The Geology of the Moon: Geochemistry and Petrology of Lunar Basalts

Thesis

NATURAL HISTORY MUSEUM

The Open University

PhD Thesis

The Geology of the Moon: Geochemistry and Petrology of Lunar Basalts

Lydia Hallis

(MSci Geology, Imperial College London)

Supervisors:
Dr Mahesh Anand (The Open University)
Prof. Sara Russell (The Natural History Museum, London)
Dr Ian Franchi (The Open University)

20/04/10

DATE OF SUBMISSION : 23 APR 2010
DATE OF AWARD : 29 JUN 2010

PAGE
NUMBERING
AS
ORIGINAL

ABSTRACT

The aim of this research is to determine any genetic relationships between high- and low-Ti lunar basalts in terms of petrology, mineralogy, geochemistry and geochronology, using a set of Apollo samples. SEM images, mineral compositions, and major- and trace-element data indicate that the high and low-Ti mare-basalts form two distinct groups, both mineralogically and chemically. Apollo 12 and 15 low-Ti basalts were produced from similar source regions, whereas the Apollo 11 and 17 basalts show greater source region compositional variation. Pb-Pb age dating of low-Ti and high-Ti samples confirm previous observations indicating the former are generally younger than the latter. Geochemical modelling suggests that the low-Ti basalts formed from < 10 % partial melting of a depleted Moon source, followed by olivine fractionation. The high-Ti basalts were probably formed as a result of < 15 % partial melting of relatively incompatible-element-enriched source regions, followed by multi-phase crystal fractionation. The REE content of Apollo 14 low-Ti, high-Al basalt 14053 can be reconstructed by ~ 10 % partial melting of a depleted Moon source, followed by olivine fractionation and 1.5 % simultaneous assimilation of a KREEPy/granitic crustal component. The REE contents of Apollo 11 high-Ti, high-K basalts match well with 10 % KREEP assimilation, along with multi-phase fractionation from a parental melt similar to Apollo 11 orange glass. Setting aside the different parental melt evolutions, bulk-rock elemental evidence clearly indicates that the high- and low-Ti mare-basalts were produced by compositionally different source regions. This conclusion is supported by different oxygen isotope compositions of the high- and low-Ti basalts. However, oxygen isotope data implies that rather than a bi-modal system, a mare-basalt compositional continuum exists. This continuum fits well with the heterogeneous cumulate source model for mare-basalt formation. Our oxygen isotope data reveal no detectable difference between the $\Delta^{17}O$ of the Earth and Moon, with implications for the viability of the giant impact origin of the Moon.

KEYWORDS: Moon, mare-basalts, mineralogy, petrology, oxygen isotopes, Giant-Impact.

STATEMENT OF ORIGINAL AUTHORSHIP

All of the research within this thesis is original, and has not been used for submission in any previous degree courses. Where the research has been submitted for publication in a scientific journal a suitable reference is made in the manuscript (Chapter 5). Where previously published research is invoked the relevant publications are referred to in the text, and listed in the reference list.

ACKNOWLEDGEMENTS

I would like to thank NASA's CAPTEM facility for the provision of Apollo samples. Mahesh Anand, Sara Russell and Ian Franchi are thanked for their supervision and guidance over the course of my research. Anton Kearsley, John Spratt, Lauren Howard, Catherine Unsworth and Stanislav Strekopytov are thanked for their help with analytical techniques at the Natural History Museum, and Sam Hammond, Nick Rogers, Richard Greenwood, and Jenny Gibson for their help with analytical techniques at the Open University. MORB sample RD32 was kindly supplied by Peter van Calsteren of the Open University. Martin Miller and Katie Joy are thanked for their statistical and mineralogical guidance, respectivley.

I would also like to thank my parents, Elizabeth and Michael Hallis, for their personal and financial support, as well as my partner, David Gent.

CONTENTS

FIGURE LIST

1. INTRODUCTION

2. METHODOLOGY

3. MINERALOGY

5. OXYGEN ISOTOPES

6. AGES OF MARE-BASALTS

7. DISSCUSSION

TABLE LIST

1. INTRODUCTION

2. METHODOLOGY

3. MINERALOGY

4. BULK CHEMISTRY

5. OXYGEN ISOTOPES

6. AGES OF MARE-BASALTS

ABREVIATIONS

$\delta^{18}O/^{17}O$: per mil (‰) variations from VSMOW.

$\Delta^{17}O$: the ordinate deviation from a reference (mass-dependent) fractionation line on the logarithmic form of the oxygen three-isotope plot.

A11, A12, etc: denotes Apollo 11, Apollo 12, etc, samples/mission.

Ab: albite feldspar.

AFC: assimilation-crystal fractionation modelling.

An: anorthite feldspar

An#: feldspar anorthite content (Ca/(Ca+Na+K))*100.

Ap: apatite.

Arm: armalcolite.

CCD: charge coupled device.

CHUR: chondritic uniform reservoir.

Cpx: clinopyroxene.

Di: diopside.

EDS: energy dispersive X-ray spectrometer.

EMP: electron microprobe.

En: enstatite.

Fa/Fay: fayalite.

Fo: forsterite.

Fs: ferrosilite.

Hd: hedenbergite.

HREE: heavy rare-earth element.

ICP-AES: inductively-coupled-plasma atomic-emission-spectrometer.

ICP-MS: inductively-coupled-plasma mass-spectrometer.

Ilm: ilmenite.

IPA: isopropyl alcohol.

JSC: Johnson Space Centre.

K-feld: potassium feldspar.

KREEP: a potassium, rare-earth element and phosphorus rich lunar lithology.

LA-ICP-MS: laser-ablation inductively-coupled-plasma mass-spectrometer.

LCROSS: Lunar Crater Observation and Sensing Satellite.

LHB: late heavy bombardment.

LMO: lunar magma ocean.

LREE: light rare-earth element.

LRO: lunar reconnaissance orbiter.

Meri: (RE)-merillite.

Meso: mesostasis.

Mg#: (Mg/(Mg+Fe))*100

MORB: mid ocean-ridge basalt.

MREE: mid rare-earth elements.

NIST: National Institute of Standards and Technology.

Ol/Olv: olivine.

Opx: orthopyroxene.

Or: orthoclase feldspar.

Phos: phosphate.

PKT: Procellarum KREEP terrain.

Plag: plagioclase feldspar.

Px: pyroxene.

Pyroxf: pyroxferroite.

REE: rare-earth element.

SC: surface contamination.

SELENE: selenological and engineering explorer.

SEM: scanning electron microscope.

SHRIMP: sensitive high-resolution ion-microprobe.

Sil: Silica.

SIMS: secondary ion mass spectrometer.

Tro: troilite.

VHK: very high potassium basalt.

VLT: very low titanium basalt.

VSMOW: vienna standard mean ocean water.

WDS: wavelength dispersive X-ray spectrometry.

Wo: wollastonite.

1. INTRODUCTION

The Earth-Moon system is unique within our solar system. The mass ratio of the system is very high (Moon/Earth = 1/81.3) - despite the Moon's relatively low density in comparison to the terrestrial planets - as is the angular momentum (Taylor et al., 2006). The Moon is virtually dry - although recent data from the LCROSS mission, along with detailed analysis of lunar apatite grains, indicate water is present on the Moon (e.g., Saal et al., 2008; Greenwood et al., 2010; McCubbin et al., 2010; Shearer et al., 2010). It is also geologically complex, and has an orbit neither within the equatorial plane nor that of the ecliptic. In contrast, Mars has two very small rocky moons believed to be captured asteroids of primitive compositions, while the outer planets' satellites consist of mostly ice-rock mixtures. Lack of atmospheric, biological, and recent wide-scale geological activity has preserved large regions of the Moon's primary crust from erosion for ~ 4.5 Ga (Hanan and Tilton, 1987), a scale of preservation not possible on our active and dynamic planet. For this reason the study of lunar samples is critical for our understanding of the Earth and Moon's formation, lunar evolution, and that of small planetary bodies in the solar system. It is also vital for the refinement of current theoretical models of the formation of the Earth-Moon system.

1.1. Origin of the Moon and its Lithologies

1.1.1. Hypotheses. The origin of the Moon has been debated for centuries. There were two main hypotheses for the origin of the Moon prior to the 1960's space race and the return of lunar rock samples to Earth. The first argued that the Moon formed along side the Earth as a sister planet (Schmidt, 1959), whereas the second suggested that at some point in the Earth's history its gravitational field captured a body formed elsewhere in the solar system (Gerstenkorn, 1955). The turning point in our understanding came in the years after six

Apollo manned missions and three Luna unmanned probes returned > 380 kg of rock and soil from the lunar surface. During 1975 and 1976, a theory evolved that combined elements of both 'classical' hypotheses and came to be known as the Giant-Impact hypothesis (Hartmann and Davis, 1975; Cameron and Ward, 1976). The Giant-Impact theory proposes that 40-50 Ma after the birth of the solar system (Asphaug and Canup, 2001; Halliday 2003, 2004), when the Earth was 70-90 % of its present mass, a Mars-sized body collided with our planet. This impact threw large amounts of material into space, forming debris rings, much like those currently visible around Saturn. Computer modelling suggests approximately 70 % of this debris originated from the impactor with only the remaining 30 % thrown out from the upper portions of the silicate Earth (Canup et al., 2004). These models also indicate that the debris accreted over a very short period, forming the lunar globe between 10 and 100 years after the impact (Thompson and Stevenson, 1988). This theory best explains the Earth-Moon system's high angular momentum, volatile element depletion, the similarities between inferred lunar and silicate Earth compositions, and lunar global geology - though some authors argue co-accretion cannot be ruled out on the basis of this evidence (Morishima and Watanabe, 2001).

1.1.2. The Lunar Magma Ocean: Anorthosite Primary Crust. The results from geophysical surveys conducted on the lunar surface by the Apollo astronauts suggested that the lunar interior is differentiated; therefore the Moon is not a primitive, undifferentiated, homogeneous body, as previously suggested (Urey, 1966). Instead it has a structure much like the terrestrial planets - with a possible core, mantle and crust (e.g., LSPET, 1969; Turkevich, 1971; Hood and Zuber, 2000). Early during the study of the Apollo 11 samples the concept of a lunar magma ocean (LMO) arose on the basis of a minority of light coloured anorthosite grains that were found within the dark grey basaltic soil present at this site (Smith et al., 1970; Wood et al., 1970a,b). Anorthosite is relatively rare on Earth, generally only forming at the top of large magma chambers as a floating 'scum' layer,

analogous to slag formed in a blast furnace. It is composed of a high percentage (generally 85-95 %) of relatively low density anorthite feldspar ($CaAl_2Si_2O_8$). Feldspar with high albite content (lower than An_{75}) is very rare because of the Moon's depletion in Na and other volatile elements (e.g., Wasson, 1971; Drake, 1986). The presence of anorthosite within Apollo 11 basaltic soil samples indicates that these grains are not native to the site, but were probably relocated as impact ejecta from the much lighter coloured lunar highlands terrain - a fact confirmed by subsequent Apollo missions and remote sensing data and sample analysis (e.g., Korotev and Gillis, 2001). The realisation that a significant proportion (~75 %) of the lunar crust is composed of anorthosite suggested a global scale compositional separation. The only way this separation could have been achieved was by deep melting to form a global magma ocean with temperatures of around 1400 °C (Warren, 1985). This melting could have been caused by energy release resulting from accretion, assisted by the heat from radioactive elements such as ^{235}U, ^{238}U, ^{232}Th and ^{40}K (Pritchard and Stevenson, 2000). As anorthite feldspar is less dense than most minerals, models suggested that it would float towards the surface of the LMO, creating a feldspathic outer crust (e.g., Warren, 1985; Wieczorek and Zuber, 2001), although more recent research has questioned the method of flotation (Elkins-Tanton et al., 2004). Estimates of magma ocean depth vary from 500 km to whole Moon melting (e.g., Ryder et al., 1991; Elkins-Tanton et al., 2002). These calculations are based on mass balance arguments concerning the abundance of plagioclase and incompatible elements within the crust, in addition to estimates of the depth of mare-basalt source regions. Hf-W and Sm-Nd isotope data suggest that the LMO crystallised 30-50 Myr after the start of the solar system (Kleine et al., 2002). However, recent data suggests that crystallisation was protracted; the last remnants of the LMO did not crystallise before ^{182}Hf became extinct at approximately 60 Ma (Touboul et al., 2007). It is believed that this global magma ocean could only have been created by the high pressures and temperatures produced during lunar accretion (Pritchard and Stevenson, 2000).

1.1.3. KREEP. As the magma ocean crystallised, a residual liquid rich in incompatible trace-elements evolved (Lucey et al., 2006). This residual melt is known as urKREEP (a primitive melt rich in potassium (K), rare earth elements and phosphorus). Although the incompatible-element concentration in each KREEPy rock may vary considerably, the ratios of these elements are always remarkably constant, no matter where the sample was collected (Warren and Wasson, 1977, 1979; Heiken et al., 1991). This implies that all KREEPy rocks crystallised from a single global source, endorsing the magma ocean theory (Shearer and Borg, 2004). It is believed that urKREEP formed after ~99 % of the magma ocean had crystallised, the remaining liquid oozed its way into the lower crust altering the original rock composition. This residual magma also contained abundant silica, FeO and incompatible heat producing elements, therefore concentrations of this material at depth could have remained molten for hundreds of millions of years (Soloman and Longhi, 1977). Although no pure urKREEP sample has ever been collected from the surface - or found on Earth as a lunar meteorite - it is believed that partial melting of lower crustal rock contaminated with urKREEP was the source for KREEP basalts, such as those returned by the Apollo 15 mission (Warren and Wasson, 1979a; Halliday, 1995). This source of trace-element rich material within the lower crust may have been assimilated into any subsequent rising melt; both Mg-suite and mare-basalt magmas were (arguably) affected (Halliday, 1995).

1.1.4. The Mg- and Alkali-suite. The lunar highlands do not consist of 100 % anorthosite, they contain a small percentage of magnesian suite lithologies with higher Mg and Fe abundances. These lithologies include dunites, troctolites, norites and gabbronorites which are younger than the anorthosite primary crust (4.43-4.17 Ga –Taylor et al., 1993). It is generally accepted that the Mg-suite plutonic rocks intruded the pre-existing LMO derived anorthositic crust to form layered intrusive complexes; possible models of formation are briefly discussed in Figure 1.1a. The even less abundant alkali-suite (Hubbard et al., 1971;

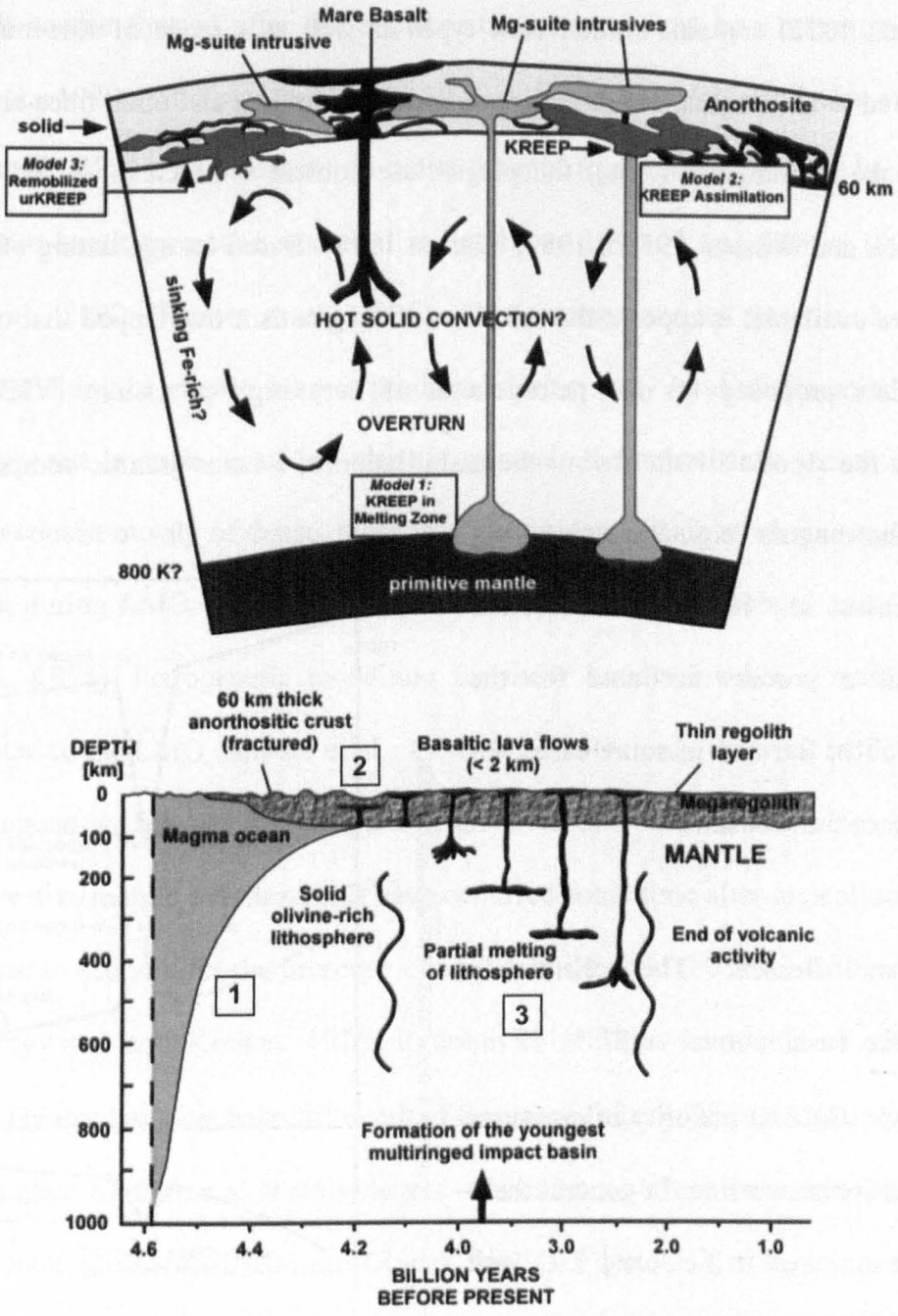

Figure 1.1: The Mg-suite and lunar magma ocean evolution. **a)** Schematic cross section through the magma ocean to ~800 km depth. The anorthosite crust forms to ~ 60 km depth from buoyant plagioclase cumulates. Three models are shown for the origin of the Mg-suite rocks, model 1 shows KREEP delivered to depth by convective overturn and mixing with Mg-rich ultramafic cumulates. Model 2 is similar but KREEP is assimilated at the base of the crust and model 3 involves mobilization of urKREEP caused by decompressional melting, triggered by basin-forming impact events (after Papike et al., 1998). **b)** Evolution of the lunar magma ocean, crust and mantle as a function of time. This simplified geological cross section shows (1) the evolution of the magma ocean to give anorthosite primary crust, olivine rich lithosphere and KREEP residual magma (2) emplacement of igneous plutons (e.g. Mg-suite) and (3) the later partial melting of the mantle and the formation of mare basaltic lavas. Timescale not linear, after Stöffler and Ryder (2001).

Brown et al., 1972) contains similar rock types as well as a range of siliceous plutonic rocks referred to as granites. These rocks are enriched in alkali and other trace elements, in relation to the anorthosites (An_{96}) the plagioclase content is much more sodic ($An_{82\pm8}$) (e.g., Warren and Wasson 1979b, 1980; Warren 1993). Based on age dating of the small sample suite available, it appears that alkali-suite magmatism overlapped that of the Mg-suite. Models proposed for the petrogenesis of very high potassium (VHK) basalts collected at the Apollo 14 site favour the assimilation of a lunar granitic component by a high-alumina magma (e.g., Shervais et al., 1985b; Neal et al., 1989a,b), see section 1.2.5. Such a process accounts for the elevated K, Rb, Ba, and in some cases, Hf abundances of these basalts.

1.1.5. Mare Basalts. The chemically diverse mare basalts cover ~ 17 % of the lunar surface, the vast majority of eruptions were on the lunar nearside. In general these basalts are enriched in FeO and TiO_2 and depleted in Al_2O_3 and CaO. They also have higher CaO/Al_2O_3 ratios than lunar highland lithologies (Heiken et al., 1991). These chemical differences are reflected in mineralogy; the mare basalts are enriched in pyroxenes and depleted in plagioclase relative to the highland anorthosites (e.g., Taylor, 1982). The depletion of strontium (Sr) and europium (Eu^{2+}), both of which preferentially enter plagioclase during magma crystallisation (Figure 1.2), suggest the

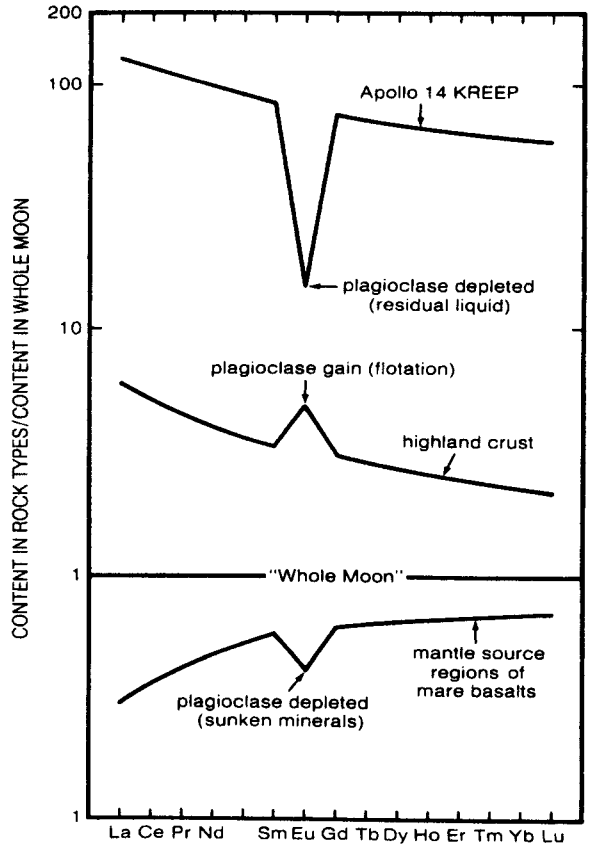

Figure 1.2: REE concentrations and europium anomalies in the plagioclase-rich lunar crust, mare-basalt source regions and KREEP basalts from the Apollo 14 site. The europium anomalies are a result of the accumulation or removal of Eu-enriched plagioclase (after S.R, Taylor, 1982).

mare-basalt source formed after the anorthositic primary crust had begun to crystallise (Wood et al., 1970a; Hubbard and Gast, 1971; Urey et al., 1971; Helmke et al., 1973; Vaniman et al., 1991). Experiments on melts thought to represent primary lunar magmas indicate mare-basalt formation occurred at depths of 100-300 km (Ryder 1991; Elkins-Tanton et al., 2002; Shearer et al., 2006). The common model for mare-basalt origin involves re-melting of mantle sources produced during early lunar differentiation. Just as the primary crust is made up of low density minerals the mare-basalt source regions are believed to consist mostly of dense, more iron rich minerals such as olivine and pyroxene, which sank during LMO crystallisation (Wood et al., 1970a,b; Hubbard and Gast, 1971; Urey et al., 1971). Petrogenetic modelling for these basalts invokes a mafic cumulate source related to the LMO (Snyder et al., 1992). This is the only unifying model for mare-basalt petrogenesis, but the details are still under debate. Most authors now agree that major convective mantle overturn must have occurred some time after crystallisation of the primary crust to account for the presence of abundant ilmenite ($FeTiO_3$) within some mare basalts (Ringwood and Kesson, 1976; Ryder, 1991; Elkins-Tanton et al., 2002). This overturn is believed to have been the result of late stage (after > 95 % LMO crystallisation) Ti-rich cumulate formation at shallow levels - ilmenite could not have crystallised on the Moon at depths greater than 100 km (Ryder, 1991 – Figure 1.3). The presence of these dense Ti-rich layers above less dense olivine and pyroxene cumulates is thought to have produced a wide scale density instability, resulting in mantle overturn via diapiric redistribution. This overturn model is also supported by the presence of strong negative Ti and Ta-Nb anomalies in mare-basalts and KREEP (Ta and Nb are assumed to partition similarly), resulting from the fact that Nb is nearly neutral and Ti strongly compatible during the crystallisation of ilmenite (McCallum and Charette, 1978). As might be expected, the elemental abundance trends of high-Ti Apollo 17 basalts shows positive Ta-Nb and Ti anomalies, indicating accumulation of ilmenite in the source region. Surprisingly, the low-Ti Apollo 15 basalts also show definite relative excesses of Ta-Nb

and Ti, indicating ilmenite accumulation. Thus the large range of TiO_2 in mare volcanics is apparently the result of a nearly continuous variation in the amount of ilmenite in the source region. Simple re-melting of static cumulates (e.g., Taylor and Jakes, 1974) does not account for this variation. A dynamic process in which high-level late stage ilmenite (± augite) cumulates sink into a less dense, less differentiated interior is required (Kesson and Ringwood, 1976). Incomplete mixing of these ilmenite cumulates at mare-basalt source region depths may explain the differing ilmenite contents within mare-basalts at the surface.

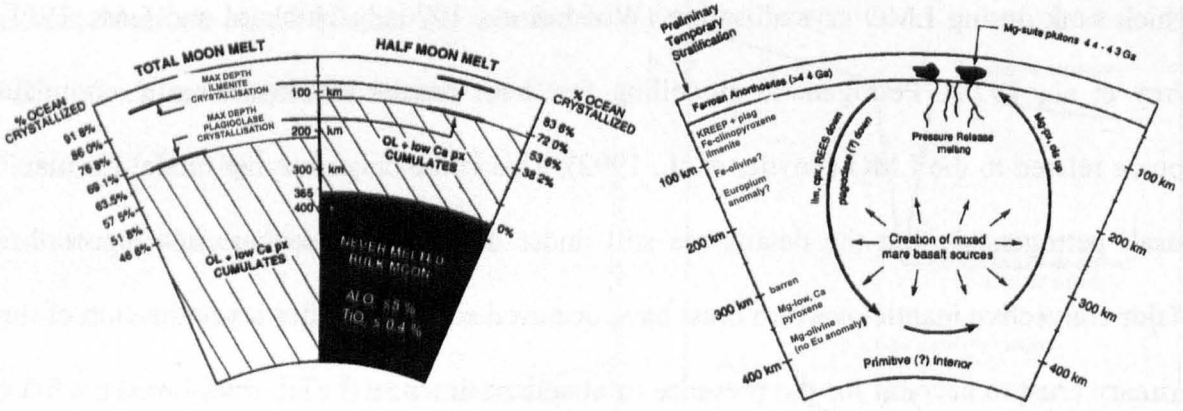

Figure 1.3: The lunar interior and cumulate mantle overturn. **a)** A model for the original stratification of a crystallised magma ocean, showing the deepest appearances of plagioclase and ilmenite during crystallisation (after Ryder et al., 1991). The left side of the figure assumes whole Moon melting while the right side assumes an ocean originally only half the depth of the Moon. **b)** A schematic view of the mainly solid-state overturning of gravitationally unstable hot lunar mantle immediately following magma ocean crystallisation, major chemical effects are shown (after Ryder et al., 1991). Mechanical mixing creates complicated mare-basalt sources for later melting; the pressure release of upwelling magnesian olivine-dominated material causes immediate melting to produce ultramafic magmas that are intruded into and assimilate the crust (the Mg-suite plutons).

Most of the melts produced in this way began to crystallise (and so fractionate) before reaching the surface, and some assimilated materials from surrounding rocks. For example, urKREEP and Mg-suite granite assimilation (section 1.1.5) is thought to have produced the KREEP basalts and a number of the high-K mare-basalts, respectively (Neal and Taylor,

1992 and references therein). Currently the oldest known mare-basalt is Kalahari 009, a basaltic meteorite believed to be a sample of crypto-mare (mare-basalt flows later covered with younger regolith). U-Pb, Sm-Nd, and Lu-Hf dating suggest this basalt crystallised at 4.35 Ga (Schultz et al., 2007; Terada et al., 2007; Sokol et al., 2008). From remote sensing data, large scale extrusion of basaltic lava on the Moon is known to have occurred at 3.9 Ga while the lunar surface was enduring the late heavy bombardment. Proof of this can be seen in a number of large, late craters, where mare basalts have flooded the crater floor (Heiken et al, 1991, Bugiolacchi, 2006). After the cessation of bombardment there followed a period of mare-basalt eruption (approximately 1 billion years); from ~2.9 Ga to the present day there appears to have been little volcanic activity on the surface, excepting areas of the Procellarum basin where basalts are thought to have erupted as recently as 1.2 Ga (Hiesinger et al., 2003).

1.1.6. Other Volcanic Products. A minority of mare-magmas on the Moon contained large amounts of gas (probably CO_2 and CO) which was explosively released when they welled up close to the surface (e.g., Nicholis and Rutherford, 2005, 2009; Heiken and McKay, 1977, 1978; Gaddis et al., 1999). When these magmas reached the surface they erupted from volcanic vents in a fountain of molten droplets, much like the lava fountains found at terrestrial basaltic volcanoes (e.g., Mauna Loa, Hawaii). These sub-millimetre droplets fell to the ground as glass beads of various compositions and colours (e.g., Coombs, 1992). This type of pyroclastic deposit was discovered at the Apollo 11, 15 and 17 sites in association with mare-basalt vents. Glass beads were also discovered in lunar soils collected by the Luna landers - the low gravity and near perfect vacuum conditions on the Moon allowed droplets to spread over a wide area. More recently remote sensing studies have uncovered nearly 100 pyroclastic deposits (Gaddis et al., 1985, 1999). They are commonly dark and smooth-surfaced, observed in association with sinuous rills, irregular depressions, or endogenic craters within the highlands. They can also be found on the

floors of old impact craters situated along the margins of many of the major mare-basalt filled impact basins on the lunar near side. A small number of pyroclastic deposits are visible on the lunar far-side; examples are found in the floor of Schrodinger Crater (Shoemaker et al., 1994) and in the Apollo Basin (Robinson et al., 1996). However, the two best studied deposits are the green glasses of Apollo 15 and the orange soils (made up mostly of glass and ash) of Apollo 17. The latter were comprised of > 90 % glass beads with an average size of 44 μm at the Shorty crater site. Below the orange soil lay a darker layer containing skeletal olivine and ilmenite crystals, suggesting it cooled at a slightly slower rate (Schmitt, 1989; Taylor, 1989). Apollo 15 green glasses alone can be separated into five distinct chemical groups, implying at least five separate magmas erupted at this site, giving an indication of the complex nature of lunar volcanism (Delano, 1979).

1.2. Lunar Regolith and Breccias

Impacts are the most important metamorphic process on the Moon because they alter the texture of rocks and produce new ones such as glasses, impact melts and fragmental rocks known as breccias. Because of the extreme old age of the lunar surface (especially the anorthositic primary crust in the highlands) numerous large impacts and countless smaller ones have caused shattering, burial, exhumation and transportation of individual particles in a random fashion. Intense impact activity during late heavy bombardment (LHB) ensured that the crust was shattered and fragmented down to depths of several kilometres, producing a global layer of impact debris or megaregolith (e.g., Short and Forman, 1972; Toksöz et al., 1973; Hörz et al., 1977; Cashore and Woronow, 1985). Additional fracturing of in-situ crust is believed to stretch down to 25 km (Hörz et al., 1991). Over geologic time as the inner solar system became less turbulent the frequency of large impacts decreased. Smaller impacts therefore became the main source of lunar erosion, resulting in an accumulated fine-grained powdery layer above the megaregolith known as the regolith (Figure 1.4). The composition of the regolith is largely controlled by the underlying

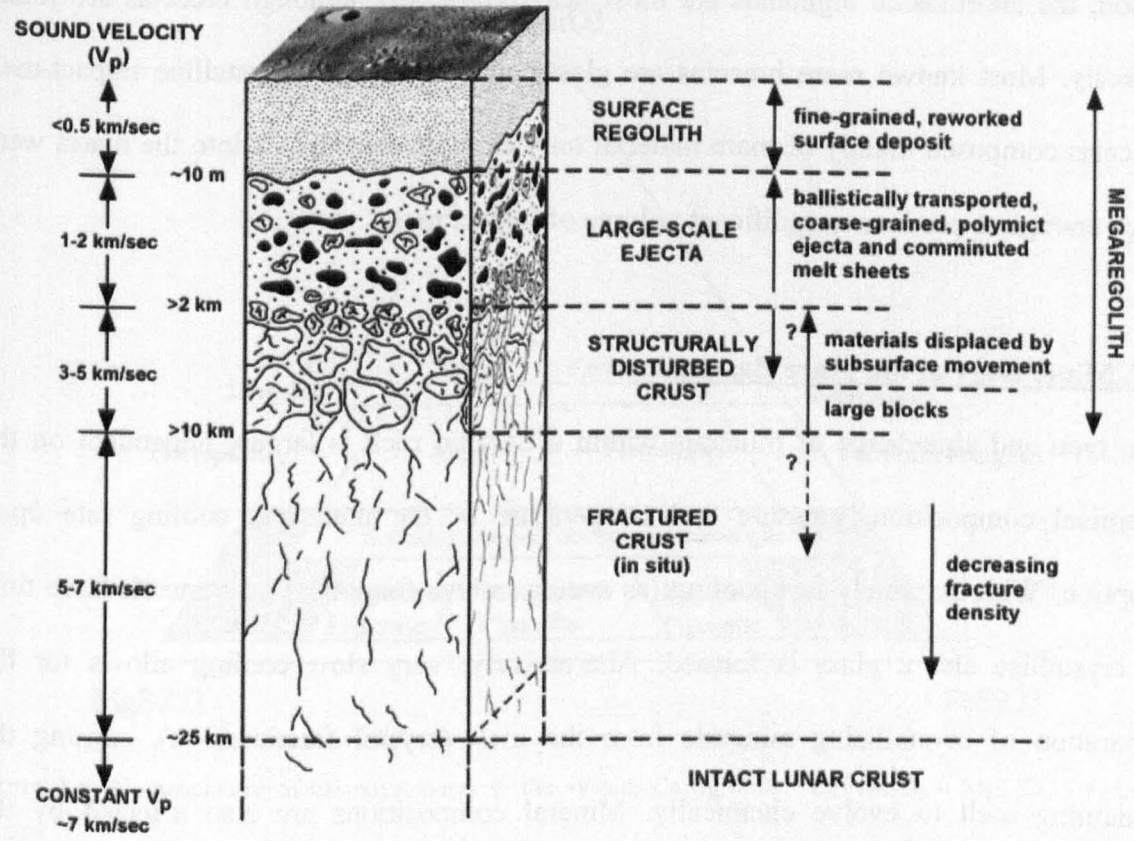

Figure 1.4: Regolith structure. Depth values are uncertain as they vary from region to region (after Hörz et al., 1991).

'bedrock' (which may itself be megaregolith). Regolith samples from the Apollo sites show only narrow compositional variation (e.g., Rhodes et al., 1977; Hörz, 1978), therefore we can be relatively confident that any sample collected from the surface relates to the local geology, unless its age and composition suggest otherwise. Breccias on the Moon are formed when disaggregated or melted materials from older rocks (the result of meteorite impacts) are bound together to form a new rock. These materials can exist as mineral and lithic fragments, and crystallised or glassy impact melt (Lucey et al., 2006). Large fragments are known as clasts and the material binding the clasts is known as matrix. Breccias are lithified by heat and shock from meteorite impacts. Most lunar breccias are polymict, meaning they contain material from various rocks, but some may be dimict (two source rocks) or even monomict (one source rock). As breccia formation is dependent on meteorite impacts, the older a surface the more brecciated it will become. Therefore, on the

Moon, the anorthositic highlands are most heavily affected, although breccias are found globally. Most known mare breccias are glassy; it is likely that crystalline impact-melt breccias composed mainly of mare material only exist where impacts into the maria were large enough to produce a significant volume of impact melt.

1.3. Mineralogy of the Mare Basalts

The type and abundance of minerals within a basaltic rock is largely dependent on the chemical composition, pressure and temperature of the melt and cooling rate upon eruption. With extremely fast cooling (as occurs in lava fountains) no minerals have time to crystallise and a glass is formed. Alternatively, very slow cooling allows for the separation of crystallising minerals from the melt (crystal fractionation), causing the remaining melt to evolve chemically. Mineral compositions are also affected by the crystallisation sequence, which is dependent on the melt composition, cooling rate and extent of crystal fractionation. As the melt composition is generally controlled by the source, a number of key parameters can be determined if the composition of this source is known. Temperature and pressure of the source region (giving the depth of melt generation) are the most useful parameters that can be calculated in this way, but cooling rate and the partial pressures of certain volatile gases can also be determined. Minerals containing water (such as amphiboles and micas) as well as those containing oxidised iron (Fe^{3+} rather than Fe^{2+}) are largely absent on the Moon. The four major phases within mare-basalts are pyroxene, plagioclase feldspar, olivine and metal oxides (ilmenite, armalcolite and spinel). Other minor minerals formed towards the end of crystallisation, including silica (cristobalite or tridymite polymorphs), potassium feldspar, zircon and other Zr-bearing silicates, tranquillityite, phosphates (apatite and whitlockite), metallic iron and iron sulphide (troilite). Small amounts of late-stage glass may also be preserved. These lunar minerals are described in detail below.

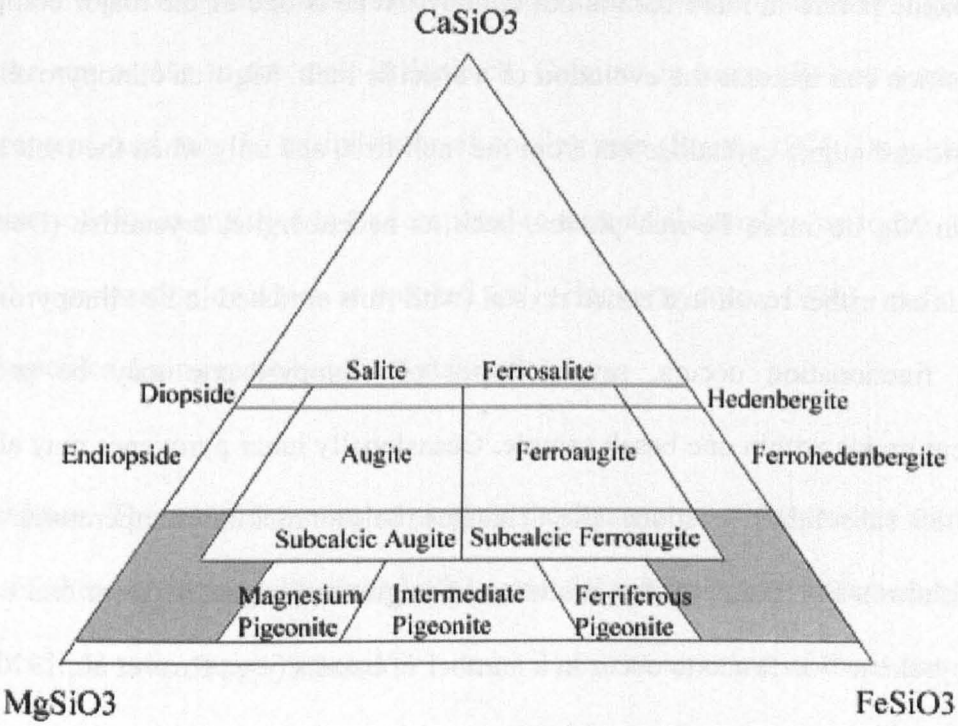

Figure 1.5: Nomenclature of clinopyroxenes in the system $CaMgSi_2O_6$ - $CaFeSi_2O_6$ – $MgSiO_3$ – $FeSiO_3$ (Poldervaart and Hess, 1951).

1.3.1. Pyroxene. The pyroxene group includes both orthorhombic and monoclinic minerals (orthopyroxene and clinopyroxene, respectively). While the orthopyroxene sub-group consists largely of the compositional series $MgSiO_3$-$FeSiO_3$ the clinopyroxenes can have a wide range of chemical compositions. However, the latter can be roughly considered as members of the four-component system $CaMgSi_2O_6$-$CaFeSi_2O_6$-$MgSiO_3$-$FeSiO_3$ (Poldervaart and Hess, 1951) (Figure 1.5). In the pyroxene structure, the M1 and M2 sites provide a range of site volumes, and the general formula can be expressed as:

$$X_{1-p}\,Y_{1+p}\,Z_2O_6 \qquad (1)$$

Where: X = Ca, Na; Y = Mg, Fe^{+2}, Mn, Li, Ni, Al, Fe^{+3}, Cr, Ti; and Z = Si, Al

In the orthopyroxene series $p \approx 1$ and the content of trivalent ions is small. In clinopyroxenes, the value of p varies from zero to one (Deer et al., 1966; Papike, 1987).

Orthopyroxene is rare in mare basalts but clinopyroxene is one of the major components; its composition can indicate the evolution of a specific melt. Mg-rich clinopyroxenes such as pigeonite and augite crystallise out from the melt first, and only when the melt becomes depleted in Mg do more Fe-rich phases, such as hedenbergite, crystallise (Deer et al., 1966). This can either result in a zoned crystal (with rims enriched in Fe-clinopyroxene), or if crystal fractionation occurs, several types of clinopyroxene may be present as independent grains within one basalt sample. Occasionally lunar pyroxenes may also show evidence of subsolidus reactions (i.e. changes below melting temperature, such as recrystallisation). For example, the exolution of augite and pigeonite from one originally uniform pyroxene was found to occur in a number of basalts (e.g., Ross et al., 1970; Papike et al., 1971; Takeda et al., 1975). Cooling rates have been calculated from exolution lamellae in lunar clinopyroxenes, with results ranging from 1.5-0.2 °C/hr for lava flows 6 m thick at the Apollo 15 site (Takeda et al., 1975). One of the major differences between lunar and terrestrial pyroxenes is the lack of Fe^{3+} in the former, reflecting the Moon's reducing environment. The most abundant basalts on Earth are the mid ocean ridge basalts (MORB), which are Mg-rich compared to mare basalts, indicating the mare source regions are relatively Fe-rich. Ionic substitutions also vary between these two groups; in terrestrial pyroxenes the most important substituting elements are Fe^{3+} + Al and Ti^{4+} + 2Al (Papike and Bence, 1978), whereas the most important ionic substitutions in lunar pyroxenes are Ti^{4+} + 2Al, Cr^{3+} + Al and Al (octahedral) + Al (tetrahedral). This variation is because of the absence of significant Fe^{3+} on the Moon.

1.3.2. Olivine. The chemical formula for olivine is $(MgFe)_2SiO_4$, where fayalite is the Fe-rich end member and forsterite is the Mg-rich end member. Although there is significant Fe-Mg variation in both groups of olivine, lunar olivines commonly have very high Fe contents (Fa_{80-100}) and even the most Mg-rich (Fa_{20}) are depleted in magnesium compared to Mg-rich terrestrial olivines. This again reflects the Moon's enrichment in Fe relative to

the Earth. As with clinopyroxenes, the Fe content of an olivine crystal will often increase towards the rim as Mg in the melt is depleted. Calcium in lunar olivines varies directly with Fe content, and may be an indicator of cooling rate (Smith, 1974; Donaldson et al., 1975). Lunar olivine is enriched in Cr compared to terrestrial samples (up to 0.6 wt % vs. ~ 0.1 wt %), a proportion of which is reduced Cr^{2+} (Haggerty et al., 1970) - indicating low oxygen fugacities during mare-basalt crystallisation.

*1.3.3. **Feldspar.*** The most common mineral in the lunar crust, feldspar has a framework structure of three-dimensionally linked SiO_4 and AlO_4 tetrahedra (reviewed by Papike, 1988). The Si:Al ratio varies between 3:1 and 1:1, so the ordering of these two elements can lead to discontinuities in the crystal lattice. Within this framework of tetrahedra much larger cations such as Ca, Na, K, Fe, Mg and Ba can be accommodated. A solid solution series exists for feldspars between the end members albite ($NaAlSi_3O_8$) and anorthite ($CaAl_2Si_2O_8$) with some substitution by potassium to create orthoclase feldspar (Figure 1.6). Lunar plagioclase feldspars are mostly > 90 % anorthite, as the Moon is depleted in alkali elements relative to the Earth (Lucey et al., 2006). Rare orthoclase feldspars formed in residual melts on the Moon and consequently are relatively enriched in other incompatible elements, for example Ba can be present in these grains in concentrations >10 wt %. Orthoclase feldspar is found in relatively high abundances in the KREEP basalts (e.g., Steele et al., 1972) and often within the mesostasis of mare basalts (e.g., Keil et al., 1971).

*1.3.4. **Ilmenite.*** The most abundant oxide mineral in lunar rocks, ilmenite ($FeTiO_3$) makes up 15-20 vol % of the high-Ti mare basalts, although these figures vary at different sites (Neal and Taylor, 1992). As would be expected, the higher the TiO_2 content of the magma from which the lunar rock crystallised, the higher the ilmenite content. Its structure is hexagonal and consists of alternating layers of Ti- and Fe-containing octahedra (Deer et

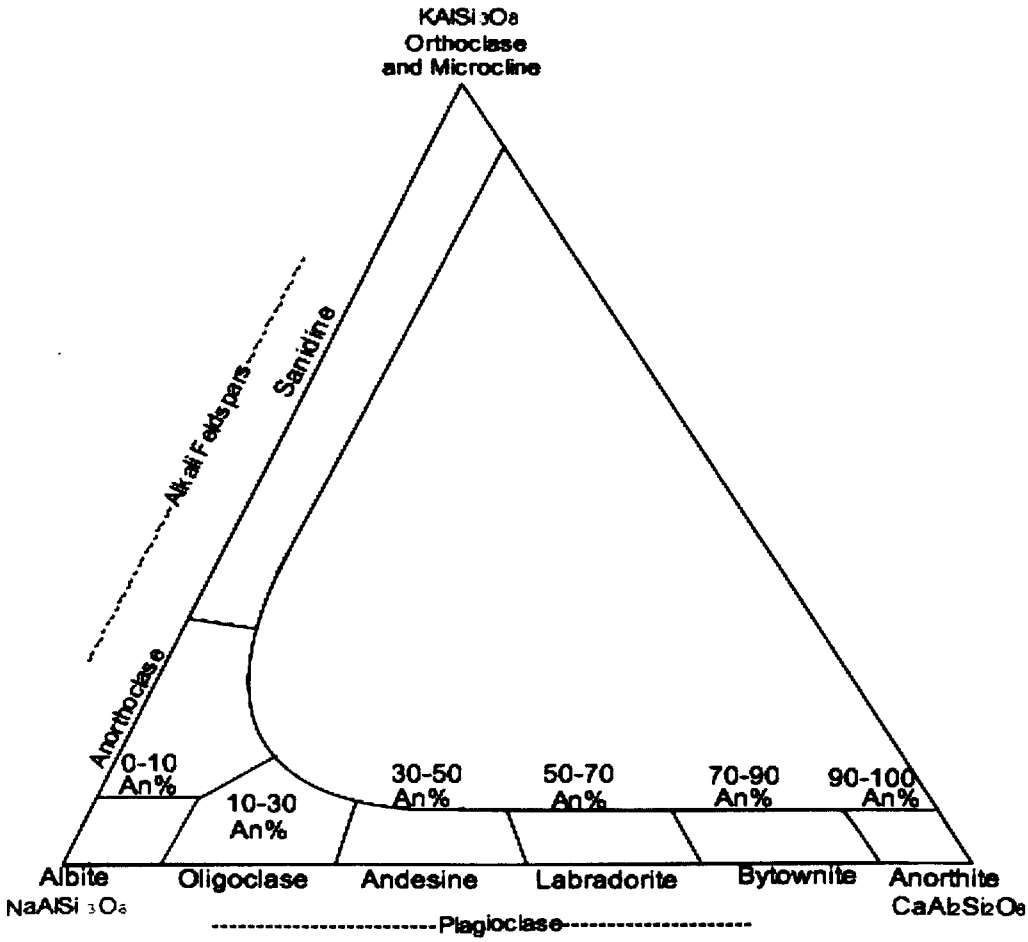

Figure 1.6: Feldspar ternary diagram showing the solid solution between anorthite - albite - orthoclase. Note that in terrestrial samples a solid solution between anorthite and orthoclase is not possible but rare lunar feldspars do plot within this forbidden compositional zone. After Deer et al. (1966).

al., 1966). Most lunar ilmenite contains magnesium as a result of the solid solution that exists between ilmenite and geikielite ($MgTiO_3$) – a mineral not present on the Moon in its pure form. Therefore, compositions of lunar ilmenites plot between $FeTiO_3$ and $MgTiO_3$ - variation from $FeTiO_3$ is expressed as wt % MgO. MgO contents within ilmenite can range from 0.3-6 wt % (El Gorsey et al., 1971b). In general, ilmenite composition reflects the magmatic chemistry of the source region - ilmenites with the highest Mg contents are those from sources rich in Mg. Other minor elements within ilmenite include Mn, Cr, Al and V; these are partitioned between co-existing ilmenite and spinel phases. In addition, ZrO_2 has been reported within ilmenites from Apollo 14 and 15 (El Goresy et al., 1971a,b: Taylor et al., 1973), and partitioning of ZrO_2 between ilmenite and ulvöspinel (Fe_2TiO_4) has been

used both as a geothermometer and a cooling-rate indicator (Taylor et al., 1975). In Apollo 17 samples, ilmenite is closely associated with armalcolite ($(Fe_{0.5}Mg_{0.5})Ti_2O_5$), where it occurs as mantles on armalcolite crystals. This is probably because of the reaction of the earlier-forming armalcolite with melt during crystallisation (Haggerty, 1973; Williams and Taylor, 1974).

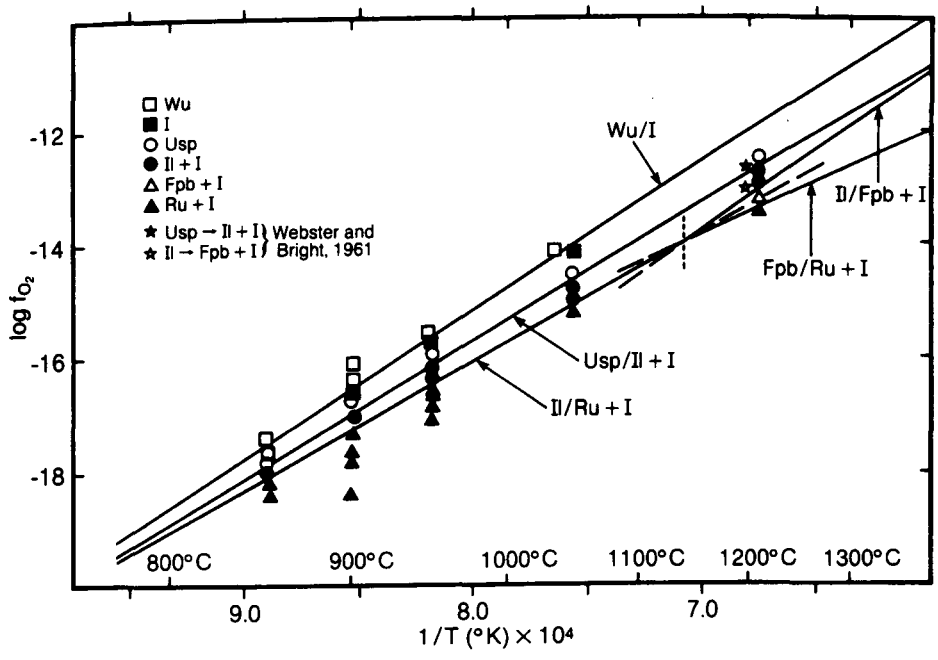

Figure 1.7: Stability relations of several Fe- and Ti-bearing minerals shown as a function of oxygen fugacity (fO_2) and temperature (T). Abbreviations: Wu = Wüstite; I = iron; Usp = ulvöspinel; Il = ilmenite; Fpb = ferropsuedobrookite; Ru = rutile. Adapted from Taylor and McCallister (1972). The Il/Ru+I and Usp/Il+I represent the separate nature of the ilmenite and ulvöspinel stability curves.

Ilmenite is commonly associated with ulvöspinel, a high-Ti spinel (section 1.3.5). Analysis of the two mineral's stability curves (Figure 1.7) for temperature and oxygen fugacity (fO_2) reveals that they are significantly different, hence these minerals did not co-crystallise in lunar samples (Taylor et al., 1973). The data suggest that in these mineral assemblages ilmenite is formed by solid-state reduction of ulvöspinel at temperatures below the melting point. In rare cases there is also evidence for the subsolidus reduction of ilmenite to rutile (TiO_2) and native Fe, or to chromite ($FeCr_2O_4$) + rutile + native Fe. In going from reduced

to oxidising conditions at temperatures below 1150 °C, the reaction sequence is rutile + iron + oxygen = ilmenite; ilmenite + iron + oxygen = ulvöspinel; and iron + oxygen = wüstite (FeO). At higher temperatures the mineral ferropseudobrookite ($FeTi_2O_5$) appears in the sequence. (Heiken et al., 1991).

1.3.5. Spinel. This group of oxides is the second most abundant in lunar samples; a number of Apollo 12 and 15 basalts contain up to 10 vol % spinel (Lucey et al., 2006). The general structural formula is $^{IV}A^{VI}B_2O_4$ where IV and VI refer to tetrahedral and octahedral polyhedra of oxygen atoms. In a normal spinel structure the divalent cation (e.g., Fe^{2+}) occupies only the tetrahedral sites, and the two sites each contain only one type of cation (e.g., $FeCr_2O_4$) (Deer et al., 1966). In lunar spinels, the divalent cations (usually Fe^{2+} or Mg^{2+}) occupy site A and the higher charge cations (such as Cr^{3+}, Al^{3+} and Ti^{4+}) occupy site B. Other cations commonly present include V, Mn and Zr (Haggerty, 1972).

An inverse spinel is created when the divalent cation also occupies half the B sites (e.g., $Fe(Fe,Ti)_2O_4$). The Johnston compositional prism (Figure 1.8) shows all the members of the spinel group, end members include chromite ($FeCr_2O_4$), ulvöspinel (Fe_2TiO_4), hercynite ($FeAl_2O_4$) and spinel ($MgAl_2O_4$). Most lunar spinels have a composition that can be represented within the three component system $FeCr_2O_4$ – Fe_2TiO_4 – $FeAl_2O_4$, so it is possible to represent them in a two dimensional trigonal plot with most points falling between chromite and ulvöspinel. In lunar samples, chromite was the first to crystallise from the melt. As the residual liquid became depleted in Al_2O_3, MgO and Cr_2O_3, later spinels, or spinel rims, became enriched in TiO_2 and FeO causing the overall composition to move towards ulvöspinel (Papike et al., 1998). In most basalt samples containing chromites and chromian ulvöspinels, the latter phase occurs as overgrowths around chromite cores. Contact between these two phases is often sharp, indicating a cessation in

growth before ulvöspinel crystallisation. However, a minority of lunar rocks (e.g., Apollo 12 basalt sample 12018) contain spinels with a gradational boundary between the two

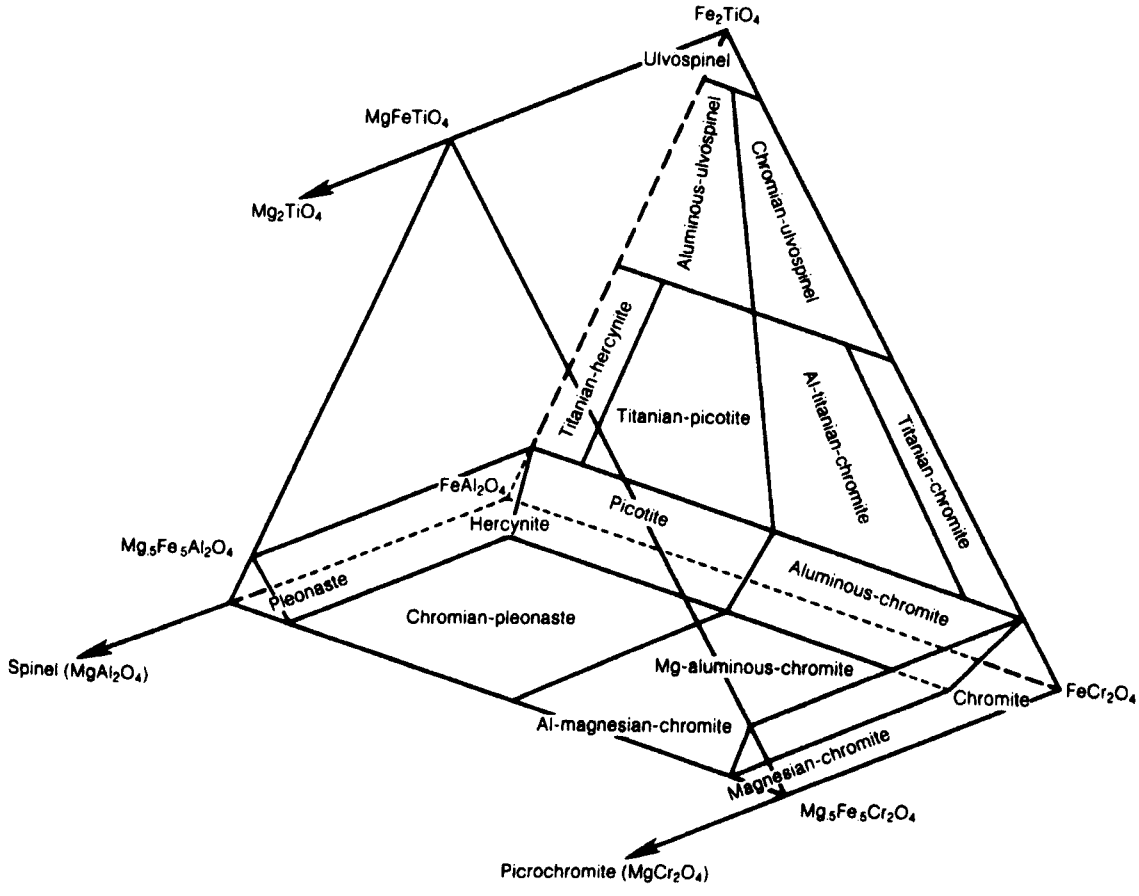

Figure 1.8: Modified Johnston prism showing the chemical varieties of spinel. End members are chromite $(FeCr_2)_4$, ulvospinel Fe_2TiO_4 and hercynite $FeAl_2O_4$. After Haggerty (1972).

growth phases, indicating continuous growth or later re-equilibration by solid state diffusion within the crystal. As discussed in section 1.3.4 ulvöspinel may be reduced to ilmenite and native iron once the rock has crystallised. This late subsolidus reduction enriches the spinel with residual components and its composition moves back towards chromite (Haggerty, 1978).

*1.3.6. **Armalcolite.*** This rare oxide is named after the three Apollo 11 astronauts (Armstrong, Aldrin and Collins) as it was first discovered in Ti-rich basalts from this site. Its chemical formula is $(Fe_{0.5}Mg_{0.5})Ti_2O_5$, but the armalcolite name is used to describe any

solid solution that has a composition varying between $FeTi_2O_5$ and $MgTi_2O_5$ (Lucey et al., 2006). The crystal structure is similar to that of ferropseudobrookite, but a significant amount of Ti is present as Ti^{3+} rather than Ti^{4+} (Wechsler et al., 1976) because of the reducing conditions at the lunar surface. Armalcolite is restricted to rocks that have a high-Ti content and have cooled rapidly, (e.g., a number of Apollo 17 mare basalts).

1.3.7. Other Oxides. The only other oxides of significant abundance are rutile (TiO_2), tranquillityite ($Fe_8(Zr,Y)_2Ti_3Si_3O_{24}$), zirconolite $(Ca,Fe)(Zr,REE)(Ti,Nb)_2O_7$ and baddeleyite (ZrO_2). Rutile is generally associated with ilmenite and/or armalcolite as it is a reduction product of these oxides. Less common grains of primary rutile are also associated with ilmenite; these euhedral grains often contain Nb, Cr, Ta and REE (Marvin, 1971). Baddeleyite is common in certain Apollo 14 clast-poor impact-melt rocks, where it is associated with schreibersite ($(Fe,Ni,Co)_3P$) (El Goresy et al., 1971a). It is believed that these two minerals are the result of meteoritic contamination incorporated into the original melt by large impact events. Tranquillityite is only known to occur on the Moon, it was first discovered in Apollo 11 mare basalts from the Tranquillity Basin, formed as a result of the high-Ti content of these basalts. Altogether oxides can make up as much as 20 % vol of the high-Ti mare basalts (Neal and Taylor, 1992).

1.3.8. Sulphides. As low oxygen fugacities on the Moon do not permit the formation of sulphates (SO_4^{2-}) all sulphur is present as sulphide minerals. Troilite (FeS) is the most common lunar sulphide - although it never forms more than 1 vol % it is ubiquitous in lunar rocks and is commonly associated with native iron, ilmenite and spinels (Papike et al., 1998). Oxygen fugacity is a measure of the amount of oxygen in a reservoir available to react (similar to partial pressure), and is often represented as $\text{Log } fO_2$ (Wieczorek et al., 2006). The presence of metallic iron and troilite (FeS) in mare basalts indicates that they crystallised at oxygen fugacities below the iron-wüstite (Fe-FeO) buffer (El Goresy et al.,

1972) (Figure 1.9). This observation is further supported by the presence of Ti and Cr in reduced valence states and the absence of Fe^{3+}. The range of temperature and fO_2 for mare-basalt crystallisation is relatively small, varying from 10^{-13} at 1200 °C to 10^{-16} at 1000 °C (Wellman, 1970; Sato and Helz, 1971; Sato et al., 1973). It is currently unclear whether these reducing conditions reflect reducing crustal and mantle environments or reduction processes during magma transport and eruption, though most researchers seem to favour the former (Delano, 1990; Fogel and Rutherford, 1995; Weitz et al., 1997).

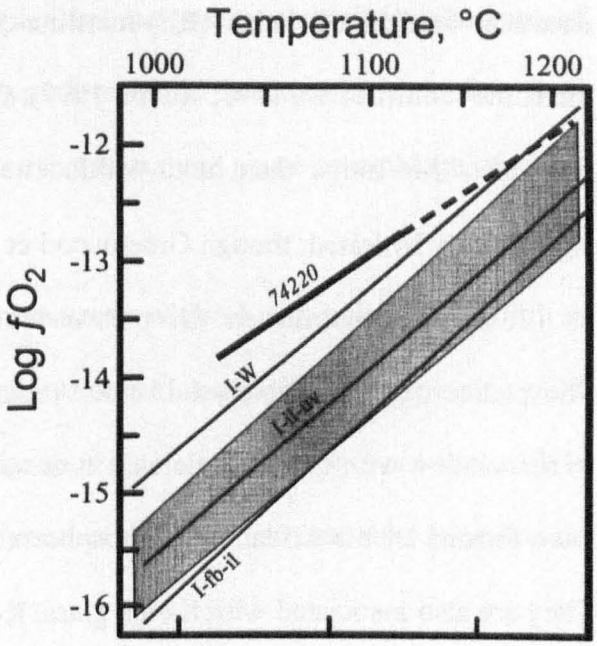

Figure 1.9: Oxygen fugacity as a function of temperature for several buffers relevant to the lunar interior. These include iron-wüstite (I-W), iron-ilmenite-ulvöspinel (I-il-uv) and iron-ferrobustamite-ilmenite (I-fb-il). Patterned region represents the range of fO_2 corresponding to the crystallisation of mare basalts. 74220 = Apollo 17 orange glass (adapted from Wieczorek et al., 2006).

Troilite is almost always a late-stage crystallisation product in mare basalts, but secondary troilite may form in solid rocks. Other sulphides present in lunar rocks (though too rare to be of much geologic significance) are chalcopyrite ($CuFeS_2$), cubanite ($CuFe_2S_3$), pentlandite ($(Fe,Ni)_9S_8$), mackinawite ($Fe_{1+x}S$) and sphalerite ((ZnFe)S) (Taylor and Williams, 1973).

1.3.9. Phosphates. Of the ~ 0.5 wt % P_2O_5 that lunar basalts contain most is locked into the minerals (RE)-merillite ($Ca_{16}(REE)_2(Mg,Fe)_2(PO_4)_{14}$) and apatite ($Ca_5(PO_4)_3(OH,F,Cl)$) (e.g., Friel and Goldstein, 1977). Lunar (RE)-merillite is similar to terrestrial whitlockite, but contains a greater amount of REE and Y (Albee and Chodos, 1970). Structural and

chemical studies of lunar (RE)-merillite indicate a close affiliation with meteoritic merrillite (Jolliff et al., 1993; Rubin, 1997), which is why it is now referred to as rare earth (RE)-merrillite rather than lunar-whitlockite. Lunar apatite is commonly F-rich and not significantly hydrated, though Greenwood et al. (2010), Liu et al. (2010) and McCullum et al. (2010) have confirmed the presence of small amounts of water in lunar apatite. Phosphates are late-stage crystallisation products in mare basalts and are sometimes found in association with metal particles - in these cases it is believed that the phosphates may have formed by the oxidation of phosphorous from the metal (Friel and Goldstein, 1977). They are also associated with K-rich glass, K-feldspar and silica in the mesostasis.

1.3.10. Silica. All three polymorphs of silica exist in lunar rocks, the high temperature phase cristobalite, the high pressure phase tridymite and the low temperature, low pressure phase quartz. Mare basalts mostly contain trydimite and cristobalite and these can be distinguished by their textures and habits. Cristobalite in mare basalts is present as anhedral masses containing conchoidal fractures. These fractures are caused by cooling - as temperature decreases, cristobalite becomes unstable and converts to tridymite, shrinking slightly in the process (Dence et al., 1970; Champness et al., 1971). Cristobalite is a late-stage mineral within these basalts whereas tridymite forms early in the crystallisation sequence, producing elongated laths (Klein et al., 1971). It is not possible to determine whether the cristobalite grains present in lunar samples have completely converted to tridymite without analysing the crystal structure of each grain (e.g., using Raman spectroscopy). As this type of analysis is beyond the scope of this study, our mineralogical analysis groups these phases together as silica.

1.3.11. Pyroxferroite. This mineral is a pyroxenoid with the chemical formula $Ca_{1/7}Fe_{6/7}SiO_3$. The high Fe content of pyroxferroite means it plots within the forbidden region near the Fe-apex of the pyroxene quadrilateral (Figure 1.5). Pyroxenes with Fe

content this high cannot exist in terrestrial samples, but are present on the Moon because of the low oxygen fugacity (section 1.3.8). Pyroxferroite is metastable, therefore it is commonly found alongside its break down components; a three phase assemblage of silica, Ca-Fe pyroxene (hedenbergite) and fayalite.

1.3.12. FeNi Metal. Native iron metal occurs commonly within lunar rocks and regolith as a result of low oxygen fugacity. In pristine igneous rocks, such as the mare basalts, FeNi metal forms in trace to minor amounts via indigenous igneous processes (Reid et al., 1970; Goldstein et al., 1974; Ryder et al., 1980; Warren et al., 1987), commonly as grains no larger than 100 μm.

1.4. The Apollo and Luna Sites and Samples

Six Apollo missions and three Luna automated missions successfully landed on the lunar surface, returning soil and rock samples to Earth. Of these Apollo 11 and 12, and Luna 16 and 24 landed on the smooth maria, Apollo 16 and Luna 20 explored the rougher terrain of the anorthosite highlands, and Apollo 14, 15 and 17 bridged the gap between the two, returning samples of basalt and anorthosite (Figure 1.10).

1.4.1. Apollo 11. The Apollo 11 mission returned 21.6 kg of samples (mostly mare basalts) from the south-western part of Mare Tranquillitatis (Figure 1.10). These mare deposits are believed to be relatively thin (in places no more than a few 100 m) and crossed by ejecta rays from the Theophilus, Alfaganus and Tycho craters (Shoemaker et al., 1970a). Although the landing site is not directly crossed by any of the rays there is a possibility that the surrounding area contains material from these craters. The basalt samples were dated at 3.57-3.88 Ga (e.g., BVSP, 1981 and references therein), the first proof that volcanism on the Moon is ancient by terrestrial standards. The site is 400 m west of West crater, a sharp rimmed, rayed crater approximately 180 m in diameter and ~30 m deep (Hiesinger and Head, 2006). Beaty and Albee (1978) suggested that most of the samples collected from

this site were ejecta from West crater. The regolith at this site is 3-6 m deep. Despite its location 40-50 km away from the nearest highland terrain the Apollo 11 regolith was found to contain up to 28 % anorthosite material, believed to be Imbrium ejecta excavated via impacts from beneath the thin surface basalt flows. Five chemically distinct groups of

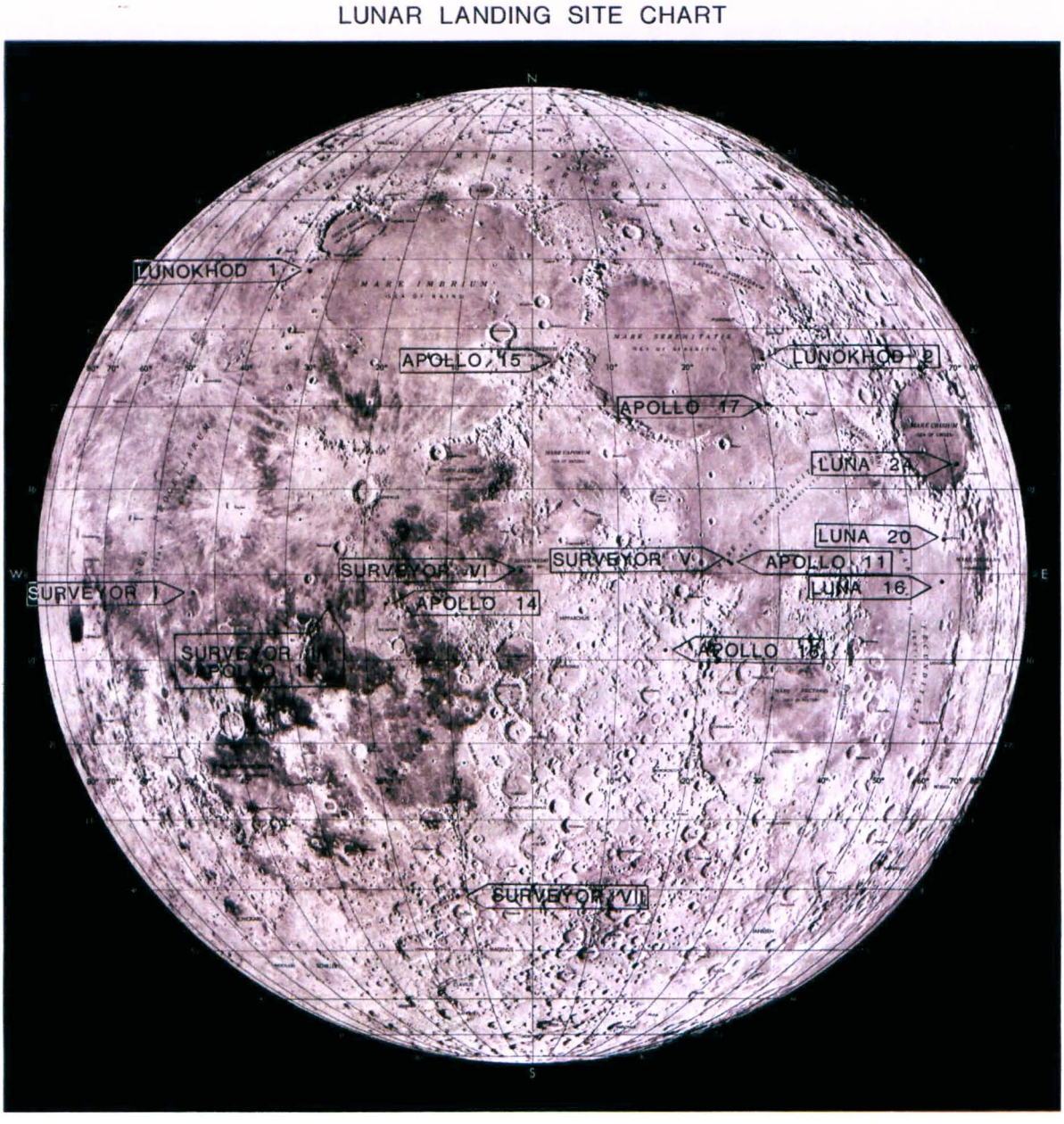

Figure 1.10: Map of the near side of the Moon, showing all Apollo and Luna landing sites, and those of the earlier Surveyor and Lunokhod probes (no sample return). Image courtesy of the Lunar and Planetary Institute, Houston.

basalt have been identified from this site (Table 1.1), suggesting at least five different basalt flows in the surrounding area. However, during this initial mission the astronauts

never ventured further than 60 m from the lunar module and each sample's location was not precisely recorded. Therefore, it is difficult to determine how representative the Apollo 11 sample collection is of the surrounding area's geology (Figure 1.11).

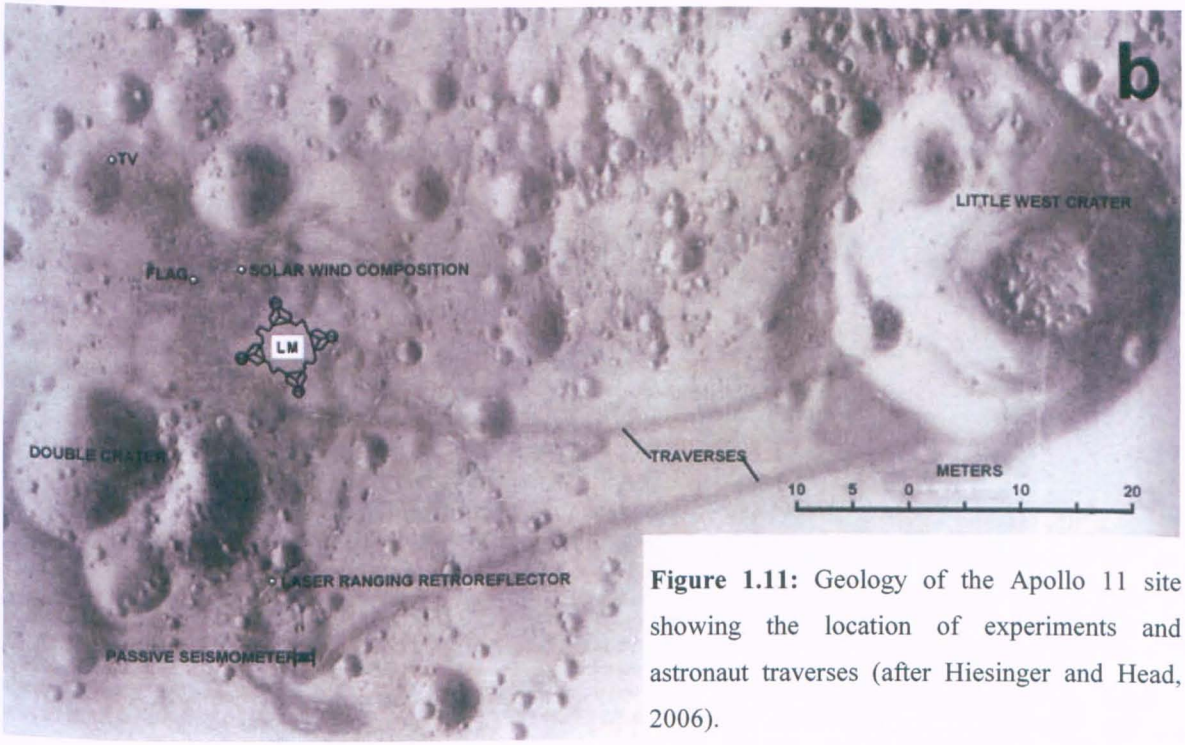

Figure 1.11: Geology of the Apollo 11 site showing the location of experiments and astronaut traverses (after Hiesinger and Head, 2006).

1.4.2. Apollo 12. This site is located in the south-eastern portion of Oceanus Procellarum (Figure 1.10). Basalt flows within this region are relatively lightly cratered compared with those at the Apollo 11 site, suggesting they are younger. These basalts fit into at least three compositional groups - the olivine, pigeonite and ilmenite basalts (Rhodes et al., 1977; Neal et al., 1994a,b – Table 1.1). They range in age from 3.29 to 3.08 Ga (BVSP, 1981; Snyder et al., 2000; Nyquist and Shih, 1992). As the ejecta rays from Copernicus crater cross the Apollo 12 site it was hoped that some of the samples could be dated to assign an exact age to the crater. Although it has not currently been proven that any of the samples are Copernicus ejecta, non-volcanic materials from this site record a major disturbance in the area at 800-900 Ma, which probably relates to this impact event (Hiesinger and Head, 2006). Exposures of non-mare material near the landing site (mostly part of the older Fra Mauro formation as seen at the Apollo 14 site – section 1.4.3) suggest the basalt flows are

thin here (Head, 1975). The regolith is also thin, with craters only 3 m deep appearing to penetrate into the basaltic bedrock (Hiesinger and Head, 2006). In all 34.3 kg of material was collected, including a small amount of KREEP-rich glass containing anorthosite, felsite and KREEP basalt lithic fragments (Wentworth, 1994). These glasses appear to

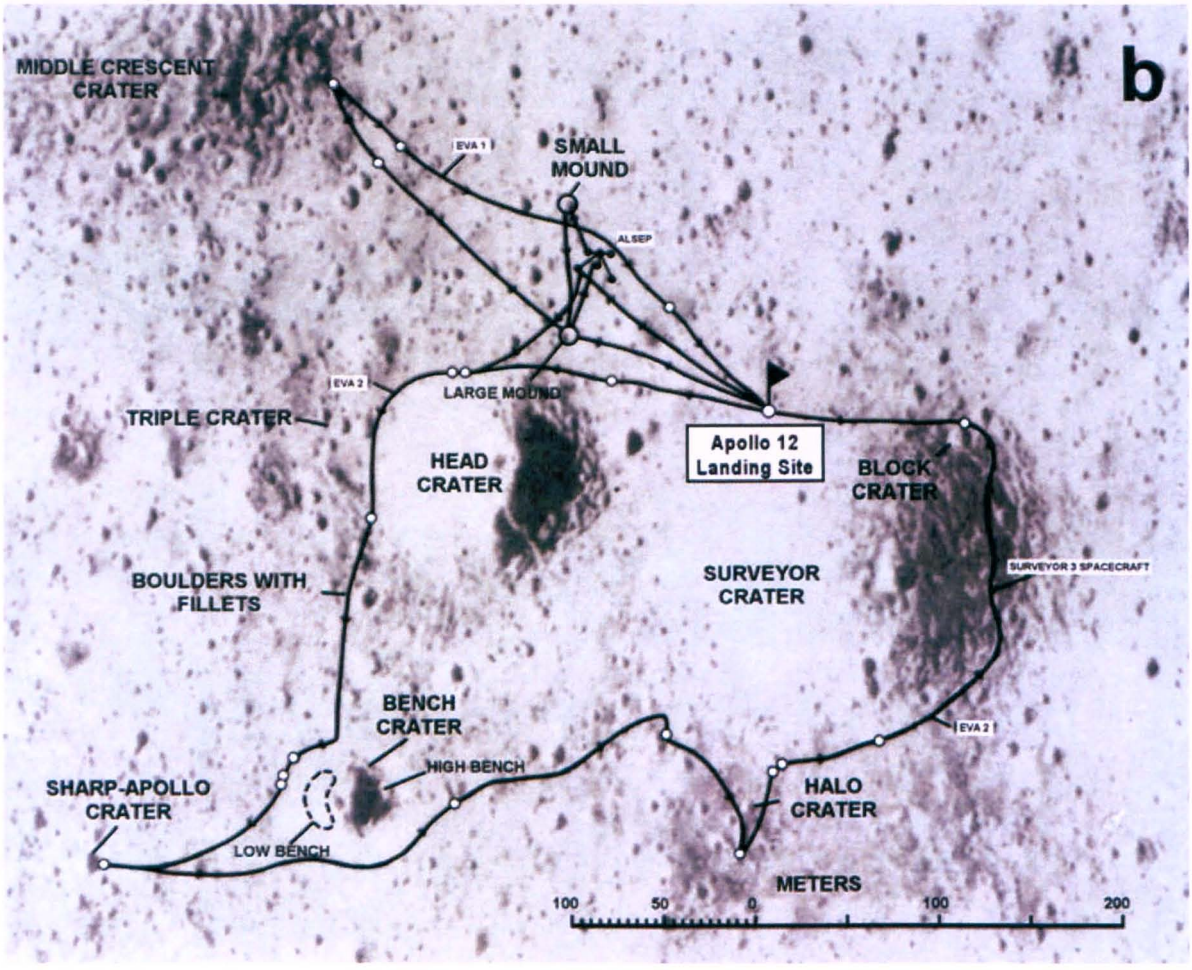

Figure 1.12: Geology of the Apollo 12 site showing the location of experiments and astronaut traverses (after Hiesinger and Head, 2006).

represent impacted surface material similar to that exposed in the Fra Mauro Formation, probably incorporated into the Apollo 12 regolith via lateral and vertical mixing (Jolliff et al., 2000). The scale of astronaut traverses was much larger at this site, and sample collection was recorded in a more ordered fashion with detailed photographs. For this reason the geology can be reconstructed with relative accuracy (Figures 1.12 and 1.18).

1.4.3. Apollo 14. The Apollo 14 mission landed within a highland region, north of the Fra Mauro crater (Figure 1.13). This site was believed to contain ejecta from the Imbrium basin impact event, and as with the Apollo 12 mission the aim was to date the ejecta. The 42.3 kg of material collected consists of complex polymict breccias, impact melt breccias and clast poor impact melts with basaltic and KREEP-rich compositions (Shervais and

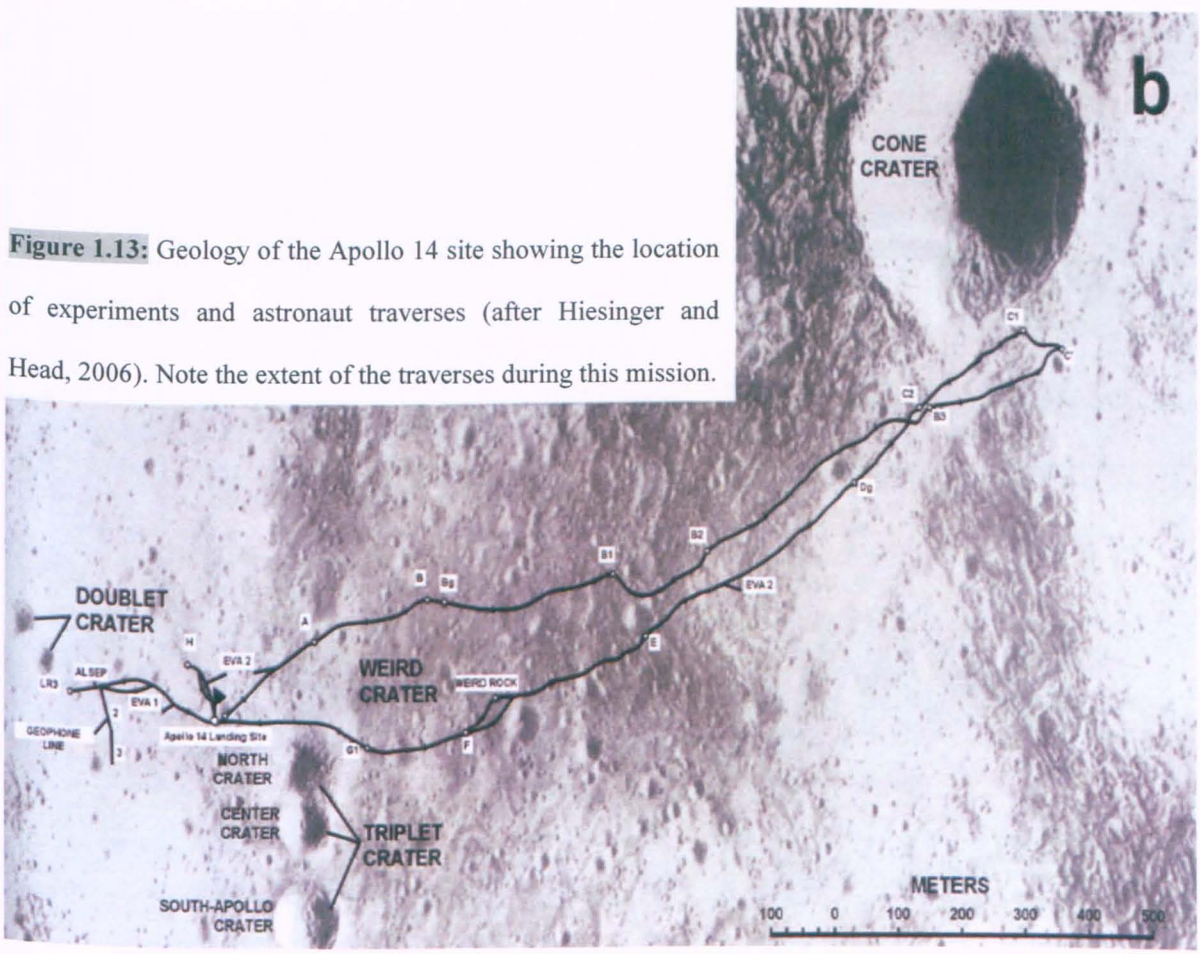

Figure 1.13: Geology of the Apollo 14 site showing the location of experiments and astronaut traverses (after Hiesinger and Head, 2006). Note the extent of the traverses during this mission.

McGee, 1998). Analysis of this material produced ages between 3.8-3.9 Ga, however, this is only the age at which they were assembled into their present form. Later studies proved that ejecta deposits consist of basin ejecta and admixed local material - hence the true origin of these rocks is still disputed (Morrison and Oberbeck, 1975; Wilhelms, 1987; Haskin, 2002; Neal and Kramer, 2006). Petrologic study of Mg-suite cumulates from the Apollo 14 site demonstrated the unique character of the western highlands (Warren et al., 1987, 1990; Shervais, 1989; Snyder et al., 1995). These lithologies are characterised by

high concentrations of incompatible trace-elements compared with their eastern counterparts.

1.4.4. Apollo 15. The Hadley-Apennine region was much further north than any previous landing site (Figure 1.10), and it was also the first complex, multiple-objective landing site and the first to utilise the Lunar Rover. This site was chosen to investigate firstly the massifs and highlands at the edge of the Imbrium basin and secondly the mare lavas and landforms of Palus Putredinis (Howard and Head, 1972). The mare material collected consists of two distinct types, quartz-normative and olivine-normative (Table 1.1), both with measured ages of 3.3 Ga (e.g., Rhodes and Hubbard, 1973; Chappell and Green, 1973; Dowty et al., 1973). Other samples included anorthosites, Mg-suite plutonic rocks, impact melts and granulites (many of which occur as clasts in regolith breccias), non-mare KREEP-rich basalts and emerald green, ultramafic glasses of pyroclastic origin (Elkins-Tanton et al, 2002). This is one of the most petrologically complex regions visited by the Apollo missions, a fact better appreciated because of the Lunar Rover, which enabled astronauts to visit a wide range of sites and return 77.3 kg of material to earth (Figure 1.14).

1.4.5. Apollo 16. This mission was sent to the central lunar highlands near the Descartes crater (Figure 1.10). The main objective was to sample two lithologies from the highlands, firstly the smooth Cayley plains and secondly the hilly Descartes material (Figure 1.15). As this site was hundreds of kilometres away from any mare-basalt flows it also allowed for the collection of purely highland material. The pre-mission expectations were that all samples collected would have a volcanic origin, but they were found to be impact products, mostly polymict breccias and impact melts with a minority of pristine anorthosites (e.g., Stoffler et al., 1985; Haskin et al., 2002). These impact products are thought to be ejecta deposits related to the formation of the Imbrium and Nectaris basins. Some of the samples

were identified as ejecta from the Nectaris basin and dated at 3.92 Ga (e.g., Wilhelms, 1987; Stöffler and Ryder, 2001). Freeman (1981) reported that the regolith thickness in this region ranges from 3 to 15 m. In all 95.7 kg of material was sampled from this site.

1.4.6. Apollo 17. The Apollo 17 landing site is close to the south-eastern rim of the Serenitatis basin, within the Taurus-Littrow valley close to the highland/mare boundary

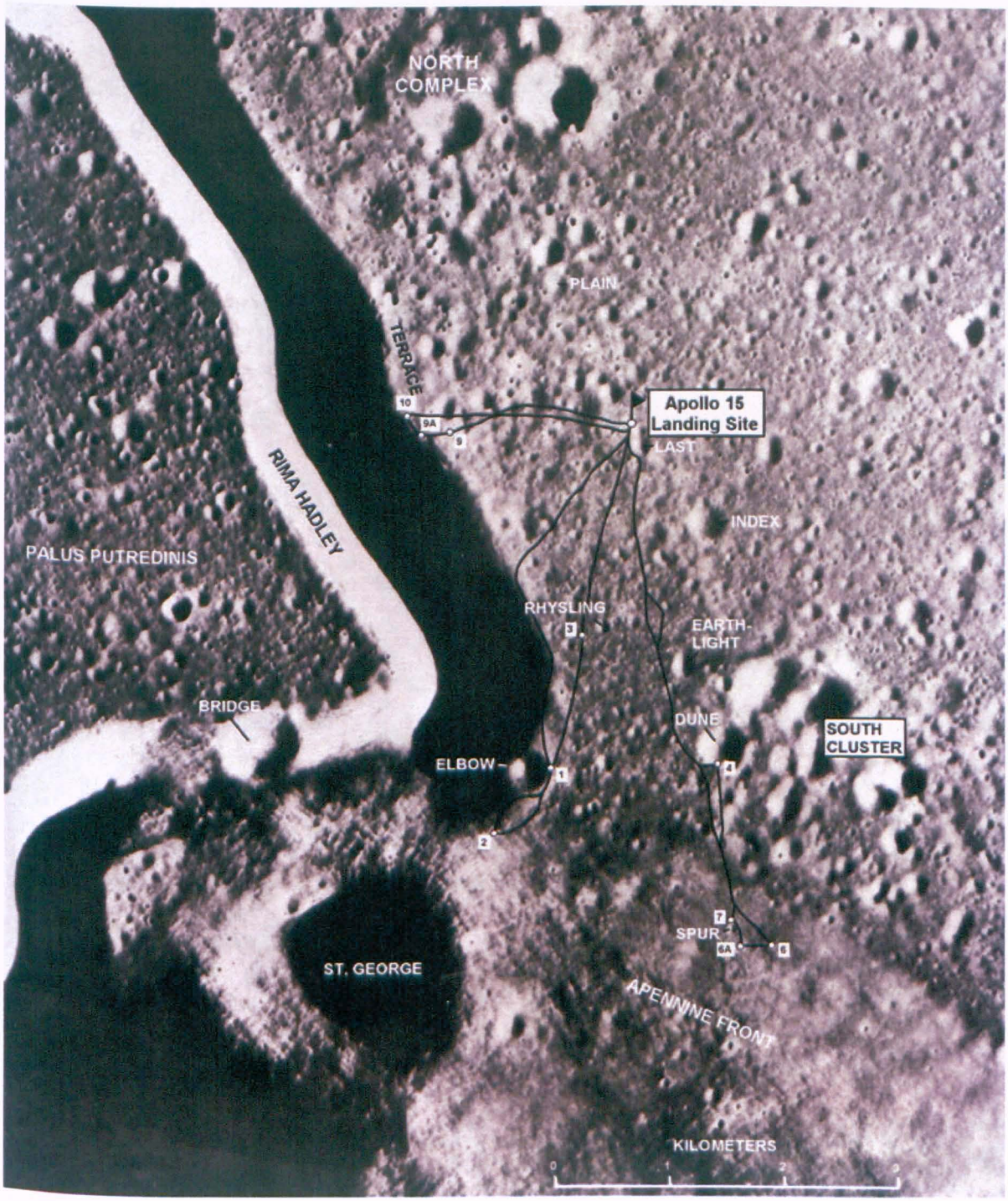

Figure 1.14: Geology of the Apollo 15 site showing the regional geology and location of sites visited in the Lunar Rover (after Hiesinger and Head, 2006). Note the scale of this image is in kilometres.

(Figures 1.10 and 1.16). The objectives of this mission were firstly to analyse two highland massifs - where rocks from the deep crust might be found as ejecta from Serenitatis and other basins, and secondly to study the valley subfloor and examine a low albedo deposit which discontinuously mantles both highlands and mare. The change in focus, from exploration to scientific investigation, over the course of the Apollo program meant that during this last Apollo mission over 110 kg of lunar material was collected. The valley

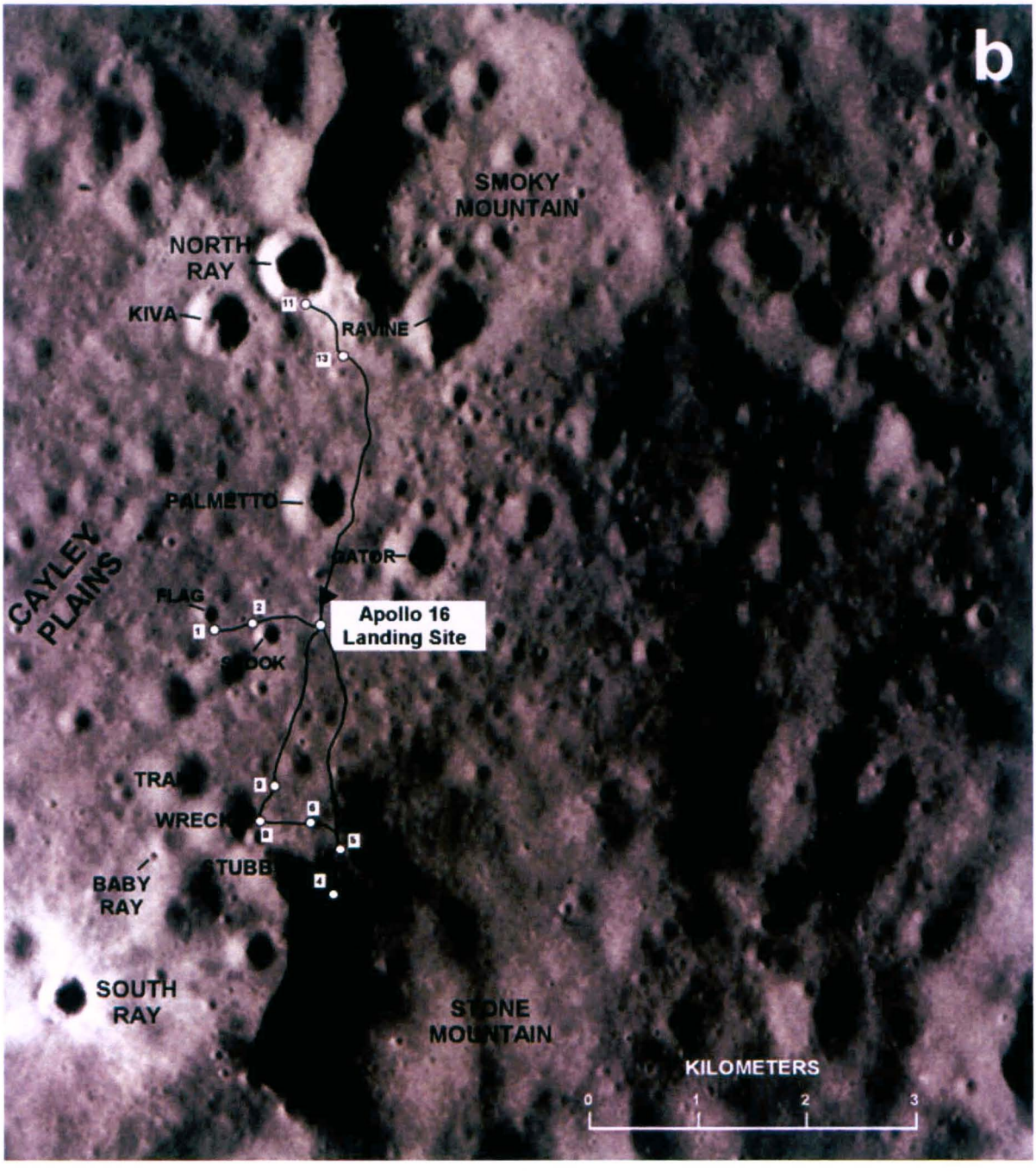

Figure 1.15: Geology of the Apollo 16 site showing the regional geology and location of sites visited in the Lunar Rover (after Hiesinger and Head, 2006). Note the scale of this image is in kilometres.

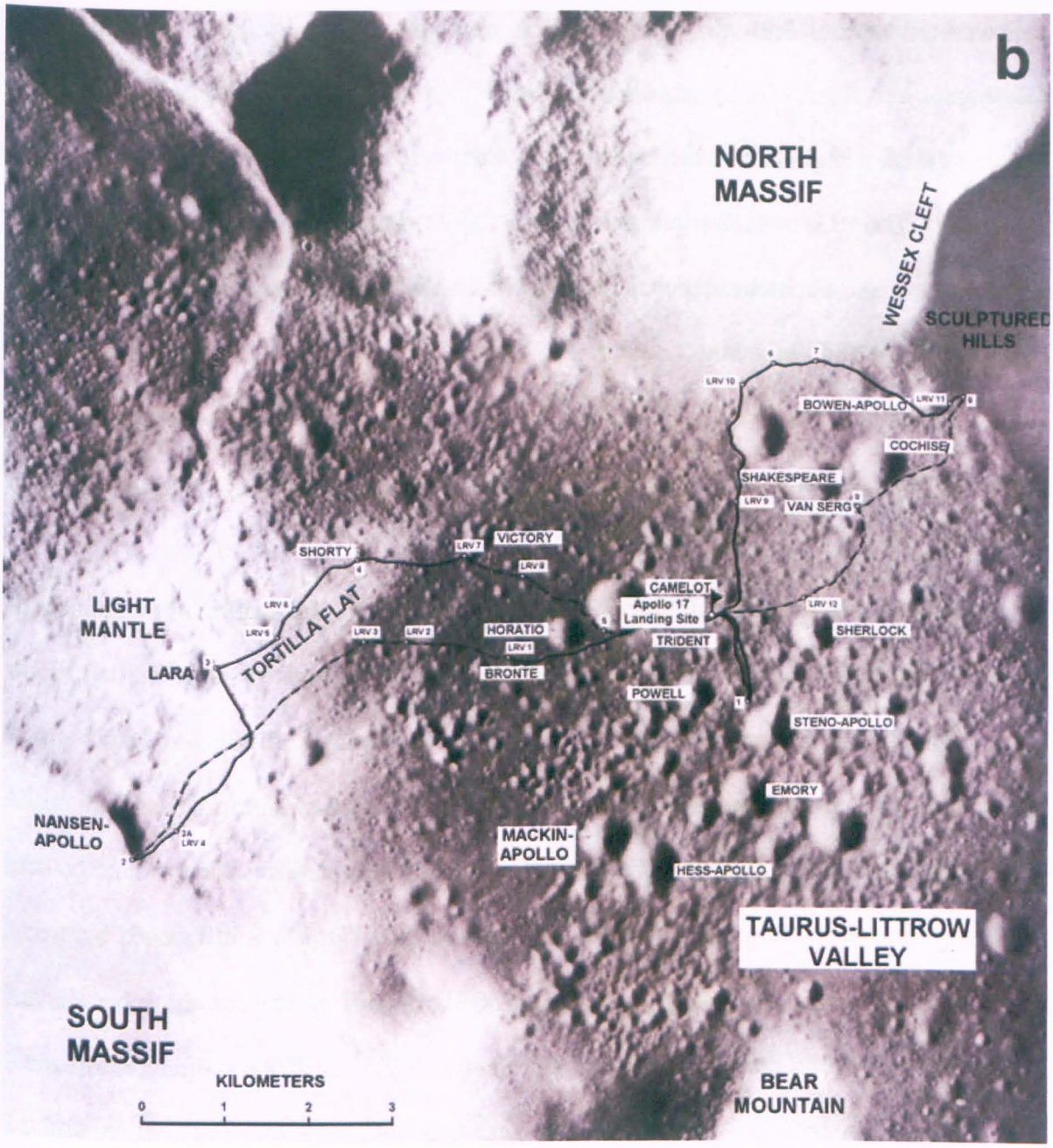

Figure 1.16: Geology of the Apollo 17 site showing regional lithologies and location of sites visited in the Lunar Rover (after Hiesinger and Head, 2006). Note the scale of this image is in kilometres.

subfloor was found to consist of several chemical subgroups of high-Ti basalts, with an age range of 3.75-3.7 Ga (e.g., Neal et al., 1990; Paces et al., 1991; Neal and Taylor, 1992; Premo and Tatsumoto, 1992). Remote-sensing Clementine spacecraft data obtained for NASA's landing site, coupled with sample data, seem to indicate that the highland massifs around the valley consist of a complex mix of impact melt breccias and plutonic Mg-suite rocks (Weitz et al., 1998; Jolliff et al., 1999; Robinson and Jolliff, 2002). The impact melts

were created around 3.87 Ga, an age which may reflect that of the Serenitatis basin (Hiesinger and Head, 2006). A dark mantle deposit of orange and black pyroclastic fragments with a high-Ti basaltic composition was located on the valley floor, which has an age of ~ 3.64 Ga (McKay and Wentworth, 1992). A lighter mantle unit at the site appears to be an avalanche deposit, probably initiated by the impact of ejecta from the Tycho crater, ~ 2000 km away (Lucchitta, 1977). Regolith at this site was found to be ~ 15 m thick. Along with the Apollo 15 landing site, the Taurus-Littrow valley was found to be one of the most complex Apollo landing sites (Figure 1.16).

1.4.7. Luna Missions. From 1970-1976, the U.S.S.R successfully landed three unmanned sample return missions on the eastern nearside of the lunar surface (Figure 1.10). Each lander drilled a shallow core into the regolith which was returned to Earth. In 1970, Luna 16 was the first successful automated Soviet sample return mission. This small probe landed just north of Mare Fecunditatis at the far east of the lunar near side. The site consists of a series of thin basalt flows, ~ 300 m thick. The area was influenced by ejecta from Langrenus (132 km away), Tauruntius (56 km away) as well as the more distant Theophilus and Tycho craters (McCauley and Scott, 1972). The 101 g sample returned is a dark gray regolith drill core which reached 35 cm depth (Vinogradov, 1971). It consists of moderately high-Ti, high-Al mare-basalt fragments, age dated to approximately 3.41 Ga. These basalts are among the most Fe-rich and Mg-poor ever returned from the Moon, they are also the most Al-rich mare basalts yet sampled (McCauley and Scott, 1972; Ma et al., 1979).

In 1972, Luna 20 landed just north of the Luna 16 sampling site, in the highlands south of Mare Crisium. The highland regolith at this site contained lithic fragments of granulites, anorthosites, impact melts and polymict breccias (Heiken and McEwen, 1972). This site is influenced by Apollonius C, a 10 Ka crater only a few kilometres east. Luna 20 returned 50

g of light grey regolith, containing breccia fragments of anorthositic-noritic-troctolitic composition and impact melts of noritic-basaltic composition. It is important to note the higher concentrations of MgO at the Luna 20 site relative to the Apollo 16 site; this is believed to be because of the addition of an unknown mafic-highland material present at the Luna 20 site (Papike et al., 1998). In addition, K and P concentrations are lower here, and it has been argued that these samples have not been contaminated with KREEP-rich Imbrium ejecta and that they represent middle to lower crustal material ejected by the Crisium impact (Fernandes et al., 2000; Cohen et al., 2000).

The Luna 24 (1976) sampling site was north again, in the southern region of Mare Crisium, within its inner ring. Head et al. (1978) estimated the thickness of the basalt at this site to be 1-2 km using remote sensing techniques. These authors also identified several distinctive basalt types within the Mare Crisium. The mission returned 170 g of fine-grained mare regolith within a 1.6 m drill core, from which four layers of stratigraphy were identified (Barsukov, 1977). The ages of basaltic fragments from this core range from 3.6-3.4 Ga and are very low in TiO_2, low in MgO, and high in Al_2O_3 and FeO (Laul et al., 1978).

1.5. Petrology of the Crystalline Mare-Basalts

From mare-basalt bulk compositions it is apparent that the most useful lithologic discriminate is TiO_2. Papike et al. (1976) and Papike and Vanimann (1978) defined three compositional groups based on TiO_2 content: very low-Ti basalts (< 1.5 wt % TiO_2), low-Ti basalts (1-5 wt % TiO_2) and high Ti-basalts (9-14 wt % TiO_2). Neal and Taylor (1992) argued that secondary and tertiary divisions can be made using Al_2O_3 (i.e. < 11 wt % = low-Al, > 11 wt % = high-Al) and K contents (i.e. < 2000 ppm = low-K and > 2000 ppm = high-K) (Figure 1.17). These divisions yield a classification containing twelve categories, of which six have been identified in the Apollo and Luna collections. The following text

aims to briefly describe the textural and mineralogical characteristics of each of these six groups along with the locations from which they were collected.

1.5.1. High-Ti, low-Al, low-K basalts. This group was preferentially sampled at the Apollo 11 and 17 sites. Apollo 17 samples can be divided into those similar to Apollo 11 low-K basalt samples and those which contain higher abundances of olivine, ilmenite and armalcolite (sometimes known as the very high-Ti basalts). The former group (know as type A - Table 1.1), along with the Apollo 11 low-K group (types B1, B2 and B3), contain fine- to medium-grained, vesicular rocks with subophitic to ophitic textures and average grain sizes ranging from 0.25-1.5 mm (Papike et al., 1998). The ophitic textures are defined by pyroxene either partially enclosing subhedral plagioclase (An_{94-77}) (subophitic) or totally enclosing it (ophitic) (Papike et al., 1976). Pyroxenes are strongly zoned and commonly display discontinuous rims of pyroxferroite (Chao et al., 1970a) often decomposed to a fine-grained intergrowth of hedenbergite (Ca-Fe-rich pyroxene), silica and fayalite (Ware and Lovering, 1970; Lindsley et al., 1972). In slowly cooled samples pyroxenes are euhedral and exhibit well-developed sector zoning. Large early-formed crystals of olivine (Fo_{80-60}) occur in finer-grained lithologies, whereas in coarser-grained samples olivine is sparse to absent. These olivines may be mantled by Ti-rich pyroxene

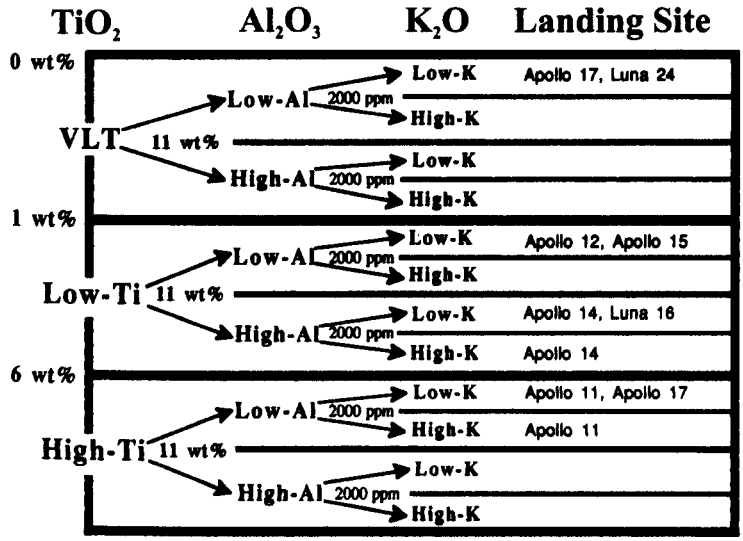

Figure 1.17: Neal and Taylor (1992) classification of mare basalts based on TiO_2, Al_2O_3 and K_2O content.

Table 1.1: Mare basalt types.

Mission	Basalt Type	Basalt Type	References
Apollo 11	High-Ti, Low-Al, High-K: Type A	> 2000 ppm K_2O plus elevated incompatible element (particularly La, 20-40 ppm) and P_2O_5 contents. ~3.6 Ga.	Geiss et al. (1977) Papanastassiou et al. (1977) Haskin et al. (1970) Philpotts and Schnetzler (1970) Beaty and Albee (1978) Beaty et al. (1979a,b) Ma et al. (1980) Rhodes and Blanchard (1980) Neal and Taylor (1992) Neal et al. (2001)
Apollo 11	High-Ti, Low-Al, Low-K: Type B1	Intermediate K (< 1000 ppm), low La (<10 ppm), ~3.72 Ga.	Geiss et al. (1977) Papanastassiou et al. (1977) Beaty and Albee (1978) Beaty et al. (1978a,b) Guggisberg et al. (1979) Ma et al. (1980) Rhodes and Blanchard (1980) Neal and Taylor (1992)
Apollo 11	High-Ti, Low-Al, Low-K: Type B2	low K (< 750 ppm), intermediate La (25-10 ppm), ~3.90 Ga.	Geiss et al. (1977) Papanastassiou et al. (1977) Beaty and Albee (1978) Beaty et al. (1978a,b) Guggisberg et al. (1979) Ma et al. (1980) Rhodes and Blanchard (1980) Neal and Taylor (1992)
Apollo 11	High-Ti, Low-Al, Low-K: Type B3	low K (< 750 ppm), low La (<10 ppm), ~3.76 Ga.	Geiss et al. (1977) Papanastassiou et al. (1977) Beaty and Albee (1978) Beaty et al. (1978a,b) Guggisberg et al. (1979) Ma et al. (1980) Rhodes and Blanchard (1980) Neal and Taylor (1992)
Apollo 12	Olivine basalt	Accumulated olivine results in Mg# >45, Rb/Sr ratio is >0.008, TiO_2 is low (~2.0 - 3.5 wt %).	Compston et al. (1971) Papanastassiou and Weasserburg (1971a) James and Wright (1972) Walker et al. (1976) Rhodes et al. (1977) Baldridge et al. (1979)
Apollo 12	Pigeonite basalt	Mg# <45, Rb/Sr ratio is >0.008, TiO_2 is intermediate (~3.0 - 5.0 wt %).	Compston et al. (1971) Papanastassiou and Weasserburg (1971a) James and Wright (1972) Walker et al. (1976) Rhodes et al. (1977) Baldridge et al. (1979)
Apollo 12	Ilmenite basalt	Mg# is variable, Rb/Sr ratio is <0.008, TiO_2 is high (~3.0 - 6.0 wt %).	Compston et al. (1971) Papanastassiou and Weasserburg (1971a) James and Wright (1972) Walker et al. (1976) Rhodes et al. (1977) Baldridge et al. (1979)
Apollo 14	High-Al	14 -11 wt % Al_2O_3, <0.3 wt % K_2O, K/La ratio ~ 100, age ~ 4.3 Ga.	Warner et al. (1980) Dickinson et al. (1985) Shervais et al. (1985a) Neal et al. (1988a, 1989)
Apollo 14	Very high-K	14 -11 wt % Al_2O_3, >0.3 wt % K_2O, K/La ratio ~ 150, K_2O/Na_2O ratio >1, high concentrations of Rb and Ba.	Warner et al. (1980) Dickinson et al. (1985) Shervais et al. (1985a) Neal et al. (1988a, 1989)
Apollo 15	Olivine Normative	18 - 24 wt % FeO, 8 - 17 wt % MgO, La < 6.5 ppm, Sm < 4.5 ppm, ~3.2 Ga.	Chappell et al. (1972) Maxwell et al. (1972) Rhodes (1972) Chappell and Green (1973) Cuttitta et al. (1973) Helmke et al. (1973) Nava (1974) Nyquist (1977)
Apollo 15	Quartz Normative	18 - 24 wt % FeO, 8 - 17 wt % MgO, La < 6.5 ppm, Sm < 4.5 ppm, ~3.2 Ga.	Chappell et al. (1972) Maxwell et al. (1972) Rhodes (1972) Chappell and Green (1973) Cuttitta et al. (1973) Helmke et al. (1973) Nava (1974) Nyquist (1977)
Apollo 17	Type A	Similar major element abundances to Type B, but 50 - 60 % higher incompatible trace element abundances	Rhodes et al. (1976) Warner et al. (1979) Neal et al. (1990a,b)
Apollo 17	Type B	Similar major element abundances to Type A, but 50 - 60 % lower incompatible trace element abundances. Can be divided into type B1 and B2, where B2 contains slightly higher La ppm	Rhodes et al. (1976) Warner et al. (1979) Neal et al. (1990a,b)
Apollo 17	Type C	Higher MgO and Cr_2O_3 contents than Type A and B, REE abundances similar to Type A, contain high Fo olivines (Fo_{90}).	Rhodes et al. (1976) Warner et al. (1979) Neal et al. (1990a,b)

(Papike et al., 1976). Ilmenite is present as elongated blades in the subophitic samples, grading into equant, anhedral grains in the ophitic samples. Cr-Ti spinels occur as inclusions within olivines and are mantled by ilmenite within the mesostasis. The mesostasis can contain cristobalite, tridymite, ulvöspinel, apatite, whitlockite, pyroxferroite, fayalite, metallic iron (FeNi), troilite and tranquillityite (Lovering and Ware, 1970) as well as more common plagioclase and clinopyroxene. The general crystallisation sequence for these magmas is olivine → spinel → ilmenite → pyroxene + plagioclase (Papike et al., 1976; Longhi, 1987, 1992). Beaty and Albee (1978), Beaty et al. (1979a,b), and Rhodes and Blanchard (1980) demonstrated that various Apollo 11 high-Ti, low-K samples represent different basaltic units (types B1, B2 and B3 - Table 1.1) and cannot be related by surface or near-surface crystal-liquid fractionation. This is best demonstrated by plotting bulk rock Co against the La/Sm ratio for each sample. Apollo 11 high-Ti, low-K basalts also contain higher abundances of Hf, and have higher La/Yb and La/Sm ratios than their Apollo 17 counterparts, thus the Apollo 11 samples were generated from sources more enriched in light rare earth elements (LREE) (Neal and Taylor, 1992).

The more olivine and Ti-rich mare basalts collected from the Apollo 17 site (types B and C and the majority of the unclassified basalts – Table 1.1) are mineralogicaly and texturally distinct, and they vary from vitrophyres to microgabbros (Ridley and Brett, 1973; Hodges and Kushiro, 1974; Longhi et al., 1974; Meyer and Boctor, 1974; Papike et al., 1974, 1976; Dymek et al., 1975a). In the vitrophyres, microphenocrysts of olivine, armalcolite and spinel are set in a fine-grained, spherulitic, quenched intergrowth of clinopyroxene, plagioclase, ilmenite, tridymite, glass, troilite and FeNi. Olivine is commonly skeletal and mantled by titano-augite, which in coarser-grained samples (microgabbros) may occur as discrete grains with olivine inclusions. Armalcolite is mantled by ilmenite in fine-grained samples and appears as inclusions in clinopyroxene, but rarely within plagioclase. The matrix of the microgabbros is similar to that of the other high-Ti, low-K basalts except that

pyroxferroite or its breakdown constituents have not been identified. Crystallisation sequences within these very high-Ti basalts are complex and generally change with cooling rate. Experimental studies by Kesson (1975) and Walker et al. (1975) concluded that high-Ti magmas similar to these were parental to other high-Ti, low-K basalts at the Apollo 11 and 17 sites. Low pressure fractional crystallisation of armalcolite and olivine may link the lithologies. As with the Apollo 11 basalts compositional differences between the Apollo 17 samples cannot be reconciled by near-surface fractional crystallisation of liquidus phases. Therefore, differing basaltic types at this site require distinct source regions (Shih et al., 1975; Rhodes et al., 1976; Warner et al., 1979; Ryder, 1990).

*1.5.2. **High-Ti, low-Al, high-K basalts.*** Collected only from the Apollo 11 site (known as type A – Table 1.1), these basalts tend to be finer-grained (average grain size 0.2-0.7 mm) with granular to intersertal textures (Chao et al., 1970b; James and Jackson, 1970). However, in coarser-grained examples pyroxene grains can reach 2.5 mm in length. Anhedral laths of plagioclase (An_{82-75}) enclosing subhedral grains of pyroxene and ilmenite are commonly observed in the coarser-grained samples, while the finer-grained basalts show irregular fan-shaped spherulitic intergrowths of plagioclase (An_{81-73}) and pyroxene (Papike et al., 1998). In the coarser grained samples pyroxene zones from pigeonite to Ti and Fe-rich augite, and may contain olivine inclusions. These olivine inclusions may in turn contain inclusions of Cr and Cr-Ti spinel. Matrix within this group of samples has a similar composition to that of other high-Ti samples. The apparent crystallisation sequence derived from these textures is olivine + armalcolite → pyroxene (reaction between olivine and melt) → ilmenite (reaction between armalcolite and melt) → plagioclase (Papike et al., 1976). The high-K group contains lower abundances of plagioclase than other high-Ti basalts (~20 % modal abundance compared to 31 % for the Apollo 11 low-K basalts and 23 % for the very high-Ti Apollo 17 basalts (Papike et al., 1976)). Enrichments in La and K within these samples suggest a certain amount of KREEP assimilation, although lack of

LREE enrichment may suggest source-region mixing rather than assimilation (Neal and Taylor, 1992). Mineralogical, major-element and trace-element compositions suggest that samples are all from the same basaltic unit (Beaty and Albee, 1978; Grove and Beaty, 1980; Neal and Taylor, 1992 and references therein).

1.5.3. Low-Ti, low- Al, low-K basalts. These basalts were returned from the Apollo 12, and 15 sites. The Apollo 12 samples are sub-categorised into pigeonite, olivine and ilmenite basalts, while the Apollo 15 basalts are divided into olivine-normative and quartz-normative types (Table 1.1). Textures amongst these basalts vary widely, from the highly porphyritic Apollo 12 pigeonite basalts with pyroxene phenocrysts up to a few centimetres in length, to the Apollo 15 olivine vesicular vitrophyres with grains no larger than 0.5 mm. Clinopyroxene zones from pigeonite cores to rims of augite, and is commonly zoned to pyroxferroite (Papike et al., 1976).

In Apollo 12 pigeonite basalts opaque inclusions range from spinels rimmed with ulvöspinel in the pigeonite cores to ilmenite in the augite rims. Plagioclase occurs as anhedral to subhedral laths intergrown in the mesostasis with pyroxene and anhedral laths of ilmenite. Olivine (Fo_{75-30}) is also present (4 vol %) (Heiken et al., 1991). Additional accessory phases include late stage glasses, silica, sulphides, phosphates, metallic iron and alkali feldspar (Papike et al., 1976; Baldridge et al., 1979). The pigeonite basalts probably represent samples of thin units in which cooling rate, rather than near-surface fractionation, affected textures, crystallisation sequence and modal mineralogy. The general crystallisation sequence is Cr-spinel → ulvöspinel → olivine → pigeonite → augite → plagioclase → ilmenite (Papike et al., 1998).

Apollo 12 olivine and Apollo 15 olivine- and quartz-normative basalts are similar in texture and mineralogy. They are fine- to medium-grained (0.5 to 4 mm) and range from

olivine vitrophyres to microgabbros or olivine cumulates (mostly Apollo 12). In rapidly cooled samples olivine is skeletal. In coarser-grained examples olivine is either partially mantled by augite or exists as inclusions within pyroxene (Baldridge et al., 1979; Neal et al., 1992). Pyroxene may form subhedral laths with pigeonite cores and augite mantles that zone outwards to pyroxferroite, blocky ilmenite exists within the matrix. The Apollo 15 olivine-normative basalts contain olivine which zones further towards fayalite than that found in any of the Apollo 12 olivine basalts. The general crystallisation sequence is olivine + spinel → pigeonite → augite → plagioclase → ulvöspinel → ilmenite (Papike et al., 1998).

Apollo 12 ilmenite basalts are low-Ti basalts with an overall higher modal abundance of ilmenite (but still only 2.7-5.0 wt % TiO_2). Fine-grained samples consist of abundant olivine (16 vol %, Fo_{80-50}) mantled by titano-augite and set in a quenched groundmass of pyroxene, ilmenite and plagioclase (An_{94-87}) (Brett et al., 1971). In coarser-grained samples olivine is far less abundant, whereas highly-zoned pyroxene and grains of cristobalite are more abundant. Fayalite and phosphates are common accessory minerals. The general crystallisation sequence for ilmenite basalts is olivine → Cr-spinel → pigeonite → augite + plagioclase + ulvöspinel + ilmenite (Papike et al., 1998). Major- and trace-element data (Neal and Taylor, 1992 and references therein; Neal et al., 1994a,b), in addition to site geology (Rhodes et al., 1977), imply that the Apollo 12 olivine, pigeonite and ilmenite basalts formed in three distinct basaltic layers (Figure 1.18).

The olivine-normative and quartz-normative Apollo 15 basalts were first distinguished as two distinct suites of low-Ti mare basalts on the basis of major-element chemistry (Chappell et al., 1972; Maxwell et al., 1972; Rhodes, 1972; Chappell and Green, 1973; Cuttitta et al., 1973; Helmke et al., 1973; Nava, 1974). The olivine-normative basalts have a slightly greater compositional range than the quartz-normative basalts, but both have

similar ages and isotopic characteristics (Nyquist, 1977). Average ages suggest that the former suite is slightly younger than the latter (3.2 vs. 3.3 Ga). Rhodes and Hubbard (1973) and Chappell and Green (1973) concluded that the two groups could not be related by simple fractional crystallisation of a common parental magma or partial melting of a common source. However, recent research by Schnare et al. (2008) proposes a model for multi-layer, shallow-level crystal fractionation which appears to reconcile compositional differences between the two groups and therefore suggests they share a common source.

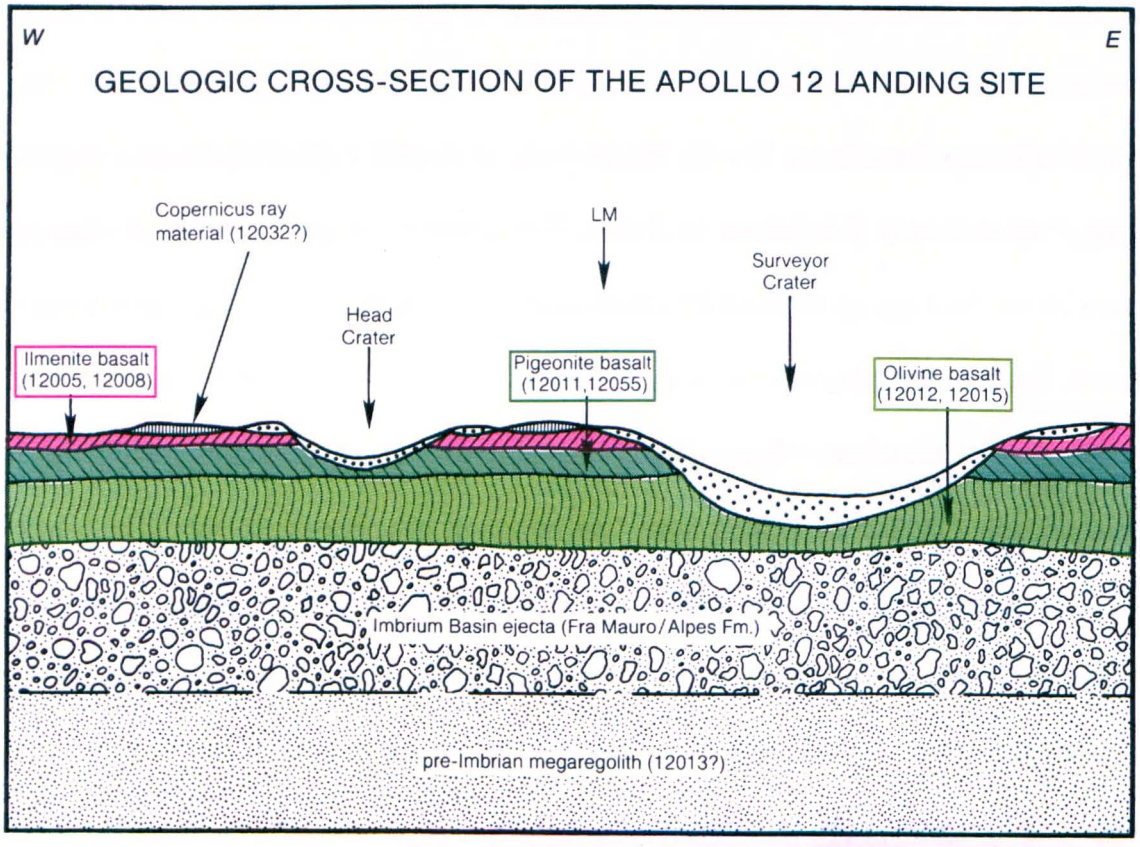

Figure 1.18: The stratigraphy of the Apollo 12 landing site, showing olivine, pigeonite and ilmenite basalts as distinct layers (with example basalt sample numbers shown). As the olivine basalts are beneath the pigeonite and ilmenite layers these must be the oldest, and the ilmenite group must be the youngest (though the accuracy of isotopic age dating techniques cannot currently distinguish between these three sample types). After Rhodes et al. (1977).

1.5.4. Low-Ti, high-Al, low-K basalts. Felspathic basalts were collected from the Apollo 12 and 14 and Luna 16 sites (Table 1.1). They have modal abundances of plagioclase

above 38.5 % and high concentrations of Al_2O_3 (> 11 %) (Papike et al., 1998). However, it now seems probable that the Apollo 12 feldspathic basalts are simply samples with unrepresentatively high amounts of feldspar – only three samples from this site were ever classified as feldspathic and two of these were subsequently reassigned to other groups based on bulk-rock chemistry (Neal et al., 1994a). For this reason the Apollo 12 feldspathic basalts are not described here. True feldspathic basalts typically display ophitic to subophitic textures, with some Luna 16 clasts appearing vitrophyric (Shervais et al., 1985a,b). In subophitic examples early olivine (Fo_{70-65}) occurs as anhedral phenocrysts whereas late-stage olivine (Fo_{20-0}) occurs only in the groundmass, in Apollo 14 sample 14053 this late stage olivine has been reduced to metallic iron and SiO_2 (El Gorsey et al., 1972). Pyroxene occurs in a fine-grained matrix with plagioclase and ilmenite, or as large strongly-zoned laths (5 mm) commonly enclosing plagioclase. Minerals in the mesostasis include spinel, silica, troilite, and residual K-rich glass (Gancarz et al., 1971; Albee et al., 1972; Longhi et al., 1972; Shervais et al., 1984a,b, 1985a; Dickinson et al., 1985; Neal 1989a,b). Over 45 high-Al clasts were discovered within Apollo 14 polymict breccia 14320, displaying a wide range of textures but all enriched in incompatible trace-elements relative to other Apollo 14 high-Al samples (Shervais et al., 1984a,b; 1985a; Dickinson et al., 1985). The Apollo 14 samples can be separated into 5 groups based on mineral chemistries and bulk-rock REE content (Shervais et al., 1985a; Dickinson et al., 1985), but it is still debated whether these groups are real or simply a product of short range regolith mixing. Upon the collection of more trace-element data Neal et al. (1988, 1989a,b) concluded that separation of these samples into five groups was not justified, and that there was in fact a continuum of compositions throughout the sample suite. It has been suggested that the high-Al content of Apollo 14 basalts was caused by impact melting – trace-element, petrographic and isotopic data are consistent with an impact-melt derived origin (Snyder and Taylor, 2001) – or alternatively mixing with a KREEPy component at the source (Neal and Taylor, 1992 and references therein). Most recently Neal and Kramer

(2006) classified the Apollo 14 high-Al basalts into three groups (A, B and C) based on age and assimilation-crystal fractionation (AFC) modelling. Their data suggest group A (4.3 Ga) evolved through closed-system crystal fractionation, whereas group B (4.1 Ga) and group C (3.9 Ga) require open-system evolution involving combined assimilation of a KREEP/granite component and crystal fractionation.

Although a number of the Luna 16 clasts are similar to the Apollo 14 high-Al basalts the remainder are distinctly lower in MgO and Cr. Sample size has hampered the study of these basalts, at the Apollo 14 site mostly polymict breccias with small clast sizes were collected and Luna 16 only returned 100 g of regolith material. Until the recent discovery of the first crypomare lunar meteorite (Terada et al., 2007; Sokol et al., 2008) the Apollo 14 samples were recognised as the oldest known mare basalts at 4.3 Ga (Taylor et al., 1983; Dasch et al., 1987).

1.5.5. Low-Ti, high-Al, high-K basalts (VHK). Very high-potassium basalts (VHK) were only found at the Apollo 14 site (Table 1.1), they have similar chemistries to other high-Al basalts found at this site with the exception of a much higher K_2O content (0.3 wt %) along with enrichments in Rb and Ba (Shervais et al., 1985b). They are medium- to coarse-grained with subophitic to ophitic textures. They contain two generations of olivine, the early olivine phenocrysts (Fo_{73-61}) and groundmass olivine (Fo_{50-36}). Pyroxene phenocrysts are zoned from Mg-pigeonite to augite, and plagioclase forms small laths that range in composition from An_{95} to $An_{78.5}$. Ilmenite is bladed and spinels occur as inclusions within olivines and pyroxenes, and as a phase within the groundmass. Orthoclase feldspar (Or_{84-95}), and K and Si-rich glasses are ubiquitous in the mesostasis (Warner et al., 1980; Shervais et al., 1984b, 1985b; Goodrich et al., 1986; Shih et al., 1986; Neal et al., 1988b). The general crystallisation sequence is olivine + spinel → pigeonite → plagioclase →

augite (Papike et al., 1998). Neal and Taylor (1992) argued that these are the products of parental high-Al magma assimilating lunar granite within the anorthosite crust.

1.5.6. Very low-Ti, low-Al, low-K basalts (VLT). These basalts were first discovered in the deep drill cores from the Apollo 17 site (Taylor et al., 1977; Vaniman and Papike, 1977a,b,c) and later as clasts within samples from this site (Table 1.1). They are also the dominant lithology returned by Luna 24 (Ma et al., 1977, 1978; Ryder and Marvin, 1978). Most fragments returned from both missions are extremely small - the largest fragments have dimensions of 2-4 mm. They are vitrophyric to coarse-grained subophitic (Apollo 17) - ophitic (Luna 24) rocks. The vitrophyres contain chromites, and skeletal grains of olivine (Fo_{75}) and pyroxene. Pyroxenes are zoned from pigeonite to thin mantles of augite and are held within a pale yellow/green to colourless glass (Vaniman and Papike, 1977c). In the coarser grained lithologies olivine (Fo_{76-05}) in contact with pyroxene is zoned and partially reabsorbed. Chromite occurs as inclusions within this olivine. Fe enrichment in the coarser grained pyroxenes is more extensive and the mantles are intergrown with plagioclase (An_{96-86}) in Apollo 17 samples. The groundmass contains iron metal, ilmenite, silica, troilite, ulvöspinel, and glass (Vaniman and Papike, 1977c; Taylor et al., 1978; Warner et al., 1978a; Papike and Vaniman, 1978, James and McGee, 1980; Ma et al., 1978; Ryder and Marvin, 1978). The general crystallisation sequence of Apollo 17 VLT basalts is: olivine + chromite → pigeonite → plagioclase + augite → ilmenite + ulvöspinel (Vaniman and Papike, 1977c). Luna 24 basalts are the only samples to exhibit a positive Eu anomaly (Neal and Taylor, 1992).

1.6. Comparisons between Mare and Highland Sample Collections

Table 1.2 shows the modal proportions of major minerals in soils from both highland and mare landing sites. The Apollo 16 site was well within the highlands and its composition of almost 70 % plagioclase contrasts dramatically with the plagioclase content of soil from

the Apollo 11 site (approximately 21 %), the latter is richer in pyroxene and mare glass (though the olivine content is relatively stable). These two sites illustrate the mineralogical difference between highland anorthosites and lowland mare basalts.

Table 1.2: Mineral modal abundance in mare and highland soils. Modified from Papike et al. (1998).

Mineral	Apollo 11 (M)	Apollo 12 (M)	Apollo 17 (M)	Apollo 17 (H)	Apollo 16 (H)
Plagioclase	21.4	23.2	34.1	39.3	69.1
Pyroxene	44.9	38.2	30.1	27.7	8.5
Olivine	2.1	5.4	0.2	11.6	3.9
Silica	0.7	1.1	-	0.1	0.0
Ilmenite	6.5	2.7	12.8	3.7	0.4
Mare Glass	16.0	15.1	17.2	9.0	0.9
Highland	8.3	14.2	4.7	8.5	17.1
Others	-	-	0.7	-	-
Total	**99.9**	**99.9**	**99.8**	**99.9**	**99.9**

(M) Denotes mare. (H) Denotes highland.

1.7. Lunar Meteorites

There are currently 54 known lunar meteorites (as of April 20th 2010, see www-curator.jsc.nasa.gov/lunar/index), which are commonly represented by numerous separate stones (Table 1.3). These samples were blasted off the Moon by meteorite impacts and eventually fell to Earth up to several million years after they left the Moon. It is not known where on the Moon any of the meteorites originated or for certain how many of them are launch-paired (sourced from the same region and launched by the same impact). However, these samples are an important source of information; they originate from a wider range of lunar locations than the Apollo and Luna collections, so help us to understand the Moon's lithologies on a global scale. One major difference between basaltic meteorites and collected basalt samples is that the former are all either low or very low-Ti, implying that high-Ti mare basalts are rarer than originally thought, and that the Apollo sites are located in, or affected by, an anomalously Ti-rich terrain (section 1.8.5).

Table 1.3: Lunar meteorites listed in order of increasing Al_2O_3 concentration within each group.

Name	Lunar Rock Type	Mass (g)	TiO_2 (%)	Al_2O_3 (%)	FeO (%)	MgO (%)	Mg' (%)	Th µg/g
Mare Basalts:								
Dhofar 287	Mare basalt & regolith	154	*2.8*	*8.4*	*22*	*13*	*52*	*0.9*
	breccia		Na	Na	Na	Na	Na	Na
NWA 032/479	Mare basalt	~456	3.1	9.2	22	7.8	39	2.0
Asuka 881757	Mare basalt	442	2.4	9.8	23	6.3	33	0.4
LAP 02205/ 02224/ 02226/ 02436/ 03632/ 04841/NWA 4734	Mare basalt	3303	3.2	9.9	22	6.3	34	2.0
Yamato 793169	Mare basalt	6	2.2		22	5.9	33	0.7
MIL 05035	Mare basalt	142		*8*	21			0.3
NWA 4898	Mare basalt	137						
KREEP impact melt breccia:								
Sayh al Uhaymir 169	Impact melt breccia	206	2.2	15.9	10.7	11.1	65	32.7
	and regolith breccia		2.5	17.4	11.1	7.9	56	8.4
Mixed (feldspathic-basaltic) breccias:								
NWA 773/2700/2727/2977/3160	Olivine gabbro and	1123	0.3	4.7	19.4	26.3	71	1.3
	regolith breccia		0.9	9.0	19.0	13.6	56	2.1
Kalahari 008/ 009	Fragmental breccia and	13,500	n.a.	13	16	8.5	49	n.a.
	regolith breccia	598	n.a.	28	4.5	4.4	64	
EET 87521/ 96008	Fragmental breccia	84	0.8	14	18	8	43	0.9
NWA 3136	Regolith breccia	95	1.2	14	15	10	55	1.3
QUE 94281	Regolith breccia	23	0.7	16	14	8.3	52	0.9
MET 01210	Regolith breccia	23	1.6	17	16	6.1	40	0.9
Yamato 793274/ 981031	Regolith breccia	195	0.7	18	12	8.9	56	1.1
Cacalong Creek	Regolith breccia	19	0.8	21	9	*8*	*60*	4
Yamato 983885	Regolith breccia	289	0.5	22	9	8	62	2
NWA 4472	Breccia	64						
NWA 4485	Breccia	188						
NWA 4884	Regolith Breccia	42						
Dho 1180	Fragmental breccia	115		22.6	9.6			0.9
NWA 2995	Fragmental breccia	538						
SaU 300	Impact melt breccia	153	0.26	20-24				0.46
Feldspathic Breccias :								
ALHA 81005	Regolith breccia	31	0.27	25.9	5.5	8.2	73	0.31
Yamato 791197	Regolith breccia	52	0.34	26.2	6.2	6.1	64	0.34
NWA 001	Regolith breccia	262	0.27	26.4	5.6	5.6	64	0.24
PCA 02007	Regolith breccia	22	0.29	26.5	6.2	6.9	66	0.41
Dhofar 025/ 301/ 304/ 308	Regolith breccia	772	0.30	27	4.9	6.6	71	0.6
Specimen 1153	Regolith breccia		*0.18*	*27*	*5.2*	*3.9*	*57*	n.a.
Dar al Gani 262	Regolith breccia	513	0.21	27.9	4.5	5.5	68	0.39
QUE 93069/ 94269	Regolith breccia	25	0.25	28.3	4.4	4.6	65	0.52
Yamato 82192/ 82193/ 86032	Fragm. / reg. breccia	712	0.19	28.5	4.4	5.2	68	0.20

Dar al Gani 400	Regolith breccia	1425	0.18	28.5	3.6	4.8	70	0.34
MAC 88104/ 88105	Regolith breccia	724	0.24	28.7	4.3	4.1	63	0.39
Dhofar 026/ 457-468	Granulitic breccia	709	0.2	28.8	4.3	4.8	67	0.39
NWA 482	Impact-melt breccia	1015	0.17	29.1	3.8	4.2	66	0.23
Dhofar 302/ 303/ 305/ 306/ 307/ 309/ 310/ 311/ 489/ 730/ 731/ 908/ 909/ 911/ 950/ 1085	Impact melt breccia	1041	*0.14*	*29*	*3*	*5*	*75*	*0.06*
Dhofar 081/ 280/ 910/ 1224	Fragmental breccia	572	*0.12*	*32*	*3.1*	*2.6*	*60*	*0.2*
JaH 348/Dhofar 1436	Regolith Breccia	19/24	0.26	30.8	4.49	3.94		
Dar al Gani 996	Fragmental breccia	12						
Dhofar 490/ 1084	Fragmental breccia	124						
Dhofar 773	Granulitic (?) breccia	459						
Dhofar 925/ 960/ 961	Impact melt / breccia	106						
GRA 06157	Anorthositic breccia	0.8						
LRA 06638	Anorthositic breccia	5.29						
NWA 2998	Anorthositic breccia	163						
NWA 3163	Granulitic breccia	1634						
Dhofar 1428	Granulitic breccia	213						
NWA 2200	Impact melt breccia	552						
NWA 4932	Impact melt breccia	93						
SaU 449	Impact melt breccia	17						
NWA 4819	Regolith Breccia	234			6.4			
NWA 4936	Regolith Breccia	172						
NWA 5000	Regolith Breccia	11528						0.4

ALHA= Allen Hills, EET= Elephant Moraine, LAP= LaPaz Icefield, MAC= MacAlpine Hills, MET= Meteorite Hills, NWA= Northwest Africa, PCA= Pecora Escarpment, QUE= Queen Alexandra Range, SaU = Sayh al Uhaymir, JaH = Jiddat al Harasis. Concentration data in italics is uncertain, meteorites listed together are believed to be paired. Mg'= bulk mole % Mg/(Mg+Fe). This table is adapted and extended from Lucey et al. (2006). See also www-curator.jsc.nasa.gov/lunar/index.

1.8. Remote Sensing of the Lunar Surface

Remote sensing is the determination of the physical or compositional state of a surface without physical contact. While the parameters derived remotely are currently very limited compared to laboratory analyses of lunar samples, remote sensing can offer a synoptic view inaccessible in any other way. The physical topography of the lunar surface has been studied in ever increasing detail since the invention of the telescope at the beginning of the 17^{th} century. Ground-based equipments are still used in remote sensing, although from a lunar point of view the post-Apollo orbiting space probes have proved more enlightening, especially in terms of global-scale compositional data. Compositional remote sensing of the Moon is broadly divided in two categories on the basis of physical technique and

spatial resolution: mineralogical remote sensing utilises spectral analysis of reflected (and potentially emitted) light from the lunar surface to resolve mineralogical parameters at a scale of 10's to 100's of metres, while elemental remote-sensing exploits energy dependent variations in neutron, X-ray or gamma-ray flux to determine elemental compositions to 10's to 100's of kilometres (Lucey et al., 2006). The signal available for mineralogical remote-sensing is much stronger than for elemental analyses; therefore while the former can be studied from Earth (e.g., the visible difference between mare and highland regions) the latter data can only be collected in orbit. The Apollo missions carried the first elemental sensors to the Moon, providing important elemental data for a significant proportion of the lunar surface and setting a baseline for future missions. For example, the Apollo 15 and 16 missions carried gamma and X-ray spectrometers (Pieters and McCord, 1975; McCord et al., 1976; Johnson et al., 1977; Pieters, 1978). Ground-based astronomy and Apollo photography also helped to establish the requirements for spectral (mineralogical) observations. The following text aims to summarise the achievements of post-Apollo remote sensing orbiters.

1.8.1. Galileo (18th Oct 1989 - 21st Sept 2003). In 1990 and 1992 the Galileo spacecraft used the Earth/Moon system for gravity assist manoeuvres to gain enough momentum for its journey to Jupiter. During the first flyby, Galileo imaged the western nearside and parts of the farside that were not illuminated during the Apollo missions, thus becoming the first mission to obtain multispectral images of the Moon since Mariner 10 (Head et al., 1993). These images led to investigations of the crustal diversity of the western hemisphere, the geology of several lunar impact-basins (e.g., the Orientale and South Pole-Aitken basins), the western maria, and related deposits and post-Imbrium impact craters (e.g., Greeley et al., 1993; Head et al., 1993; McEwen et al., 1993; Pieters et al., 1993). During the second flyby, the probe produced multispectral images of the north-central nearside (e.g., Belton et al., 1994).

1.8.2. Clementine (25th January - 3rd May, 1994). This probe had five different imaging instruments on board: a UV-visible camera (415-1000 nm wavelength), a near-infrared (NIR) camera (1100-2690 nm), a long-wave infrared camera for thermal imaging (8000-9500 nm) (Lawson et al., 2000), a laser ranger (LIDAR) high-resolution camera (400-800 nm) and the Star Tracker camera (visible wavelengths, for photographing more distant objects) (Nozette et al., 1994). The lunar objectives of this mission were to assess the surface mineralogy and obtain laser-ranging altimetry from latitudes between 60 ° north and south. Clementine collected multispectral images from almost the entire surface, including detailed images of the south pole region and the lunar farside, revealing the geology of these regions for the first time (Nozette et al., 1994; Shoemaker et al., 1994; Lucey et al., 1995; 1998; 2000; Blewett et al., 1997; Otake and Mizutani, 2006). Laser altimetry allowed for the creation of detailed topographical maps and the identification of ancient multi-ring impact basins, as well as producing sharper views of impact craters (Lucey et al., 1994; Pieters et al., 1994; Spudis et al., 1994) (Figure 1.19). Data collaboration from the altimeter and an S-band microwave transponder (for the collection of gravitational data) also on board allowed the internal shape and structure of the Moon to be uncovered. This data indicate that the farside crust is on average thicker (68 km) than the nearside crust (60-45 km) and that the lunar lithosphere has large density variations, therefore it must support relatively large elastic stresses (Zuber et al., 1994; Wieczorek et al., 2001). Clementine also provided the first hints that there may be water-ice on the Moon. The Moon has a number of permanently shadowed craters near the poles with continuous temperatures of −190 °C, these craters may act as cold-traps for water from incoming comets and meteoroids (e.g., Feldman et al., 1998b). The spacecraft searched for ice using a Bistatic Radar Experiment; S-band radio signals were transmitted through the high gain antenna towards a target on the lunar surface, where they were reflected back and received by a 70 m Deep Space Network (DSN) antenna on the Earth. Frozen volatiles such as water-ice are much more reflective to S-band radio waves than lunar rocks, and

radio waves also have different characteristics when reflected by ice as opposed to silicates. Analysis of the signals returned from orbit 234 showed reflection characteristics suggestive of water-ice in the permanently shadowed areas near the south pole (Nozette et al., 1996).

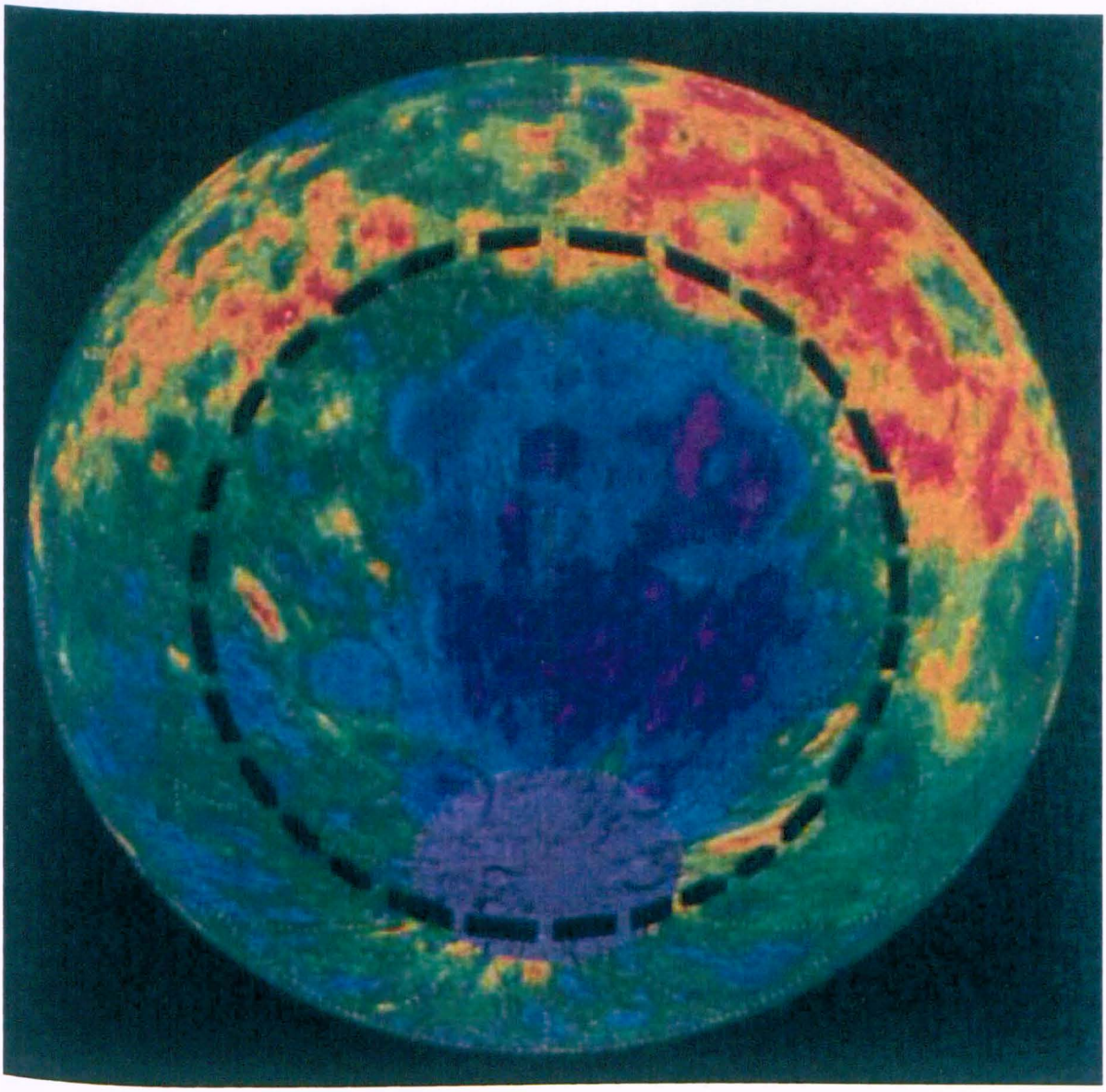

Figure 1.19: Orthographic view of the Moon centred at 50° S, 180° (approximate centre of the South Pole-Aitken basin) with Clementine altimetry colour coded by elevation (red = + 7 km, purple = - 8 km). Average basin depth is approximately 12 km from rim to floor, the grey region near the pole has no altimetry coverage. After Spudis et al. (1994).

1.8.3. Lunar Prospector (7th January, 1998- 31st July, 1999). This spacecraft carried six instruments: a Gamma Ray Spectrometer (GRS), a Neutron Spectrometer, a

Magnetometer, an Electron Reflectometer, an Alpha Particle Spectrometer (APS) and a Doppler Gravity Experiment. The GRS was designed to detect radioactive elements within the lunar crust, most importantly U, Th, and K which were used to accurately map areas rich in KREEP. It was also able to detect elements that emit gamma rays as a result of stray neutron absorption. These neutrons are the product of cosmic ray or solar wind particle impacts. For example, Fe, Ti, O, Si, Al, Mg, and Ca. Therefore, GRS proved a useful tool in distinguishing different lithologies (e.g., Kramer et al., 2008; Binder, 1998; Lawrence et al., 1998; 2003) (Figure 1.20). The Neutron Spectrometer was designed to detect minute amounts of water-ice at a level of less than 0.01 %. This instrument was also used to measure the abundance of hydrogen implanted by solar wind (Feldman et al., 1998a) and to detect elements such as Ti, Fe and incompatible elements (Elphic et al., 1998; 2000). The APS was designed to detect radon outgassing events on the surface of the Moon by recording alpha-particle signatures from the radioactive decay of radon gas and its daughter product polonium (Lucey et al., 2006). These putative outgassing events, in which radon, nitrogen, and carbon dioxide are vented, are hypothesised to be the source of the tenuous lunar atmosphere, and may be the result of low-level volcanic/tectonic activity. However, the APS was damaged during probe launch limiting its analytical capacity, in addition, the Sun spot activity during the months of analysis caused interference to such a degree that no significant results have currently been gained from this instrument. The Doppler Gravity Experiment (DGE) was the first polar, low-altitude mapper of the lunar gravity field - Clementine had previously produced a relatively low-resolution map, but the Prospector DGE obtained data approximately five times as detailed (200 km surface resolution). The purpose of the DGE was to learn about the surface and internal mass distribution of the Moon, accomplished by measuring the Doppler shift in the S-band tracking signal as it reaches Earth, which can be converted to spacecraft accelerations. The accelerations can be processed to provide estimates of the lunar gravity field, from which the location and size of mass anomalies affecting the spacecraft's orbit can be modeled

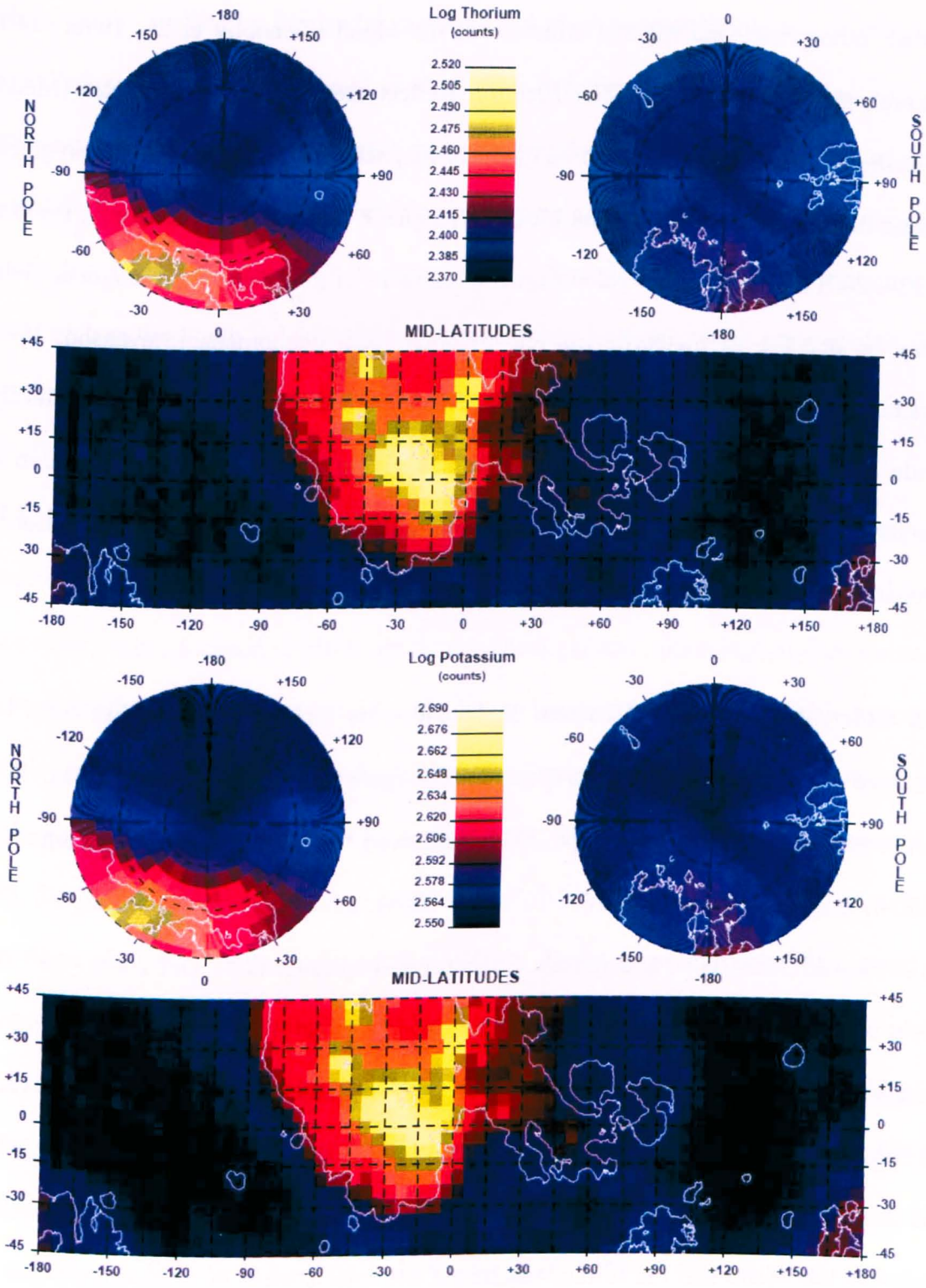

Figure 1.20: Colour-coded maps of **(a)** the log of thorium and **(b)** the log of potassium counting rate as measured by the Lunar Prospector GRS. The rectangular panels show a Mercator projection for latitudes of 45° S to 45° N, and the circular panels show stereographic projections for latitudes of 45° to 90° at the north and south poles. The data are binned into equal area pixels that have a size of 5° latitude by 5° longitude at the equator. Contours of albedo data taken from Clementine data are shown for latitudes between 70° S and 70° N. After Lawrence et al. (1998).

(Binder, 1998). Estimates of the surface and internal mass distribution give information on the crust, lithosphere, and internal structure of the Moon (Konopliv et al., 1998; 2001; Wieczorek and Phillips, 1999). The Electron Reflectometer and magnetometer (MAG) were designed to collect information on the lunar magnetic fields. The Moon has no global magnetic field, but it does have weak localised magnetic fields at its surface (e.g., Hood et al., 1979; 2001). These may be paleomagnetic remnants of a former global magnetic field, or may be because of meteorite impacts or other local phenomena (Stevenson, 1980; Williams et al., 2001; Garrick-Bethell, 2009). This experiment helped map these fields and provide information on their origins, as well as giving an idea of the distribution of minerals on the lunar surface, aiding in the determination of the size and composition of the lunar core, and providing information on the lunar induced magnetic dipole.

1.8.4. Other, More Recent, Missions. In recent years lunar exploration has been less dominated by NASA. First, the European Space Agency (ESA) launched the SMART-1 mission (27th Sept 2003 – 3rd Sept 2006), followed by the Japanese Space Agency's SELENE mission (14th Sept 2007 – 10th June 2009), the Chinese probe Chang'e-1 (24th Oct 2007 – 1st Mar 2009) and India's Chandrayan-1 mission (22nd Oct 2008 - 29th Aug 2009). At present the US Lunar Reconnaissance Orbiter (LRO) is fully operational (launched 18th June, 2009), and on the 9th of October 2009 its Lunar Crater Observation and Sensing Satellite (LCROSS) confirmed the presence of water-ice in the lunar regolith. This enhanced flux of lunar missions is paving the way for combined international efforts to explore the Moon and the further reaches of the solar system in the coming years and decades. Such efforts are likely to be multi-national in approach, utilising both robotic and human exploration techniques. SELENE and Chang'e-1 focused on high resolution imaging of the lunar surface and the lunar surface environment; in particular SELENE's topographical videos and images show craters and other surface detail with a resolution better than 10's of meters. In addition, new telescopic equipment on Earth, along with the

Hubble space telescope and LRO have allowed us to view details as small as the debris left behind on the surface by the lander missions and map separate lithologies on the surface (e.g., Robinson et al., 2007; Araki et al., 2009). A future Lunar space station will allow astronauts to acclimatise and practice maneuvers under low gravity conditions, as well as providing a unique stage for scientific experiments and astronomical observations. In addition, a permanent base will facilitate thorough exploration and sample return from areas, such as the South Pole-Aitken basin, which may hold the key to lunar evolution and therefore planetary body accretion in the solar system.

1.8.5. Remote Sensing Analysis of Mare Basalts. The above mentioned orbiting missions have returned multispectral data to Earth, and in particular, the Clementine and Lunar Prospector probes focused on determining the chemical and mineralogical composition of the lunar surface in an attempt to relate this data to lunar samples here on Earth. Successful completion of these objectives resulted in the production of global maps of elements such as Th, K, Ti, Fe, Ca, Si, Mg, Al (e.g., Kramer et al., 2008; Binder, 1998; Lawrence et al., 1998, 2003; Shoemaker et al., 1994; Nozette et al., 1994; Lucey et al., 1995, 1998, 2000; Blewett et al., 1997; Otake and Mizutani, 2006). These maps not only highlighted the difference between the anorthositic highlands terrain and the mare basalts but also picked up distinct anomalous regions within the basalts, specifically the Procellarum KREEP terrain (PKT). This region differs from others on the Moon primarily by its KREEP-rich geochemistry and prolonged volcanic history. Mare basalts erupted here from at least 4.2 Ga (data from an Apollo 14 breccia clast - Taylor et al., 1983) to 900 ± 400 Ma (calculated via crater counting - Schultz and Spudis, 1983). Data from Lunar Prospector shows the surface abundance of incompatible elements such as Th, K, Gd, Sm, and by inference, the other elements which make up KREEP, are highly concentrated in this region, which encompasses Oceanus Procellarum, Mare Imbrium and the adjoining mare highlands (Lawrence et al., 1998, 2000; Elphic et al., 2000) (Figure 1.20). Oceanus Procellarum

represents the largest contiguous expanse of mare basalts despite the fact that the region possesses a relatively thick crust, therefore, it is not an obvious basin setting (Wieczorek et al., 2001). More than 60 % of all mare basalts by area are located here, and although only ~20 % of mare basalts have TiO_2 content above 5 wt %, more than half of the PKT basalts have at least this amount (Haskin et al., 2000). Prolonged volcanic activity along with incompatible-element enrichment seem to suggest the final dregs of the lunar magma ocean accumulated below this region, although the reason for this is still disputed (e.g., Warren, 2001; Parmentier et al., 2002). High abundance of radioactive elements within the PKT would have helped to prolong volcanic activity (Wieczorek and Phillips, 2000; Parmentier et al., 2002) but the reason for earlier eruptions in this region is less certain. Whatever the reasons, the PKT is one of the most geologically varied areas of the Moon. Coincidentally, all of the Apollo basalts were either collected from within this region (Apollo 12, 14 and 15) or from areas close to its boundaries (Apollo 11 and 17 – Apollo 16 collected no basalts). There is, therefore, a good record of basaltic eruptions in this region but other regions are underrepresented in the sample collection. As remote sensing has shown that the PKT is anomalous, the Apollo collection is believed to be biased towards incompatible-element and Ti-rich samples. However, this bias can be partly eliminated by taking into account remote-sensing data and lunar meteorites.

1.9. The Ages of Mare Basalts

Global element maps derived from remote-sensing data have been used in conjunction with high-resolution visible wavelength photography to determine the ages of compositionally different mare regions via crater counting. A number of results centred on the Imbrium basin suggest that the low-Ti mare basalts are older than the high-Ti (e.g., Bugiolacchi et al., 2006, 2008; Otake and Mizutani, 2006). This relationship is contradicted by isotopic measurements of the Apollo samples, where the high-Ti basalts are older than the low-Ti basalts (Table 1.4). However, the research of Hiesinger et al. (2003, 2010) suggests that on

a global scale there is no relationship between mare-basalt TiO_2 content and age. This research indicates that the older mare basalts are located predominantly on the eastern and southern nearside, and in patches of mare peripheral to the larger maria, in contrast to the younger basalts which are located on the western nearside (Oceanus Procellarum). While the crater counting method is acknowledged to be less accurate than laboratory-based sample analysis, both methods appear to roughly agree at the Apollo and Luna sites. However, it should be noted that the laboratory based analyses were used to calibrate the crater counting method on the Moon.

Table 1.4: Crystallisation ages of mare-basalt flows at the Apollo and Luna landing sites.

Landing Site	Basalt Type	Absolute Age (Ga)
Apollo 11	High-K basalts	**3.58 ± 0.01**
	Low-K basalts, group B1,3	3.70 ± 0.02
	Low-K basalts, group B2	**3.80 ± 0.02**
	Low-K basalts, group D	3.85 ± 0.01
Apollo 12	Olivine basalt	3.22 ± 0.04
	Pigeonite basalt	3.15 ± 0.04
	Ilmenite basalt	3.17 ± 0.02
Apollo 15	Olivine Normative basalt	**3.30 ± 0.02**
	Quartz Normative basalt	3.35 ± 0.01
	Green Glass	~3.3 - 3.4
	Yellow Glass	3.62 ± 0.07
Apollo 17	High-Ti basalt, group A	**3.75 ± 0.01**
	High-Ti basalt, group B	3.70 ± 0.02
	High-Ti basalt, group C	**3.75 ± 0.07**
	High-Ti basalt, group D	3.85 ± 0.04
	Orange glass	~3.5 - 3.6
Luna 16	High-Al basalt	3.41 ± 0.04
Luna 24	Very Low-Ti (VLT) basalt	**3.22 ± 0.02**
Lunar meteorite Asuka 881757	Basalt (gabbroic)	3.87 ± 0.06
Lunar meteorite Kalahari 009	Basalt (crypto-mare)	4.35 ± 0.15
Lunar meteorite LAP 02205	Low-Ti basalt	2.99 ± 0.01

Data compiled from various sources; see Snyder et al. (2000); Burgess and Turner (1998); Nyquist and Shih (1992); Dalrymple and Ryder (1993); Terada et al. (2007); Rankenburg et al. (2007); Spangler et al. (1984) and references therein. Crater counting ages for surface flows are given in bold (Stöffler and Ryder, 2001).

1.10. Research Background - Unanswered Questions

Previous research into our Moon's formation and evolution has produced a number of theories, some more widely accepted in the community than others. A number of these

theories attempt to define the conditions required for the creation of specific mare-basalt types and, therefore, establish their source region characteristics. Neal and Taylor (1992) provided the first thorough review of the post-Apollo, sample-based research and attempted to summarise the most probable formation conditions for each mare-basalt type. Since then, a number of authors have focused on a single type of basalt or the formation of basalts at a single site, but none have tried to further clarify the genetic relationships between different basalt types as a whole. Many workers argue that because of the limited number of sampling sites, and the location of these sites within or close to the PKT (section 1.8.5), further sample return missions are needed to comprehensively establish the composition and formation conditions of mare basalts. However, of the 382 kg of material which has been collected by the Apollo astronauts, a surprisingly high percentage has never been analysed in detail. In addition, it is often the case that samples which were initially studied in the 1970's were subsequently passed over for more recently returned Apollo samples (e.g., some Apollo 15 samples may have been passed over for newly returned Apollo 16 samples), and, more recently, newly discovered meteorites. As a result, individual Apollo samples commonly have patchy research histories. For example, the major- and minor-element chemistries of most samples have been analysed (commonly twice or more in the 1970's) but trace-element data are often missing or incomplete. In some cases, even the basic mineralogy of a sample has not been recorded, and numerous samples have not been dated. Therefore, although a more varied sample collection is needed, the complete analysis of the present Apollo collection - as well as utilisation of new state-of-the-art techniques, for chronological, mineralogical and chemical analysis - will help to clarify mare-basalt relationships and answer some of the questions left open by previous research. Some of these unanswered questions include:

1. Do all mare basalts fit into the classification of Neal and Taylor (1992) - is further subdivision necessary?

2. How did high- and low-Ti mare basalts evolve – is the mantle overturn model in line with genetic relationships observed between the two sample types?

3. Do certain types of mare basalt (e.g., the Apollo 14 high-Al basalts) originate from source regions containing a KREEP component, or was KREEP-rich material assimilated by the melt? Could there have been overlap between KREEP and mare basaltic activity on the Moon?

4. What are the precise parental melt compositions for each mare-basalt group? What does this suggest about the source region composition?

5. Is the Giant-Impact hypothesis still the most suitable hypothesis for the formation of the Earth-Moon system?

1.11. Research Aims and Objectives

The main aim of this research is to determine the genetic relationships between high- and low-Ti lunar mare basalts in terms of petrology, mineralogy, chemistry and chronology using a set of Apollo mare-basalts.

Objectives:

1. Determine the mineralogy and petrology of the samples (from polished thin-sections) using optical microscopy, secondary electron microscope and electron microprobe techniques.

2. Classify each sample (rock chips) in terms of bulk-rock major- and trace-element compositions using data acquired from solution ICP-AES and ICP-MS, respectively.

3. Ascertain the mineral trace-element chemistry in each sample (from polished thin-sections) using the laser ablation ICP-MS technique.

4. Acquire U-Pb/Pb-Pb ages of appropriate samples (from polished rock thin-sections) using sensitive high-resolution ion-microprobe (SHRIMP) analysis of phosphates.

5. Use laser fluorination mass-spectrometry to measure the three oxygen isotope composition of powdered lunar samples, and resolve the differences in $\delta^{18}O$ between low- and high-Ti mare basalts. Compare $\Delta^{17}O$ values of lunar basalts with those of terrestrial samples in an attempt to further evaluate the Giant-Impact theory.

6. Use the above acquired dataset, along with that of previous works, to compare, contrast and group lunar basalts, and then establish the petrogenesis of these samples in the context of lunar magma ocean crystallisation and differentiation.

1.12. Samples

Basalt samples were obtained from NASA's Apollo sample collection at JSC (Table 1.5). We received one thin section (30 μm thickness) and one rock chip (250 mg) for each

Table 1.5: The sample set.

Mission	Sample	Type
Apollo 11	10017	High-Ti, Low-Al, High-K: Type A
	10020	High-Ti, Low-Al, Low-K: Type B3
	10049	High-Ti, Low-Al, High-K: Type A
	10050	High-Ti, Low-Al, Low-K: Unclassified
	10057	High-Ti, Low-Al, High-K: Type A
	10058	High-Ti, Low-Al, Low-K: Type B1
	10072	High-Ti, Low-Al, High-K: Type A
Apollo 12	12016	Low-Ti, Low-Al, Low-K: Ilmenite
	12040	Low-Ti, Low-Al, Low-K: Olivine
	12047	Low-Ti, Low-Al, Low-K: Ilmenite
	12051	Low-Ti, Low-Al, Low-K: Ilmenite
	12052	Low-Ti, Low-Al, Low-K: Pigeonite
	12064	Low-Ti, Low-Al, Low-K: Ilmenite
Apollo 14	14053	Low-Ti, High-Al, Low-K
Apollo 15	15016	Low-Ti, Low-Al, Low-K: Olivine-Normative
	15386	KREEP
	15555	Low-Ti, Low-Al, Low-K: Olivine-Normative
Apollo 17	70017	High-Ti, Low-Al, Low-K: Unclassified
	70035	High-Ti, Low-Al, Low-K: Unclassified
	70215	High-Ti, Low-Al, Low-K: Type B2
	74275	High-Ti, Low-Al, Low-K: Type C
	75055	High-Ti, Low-Al, Low-K: Type A

sample. Sample selection was based on previously published information regarding basalt type, age, and the location it was collected from, with the aim of analysing as many different variations of basalt from as many different lunar sites as possible. Our sample set consists of seven Apollo 11 and five Apollo 17 basalts (high-Ti), six Apollo 12, one Apollo 14 and two Apollo 15 basalts (Low-Ti), and one Apollo 15 KREEP basalt.

2. METHODOLOGY

This chapter provides details of all the data collection techniques utilised during this research, and explains the rationale behind their selection.

2.1. Thin-Section Imaging

2.1.1. Optical Microscopy. One of the most important factors in the analysis of any rock thin-section is to know which area of the section is under investigation. Therefore, a detailed image of the whole section is essential. During the course of our research all rock thin-sections were initially studied using an optical microscope at × 5 magnification. Plain- and cross-polarised transmitted light were used to distinguish silicate minerals; reflected-light microscopy was used to study opaque phases (e.g., oxides, sulphides and metals). Low-magnification optical microscope images were also useful as a guide when observing individual thin-sections at higher resolution using the JEOL 5900LV scanning electron microscope (SEM) at the Natural History Museum. These high-resolution images were used for calculating modal mineralogy, textural observations, and to serve as maps for electron microprobe analysis (section 2.2).

2.1.2. Scanning Electron Microscopy. The SEM technique uses an electron beam focused onto the surface of a sample (thin-sections in our case). Electrons which originate in the electron beam, and are reflected (or back-scattered) from the sample surface via elastic scattering, are detected by a backscatter detector. These data are displayed as a greyscale image, where bright areas on the image represent a high number of backscattered electrons, and dark areas represent low levels of electron backscatter (i.e. high levels of electron absorption). The higher the proportion of heavy elements (e.g., Fe) within a material, the more electrons will be backscattered, as there is less space between the nuclei of heavy

atoms for an electron to pass through. Therefore, areas with a high percentage of heavy elements will appear brighter on a backscatter image, and those with mostly light elements (e.g., Si, Mg, Al) will appear darker. For this reason the backscatter detector is used to detect the contrast between areas of different chemical composition (Goldstein et al., 1981).

The elemental composition of a sample can be determined using an energy dispersive X-ray spectrometer (EDS). This spectrometer contains an Li-doped silicon crystal detector, maintained at very low temperatures using liquid nitrogen to avoid damage. At rest, an atom within the sample contains ground state (or unexcited) electrons in discrete energy levels (electron shells) bound to the nucleus. The incident electron beam may excite an electron in an inner shell, ejecting it from the shell while creating an electron hole at the electron's former position. An electron from an outer, higher-energy shell then fills the hole, and the difference in energy between the higher-energy shell and the lower energy shell is released in the form of an X-ray (Figure 2.1). The number and energy of the X-rays emitted from a specimen can be measured by the EDS - X-rays create currents of different strengths at the silica crystal detector, depending on their wavelength. As the energy of the X-rays is characteristic of the difference in energy between the two electron shells, and of the atomic structure of the element from which they were emitted, this allows the elemental composition of the specimen to be measured (Goldstein et al., 2003). X-ray images can be built up for a whole thin-section giving the relative abundance (in greyscale) of different elements in any given area. Assigning false colours to a number of elements allows false colour images to be produced, where different mineral phases can be distinguished. Data collection and analysis with EDS is a relatively quick and simple process because the complete spectrum of X-ray energies is acquired simultaneously. After areas of further interest were identified, the EDS was additionally employed to produce spot spectra, yielding a quantitative estimate of major-element composition to within ~ 0.1 wt %.

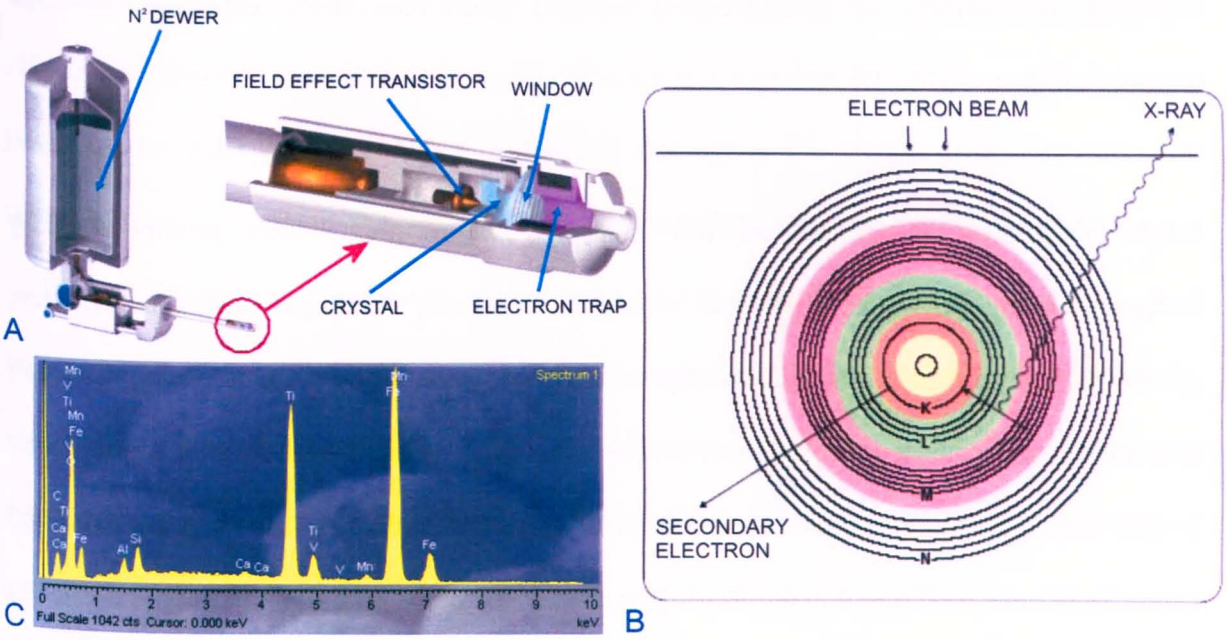

Figure 2.1: Energy dispersive X-ray spectrometry in a scanning electron microscope. **(a)** Internal structure of the EDS detector (image revised from xraymicroanalysis.com). **(b)** EDS works by detecting X-rays emitted from a specimen because of changes in atomic electron energy states caused by the SEM electron beam. Atomic ground state electrons within the inner K shell are excited by the incident electron beam and emitted as secondary electrons, creating an electron hole within the low energy K-shell. An electron from a higher energy outer shell subsequently fills this hole, releasing its extra energy in the form of an X-ray (image from xraymicroanalysis.com). **(c)** Example EDS spectrum from INCA software, showing counts vs. energy (keV) for separate elements at a specific point on a sample.

Secondary electron detectors collect low-energy (<50 eV) secondary electrons, that are ejected from the inner K-orbitals (electron shells) of the specimen atoms by inelastic scattering interactions with beam electrons (Goldstein et al., 1981). Because of their low energy, these electrons originate within a few nanometers from the sample surface. Therefore, images produced in this way are useful for detecting surface topography and contamination.

Both backscatter and X-ray images were produced for this study, with × 200 magnification or greater (section dependent) yielding a surface resolution of 1-10 μm. This high spatial

resolution is essential for distinguishing mineral grain boundaries, especially in fine-grained samples.

2.1.3. Calculation of Mineral Modes. X-ray elemental images were processed using Oxford Instruments INCA software, which automatically montages individual frames, generating a high-resolution digital image of each thin-section. INCA's phasemap function also allows for accurate calculation of modal mineralogy using a trigonal plot of elements; in this way the volume percentage (vol %) of different mineral phases can be extracted from X-ray images. For example, plotting Si, Fe and Al helps distinguish clinopyroxene (Si and Fe-rich), olivine (more Si and Fe-rich than clinopyroxene) and feldspar (Si and Al-rich) into three clusters. High spatial-resolution in these images ensures grain boundaries are sharp, therefore, very few pixels show mixed signatures (e.g., half feldspar, half clinopyroxene). The error on these modal calculations is ~ 1 vol %, mainly because the boundaries of each group on the trigonal plot have to be judged by eye. This error is also dependant on the grain size of a sample; the larger the mineral grains the fewer boundary areas and so the lower the error. However, the backscatter images are available as a guide (Figure 2.2) which helps reduce the error. The modes of minor minerals were also calculated via SEM X-ray image pixel counting using Photoshop software. If a large discrepancy was detected between the results of these two methods for a particular sample, the phasemap modes were recalculated until all minor minerals agreed to within 0.5 vol %. Prior to modal calculations, reliability tests were performed for both methods based on reproducibility. These tests showed that the INCA phasemap method was more accurate than the pixel counting method for our samples.

2.2. Electron Microprobe (EMP) Analysis

Once the sections were imaged in detail, areas of interest were identified. Electron microprobe analysis uses wavelength dispersive X-ray spectrometry (WDS); a technique

that has a much improved spectral resolution in comparison to EDS. This high resolution allows for enhanced chemical analysis of minerals in a polished thin-section, with detection limits of the order of 0.01 wt % and minimal damage to the sample (only the outer few microns directly beneath the beam, which is generally 1 μm in diameter). The Cameca SX50 and SX100 are wavelength dispersive electron microprobes capable of automated elemental analysis of materials in polished thin-sections or blocks. Analysis is achieved by focusing a beam of electrons onto the sample surface, producing secondary X-rays with wavelengths or energies characteristic of the elements present. The analysis of standard materials is required prior to every analytical run, to allow for accurate wavelength peak area comparisons, hence elemental identification (Long, 1967). Quantitative analyses can

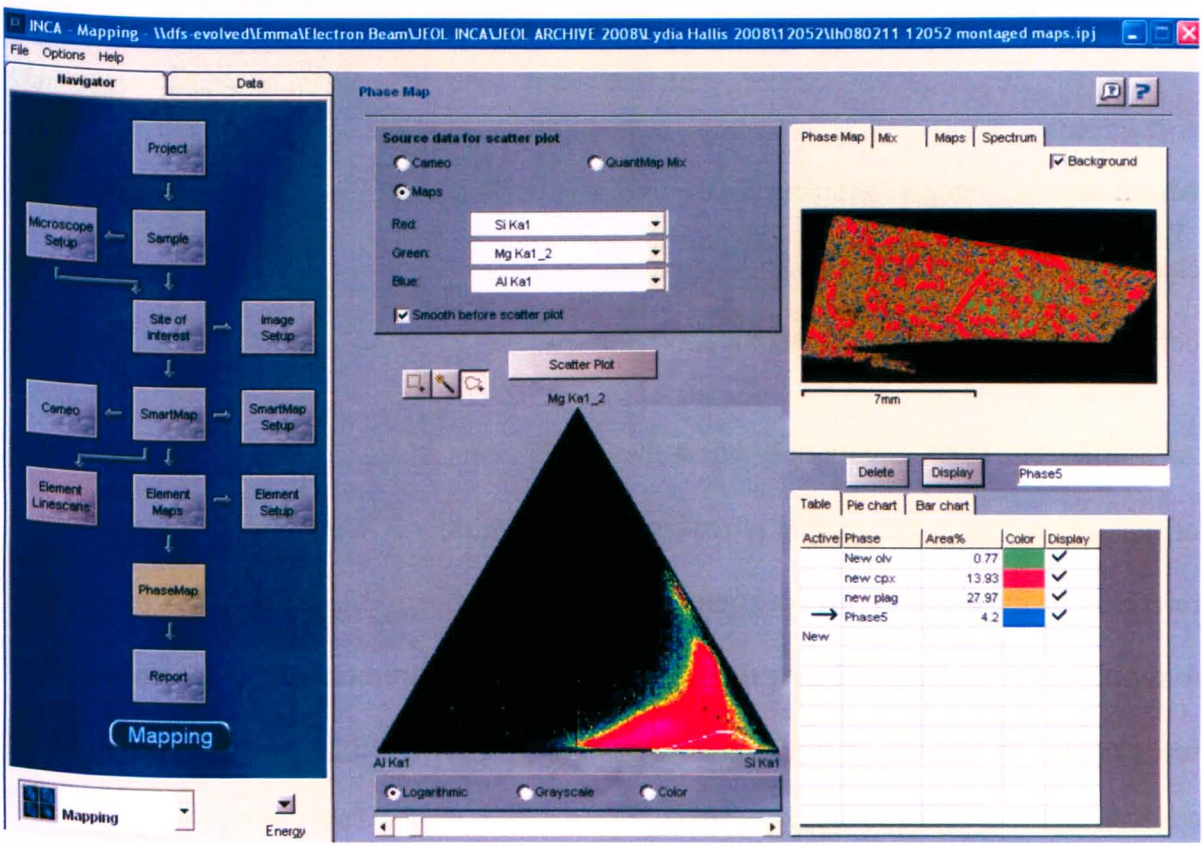

Figure 2.2: INCA software phasemap function as a tool for the calculation of modal mineralogy. The trigonal plot (central) shows pixel density for certain ratios of Mg, Si and Al where pink represents the highest density and blue the lowest. The white line is drawn by hand to estimate group boundaries. Precision can be enhanced by comparing the outlined group with mineral phases on a backscatter electron image of the sample (top right). In this example the outlined phase is mesostasis, highlighted in blue on the backscatter image.

be obtained for elements with an atomic number greater than five (boron) to within 0.02 wt %. In addition to point analysis, X-ray elemental maps can be obtained showing the spatial distribution of elements in selected areas of the sample surface, hence false colour maps can be generated as with the JEOL 5900LV. The difference in the data collection technique with WDS influences the collection period, as the spectrum is acquired sequentially rather than simultaneously (Figure 2.3). The Natural History Museum's Cameca SX50 has four WDS multi-crystal spectrometers, and the Cameca SX100 has five. These spectrometers function by utilising different analysing crystals of specific lattice spacing to diffract the characteristic X-rays from the sample onto the detector (Figure 2.3). The wavelength of the X-ray diffracted into the detector can be selected by varying the position of the analysing crystal with respect to the sample, according to Bragg's law:

$$n\lambda = 2d \sin \theta \quad (1)$$

where; n = an integer referring to the order of diffraction; λ = the wavelength of the characteristic X-ray; d = the lattice spacing of the diffracting material; θ = the angle between the X-ray and the diffractor's surface.

As a diffracted beam occurs only when these conditions are met, interference from peaks of other elements in the sample is reduced. However, only X-rays from one element at a time may be measured on the spectrometer, and the position of the crystal must be changed to tune to another element, hence the need for multiple spectrometers. Popular crystal types include lithium fluoride (LIF), pentaerythritol (PET) and thallium acid phthalate (TAP). Each crystal type covers a range of elements.

2.3. Laser Ablation ICP-MS

The concentration of trace-elements in mineral grains can be measured via time-resolved analysis using laser-ablation inductively-coupled-plasma mass-spectrometry (LA-ICP-

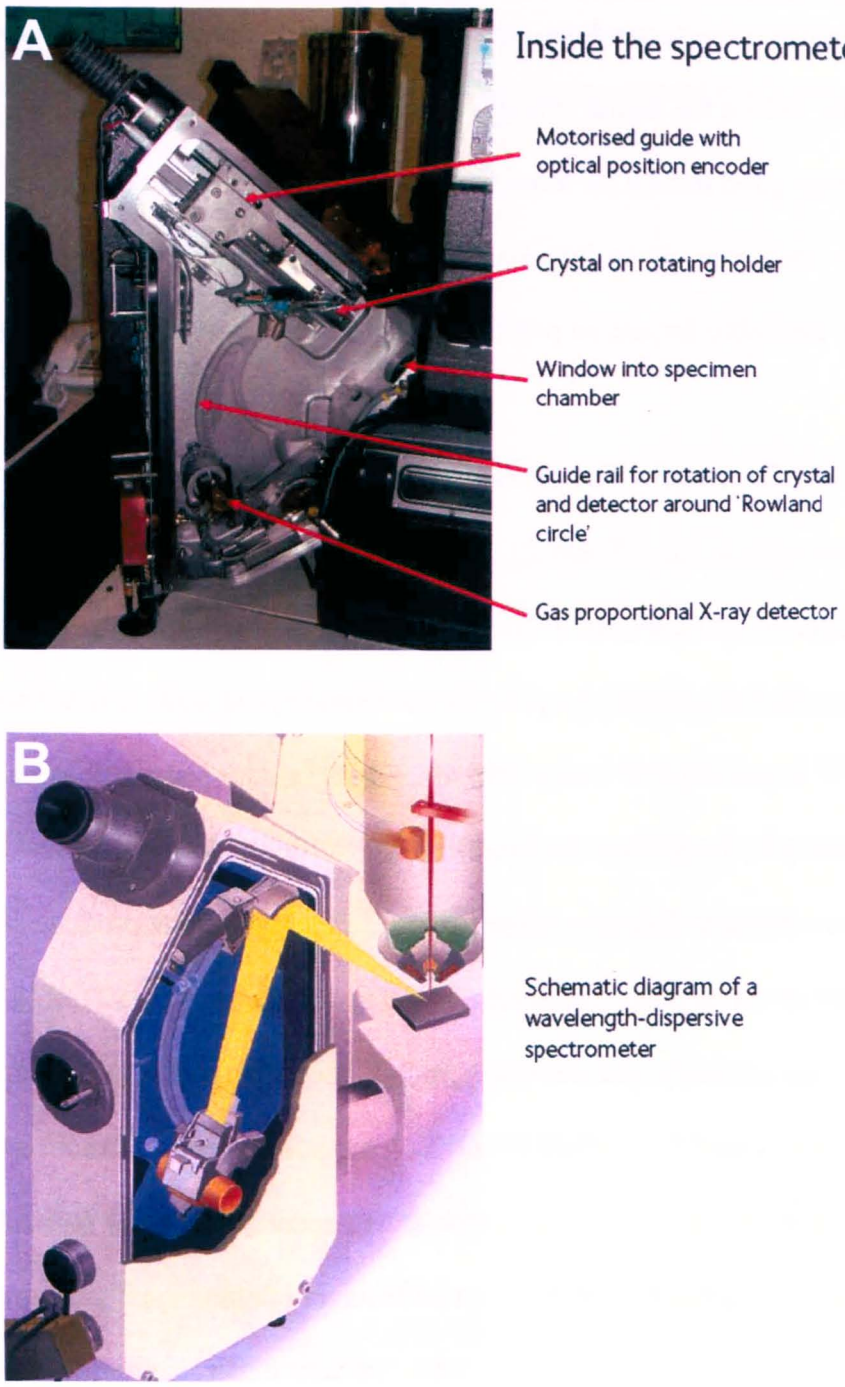

Figure 2.3: The electron microprobe. **(a)** Inside one of the four WDS detectors of the Natural History Museum's Cameca SX50 (image courtesy of the EMMA laboratories, NHM). **(b)** Diagram of a WDS showing the electron beam over the sample causing X-ray emission; these X-rays are subsequently deflected by the crystal and X-ray counts recorded via the detector (image courtesy of Oxford Instruments).

MS). This technique is usually carried out on thick sections (> 60 μm thickness compared to thin-section thickness of ~ 30 μm) to extend the analysis time, hence produce a stronger

signal. However, because of the precious nature of our samples, thick sections were not available. Therefore, we decided to analyse the thin-sections that we were allocated. Although this did reduce the signal strength to below detection limits for a few samples, we were able to obtain good results for most samples. Despite the fact that laser ablation leaves pits within the specimen, it is largely accepted as a non-destructive technique. It is therefore highly desirable for use on precious samples, such as Apollo mare-basalts.

2.3.1. LA-ICP-MS Technique. The instrument at the Open University is an Agilent 7500s ICP-MS coupled with a New Wave 213 Nd:Yag deep UV (213 nm) laser system. The technique involves *in-situ* analysis of individual mineral grains by ablating with a pulsed laser beam. Samples are ablated in a pure He atmosphere, the analyte is carried in He and then mixed with Argon via a Y connector before entering the plasma. Plasma is produced inside the ICP torch by creation of an intense magnetic field - Ar gas is ionised in this field and the inelastic collisions between these ions and other Ar atoms produce stable plasma with a temperature of around 7000 K. The use of He gives a 2-3 fold increase in sensitivity, and significantly reduces background intensity (e.g., Günther and Heinrich, 1999). The plasma is used to produce ions which are subsequently introduced to the mass spectrometer. These ions are separated and collected according to their mass/charge ratios; therefore ICP-MS is extremely sensitive to a wide range of elements.

2.3.2. Analytical Protocol. For this study, data were acquired across the mass range from ^{7}Li to ^{238}U and the total time for each analysis was 240 s. During the first 120 s, the gas blank was measured, during this time the laser beam was blocked by a shutter. This shutter was then removed, ablation takes place for 60 s and the transient signals from the analyte are acquired for a further 60 s. A 60 s wash out period was carried out between analyses. With a 60 μm beam spot, detection limits are ~10 ppb for lithophile trace-elements (see Table 2.1 for operating conditions). Synthetic doped glass NIST 612 was used

Table 2.1: LA-ICP-MS operating conditions (after Hammond, 2006).

	Conditions used
Scan parameters	
Detection modes	Dual (analogue and pulse detector are cross-calibrated prior to each session)
Dwell time	10 - 100 ms
Integration time	10 ms
Laser	
Laser	UP-213 (New Wave Research)
Type	Nd:YAG frequency quintupled
Wavelength	213 nm
Repetition rate	10 Hz
Spots	
Ablation duration	60 s
Spot size	80 μm
Energy	0.8 mJ

for external calibration (Pearce et al., 1997), while calcium acted as an internal standard by comparing LA-ICP-MS CaO wt % abundance with previously measured EMP CaO wt % abundance. The external NIST glass standard was analysed twice at the start of each run, after every 8 or 9 ablations, and twice at the end of each run, showing an analytical precision of 3 %. Detection limits are usually between 1 and 10 ppb (Hathorne et al., 2003). Raw data were reduced using Glitter software (Van Achterbergh et al., 2001), which enables the user to view each signal and set the limits for background and aerosol counts (Figure 2.4). This process is very important as often spurious results (for example, data spikes resulting from mineral inclusions) can affect the dataset if not removed. There is also a risk that the laser beam can penetrate to underlying mineral phases or the glass slide (especially with thin-section analysis), but this problem can be overcome by careful selection of the time resolved signal.

2.4. Sample Preparation for Bulk-Rock Analysis

Each ~ 250 mg sample rock chip was powdered for bulk-rock chemical analysis. A clean laboratory suite at the Open University, used only for the preparation and analysis of

meteorite samples, was employed for this process (Figure 2.5). We utilised the main area of the laboratory, which operates well in excess of Class 1000 (< 1000 particles in the air

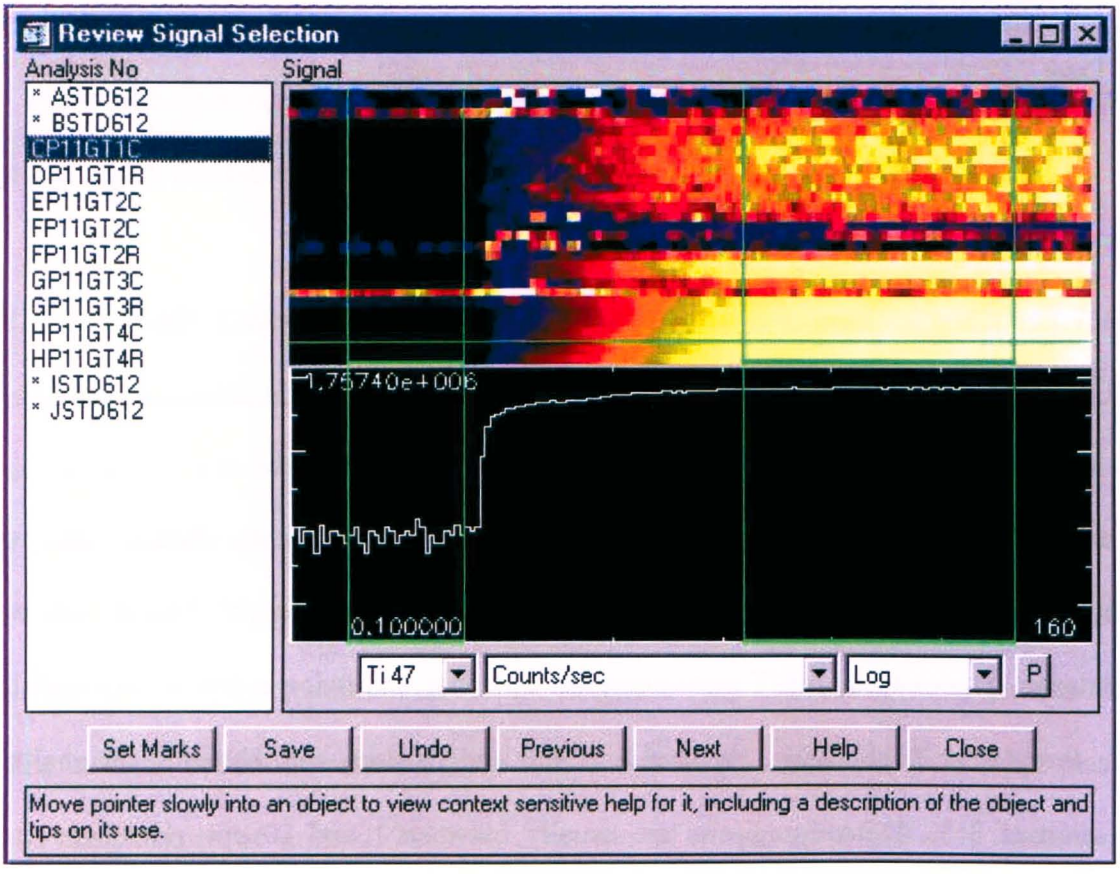

Figure 2.4: An example of Glitter's signal selection application. The green boxes denote selected sections of background (on the left of the black screen) and aerosol signal (on the right of the black screen) which will be included in the final dataset. This signal processing is needed to remove any spurious data.

per cm^3), meaning terrestrial contamination is kept to a minimum in this facility. Two agate (hydrated SiO_2) pestles and mortars were used for grinding - in both cases these had only ever been used to grind Martian meteorites, hence removing the risk of metal contamination (as would be the case if they had been used for grinding undifferentiated or iron meteorites). The cleaning procedure for these pestles and mortars is listed below:

1. The pestle and mortar was initially cleaned with acetone and heavy duty synthetic wipes packed in a clean environment. This process was performed to remove any visible remains of previous crushing.

Figure 2.5: Preparing sample powders in the clean laboratories of the PSSRI department at the Open University. **(a)** Clean suits and gloves were worn at all times, **(b)** the samples were crushed using an agate pestle and mortar and **(c)** each chip was weighed on a weighing plate both before and after crushing.

2. Approximately five minutes of grinding with de-ionised water and pure quartz sand was performed to remove any detritus remaining on the agate surface.

3. The quartz sand was removed by washing with copious amounts of de-ionised water.

4. The pestle and mortar were re-cleaned with acetone

5. The pestle and mortar were cleaned with IPA (a 70/30 mix of IPA and de-ionised water).

6. A pure N_2 source was utilised to visibly dry the pestle and mortar, which was then wrapped in pure aluminium foil and placed in an oven at 150 °C for 20 minutes.

7. After 20 minutes the pestle and mortar was removed from the oven and left to cool for a further 20 minutes (still wrapped in foil).

8. The bench and surrounding area were cleaned with IPA before a layer of pure aluminium foil was placed over the bench to create a new working area.

9. Two pestles and mortars were used in rotation to speed up the process.

10. All foil and wipes were used only once and then discarded. Latex gloves were replaced every time a new sample was crushed.

The above process was performed before every chip was powdered. The following process was then completed:

1. The chip was placed on a piece of pure aluminium foil and weighed to an accuracy of 0.01 g on a weighing plate (Figure 2.5c).

2. It was transferred to the clean pestle and mortar and crushed (this took between 5 and 15 minutes depending on the hardness of the sample). At this point the relative hardness of the sample was recorded and specific notes taken.

3. To prevent any parts of the chip jumping out of the pestle and mortar a pure aluminium foil wall was created around the perimeter to deflect escaping particles back into the vessel.

4. Once crushing was completed (when the powder achieved a chalky texture) it was placed within a previously weighed air tight vial. These vials had never been used before and had previously been washed in alcohol and baked dry in an oven overnight. Transfer was achieved by tipping the powder from the mortar onto a piece of thicker pure aluminium foil, folded to have a v-shaped cross-section. The v-shaped foil rested

on top of a third layer of foil ~10 cm in diameter (to catch any spilt powder). Once on the v-shaped foil the powder was tipped into the vial (with the use of tweezers cleaned with IPA). Once the vial contained all the powder it was re-weighed, thus the amount of material lost during powdering (if any) could be recorded.

5. The vial was labelled and stored in the laboratory until required for further analysis.

6. If at any point during this process some particles escaped they were picked up from the foil workspace using tweezers (in the case of solid particles), or if the spillage occurred after powdering the second layer of foil could be raised and the powder again tipped onto the v-shaped foil funnel.

2.5. Inductively Coupled Plasma Atomic Emission Spectroscopy (ICP-AES)

ICP-AES can be used to accurately determine the major-element chemistry of bulk-rock powders. Although it is a destructive technique, only a small amount of sample is needed to produce a large volume of sample solution, which can be stored and re-analysed years later. The vast majority of our samples had not been analysed for major-elements since the 1970's. Therefore, for the sake of completeness, it was decided to create a dataset with uniform conditions and smaller errors than the previous datasets, which were obtained in numerous laboratories employing different techniques.

*2.5.1. **Sample Digestion.*** Before the samples were analysed via ICP-AES a delicate procedure was followed in the wet chemistry laboratory of the Natural History Museum to dissolve each sample powder in an acid solution:

1. 40 mg of the powdered sample was weighed out into a clean platinum-gold alloy crucible (90 % Pt, 10 % Au) using a weighing plate with a precision of up to 1 μg.

2. The powder was then treated with a few drops of de-ionised water (with a resistivity of 18 Ω) and ½ ml concentrated nitric acid (HNO_3) and placed in a sand bath at 80 °C until all liquid evaporated. This process removes any metallic iron (Fe^0) and sulphides which may react with the crucible on heating. However, sulphides and HNO_3 react to form volatile H_2S which evaporates along with the liquids, therefore bulk-rock sulphur content cannot be reliably analysed using this technique.

3. A second dose of HNO_3 was added to any sample acquiring a yellow colour after evaporation of the liquid.

4. Once dry, the powders were removed from the sand bath and left to cool. 120 mg of lithium meta-borate was then weighed out into the crucibles, in addition to the 40 mg of dried sample powder.

5. Each crucible in turn was then heated over a Bunsen burner to ~ 1000 °C and the melt was slowly manipulated until it resembled a glass bead, a process known as fusion. Lithium meta-borate reacts with the powdered sample at high temperatures to ensure all the grains melt during fusion, even those with melting temperatures higher than 1000 °C.

6. Once the glass bead has formed and encapsulated all material within the crucible (normally after 10-15 minutes heating) the bead was manipulated onto the wall of the crucible and removed from the heat. After carefully transferring the crucible to a position above the laboratory sink, de-ionised water was aimed directly at the external wall of the crucible where the bead was fixed. This rapidly cooled the bead which we were then able to remove from the wall with a little tapping on a pre-cleaned heat proof tile.

7. The detached bead was immediately dropped into a corresponding teflon beaker containing 40 ml of 1.56 M HNO_3. This beaker was placed on a magnetic stirring plate and the bead left to dissolve over night (Figure 2.6).

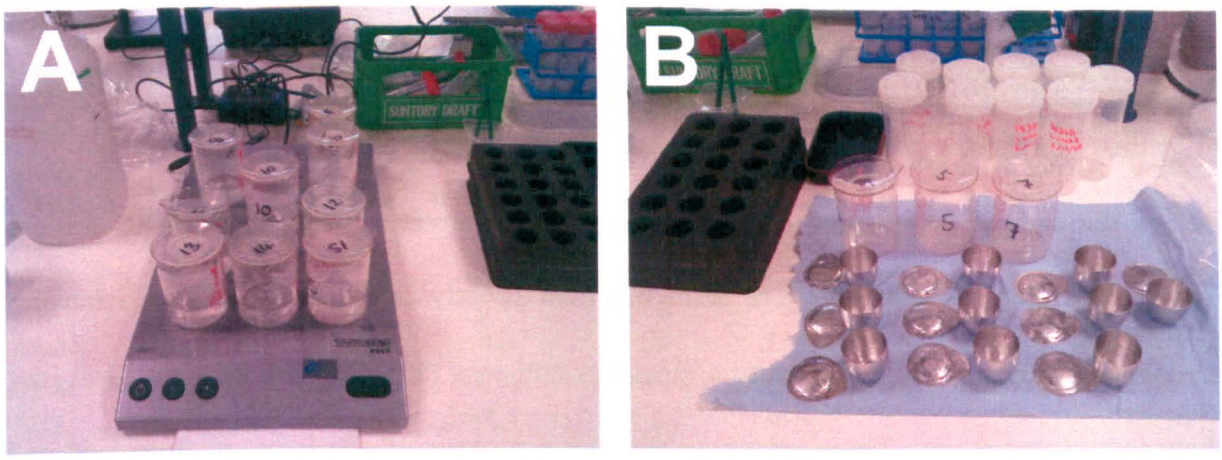

Figure 2.6: Digestion prior to ICP-AES analysis. **(a)** Beakers containing fusion beads and acid solution on a magnetic stirring plate, **(b)** Pt-Au crucibles used for fusion.

8. The empty crucible was then filled with HNO_3 from this beaker to cover the point where the bead attached to the wall. This process ensures that no material is left in the crucible as the acid will dissolve anything remaining within a few hours. After this time the acid solution was returned to the beaker.

9. Once the crucibles were all emptied of acid they were heated over the Bunsen burners for 15 minutes with a hot flame (~950 °C). Finally they were washed out with ½ ml concentrated hydrochloric acid (HCl) to remove any last adhering material which was also transferred to the corresponding sample's beaker.

10. The next day the acid solutions in each beaker were made up to 100 ml by transferring the solution to a glass volumetric flask and then adding de-ionised water. The final solution was stored in a plastic tube for analysis.

11. Any solutions showing signs of incomplete dissolution were placed in an ultrasonic bath to break up the remaining particles.

2.5.2. ICP-AES Analysis. Inductively-coupled-plasma atomic-emission-spectrometry (ICP-AES) is a type of emission spectroscopy that uses inductively coupled plasma to produce excited atoms and ions. Once excited, they emit electromagnetic radiation at wavelengths unique to that particular element (Mermet, 2005), the intensity of this emission is indicative of the element's concentration within the sample. Plasma is produced inside the ICP torch by the method previously described for laser ablation (section 2.3.1). Before the sample is introduced to the plasma it is converted from solution to aerosol within a nitrogen gas nebulizer. The aerosol is then directly discharged into the plasma and aerosol molecules collide with plasma electrons and ions until they are broken down into their constituent atoms. These atoms go through a process of continual electron loss and recombination, giving off characteristic electromagnetic wavelengths for each element during this process. Nitrogen gas and lenses are used to focus the emitted wavelengths onto a diffraction grating where they can be separated into their component radiation in the optical spectrometer. Wavelength intensity is measured with a photomultiplier tube (which can multiply a signal by 100 million times). By comparing the measured intensities with known standards, the concentration of each element within the unknown sample can be determined.

After our first analytical run it became apparent that some elements in a number of samples were above the calibration of the standards used (Table 2.2), meaning concentrations of these elements in the first solution (10 ml of the total 100 ml, 1 % nitric acid plus fusion bead) were very high relative to the standards. For more precise results we created further diluted solutions by 5, 10 and 50 times, to account for the elements only slightly above calibration (the 5 times dilution) and elements a long way above calibration (the 50 times dilution). These three dilutions were produced by placing 200 µl, 1000 µl (1 ml) and 2000 µl (2 ml) of the 1 % solution into separate vials and making them all up to 10 ml with de-ionised water, so for every sample three different concentrations of solution were analysed.

The analytical precision for our samples was always < 1 %, and in 75 % of cases it was < 0.6 %.

Table 2.2: ICP-AES external standards (major elements = wt %, minor elements = ppm).

	BE-N	BHVO-1	BCR-1	AGV-1	GSP-1	JG-1	NIM-G
Lithology	Basalt	Basalt	Basalt	Andesite	Granodiorite	Granodiorite	Granite
Al_2O_3	10.07	13.80	13.64	17.15	15.10	14.20	12.08
CaO	13.87	11.40	6.95	4.94	2.07	2.18	0.78
Fe_2O_3	12.84	12.23	13.41	6.77	4.29	2.14	2.02
K_2O	1.39	0.52	1.69	2.92	5.51	3.97	4.99
MgO	13.15	7.23	3.48	1.53	0.96	0.74	
MnO	0.20	0.17	0.18	0.09	0.04	0.06	
Na_2O	3.18	2.26	3.27	4.26	2.80	3.39	3.36
P_2O_5	1.05	0.27	0.36	0.49	0.28	0.10	
SiO_2	38.20	49.94	54.11	58.84	67.22	72.30	75.70
TiO_2	2.61	2.71	2.24	1.05	0.65	0.26	0.09
Sum	**96.56**	**100.53**	**99.33**	**98.04**	**98.92**	**99.34**	**99.02**
Ba	1025	139	681	1226	1310	462	120
Cr	360	289				64.6	
Ni	267	121					
Sr	1370	403	330	662	234	184	
Y	30	27.6	38	20	26	28.5	143
Zr	260	179	190	227	530	114	300

2.6. Solution ICP-MS

Previous trace-element data are sparse and incomplete for the majority of the samples investigated in this study, especially for the rare earth elements. For this reason we decided to analyse the samples via a high-precision technique such as ICP-MS. ICP-MS is used to determine the trace-element chemistry of bulk-rock powders. Like ICP-AES, it is a destructive technique, but the ICP-MS system at the Open University has been optimised such that it requires a very small amount of powder and yields very precise results.

2.6.1. Solution Preparation. All acids used in the dissolution procedure were teflon distilled (TD) grade, unless otherwise stated. All water used was purified through a millipore filtration system (MQ) to a resistivity of >18.2 MΩ. Dilute acids were produced from dilution of TD grade acids with MQ H_2O. Rock powders (0.01 g), along with relevant

reference materials and procedural blanks, were digested in clean Teflon vials using a few drops of concentrated HNO_3, and 200 µl concentrated HF. Andesite AGV-1, dolerite DNC-1, diabase W-2, and basalts BIR-1 and BHVO-1 were used as reference materials (Eggins et al., 1997). After 48 hours on the hotplate, at 130 °C, the solution was dried down, and refluxed in 1 ml 6M HCl for 24 hours at 130 °C. Following this the sample was refluxed in 1 ml conc. HNO_3 for a further 24 hours. On the addition of HNO_3, we observed the formation of a fine-grained white residue, presumably because of the high Ti content of our samples. We therefore made the decision to run our samples in a mixed HNO_3/HCl acid matrix. Samples were then taken up in 0.6 ml conc. HNO_3 and 0.6 ml 6M HCl, before being transferred into a cleaned nalgene vial. Samples were made up to 20 ml with MQ H_2O to form a 2 % HNO_3 solution (i.e. a 2000 fold dilution of the original rock-powder) with a trace of HCl.

2.6.2. ICP-MS analysis. Trace-element concentrations were determined by ICP-MS (Agilient 7500a) at the Open University. This instrument is fitted with a standard quartz spray chamber and a Babington nebuliser. Samples were aspirated at approximately 400 µl min^{-1} with count rates of the order of 3-5 x 10^7 cps/ppm. Oxide interferences were kept low at 0.3 % CeO^+/Ce^+ and doubly charged species at $\leq$ 1 % (Ce^{++}/Ce^+). Analyses were standardised against five reference materials (BIR-1, BHVO-1, W-2, DNC-1, AGV-1) that were measured at the beginning of each analytical run. An internal standard, containing Be, Rh, In, Tm, Re and Bi, was run along with the samples and reference materials. The basaltic reference material DNC-1 was also analysed as an "unknown" sample every 6 samples, together with one 2 % HNO_3/HCl blank, in order to monitor instrumental drift and to assess the external reproducibility of the data. The measured concentrations of elements in DNC-1 are routinely within 10 % difference of published values (Eggins et al., 1997) with a few exceptions and commonly show < 5 % difference (Table 2.3). Detection limits for trace elements with atomic masses greater than 85 are usually less than 10 ppt in

Table 2.3: Measured vs. published ICP-MS selected trace-element data for DNC-1 monitor

	Measured (ppm)							Published (ppm)	RD* %
Element	DNC-1 (1)	DNC-1 (2)	DNC-1 (3)	DNC-1 (4)	DNC-1 (5)	Average	2σ Error		
Li	5.12	5.32	5.30	5.29	5.25	5.26	0.16	5.10	-3.06
Sc	32.31	33.03	33.06	32.88	32.87	32.83	0.61	31.00	-5.90
Ti	2960.00	3053.00	3061.00	3030.00	3056.00	3032.00	83.94	2878.00	-5.35
V	149.60	153.70	153.90	151.70	152.60	152.30	3.50	148.00	-2.91
Co	57.93	59.02	58.82	57.00	57.79	58.11	1.64	55.00	-5.66
Ni	267.00	272.30	271.30	266.40	266.60	268.72	5.68	247.00	-8.79
Ba	101.50	104.70	105.10	103.50	104.20	103.80	2.84	118.00	12.03
La	3.57	3.71	3.71	3.66	3.67	3.66	0.11	3.53	-3.75
Ce	7.97	8.22	8.21	8.06	8.14	8.12	0.21	8.19	0.84
Pr	1.09	1.12	1.12	1.11	1.11	1.11	0.03	1.10	-0.73
Nd	4.81	4.96	4.93	4.88	4.91	4.90	0.12	4.86	-0.74
Sm	1.41	1.47	1.45	1.45	1.45	1.45	0.04	1.40	-3.26
Eu	0.58	0.60	0.61	0.59	0.59	0.59	0.02	0.60	1.38
Gd	1.99	2.04	2.03	2.00	2.01	2.02	0.05	2.00	-0.76
Tb	0.38	0.41	0.40	0.39	0.39	0.40	0.02	0.39	-1.52
Dy	2.67	2.78	2.78	2.73	2.72	2.74	0.09	2.76	0.81
Ho	0.63	0.66	0.66	0.65	0.66	0.65	0.03	0.65	-0.12
Er	1.91	1.97	1.99	1.95	1.96	1.96	0.06	1.90	-3.07
Yb	1.91	1.99	1.97	1.93	1.95	1.95	0.06	1.97	1.06
Lu	0.30	0.31	0.32	0.31	0.31	0.31	0.01	0.31	0.03

*RD = Relative Difference, calculated by (1-(measured/published value))*100

solution (equivalent to 20 ppb in the rock) but are somewhat higher for lighter elements (less than 100 ppt in solution, 200 ppb in the rock). Precision is routinely better than ± 3 % for all elements.

2.7. Laser-Fluorination Dual-Inlet Mass-Spectrometry

Laser-fluorination is used to determine oxygen isotope abundances; it can be used to measure ^{18}O, ^{17}O and ^{16}O. The system at the Open University has an international reputation for three oxygen isotope analysis using the laser-fluorination system. Although laser-fluorination is a destructive technique, the amount of material needed is very small (2 mg), and preparation time is also minimal.

2.7.1. Sample Preparation. The instrument at the Open University consists of an infrared CO_2 (10.6 μm) laser and high resolution Micromass Prism III dual-inlet mass-spectrometer. For this study 2 mg of each sample powder was placed into a small well (3 mm diameter and 4 mm depth) within a pure nickel sample tray. Each tray contains 22 wells allowing for the analysis of 8 samples (in duplicate) along side 6 external standards (Figure 2.7). Once full, this tray was transferred to the sample chamber of the laser-fluorination system, the upper half of which consists of a BaF_2 window (3 mm thick). The sample chamber is heated to ~ 70 °C with bake out tape and evacuated overnight $< 5 \times 10^{-8}$ Torr (base vacuum). Each powder is then fused under low level laser heating (~ 11 % maximum laser output) to prevent well to well contamination and to ensure a complete reaction. During the heating operation the beam power is gradually increased from ~ 20 to 100 % of the total available. Progress of the fusion (and subsequent fluorination process) can be monitored using a CCD video camera, viewing the sample along the axis of the laser beam.

2.7.2. Laser-Fluorination Analysis. After sample fusion, the chamber is evacuated again (overnight and with bake-out) to base vacuum. Prior to sample fluorination, the reaction chamber is exposed to BrF_5 vapour (~ 260 Torr) at room temperature to 'condition' internal surfaces and remove any remaining traces of adsorbed water vapour. A system 'blank' check is then undertaken; an aliquot of BrF_5 vapour is admitted to the chamber as for sample analysis, after 2 minutes, any O_2 formed is isolated and purified as described below. Generally, the system blank yield is ~ 30 nmol O_2 or less. System performance is checked by analysing external standards and ensuring that the attendant $\Delta^{17}O$ value

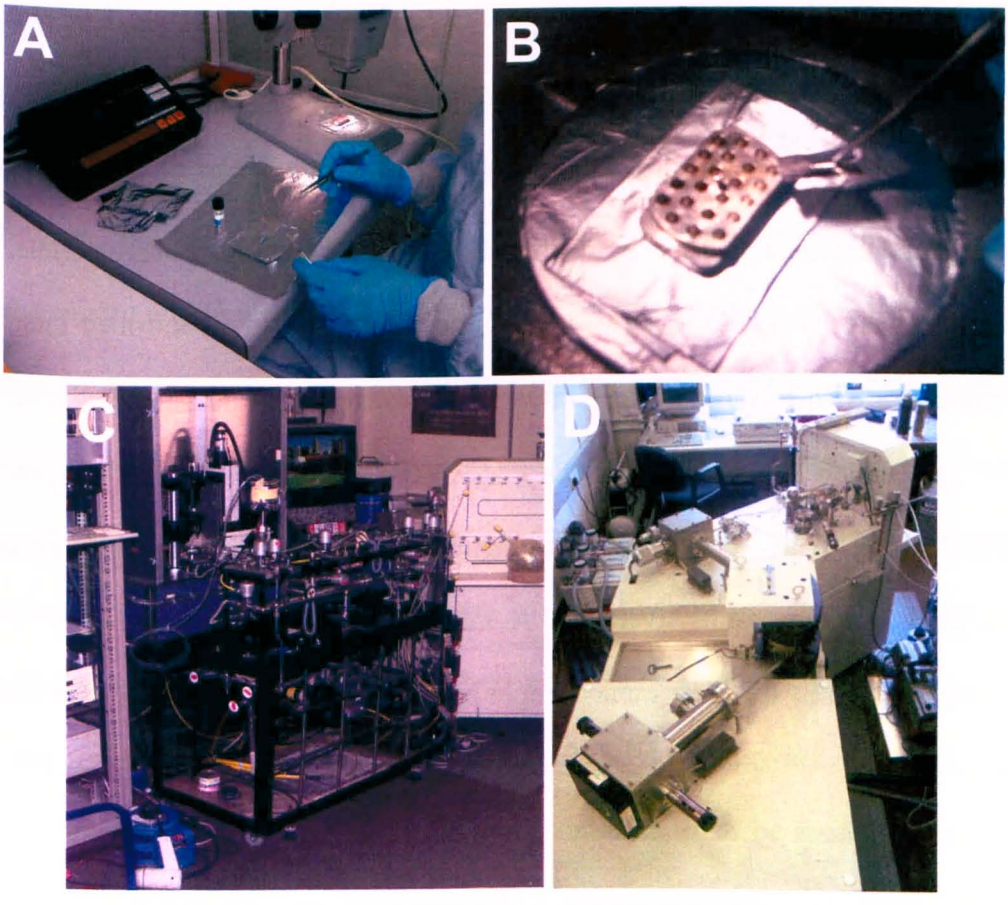

Figure 2.7: Laser-fluorination at the Open University. **(a)** Weighing out the samples for laser-fluorination, and placing 2 mg of powder into the small wells within a nickel sample tray **(b)**. **(c)** The laser system. **(d)** The dual inlet Micromass PRISM III mass-spectrometer coupled with the laser.

(defined in chapter 5) is zero within the limits of analytical precision. The system precision for $\delta^{17}O$ is 0.04 per mil, and 0.08 per mil for $\delta^{18}O$, producing an error of 0.024 for $\Delta^{17}O$

(all values 1 sigma). The external standards analysed were powdered UWG-2 garnet. Prior to the fluorination reactions, laser transmission is increased to ~ 82 % of the maximum value. For each analysis, an aliquot of BrF_5 vapour is expanded into the sample chamber to give a pressure of 210 ± 3 Torr. To ensure that there are no residual traces of O_2 present, the BrF_5 aliquot is first condensed at -196 °C (on a liquid nitrogen trap) and any non-condensed volatiles removed by pumping to base vacuum, prior to warming the BrF_5 to room temperature and admitting it to the sample chamber. The chamber is then isolated from the rest of the extraction line and an individual sample (or standard) heated to melting, in a controlled manner, by the laser. During the course of sample fluorination, which takes approximately 2 minutes in total, the laser power is gradually increased from ~ 20 to 100 % of the maximum value. Silica is converted to gaseous products SiF_4 and O_2 during this process. O_2 formed during fluorination is purified and SiF_4 removed via a series of cryogenic and chemical traps. It is then frozen onto 13X molecular sieve pellets, cooled via liquid nitrogen. From here it can be heated and so released in a controlled manner into the Micromass PRISM III dual inlet mass spectrometer and measured relative to the reference gas, which is calibrated directly against Vienna standard mean ocean water (VSMOW) (Miller et al., 1999). For each sample/standard at least three aliquots of O_2 were analysed and the results averaged. A minimum of two replicates (2 × 2 mg of powder) were analysed for each lunar sample and the results averaged to give one value per sample.

2.8. Sensitive High Resolution Ion Microprobe (SHRIMP)

Isotope systems used as geochronometers for lunar samples include Ar-Ar, K-Ar, Rb-Sr, Nd-Sm, Pb-Pb and U-Pb. The use of two or more of these systems on a single sample gives independent verification of that sample's age if the two results agree within error. Previous chronological data for our samples (and the mare basalts in general) are patchy and have widely varying errors. The SHRIMP technique allows for the determination of Pb-Pb and

U-Pb ages, therefore giving two independent age estimates from one set of non-destructive analyses. However, SHRIMP analysis is time consuming and only a limited number of laboratory days were available for measurements Therefore, we carefully selected samples that had not previously been dated and/or those which were most likely to yield accurate results (based on phosphate content and condition).

2.8.1. The SHRIMP Technique. The SHRIMP is a large-diameter, double focusing secondary ion mass spectrometer (SIMS). It can measure isotopic and elemental abundances *in-situ* in minerals down to a spatial resolution of 5 μm. Therefore, it is particularly well adapted for the analysis of complex or small mineral grains. It differs from SIMS on account of its larger mass analyser, a feature developed in order to maintain sensitivity at high mass resolutions. As with LA-ICP-MS, a small pit is produced in the mineral grain, but the technique is largely non-destructive as the measurements are performed *in-situ* within a thin- or thick-section. U-Pb geochronology is the most common application of the instrument, though the SHRIMP can be used to measure other isotopic and elemental abundances. During analysis, a beam of primary ions (O_2^-) is accelerated towards the target and used to sputter secondary ions from the sample. These secondary ions are accelerated through the large mass analyser, which separates them according to their mass-charge ratio. The quadrupole lens and electromagnet further process the ions before they reach the mass spectrometer (Figure 2.8) where they are identified. For U-Pb and Pb-Pb analysis various isotopes of uranium and lead can be measured successively, along with reference peaks (e.g., ThO^+ and UO^+). Since the sputtering yield differs between ion species and changes with time depending on the ion species (because of increasing crater depth, charging effects and other factors), the measured relative isotopic abundances do not relate to the real relative isotopic abundances in the target. Corrections are determined by analysing a standard material, and determining an analytical-session specific calibration factor (Claoué-Long et al., 1995).

2.8.2. Analysis at Hiroshima University. Our analysis was carried out by employing the SHRIMP II at the University of Hiroshima, Japan. SHRIMP II uses the same ion optical design as the original SHRIMP of the early 1980's. However, with its modified secondary extraction geometry, SHRIMP II gives a three fold increase in the extracted secondary ion yield (Figure 2.9). Before our analysis was undertaken, each target grain had to be located and imaged using the backscatter detector attached to the NHM's JEOL 5900LV. These high-resolution images are necessary as the SHRIMP only has a standard video camera for sample guidance with no zoom capabilities, making target grain identification difficult. This problem is enhanced as each thin-section must be gold coated to enable the conduction of ions across the surface. Gold coating reduces the build up of charged particles on the sample surface, minimising interference with the primary beam. Surface conductivity is monitored with a voltmeter once the sample is secured in a metal holder. If the reading is constant over the whole section then it can be placed into the sample chamber, if not the sample holder is adjusted and/or the gold coat re-applied to increase conductivity.

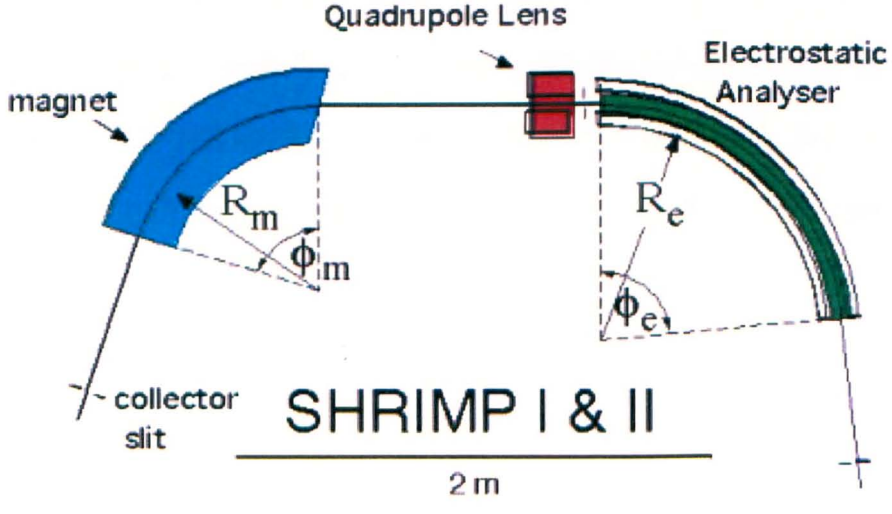

Figure 2.8: SHRIMP plan view. Secondary ions sputtered from the sample surface are accelerated along the instrument. As they move through the large electrostatic analyser they are separated according to mass-charge ratio, the quadrupole lens then selectively stablises certain ions which travel through the electromagnet to the detector (Compston et al., 1984). This manipulation ensures that when the ions reach the collector they are separated and can be individually identified. Image adapted from shrimprg.stanford.edu.

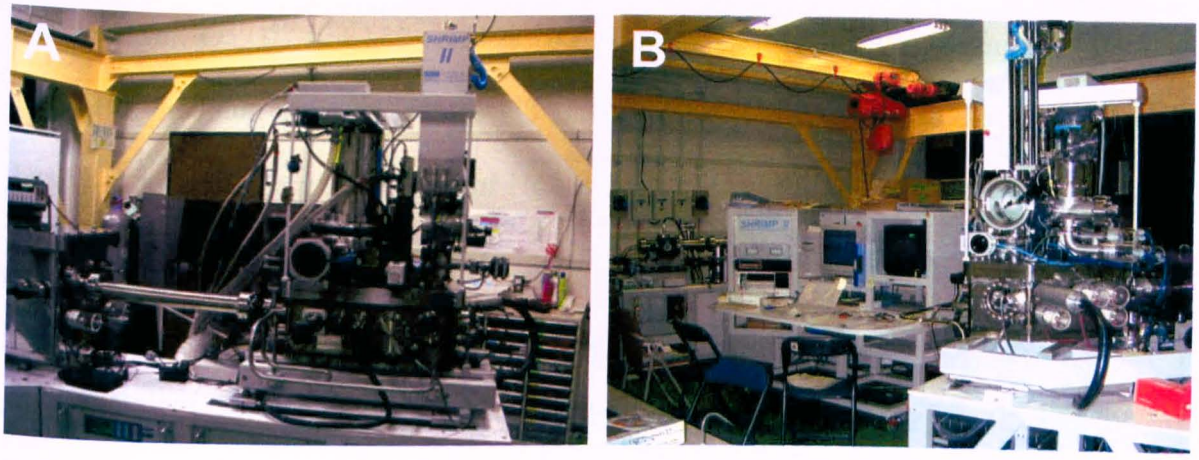

Figure 2.9: The SHRIMP II at Hiroshima University. **(a)** Sample chamber which is kept at a high vacuum to prevent atmospheric disturbance to the primary beam. The secondary ions are removed from the sample chamber and travel to the electrostatic analyser (left of image) via the visible metal tube. **(b)** Sample chamber (foreground right), control panel (centre) and collector (background left), the electrostatic analyser and magnet are hidden behind the control panel.

From the time the samples are placed within the chamber it takes 3-4 hours to reach the correct vacuum pressure. After this period of time elapses the search for the target grains begins, once found their location can be recorded. During our target location it was often necessary to check the target grain by briefly turning on the beam and observing if the spectral peaks produced were in accordance with the target's mineral type. Finding the spot where the highest number of counts reaches the detector is also a useful way of determining the best location on the grain for analysis. Before every analysis, a 20 μm diameter area of the sample surface was rastered for 2 minutes to remove the gold coat and possible surface contaminants. Then using Kohler illuminations, a ~ 6 nA mass filtered O_2^- primary beam was used to sputter a 30 mm diameter flat-bottomed crater and secondary positive ions were extracted for mass analysis (Sano et al., 1999). The source and collector slits were set to 80 mm and 100 mm, respectively. A mass resolution of 5800 at 1 % peak height was employed to separate $^{40}Ca_2{}^{31}P^{16}O_3{}^+$ from $^{143}Nd^{16}O^+$ in the apatite standard with adequate flat topped peaks. No isobaric interferences were found in the mass range over ^{206}Pb and ^{207}Pb. The magnet was cyclically peak-stepped through a series of mass

numbers, ranging from mass 159 for $^{40}Ca^{31}P^{16}O_3^+$ to mass 254 for $^{238}U^{16}O^+$. These steps included the background mass number at 204.1, Pb isotopes at mass numbers 204, 206, 207, and 208, mass 209 for $^{208}PbH^+$ (to assess PbH interference), mass 238 for ^{238}U and mass 248 for the $^{232}Th^{16}O$ peak (Sano et al., 1999).

Throughout an analytical session certain factors must be regulated to maintain high precision, for example the primary column and source chamber pressures should be kept at 3.5-4.5 and ~ 2 Torr respectively, by manual adjustment of the oxygen flow. In addition, the primary beam current and alignment are monitored and the secondary ion detection maximised before every analysis. PRAP apatite from the Prairie Lake circular complex was used as a standard, as grains from this complex are relatively large and contain high U concentrations (Sasada et al., 1997). Standard analysis took approximately 20 minutes whereas that of the sample was considerably longer (~ 2 hours). In general, standards were analysed in groups of three at the beginning and end of a session, and after every 4-5 sample analyses. Analytical errors are generally less than 2 % (Nemchin et al., 2008).

Raw data processing was undertaken using Isoplot software (Ludwig, 2000), a geochronological toolkit for Microsoft Excel, created to interpret radiogenic isotope data. We used Isoplot to construct Pb-Pb isochrons. Any data points with insufficient counts above background levels were excluded (see chapter 6 for further details on data processing procedures).

3. MINERALOGY

3.1. Sample Descriptions

We investigated the petrography and mineral chemistry of mare-basalt samples using optical microscopy, scanning electron microscope (SEM) and electron microprobe techniques, the complete data sets of which can be found in appendix A and B. These investigations allowed observations of various textural and mineralogical characteristics for each lunar basalt sample. Each sample is individually described in the following section and the modal abundance data (vol %) for the entire sample set is given in Table 3.1.

Table 3.1: Modal mineralogy (vol %) for the samples studied in this work.

Sample[1]	Pyroxene[2]	Plagioclase[3]	Olivine[4]	Ilmenite[5]	Spinel[6]	Armalcolite[7]	Silica[8]	Troilite[9]	Mesostasis[10]	Phosphates[11]	Sum
10017	47	29		10				0.06	14.19	trace	100
10020	48	33	5	14	0.13*			trace	trace	trace	100
10049	50	33	trace	15			1.40	0.40	trace	trace	100
10050	51	33	1	14			1.55	0.17	0.10	trace	100
10057	56	36	trace	8				0.04	trace	trace	100
10058	51	32		11			4.92	0.35	trace	trace	100
10072	45	39	1	15				0.03	trace	trace	100
12016	51	31	14	4	0.57			0.02	trace		100
12040	55	19	22	3	0.14			0.05	trace	trace	100
12047	51	39	1	6	0.25		2.95	0.35		trace	100
12051	60	30		7	0.07		2.84	0.26		trace	100
12052	62	32	2	3	0.29		1.37	0.22			100
12064	62	27		5	0.54		3.82	0.11	1.21	0.27	100
14053	59	34	3	2	0.26		0.92	0.13	trace	trace	100
15016	61	23	12	1	2.83			trace	trace	trace	100
15386	33	51		3	0.01		2.68	0.11	10.50	0.58	100
15555	56	31	11	1	0.64		0.52	trace	trace	trace	100
70017	53	28	1	17	0.06	0.20	0.32	0.09	trace	0.03	100
70035	52	29		18	trace	0.21	1.39	0.12	trace	trace	100
70215	63	12	7	17	0.08	0.11	0.02	0.02			100
74275	51	22	9	15	1.86	0.93	0.28	0.41			100
75055	55	31		10			3.62	0.11	trace	trace	100

[1]Numbers beginning with 10, 12, 14, 15 and 70 represent samples from the Apollo 11, 12, 14, 15 and 17 sites respectively. [2]pyroxene = clinopyroxenes of the solid solution system diopside ($CaMgSi_2O_6$) - hedenbergite ($CaFeSi_2O_6$) - enstatite ($MgSiO_3$) - ferrosilite ($FeSiO_3$), plus orthopyroxenes within sample 15386 ($MgSiO_3$ - $FeSiO_3$). [3]plagioclase = albite ($Na(AlSi_3O_8)$) - anorthite ($CaAl_2Si_2O_8$). [4]Olivine = Fayalite (Fe_2SiO_4) - Forsterite (Mg_2SiO_4). [5]ilmenite ($FeTiO_3$). [6]spinel = in general a solid solution between chromite ($Fe^{+2}Cr_2O_4$) and ulvöspinel ($Fe^{+2}_2TiO_4$) with a small proportion of hercynite ($Fe^{+2}Al_2O_4$). [7]armalcolite ($(Fe,Mg)Ti_2O_5$). [8]silica (SiO_2). [9]troilite (FeS). [10]mesostasis = interstisial material mostly too fine grained for analysis, frequently containing patches of K-feldspar ($KAlSi_3O_8$), glass and fine grained crystals of the preceding minerals. [11]Phosphates = apatite ($Ca_5(PO_4)_3(F,Cl)$ and (RE)-merillite ($Ca_{18}(Mg,Fe)_2(Y,REE)_2(PO_4)_{14}$). *Though the INCA phasemap tool has an error of ~ 1 % the modes of minor minerals were calculated based on phasemap data and SEM x-ray image pixel counting.

3.1.1. 10017,372: Apollo 11 High-Ti, Low-Al, High-K Mare Basalt. Sample 10017,372 displays a fine grained, granular texture containing irregular vesicles up to ~ 2 mm diameter. Circular vesicles are less common and do not exceed 1 mm (Figure 3.1). Grain size is phase dependent, plagioclase and pyroxene occur as elongated grains with lengths up to 500 μm, whereas ilmenite and silica grains rarely reach 100 μm in length. Ilmenite is

irregular, cubic or acicular in contrast to anhedral, partially intergrown pyroxene and plagioclase. Anhedral and subhedral silica grains are associated with plagioclase and small areas (< 250 μm) of mesostasis. Minor minerals include F-rich apatite, (RE)-merillite, troilite and FeNi, all of which are < 100 μm and are associated with mesostasis (Figure 3.2).

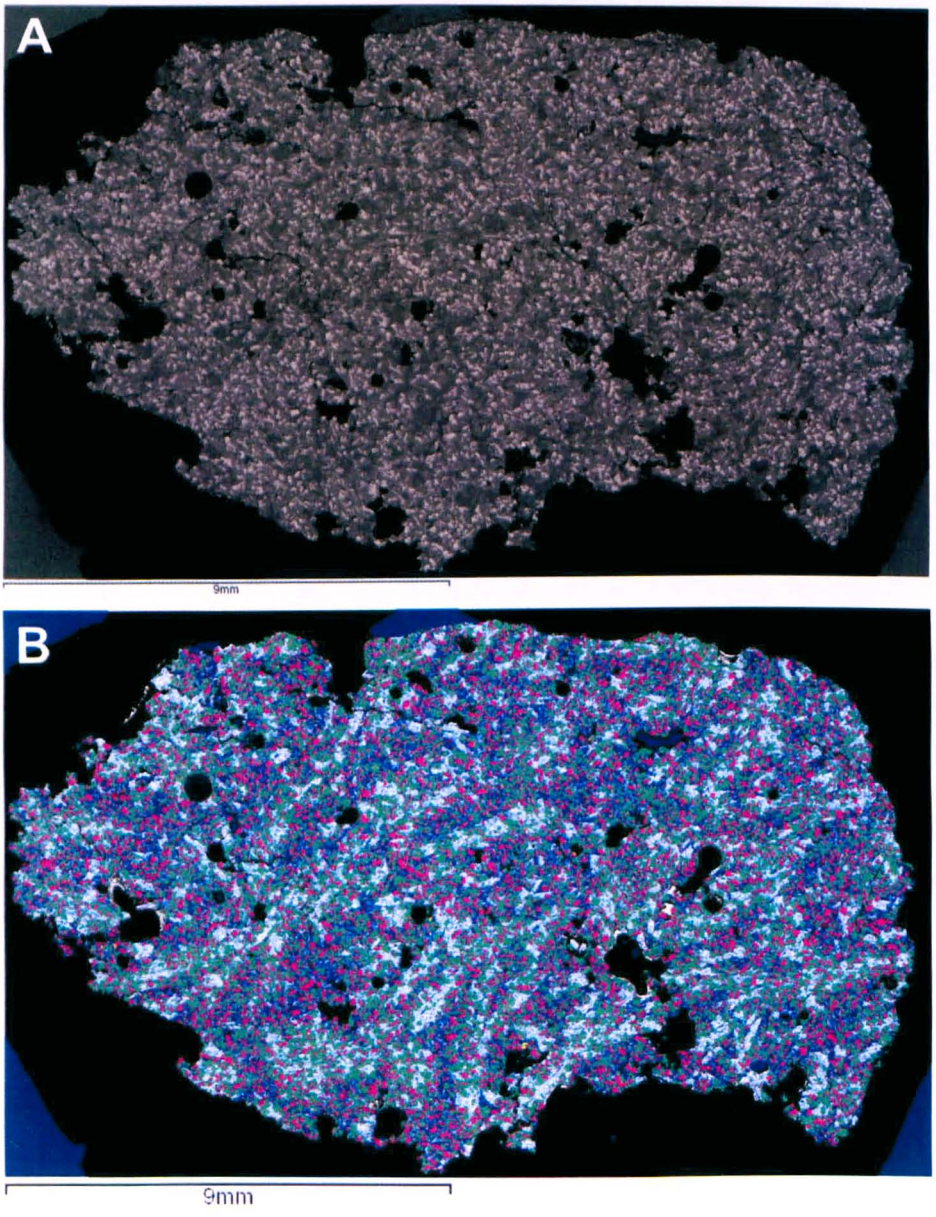

Figure 3.1: Apollo 11 sample 10017. **(a)** Greyscale backscatter image where brighter areas are richer in heavy elements such as Fe, e.g. ilmenite appears bright because of high Fe and Ti content. **(b)** False colour x-ray image where red = Fe, green = Mg, blue = Si, white = Al, pink = Ti and yellow = S. This false colour image therefore shows pyroxene in green (olivine is bright green where present in some other images), plagioclase in white, silica in blue (including some of the glass slide around the edges of this image), ilmenite in pink and troilite in yellow.

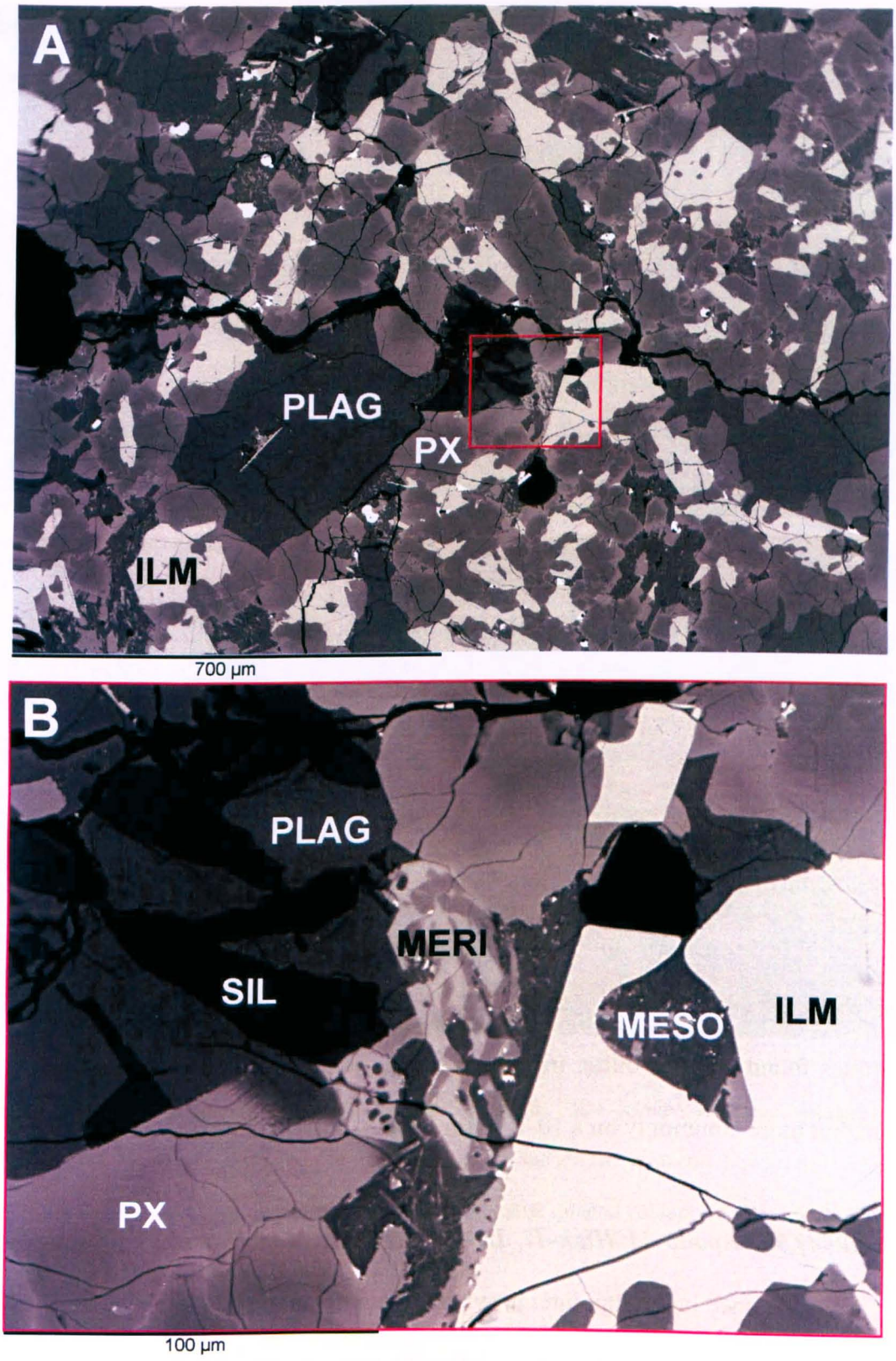

Figure 3.2: Apollo 11 sample 10017 minor minerals. **(a)** High resolution backscatter image of this basalt's granular texture, where plag = plagioclase, px = pyroxene and ilm = ilmenite. **(b)** High resolution backscatter image of an area of mesostasis and associated minor minerals, where meso = mesostasis, sil = silica and meri = (RE)-merillite. (RE)-merillite needles are visible within the mesostasis below the main (RE)-merillite grain. This grain contains bright zones with a high proportion of rare earth elements (REE) and darker zones containing comparatively low abundances of REE.

These phases are mostly irregular (excepting a number of (RE)-merillite needles) and are commonly intergrown. Mesostasis appears to contain K-feldspar and/or K-rich glass, but because of small grain size (< 10 μm) these could not be distinguished.

3.1.2. 10020,232: Apollo 11 High-Ti, Low-Al, Low-K Mare Basalt. There appears to be two generations of ilmenite within this sample, roughly half the grains are irregular (< 0.5 mm) while the remaining half are acicular/needles (up to 1.5 mm in length) (Figure 3.3). Plagioclase has similar textures but is slightly shorter (< 1 mm in length, commonly < 0.5 mm). Pyroxene is present as large irregular masses sub-ophitically enclosing ilmenite and plagioclase grains, because of this it is difficult to distinguish separate grains but the largest mass of pyroxene is ~ 2 by 1 mm (Figure 3.4). Olivine grains display a subhedral granular texture (<1 mm diameter), and are associated with Cr-rich spinels (< 100 μm diameter) that commonly form inclusions within olivine. Acicular silica is associated with areas rich in plagioclase and minor minerals. Phosphate phases are rare and very small (< 5 μm) within this thin section, precluding further mineralogical identification of these grains. Troilite (< 50 μm) and tranquillityite (< 10 μm) are associated with very rare and small areas of mesostasis consisting mostly of K-feldspar and pyroxferroite. FeNi blebs are sometimes found within troilite. Irregular vesicles of up to 2 mm diameter occur in this section, but more commonly on a 10-100 μm scale.

3.1.3. 10049,94: Apollo 11 High-Ti, Low-Al, High-K Mare Basalt. This sample has a uniform fine-grained but vuggy intergrown texture with an average grain size of ~ 200 μm with rare 500 μm grains (Figure 3.5). Irregular vesicles are common, the largest has a diameter of 1.5 mm but diameters of ~500 μm are more frequent. Euhedral, skeletal, pyroxene cores are rimmed by a later anhedral, Fe-rich pyroxene overgrowths. A number of these cores sub-ophitically enclose bladed ilmenite or contain ilmenite inclusions, and sometimes rare olivine is also associated. Anhedral plagioclase is associated with areas of

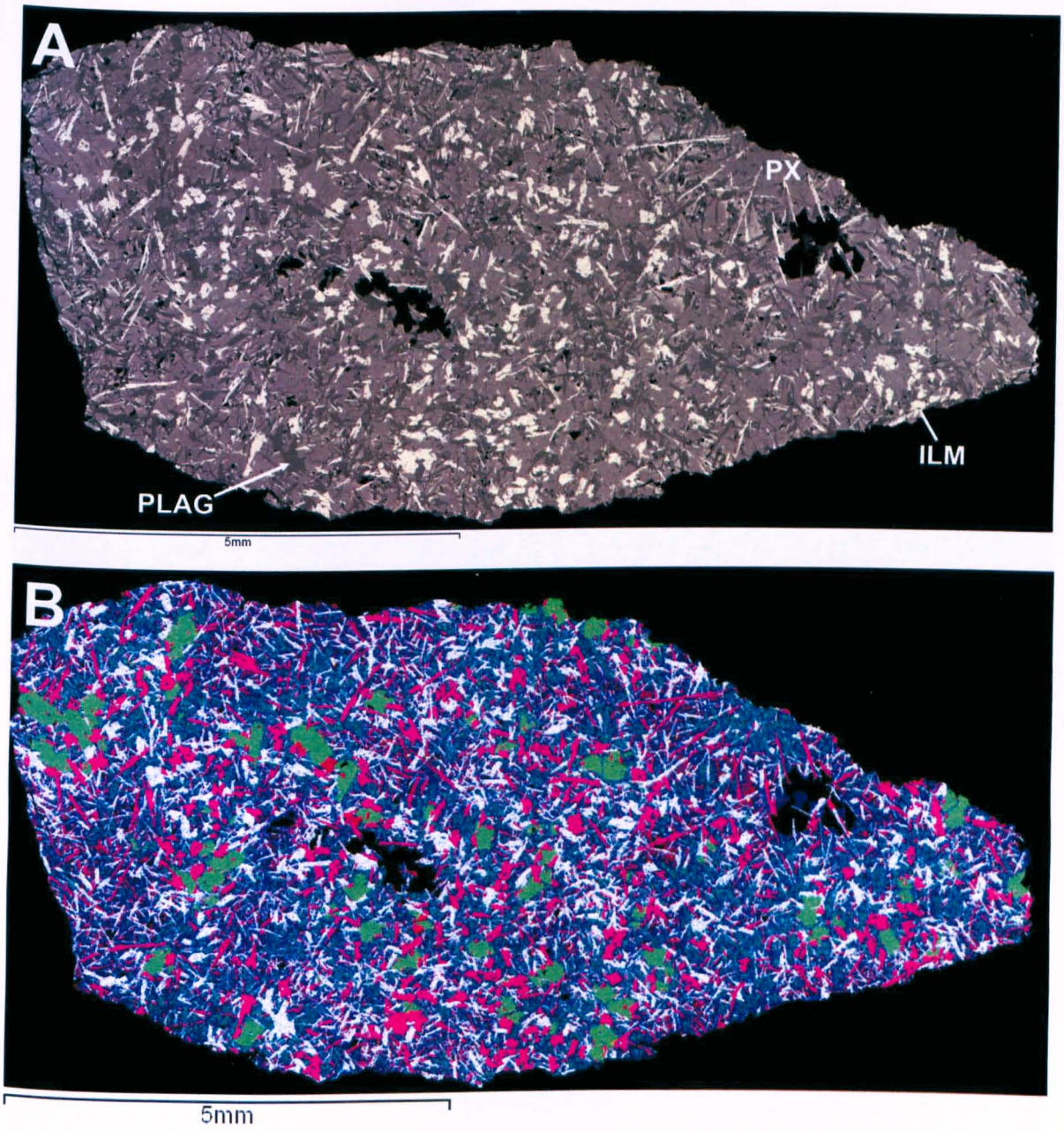

Figure 3.3: Apollo 11 sample 10020. **(a)** Backscatter image. **(b)** False colour x-ray image (element key as with Figure 3.1b). The bright green areas of this image are olivine grains; pyroxene shows a more blue-green colour. The red grains associated with olivine are spinel. All other mineral colours are as in Figure 3.1b.

mesostasis containing K-rich glass and feldspar (Figure 3.6). Rare ilmenite resorbtion hollows contain plagioclase or Fe-rich clinopyroxene inclusions. Troilite is often found within plagioclase or at its margins, however the largest troilite grains are associated with vugs (< 250 μm). FeNi blebs (< 5 μm) are associated or included within troilite. Phosphate phases are widespread but rarely exceed 10 μm, precluding further mineralogical identification. Silica is rare, < 10 μm, and associated with plagioclase and mesostasis.

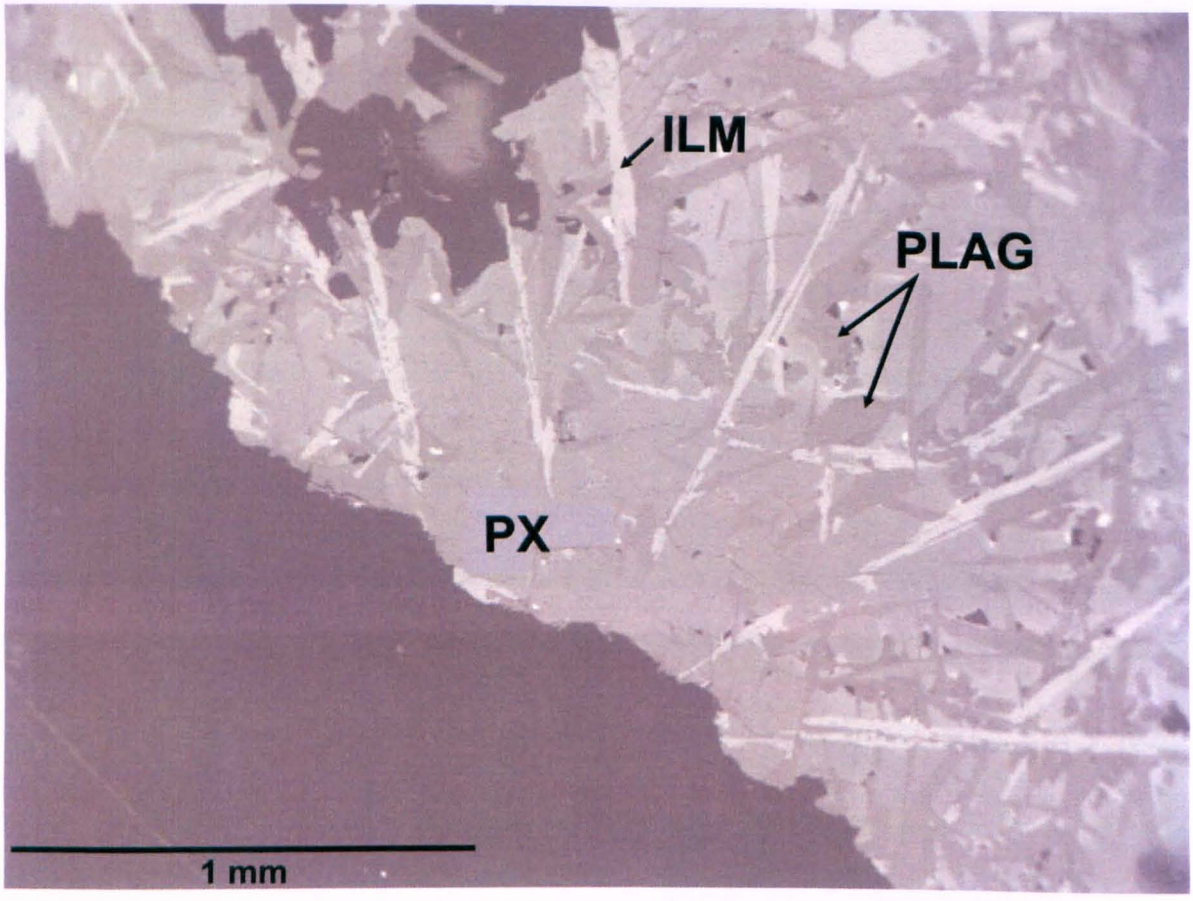

Figure 3.4: Apollo 11 sample 10020 high resolution backscatter electron image. This image shows a large pyroxene grain intruded with ilmenite blades.

3.1.4. 10050,168: Apollo 11 High-Ti, Low-Al, Low-K Mare Basalt. Coarser grained than samples 10017 and 10020, this sample contains anhedral and subhedral masses of pyroxene (up to 2 mm diameter) sub-ophitically intergrown with acicular plagioclase (up to 1 mm). Irregular and semi-cubic plagioclase clusters occur at pyroxene grain boundaries, associated with embayed and resorbed blocky sieve textured ilmenite grains up to 2 mm in diameter (Figure 3.7). Voids within these grains contain pyroxene, plagioclase, silica and K-feldspar. Rounded and partially resorbed olivine grains are present within pyroxene masses, olivine voids contain mostly pyroxene with some ilmenite needles. Bladed and anhedral silica is associated with areas of mesostasis containing K-feldspar (< 50 μm), troilite (< 400 μm), FeNi (< 100 μm – both within troilite and as independent grains), and F-rich apatite (< 50 μm). Pyroxferroite is found at a number of clinopyroxene-ilmenite grain boundaries but in

this sample it has mostly broken down into an intergrowth of silica, fayalite and Ca, Fe-rich pyroxene (Figure 3.8). Irregular vesicles range from 0.5-2 mm diameter.

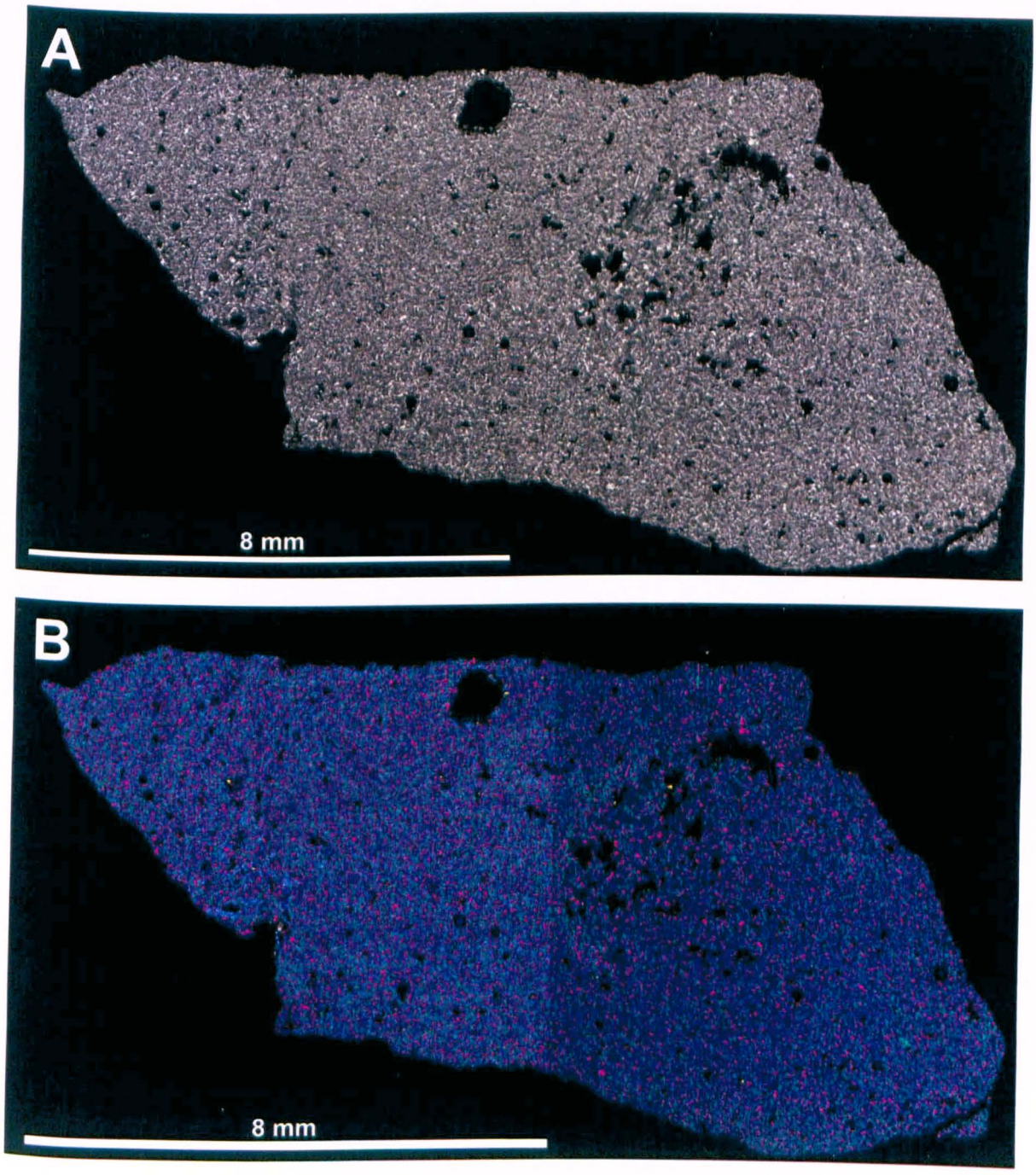

Figure 3.5: Apollo 11 sample 10049. **(a)** Backscatter image. **(b)** False colour x-ray image (elemental key as in Figure 3.1b). The slight variation in colour for the two halves of this image is because of the availability of Al x-ray data rather than any compositional difference, EDS detection of Al (shown in white) failed for the right half of this image montage.

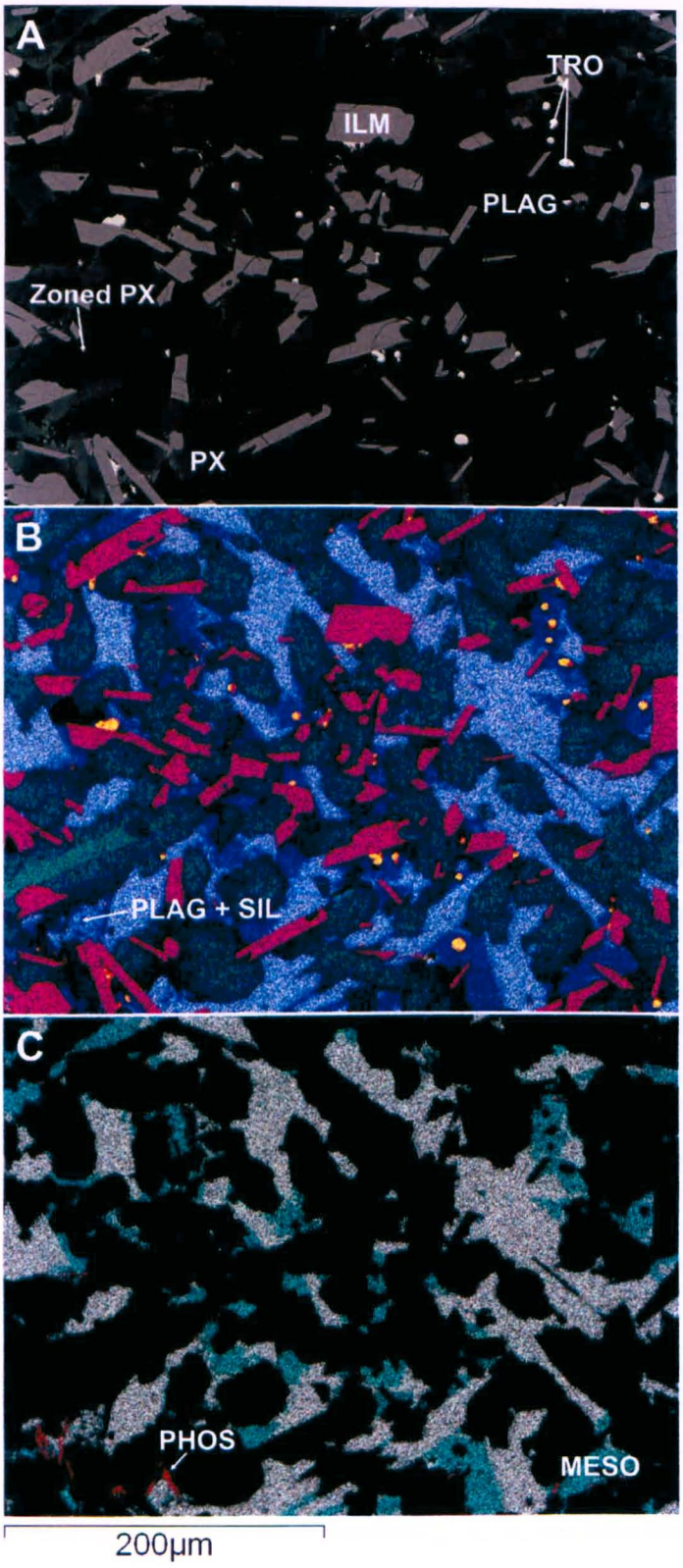

Figure 3.6: Apollo 11 sample 10049 high resolution images. **(a)** Backscatter image showing the zoned nature of pyroxene grains, a euhedral, Mg-rich core is particularly evident within the large grain to the left of the image. **(b)** False colour x-ray image (elemental key as in Figure 3.1b) highlighting troilite (yellow - tro), associated FeNi blebs (red) and mesostasis (blue). **(c)** False colour x-ray image where Al = white, K = blue and P = red, this image highlights the K-rich nature of the mesostasis, separates mesostasis from silica and shows phosphate rich phases (phos) associated with mesostasis and Fe-rich pyroxene.

3.1.5. 10057,64: Apollo 11 High-Ti, Low-Al, High-K Mare Basalt. This sample's texture is very similar to that of 10049,94, with bladed ilmenite, anhedral plagioclase and two stage pyroxene growth (Figure 3.9). Troilite (up to 100 μm) associated with vesicles and the minor mineral phases associated with mesostasis are also common for both samples. However, average grain sizes are slightly larger within 10057,64 at around 200-300 μm, with a number of acicular plagioclase grains showing lengths over 1 mm (Figure 3.10). Irregular and circular vesicles are also more common, varying from 2 mm to 100 μm in diameter.

3.1.6. 10058,254: Apollo 11 High-Ti, Low-Al, Low-K Mare Basalt. Sample 10058,254 contains large anhedral pyroxene grains up to 3 mm diameter that are zoned with Fe-rich compositions at the rim, and these grains are sub-ophitically intergrown with plagioclase (< 1 mm) and ilmenite (< 2 mm). Plagioclase is present both as laths and irregular masses while ilmenite is mostly irregular and partially resorbed (Figure 3.11). Pyroxene, plagioclase, K-feldspar and troilite are present within the resorbtion voids of ilmenite. Irregular and acicular silica (up to 1.5 mm long) is associated with plagioclase and areas of Fe-rich pyroxene as are relatively large irregular troilite grains (up to 500 μm) with FeNi inclusions (up to 100 μm). Small areas of mesostasis (< 200 μm) are made up mostly of silica, K-feldspar and Fe-pyroxene (Figure 3.12). F-rich apatite (< 50 μm), troilite, FeNi blebs and baddeleyite (< 10 μm) also occur in the mesostasis. The residual breakdown products of pyroxferroite (silica, Ca,Fe-rich pyroxene and fayalite) form a symplectite texture associated with the mesostasis (< 150 μm). Towards the bottom right of this thin section (Figure 3.11) is a comparatively large (~ 200 μm) anhedral grain of metal consisting of 85 % Fe, 13 % Cr, and 0.15 % Ni along with other low amounts of Co, Si, Ca and Ti. None of the other samples contain metal grains with this ratio of Fe/Cr/Ni. Its presence at the edge of the section initially suggested it was a contaminant, however it appears to be

attached to a pyroxene grain boundary. Therefore it probably is a large Fe metal grain from within this sample with an unusually high Cr content.

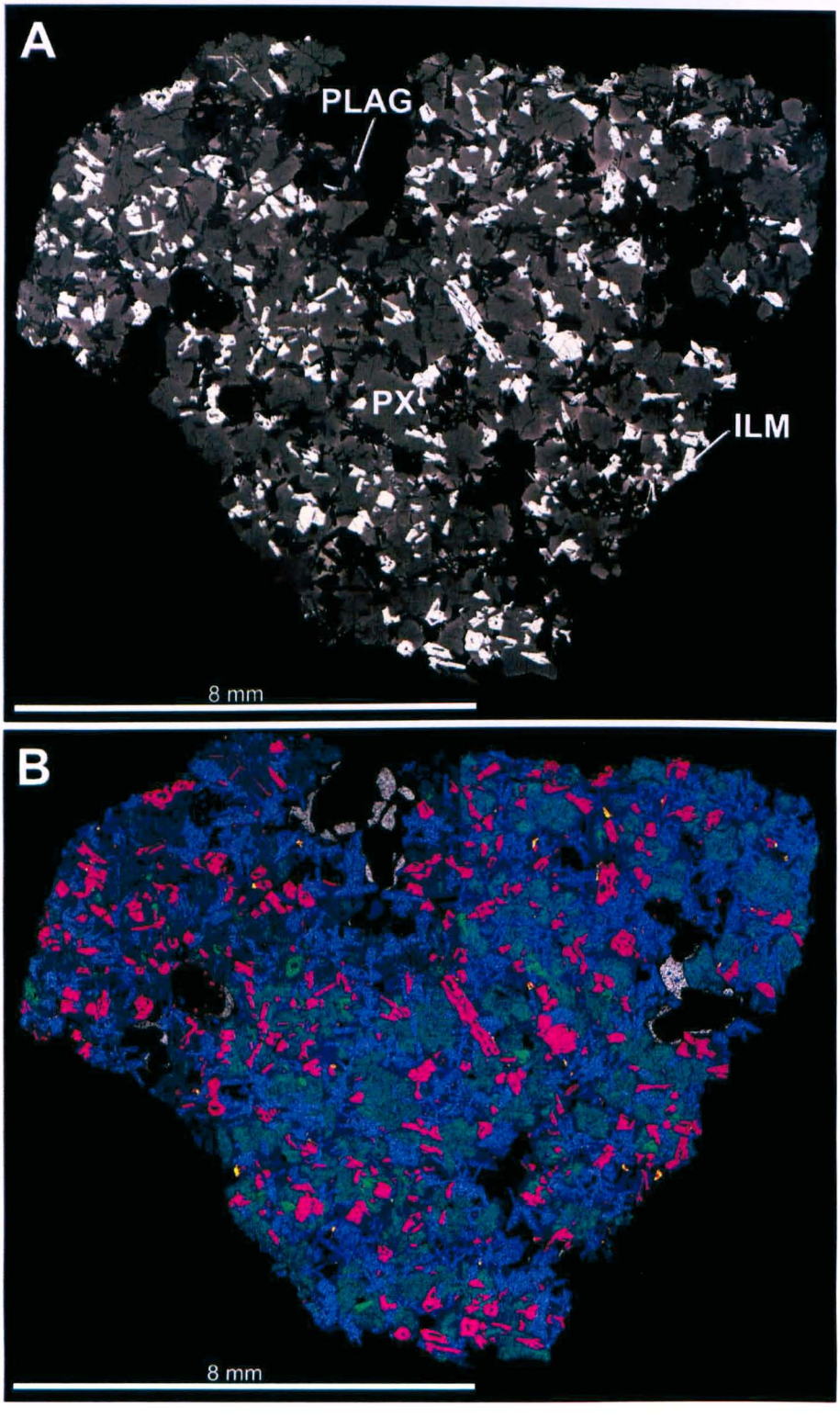

Figure 3.7: Apollo 11 sample 10050. **(a)** Backscatter image. **(b)** False colour x-ray image (elemental key as in Figure 3.1b). Bright green grains in the latter are rounded olivine cores within pyroxene grains, white areas around vugs are Al-rich resin (used to stick the thin section to the glass slide), and plagioclase is light blue whereas silica is strong blue.

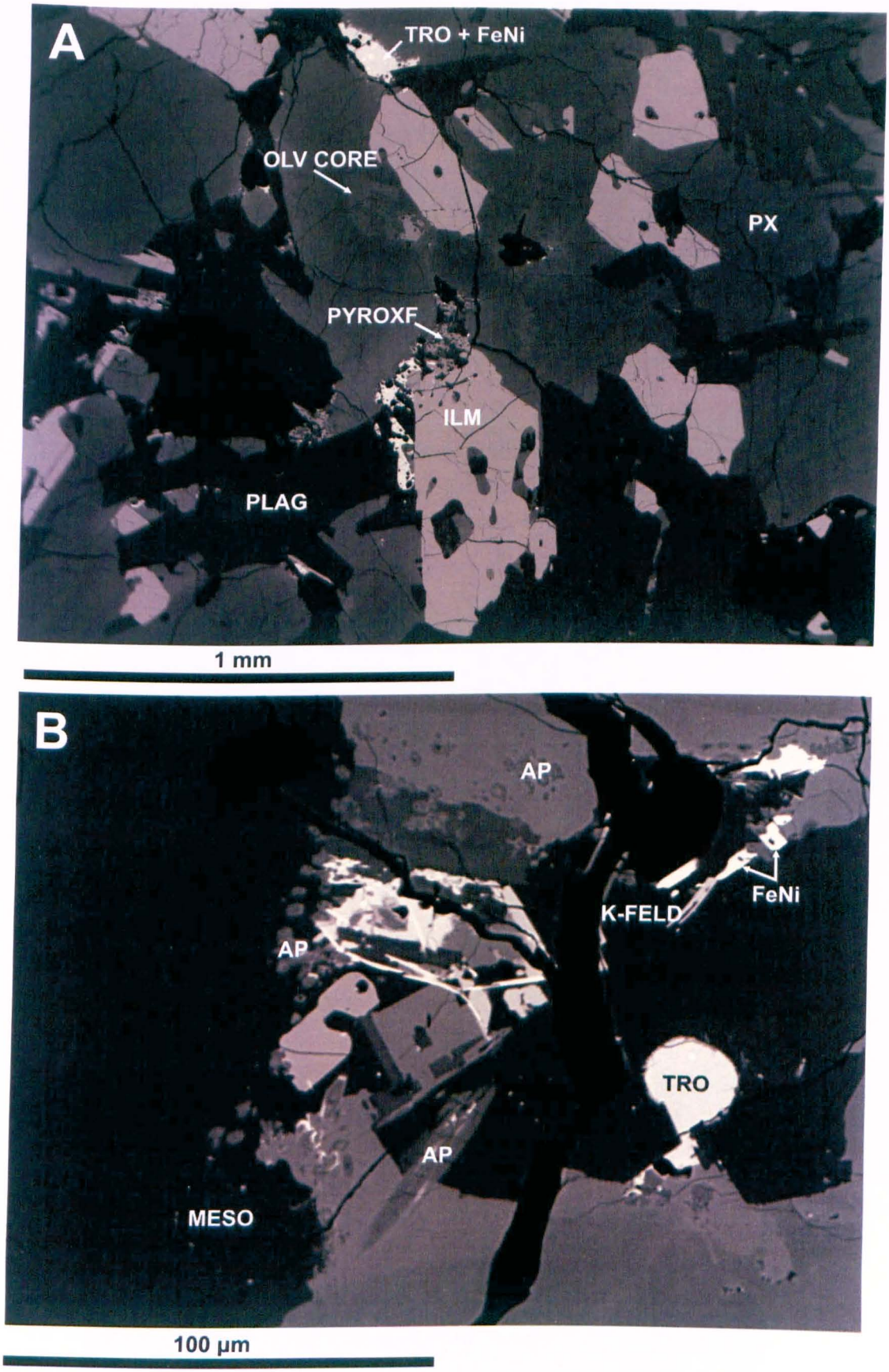

Figure 3.8: Apollo 11 sample 10050 high resolution backscatter electron images. Highlighting **(a)** olivine (olv) core and pyroxferroite (pyroxf) degraded to fayalite, silica and FeCa-rich pyroxene, **(b)** an area of mesostasis with associated apatite (ap), K-feldspar (K-feld), troilite (tro) and FeNi metal.

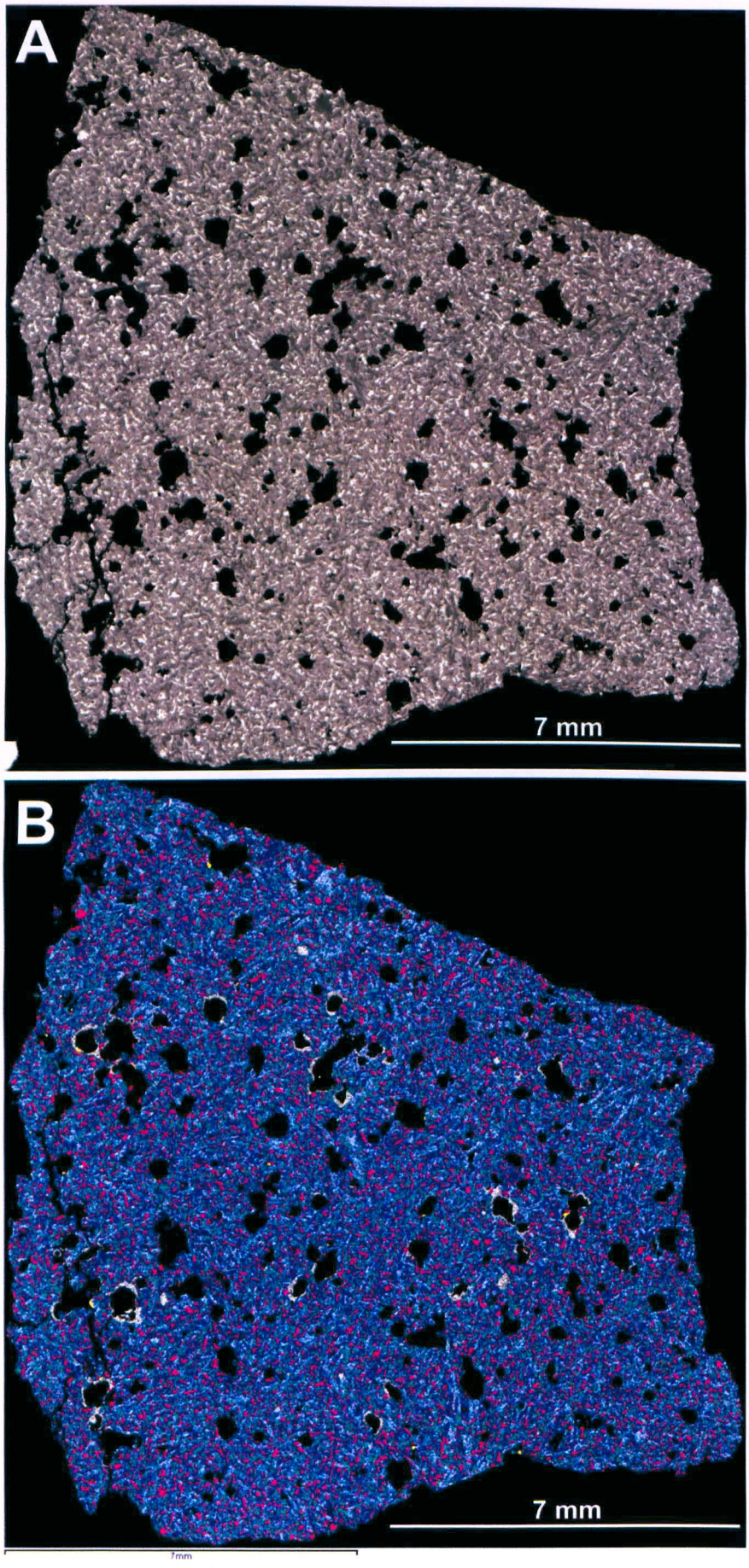

Figure 3.9: Apollo 11 sample 10057. **(a)** Backscatter image. **(b)** False colour x-ray image (elemental key as in Figure 3.1b), both highlighting the granular texture of this sample and its similarity to sample 10049.

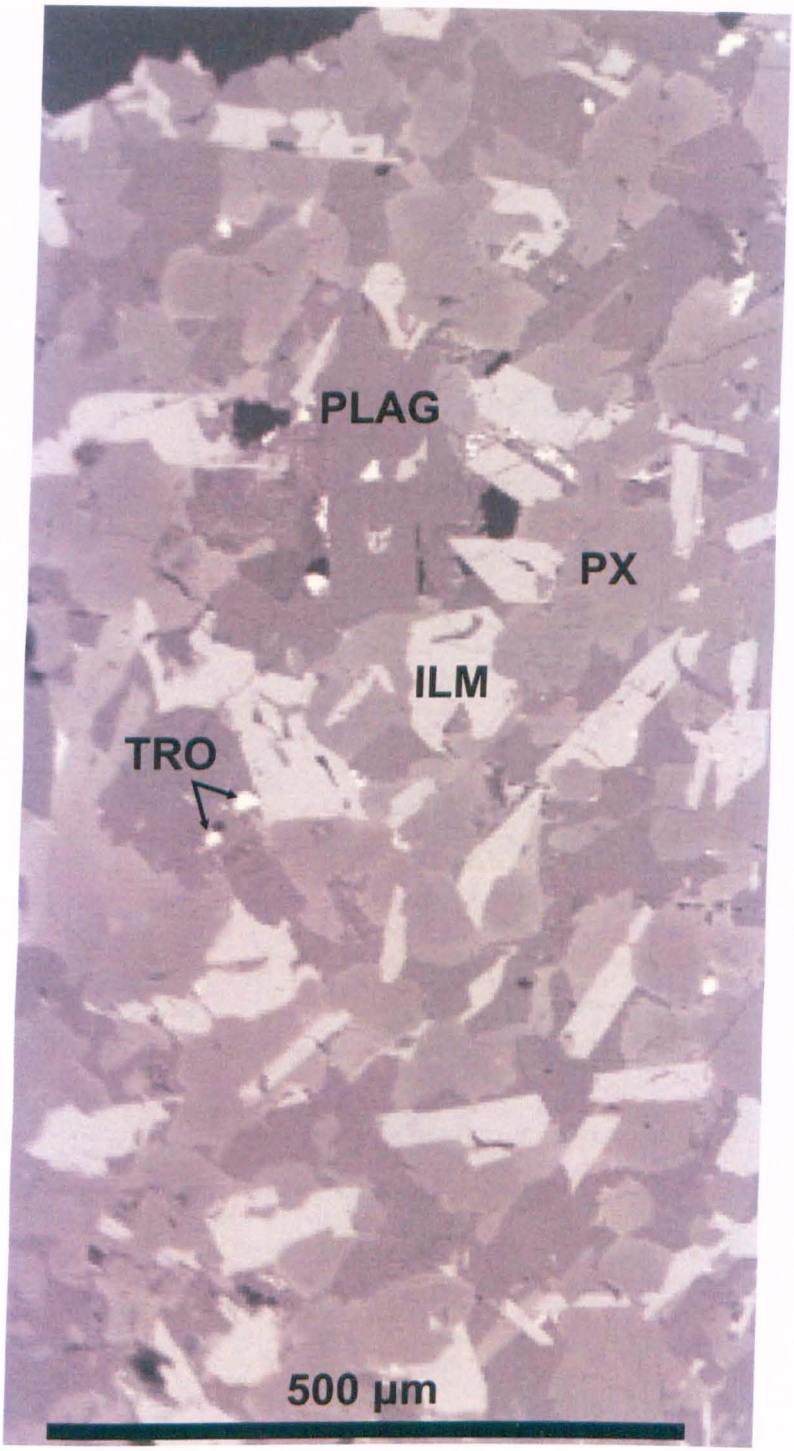

Figure 3.10: Apollo 11 sample 10057 high resolution backscatter electron image. This image shows granular texture with ilmenite intruding pyroxene and commonly anhedral plagioclase at grain boundaries.

3.1.7. 10072,40: Apollo 11 High-Ti, Low-Al, High-K Mare Basalt. Pyroxene and ilmenite are the dominant minerals in this sample (Figure 3.13). The former occurs as 1 mm sized anhedral masses, with Mg-rich cores and Fe-rich rims, with smaller (< 100 µm) Fe-pyroxene is also visible between larger grains. The latter is skeletal and exists as blades (up

to 2 mm) or needles (up to 1 mm). Inclusions within ilmenite blades contain pyroxene, plagioclase, K-feldspar and glass. Olivine is present as rare rounded grains within pyroxene (< 700 μm) with the exception of one large (1.7 mm diameter) lens shaped, embayed olivine grain which is not included or intruded by any other phase (Figure 3.14). Bladed or acicular plagioclase crystals are found around the margins of large clinopyroxene masses, inter-grown with Fe-rich pyroxene. Irregular troilite grains up to 500 μm in length are randomly dispersed and do not contain FeNi blebs. Phosphate phases are rare (<0.01 %) within in this sample, and occur as needle clusters less than 50 by 10 μm, too small for mineralogical identification. Small areas of mesostasis (< 200 μm) are associated with Fe-rich pyroxene and consist of interstitial glass enriched in K, Al and Ca (Figure 3.15). Irregular vesicles from 3 mm to < 100 μm diameter are common in this sample.

3.1.8. 12016,39: Apollo 12 Low-Ti, Low-Al, Low-K Mare Basalt. Sample 12016,39 contains ~ 1 mm-sized subhedral pyroxene grains with Mg-rich cores zoning to Fe-rich rims (Figure 3.16). These pyroxene grains sub-ophitically include irregular, commonly bladed and partially resorbed ilmenite (< 700 μm), and subhedral olivine (< 1 mm) with normal zoning. Ilmenite resorbtion hollows contain pyroxene, plagioclase and silica. Spinel (< 200 μm) of varying Cr and Ti compositions (section 3.2.5) is associated with pyroxene and olivine, though there appears to be no relationship between spinel composition and phase association. For example, Cr-rich spinels are not preferentially associated with olivine. Largely mm-sized subhedral-anhedral plagioclase surrounds the above phases, rarely displaying an intergrown texture with areas of Fe-rich pyroxene. Troilite and silica (both < 250 μm), F-rich apatite needles (< 30 μm in length), FeNi blebs within troilite (< 5 μm), and rare mesostasis (< 0.01 %, < 30 μm diameter), are also associated with areas of Fe-rich pyroxene (Figure 3.17). Irregular voids are visible in this thin section, the largest of which is 1 mm in length.

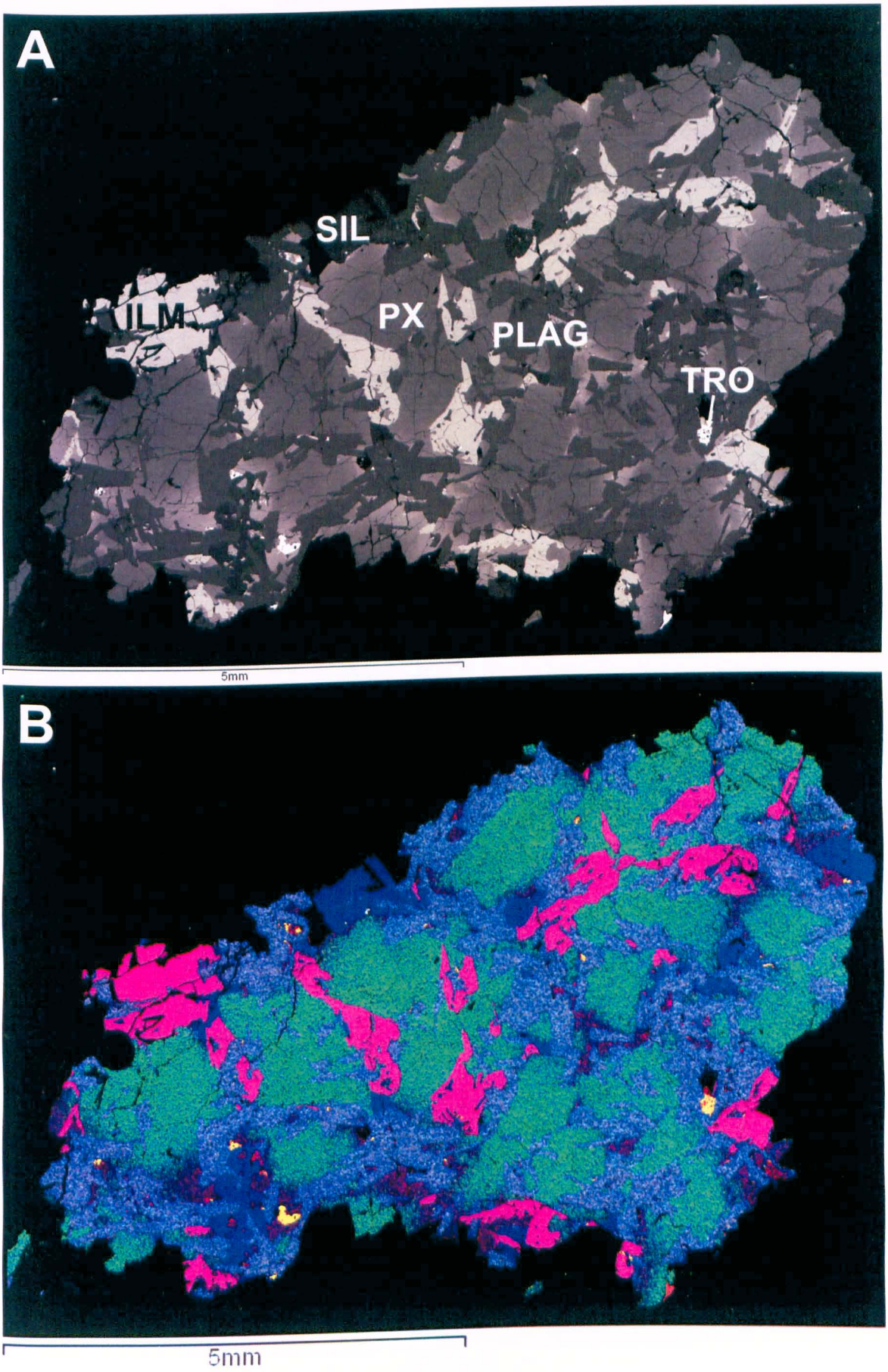

Figure 3.11: Apollo 11 sample 10058. **(a)** Backscatter image. **(b)** False colour x-ray image (elemental key as in Figure 3.1b). A large Fe metal grain rich in Cr is shown in red at the bottom right of the latter image.

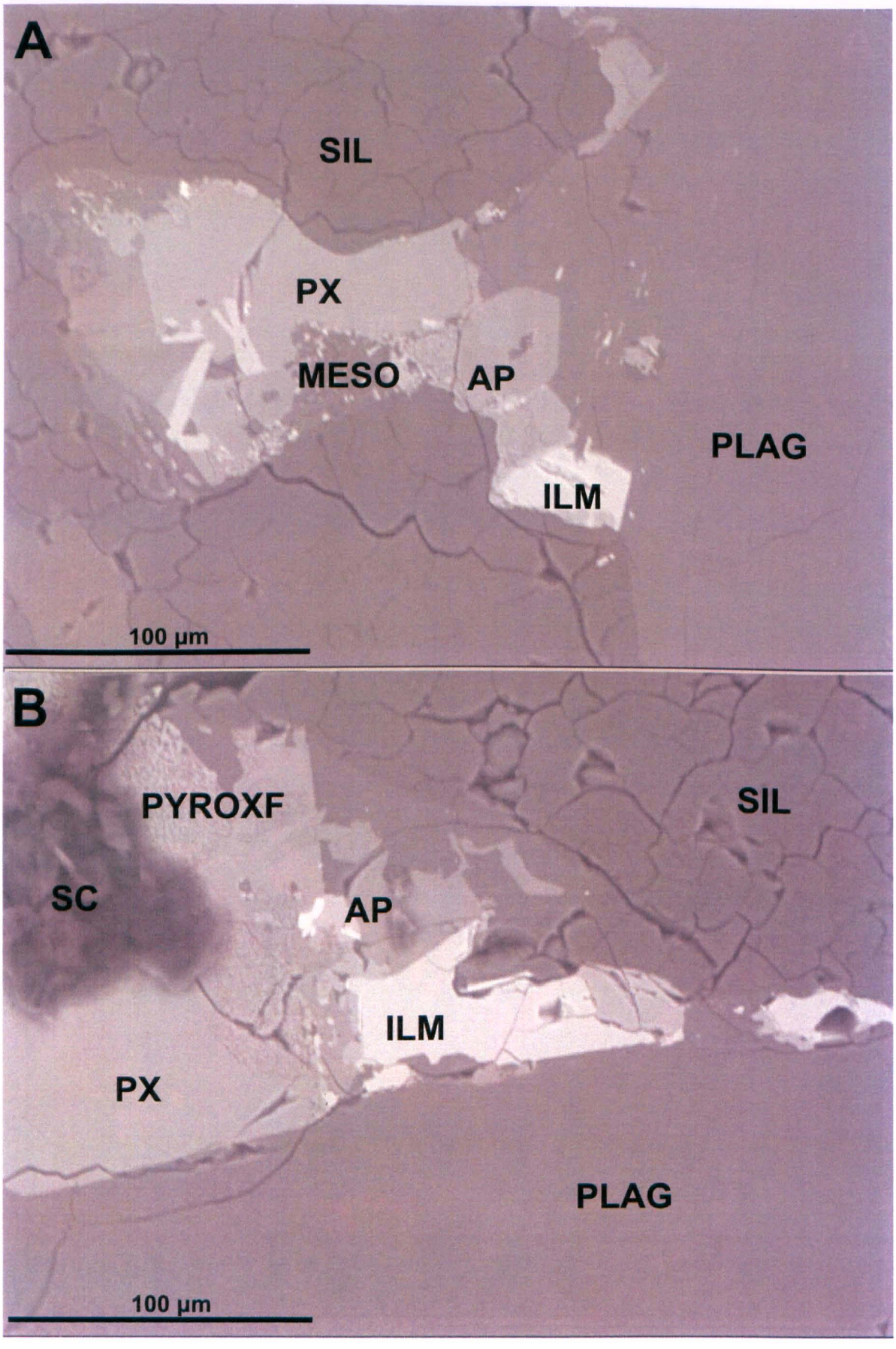

Figure 3.12: Apollo 11 sample 10058 high resolution backscatter electron images. Highlighting **(a)** mesostasis and associated minerals, **(b)** pyroxferroite. The latter also shows surface contamination (sc) towards the left of the image.

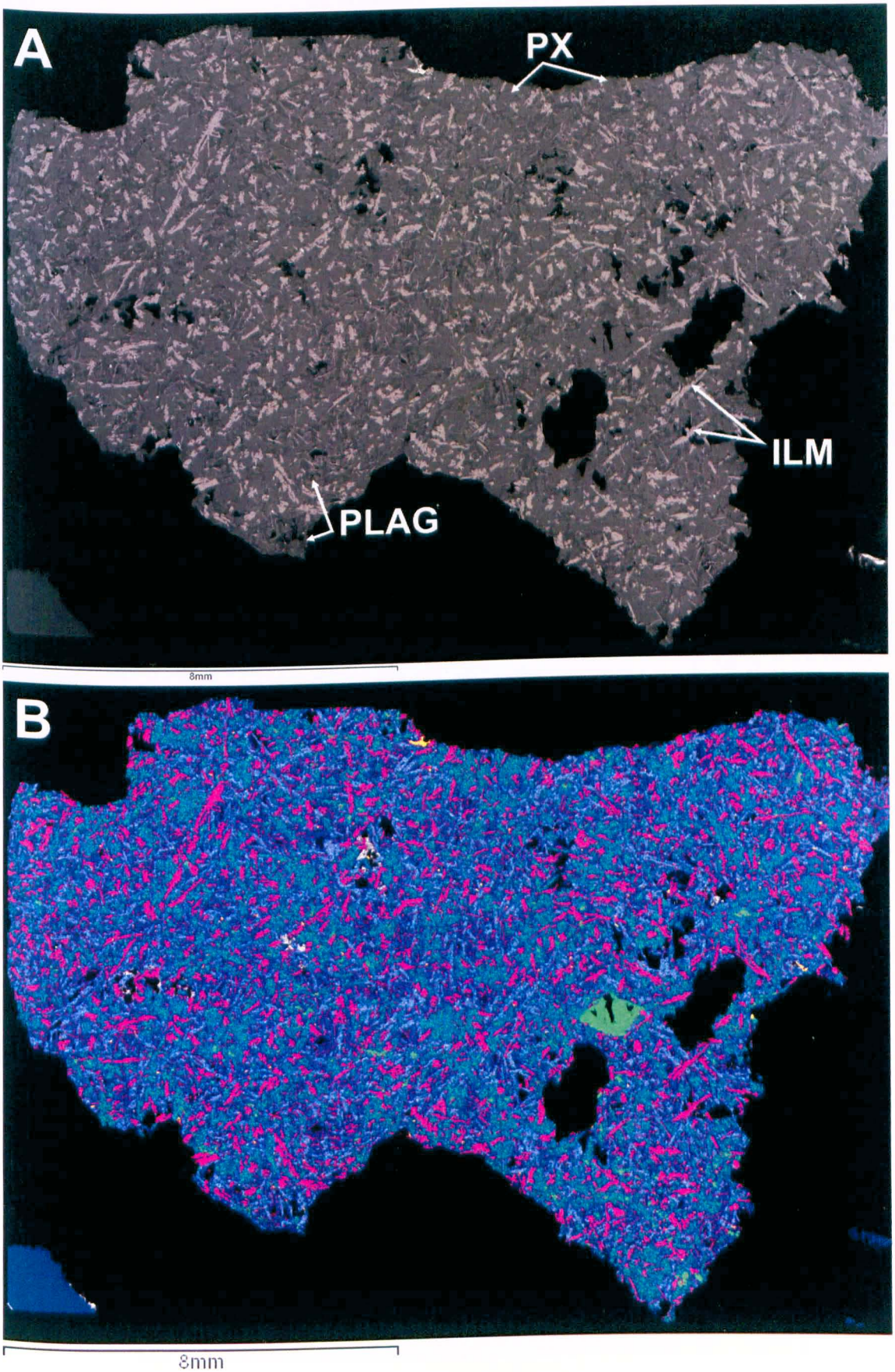

Figure 3.13: Apollo 11 sample 10072. **(a)** Backscatter image. **(b)** False colour x-ray image (elemental key as in Figure 3.1b). The obvious bright green grain to the right of the latter image is an embayed olivine grain, smaller olivine cores are visible within pyroxene.

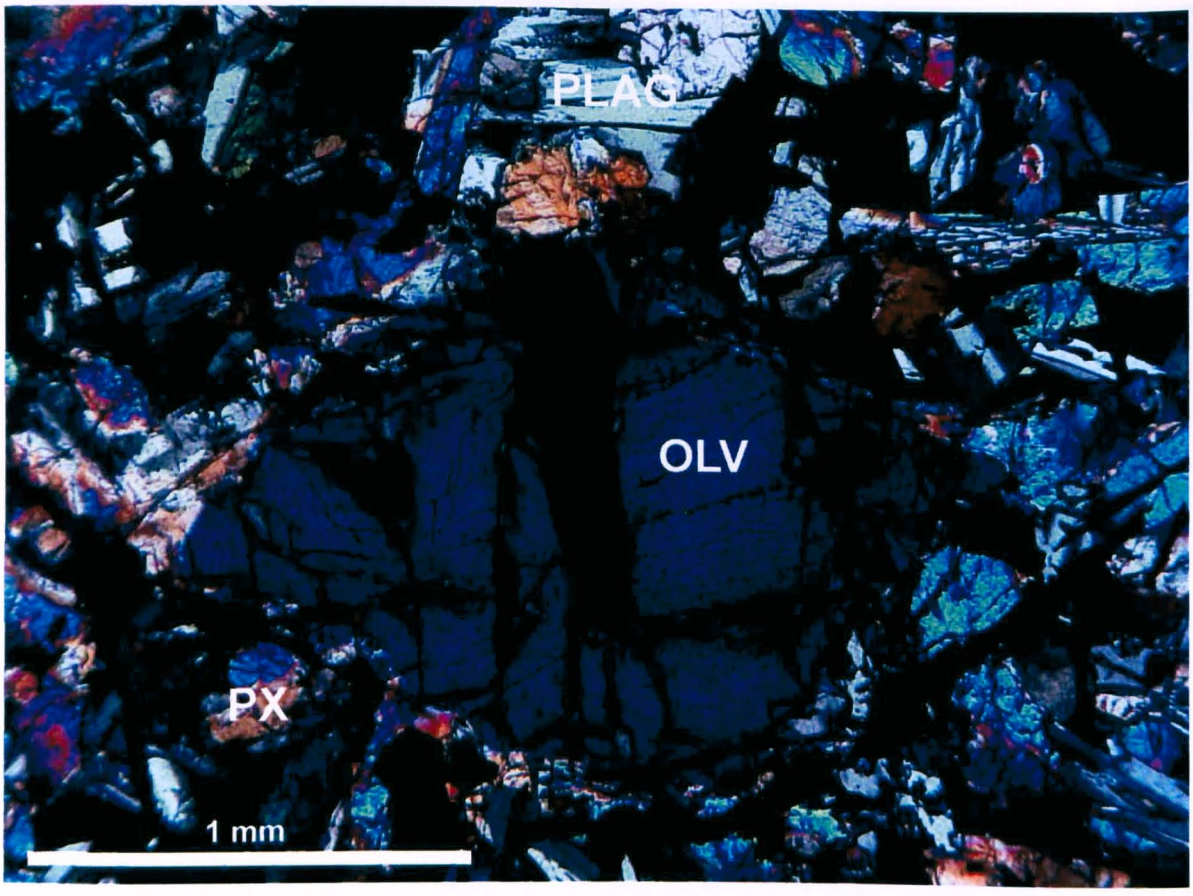

Figure 3.14: Apollo 11 sample 10072 optical microscope crossed polarised light (XPL) image. This image displays the sole large olivine grain found within this sample, which shows signs of pyroxene embayment at its edges but no intrusions or included phases.

3.1.9. 12040,44: Apollo 12 Low-Ti, Low-Al, Low-K Mare Basalt. This sample contains subhedral, zoned olivine (< 2 mm) grains (Figure 3.18). Fe-rich olivines are associated and often intergrown with irregular ilmenite (< 1.5 mm) commonly showing resorbtion hollows (Figure 3.19). Pyroxene crystals up to 4 mm in length surround the more Mg-rich olivine grains, both of which are associated with spinels of varying compositions (as in sample 12016,39). Fe-rich olivine and ilmenite are mostly observed at pyroxene grain boundaries, as is troilite (< 100 μm) containing FeNi blebs (< 30 μm). Anhedral plagioclase (mm-sized) occurs at pyroxene grain boundaries but is also found intergrown with pyroxene. Mesostasis containing K-feldspar (< 200 μm), F-rich apatite (< 50 μm), (RE)-merillite (< 30 μm) and baddeleyite (< 5 μm) are associated with plagioclase. No vesicles are visible in this thin section.

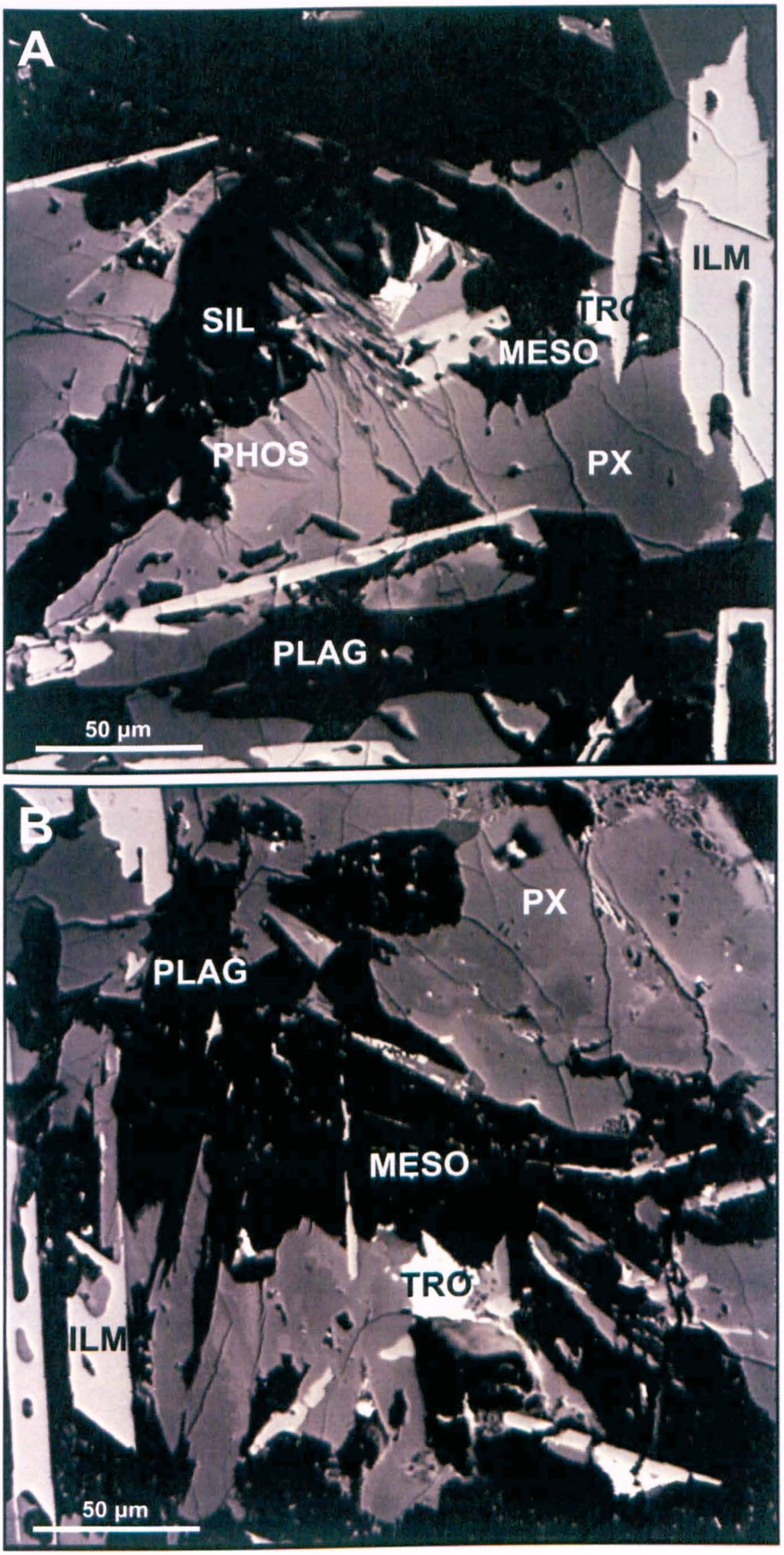

Figure 3.15: Apollo 11 sample 10072 high resolution backscatter electron images. Highlighting **(a)** rare phosphate (phos) phases, **(b)** mesostasis and associated minerals.

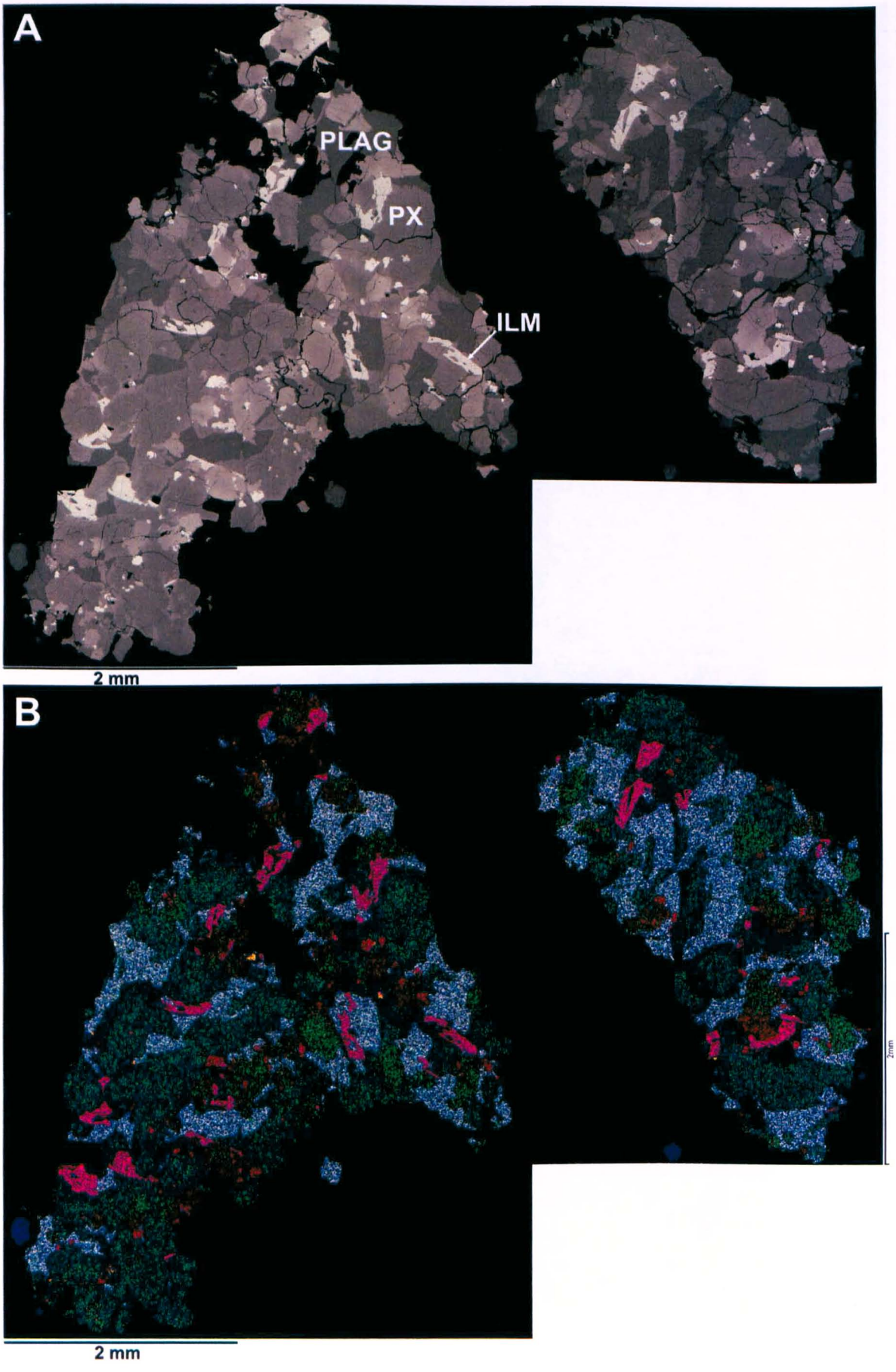

Figure 3.16: Apollo 12 sample 12016. **(a)** Backscatter electron image. **(b)** False colour x-ray image (key as in Figure 3.1b). The latter highlights olivine zonation from Mg-rich (green) to Fe-rich (red).

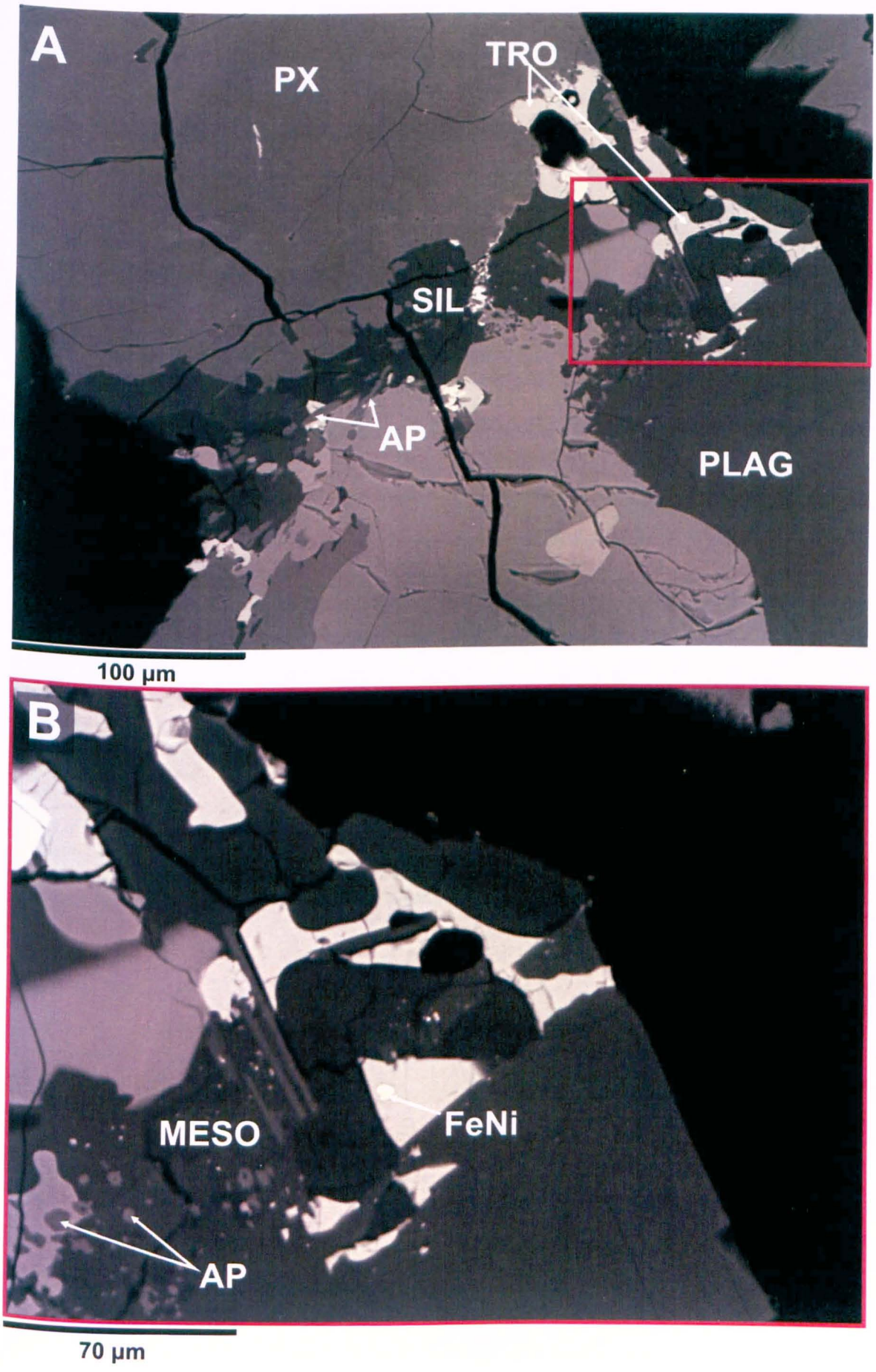

Figure 3.17: Apollo 12 sample 12016 high resolution backscatter electron images. Showing **(a)** minor minerals silica, troilite and apatite, **(b)** mesostasis.

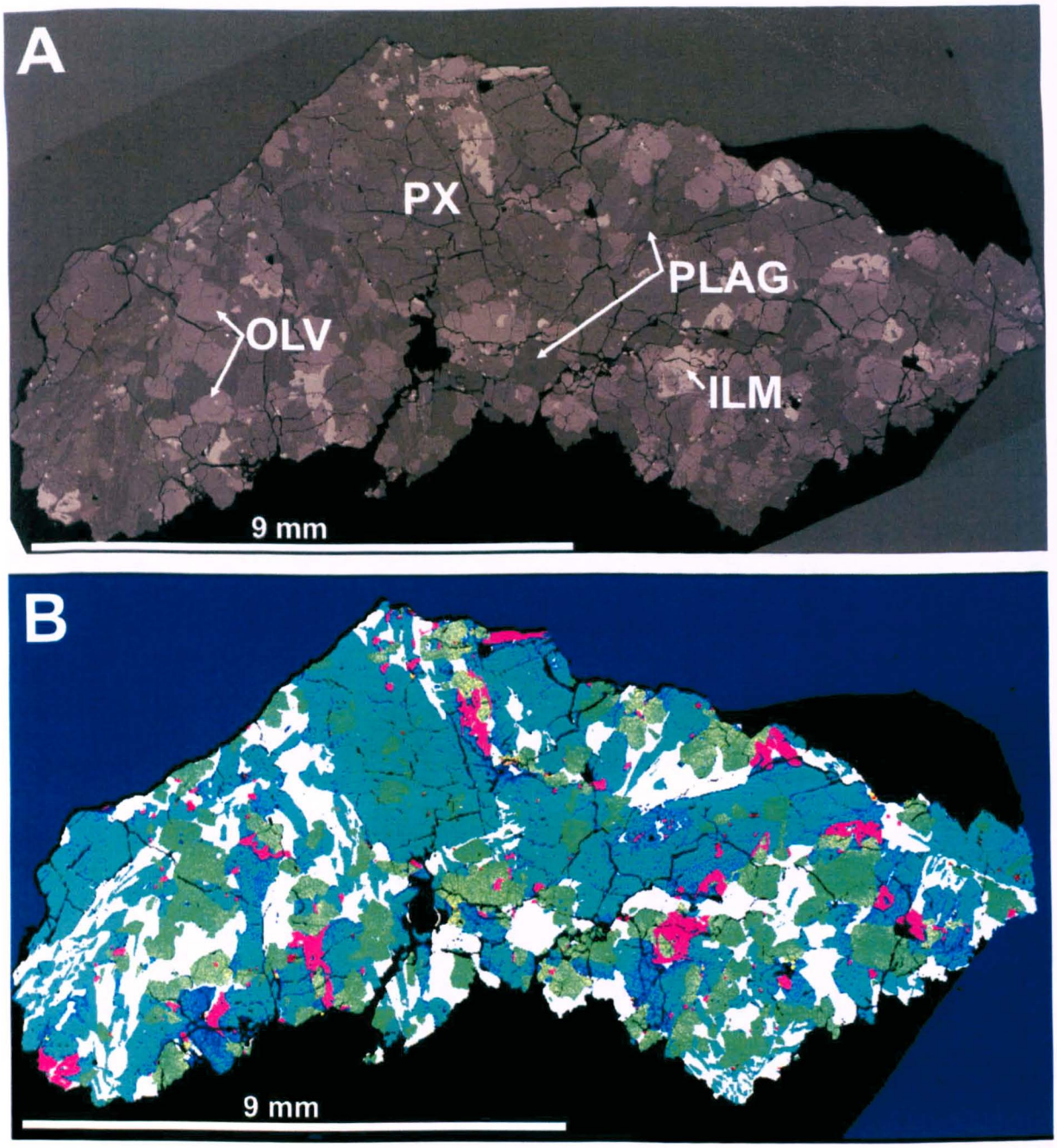

Figure 3.18: Apollo 12 sample 12040. **(a)** Backscatter electron image. **(b)** False colour x-ray image (elemental key as in Figure 3.1b).

3.1.10. 12047,9: Apollo 12 Low-Ti, Low-Al, Low-K Mare Basalt. Sample 12047,9 contains circular vesicles up to 2 mm diameter and displays a hollocrystalline texture (Figure 3.20). Subhedral to anhedral pyroxene (< 2 mm) dominates this sample, zoned to Fe-rich compositions at grain rims. A smaller number of subhedral, Mg-rich pyroxenes are also present. Acicular plagioclase and ilmenite (both < 2 mm in length) are associated with these pyroxene rims and are mostly encapsulated by pyroxene. A number of ilmenite grains contain resorbtion hollows filled with feldspar and Fe-rich pyroxene. The most Mg-

rich pyroxene cores enclose rounded, embayed and partly resorbed olivine (< 1 mm); pyroxene cores and olivine appear to cluster together. Spinels (< 70 μm) with varying Cr and Ti contents are found within olivine or Mg-rich pyroxene. Minor minerals include anhedral silica (< 500 μm), K-feldspar, associated with plagioclase (< 100 μm), troilite (< 70 μm), F-rich apatite (< 100 μm) and rare fayalite at the extreme edge of pyroxene rims (< 20 μm). This fayalite is a by-product of pyroxferroite break-down and is associated with areas of Fe-rich pyroxene and apatite grains (Figure 3.21).

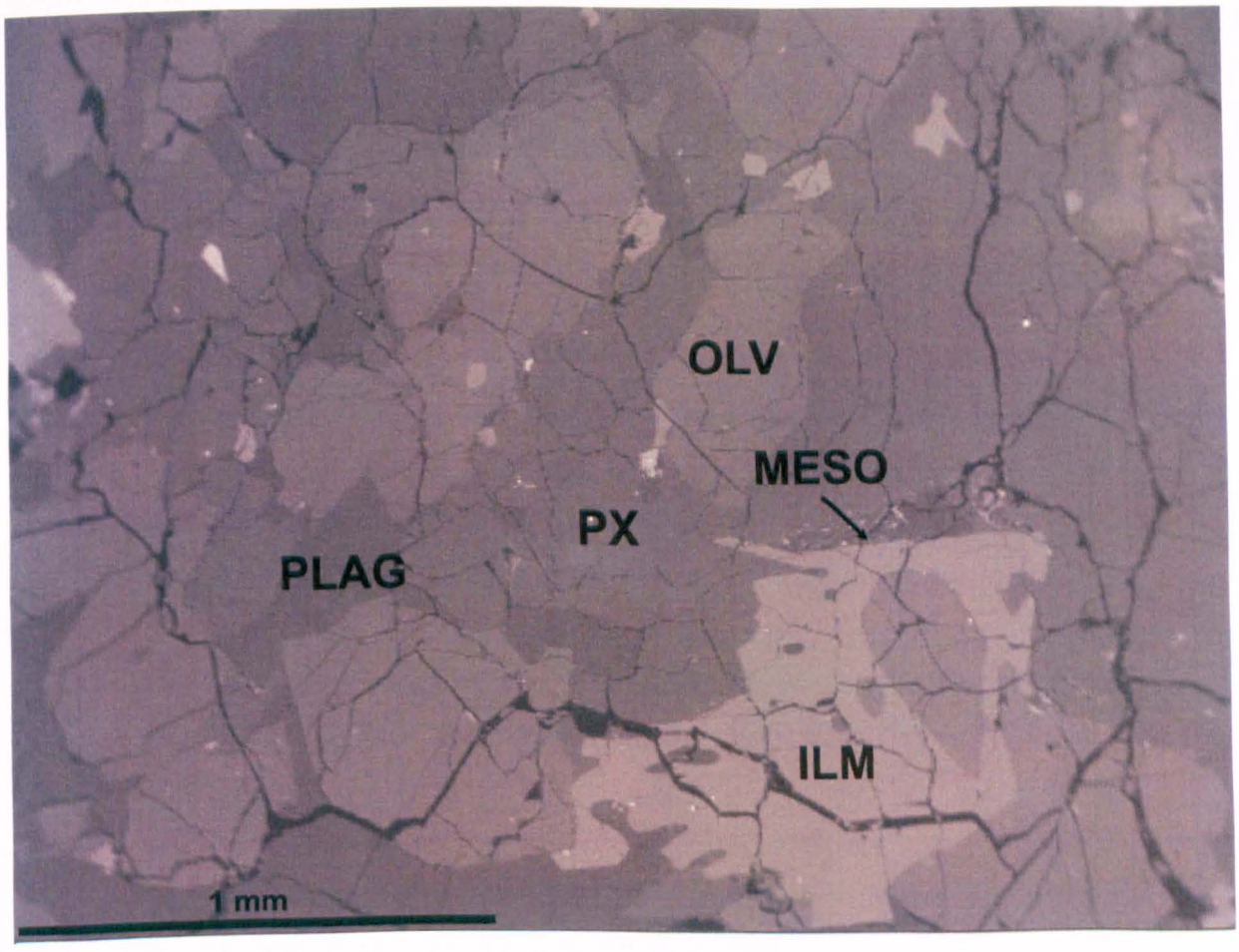

Figure 3.19: Apollo 12 sample 12040 high resolution backscatter electron image. The mesostasis and ilmenite resorbtion hollows are highlighted.

3.1.11. 12051,59: Apollo 12 Low-Ti, Low-Al, Low-K Mare Basalt. Plagioclase, pyroxene and ilmenite dominate this hollocrystalline sample (Figure 3.22). Euhedral Mg-rich pyroxene cores (< 3 mm) are overgrown with anhedral Fe-rich rims, the boundary between these two types of pyroxene may be sharp or disbursed. In rare instances, Fe-rich pyroxene

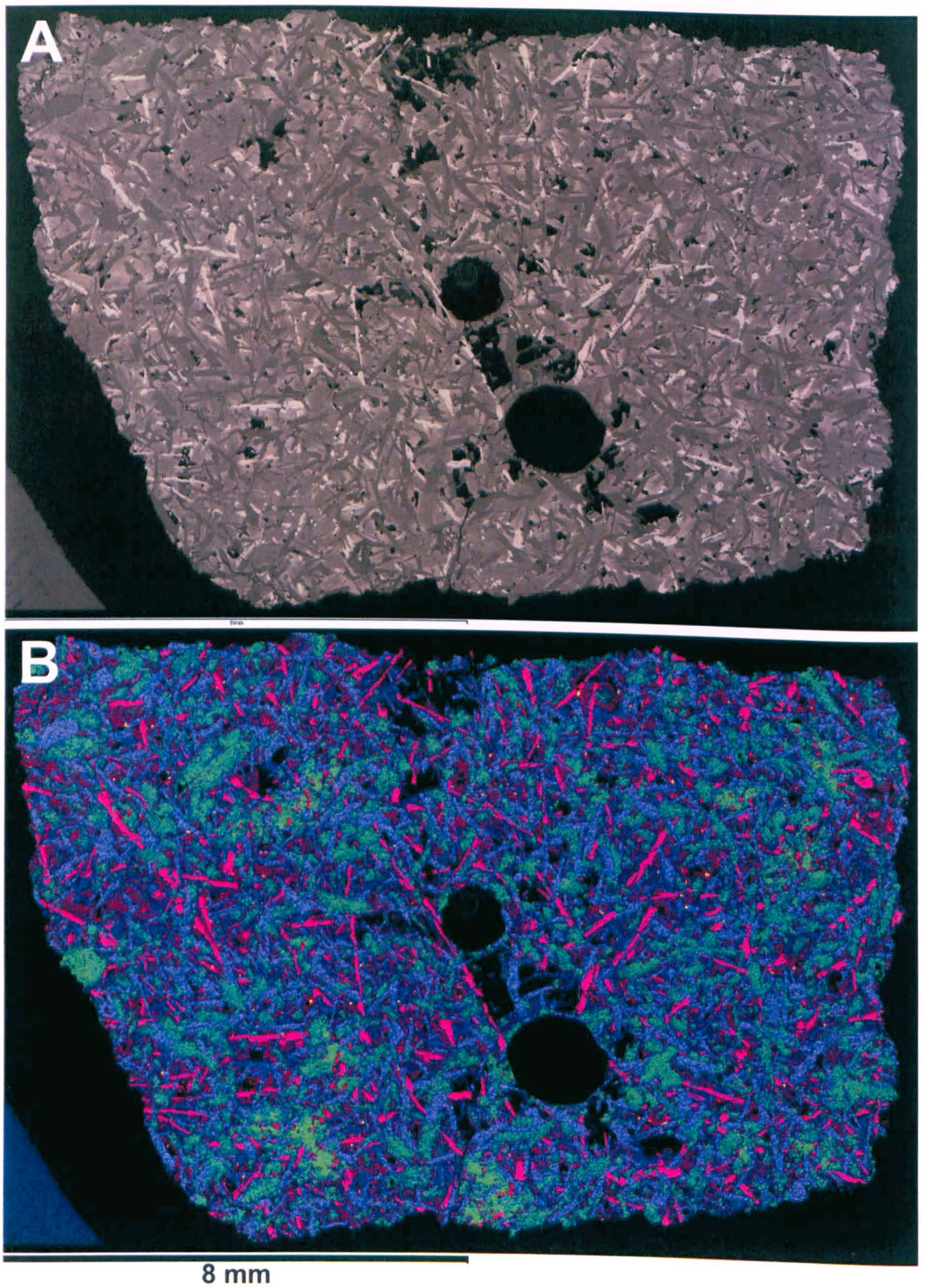

Figure 3.20: Apollo 12 sample 12047. **(a)** Backscatter electron image. **(b)** False colour x-ray image (elemental key as in Figure 3.1b). This latter image highlights olivine and Mg-rich pyroxene clusters as well as the existence of a small number of relatively large subhedral Mg-rich pyroxenes.

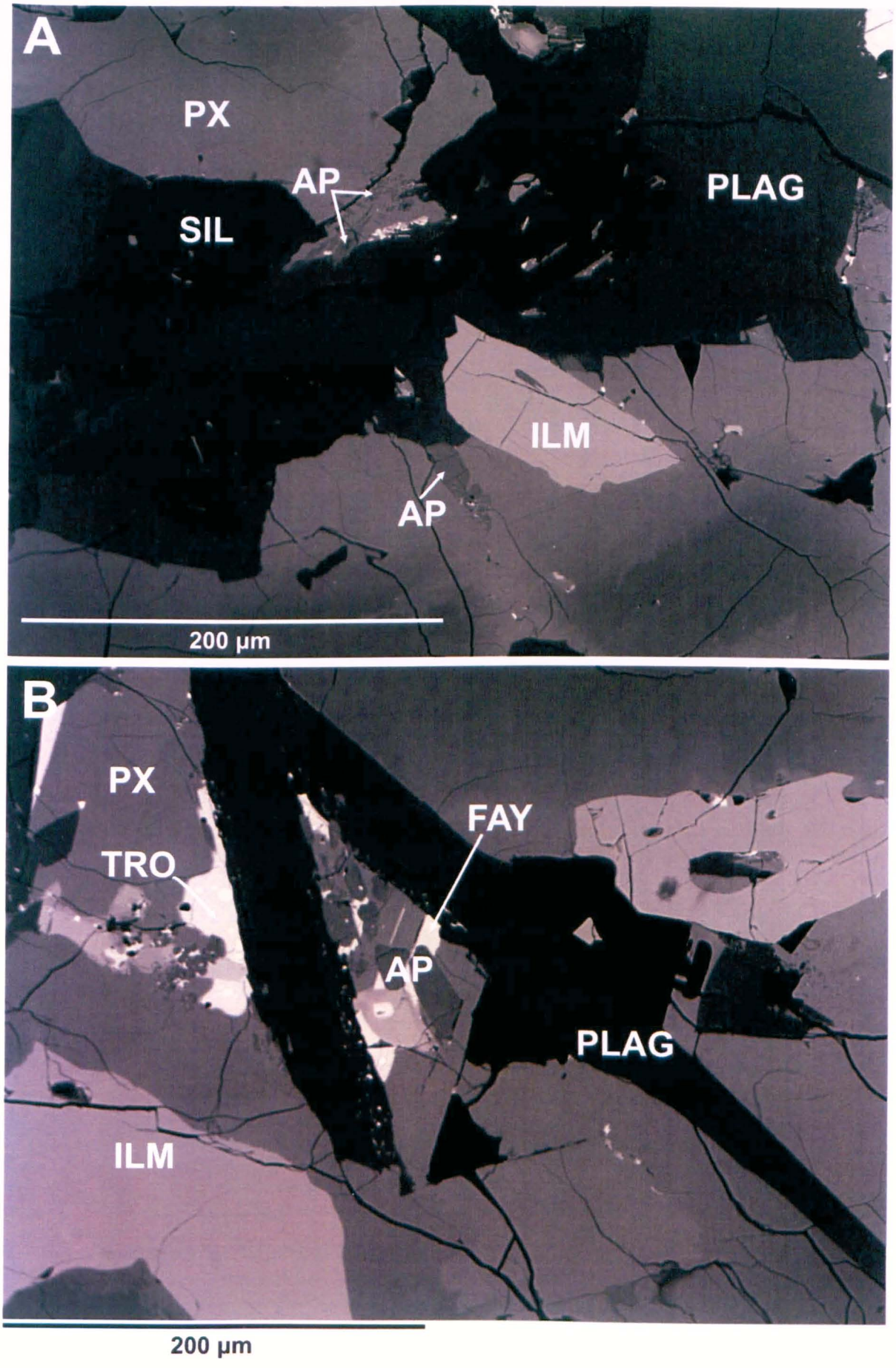

Figure 3.21: Apollo 12 sample 12047 high resolution backscatter electron images. Highlighting **(a)** silica and apatite, **(b)** troilite and fayalite.

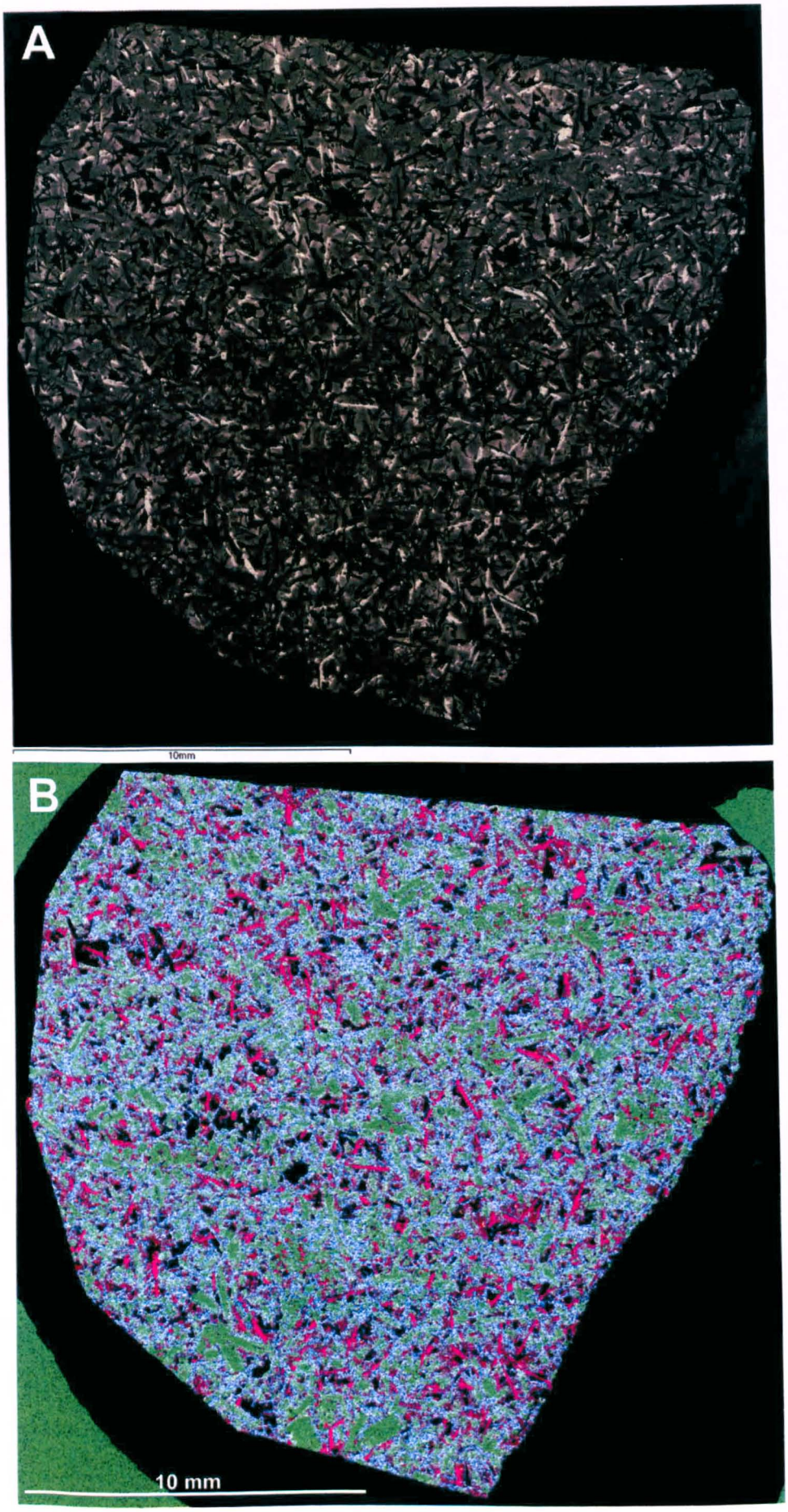

Figure 3.22: Apollo 12 sample 12051. **(a)** Backscatter electron image. **(b)** False colour x-ray image (elemental key as in Figure 3.1b).

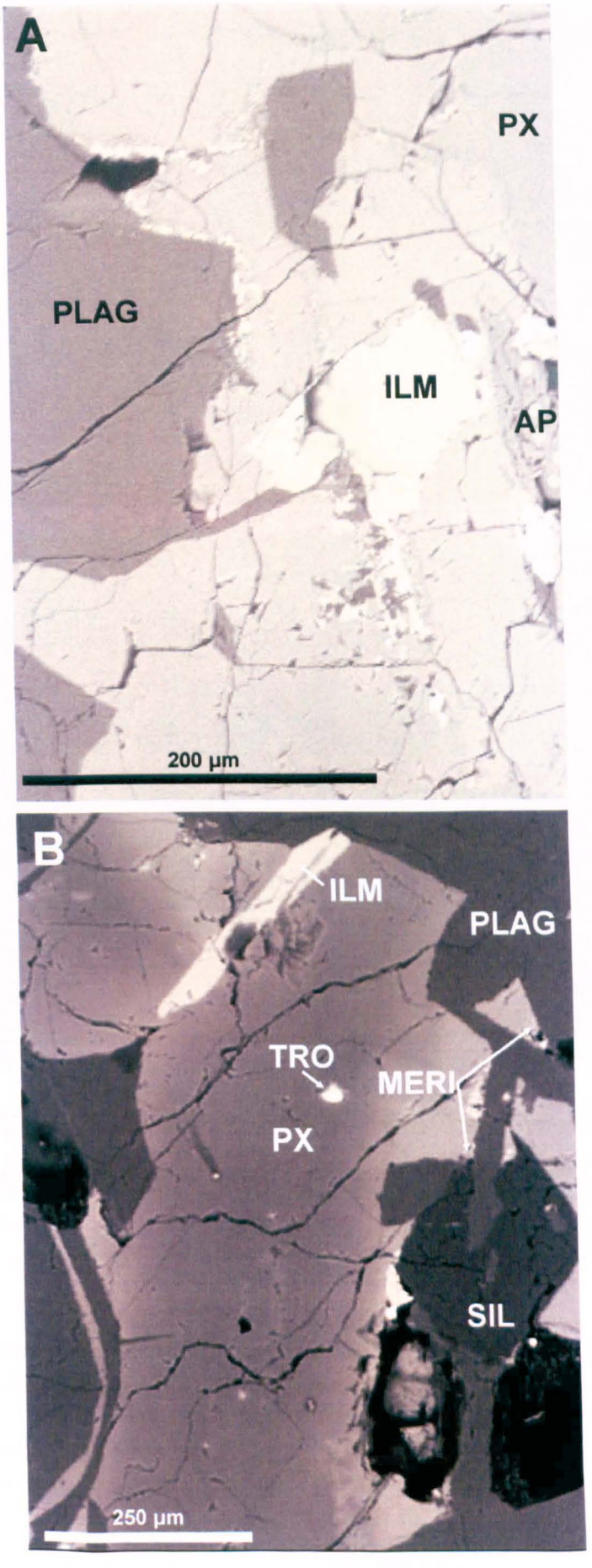

Figure 3.23: Apollo 12 sample 12051 high resolution backscatter electron images. Highlighting **(a)** apatite and **(b)** silica and (RE)-merillite. (RE)-merillite in these images is generally harder to distinguish than apatite as it has less pronounced boundaries and a similar brightness to pyroxene.

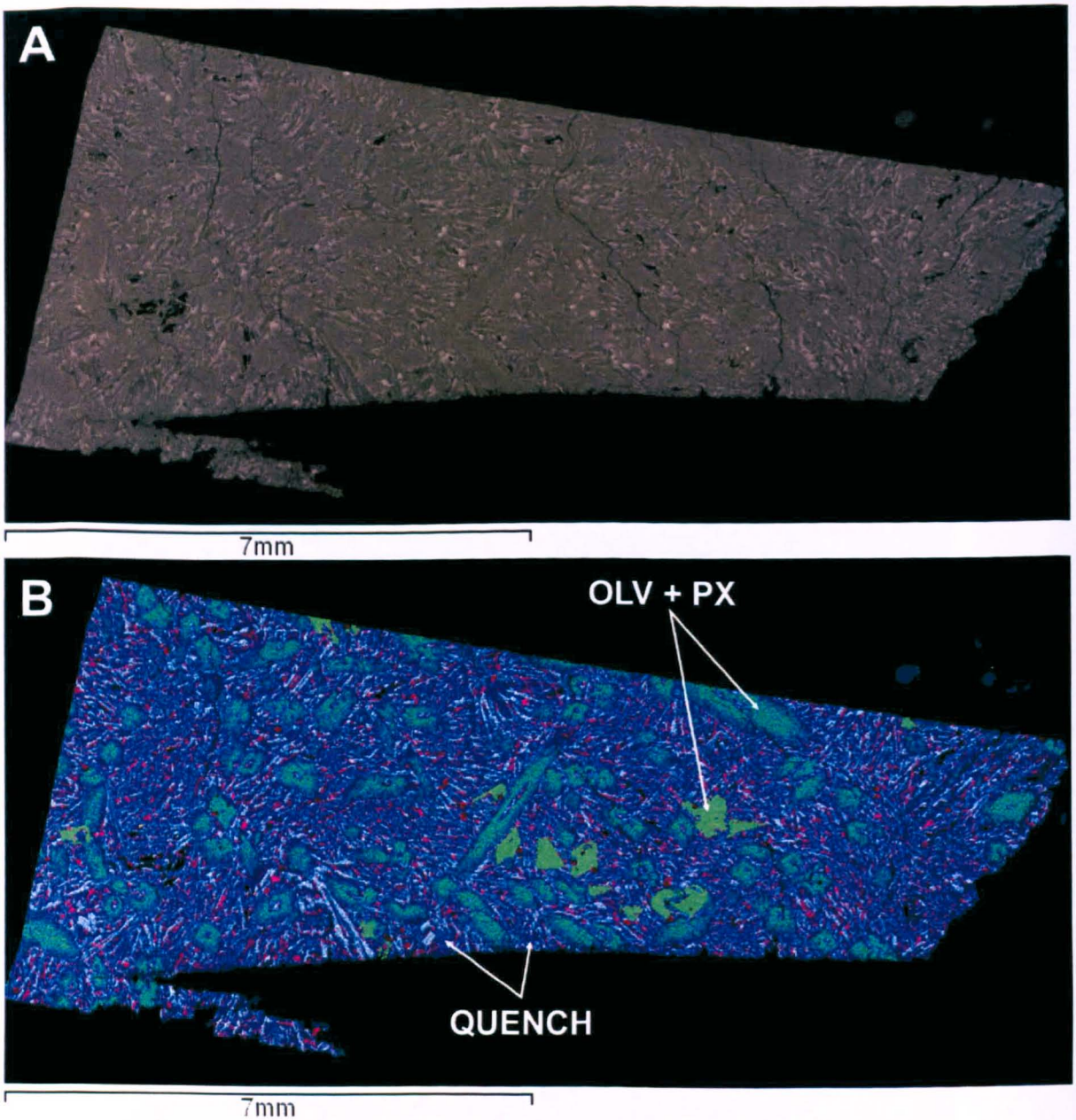

Figure 3.24: Apollo 12 sample 12052. **(a)** Backscatter electron image. **(b)** False colour x-ray image (elemental key as in Figure 3.1b). The latter image shows how olivine, pyroxene and spinel (in red) phenocrysts are frozen within a quench textured groundmass.

rims develop into pyroxferroite, found along with its breakdown products, silica, Ca-Fe pyroxene and fayalite, though these areas never reach more than ~ 100 μm diameter. Spinels (< 200 μm) of varying Cr and Ti compositions are associated with Mg-rich pyroxene, forming defined clusters. Long blades and laths of plagioclase (up to 2 mm) are sub-ophitically enclosed by pyroxene grains excepting the most Mg-rich pyroxene cores. Ilmenite blades (< 800 μm) and smaller anhedral grains are commonly found at pyroxene

grain boundaries or within the anhedral Fe-rich pyroxene overgrowths. Rare ilmenite resorbtion hollows can contain Fe-rich pyroxene, plagioclase, K-feldspar, silica and troilite. Silica (< 1 mm) is present as anhedral masses often intergrown with plagioclase and K-feldspar (< 200 μm). Silica is also associated with troilite (< 150 μm) containing FeNi blebs (< 50 μm), pyroxferroite (< 100 μm), (RE)-merillite and F-rich apatite (< 100 μm) (Figure 2.23). Irregular shaped vesicles are rare and small (200 μm) in this thin section.

3.1.12. 12052,339: Apollo 12 Low-Ti, Low-Al, Low-K Mare Basalt. Sample 12052,339 contains phenocrysts of elongated subhedral zoned pyroxene (up to 2.5 mm), subhedral olivine (< 700 μm) and associated chromite spinel (200 μm) (Figures 3.24 and 3.25). Pyroxene phenocrysts commonly exhibit skeletal 'soda straw' texture (appearing hollow along their length), zonation can be observed under an optical microscope - the rosy tint of pyroxene rims under plane polarised light indicates augite composition (Figure 3.26), which is further supported by mineral chemical analysis (section 3.2.1). Phenocrysts are set within a fine-grained quench textured groundmass consisting of intergrowths of radiating elongated plagioclase (< 1 mm), anhedral Fe-rich pyroxene (< 1 mm), bladed ilmenite (< 200 μm long), silica (< 100 μm) and troilite (< 100 μm). These groundmass crystals do not penetrate the phenocrysts, although olivine and pyroxene margins are slightly embayed. Troilite (< 30 μm) containing FeNi blebs (< 10 μm) commonly mantles spinel, in addition to occurring in the groundmass. It is not possible to distinguish any phosphate phases or other minor minerals because of the fine grained nature of the groundmass. Small (< 500 μm) irregular shaped vesicles are rare.

3.1.13. 12064,136: Apollo 12 Low-Ti, Low-Al, Low-K Mare Basalt. Sample 12064,136 exhibits one of the coarsest textures among all our samples, containing ilmenite blades up to 3 mm in length (Figure 3.27). Subhedral to anhedral, highly-zoned clinopyroxene (< 2 mm)

is inter grown with anhedral plagioclase (< 2 mm). SEM backscatter electron (BSE) images suggest that in a number of areas the iron content of pyroxene is comparable to that of ilmenite, this Fe-pyroxene commonly grades into pyroxferroite (and symplectite texture of silica, fayalite and Ca-rich pyroxene representing pyroxferroite breakdown products) where it is surrounded by ilmenite. Ilmenite blades and skeletal silica laths (up to 2 mm in length) are associated with Fe-rich pyroxene but are not associated with Mg-rich pyroxene cores. These cores commonly appear as skeletal ghost crystals within surrounding Fe-rich pyroxene and are rarely associated with irregular spinel (< 500 μm). The latter occur in two generations; Cr-rich spinel exists as 100-200 μm anhedral and subhedral grains mantled by Ti-rich spinel which also occurs as isolated anhedral grains up to 300 μm diameter. Silica is mostly associated with ilmenite. In addition, it occasionally shows intergrowth textures with plagioclase. Minor minerals include anhedral troilite (< 100 μm), elongated F-rich apatite (< 300 μm in length), K-feldspar (< 100 μm), pyroxferroite (< 700 μm – with breakdown products composed of silica, Ca, Fe-rich pyroxene and fayalite) and baddeleyite (< 10 μm). These are all associated with Fe-rich pyroxene areas (Figure 3.28). In this thin section, a single area (~ 1.5 mm diameter) of mesostasis is present containing numerous apatite and troilite inclusions, with pyroxferroite at its edge as well as surrounding silica and ilmenite blades. The coarse-grained texture and absence of glass in this sample indicate relatively slow cooling. This sample contains no vesicles. Fayalite is known to exist in sample 12064 in trace amounts (Kushiro et al., 1971) but none was found in this thin section.

3.1.14. Sample 14053,19: Apollo 14 Low-Ti, High-Al, Low-K Mare Basalt. Sample 14053,19 is dominated by anhedral zoned-pyroxene grains (up to 2 mm) with Mg-rich cores and Fe-rich rims (Figure 3.29). These cores contain inclusions of anhedral, slightly rounded olivine (up to 1.5 mm) and spinel (< 500 μm). Two groups of spinel are present, (i) subhedral Cr-rich spinel with slight zonation towards more Ti-rich spinel and (ii) anhedral Ti-rich grains. Both varieties are associated with Mg-rich pyroxene cores and can be found

as inclusions within olivine. Subhedral to euhedral, acicular or bladed plagioclase (up to 1 mm in length) is commonly associated with Fe-rich pyroxene, however smaller blades can be found within Mg-pyroxene cores and olivine. Irregular ilmenite (up to 1 mm) is rare compared to plagioclase and is entirely associated with Fe-rich pyroxene at pyroxene grain boundaries. Ilmenite resorbtion hollows are common and mostly contain Fe-rich pyroxene, plagioclase, silica and troilite. Irregular silica (up to 1 mm but commonly < 700 μm) is also associated with Fe-rich pyroxene rim areas as is troilite (< 150 μm), FeNi (< 100 μm), K-rich glass (< 500 μm – often but not exclusively found with plagioclase), pyroxferroite and its degraded components (< 300 μm), F-rich apatite (disarticulated needles up to 500 μm long), mesostasis (< 100 μm) and (RE)-merillite (< 100 μm) (Figure 3.30). FeNi is usually mantled rather than enclosed by troilite in this sample. Irregular vesicles are rare and small (< 700 μm).

3.1.15. 15016,7: Apollo 15 Low-Ti, Low-Al, Low-K Mare Basalt. Sample 15016,7 contains the largest spherical vesicles among all our samples (up to 4 mm diameter) (Figure 3.31). It contains subhedral-anhedral zoned pyroxene (up to 2 mm), with highly zoned subhedral olivine (up to 1 mm) and Cr-spinel (< 200 μm) within the Mg-rich pyroxene cores. Acicular plagioclase (< 1.5 mm) is intergrown with the Fe-rich rims of pyroxene, irregular ilmenite (< 500 μm) and minor minerals are also associated with these rims. In addition, the smaller spinel grains (< 100 μm) appear to cluster around the vug edges. Minor phases include silica (< 200 μm), troilite (< 50 μm) containing FeNi blebs (< 10 μm), K-rich glass (< 150 μm), F-rich apatite (< 50 μm), (RE)-merillite (< 50 μm) and mesostasis (< 50 μm) (Figure 3.32).

3.1.16. 15386,46: Apollo 15 KREEP Basalt. Sample 15386,46 is dominated by anhedral plagioclase (up to 2 mm) intergrown with zoned acicular or irregular subhedral pyroxene

(< 1.5 mm). Pyroxene cores are Mg-rich compared to the rims, which appear embayed and partially resorbed but traces of euhedral outlines still remain (Figure 3.33). The Mg-rich

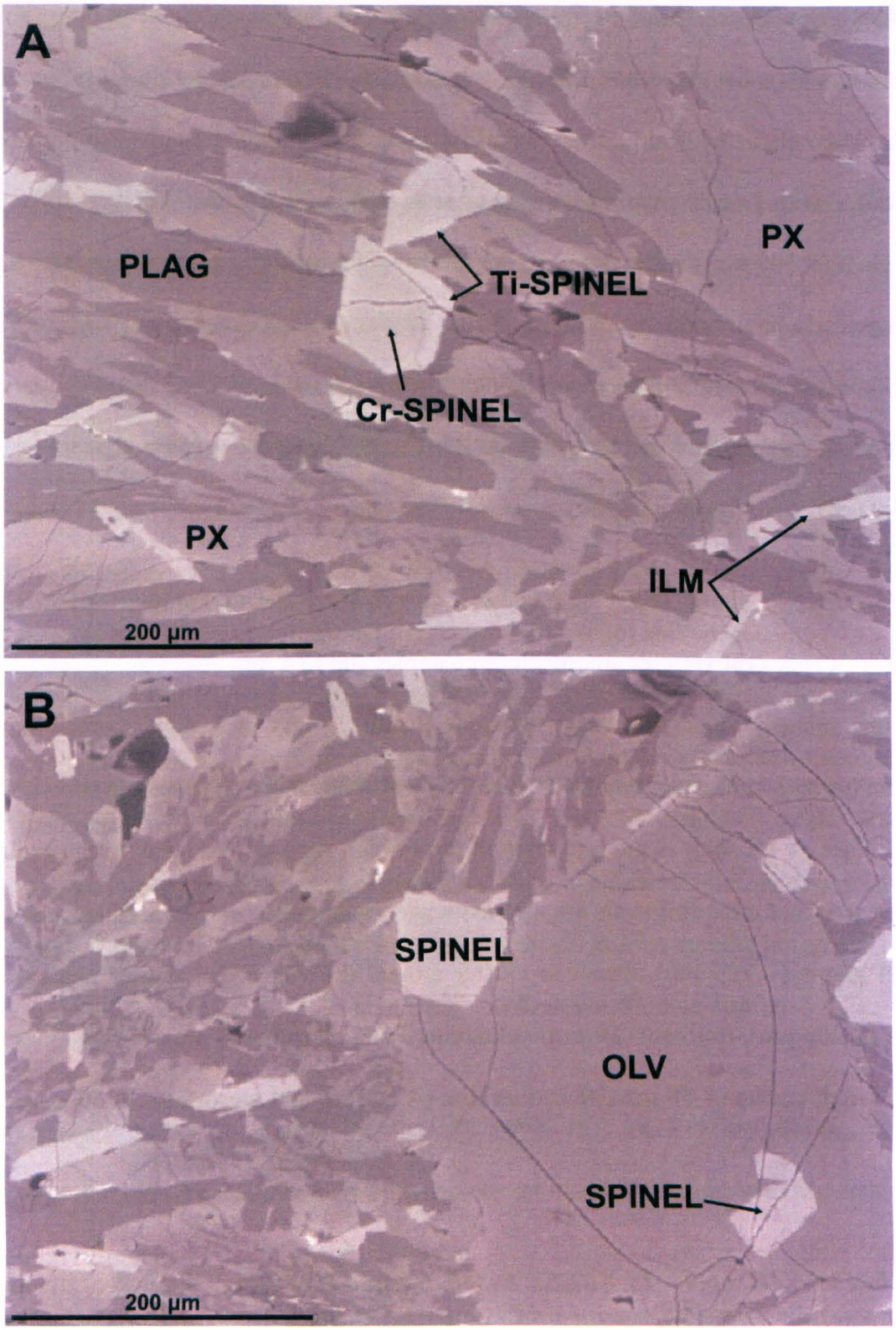

Figure 3.25: Apollo 12 sample 12052 high resolution backscatter electron images. Showing **(a)** Cr-spinel phenocrysts with Ti-spinel overgrowth, **(b)** spinel associated with olivine phenocrysts.

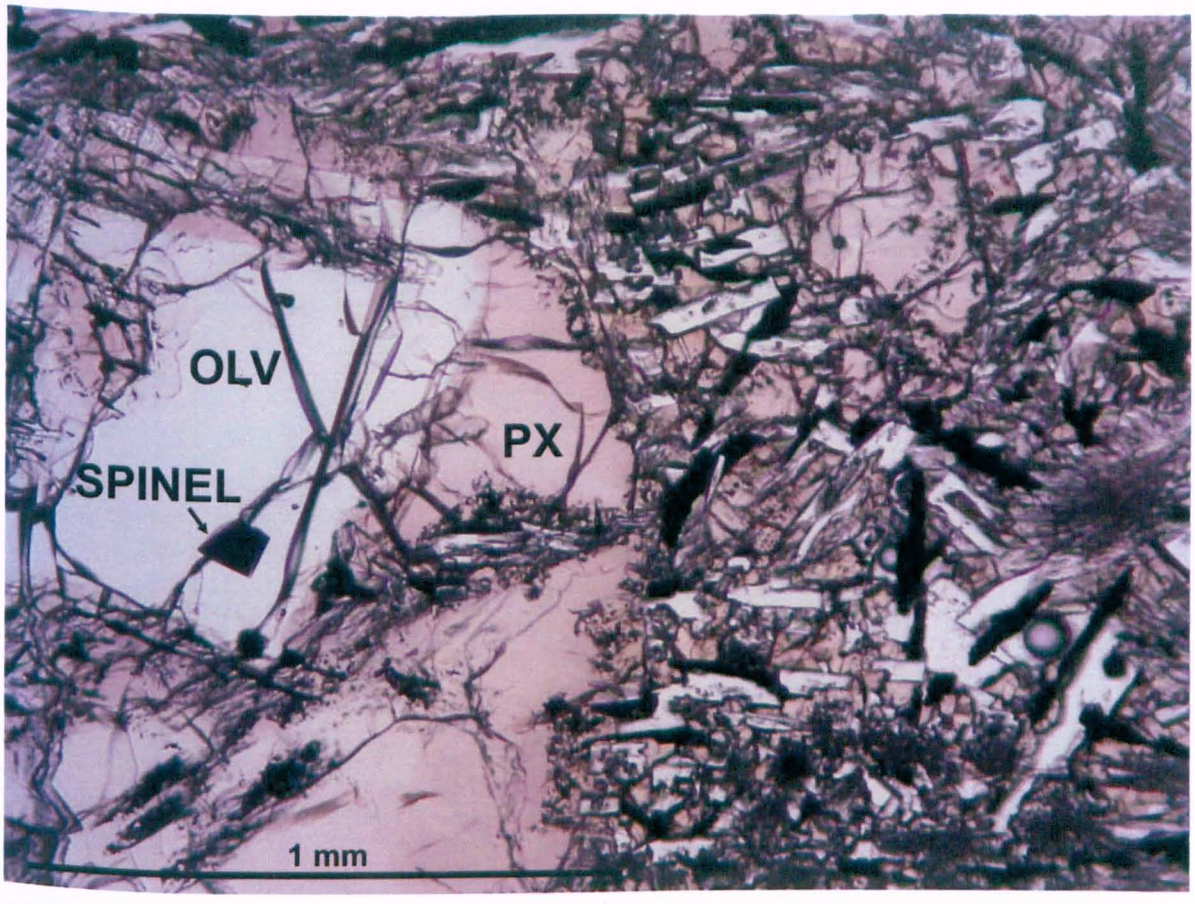

Figure 3.26: Apollo 12 sample 12052 plain polarised light (PPL) optical microscope image. The rosy colour of pyroxene is because of high Ti content, indicative of an augitic rather than pigeonite composition.

cores are not included or penetrated by any other phase, but the surrounding Fe-rich rims contain small anhedral Cr-rich spinels (< 100 μm). Plagioclase is associated with troilite (<100 μm) containing FeNi (< 20 μm); these are the only phases to form inclusions within plagioclase though other minerals show sub-ophitic relationship with plagioclase near the grain boundaries. Other minerals associated with plagioclase include acicular grains (< 700 μm in length) and needles of ilmenite (up to 1 mm in length), irregular silica (< 500 μm), disarticulated needles and acicular grains of F-rich apatite (700 μm and 300 μm in length respectively), acicular (RE)-merillite (< 250 μm in length) and baddeleyite (< 10 μm) (Figure 3.34). Areas of mesostasis (up to 700 μm diameter) within this sample are particularly abundant, containing mostly K-rich glass and Fe-rich pyroxene in addition to minor minerals (silica and independent FeNi blebs are especially associated). A number of irregular vesicles occur in this sample with a maximum diameter of 1 mm.

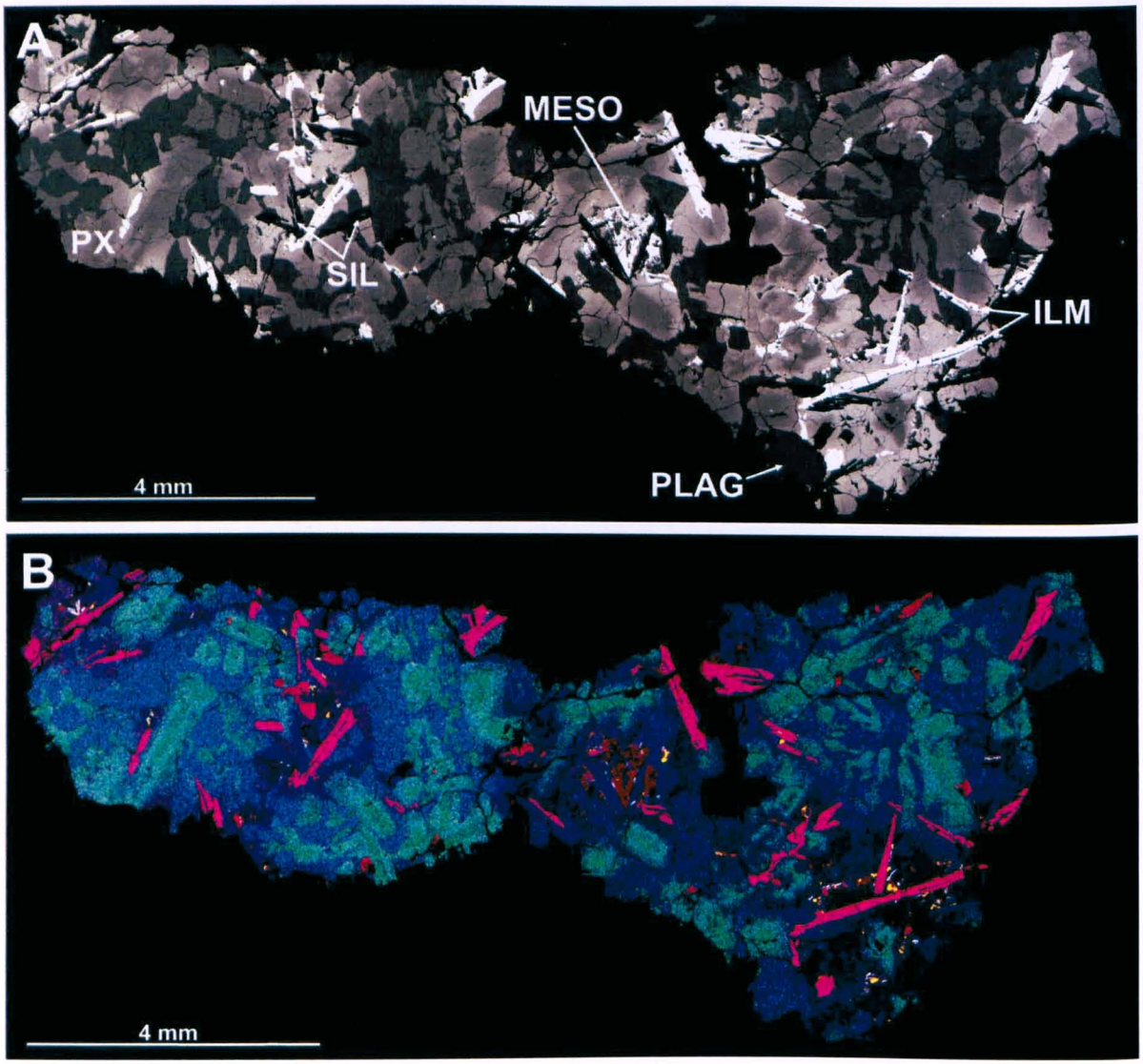

Figure 3.27: Apollo 12 sample 12064. **(a)** Backscatter electron image. **(b)** False colour x-ray image (elemental key as in Figure 3.1b except Ca = white rather than Al). This sample is highly zoned as can be seen by the transition of pyroxene from Mg-rich (dark grey) to Fe-rich (light grey) in the backscatter image. In addition, a large area of mesostasis is visible in the central region of this thin section (red in **b**). Ca rather than Al is represented in white, this highlights plagioclase in light blue and relatively large apatite grains in white.

3.1.17. 15555,206: Apollo 15 Low-Ti, Low-Al, Low-K Mare Basalt. Phenocrysts of zoned euhedral pyroxene (up to 3.5 mm but more commonly < 2 mm) and zoned subhedral olivine (< 1 mm) are surrounded by anhedral plagioclase in this sample (Figure 3.35). Smaller, less zoned, granular, rounded olivine can be found within the cores of pyroxene

phenocrysts. This olivine also occurs within plagioclase masses associated with small, granular, less-zoned pyroxene grains. Cr-rich spinel (< 150 μm) exists as inclusions within

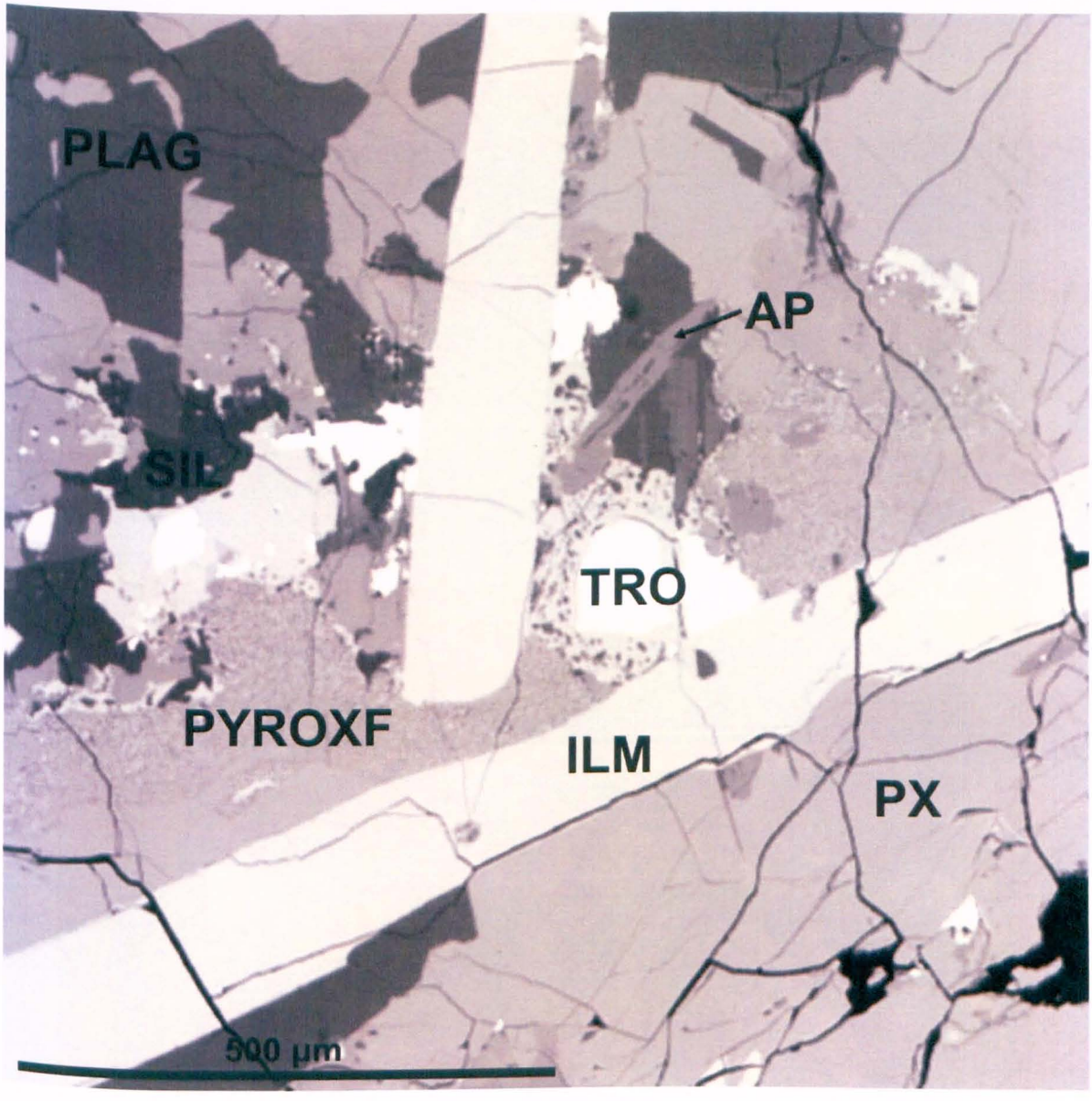

Figure 3.28: Apollo 12 sample 12064 high resolution backscatter image. Minor minerals, including silica, pyroxferroite, troilite and apatite are highlighted.

the large pyroxene and olivine phenocrysts, it is also found attached to the smaller grains of these phases within plagioclase. Comparatively rare ilmenite occurs as elongated irregular grains up to 1 mm in length and is mainly associated with Fe-rich pyroxene and olivine rims or the most fayalitic small olivine grains within plagioclase. Anhedral silica (< 500 μm), troilite (< 150 μm) and FeNi metal (< 30 μm) are also associated with these Fe-rich regions,

as are rare areas of mesostasis up to 200 μm in dimension. The mesostasis consists of K-rich glass containing Fe-pyroxene and troilite needles (both < 10 μm), zoned F-rich apatite (< 70 μm), (RE)-merillite (< 20 μm), baddeleyite (< 30 μm) and zirconolite (< 10 μm)

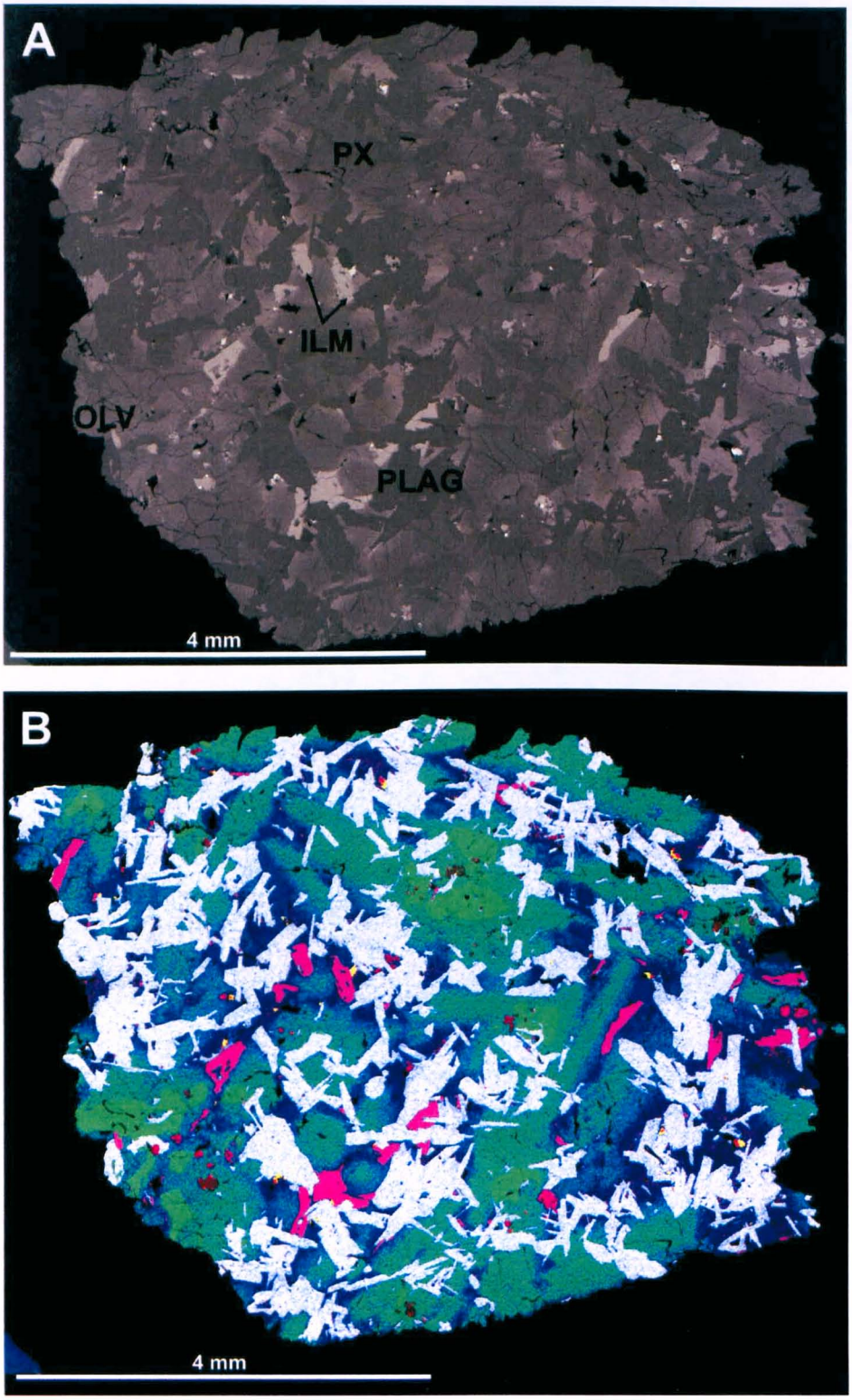

Figure 3.29: Apollo 14 sample 14053. **(a)** Backscatter electron image. **(b)** False colour x-ray image (elemental key as in Figure 3.1b).

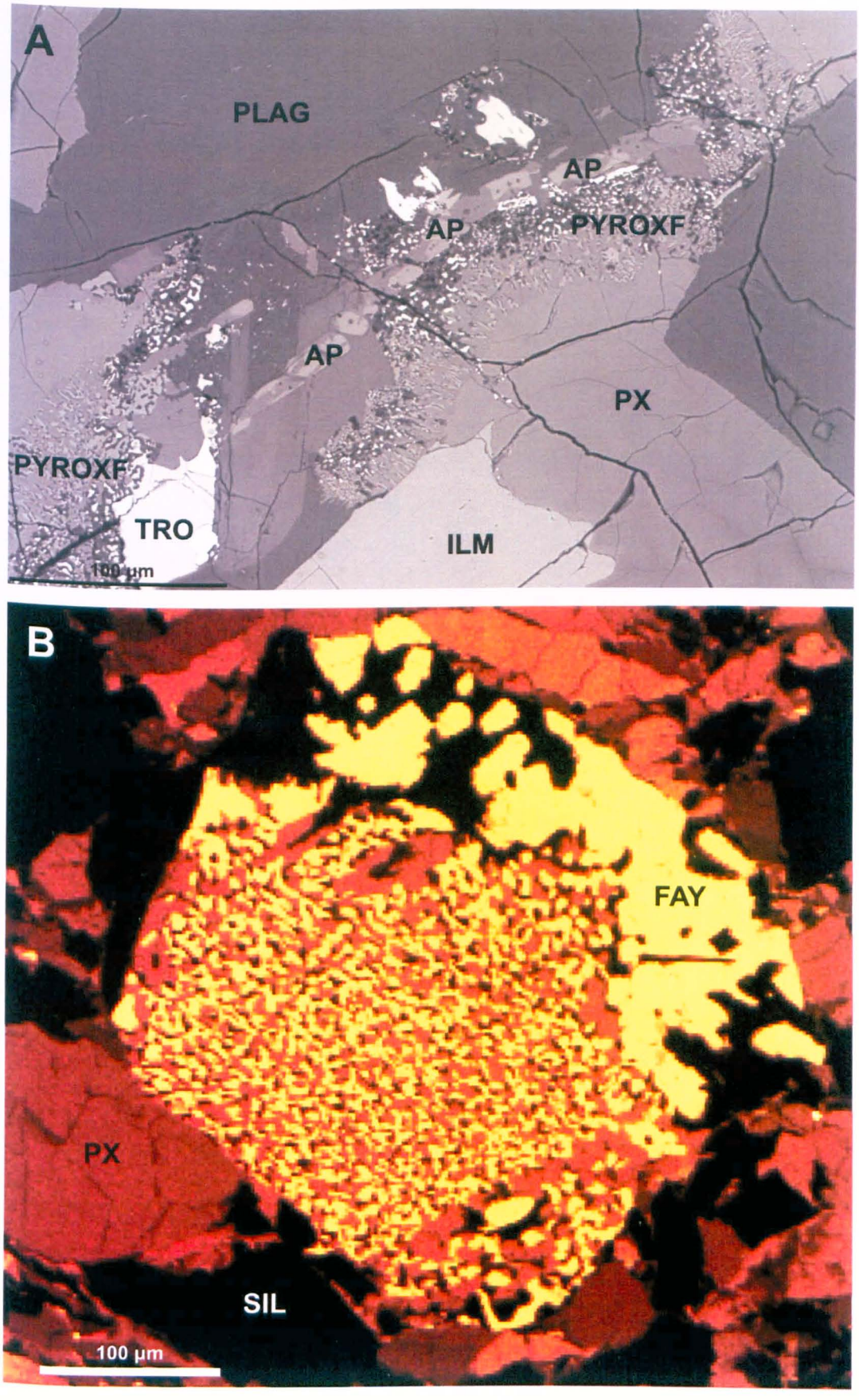

Figure 3.30: Apollo 14 sample 14053 high resolution images. **(a)** High resolution backscatter electron image displaying apatite and pyroxferroite. **(b)** High resolution x-ray image showing relative Fe content to highlight the three components of degraded pyroxferroite – silica (black), fayalite (yellow) and Fe, Ca rich pyroxene (orange).

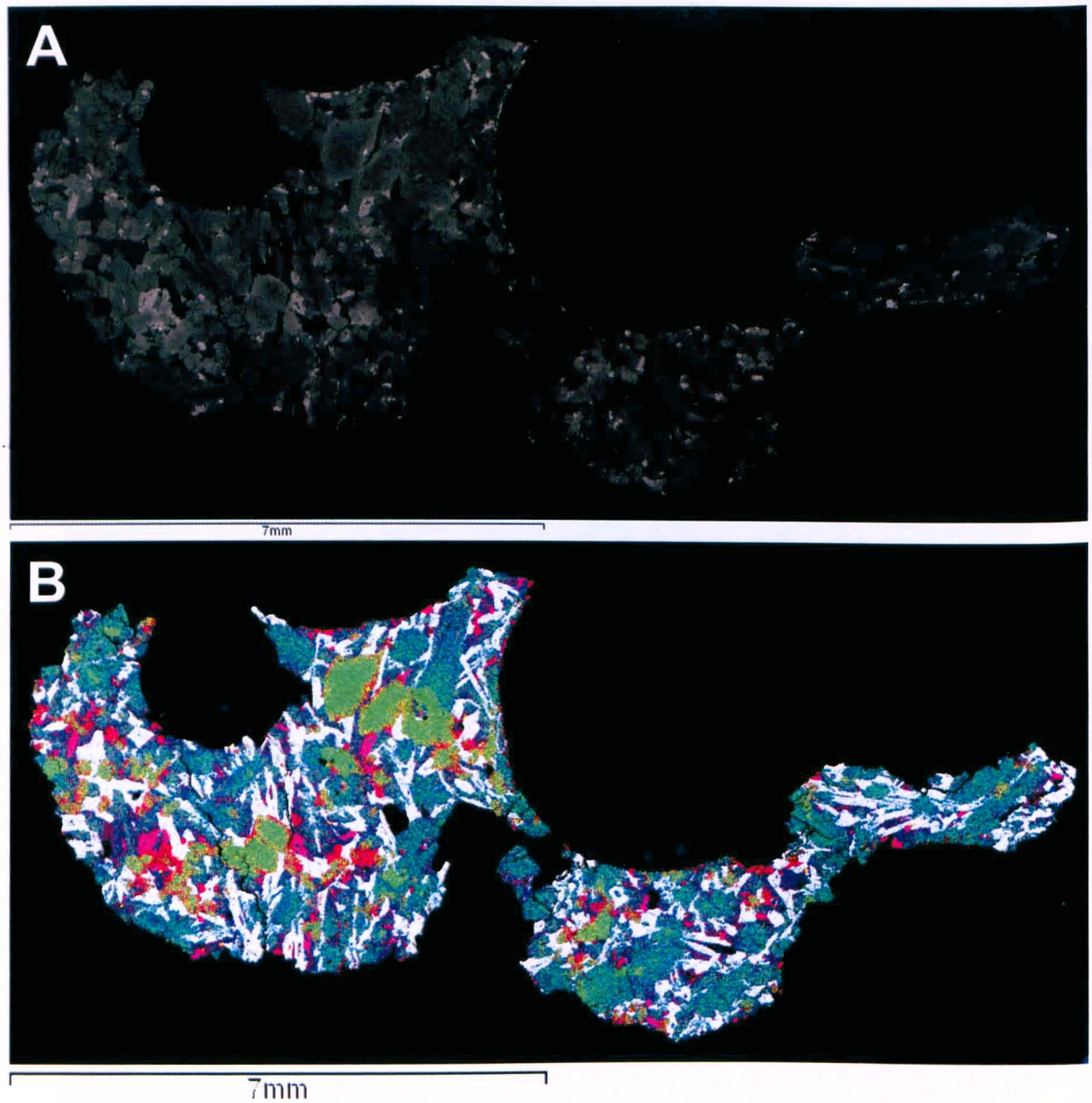

Figure 3.31: Apollo 15 sample 15016. **(a)** Backscatter electron image. **(b)** False colour x-ray image (elemental key as in figure 3.1b). Olivine is highly zoned from Mg-rich cores (green in x-ray image) to Fe-rich rims (red in x-ray image).

(Figure 3.36). Vugs are irregular but rounded and can reach up to 2.25 mm, however this thin section is of uneven thickness and it is, therefore, difficult to distinguish in this area whether holes are due to the presence of vesicles or simply the extreme thinness of the section.

3.1.18. Sample 70017,110: Apollo 17 High-Ti, Low-Al, Low-K Mare Basalt. Anhedral pyroxene (< 2 mm) is intergrown with anhedral elongated plagioclase (< 2 mm in length) in

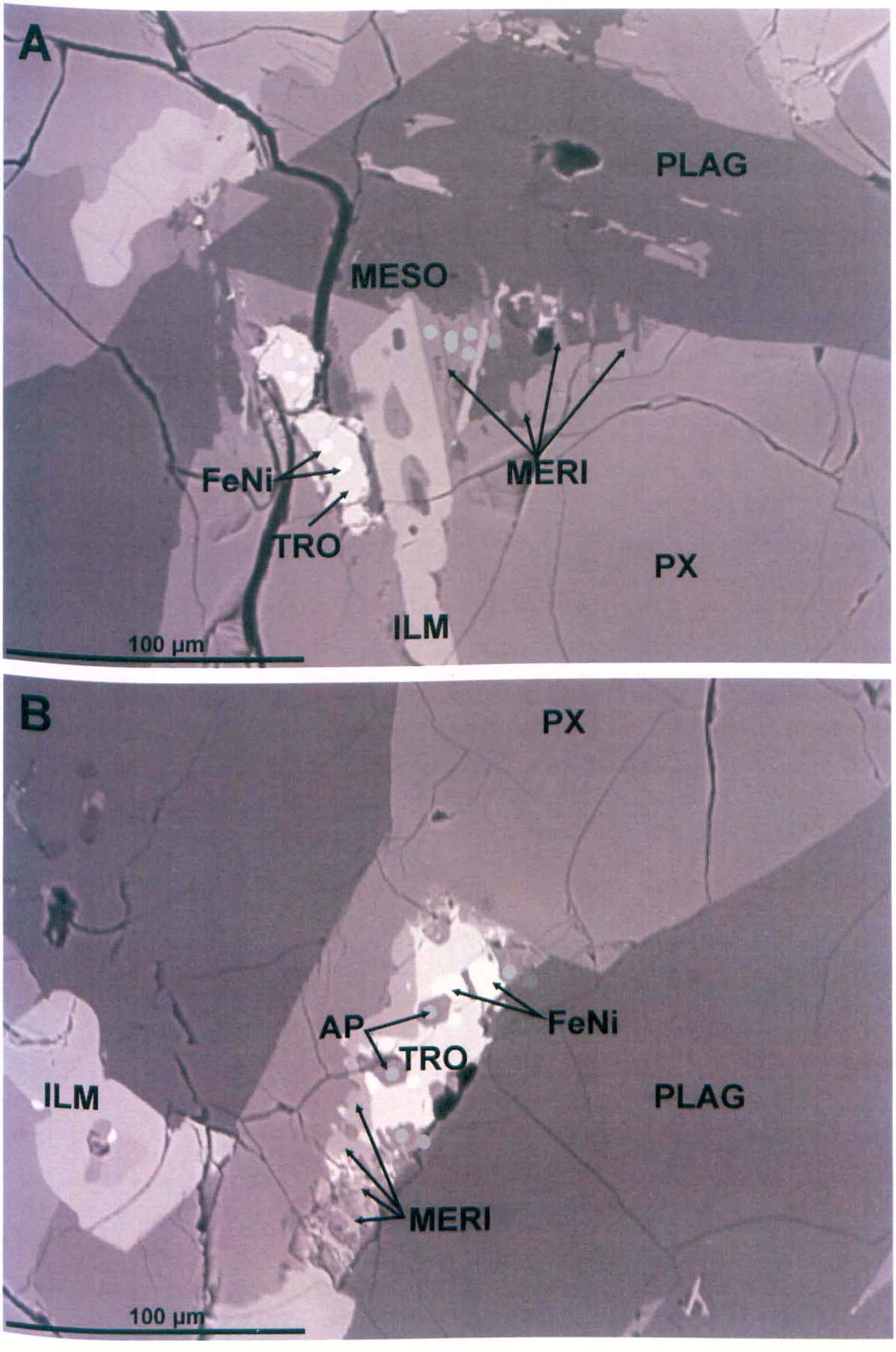

Figure 3.32: Apollo 15 sample 15016 high resolution backscatter electron images. Highlighting **(a)** mesostasis, troilite and (RE)-merillite, **(b)** troilite, (RE)-merillite and apatite.

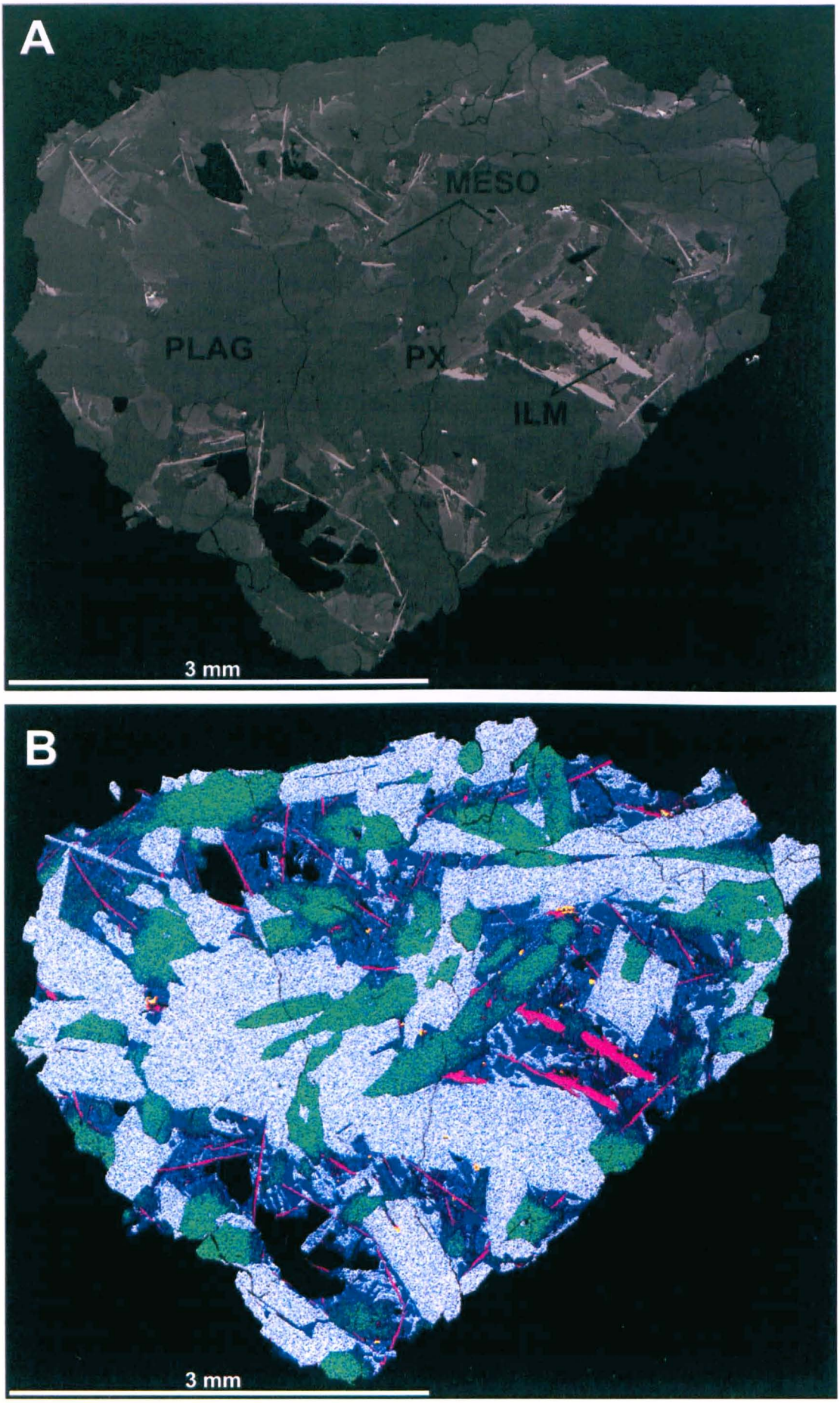

Figure 3.33: Apollo 15 sample 15386. **(a)** Backscatter electron image. **(b)** False colour x-ray image (elemental key as in Figure 3.1b). This KREEP basalt contains comparatively large areas of mesostasis.

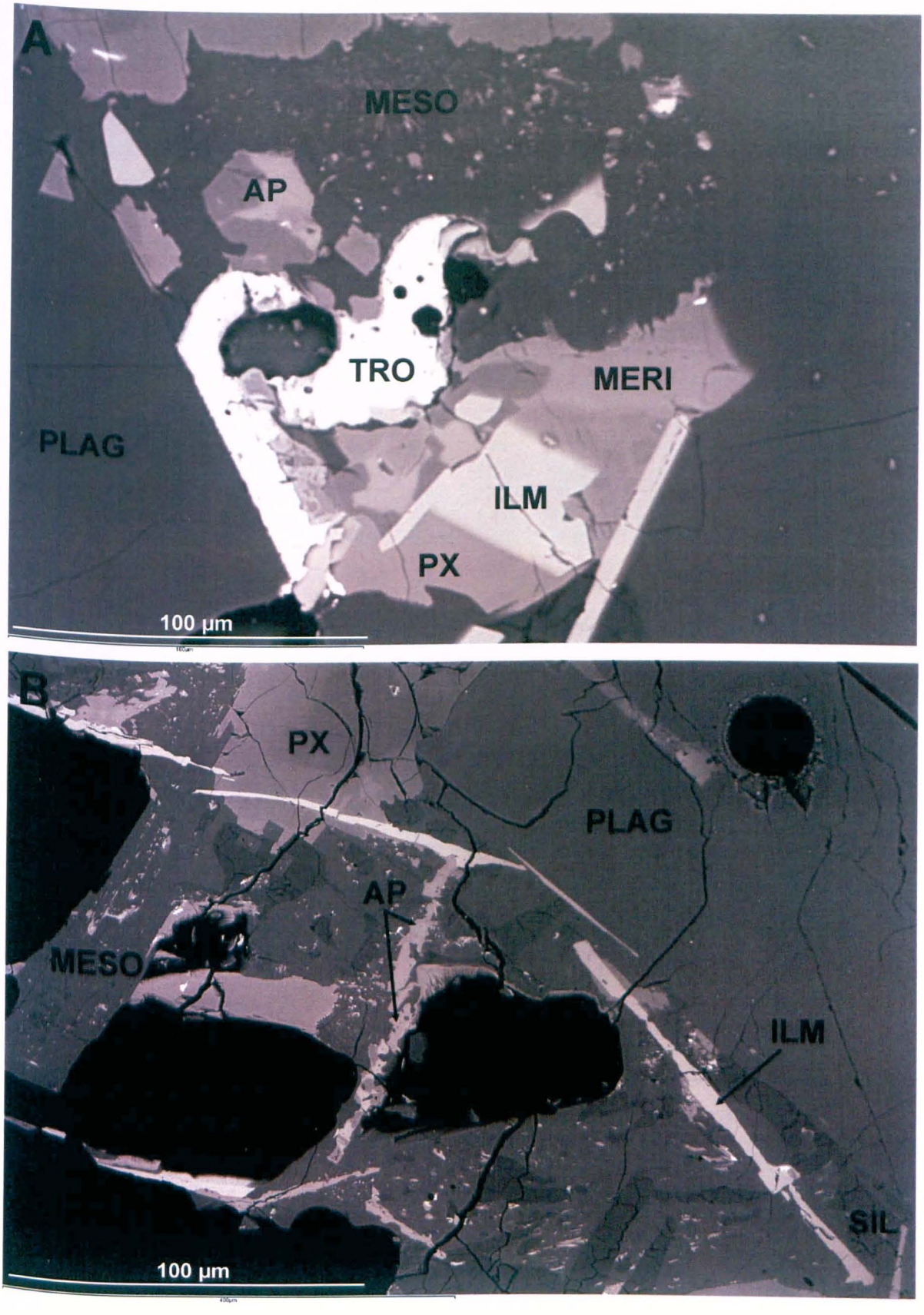

Figure 3.34: Apollo 15 sample 15386 high resolution backscatter images. Highlighting **(a)** mesostasis, troilite, (RE)-merillite and apatite, **(b)** mesostasis and disarticulated apatite needle.

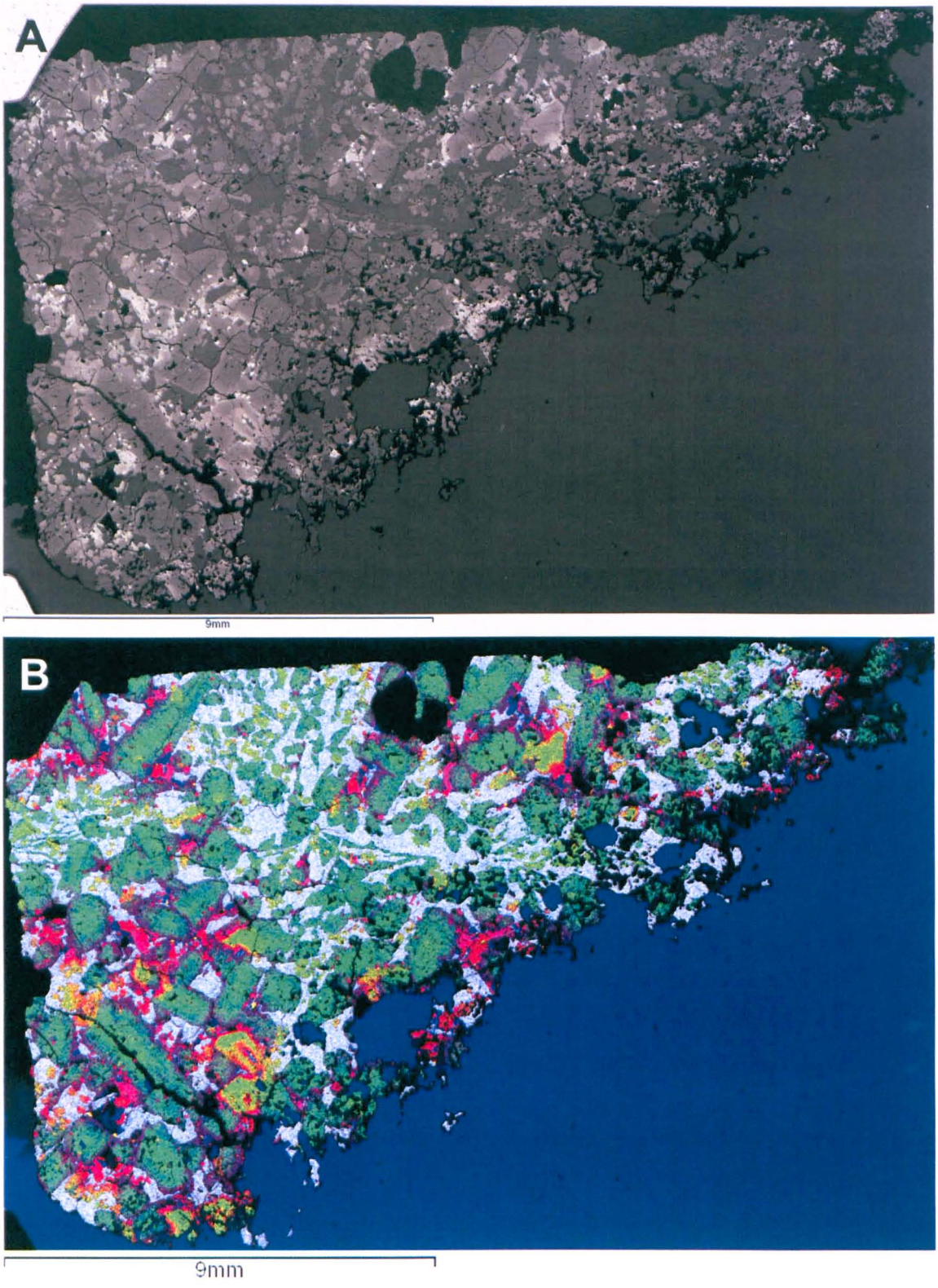

Figure 3.35: Apollo 15 sample 15555. **(a)** Backscatter electron image. **(b)** False colour x-ray image (elemental key as in Figure 3.1b). Olivine is highly zoned in this sample, as with sample 15016 (Figure 3.31).

this sample (Figure 3.37). However a number of Mg-rich pyroxene cores exist without plagioclase inclusions; in places the faint euhedral outline of these cores is still visible against the more Fe-rich rim pyroxene. Rounded olivine is found within pyroxene grains (<

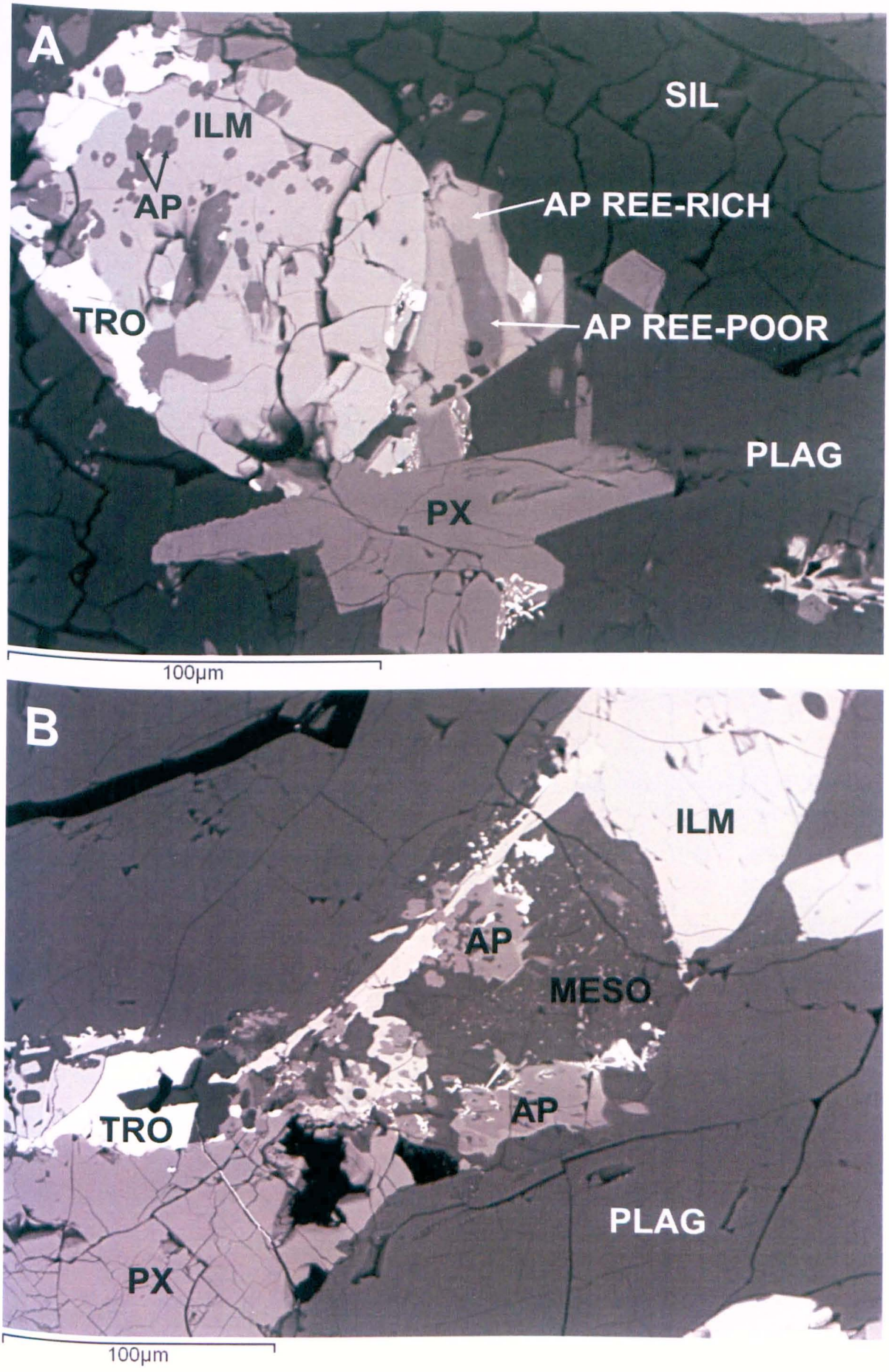

Figure 3.36: Apollo 15 sample 15555 high resolution backscatter electron images. Showing **(a)** zoned apatite with a REE-rich rim, **(b)** mesostasis and apatite.

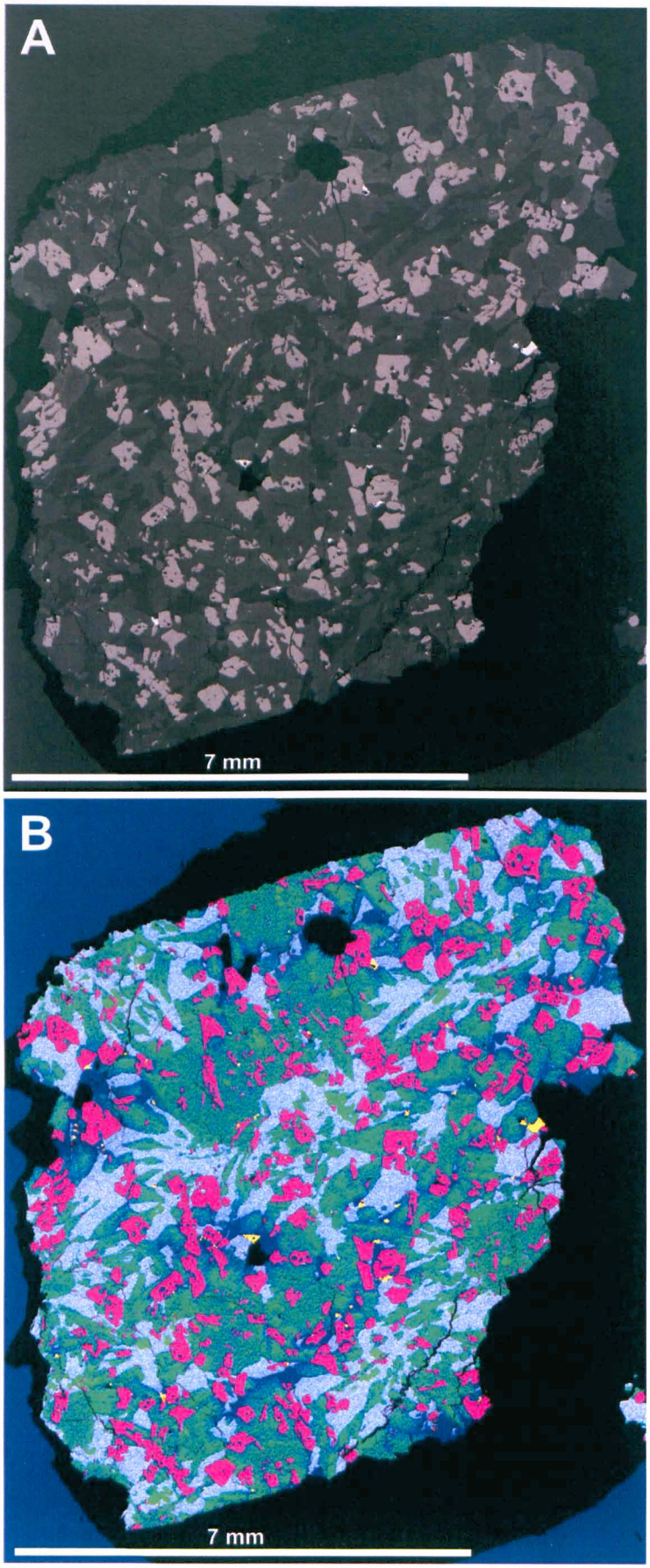

Figure 3.37: Apollo 17 sample 70017. **(a)** Backscatter electron image. **(b)** False colour x-ray image (elemental key as in Figure 3.1b).

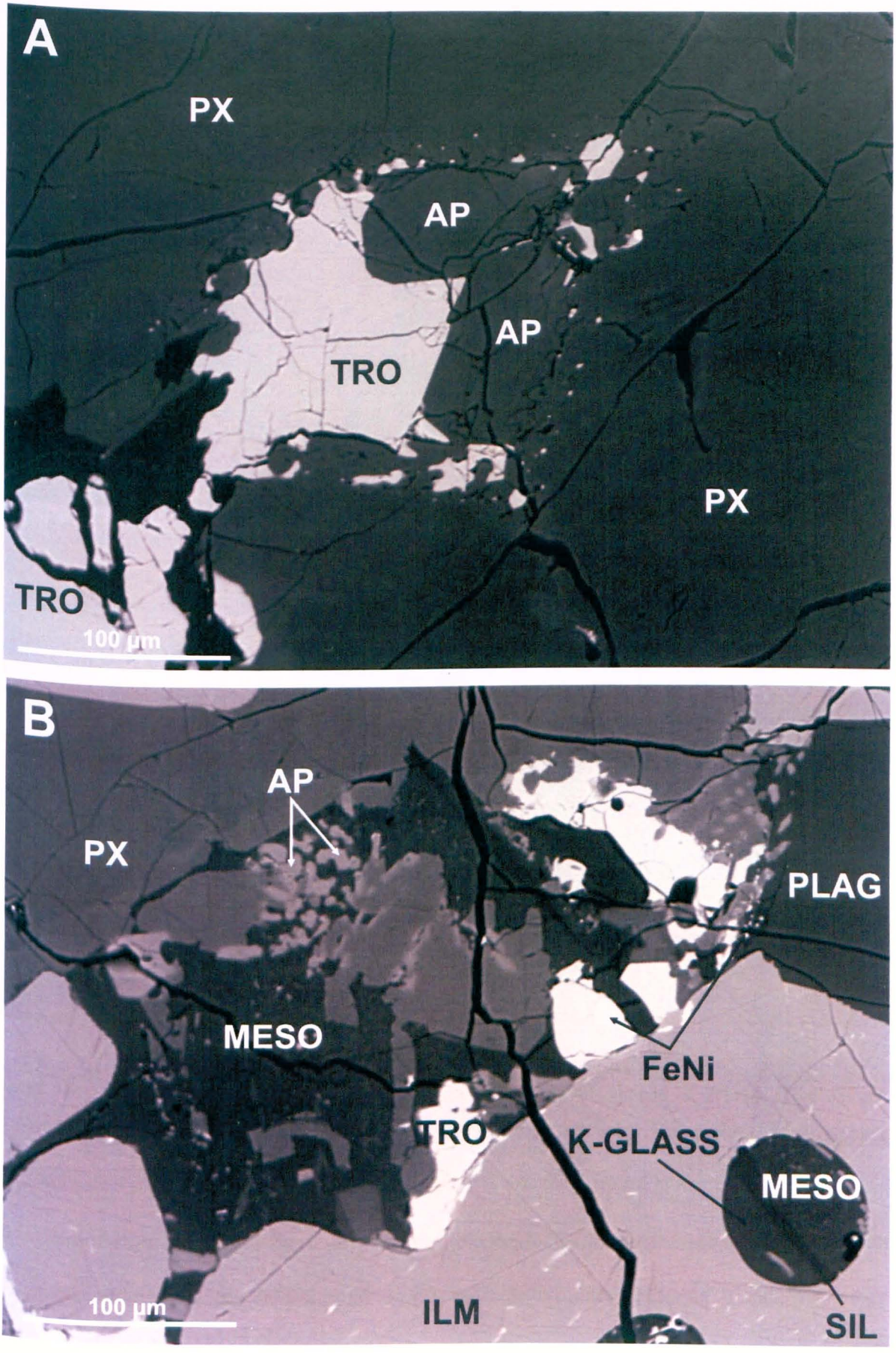

Figure 3.38: Apollo 17 sample 70017 high resolution backscatter electron images. Showing **(a)** apatite and troilite, **(b)** apatite, mesostasis and ilmenite resorbtion hollows filled with K-rich glass, silica and mesostasis.

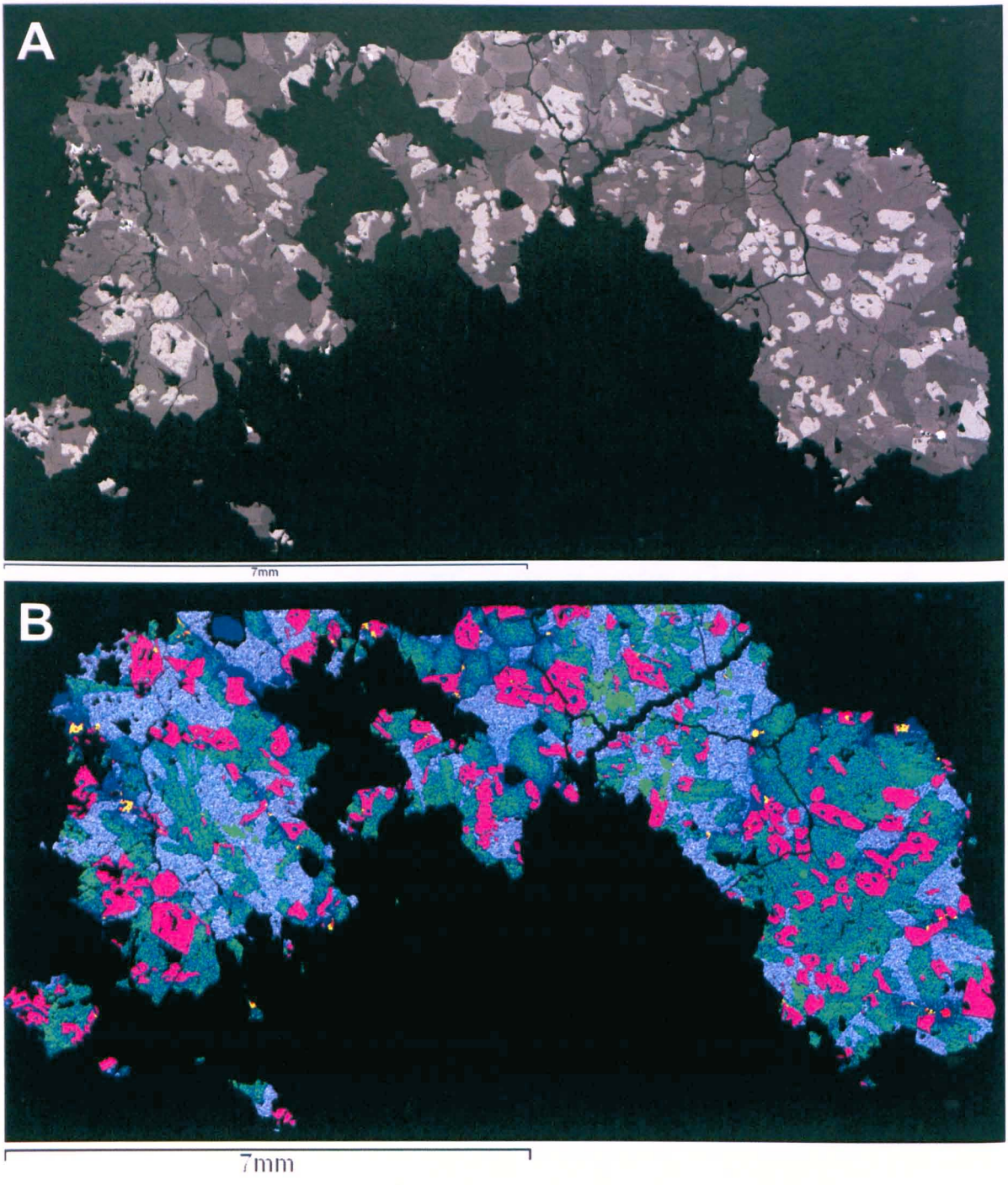

Figure 3.39: Apollo 17 sample 70035. **(a)** Backscatter electron image. **(b)** False colour x-ray image (elemental key as in Figure 3.1b).

800 μm – it also occurs within plagioclase), along with small anhedral Cr-Ti spinel (< 80 μm), acicular rounded armalcolite (< 600 μm in length) and blocky irregular, partially resorbed ilmenite (up to 1 mm), which is ubiquitous throughout the sample. Ilmenite resorbtion hollows contain mostly silica, K-rich glass, plagioclase and Fe-pyroxene. Ilmenites are associated with irregular silica (< 700 μm), troilite (< 300 μm, also present

within olivines), FeNi (< 50 μm) and areas of mesostasis (< 200 μm) (Figure 3.38). Armalcolite cores exist within a number of ilmenite grains (Table 3.1). F-rich apatite (< 100 μm) and FeNi blebs (< 10 μm) are associated with areas of mesostasis. Rare irregular rounded vesicles are visible up to 1 mm diameter.

3.1.19. 70035,195: Apollo 17 High-Ti, Low-Al, Low-K Mare Basalt. The texture of sample 70035,195 appears similar to that of 70017,110 with Mg-rich pyroxene cores associated with blocky irregular ilmenite (up to 1 mm) and rounded olivine (< 500 μm), surrounded by Fe-pyroxene and plagioclase (Figure 3.39). However, there are a number of differences; firstly, armalcolite and spinel are rare within this sample (Table 3.1). Secondly, pyroxene cores zone smoothly into Fe-rich pyroxene rims creating an anhedral mass (< 2.5 mm) rather than a euhedral core surrounded by anhedral rim material, and thirdly, plagioclase (< 2 mm) is less intergrown with Fe-rich pyroxene rims than in sample 70017,110. In addition, olivine is less abundant in this sample, as are apatite (< 40 μm - zoned) and (RE)-merillite (< 100 μm) (Table 3.1, Figure 3.40). Ilmenite shows resorbtion hollows filled with plagioclase, silica and Fe-pyroxene and is associated with anhedral silica (< 800 μm), very rare Cr-Ti spinel (< 10 μm) and troilite (up to 300 μm). Spinel is only found as inclusions within ilmenite grains and associated with sulphides, FeNi blebs and silica. K-feldspar (< 100 μm) is associated with plagioclase and areas of mesostasis (< 250 μm). Mesostasis consists of K-rich glass, plagioclase, troilite needles, FeNi blebs (up to 10 μm – also found within troilite). F-rich apatite (< 50 μm - zoned), (RE)-merillite (< 100 μm), Fe-pyroxene, baddeleyite (< 10 μm) and zirconolite (< 10 μm) are also found within these areas. Two possible tranquillityite grains (< 10 μm) were also observed, though small grain size prevented a definitive identification. Vesicles are rare and never reach more than 500 μm.

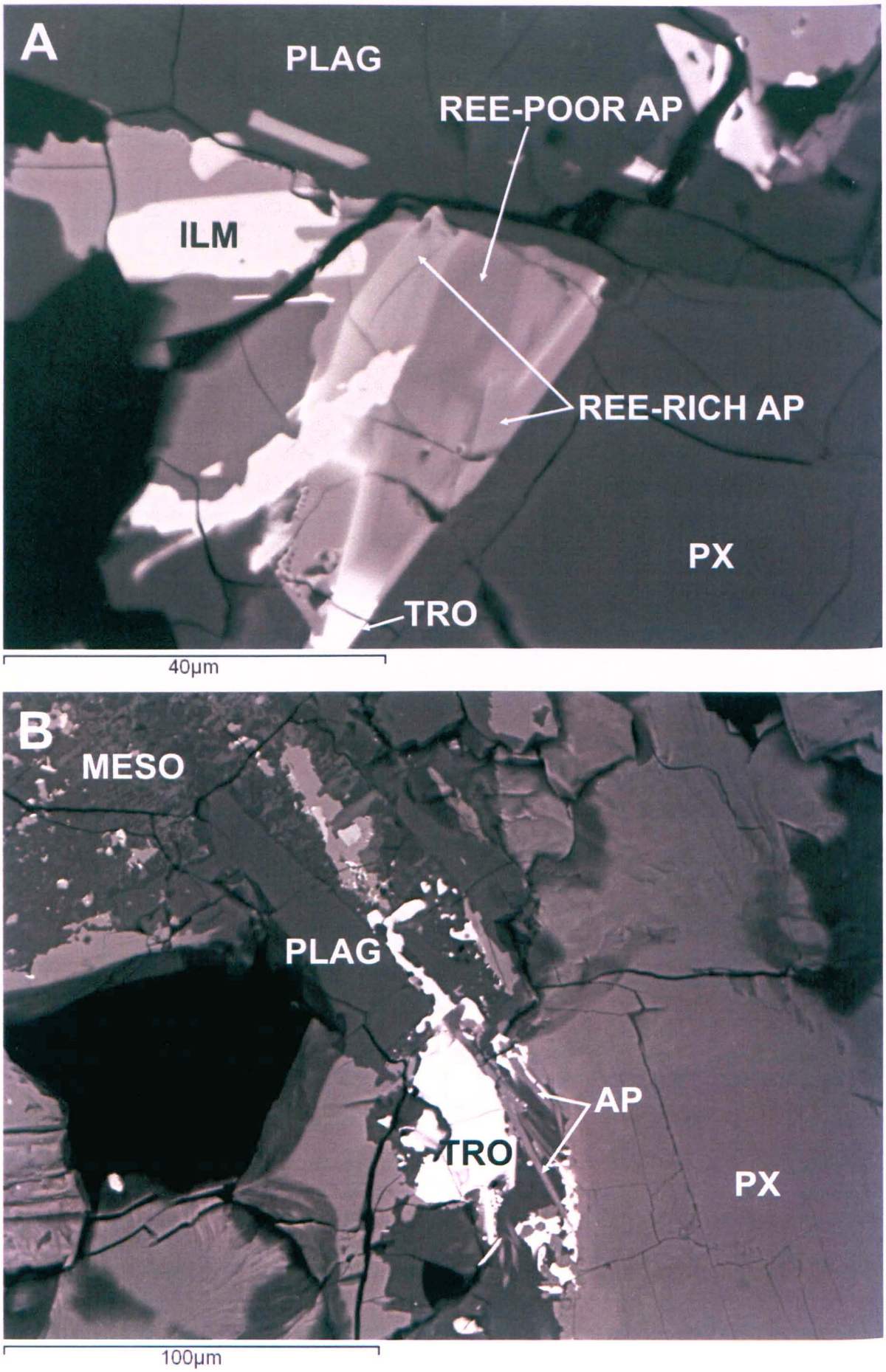

Figure 3.40: Apollo 17 sample 70035 high resolution backscatter electron images. Highlighting **(a)** zoned apatite, **(b)** Apatite needles, troilite and mesostasis.

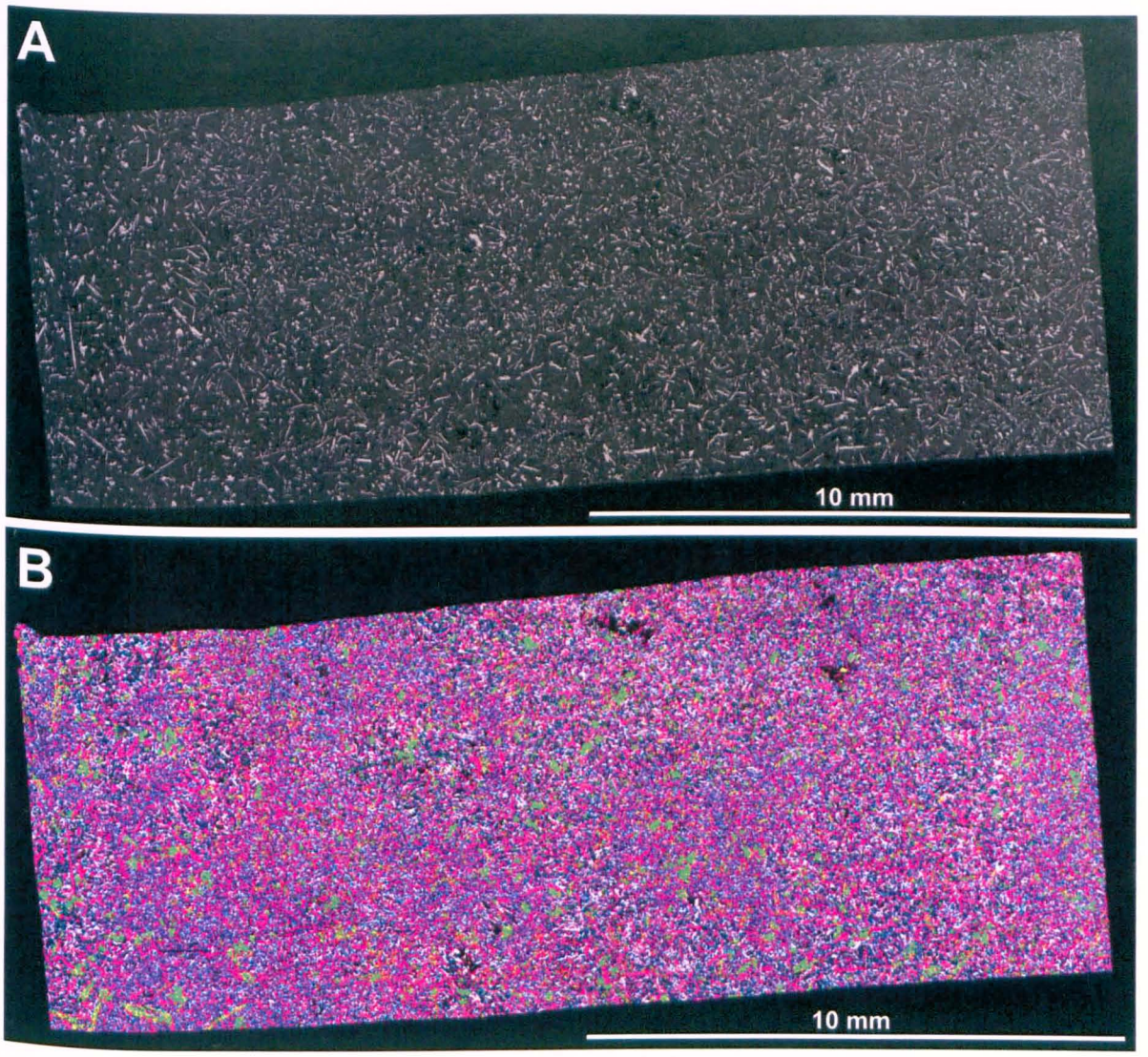

Figure 3.41: Apollo 17 sample 70215. **(a)** Backscatter electron image. **(b)** False colour x-ray image (elemental key as in Figure 3.1b). These images reflect the fine grained texture of this sample, the latter image highlights the presence of olivine phenocrysts but gives an overrepresentation of ilmenite abundance (in pink). Ilmenite is present in the groundmass along with pyroxene (green) and plagioclase (white), as these grains are less than 1 pixel creation of a false colour image advocates the dominance of the brightest colour (pink).

3.1.20. 70215,306: Apollo 17 High-Ti, Low-Al, Low-K Mare Basalt. This sample displays a quenched texture similar to sample 12052 (section 3.1.12), with phenocrysts of skeletal olivine (up to 2 mm), granular pyroxene (up to 1 mm), semi cubic Cr-rich spinel (< 150 μm) and skeletal acicular ilmenite (up to 3 mm long) (Figure 3.41). Inclusions in olivine are mostly ilmenite or pyroxene. Pyroxene phenocrysts exist in loose clusters associated with slightly coarser plagioclase needles (up to 700 μm long) than those present in the

groundmass (Figure 3.42). Acicular and skeletal ilmenite blades are homogeneously distributed, rarely containing armalcolite cores (< 10 μm). Cr-rich spinel phenocrysts (zoned to Ti-rich rims) are associated with and commonly include olivine. The quenched groundmass consists mostly of an intergrowth of radiating acicular plagioclase (up to 400 μm long), anhedral silica (< 200 μm) and anhedral pyroxene, also containing abundant ilmenite needles (< 500 μm). Troilite (< 300 μm) are associated with rare irregular vesicles (< 700 μm), smaller grains exist within the groundmass. No phosphate phases, FeNi blebs, or other minor minerals were observed in this sample, however they may be present as aphanitic grains (< 5 μm) in the groundmass.

3.1.21. 74275,310: Apollo 17 High-Ti, Low-Al, Low-K Mare Basalt. This sample is dominated by anhedral cores of pyroxene (< 700 μm), granular rounded olivine (< 350 μm) and skeletal bladed and irregular ilmenite (up to 1 mm in length) (Figure 3.43). Cr-Ti semi-cubic, subhedral, spinel (< 120 μm) is associated with and included in olivine. Pyroxene cores are cross cut by ilmenite, olivine and armalcolite, the latter existing independently as acicular grains (< 200 μm long) within pyroxene and as cores within ilmenite (< 150 μm), while the former two phases exist both within pyroxene and external to it. The remainder of the sample consists of quenched and intergrown anhedral pyroxene (only slightly more Fe-rich than pyroxene cores), acicular plagioclase (up to 700 μm in length), ilmenite needles (< 200 μm), irregular silica (< 200 μm) and K-feldspar (< 100 μm). Troilite has diameters no more than 50 μm and is only observed in the groundmass. FeNi blebs (< 5 μm) are rare and no phosphates were observed (Figure 3.44). Vesicles are rare and < 700 μm diameter.

3.1.22. 75055,49: Apollo 17 High-Ti, Low-Al, Low-K Mare Basalt. Sample 75055,49 displays a hypocrystalline texture of ilmenite, pyroxene and plagioclase (Figure 3.45). Subhedral-anhedral pyroxene (< 2 mm) is zoned with Fe-rich composition towards the grain rims (pyroxferroite in some cases). Subhedral-anhedral plagioclase is acicular (< 2

mm) as is ilmenite (< 1.5 mm) which is also commonly bladed and/or skeletal, and shows signs of resorbtion. Ilmenite resorbtion hollows commonly contain silica, pyroxene,

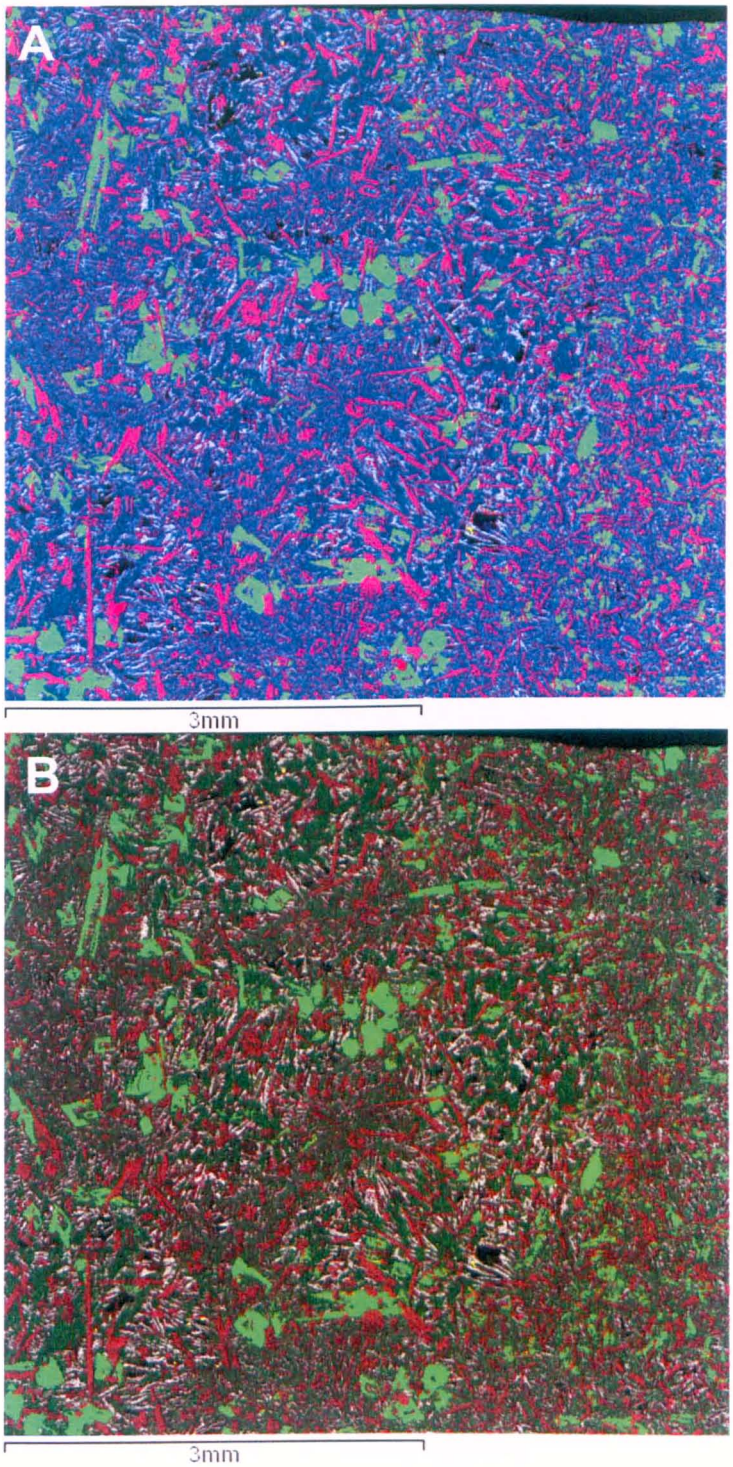

Figure 3.42: Detailed areas of Apollo 17 sample 70215. **(a)** High resolution false colour x-ray image (elemental key as in Figure 3.1b) displaying the skeletal nature of olivine and ilmenite phenocrysts. Semi-cubic spinels are shown in red. **(b)** False colour x-ray image of the same area as (a), where Al = white, Fe = red, Mg = green and S = yellow. This image highlights the clustered nature of granular pyroxene phenocrysts (dark green areas) and the relatively coarse grains of plagioclase surrounding them.

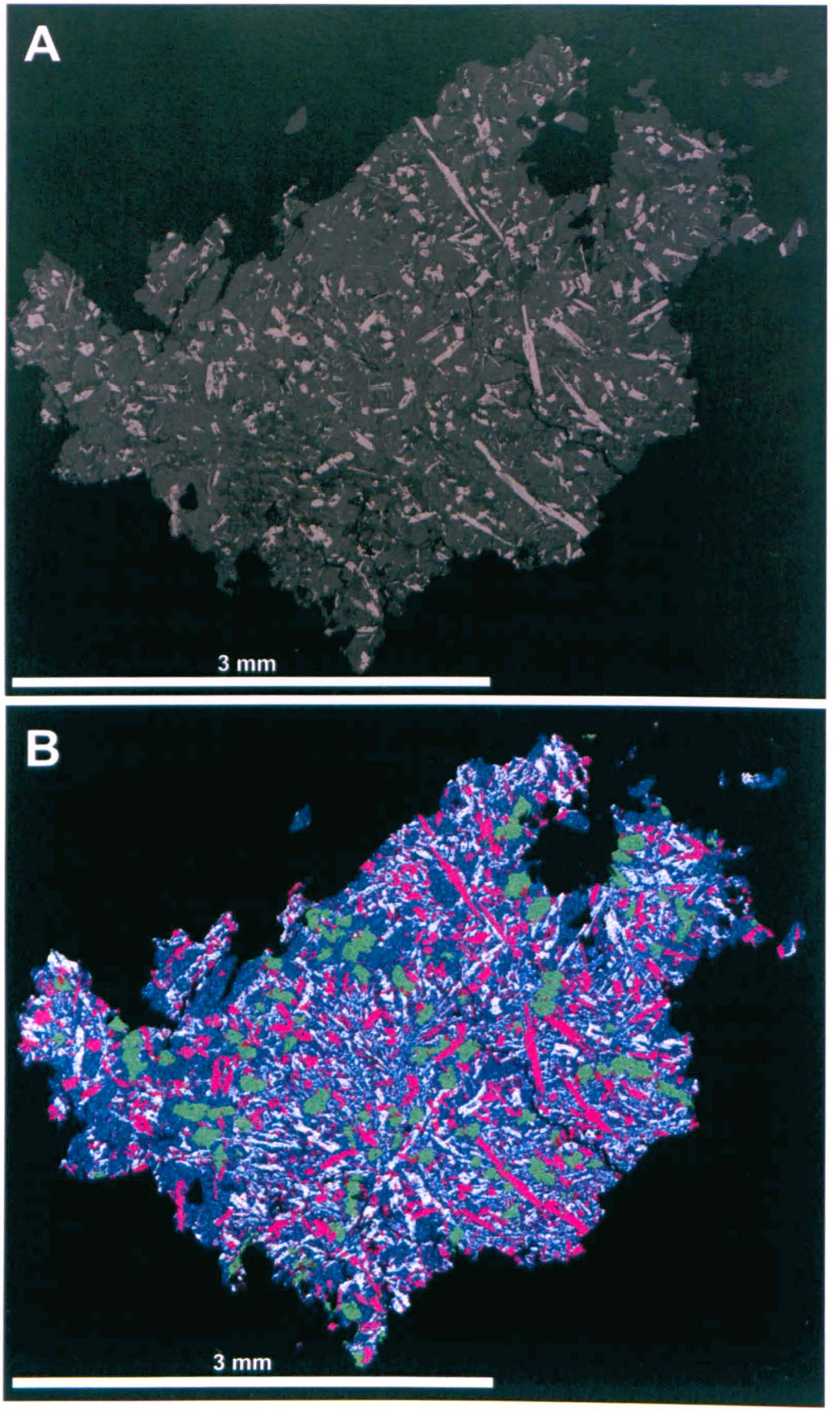

Figure 3.43: Apollo 17 sample 74275. **(a)** Backscatter electron image. **(b)** False colour x-ray image (elemental key as in Figure 3.1b).

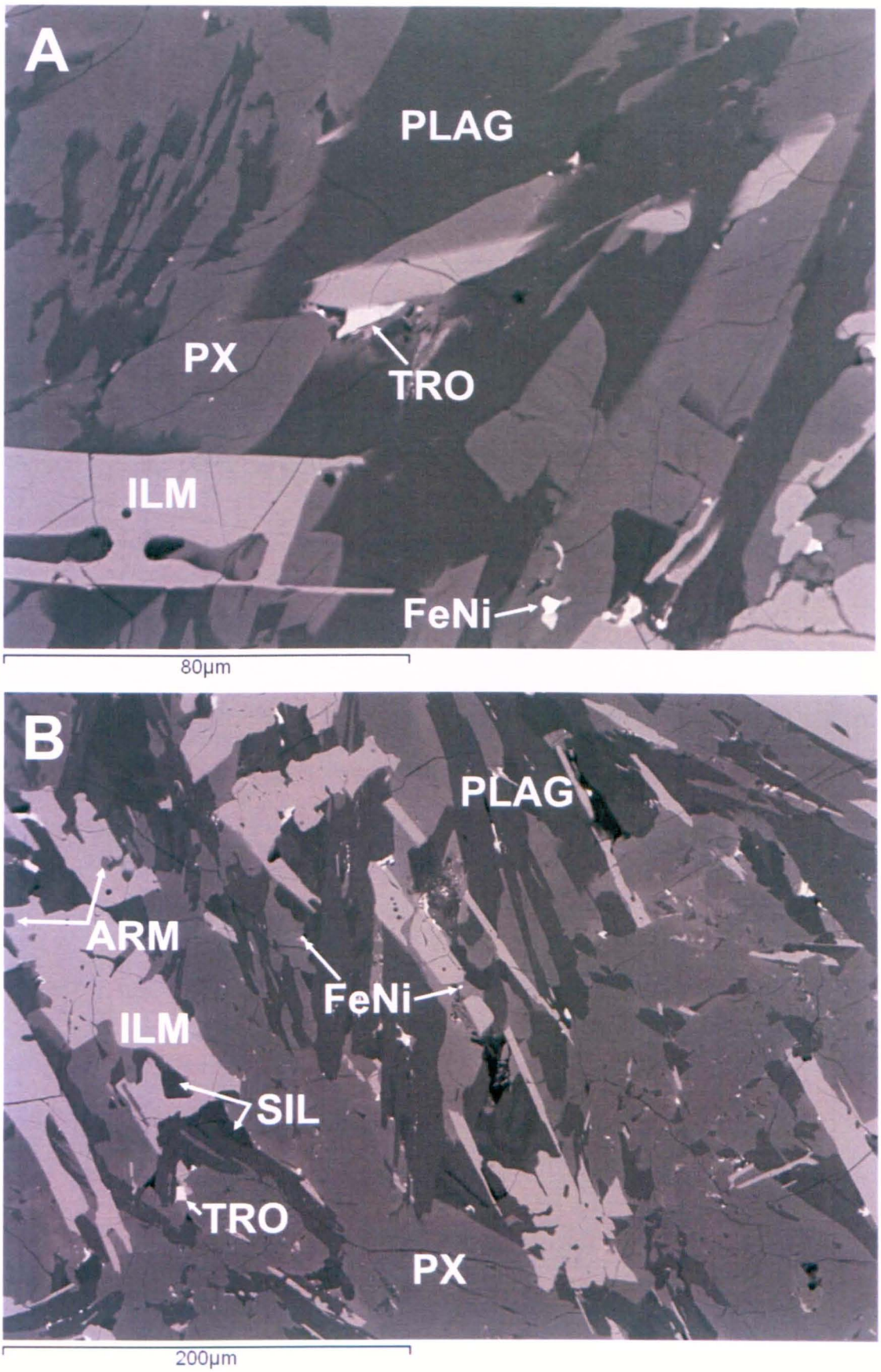

Figure 3.44: Apollo 17 sample 74275 high resolution backscatter electron images. Highlighting **(a and b)** the skeletal nature of ilmenite phenocrysts plus the intergrown texture of pyroxene and plagioclase, **(b)** ilmenite needles in the groundmass and armalcolite cores within larger ilmenite grains.

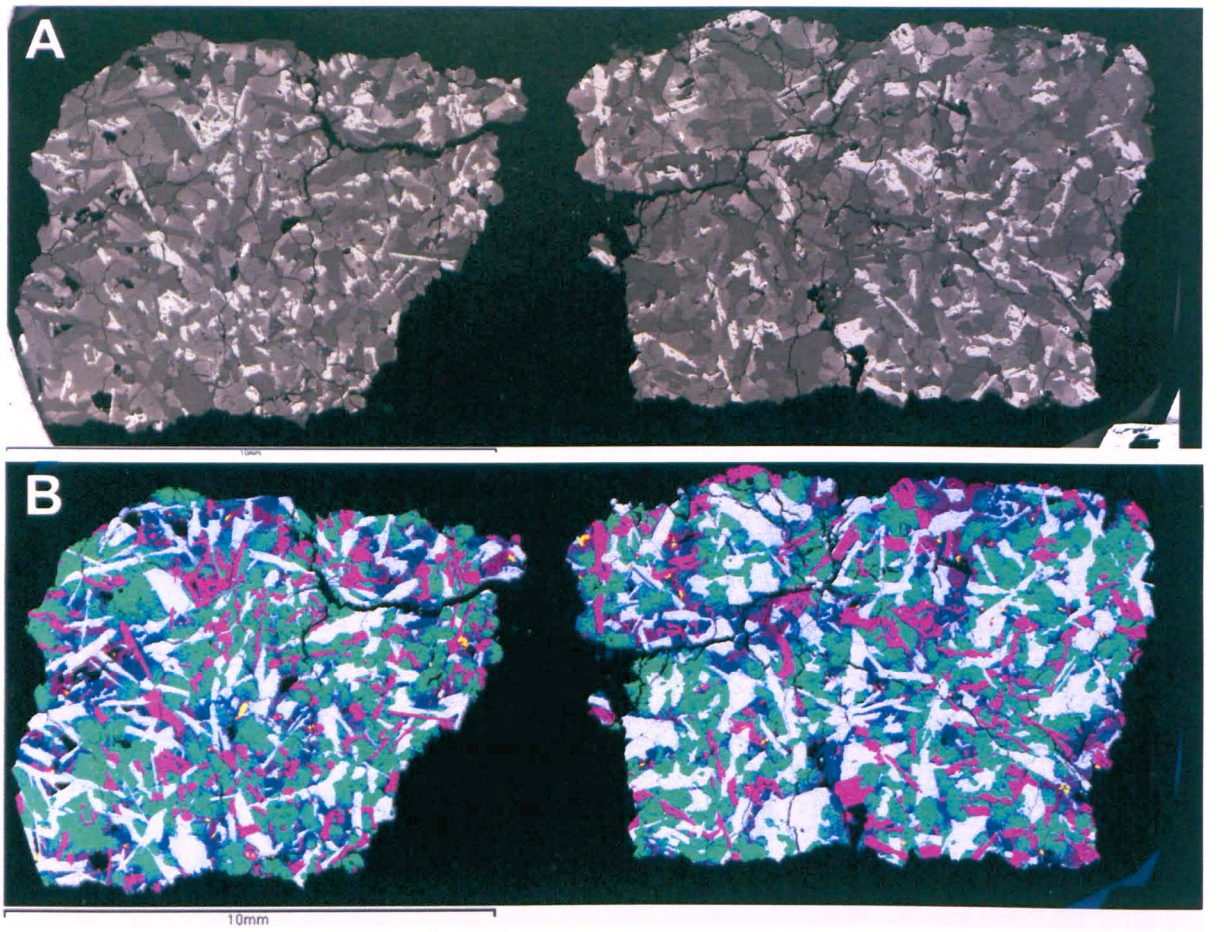

Figure 3.45: Apollo 17 sample 75055. **(a)** Backscatter electron image. **(b)** False colour x-ray image (elemental key as in Figure 3.1b).

at pyroxene, plagioclase and ilmenite boundaries. Troilite (< 200 μm) and FeNi blebs within troilite (< 50 μm) are associated with silica, as are rare F-rich apatite grains (< 150 μm), baddeleyite (< 50 μm), zirconolite (< 20 μm) and areas of mesostasis (< 300 μm, containing K-feldspar) (Figure 3.46). Vesicles are rare, irregular, rounded and < 200 μm.

3.2. Major Element Mineral Chemistry

In the following section, the major-element composition of individual mineral phases within the samples are described and these data were then used to draw mineralogical comparisons. Table 1.1 and 1.5 provide the basalt type for each specimen as per lunar nomenclature.

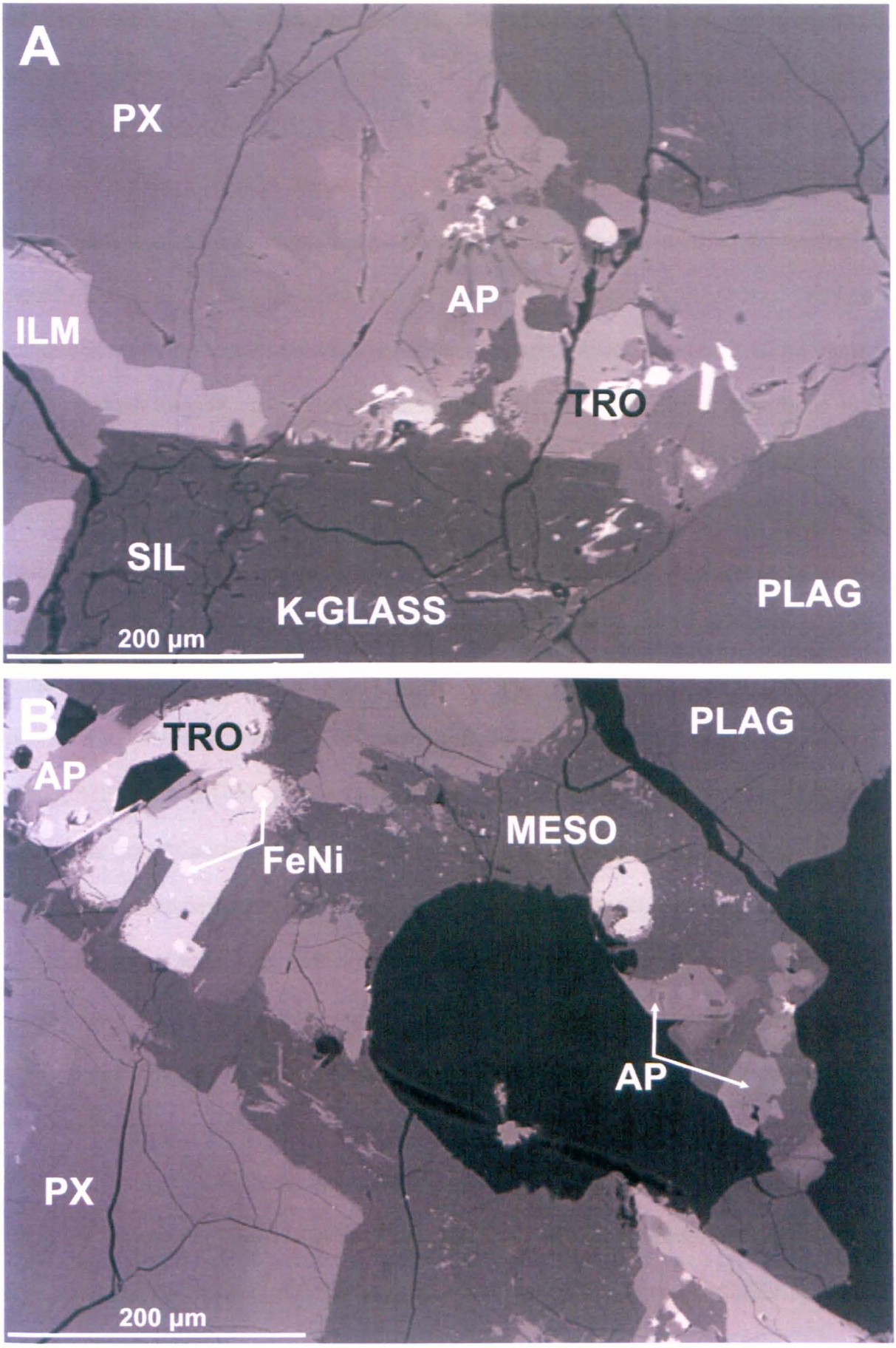

Figure 3.46: Apollo 17 sample 75055 high resolution backscatter electron images. Showing **(a)** silica, K-rich glass and troilite, **(b)** troilite, FeNi metal, apatite and mesostasis.

3.2.1. Pyroxene. Pyroxene grains from Apollo 11 samples generally exhibit varying crystallisation trends for the high-Ti, low and high-K samples within our sample set. The Apollo 11 low-K samples contain augite cores progressing through ferroaugite to ferrohedenbergite and pyroxferroite rims, while the latter contain pigeonite, subcalcic augite and augite cores with rims of ferroaugite or subcalcic ferroaugite - less Fe enriched than the low-K samples (Figure 3.47). High-K basalt pyroxene grains also appear to have definite Mg-rich cores which are large in comparison to the rim, conversely low-K samples show continuous pyroxene zonation resulting in a relatively even spread of data across the pyroxene quadrilateral. These differences in pyroxene composition and zoning patterns between the two Apollo 11 basalt types are also evident in the data of Dence et al. (1970), French et al. (1970), Lovering and Ware (1970) and Beaty and Albee (1978). Although sample 10050,168 is classified as a low-K sample (LSPET, 1969; Duncan et al., 1976; Jerde et al., 1994) it does not fit with the typical trend for this compositional group. It contains augitic cores with higher Mg# than pigeonite (77 vs. 69 respectively, where Mg# = $(Mg/(Mg+Fe^{2+}))*100$), and a number of grains fractionate to subcalcic ferroaugite compositions, similar to pyroxene grains found in the high-K basalts. Beaty and Albee (1978) stated that the most Fe-rich pyroxene in this sample is poorer in Ca (giving it a pyroxferroite composition) than equivalent grains within the other low-K samples. However, our data indicate this is not the case, as the Ca contents of the most Fe-rich pyroxene within samples 10020,232, 10050,168 and 10058,254 are Wo_9, Wo_{10} and Wo_{14} respectively. All the Apollo 11 samples studied display Ca-rich compositions for the majority (if not all) of their pyroxene cores, pigeonite cores are rare.

Apollo 17 high-Ti type A sample 75055,49 contains the same pyroxene compositions as those of the Apollo 11 high-Ti, low-K basalts, with augite cores zoning through ferroaugite to ferrohedenbergite and pyroxferroite rims. In addition the two previously unclassified Apollo 17 samples 70017,110 and 70035,195 show pyroxene data trends resembling those

of Apollo 11 high-Ti, high-K basalts, with Mg-pigeonite and augite cores zoning to subcalcic ferroaugite and ferroaugite rims (Figure 3.47). However, type B basalt 70215,306 and type C basalt 74275,310 exhibit very different zoning trends, with high-Ca augite grain cores zoning to subcalcic augite or low-Fe ferroaugite rims, showing a much sharper decrease in Ca-content during fractionation than that visible in other Apollo 17 or Apollo 11 high-Ti basalts. Previous studies show that the type B and C basalt pyroxenes can have lower amounts of Ca than observed in samples 70215,306 and 74275,310, with most varying from 40 % to 10 % Ca (Hodges and Kushiro, 1974; Longhi et al., 1974; Dymek et al., 1975). These basalt types can also contain Fe-rich pyroxene - type B basalt 71055 and type C basalt 74255 show pyroxene with compositions of $Wo_{15}En_{15}Fs_{85}$ and $Wo_{15}En_{10}Fs_{90}$ respectively (Dymek et al., 1975). A number of type A basalts contain Mg-pigeonite (Neal and Taylor, 1993) though none is observed in sample 75055,49.

The low-Ti Apollo 12 ilmenite basalts within our sample suite (basalts 12016,39, 12047,9, 12051,59 and 12064,136) exhibit continuous zonation from Mg-pigeonite, subcalcic augite and augite cores through to ferroaugite, ferrohedenbergite and even hedenbergite rims in highly zoned sample 12064,136 (Figure 3.47). Pyroxferroite is present in samples 12047,9, 12051,59 and 12064,136, with virtually Mg-free composition (ferrosilite). A slight exception to the ilmenite basalt trend is sample 12016,39, which contains Ca-rich augite and Mg-pigeonite cores zoning to a Ca-poor ferroaugite or subcalcic ferroaugite, it does not contain any extremely Fe-rich pyroxene. The trend of this ilmenite basalt appears more in line with that of olivine basalt 12040,44, which also contains Ca-rich augite cores and subcalcic ferroaugite rims (Figure 3.47). However, rims of ferriferous pigeonite and ferroaugite are also observed in the latter sample making it more compositionally diverse. Pigeonite cores are not present in sample 12040,44 and augite cores display higher Mg content than other Apollo 12 augites. This gives the impression of overall Ca decrease during the early stages of Apollo 12 olivine basalt pyroxene fractionation, in contrast to the

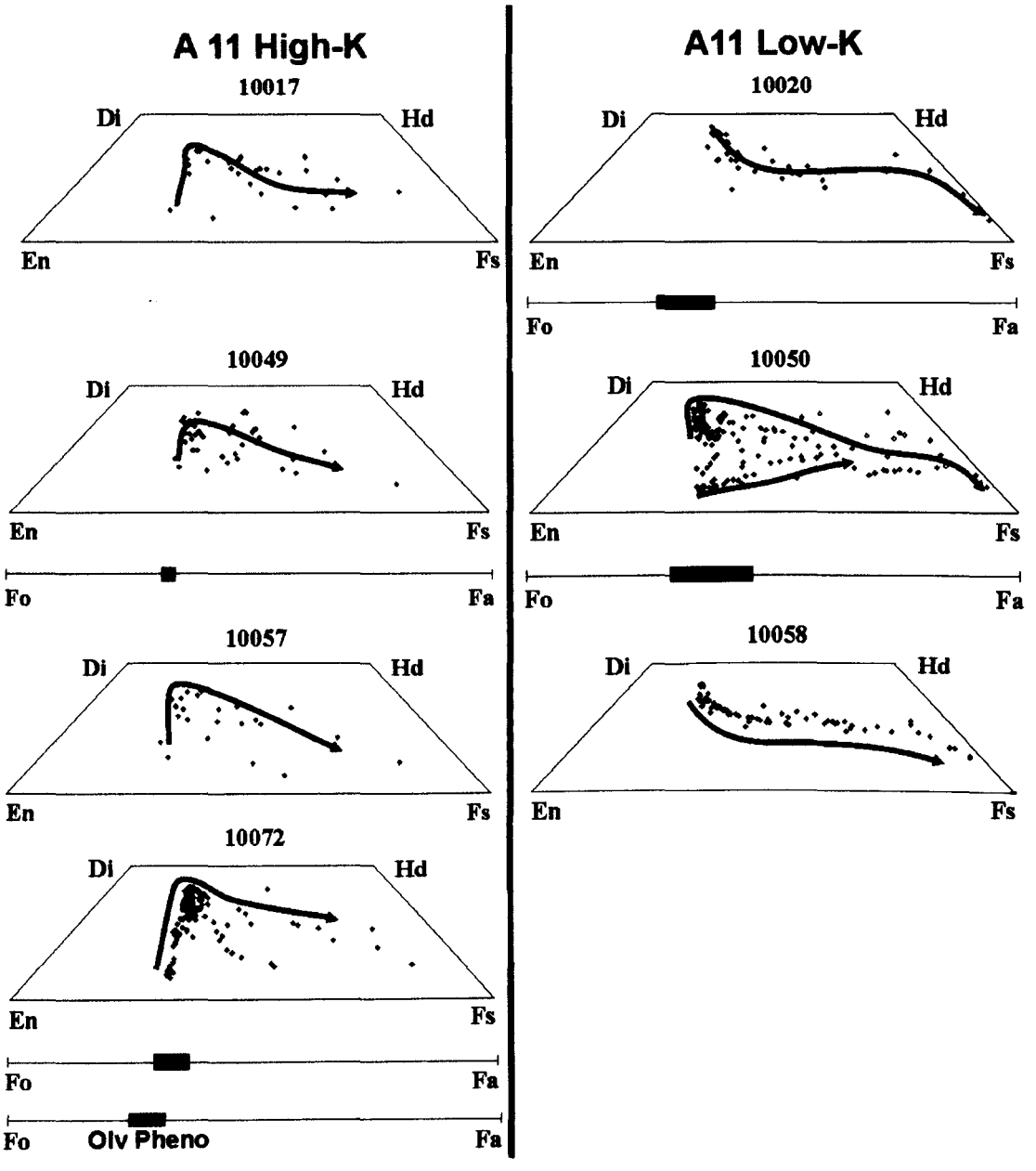

Figure 3.47: Pyroxene quadrilaterals and olivine forsterite compositions (where applicable) for each sample. Each quadrilateral shows electron microprobe data for individual pyroxene grains in terms of Mg (bottom left corner), Ca (missing top corner) and Fe (bottom right corner). Mineralogicaly a data point plotting in the extreme top left corner would be pure diopside, top right would be hedenbergite, bottom right would be ferrosilite and bottom left would be enstatite – see Figure 1.5 for a more detailed mineralogical breakdown. Arrows indicate the general crystallisation trends of the data, where two are shown the lower indactes the pigeonite trend and the upper indicates the augite trend. Olivine forsterite contents are plotted below the quadrilaterals for those samples containing olivine. The two extremes of these plots are forsterite (Mg-olivine) to the left and fayalite (Fe-olivine) to the right. Samples are grouped according to type. Sample 10072,40 contains a single large olivine phenocryst/xenocryst in addition to its native olivine grains, which is plotted on a separate forsterite diagram.

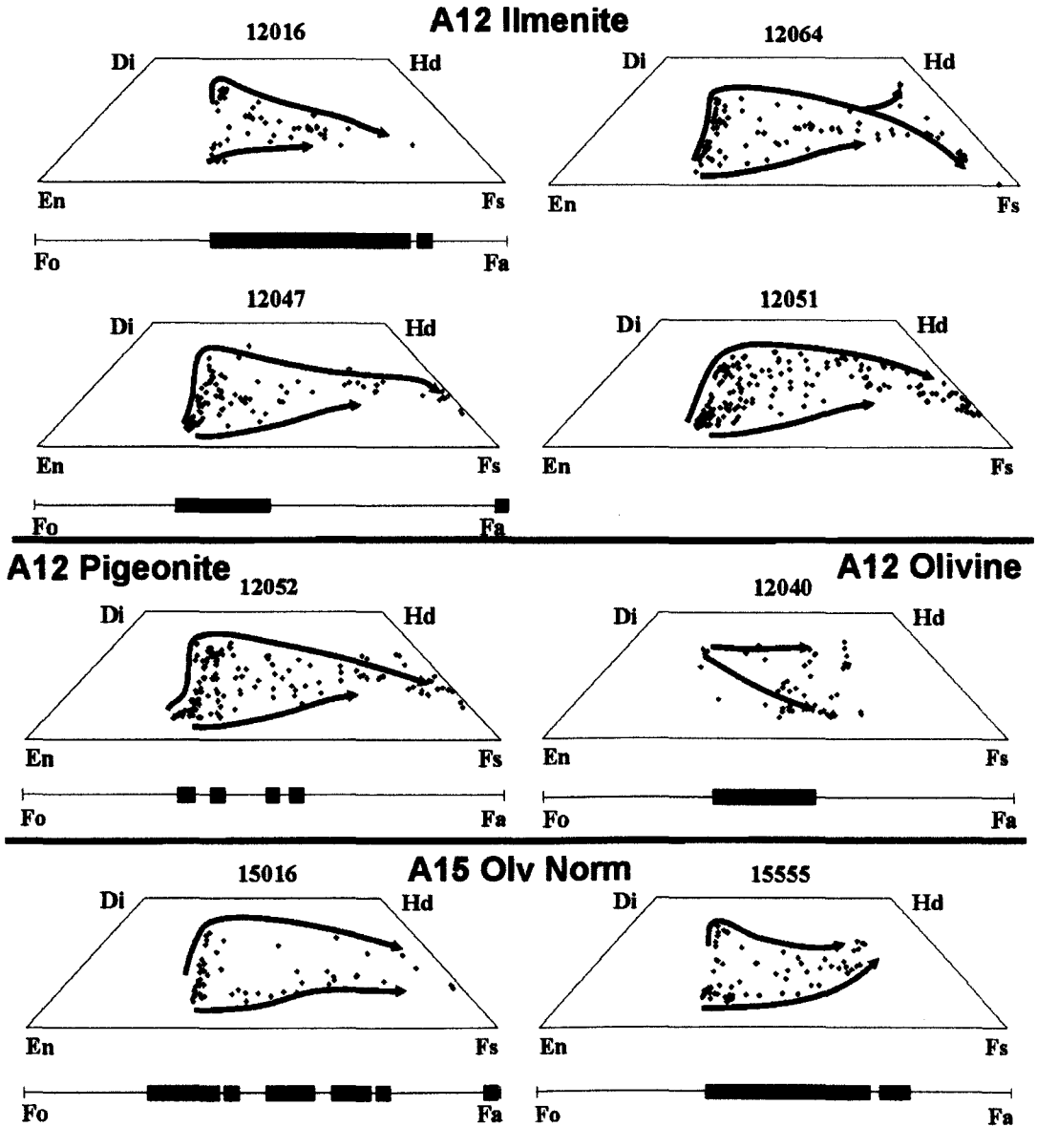

Figure 3.47: cont.

relatively continuous Ca concentration - and even slight Ca increase in some cases - visible in the ilmenite basalts at this stage (see also Brown et al., 1971; Keil et al., 1971; Klein et al., 1971; Kushiro et al., 1971; Dungan and Brown, 1977). Apollo 12 pigeonite basalt 12052,339 is compositionally similar to the ilmenite basalts, except for a slightly higher Mg# within a small number of Mg-pigeonite cores ($Mg\#_{71}$ vs. $Mg\#_{69}$ in sample 12051,59). This data are in agreement with the pigeonite basalt data of Bence et al. (1970) and Baldridge et al. (1979).

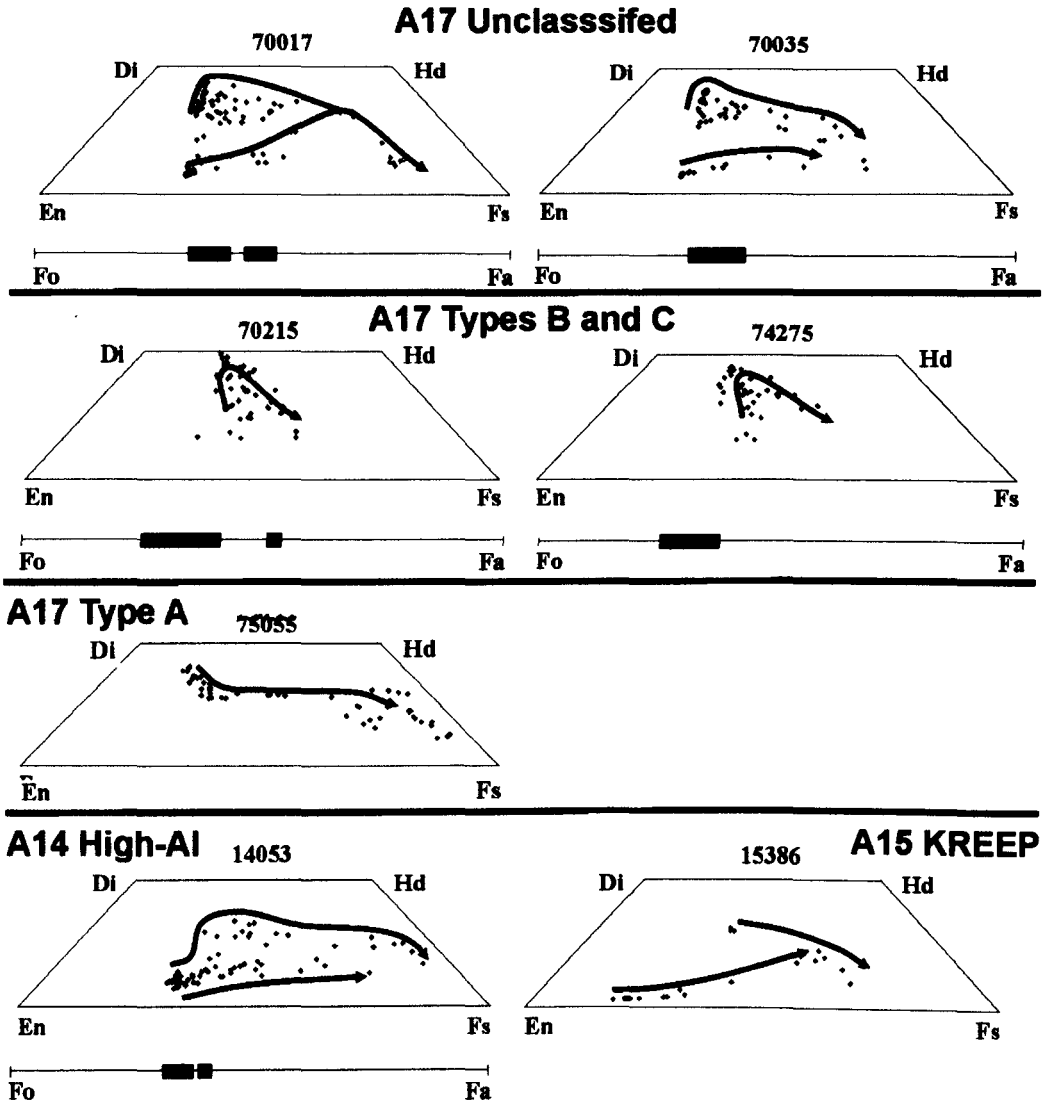

Figure 3.47: cont. 2.

Apollo 15 low-Ti olivine-normative basalts (samples 15016,7 and 15555,206 within our sample suite) exhibit a similar trend to Apollo 12 ilmenite basalts, though in both samples Ca content within pyroxene is never lower than subcalcic augite. However, previous data indicate this basalt group does contain pigeonite with a Ca content as low as Wo_5 (Kushiro, 1972). Pyroxene rims within sample 15555,206 do not zone beyond ferroaugite, but Walker et al. (1977) found pyroxene with < En_{15} in this sample. Bence and Papike (1972), Brown et al. (1972) and Dalton and Hollister (1974) observed similar pyroxene compositions for sample 15555.

Apollo 15 KREEP basalt 15386,46 and Apollo 14 low-Ti, high-Al basalt 14053,19 both contain Mg-rich pyroxene cores evolving to moderately Fe-rich rims, but the two trends are widely different in every other respect. In sample 15386,46 the grains with highest Mg content are orthopyroxene, surrounded by clinopyroxene zoning through Mg-pigeonite to subcalcic ferroaugite and ferroaugite rims, a small number of independent augite cores also exist. These data are in agreement with that of Takeda et al. (1978), though data from Steele et al. (1972) suggest that this sample contains ferroaugite and subcalcic ferroaugite with Mg contents as low as En_5. Clinopyroxene within Apollo 14 sample 14053 zones from Mg-pigeonite and subcalcic augite cores through augite to ferroaugite, subcalcic ferroaugite and rare ferrohedenbergite rims. The data trends of these two samples do not closely resemble those of any other low or high-Ti basalt type investigated in this study.

Plotting pyroxene Al/Ti ratio against Mg# assists the determination of each sample's mineral crystallisation sequence. Mg# can be viewed as a proxy for pyroxene crystallisation, decreasing over time as the melt becomes more Fe-rich. The way in which Al/Ti ratio changes with Mg# therefore indicates the timing of plagioclase and/or ilmenite co-crystallisation with pyroxene (e.g., Anand et al., 2003). For the low-Ti Apollo 12 ilmenite basalts within our sample suite these trends indicate initial data clustering at high magnesium numbers ($Mg\#_{70\text{-}63}$) and Al/Ti ratios, followed by a decrease in Al/Ti ratios beginning at $Mg\#_{65\text{-}62}$ (Figure 3.48). This suggests initial crystallisation of Mg-rich pyroxenes followed by the onset of plagioclase co-crystallisation at $Mg\#_{65\text{-}62}$. When pyroxenes had fractionated to ~$Mg\#_{55}$ and Al/Ti ratios of ~1.5-2 ilmenite became a liquidus phase and co-crystallised with plagioclase and pyroxene, therefore maintaining the Al/Ti ratio at 1-2 for all subsequently crystallising pyroxene in these samples (Table 3.2). Apollo 12 pigeonite basalt 12052,339 shows a similar trend to the ilmenite basalts but the vast majority of data points plot in the high Mg#, high Al/Ti ratio region ($Mg\#_{71\text{-}64}$, Al/Ti = 4.73-3.63). This can be explained by the presence of pyroxene phenocrysts within a

quenched groundmass. Plagioclase and ilmenite are only present within the groundmass, therefore the composition of the pyroxene phenocrysts (where the majority of measurements were taken) would not be expected to indicate either plagioclase or ilmenite co-crystallisation. Only narrow pyroxene phenocryst rims and late stage pyroxene within the groundmass shows variation to lower Mg contents ($Mg\#_{47-8}$) and Al/Ti ratios (2.44-1.68). No significant Al/Ti ratio change is visible with Mg# variation, indicating plagioclase and ilmenite crystallised together (as would be expected during quench cooling– Table 3.2). Apollo 12 olivine basalt 12040,44 initially crystallised Mg-rich pyroxene ($Mg\#_{74-70}$) with Al/Ti values of 3.35-3.76. This group has much higher Mg# and Al/Ti ratios than the remaining pyroxenes within this sample (beginning at $Mg\#_{66}$ and Al/Ti 2.8). Therefore it appears to represent a group of early grains subsequently surrounded by later, less Mg-rich, pyroxene. A large discrepancy exists between the Al/Ti ratios of the early Mg-rich pyroxene grains and the next large group of compositions at $Mg\#_{64-48}$, where the Al/Ti trend is constant between 1.7 and 2.1. As few pyroxenes show compositions between these two groups it appears there was a relative hiatus in pyroxene crystallisation between $Mg\#_{70-64}$. When pyroxene did again begin to crystallise the constant Al/Ti ratio indicates both plagioclase and ilmenite were co-crystallising alongside it.

Apollo 14 and 15 samples show similar trends on this type of diagram, with initially high Al/Ti ratios decreasing from 5-3.6 at $Mg\#_{71-60}$, to 2.8-1 at $Mg\#_{60-2}$. Compared to the Apollo 12 basalts this indicates an extended period of plagioclase co-crystallisation prior to the appearance of ilmenite in these samples. Apollo 15 olivine-normative basalts 15016,7 and 15555,206 show definite data clustering at Mg-rich compositions ($Mg\#_{69-60}$), suggesting the presence of Mg-rich cores as in the case of the majority of Apollo 12 samples. Plagioclase co-crystallisation with pyroxene continues over a 15 % change in Mg# within these samples; pyroxenes in Apollo 15 olivine-normative samples 15016,7 and 15555,206 fractionate from $Mg\#_{65-50}$, and pyroxenes in Apollo 14 sample 14053,19 fractionate from

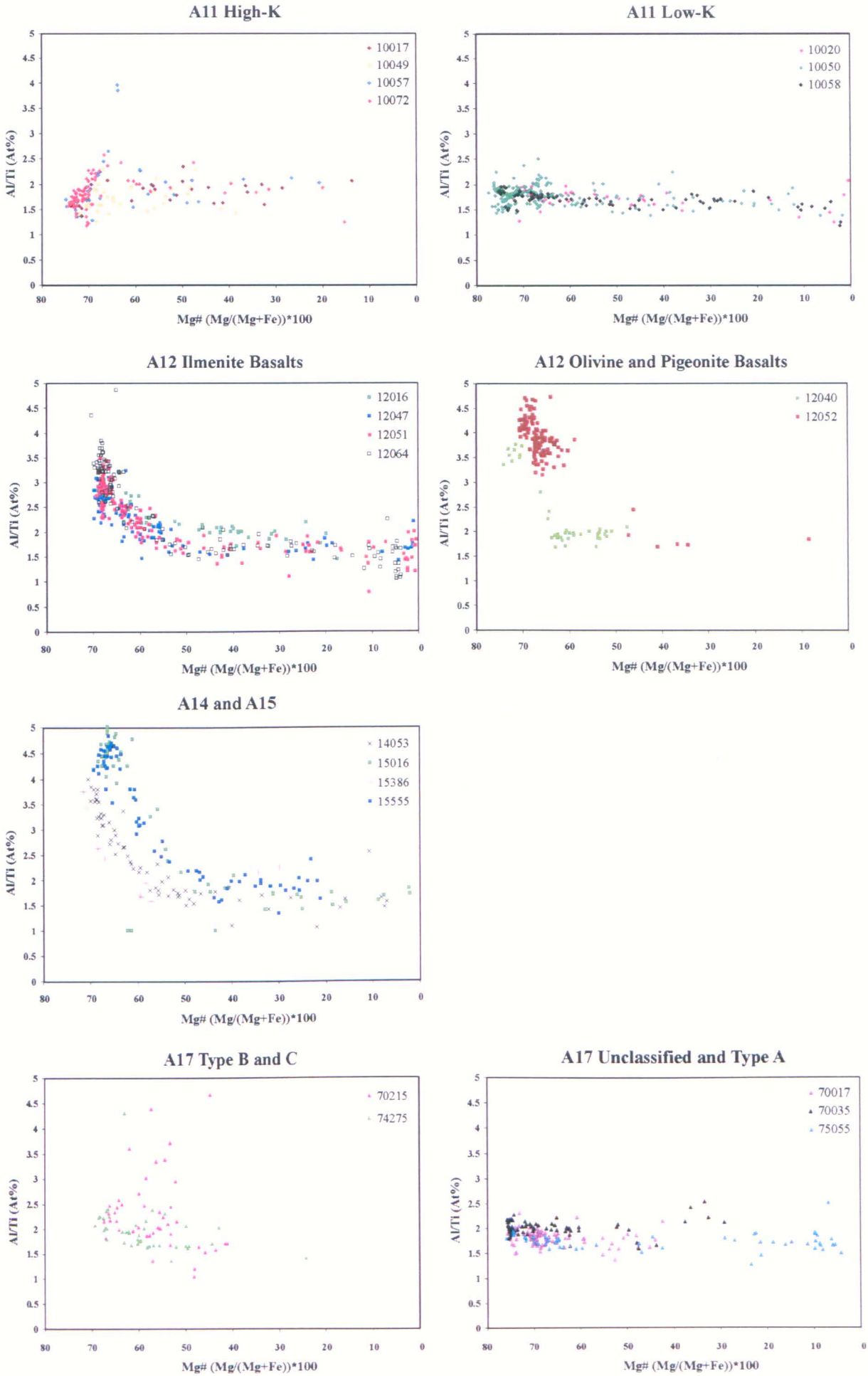

Figure 3.48: Al/Ti ratio vs. Mg# for clinopyroxene grains within individual samples.

$Mg\#_{70\text{-}55}$. Apollo 15 KREEP sample 15386,46 exhibits Al/Ti ratios in line with those of Apollo 14 basalt 14053,19 for $Mg\#_{72\text{-}57}$, with the addition of an increase in Al/Ti from 1.86 to 2.25 within late stage pyroxenes with $Mg\#_{57\text{-}30}$. This ratio increase suggests the cessation of plagioclase crystallisation at pyroxene $Mg\#_{57}$, followed by ilmenite co-crystallisation with pyroxene from this point forward (Table 3.2).

Apollo 11 and 17 high-Ti samples show little Al/Ti ratio variation, excepting hints of a ratio increase between $Mg_{69\text{-}45}$ for some samples. The ratio increase is strongest for Apollo 17 type B basalt 70215,306 and type C basalt 74275,310, where Al/Ti increases from 1.8 to 4.7 and 2.1 to 4.3 respectively. Weaker ratio increases are observed in the Apollo 11 high-K basalts, where Al/Ti changes from 1.6 to a maximum of 4.0 between $Mg\#_{74}$ and $Mg\#_{64}$. These ratio increases suggest ilmenite co-crystallisation with pyroxene, followed by additional plagioclase crystallisation from the point where the ratio begins to fall and level off ($Mg\#_{45}$ for the Apollo 17 type B and C samples, $Mg\#_{64}$ for the Apollo 11 high-K samples). To further constrain the details of the remaining high-Ti samples within our suite Mg# is compared to At % proportions of Ti and Al individually in Figure 3.49. The decrease in both Ti and Al within these samples pyroxene grains, along with the flat Al/Ti ratio trend with changing Mg# in Figure 3.48, indicates both ilmenite and plagioclase co-crystallised with pyroxene in the Apollo 11 low-K samples and remaining Apollo 17 samples (Table 3.2). Samples 75055,49 and 10020,232 both show a gap in pyroxene Mg# implying a hiatus in crystallisation. For 75055,49 this gap is between $Mg\#_{43}$ and $Mg\#_{29}$, whereas that of 10020,232 lies slightly later at $Mg\#_{36}$ to $Mg\#_{18}$.

3.2.2. Olivine. Plots of olivine Mg# show the amount of fractionation from Mg to Fe-rich compositions (forsterite to fayalite) present within each sample (Figure 3.47). The data can also be used in conjunction with pyroxene Mg# to determine crystallisation relationships. Apollo 15 olivine-normative basalts 15016,7 and 15555,206, and Apollo 12 ilmenite basalt

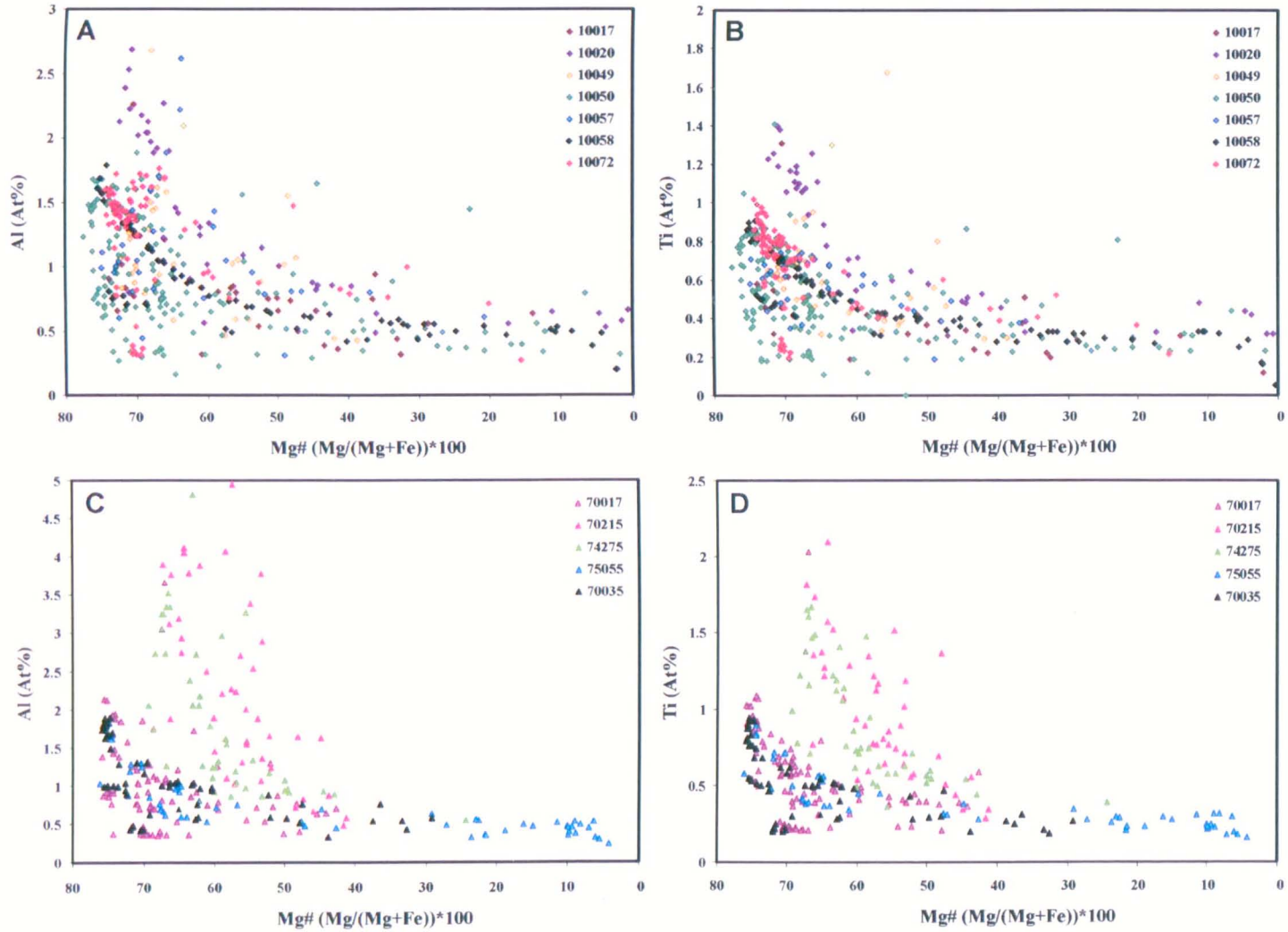

Figure 3.49: High-Ti basalt Al and Ti vs. Mg# for clinopyroxene grains in individual samples. Samples are grouped according to type. **(a)** Apollo 11 basalts Al vs. Mg#, **(b)** Apollo 11 basalts Ti vs. Mg#, **(c)** Apollo 17 basalts Al vs. Mg#, **(d)** Apollo 17 basalts Ti vs. Mg#.

12016,39, contain highly zoned olivine with $Mg\#_{69-2}$, $Mg\#_{63-24}$ and $Mg\#_{62-17}$ respectively. Previous studies show olivine compositions within the Apollo 15 olivine-normative and Apollo 12 ilmenite basalts vary even more ($Mg\#_{72-2}$, Kushiro, 1972; Walker et al., 1977 and $Mg\#_{67-2}$, Dungan and Brown, 1977), suggesting these grains nucleated early in the crystallisation sequence and continued to crystallise for a long period of time. Our data show olivine Mg# is lower than pyroxene Mg# in samples 15555,206 and 12016,39, the highest values are olivine $Mg\#_{62}$ vs. pyroxene $Mg\#_{70}$ in the former sample and $Mg\#_{63}$ vs. $Mg\#_{69}$ in the latter. This implies olivine crystallised after the earliest pyroxene grains in these basalts. Sample 15016,7 shows the opposite relationship, with maximum olivine $Mg\#_{69}$ vs. pyroxene $Mg\#_{68}$, indicating olivine was the first of the two minerals to nucleate by a narrow margin (Table 3.2). The olivine compositional data of Kushiro (1972) confirms this relationship by indicating olivine Mg content in sample 15016 can be as high as $Mg\#_{72}$. Apollo 12 olivine basalt 12040,44 contains a high modal proportion of olivine (Table 3.1), and as with samples 12016,39 and 15555,206 early olivine grains show lower Mg# than the most Mg-rich pyroxene cores ($Mg\#_{63}$ vs. $Mg\#_{74}$). This relationship is also apparent in the remaining olivine bearing Apollo 12 samples (12047,9 and 12052,339), which contain a similar amount of olivine fractionation to sample 12040,44 ($Mg\#_{63-44}$). Olivine data from Baldridge et al. (1979), Neal et al. (1994a) and McGee et al. (1977) suggest that our olivine data are slightly more Fe-rich than that observed in the other pigeonite basalt samples (Fo_{67-43} in sample 12052,399 versus Fo_{76-59} in other samples). In addition olivine basalt 12040,44 does not contain any of the more Mg-rich olivine compositions recorded in a number of other olivine basalt samples ($Mg\#_{76-42}$, Kushiro et al., 1971; Grove et al., 1973; Dungan and Brown, 1977; McGee et al., 1977; Baldridge et al., 1979).

Apollo 14 basalt 14053,19 exhibits restricted compositions of olivine ($Mg\#_{67-60}$), lower than its most Mg-rich pyroxene ($Mg\#_{71-7}$), implying olivine crystallised slightly later than

initial pyroxene nucleation. However, the presence of slightly rounded phenocrystic olivine within the most Mg-rich pyroxene cores of this sample suggests olivine began to crystallise before the earliest pyroxene (Figure 3.29). In this situation the textural evidence is most reliable because electron microprobe data may not represent the most Mg-rich olivines, or they may not be represented in our thin section (Table 3.2). The olivine and pyroxene data of Kushiro et al. (1972) also suggest early pyroxene crystallised before olivine but this dataset is sparse. In addition Gancarz et al. (1971) and Kushiro et al. (1972) detected fayalitic olivine within the mesostasis of sample 14053 ($Mg\#_{15-5}$). Patchen et al. (2004) also report the presence of fayalite but none is visible within sample 14053,19, probably due to its heterogeneous distribution. Apollo 15 KREEP basalt 15386,46 does not contain olivine.

Four of the five Apollo 17 high-Ti basalt samples contain olivine (excluding 75055,49). These grains show less fractionation than those of the Apollo 12 samples (Figure 3.47). Unclassified basalts 70017,110 and 70035,195 display olivine fractionating from $Mg\#_{67-51}$ and $Mg\#_{67-59}$ respectively, in agreement with Hodges and Kushiro (1974) and Weigand (1973). Both these samples contain initial pyroxene with higher Mg# than olivine. Conversely type B basalt 70215,306 and type C basalt 74275,310 contain early crystallised olivine with higher Mg# than pyroxene (70215,306: pyroxene $Mg\#_{67-41}$, olivine $Mg\#_{74-48}$; 74275,310: pyroxene $Mg\#_{63-26}$, olivine $Mg\#_{74-65}$). This is consistent with earlier observations for these sample groups by Hodges and Kushiro (1974), Longhi et al. (1974) and Dymek et al. (1975). Meyer and Wilshire (1974) suggested sample 74275 contains xenocrystic olivine grains with much higher Mg# than this sample's parental melt could produce ($Mg\#_{84-82}$). As our olivine data show lower Mg# than these xenocrysts and overlap with pyroxene Mg# sample 74275,310, it does not appear to contain any of the xenocrysts.

Apollo 11 basalts display a limited range in olivine compositions ($Mg\#_{58-73}$) and only high-K samples 10049,94 and 10072,40, and low-K samples 10020,232 and 10050,168 contain olivine. Type B3 sample 10020,232 shows olivine with slightly higher Mg content (Mg_{73-65}) than pyroxene ($Mg\#_{71-1}$), whereas high-K sample 10049,94 and unclassified sample 10050,168 show the opposite relationship (10049.94: olivine $Mg\#_{67}$, pyroxene $Mg\#_{72-36}$; 10050,168: olivine $Mg\#_{70-56}$, pyroxene $Mg\#_{77-2}$). These compositions are consistent with previous analyses of samples 10020, 10049 and 10050 by Beaty and Albee (1978), though these authors found olivine extended to more Fe-rich compositions within sample 10050 ($Mg\#_{69-40}$). Beaty and Albee (1978) also show type B3 basalts can contain olivine with more Fe-rich compositions than those analysed within sample 10020 (as low as $Mg\#_{40}$), the low-K B1 group samples do not contain olivine. As mentioned in section 3.1 high-K basalt 10072,40 contains two types of olivine; a large, embayed, euhedral phenocryst with $Mg\#_{74-70}$ and a number of smaller, more Fe-rich ($Mg\#_{71-65}$), partially resorbed grains found within pyroxene. The difference in Mg# between the two suggests they are of two different generations, the large phenocryst appears to have crystallised before pyroxene (based on Mg# and textural evidence) and the smaller olivine grains probably formed after initial pyroxene nucleation and co-crystallised with later pyroxene (Table 3.2). Beaty and Albee (1978) did not report the presence of any olivine with the composition of the large phenocryst, their native olivine data for this sample extend to slightly more Fe-rich compositions ($Mg\#_{70-58}$).

3.2.3. Feldspar. Plagioclase compositions are compared in Figure 3.50 using anorthite number, where An = (Ca/(Ca+Na+K))*100 (atomic proportions). Some brief observations are noted below:

- Plagioclase compositions within Apollo 14 high-Al basalt 14053,19 show the most variation within our sample set (An_{65-95} from core to rim), in agreement with the data of Kushiro et al. (1972).

- The Apollo 15 olivine-normative basalts display least variation (An_{93-88}), but previous data extends this to An_{94-78} where the cores are relatively unzoned but the rims decrease in anorthite content (Bence and Papike, 1972; Longhi et al., 1976).

- The Apollo 12 low-Ti basalts contain plagioclase with compositions similar to the Apollo 15 low-Ti olivine-normative basalts (An_{96-80} and An_{93-88} respectively). Previous studies reported plagioclase zonation between An_{95} and An_{80} (Grove et al., 1973; Dungan and Brown, 1977; Baldridge et al., 1979).

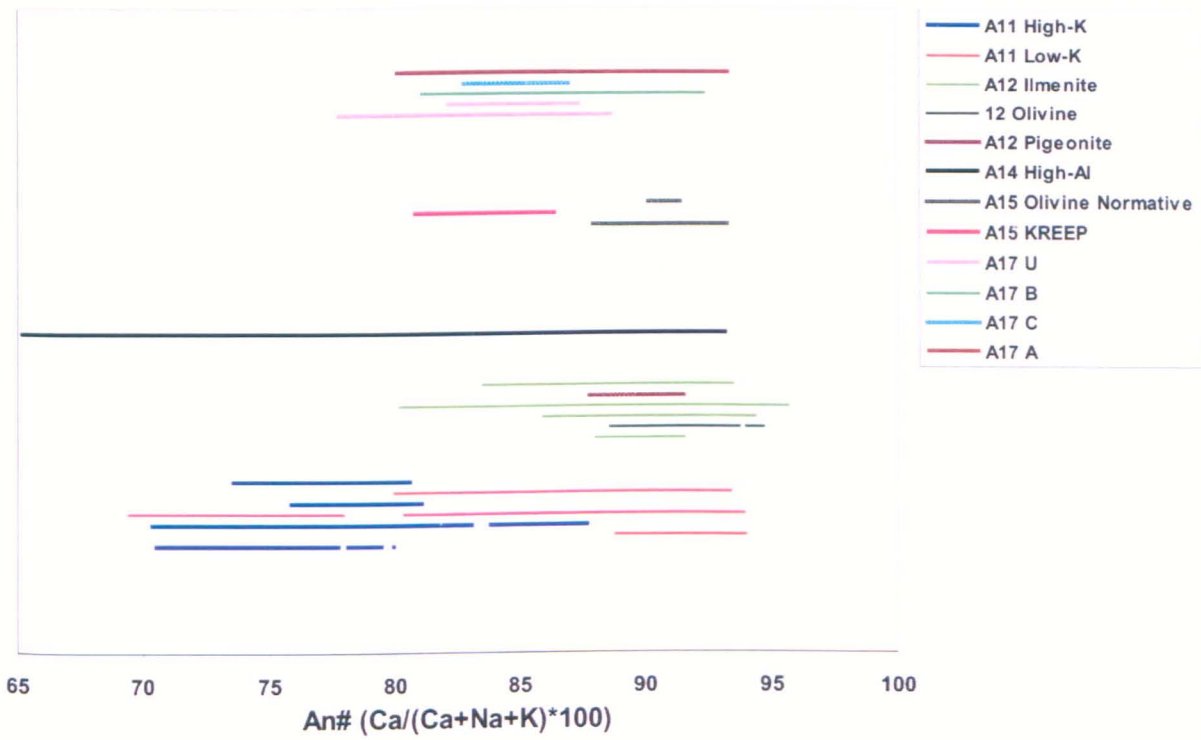

Figure 3.50: Plagioclase An# variation within individual samples. Samples are grouped according to type (see table 1.5).

- Generally plagioclase within high-Ti, high-K Apollo 11 basalts contains lower anorthite content (An_{88-70}) than that within the low-K basalts (An_{94-80}), excluding sample 10050,168 which shows variation from An_{69} to An_{94}. This relationship is

also visible in the data of Keil et al. (1970), Lovering and Ware (1970) and Stewart et al. (1970), whos combined data show the high-K basalt samples vary from An_{78} to An_{69} and the low-K samples vary from An_{91} to An_{75}.

- Apollo 15 KREEP basalt 15386,46 displays lower anorthite content (An_{81-86}) than the Apollo 15 low-Ti olivine-normative basalts (An_{88-93}). Steele et al. (1972) reported the plagioclase anorthite content of sample 15386 as An_{85-70}.

Comparing the average Mg# of olivine and the average An# of plagioclase from each sample illustrates where these basalts fit in context with other mare basalts (Figure 3.51). In general the low-Ti basalts have the highest average An# while the high-Ti basalts have higher average Mg#, however the classification is not that simple - as range bars representing the full spread of previous data show. This plot again highlights the difference in An# between the high and low-K Apollo 11 basalts as well as the similarity of Apollo 12 and 15 samples. Apollo 14 data appear to plot closest to that of Apollo 17, with higher average Mg# than any of the other low-Ti basalt types. Sample 10049,94 falls well below the other high-K Apollo 11 basalts in terms of Mg#, but this almost certainly results from sparse olivine microprobe data on account of the fine grained nature of the sample.

K-rich feldspar is present in a number of low-Ti basalts, Apollo 11 high-K basalts and Apollo 15 KREEP basalt 15386,46 However, the grains are only large enough for analysis in samples 12051,59, 10017,372, 10050,168 and 15386,46 (Figure 3.52). K-feldspar is most abundant in sample 15386,46 and these grains, as well as those within sample 10017,372, fall within the forbidden zone of the feldspar quadrilateral because of the Moon's depletion in alkali elements (sections 1.1.1 and 1.1.2). K-feldspar within sample 10050,168 was found to contain up to 13 wt % BaO.

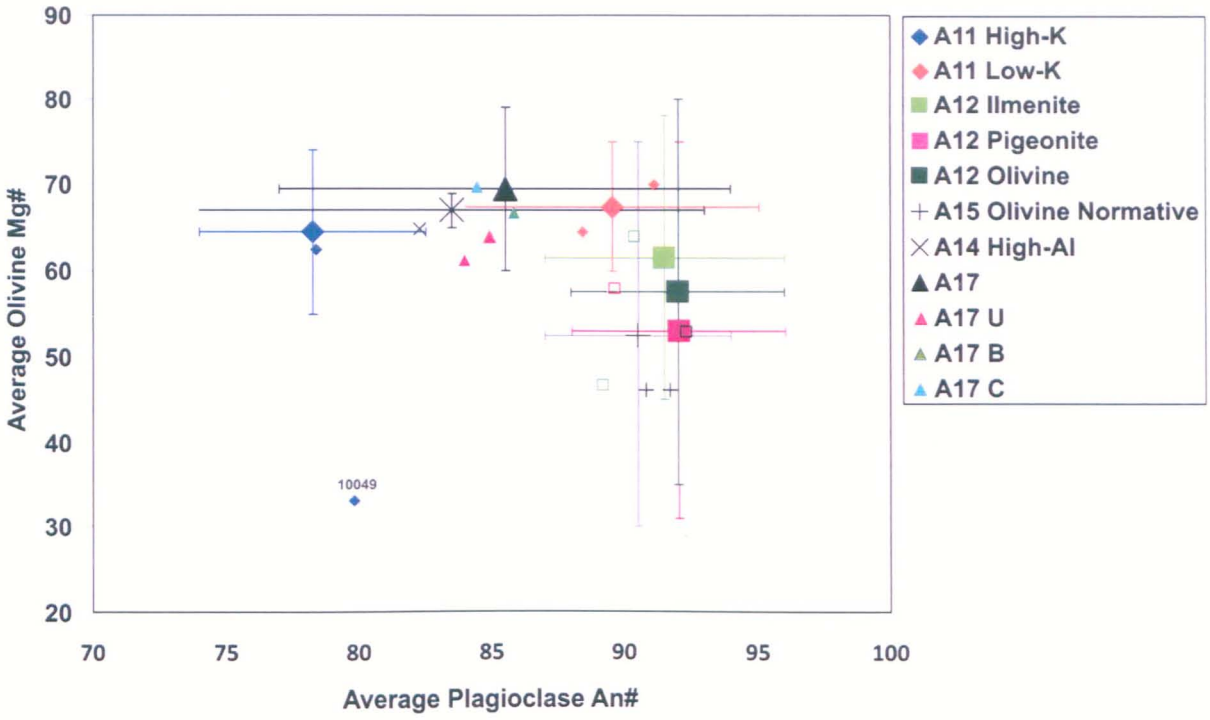

Figure 3.51: Average olivine Mg# vs. average plagioclase An#. Large symbols represent the average values of specific basalt groups, calculated from all previous data; error bars represent the spread of data. Small symbols represent our data.

3.2.4. Ilmenite. Chemical differences exist between ilmenites from different Apollo sites, specifically in terms of their MgO content. Ilmenites within the high-Ti basalts contain the highest amount of MgO (up to 6 wt % - see appendix B). In these samples, the MgO content in ilmenites appear to be positively correlated with the ilmenite modal abundance. The Apollo 17 samples with highest ilmenite modal abundance (e.g. unclassified basalts 70017,110 and 70035,195, and type B basalt 70215,306) contain high MgO (wt %) within their ilmenite, whereas Apollo 17 and Apollo 11 samples with lower ilmenite modal abundance (e.g. Apollo 17 type A basalt 75055,49) contain grains with lower MgO wt %. These relationships are apparent in Figure 3.53, which shows the relative proportions of MgO, Cr_2O_3 and MnO in our samples. Ilmenite compositions in the low-Ti basalts display a wide variation from 0-2.0 wt % MgO with varying MnO and Cr_2O_3 contents, however two samples lie outside this group. Apollo 12 olivine basalt 12040,44 and ilmenite basalt 12016,39 contain ilmenite grains with MgO wt % ranging from 2.9-3.2 and 0.5-1.2

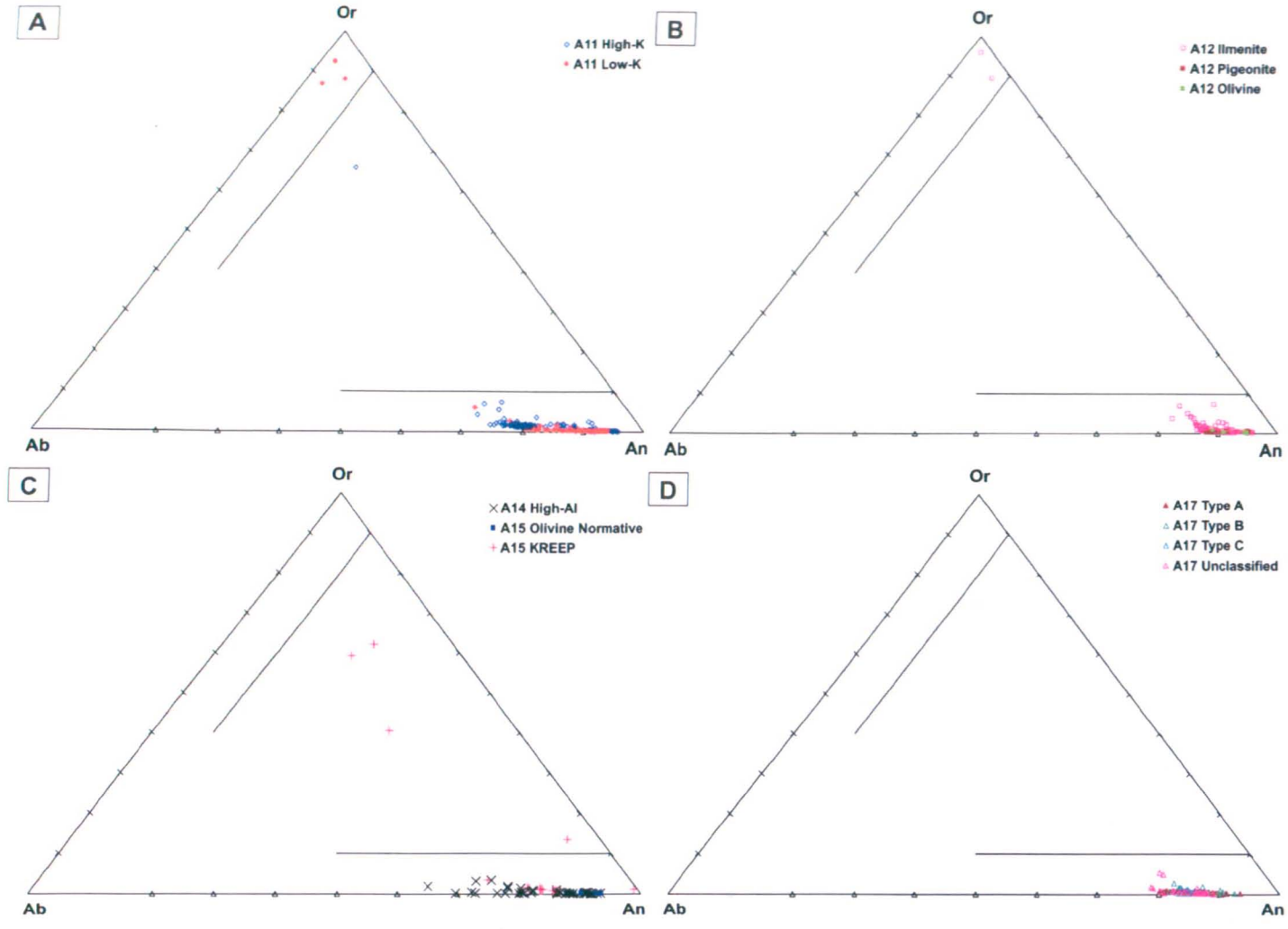

Figure 3.52: Quadrilateral plots of orthoclase (top corner), anorthite (bottom right) and albite (bottom left) percentages within plagioclase grains from individual samples. Samples are grouped according to type where **(a)** shows the Apollo 11 samples, **(b)** shows the Apollo 12 samples, **(c)** shows the Apollo 14 and 15 samples and **(d)** shows the Apollo 17 samples.

respectively, concentrations more in line with the high-Ti basalts (making these two samples plot towards the MgO corner of Figure 3.53). Of the remaining samples, Apollo 15 KREEP basalt 15386,46 shows slightly elevated Cr_2O_3 content within its ilmenite grains (0.9-0.5 wt %) and Apollo 11 low-K basalt 10058,254 shows two distinct populations of ilmenite with slightly varying MgO (0.4-0.5 and 0.6-0.7).

3.2.5. Spinel. Spinel composition ranges from chromite ($FeCr_2O_4$) to ulvöspinel (Fe_2TiO_4) and provides textural and chemical measures of melt evolution. Low-Ti and KREEP basalts contain chromites ranging to Ti-rich spinel and commonly ulvöspinel (Figure 3.54). Apollo 14 sample 14053,19 contains chromites with higher Al content than any other low-Ti sample analysed in our study; the stoichiometry of these grains was found to be

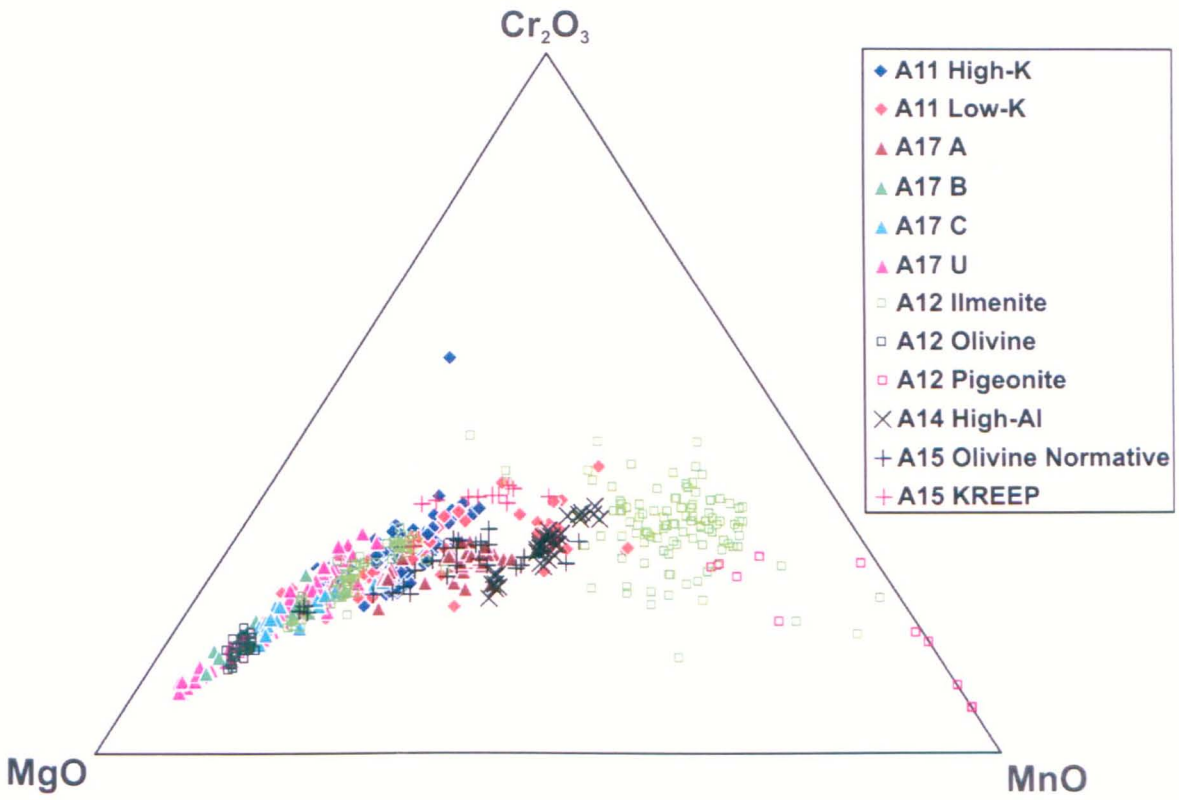

Figure 3.53: Ilmenite compositions for individual samples, grouped according to type. Cr_2O_3, MnO and MgO relative abundances are calculated using the following formula: $Cr_2O_3\# = (Cr_2O_3/ (Cr_2O_3 + MnO + MgO))*100$, where MnO and MgO can be substituted for Cr_2O_3 to give MnO# and MgO#.

incorrect as also reported by El Goresy et al. (1972). This is probably because of the extremely reduced nature of the sample, causing ulvöspinel to break down to chromite, ilmenite and Fe metal grains (Patchen and Taylor, 2004). A number of high-Ti basalts do not contain spinel but, where present, these grains display mixed Cr-Ti compositions with little variation, excepting the slightly more Al-rich composition of grains within Apollo 17 unclassified sample 70017,110.

3.2.6. Accessory Minerals. The modal abundance and composition of indigenous FeNi metal within each sample varies. No FeNi metal grains were detected in Apollo 11 high-K basalt 10072,40 or Apollo 17 type B basalt 70215,306, while high-K basalt 10049,94 and Apollo 17 type C basalt 74275,310 only contain blebs < 5 μm - too small for reliable electron microprobe analysis. Apollo 17 unclassified basalt 70017,110 displays numerous

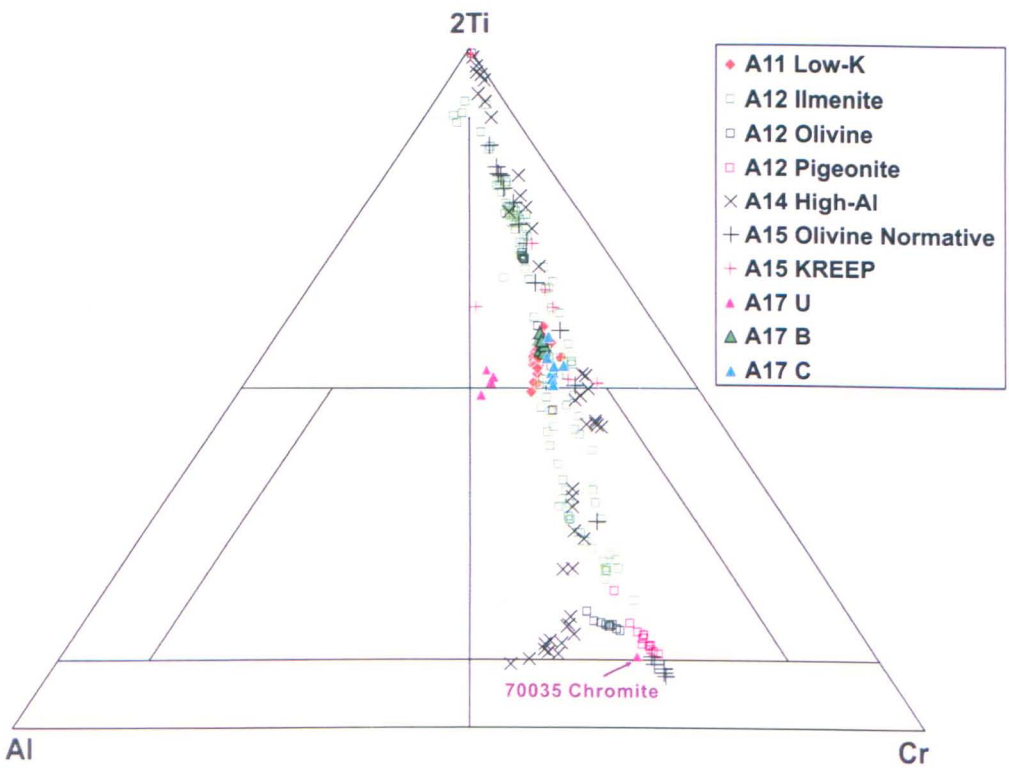

Figure 3.54: Spinel compositions for individual samples, grouped according to type. Relative abundances calculated as in figure 3.53. Compositions vary from Cr-rich (chromite) to Ti-rich (ulvöspinel).

blebs as independent grains and inclusions within troilite, containing < 1.1 wt % Co and < 0.25 wt % Ni. Apollo 11 low-K basalt 10058,254 contains a native iron bleb of 200 μm diameter with very little Ni and Co but unusually high Cr (12.33 wt %). In contrast, the Apollo 12 FeNi blebs contain ~ 1.6 wt % Co and Ni up to 3.5 wt %. This variation has been previously noted by Taylor (1982). Troilite has a very stable composition with a 1:1 ratio of FeS for all samples.

Phosphate phases are found in all samples excluding 12052,339, 70215,306 and 74275,310. Apollo 11 high-K basalts generally contain phosphates too small for quantitative analysis. However, sample 10017,372 was found to contain both apatite and (RE)-merillite. In contrast, the Apollo 11 low-K basalts only contain apatite, as do Apollo 17 type A basalt 75055,49 and unclassified basalt 70017,110. The low-Ti Apollo 15 olivine-normative basalts and Apollo 12 olivine basalt 12040,44 contain apatite and (RE)-merillite, while the Apollo 12 ilmenite basalt samples contain only apatite. (RE)-merillite is not present in any of our samples without apatite; (RE)-merillite appears to contain much higher incompatible element abundances than apatite (mostly REE, Y, with some Fe and Mg). Jolliff et al. (2006) argued that lunar (RE)-merrilite contains high REE and Y abundances because of the lack of Na in lunar rocks; this absence leaves the Na site open in the crystal lattice and it is filled by these elements. However, a REE-enriched melt is not required to crystallise (RE)-merillite in minor proportions such as those found in our samples (Jolliff et al., 1993).

3.3. Trace Element Mineral Chemistry

Thin sections are not ideal for LA-ICP-MS analysis as a 30 μm thickness yields a much shorter signal than a typical thick section (~ 150 μm). However, because the former are more widely available for both Apollo and lunar meteoritic material, it is important to try and utilise them as much as possible. Thin section analysis during this study produced

reliable trace element data sets for pyroxene and plagioclase and partial datasets for olivine. Rare earth element concentrations in rocks and minerals are usually normalised to a common reference standard as the REE in the solar system are highly variable because of the different stabilities of the atomic nuclei. REE with even atomic numbers are more stable (and therefore more abundant) than those with odd atomic numbers, producing a zig-zag pattern on a composition-abundance diagram. Chondritic meteorite normalisation (commonly using CI-chondrites) eliminates this abundance variation and allows any fractionation of the REE group relative to chondritic meteorites to be identified. Normalised values and ratios of normalised values are denoted with the subscript N (e.g., Ce_N, $(La/Ce)_N$).

3.3.1. Pyroxene. Pyroxene rare-earth-element (REE) data trends show typical light REE (LREE) depletion relative to heavy REE (HREE). This forms a positive gradient from La to Lu for all samples (La/Lu_n = 0.008-0.956, where $_n$ signifies element values are normalised to the CI chondrite values of Anders and Grevesse, 1989) – generally steep from La to Sm (0.036-0.956) and comparatively flat from Gd to Lu (0.301-1.217) (Figure 3.55). The trend includes a strongly negative Eu anomaly common to all mare-basalt pyroxenes (Eu* = chondrite-normalised $Eu/\sqrt{(Sm*Gd)}$, where anything between zero and one is a negative anomaly and anything above one is positive), and caused by inherent Eu^{2+} depletion in the lunar source regions (see section 1.1 and Figure 1.1). Despite these similarities, significant variations among REE trends for different mare-basalts do exist, and prove valuable in determining the crystallisation sequence and parental melt composition for each basalt sample. Pyroxene REE abundance increases with decreasing Mg# (i.e. fractionation - Figure 3.56) and possible change from pigeonite to augite (REE replace calcium in pyroxene lattices). Hence highly zoned pyroxene grains exhibit widely varying REE patterns (e.g. sample 12047,9), and pyroxenes in samples with less compositional variation (e.g. 10072,40) show less difference in REE abundance both

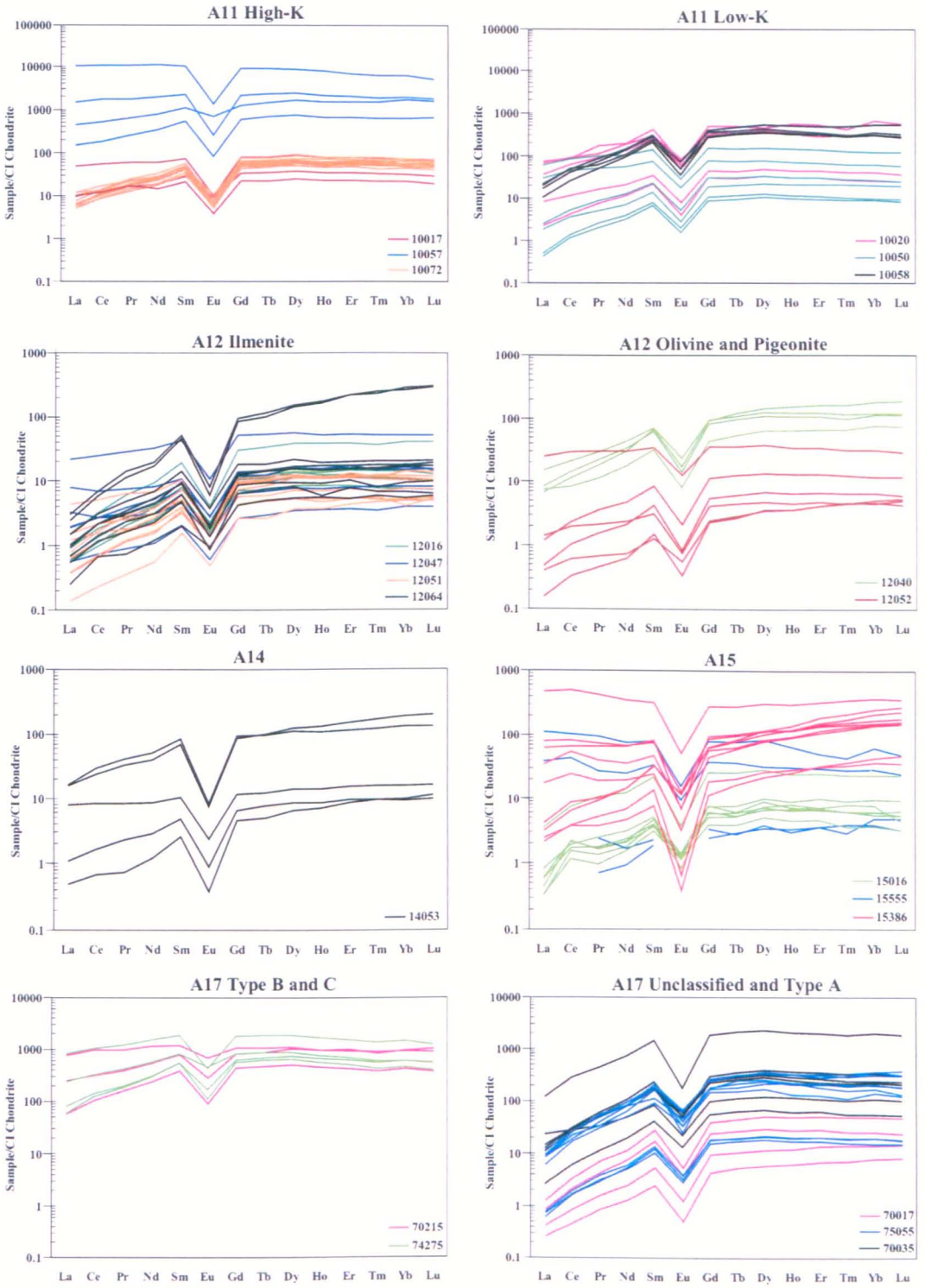

Figure 3.55: Pyroxene REE abundances normalised to CI chondrites. Samples are grouped according to type and each line represents one pyroxene grain analysis. Chondritic values from Anders and Grevesse (1989). Data from the analysis of sample 10057,64 is included in the Apollo 11 high-K plot but the fine grained nature of this sample meant more than one phase was incorporated into these ablation pits. Consequently the data are not reliable and were not investigated further.

within and between grains. A number of samples are coarse-grained, hence allowing for the analysis of both pyroxene cores and rims (e.g. sample 12064,136), therefore, giving a true indication of REE variation throughout crystallisation. However, most samples were found to be too fine grained for this type of analysis as each laser pit is ~ 80 μm diameter. For these samples the laser was aimed at the core of each grain. Therefore LA-ICP-MS data may underestimate the amount of zonation within finer grained samples; for example electron microprobe data shows much more zonation within sample 10058 than is represented in LA-ICP-MS data.

For a number of samples, LREE's are less depleted in low Mg# pyroxene (highest REE abundance). This may indicate Fe-rich pyroxene continued to crystallise after the majority of feldspar formed in these samples, as feldspar preferentially incorporates LREE's into its structure during crystallisation. However, Apollo 12 ilmenite basalt 12064,136 shows the opposite relationship, its low-Mg#, Ca-poor pyroxene has an increasingly positive gradient with highly depleted LREE and HREE enrichment. LREE depletion can be explained by the co-crystallisation of plagioclase with late stage pyroxene in this sample (Figure 3.27 and Figure 3.48). Similarly as HREE's do not readily partition into the crystal lattice of plagioclase they collect in the residual melt, where they can be taken into the pyroxene structure (Onuma et al., 1968; Philpotts, 1978). REE variation also highlights the hiatus in pyroxene crystallisation observed from the microprobe data of samples 10020,232 and 75055,49. A gap is visible between low and high REE abundance for pyroxene in both these samples (Figure 3.55).

To eliminate the effects of zoning and gain a better understanding of parental melt composition, the earliest-forming pyroxene cores of each sample were analysed for their trace element contents (Figure 3.57). Within our sample set, Apollo 12 pigeonite and ilmenite basalts and Apollo 15 olivine-normative basalts contain pyroxenes with the lowest

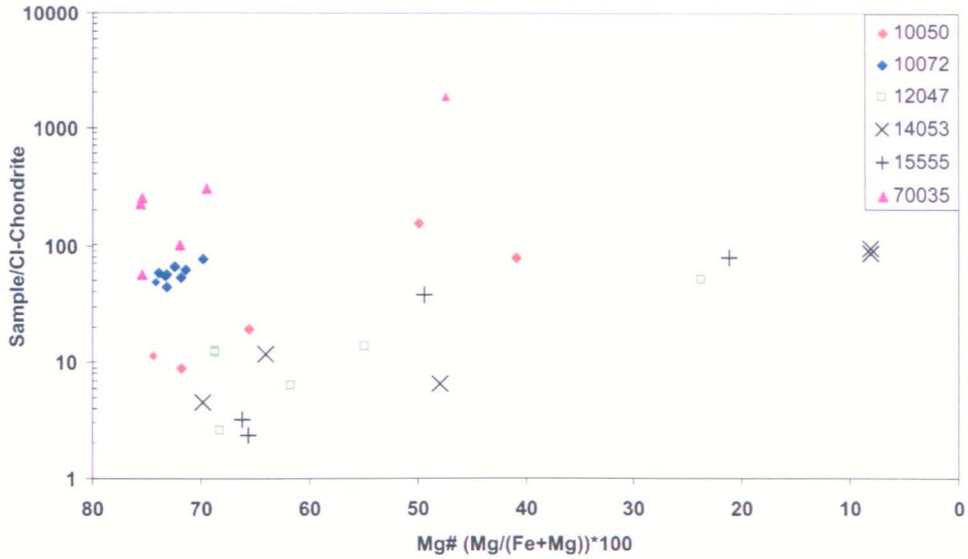

Figure 3.56: Pyroxene Mg# vs. chondrite-normalised Gd abundance. The data of these samples show the best trends of overall pyroxene REE abundance increase with decreasing Mg# within individual samples. The R2 values for these trends vary from 0.56 for sample 10072, to 0.99 for sample 15555, where 1 represents a prefect correlation. However, the statistical reliability is limited by the limited data set.

REE abundances, along with Apollo 14 high-Al basalt 14053,19 and Apollo 17 unclassified basalt 70017,110. On a chondrite-normalised REE diagram these samples plot below olivine basalt 12040,44, which contains REE abundance higher by a factor of ten than that of any other low-Ti basalt. Apollo 17 type B and C basalts 70215,306 and 74275,310 contain pyroxenes with high REE abundance and show very similar trends, while Apollo 17 type A basalt 75055,49 is relatively REE poor. Apollo 11 high-K basalts exhibit similar REE trends and abundances, however, this observation is based on data from two samples which have fine grained textures (10049,94 and 10057,64) and therefore are not suitable for mineral REE data collection. Despite this group's enrichment in whole rock K and P (Table 4.1), pyroxene REE trends do not display the typical characteristics of a KREEP rich parental melt (see Apollo 15 KREEP basalt 15386,46 and ,54 in Figures 3.57a and 4.7 respectively). Apollo 14 high-Al basalt 14053,19 does show some of these characteristics, despite relatively low REE abundance in pyroxenes. Its trends display a positive gradient from Gd to Lu (0.453-0.728), similar to (but more pronounced than) those

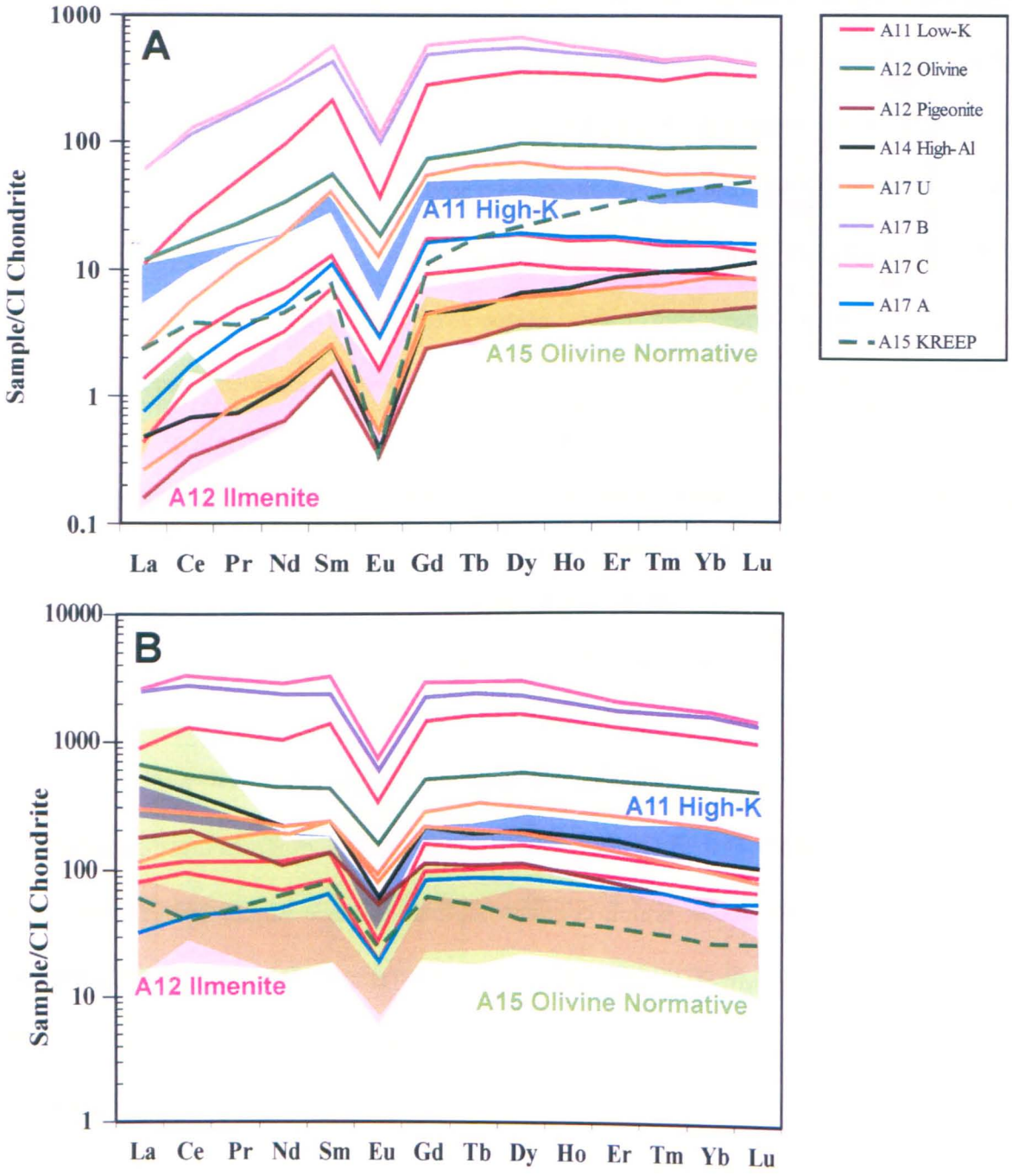

Figure 3.57: Pyroxene grains with the lowest Mg# from each sample, grouped according to type. **(a)** Mg# vs. chondrite-normalised abundance. **(b)** Mg# vs. chondrite-normalised melt abundance calculated using the augite partition coefficients of McKay et al. (1986) based on the Martian shergottite basalt system, and the pigeonite partition coefficients of McKay et al. (1991) based on the mare-basalt system. For clarity the blue shadows represent our data for the Apollo 11 high-K basalts, pink shadows represent Apollo 12 ilmenite basalts and green shadows represent Apollo 15 olivine-normative basalts. All our other samples are represented by coloured lines (see key). Chondritic values from Anders and Grevesse (1989).

visible in Apollo 12 pigeonite basalt 12052,339 and Apollo 17 unclassified basalt 70017,110 (0.483-1.154 and 0.524-0.928). In addition, it has a slightly deeper europium anomaly than other mare basalts (Eu* = 0.09-0.21 compared to 0.11-0.36), excluding the rim analyses of sample 12064,136 which have a similar europium anomaly (Eu* = 0.09-0.17). This pronounced positive HREE gradient appears to be half way between that of the mare basalts and Apollo 15 KREEP basalt 15386,46, which shows a characteristic KREEP signature with steeply positive slope (La/Lu_n = 0.011-0.384) and deeply negative Eu* (0.04-0.24) (e.g., Warren and Wasson, 1979a; Snyder et al., 1995).

Figure 3.58a shows Eu abundance versus europium anomaly for all pyroxene analyses from each sample, therefore tracking melt evolution in each case. For example, europium anomalies in pyroxenes of KREEP basalt 15386,46 range from by far the most negative (0.04) to relatively moderate (0.25) in comparison to mare-basalt samples, highlighting the transition from early formed orthopyroxene cores through pigeonite and finally to later Fe-rich augite (Figure 3.47). This pattern is seen throughout the sample set, with augite consistently exhibiting a weaker europium anomaly, in addition to overall higher REE abundance, than earlier formed pigeonite when both are present in one sample. The fact that augite contains more Ca (and therefore potential REE sites in the crystal lattice – McKay et al., 1986; James et al., 1998) may partly negate the avoidance of Eu uptake seen in other, less Ca-rich pyroxenes, - for example the Ca-poor rims of 12064,136. Excluding these rim analyses, the low-Ti Apollo 12 pyroxenes show a weak negative europium anomaly (average Eu* = 0.23), along with the low-Ti Apollo 15 olivine-normative basalts (average Eu* also = 0.23). When taken as a collective group, the high-Ti Apollo 17 basalts show a similar europium anomalies to the low-Ti basalts, but there is variation between the weak values of type B and C basalts 70215, 306 and 74275,310 (showing averages of 0.26 and 0.24 respectively) and the stronger values of unclassified basalt 70017,110 (Eu* = 0.17 average) - a sample containing a relatively high proportion of pigeonite with overall low

REE abundance (Figure 3.55). Apollo 11 high-K basalts within our sample set have a more negative average europium anomaly than the low-K group (Eu* = 0.15 and 0.19 respectively). As mentioned previously, high-Mg# pyroxene grains in 14053,19 display some of the most negative europium anomalies after those of KREEP basalt 15386,46, but the average europium anomaly for all grains is similar to mare-basalt values (Eu* = 0.14).

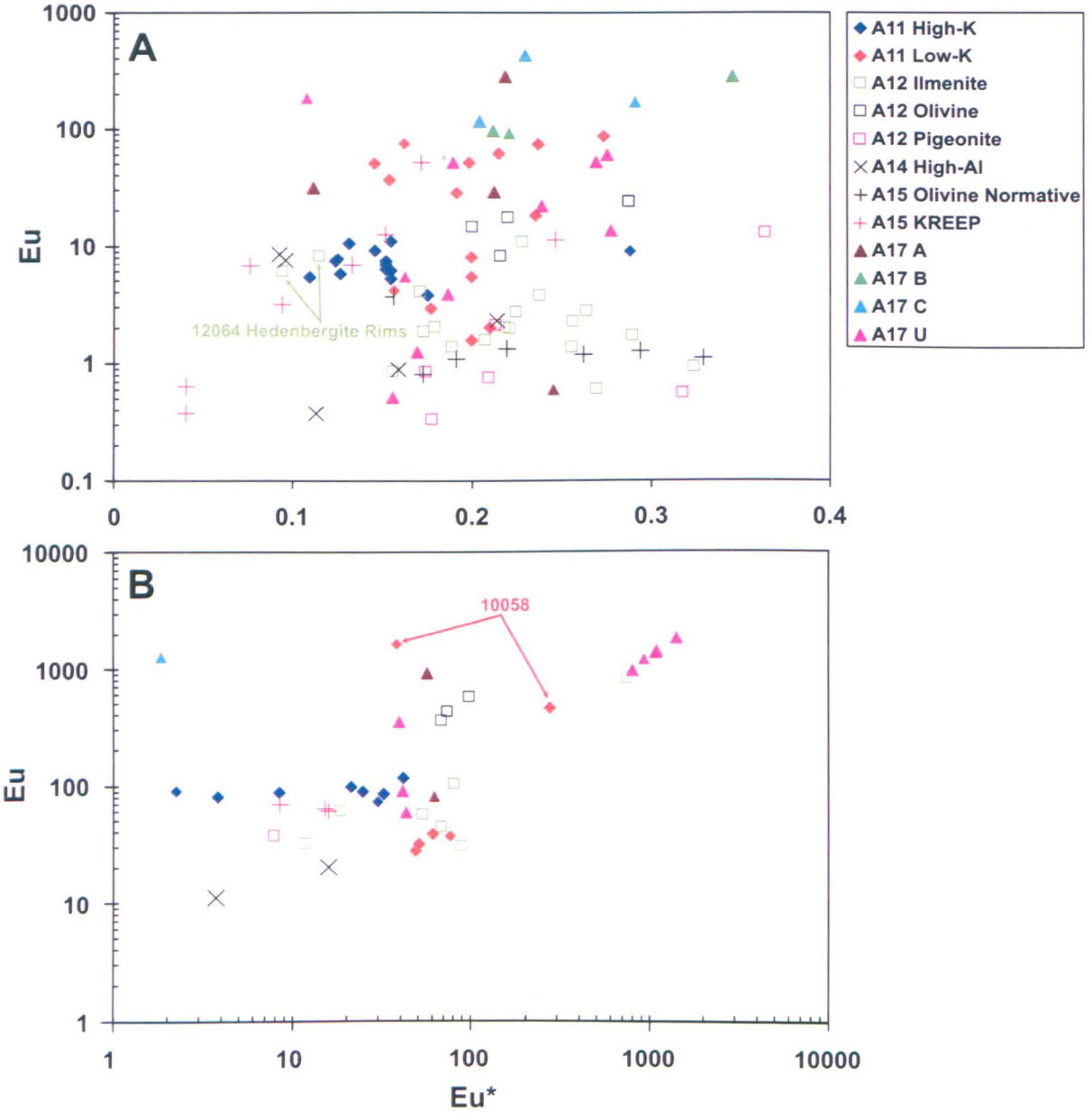

Figure 3.58: Eu abundance vs. Eu anomaly (where Eu* = chondrite-normalised Eu/√(Sm*Gd)). **(a)** Shows pyroxene grains (semi log plot) and **(b)** shows plagioclase grains within individual samples (log/log plot). Eu abundance is normalised to CI chondrite values (Anders and Grevesse, 1989).

Plots of pyroxene $(La/Yb)_n$ vs. $(Gd/Yb)_n$ (where $_n$ signifies chondrite-normalised values) shows variation in the overall REE gradient against that of the HREE (Figure 3.59). For pyroxenes (Figure 3.59a), all trends show LREE depletion ($(La/Yb)_n < 1$) while $(Gd/Yb)_n$ ratios are centred on 1. Apollo 17 type A basalt 75055,49 and unclassified basalt 70017,110 show the strongest LREE depletion with variable HREE enrichment for most grains ($(Gd/Yb)_n = 0.52\text{-}1.02$), while type B and C basalts 70215,306 and 74275,310 show weaker LREE depletion in addition to HREE depletion. Apollo 11 low-K basalts display greater LREE depletion than the high-K group, but no significant difference in $(Gd/Yb)_n$ ratio is observed – these samples have characteristically flat mid-REE (MREE) to HREE trends. The low-Ti basalts mostly show $(Gd/Yb)_n$ ratios < 1, excepting sample 15016,7 which exhibits flat trends and contains a number of pyroxenes with slight HREE depletion, much like the Apollo 11 basalts within our suite.

Additional trace element data reveal a decrease in Cr and V with Mg# in low-Ti basalt pyroxene grains, a trend not seen in the high-Ti basalts (Figure 3.60). Apollo 17 high-Ti unclassified basalt 70035,195, type B basalt 70215,306, type C basalt 74275,310 and a number of grains from type A basalt 75055,49, plus Apollo 11 low-K basalt 10058,254 and low-Ti Apollo 12 olivine basalt 12040,44, contain relatively high abundances of Sc and Cr. Apollo 15 KREEP basalt 15386,46 shows homogeneous concentrations of V, Sc and Cr throughout its pyroxene grains, irrespective of their Mg#. In addition, elevated Cr levels in these grains are consistent with the high concentration of Cr_2O_3 found in the ilmenites of this sample.

3.3.2. Parental Melt Calculations. Mare-basalt parental melt estimates were obtained using the augite REE partition coefficients of McKay et al. (1986) and the pigeonite REE partition coefficients of McKay et al. (1991). The former group of partition coefficients was selected because they were determined for low oxygen fugacity conditions (~Iron-

Table 3.2: Summary of mineralogical compositions

Sample	Type	Texture	Olivine	Pyroxene	Plagioclase	Minor Phases	REE Observations
10017	A11 High-K	fine grained, granular		Wo 6.7-36.8; En 11.1-62.5	An 80.0-80.2	tro, sil, ap, meri + FeNi	cpx and plag show little variation with Mg# and An#
10020	A11 Low-K	medium grained, subophitic cpx, ilm needles	Fo 63.7-72.7	Wo 8.8-43.5; En 0.6-47.9	An 86.5-94.0	sp, tro, sil, phos, K-feld, tran, pyroxf + FeNi	cpx show large variation with mg#, two populations apparant, few analyses for plag
10049	A11 High-K	fine grained, granular, vesiculated	Fo 66.9	Wo 11.1-39.5; En 23.1-56.1	An 73.6-88.4	tro, sil, K-feld, K-glass + FeNi	too fine grained to analyse
10050	A11 Low-K	medium grained, subophitic cpx, sieve textured ilm	Fo 55.9-69.7	Wo 8.8-41.2; En 1.6-61.5	An 72.2-94.0	tro, sil, ap, K-feld, pyroxf + FeNi	cpx show very wide variation with Mg#, plag show little variation with An#, olv abundance is high
10057	A11 High-K	fine grained, granular, vesiculated		Wo 0.55-40.0; En 3.4-59.6	An 76.8-81.9	tro, sil, K-feld, K-glass + FeNi	cpx and plag show wide variation with Mg# and An#
10058	A11 Low-K	coarse grained, subophitic cpx, irregular ilm		Wo 14.1-41.8; En 1.89-48.2	An 80.4-93.4	ap, K-feld, bad, FeNi + FeCr	cpx show little variation with Mg#, plag show moderate variation with An#
10072	A11 High-K	fine grained, skeletal ilm, anhedral cpx, rare olv phenocrysts	Fo 64.8-73.3	Wo 8.2-41.5; En 13.6-63.4	An 74.6-81.1	tro, sil, phos + glass	cpx show little variation with Mg#, but plag show wide variation with An#
12016	A12 Ilmenite	coarse grained, subophitic cpx, anhedral olv, irregular ilm	Fo 17.4-61.7	Wo 8.2-37.4; En 15.1-60.3	An 88.4-91.6	sp, tro, sil, ap + FeNi	cpx and plag show wide variation with Mg# and An#, olv abundance is high
12040	A12 Olivine	coarse grained, ophitic cpx encloses anhedral olv, intergrwn plag and irregular ilm	Fo 43.8-62.8	Wo 8.5-38.6; En 40.9-63.7	An 86.5-94.7	sp, tro, ap, meri, bad, K-feld + FeNi	cpx and plag show little variation with Mg# and An#, olv abundance is high
12047	A12 Ilmenite	medium grained, subhedral cpx, acicular plag and ilm, vesiculated	Fo 51.3-68.6	Wo 7.6-40.7; En 1.3-63.7	An 82.3-94.5	sp, tro, sil, ap, K-feld + fay	cpx and plag show wide variation with Mg# and An#
12051	A12 Ilmenite	coarse grained, subophitic cpx, bladed ilm, acicular plag		Wo 7.6-37.4; En 0.41-63.3	An 83.5-95.6	sp, tro, sil, bad, K-feld, pyroxf + FeNi	cpx ansd plag show wide variation with Mg# and An#
12052	A12 Pigeonite	fine grained, subhedral cpx, olv and spinel phenocrysts, quenched groundmass	Fo 43.4-66.9	Wo 8.6-37.7; En 0.8-64.6	An 88.0-95.2	quench texture inc. plag, ilm, tro + FeNi	cpx show wide variation with Mg#, overall abundance is low, only one plag analysis
12064	A12 Ilmenite	coarse grained, intergrown cpx and plag, acicular ilm and silica		Wo 8.0-42.2; En 2.8-63.1	An 85.4-93.6	sp, tro, sil, ap, pyroxf, K-feld + bad	cpx show wide variation with Mg#, rims show strong LREE depletion and HREE enrichment, plag shows moderate variation with An#
14053	A14 High-Al	coarse grained, anhedral cpx and olv, acicular plag, irregular ilm	Fo 59.8-67.2	Wo 7.5-33.7; En 5.8-63.7	An 65.1-93.2	sp, tro, sil, ap, K-glass, meri, pyroxf + FeNi	cpx show wide variation with Mg#, plag and olv show concave trend
15016	A15 ONB	coarse grained, subophitic cpx, anhedral olv, intergrown plag, vesiculated	Fo 25.0-70.5	Wo 10.0-36.2; En 1.9-59.2	An 88.3-93.4	sp, tro, sil, FeNi, ap, meri + K-glass	cpx show wide variation with Mg#, overall abundance of cpx and plag is low, olv abundacne is high
15386	A15 KREEP	coarse grained, subhedral cpx, intergrown plag, ilm and ap needles		Wo 2.6-30.5; En 25.6-80.1	An 81.4-86.8	sp, tro, sil, ap, meri, K-glass + bad	cpx show wide variation with Mg#, steep positive cpx and negative plag trends and strong Eu* are characteristic of KREEP basalts
15555	A15 ONB	coarse grained, poikilitic, cpx subophitically encloses olv	Fo 24.1-63.4	Wo 9.4-38.7; En 14.5-59.4	An 90.2-92.6	sp, tro, sil, ap, meri, bad + zirc	cpx show wide variation with Mg#, plag abundances are too low fro detection
70017	A17 Unclassified	coarse grained, subophitic cpx, intergrown plag, sieve textured ilm	Fo 51.4-66.7	Wo 7.5-43.5; En 13.2-65.2	An 78.8-88.8	sp, tro, sil, ap + K-glass	cpx and plag show wide variation with Mg# and An#, overall abundance of both is low, strong Eu* - especially for plagioclase
70035	A17 Unclassified	coarse grained, intergrown cpx and plag, irregular ilm, anhedral olv	Fo 58.5-70.0	Wo 6.8-40.3; En 25.2-67.1	An 82.4-93.4	tro, sil, ap, K-feld, bad, tran, zirc +FeNi	cpx show wide variation with Mg#, plag shows little variation with An# though abundance is high
70215	A17 Type B2	fined-grained, olv, spinel and cpx phenocrysts, quenched groundmass	Fo 47.8-74.3	Wo 16.3-49.3; En 29.9-55.2	An 81.9-92.5	QT inc. tro, plag + cpx	cpx show moderate variation with Mg#, overall abundance is high in cpx and olv, plag too fine grained to analyse
74275	A17 Type C	medium grained, intergrown cpx and plag, acicacular ilm, subhedral olv	Fo 64.5-74.1	Wo 16.1-44.8; En 26.7-50.3	An 83.1-87.1	sp, tro, plag, cpx ilm, sil + K-feld	cpx show moderate variation with Mg#, overall abundance is high in cpx, olv and plag
75055	A17 Type A	coarse grained, sub-ophitic cpx, accicular plag and ilm		Wo 11.3-40.4; En 3.7-47.9	An 80.4-93.4	tro, sil, ap, bad, zirc + FeNi	cpx and plag show wide variation with Mg# and An#, two populations of cpx apparent

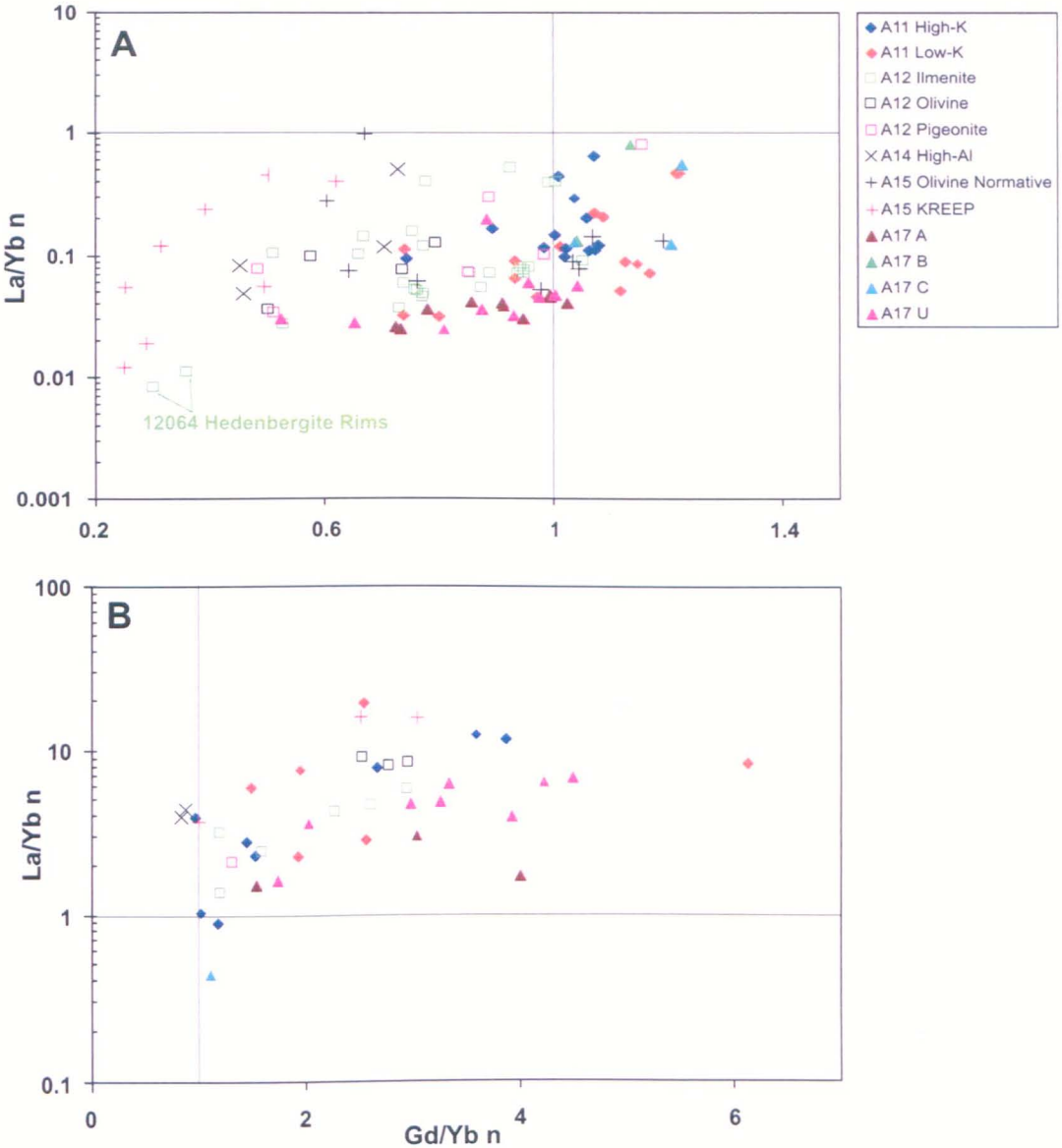

Figure 3.59: Chondrite-normalised La/Yb ratio vs. Gd/Yb ratio for pyroxene **(a)** and plagioclase **(b)**. Samples grouped by type. The grey lines cross each axis at one, any value less than one represents a positive gradient from La to Yb or Gd to Yb, any value more than one represents a negative gradient. Chondritic values from Anders and Grevesse (1989).

Wustite) and pyroxenes with similar major element compositions to those found in mare basalts (especially the Apollo 15 basalts). Both REE partition coefficient datasets were also utilised to determine the REE composition of lunar igneous melts by Snyder et al. (1995) and Schnare et al. (2008), which provided useful datasets for comparison with our calculations. The parental melt composition of Apollo 15 KREEP basalt 15386,46 was calculated using the orthopyroxene partition coefficients of Weill and McKay (1975) as

compiled by Snyder et al. (1995) based on the lunar KREEP igneous system. As pyroxene is often the first mineral with appreciable REE content to crystallise, the grains with highest Mg# (earliest formed – Figure 3.57a) can be used to determine the equilibrium parental melt composition. This is achieved by dividing the chondrite-normalised abundance of each element by the partition coefficient for that element, specific to each mineral (pigeonite, augite or orthopyroxene in the case of lunar basalts). Because partition coefficients for La are significantly different for low-Ca and high-Ca pyroxenes (over 1000 times lower for pigeonite than augite), whereas those of Lu are relatively similar, LREE depletion visible in the mineral data is absent or considerably lessened in the calculated parental melt data for pigeonites. Negative europium anomalies are still observed in all melt trends, even for Apollo 14 high-Al basalt 14053,19 (Figure 3.57b), because of the inherently europium depleted nature of the mare-basalt source regions. As with pyroxene REE data, a large difference is visible between the relatively low REE melt abundances of Apollo 17 type A basalt 75055,49 and unclassified basalts 70017,110 and 70035,195, and the high abundance of type B basalt 70215,306 and type C basalt 74275,310 – these latter two basalts show almost identical REE compositions at the time of pyroxene crystallisation. However, the texture and mineral chemistry of these samples suggests pyroxene crystallised relatively late in the mineral sequence (Table 3.2) and therefore the calculated melt REE abundances for these samples would be an overestimate, as is suggested by their whole rock REE abundance (chapter 4, section 4.2.1). The parental melt of Apollo 12 olivine basalt 12040,44 has a higher REE abundance compared to the parental melts of other low-Ti basalts.

Close agreement between the measured bulk-rock REE and the calculated parental melt REE abundance suggests a sample has undergone closed system melt evolution. Crystal accumulation and fractionation may result in a significant difference between measured and calculated REE abundance, for example olivine accumulation in the melt would

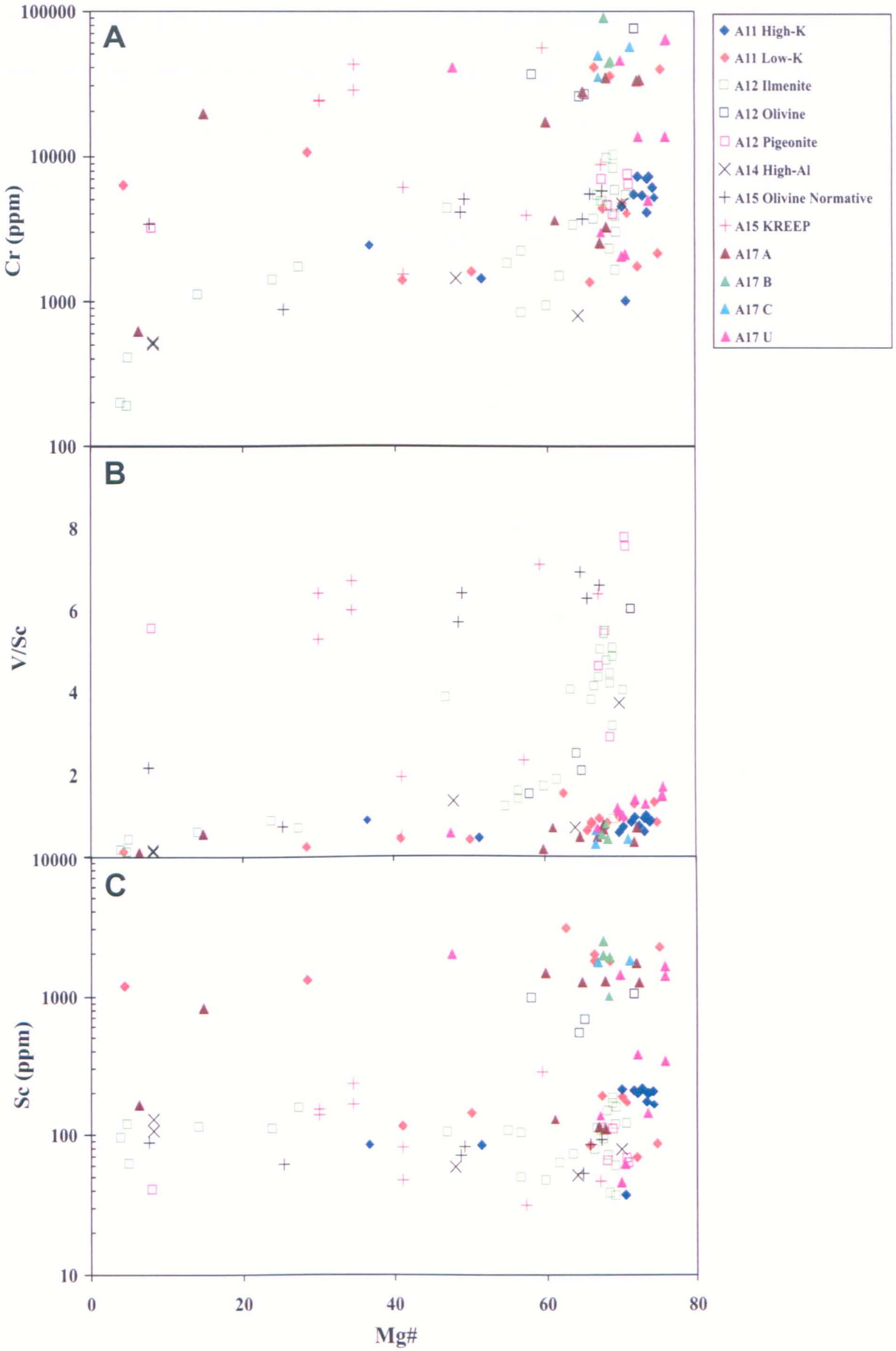

Figure 3.60: Pyroxene Mg# vs. **(a)** Cr ppm, **(b)** V/Sc and **(c)** Sc ppm for all samples.

decrease the measured bulk-rock REE content (as olivine is REE-poor), but calculated abundances based on pyroxene REE content would be unaffected. Crystal fractionation will only affect the bulk-rock REE if the fractionating phases are REE-rich (in which case bulk-rock REE will be decreased), fractionation of REE-poor phases (e.g., olivine, spinel or ilmenite) should not have a significant affect on subsequently crystallising phases.

3.3.3. Comparison with Literature Data. To our knowledge this mineral trace element dataset is currently the most comprehensive for lunar basalts, therefore possible literature comparisons are scarce. Our pyroxene REE dataset for Apollo 15 olivine-normative basalt 15016,7 agrees well with that of Schnare et al. (2008) for a different split of the same sample (Figure 3.61a). However, in terms of REE abundance, one of our extreme rim REE compositions exceeds anything reported by this previous study. Positive Ce anomalies (where Ce* = CI-chondrite-normalised $Ce/\sqrt{(La*Pr)}$) are observed in both datasets (our data = 2.62-1.20, Schnare et al., 2008 = 4.06). Our calculated parental-melt data for this sample is also comparable to our bulk-rock data and that of Schnare et al. (2008) (Figure 3.61b).

3.3.4. Plagioclase. Plagioclase REE data trends show typical LREE enrichment ($(La/Lu)_n$ = 1.10-23.84) and strongly positive europium anomalies (Figure 3.58b) because of the preferential accommodation of Eu^{2+} in the plagioclase crystal lattice. As with pyroxenes, Apollo 12 ilmenite and pigeonite basalt plagioclase REE abundances are low. Apollo 12 ilmenite basalt 12064,136 shows the lowest detectable REE abundances along with Apollo 15 olivine-normative basalt 15016,7 – samples 12047,9 and 15555,206 have abundances largely below detection limits and data for 15016 are sparse for this reason (Figure 3.62). Apollo 12 olivine basalt 12040,44 displays similar plagioclase REE abundances to those of pigeonite basalt 12052,339, and both are slightly REE enriched in comparison to ilmenite basalts from the same site. The only plagioclase REE data trend available for

sample 12052,339 shows a relatively weak europium anomaly compared to the other Apollo 12 basalts (Eu* = 8.26 versus 12.14-749.99) and flatter REE trend ($(La/Lu)_n$ = 1.69). These characteristics may indicate that the ablated material was not 100 % plagioclase, the fine-grained nature of this phase within sample 12052,339 means the 80 μm diameter ablation pit could easily have incorporated material from surrounding mineral phases. However, these data can still give an approximation of the REE abundance in plagioclase from sample 12052. Plagioclase in Apollo 17 unclassified basalts 70017,110 and 70035,195 contains much lower REE abundances than the single plagioclase analysis

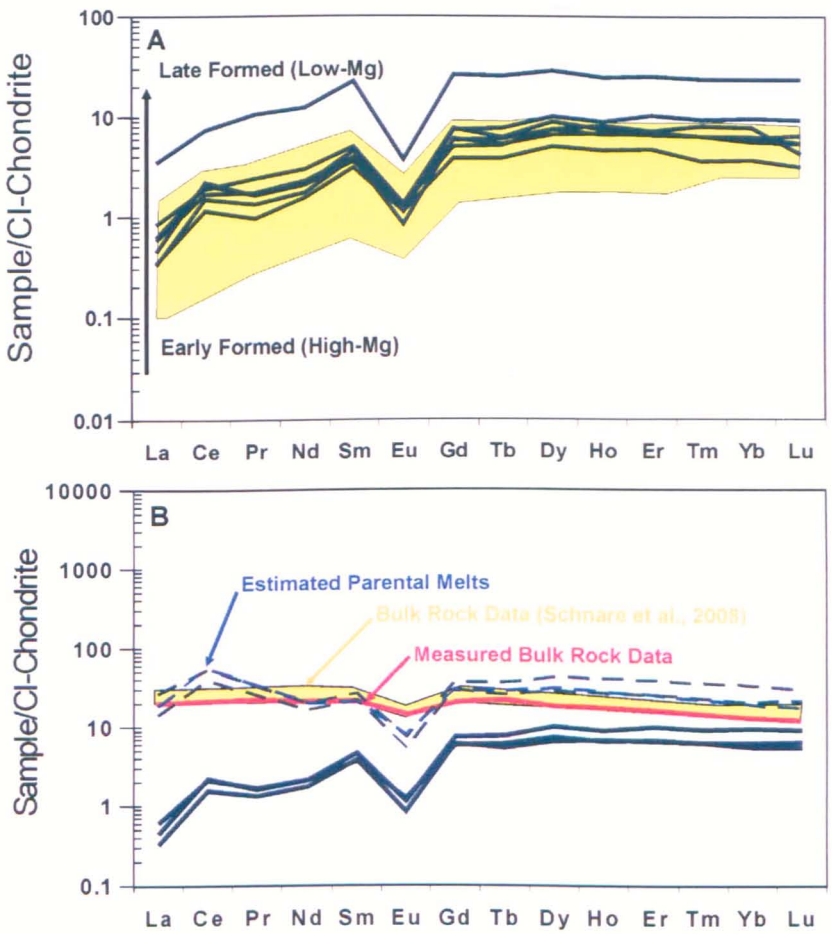

Figure 3.61: Apollo 15 olivine-normative basalt 15016 pyroxene REE data compared with that of Schnare et al., 2008 (yellow envelopes). **(a)** Chondrite-normalised abundance vs. REE. **(b)** Chondrite-normalised melt abundance vs. REE, also showing the measured bulk rock abundance of sample 15016 measured during this study (red line) and during the study of Schnare et al. (2008) (yellow envelope). Chondritic values from Anders and Grevesse (1989).

for 74275,310 type C basalt (0.1-100 versus 100-1000 times CI-chondrite values), which has slight LREE depletion and small positive europium anomaly (Eu* = 1.92). Only one set of plagioclase REE data was collected from this sample because of its fine-grained nature. In addition, it was not possible to collect any plagioclase REE data for type B basalt 70215,306 because of the fine grained nature of this sample. Apollo 11 low-K basalts have a wide spread of data from La_n <1 in samples 10020,232 and 10050,168 to >100 in sample 10058,254 (which also contains high pyroxene REE abundance). As with pyroxenes, the high-K basalts plagioclase grains contain comparable abundances of REE's, and they also show weakly positive europium anomalies in comparison to the low-K basalts (2.32-42.98 and 39.73-282.92 respectively). In highly fractionated samples (e.g. Apollo 11 low-K basalt 10072,40) a marked decrease in europium anomaly with decreasing Mg# is visible (Figure 3.62), along with a decrease in LREE enrichment as these elements become depleted in the melt ($(La/Sm)_n$ = 0.798-2.173). High-Al basalt 14053,19 also exhibits these characteristics in addition to a convex downwards trend showing enrichment from MREE's to HREE's ($(Gd/Yb)_n$ = 0.453-0.728), but this is not a highly fractionated sample. Therefore these characteristics support textural and mineralogical evidence indicating plagioclase crystallised before pyroxene in this basalt (Table 3.2). The strong enrichment from MREE's to LREE's in these plagioclase grains is a characteristic of all Apollo 14 samples ($(La/Sm)_n$ 3.26-5.17 = within our dataset and 1.03-2.51 within that of Hagerty et al., 2003).

3.3.5. Olivine. Olivine analysis achieved limited success as LREE's were generally below detection, however, a number of grains were found to contain abundances above background levels. These trends all show LREE depletion (La/Sm = 0.067-0.831) with a negative Eu* (0.13-0.69) (Figure 3.63) and in the case of Apollo 14 high-Al basalt 14053,19 the characteristic convex downward trend seen in plagioclase is again observed. The moderately compatible trace elements Co and Ni are present in relatively low

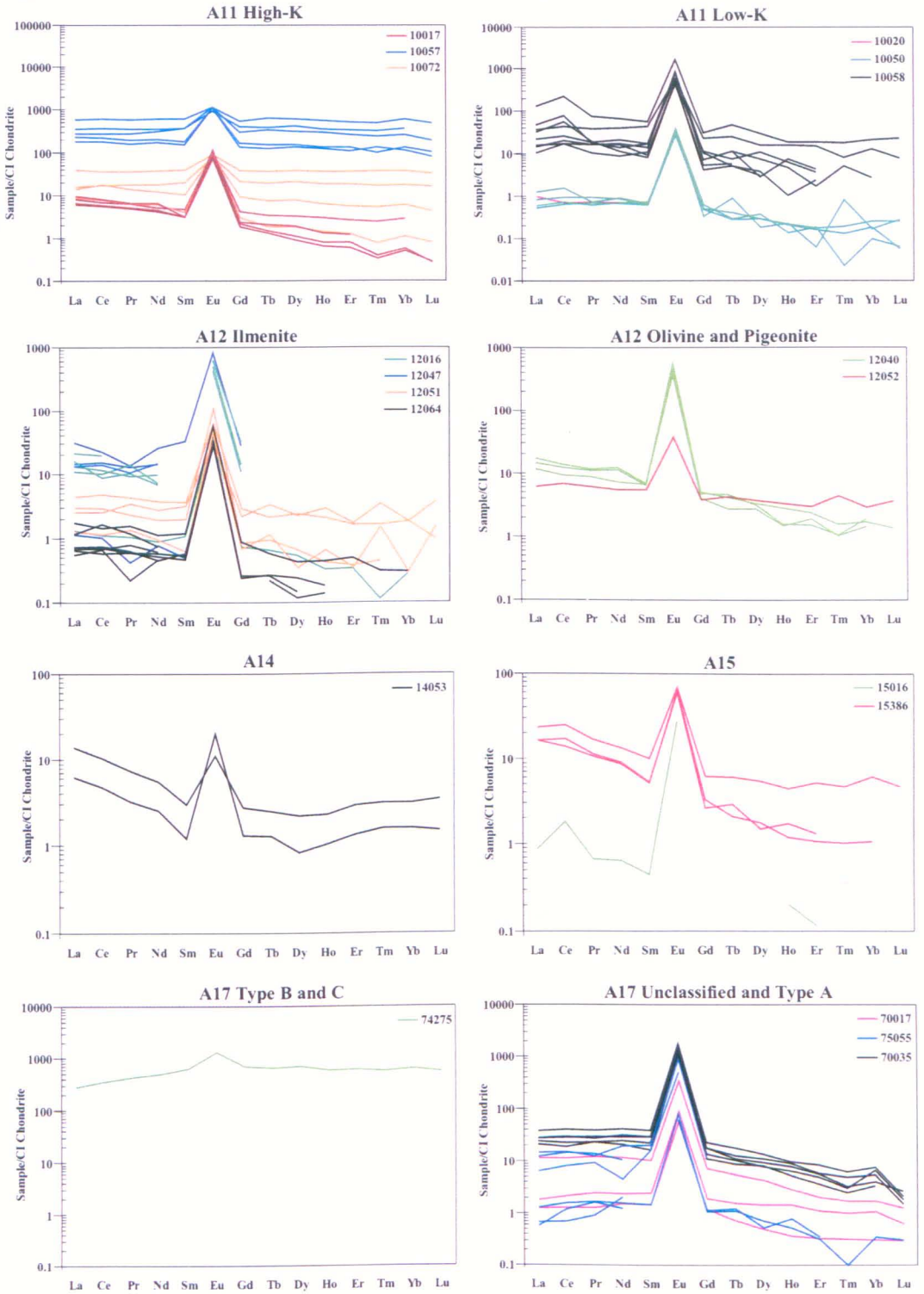

Figure 3.62: Chondrite-normalised plagioclase feldspar REE abundances. Samples are grouped according to type (scale on the y-axis differs). Each line represents one plagioclase grain analysis, data from sample 10057,64 is shown along with the other high-K Apollo 11 samples but as with pyroxene the fine grained nature of this sample makes these values unreliable. Chondritic values from Anders and Grevesse (1989).

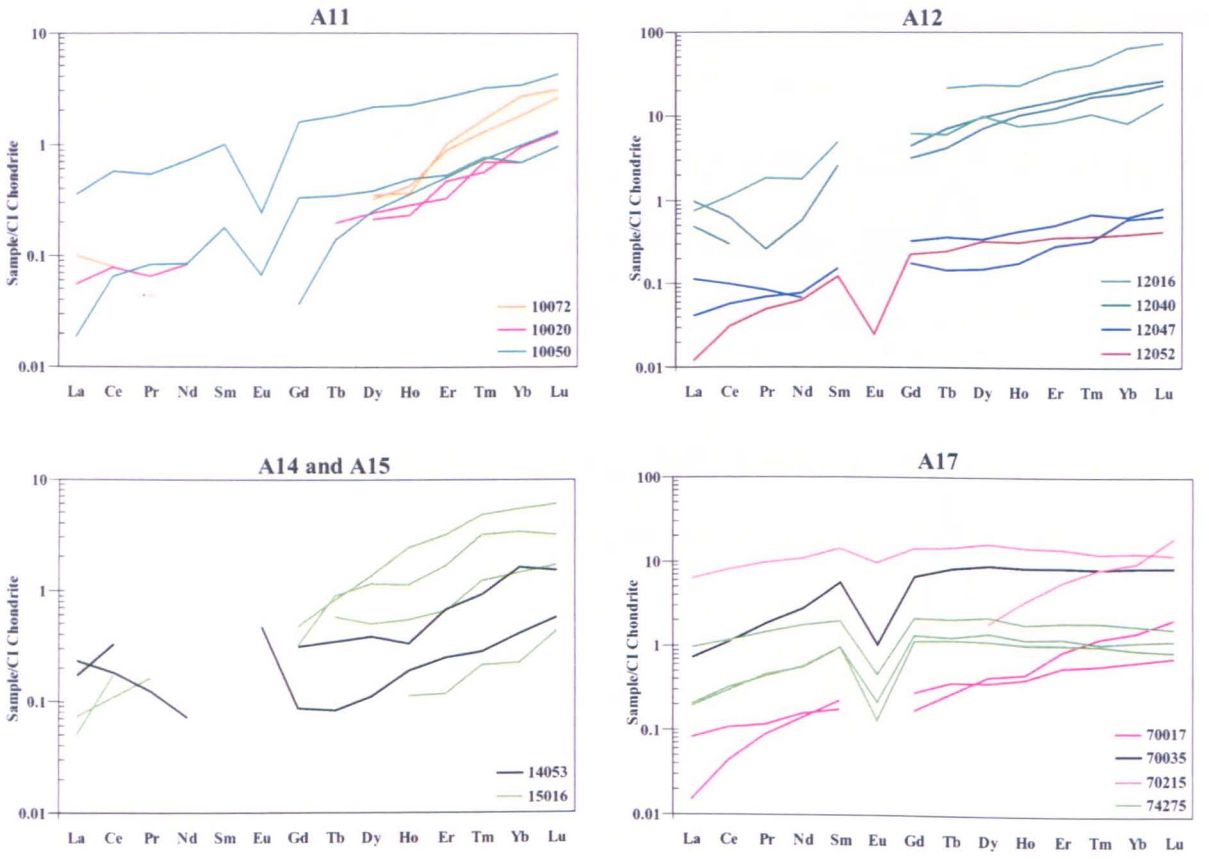

Figure 3.63: Chondrite-normalised olivine REE abundances. Samples are grouped according to type. Each line represents one olivine grain analysis. Chondritic values from Anders and Grevesse (1989).

abundance in the Apollo 11 low-K basalts, Apollo 17 type A basalt 75055,49, unclassified Apollo 17 basalts 70017,110 and 70035,195, and Apollo 12 pigeonite basalt 12052,339 (Figure 3.64). Although Co and Ni abundances generally decrease with olivine evolution, this low abundance is reflected in pyroxene and plagioclase grains within these samples, suggesting that parental melt was inherently depleted in Co and Ni.

3.4. Crystallisation Sequences

Mineral textures and compositions within a sample can be used to determine the mineral crystallisation sequence. For example, the amount of MgO within ilmenite grains can give an indication of whether this phase crystallised before or after the onset of Mg-bearing pyroxene and olivine. Based on these observations, and the bulk rock data of chapter 4, the crystallisation sequence of each basalt within our sample set was determined (Table 3.2).

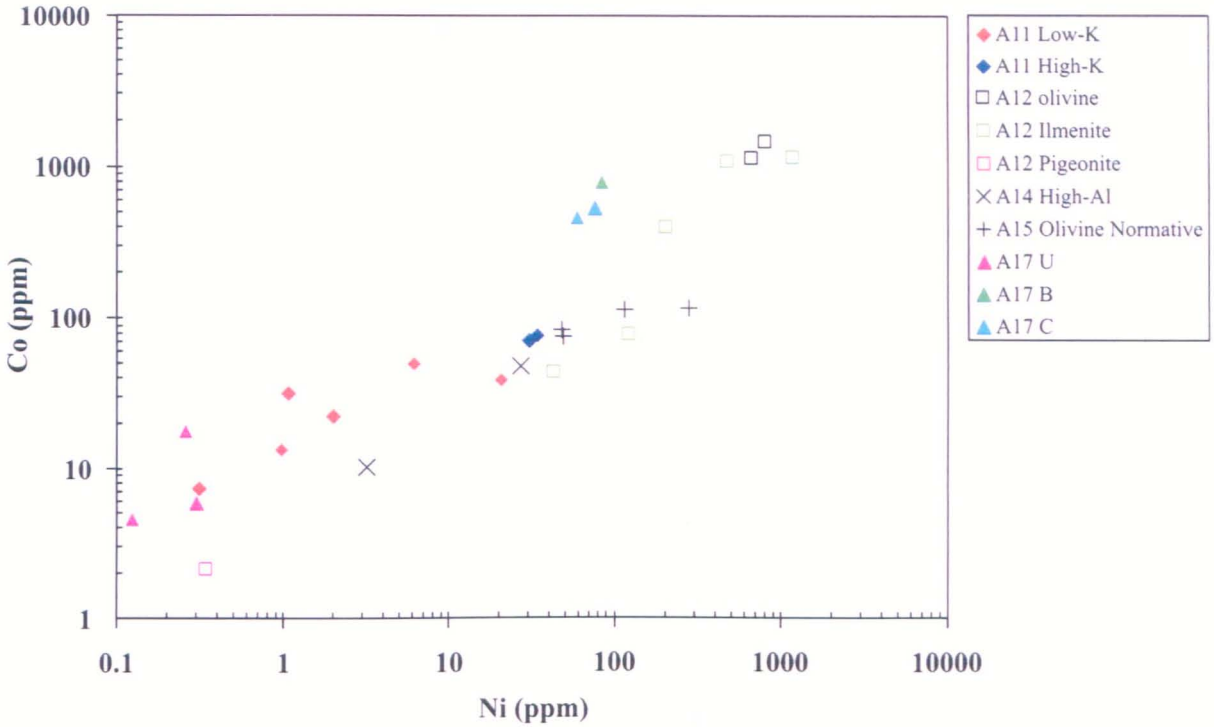

Figure 3.64: Olivine Co vs. Ni content.

Within the high-Ti basalts, ilmenite crystallised as the earliest phase, commonly (though not exclusively) crystallising alongside pyroxene in the Apollo 11 high-K basalts, pyroxene and plagioclase in the Apollo 11 low-K basalts, and armalcolite, olivine and clinopyroxene in the Apollo 17 basalts. Plagioclase often crystallised late in the high-Ti samples, a characteristic Kesson et al. (1975) stated is often a consequence of rapid cooling (i.e., suppressing nucleation of plagioclase). As quench textures are visible in Apollo 17 samples 70215,306 and 74275,310 (Figures 3.41-3.44), and Apollo 11 high-K basalts display fine-grained textures (Figures 3.1-2, 3.5-6, 3.9-10 and 3.13-15), rapid cooling appears highly likely for these samples. Apollo 12 pigeonite basalt 12052,339 also shows a quench textured groundmass surrounding pyroxene phenocrysts with a soda straw texture (elongated with hollow centres) - both features indicate this sample was rapidly cooled. Pyroxene, olivine and Cr-spinel appear to have crystallised first in the Apollo 12 and 15 low-Ti basalts, followed by plagioclase and later ilmenite. Apollo 14 high-Al basalt 14053,19 contains early crystallising olivine, followed by clinopyroxene and plagioclase crystallisation, and late stage ilmenite. Apollo 15 KREEP basalt 15386,46

Table 3.3: Sample crystallisation sequences, based on textural and mineralogical observations, and bulk-rock chemistry

	Stages of Mineral Crystallisation					
sample	**1st**	**2nd**	**3rd**	**4th**	**5th**	**6th**
10017	ilm + cpx	ilm, cpx + plag	tro, sil, ap, whit, K-feld, FeNi + meso			
10020	ilm, ol + CrTi-spinel	ol, ilm, cpx + plag	tro, sil, phos, K-feld, tran, pyroxf, FeNi + meso			
10049	ilm + cpx	ol, ilm, cpx + plag	tro, sil, K-feld, K-glass, FeNi + meso			
10050	ilm, cpx + plag	ol, ilm, cpx + plag	ol + cpx	tro, sil, ap, K-feld, pyroxf, FeNi		
10057	ilm + cpx	ilm, cpx + plag	tro, sil, K-feld, K-glass, FeNi + meso			
10058	ilm, cpx + plag	sil + tro	ap, K-feld, bad, FeNi, meso + FeCr metal			
10072	ol (embayed phencryst)	ilm + cpx	ilm, cpx + ol	ilm, cpx, ol + plag	tro, sil, phos, meso + glass	
12016	cpx + Cr-spinel	cpx, ol + CrTi-spinel	cpx, ol + plag	cpx, ol, plag + ilm	tro, sil, ap, FeNi + meso	
12040	ol (accumulation)	cpx + Cr-spinel	cpx, plag, ilm + Ti-spinel	tro, ap, whit, bad, K-feld, FeNi + meso		
12047	cpx	cpx, ol + CrTi-spinel	cpx, plag + Ti-spinel	cpx, plag + ilm	tro, sil, ap, K-feld + fay	
12051	cpx + Cr-spinel	cpx, CrTi-spinel + plag	cpx, plag + ilm	cpx, plag, ilm + sil	tro, sil, bad, K-feld, FeNi + pyroxf	
12052	cpx + Cr -spinel	cpx, ol + Cr-spinel	quench texture inc. plag, ilm, tro + FeNi			
12064	cpx + Cr-spinel	cpx, Cr-spinel + plag	Ti-spinel	ilm	sil	tro, ap, pyroxf, K-feld, bad + meso
14053	ol + Cr-spinel	Cr-spinel + cpx	plag, cpx + CrTi-spinel	plag, cpx, ilm + sil	tro, FeNi, sil + ap	K-glass, whit, meso + pyroxf
15016	ol + Cr-spinel	ol, Cr-spinel + cpx	ol, Cr-spinel, cpx + plag	ol, cpx, plag + ilm	tro, FeNi + sil	ap, whit, K-glass + meso
15386	opx	plag + opx	plag + cpx (replacing opx)	cpx, ilm, sil, ap + whit	tro, K-glass, bad + meso	
15555	cpx + Cr-spinel	cpx, CrTi-spinel + ol	cpx, ol + plag	cpx, ol, ilm + plag	tro, sil, ap, whit, bad, zirc + meso	
70017	arm + ilm	ilm + cpx	cpx, ol + CrTi-spinel	ol, cpx + plag	tro, sil, ap, K-glass + meso	
70035	ilm	ilm + cpx	cpx, ol + plag	tro, sil + FeNi	ap, K-feld, meso, bad, tran + zirc	
70215	ilm, ol + CrTi-spinel	ilm + cpx	cpx, plag + tro	QT inc. plag + cpx		
74275	arm + ilm	ilm, ol + CrTi-spinel	cpx	cpx + plag	sil	QT inc. cpx, plag, ilm, sil, K-feld + tro
75055	ilm, cpx + plag	tro, sil, ap, bad, zirc, FeNi + meso				

Mineral abbreviations: ap = apatite, arm = armalcolite, bad = baddeleyite, cpx = clinopyroxene, K-feld = K-feldspar, meso = mesostasis, opx = orthopyroxene, phos = phosphate, plag = plagioclase, pyroxf = pyroxferroite, QT = quench texture, sil = silica, tran = tranquillityite, tro = troilite, whit = whitlockite, zirc = zirconolite.

contains early orthopyroxene cores surrounded by later clinopyroxene rims, as these cores are rounded some resorbtion appears to have occurred. Plagioclase is a relatively early phase in this sample, whereas ilmenite only appears to have formed towards the end of crystallisation. Ilmenite also crystallises late in these two low-Ti samples. Within the melts of Apollo 11 low-K basalts 10050,168 and 10058,254, and Apollo 17 type A basalt 75055,49 ilmenite, pyroxene and plagioclase appeared on the liquidus simultaneously. O'Hara et al. (1974) argued that this is a consequence of shallow level fractionation under low pressures.

3.5. Discussion

The diversity of textures in lunar basalts investigated in this study highlights the range of basalt types present in the Apollo collection. For example, there is wide variation between the textures of the Apollo 12 ilmenite basalts as well as the Apollo 11 low-K basalts (Figures 3.5, 3.7, 3.10, 3.18, 3.22 and 3.24). Mineralogy also changes within the petrological groups; for example Apollo 11 low-K basalt 10020,232 contains spinel and a lot more olivine than the other samples within this group (Table 3.1); sample 10058,254 contains no olivine and neither this sample nor sample 10050,168 contain spinel. Other groups show greater similarity; the high-K basalt samples 10017,372, 10049,94 and 10057,64 display similar textures with only sample 10072,40 showing a slightly coarser–grained texture. Samples 10049,94 and 10057,64 are particularly similar, possibly suggesting these two rocks were sourced from the same place on the surface (as is suggested by chemical analysis – chapter 4). The fact that all Apollo 11 basalts were collected within 60 m of the lunar lander makes this a real possibility. The Apollo 15 olivine-normative basalts 15016,7 and 15555,206 also exhibit similar textures and mineralogies (Table 3.1).

3.5.1. Apollo 12 and 15 Low-Ti Basalts. It is clear from the above mineralogical and chemical evidence that the Apollo 12 and 15 low-Ti basalts contain more diverse compositions of clinopyroxene, olivine and spinel compared to the high-Ti basalts of Apollo 11 and 17. The Apollo 12 ilmenite basalts within our sample set contain higher ilmenite modal abundances than the pigeonite and olivine basalts (4-7 vol % compared to 3 vol % and 3 vol % respectively). Olivine basalt 12040,44 is olivine-rich (22 vol %) whereas the former two basalt types are olivine-poor (0-14 vol %). These observations are in agreement with the data and sample classifications of James and Wright (1972), Rhodes et al. (1977), Walker et al. (1976a), and Baldridge et al. (1979). The zoned nature of olivines in 12016,39, 15016,7 and 15555,206 indicates that these grains grew within a constantly evolving melt. In comparison, olivine basalt 12040,44 contains relatively unzoned olivines which are more Fe-rich than a number of clinopyroxene grain cores, implying these grains re-equilibrated with the melt. Meyer and Wiltshire (1974) and Baldridge et al. (1979) suggested that these grains accumulated within the Apollo 12 olivine basalt parental melt. This hypothesis is supported by the high bulk-rock MgO content observed in the sample relative to olivine forsterite content (Figure 4.6). Previous studies of Apollo 12 mare basalts (Compston et al., 1971; Papanastassiou and Wasserburg, 1971a; James and Wright, 1972; Walker et al., 1976a; Rhodes et al., 1977; Baldridge et al., 1979; Neal et al., 1994a,b) argued that the olivine, pigeonite and ilmenite basalts cannot be related by crystal fractionation or accumulation, and that these three groups represent three separate source regions. Two groups were established based on differences in petrography and major-element chemistry (mainly ilmenite and TiO_2 content), the olivine-pigeonite group and the ilmenite group (James and Wright, 1972). Subsequently Rhodes et al. (1977) found that the trace-element and isotopic variability within the olivine-pigeonite group was greater than would be expected from simple closed-system fractional crystallisation. Therefore, these authors proposed splitting the group into two groups. Neal et al. (1994a,b) confirmed this seperation based on each groups Mg# and Rb/Sr ratios (section 4.2.2; Figure 4.12).

Detailed petrological studies of pigeonite basalt samples 12007, 12011 and 12043 (Baldridge et al., 1979), sample 12019 (Neal et al., 1994a) and sample 12039 (McGee et al., 1977) show that our pyroxene and plagioclase compositional data for sample 12052,339 are typical of the pigeonite basalt group, though olivine data is slightly more Fe-rich (Fo_{67-43} in sample 12052,399 versus Fo_{76-59} in other pigeonite basalt samples). Olivine basalt 12040,44 does not contain any of the more Mg-rich olivine grains recorded in a number of other olivine basalt samples ($Mg\#_{62-43}$ versus $Mg\#_{76-42}$ for the entire group, Kushiro et al., 1971; Grove et al., 1973; Dungan and Brown, 1977; McGee et al., 1977; Baldridge et al., 1979). Pyroxene and olivine compositions of the ilmenite basalt samples 12005 and 12008 are relatively unzoned towards Fe-rich compositions compared to our ilmenite basalt data (Dungan and Brown, 1977), but this is probably because of a limited dataset. The data of Busche et al. (1971) and Keil et al. (1971) show pyroxene and olivine compositions similar to samples 12047, 9, 12051,59 and 12064,136 with the addition of a number of Ca-rich ferroaugite compositions.

Olivine basalt 12040,44 contains only moderately zoned pyroxenes ($Mg\#_{74-48}$) with high REE abundance (1-1000 times CI-chondrite abundances). The REE abundance of both pyroxene and plagioclase grains within this sample are much higher than in any other low-Ti basalt (1-1000 and 1-100 compared to 0.1-100 and 0.1-10 times CI-chondrite abundances), excluding the REE-rich pyroxene rims of sample 12064,136. It is possible that this high REE abundance was caused by late crystallisation of pyroxene in sample 12040,44, after olivine had been crystallising for some time. Under these conditions, pyroxene would begin to crystallise in a melt much more enriched in REE (as olivine does not take REE's into its crystal lattice), but relatively depleted in Mg. However, the observed Mg content of pyroxene grains in basalt 12040,44 are too high for this to have occurred in the extreme (En_{63-39}). Therefore, these grains appear to have crystallised from a parental melt inherently rich in REE than the Apollo 12 pigeonite and ilmenite basalt parental melts.

High MgO contents in ilmenite grains from this sample relative to those in other low-Ti samples (MgO = 2.9-3.2 versus 0-2 wt %), and the presence of Mg-rich early pyroxenes ($Mg\#_{74-70}$), indicate that the samples parental melt was inherently Mg-rich irrespective of olivine accumulation. High Ni and Co content in this basalt's olivine grains (e.g., Ni = 797-658 ppm in sample 12040,44 compared to 470-0.3 ppm in the other Apollo 12 basalts) suggests they crystallised from a primitive melt (Papike et al., 1999). Pyroxene grains also contain high compatible element contents (e.g., Sc = 1043-544 ppm in sample 12040,44 compared to 187-37 ppm in the other Apollo 12 basalts), implying they too crystallised from a primitive melt. Therefore the parental melt of sample 12040,44 appears to have been more primitive compared to the parental melts of the pigeonite and ilmenite basalt samples represented in our suite.

Ilmenite basalt 12016,39 contains the next highest modal abundance of olivine (Table 3.1); bulk-rock MgO content (Table 4.1) and ilmenite MgO content (0.5-1.2 wt %, Figure 3.53) indicates that it is the most primitive ilmenite basalt sample represented in our sample set. This is in agreement with the major-element data of Rhodes et al. (1977) which showed that only sample 12005 contains greater bulk rock MgO wt % than 12016,39 in this group. Pigeonite basalt 12052,339 and the ilmenite basalts are similar in terms of major-element mineral-chemistry and mineral REE and trace-element abundances (Sc, V and Cr – Figure 3.60). REE parental melt calculations imply that although REE abundance is similar in pyroxenes from ilmenite basalts and pigeonite basalt 12052,339, the REE melt abundance in 12052,339 is higher, especially for the LREE's. As only the pigeonite phenocrysts were large enough to ablate successfully in sample 12052,339, melt compositions were calculated using the pigeonite partition coefficients of McKay et al. (1991) rather than the augite partition coefficients of McKay et al. (1986) used for other samples. As the rims of these phenocrysts are augite the 80 μm laser pit may have incorporated both pigeonite and augite, or the laser may have ablated into augitic material. Therefore the calculated parental

melt REE abundances of sample 12052 may not be reliable. Despite the mineralogical similarities between pigeonite basalt 12052,339 and the ilmenite basalts within our sample set, differing ilmenite abundances and incompatible element ratios (Figure 4.10-4.12) provide proof that these samples most likely originated from different source regions. Therefore, there appears to be material originating from at least three separate source regions at the Apollo 12 site.

Two basalt groups were originally identified at the Apollo 15 site, the olivine-normative and quartz-normative basalts, (Rhodes, 1972; Maxwell et al., 1972; Chappell et al., 1972; Chappell and Green, 1973; Helmke et al., 1973; Cuttitta et al., 1973; Nava, 1974; Nyquist, 1977), the latter are not present in our sample set. Both groups are now believed to originate from a single source region - any difference in major-element chemistry can be accounted for by varying amounts of crystal fractionation at separate levels in the lunar crust (Ryder and Schuraytz, 2001; Schnare et al., 2008). Olivine-normative basalts analysed in this study display the lowest ilmenite modal abundances of all the samples (along with KREEP basalt 15386,46). The low TiO_2 abundance of these samples is reflected by slightly elevated MgO wt % in ilmenite compared to Apollo 12 samples (excluding olivine basalt 12040,44 and ilmenite basalt 12016,39 discussed above), as well as relatively Ti-poor pyroxenes. Major, minor and trace element mineralogical analyses reveal the similarity between Apollo 12 and 15 low-Ti basalts. Sc, V and Cr content within pyroxene, Co and Ni content within olivine and REE content within pyroxene and olivine all suggest that the Apollo 15 olivine-normative basalts share most similarities with the Apollo 12 ilmenite basalts (Figures 3.55, 3.60, 3.63 and 3.64).

3.5.2. Apollo 15 KREEP Basalt. Sample 15386,46 contains plagioclase with comparatively low An# and relatively abundant orthoclase as a result of elevated K in the parental melt. It also contains orthopyroxene at the core of larger clinopyroxene grains and

abundant phosphates as mentioned in preceding sections. Our pyroxene compositional data agree well with the data of Dowty et al. (1976) for Apollo 15 KREEP basalt 15382 which shows orthopyroxene cores (En_{82}) zoning to Mg-pigeonite and augite. This is also consistent with the pyroxene compositions of Apollo 14 KREEP basalt 14310 (Brown et al., 1972; Bence and Papike, 1972). Spudis and Hawke (1986) stated that KREEP basalts typically contain 40-50 % plagioclase, 30-40 % low-Ca pyroxene, and minor cristobalite, ilmenite, apatite, (RE)-merillite and Si- and K-rich glass. Pyroxene REE data for KREEP basalt 15386,46, exhibit characteristic steep trends ($(La/Lu)_n$ = 0.011-0.384), deeply negative europium anomalies (0.04-0.24) and REE abundances are high in both pyroxene and plagioclase (1-1000 and 1-100 CI-chondrite abundance, respectively). As high-REE phases such as apatite, (RE)-merillite, K-feldspar and glass are present in relatively high abundances in this sample (Table 3.1) the bulk-rock REE content is accordingly higher than that of the mare basalts (Figure 4.7). All these features, along with successful Rb-Sr (3.94 ± 0.01) and Sm-Nd (3.85 ± 0.08) age dating (Nyquist et al., 1975; Carlson and Lugmair, 1979), indicate that 15386,46 is a typical KREEP basaltic sample (e.g., Warren and Wasson, 1979a; Snyder et al., 1995) and therefore, it did not originate from the same cumulate source regions as the mare basalts.

Homogeneous concentrations of Cr, V, Sc from the core to the rim of pyroxenes in sample 15386,46 suggest low levels of crystal fractionation in the melt. The abundance of Cr is comparatively high in these grains, as well as in ilmenite. However, spinel modal abundance is low. The formation of chromite and ulvöspinel both require a Fe-rich melt, therefore, spinel probably failed to form excessively in this sample due to the low abundance of available Fe in the melt at the time of crystallisation. McKay and Weill (1976) noted this high Mg/Fe ratio in the bulk-rock chemistry of sample 15386 and other KREEP basalts as evidence that the formation of these basalts can not be explained by

partial melting of the mare-basalt source. Therefore, the Apollo 15 site contains material from at least two sources, the mare-basalt source and the KREEP basalt source.

3.5.3. Apollo 14 High-Al Basalt. As our mineralogical data are consistent with the data of Hagerty et al. (2005), it appears that sample 14053,19 is a typical Apollo 14 high-Al basalt. Both sample 14053,19 and Apollo 15 KREEP basalt 15386,46 contain a high modal abundance of plagioclase (Table 3.1) because of their high-Al content. Plagioclase in sample 14053,19 shows a wide variation in An# (Figure 3.50), and enrichment in HREE's. These characteristics, as well as textural evidence and strongly negative europium anomalies in a number of pyroxene grains (Eu* = 0.09-0.21), imply that plagioclase crystallised prior to some pyroxene in this melt. The relatively high-Al content of early chromite spinels compared to those of other samples is also indicative of a high-Al melt. The more Ti-rich spinels do not contain excess Al, as by this point in the crystallisation sequence co-crystallising plagioclase had begun to preferentially accumulate Al from the melt into its crystal structure. The strong LREE enrichment visible in olivine and plagioclase is a common feature of Apollo 14 basalts (Hagerty et al., 2003). Pyroxene REE trends for Apollo 14 high-Al basalt 14053,19 and Apollo 15 KREEP basalt 15386,46 display a deeply negative europium anomaly (Eu* = 0.09-0.21 and 0.04-0.24, respectively) compared to the other basalts in our sample set (Figure 3.55; 0.11-0.36). They also show a positive gradient for the HREE's ($(Gd/Yb)_n$ = 0.45-0.73 and 0.25-0.62, respectively) compared to the other basalts ($(Gd/Yb)_n$ = 1.22-0.48). These REE abundance similarities indicate that sample 14053,19 may have been produced via hybridisation between mare-basalt and KREEPy magma, in agreement with other studies of the Apollo 14 high-Al basalts (e.g., Dickinson et al., 1985: Dasch et al., 1987; Hughes et al., 1990; Neal and Taylor, 1990; Shervais and Vetter, 1990; Neal and Kramer, 2006). While most authors now agree a KREEP-rich component was assimilated into the melt rather than mixed in at the source, the exact composition and proportion of the assimilant is still under debate

(e.g., Dasch et al., 1987; Neal and Taylor, 1990; 1992; Neal and Kramer, 2003; 2006). Dickinson et al. (1985) and Shervais et al. (1985a) divided the Apollo 14 high-Al basalts into five groups based on LREE enrichment or depletion, where group 1 showed the most enrichment and group 5 the most depletion. Our REE parental melt calculations suggest the melt for sample 14053,19 contained only slight REE enrichment, in agreement with our bulk-rock REE data (Figure 4.7). Therefore, this sample should be classified as group 3, as also suggested by Neal and Kramer (2006).

3.5.4. High-Ti, Low-K Apollo 11 Basalts. As shown in Table 1.1, the Apollo 11 low-K basalts can be separated into four subgroups, based on K and La content. The B1 basalts contain intermediate K and low La, B2 contain low K, intermediate La, and B3 contain low K and La - the high-K samples (type A) contain high K and La (Beaty and Albee, 1978; Beaty et al., 1979a,b; Ma et al., 1980; Rhodes and Blanchard, 1980). These different subgroups are thought to represent at least five separate igneous events (Beaty and Albee, 1978, 1980; Beaty et al., 1979a; Rhodes and Blanchard, 1980). Within our sample set, Apollo 11 pyroxenes display differing compositions for the high- and low-K basalts, with only high-K basalts containing Mg-pigeonite cores, in addition to augite rims that are less Fe-rich than the low-K group. This observation is not fully supported by the wider sample collection, as a number of low-K Apollo 11 basalts not represented in our sample set (samples 10003, 10029, 10045, 10062 and 10092) are reported to contain Mg-pigeonite cores (Beaty and Albee, 1978), although they are relatively rare compared to augite. In addition to our low-K samples, 10044 and 10047 contain no pigeonite (Hafner and Virgo, 1970; Beaty and Albee, 1978). Low-Ti unclassified basalt 10050,168 exhibits a distinct trend, containing Mg-pigeonite with lower Mg# than some augite cores and Ca-poor, Fe-rich pyroxene rims - a characteristic also reported by Beaty and Albee (1978). Pyroxene REE data for this sample show wide variation from low abundance in grain cores (0.1-10 times CI-chondrite abundance) to much higher abundance in the rims (10-1000 times CI-

chondrite abundance). Parental melt calculations suggest that the source melt had a lower REE content than the melt of group B3 basalt 10020,232 and group B1 basalt 10058,254. This is consistent with the suggestion by Rhodes and Blanchard (1980) that sample 10050 represents a parental melt for the B1 basalts, despite the fact that it is compositionally similar to low-K group B3 basalt 10020,232 (a relationship visible in our bulk-rock chemical data – chapter 4), and mineralogicaly similar to group B2 (Beaty and Albee, 1978). Low REE abundance in 10050,168 pyroxene and plagioclase supports this theory – relatively high REE abundance combined with low Ni and Co content in olivine supports textural evidence indicating the late crystallisation of these grains. However, the presence of a substantial proportion of Ba in K-feldspar from sample 10050,168 may suggest it represents a totally separate parent melt. Group B1 basalt 10058,254 has much higher pyroxene and plagioclase REE abundance than group B3 sample 10020,232 and unclassified sample 10050,168. However, our calculated REE melt abundance values are much higher than measured bulk-rock REE values for sample 10058,168, suggesting pyroxene REE analysis for this sample was incomplete and the calculated parental melt abundance is therefore not representative (section 4.3.2). As all three samples within this group (10058, 10044 and 10047) show almost identical textures and mineral chemistries it is thought they may be from the same boulder on the lunar surface (Beaty and Albee, 1978). Our data therefore suggests group B1 is enriched in REE compared to groups B2 and B3, in agreement with the REE data of Wiesmann and Hubbard (1975). The high Cr, V and Sc content of pyroxene also testify to the evolved nature of sample 10058,254 relative to the other Apollo 11 low-K basalts within our sample suite..

3.5.5. High-Ti, High-K Apollo 11 Basalts. As indicated above, samples 10049,94 and 10057,64 have a very similar textures and mineralogies. These observations, along with similar elemental bulk-rock compositions (chapter 4), indicate that these samples may be paired. Unfortunately, the fine-grained nature of both samples made mineral REE analysis

very difficult, therefore, no dataset could be produced for either sample. Mineral major-data was also limited for these two samples, accounting for the lack of plagioclase compositional variation in sample 10057,64 (An_{81-76}, Figure 3.50) and olivine Mg content in sample 10049,94 ($Mg\#_{33}$, Figure 3.51). However, all Apollo 11 high-K basalt samples show similar pyroxene evolutionary trends, plagioclase and ilmenite major-element compositions, in addition to similar plagioclase and pyroxene REE abundances and characteristically flat REE trends. These textural and mineralogical similarities may suggest all four samples were produced from the same melt. The similarities observed in our Apollo 11 high-K samples are mirrored in the remaining samples of this group (Carter and MacGregor, 1970; Dence et al., 1970; Hollister and Hargraves, 1970; Beaty and Albee, 1978). Europium anomalies in the Apollo 11 high-K basalts are less positive for plagioclase (Eu* = 2.32-43.00) and more negative for pyroxene (Eu* = 0.11-0.29) than in the low-K basalts (Eu* = 18-283 and 0.15-0.27, respectively). As both groups contain both pigeonite and augite analyses the difference is apparently a factor of inherently low Eu concentration in the parental melts, the high-K basalt melt appears to contain less Eu than the low-K melt. The presence of these deeply negative europium anomalies within the high-K samples is supported by our bulk-rock REE data, and is probably caused by the addition of a KREEP-rich component to the melt (section 4.2.1).

Unlike the low-K basalts, the high-K basalts all contain numerous pigeonite grains. The rarity of pigeonite in the low-K samples indicates that these parental melts had higher Ca contents than the high-K melts during pyroxene crystallisation. As plagioclase grains do not show co-crystallisation texture in the latter samples, we deduce that augitic pyroxenes were the first Ca-bearing phases to crystallise. In contrast, both textural evidence and the variation of pyroxene Al content with Mg#, indicates plagioclase and pyroxene co-crystallised in the low-K basalts. Without this co-crystallisation, early forming pyroxene would have been even more Ca-rich, therefore, the parental melts of our low-K samples

appear to have been richer in Ca than that of the high-K samples. These data are supported by our bulk-rock chemical data for these samples (Table 4.1, Figure 4.3), but the difference in Ca content is not fully apparent across the entire Apollo 11 sample suite. Data from previous studies indicate that while the high-K basalts extend to lower bulk-rock CaO abundances and the low-K basalts extend to higher CaO abundances, the majority of sample analyses lie somewhere in the middle (see Figure 4.1 for references).

3.5.6. Apollo 17 High-Ti Basalts. Apollo 17 basalt types A, B1, B2 and C are classified based on their bulk-rock chemistry; type A basalts contain 50-60 % higher incompatible trace-element abundances than the type B basalts although they have similar major-element compositions (Rhodes et al., 1976; Warner et al., 1979). The defining characteristic of the type C basalts is the presence of the Mg-rich olivine grains noted by Meyer and Wiltshire (1974), Rhodes et al. (1976), Warner et al. (1979) and Neal et al. (1990b). The type B basalts can be further separated into two subgroups, where subgroup B1 has La < 5 ppm and subgroup B2 has La > 5 ppm. These Apollo 17 high-Ti mare-basalts are thought to originate from four separate sources (Rhodes et al., 1976; Warner et al., 1979a; Neal et al., 1990a; Ryder, 1990; Paces et al., 1991; Neal and Taylor, 1992) - the limited range of geochemical and isotopic compositions, along with the scarcity and distribution of type C samples (5 samples, all found at the Shorty crater - Station 4) indicate that this group may originate from a single lava flow (Paces et al., 1991; Neal and Taylor, 1993).

The Apollo 11 high-Ti sample collection is often quoted as being similar to the Apollo 17 collection, in age as well as composition (e.g., Neal and Taylor, 1992 and references therein). There are numerous similarities amongst our sample suite - mineral major- and trace-element data show Apollo 17 type A basalt 75055,49 is comparable to the Apollo 11 low-K sample 10020,232, with both showing two populations of pyroxene. Neal et al.

(1990a) observed that Apollo 17 basalt 71095 (not studied here) was even more comparable with Apollo 11 low-K basalts, reclassifying this sample as a type II, Apollo 11 low-K, high-Ti basalt. Sample 71095 falls on the fractionation line of the type A basalts but due to its extremely evolved composition relative to the type A parent, the above authors conjectured that this may be a coincidence; this sample could originate from a different source altogether. The less evolved sample 75055,49 has a similar relationship to the Apollo 11 basalts, indicating the parental melts for these two groups of basalt were compositionally similar despite the geographical separation.

Apollo 17 type B basalt 70215,306 and type C basalt 74275,310 have very high REE mineral abundances with less HREE's than LREE's in pyroxene - a characteristic not visible in type A basalt 75055,49 or either of the unclassified basalts. These two samples also display similar mineral chemistries, indicating their melts had similar major-element chemistries. However, differences in trace-element data indicate they did not originate from the same melt (section 4.2). Sample 74275,310 seems to be an uncharacteristic type C sample as it does not contain any of the Mg-rich olivine grains typical of this group. However, this could probably be accounted for by the small size of the thin-sections that we analysed (< 5 mm diameter).

Unclassified basalts 70017,110 and 70035,195 do not appear to show any mineral major- or trace-element similarities to each other or any of the remaining Apollo 17 basalts in our sample suite. These two basalts are among 11 unclassified basalts from the Apollo 17 site (Neal and Taylor, 1993). Even assuming that upon further investigation some of these are found to originate from the same source, the variety of basalt types necessitates the presence of numerous different magma bodies at this site. Such complexities within an area less than 10 km^2 highlights the complex nature of mare-basalt volcanism.

3.6. Conclusions.

- The Apollo 12 and 15 low-Ti basalts contain highly zoned and/or diverse olivine and pyroxene compositions in comparison to the Apollo 11 and 17 high-Ti basalts. Apollo 14 high-Al basalt 14053,19 and Apollo 15 KREEP basalt 15386,46 show the least olivine and pyroxene compositional variation of all the basalts within our sample suite, but the former does contain zoned plagioclase.

- The Apollo 11 low-Ti basalts and Apollo 17 type A basalt 75055,49 display similar mineral chemistries and crystallisation sequences. As they were not collected from the same site they could not have crystallised from the same melt but their parental melts appear to have been similar.

- The Apollo 11 high-K basalts show similar textures, mineral chemistries and crystallisation sequences, indicating they may have crystallised from the same melt.

- Both the Apollo 11 high-K samples and Apollo 14 sample 14053,19 contain mineral trace-element abundances indicating a low Eu abundance in their parental melts compared to the other mare-basalts. In addition, minerals within the former contain higher REE abundances than the Apollo 11 low-K basalts, and the latter shows a strongly positive gradient from Gd to Lu. All these characteristics are typical of KREEP basalts and suggest KREEP contamination.

- Based on mineral chemistry, the two high-Ti Apollo 17 unclassified basalts do not fit into any of the established groups (type A, B or C) and are not similar to each other. Therefore, the volcanic history at this site is complex.

- Unclassified low-K Apollo 11 basalt 10050,168 contains high amounts of Ba within its feldspar, a characteristic not observed in any of the other basalts within this sample set. This compositional characteristic, along with its unique texture and

pyroxene composition suggest that this sample is unrelated to the other Apollo 11 low-K basalts and may not be native to the Apollo 11 site.

- At least five separate high-Ti parental melt compositions were sampled at the Apollo 11 site (type A, B1, B2, B3 and unclassified basalt 10050), and five separate Apollo 17 high-Ti melts are represented in our sample suite alone. In contrast, only three melts are represented from the Apollo 12 site (the low-Ti olivine, ilmenite and pigeonite basalts) and the Apollo 15 low-Ti olivine-normative and quartz-normative basalts appear to all have originated from the same source. Therefore, basaltic eruptions at sites dominated by high-Ti mare basalts appear to be more diverse than those at the low-Ti sites.

To further investigate these findings and determine the detailed petrogenesis of each basalt group bulk rock major- and trace-element data must be produced and studied.

4. BULK-ROCK CHEMISTRY

The bulk-rock elemental chemistry of a sample can provide key information about its origin and evolution, including the nature and type of source regions represented within a sample set and the role of crustal contamination, crystal fractionation and accumulation within each sample. ICP-AES analysis of sample rock chips provided a comprehensive dataset for all major-elements known to be present within lunar basalts, while ICP-MS analysis provided a comprehensive trace-element dataset. The entire data set for ICP-AES and ICP-MS can be found in appendix D and E, respectively.

4.1. Major-Elements

4.1.1. Observations and Sample Comparisons. In agreement with petrographic observations, the bulk-rock TiO_2 data exhibit a dichotomy between low- and high-Ti samples (Table 4.1). However, Apollo 11 low-K basalt 10058 does not appear to belong to either of these groups. It lies in the intermediate-Ti region, showing 8.40 wt % TiO_2 - approximately 1 wt % lower than any previous data published for this sample (LSPET, 1969; Gast et al., 1970; Goles et al., 1970a; Morrison et al., 1970; Rose et al., 1970; Wiesmann and Hubbard, 1975; Duncan et al., 1976; Beaty and Albee, 1978; Rhodes and Blanchard, 1980). The Al_2O_3 content of sample 15555 is also ~ 0.7 wt % higher than the highest previous analysis (Cuttita et al., 1973). These differences can be reconciled on the grounds of sample heterogeneity. All other elemental abundances for these samples are similar to previous data, as shown in Figure 4.1.

On a plot of TiO_2 vs. Al_2O_3 wt % (Figure 4.1a), the majority of Apollo 11 and 17 basalts within our sample set cluster together in the high-Ti, low-Al region. Apollo 11 low-K basalt 10058 is the exception, as it plots just within the high-Al region. However, this is in

Table 4.1: Bulk-rock major- and minor-elements. Analytical precision = < 1 %

Mission	Apollo 11							Apollo 12						Apollo 14	Apollo 15			Apollo 17				
Sample	10017	10020	10049	10050	10057	10058	10072	12016	12040	12047	12051	12052	12064	14053	15016	15386	15555	70017	70035	70215	74275	75055
FeO	18.51	18.58	19.34	18.35	19.23	18.83	17.49	21.87	21.80	20.28	20.09	19.20	18.37	15.77	22.14	9.96	18.46	18.51	20.41	19.35	17.69	16.92
Al_2O_3	8.0	9.6	8.6	10.3	8.2	11.2	8.1	8.1	7.7	10.5	11.0	10.2	11.5	14.3	8.5	15.7	11.1	8.5	7.9	8.7	8.7	9.4
CaO	10.87	11.21	11.10	11.63	10.81	12.91	11.11	8.81	7.77	11.78	12.16	10.97	12.17	11.84	9.18	10.09	10.30	10.49	9.76	10.57	10.70	13.20
K_2O	0.32	0.06	0.32	0.07	0.29	0.09	0.30	0.04	0.04	0.07	0.07	0.06	0.06	0.12	0.04	0.61	0.02	0.04	0.08	0.04	0.08	0.04
MgO	7.19	7.59	6.89	7.69	7.24	7.37	5.92	13.18	16.17	6.67	6.48	7.49	6.27	7.71	11.69	8.12	12.37	9.85	9.25	8.61	9.97	8.01
MnO	0.23	0.27	0.25	0.26	0.24	0.24	0.25	0.28	0.27	0.27	0.27	0.27	0.26	0.25	0.28	0.15	0.25	0.27	0.27	0.25	0.26	0.25
Na_2O	0.46	0.36	0.49	0.36	0.46	0.40	0.45	0.21	0.18	0.29	0.29	0.24	0.27	0.42	0.22	0.81	0.27	0.34	0.35	0.35	0.36	0.37
P_2O_5	0.2	<	0.2	<	0.2	<	0.1	<	<	<	<	<	<	0.1	<	0.5	<	<	<	<	<	<
SiO_2	42.09	40.47	42.31	39.96	40.59	42.52	42.05	43.62	43.34	46.46	47.65	46.16	46.92	47.69	45.40	52.62	47.66	39.39	39.04	38.81	40.15	41.51
TiO_2	11.01	10.34	10.59	11.30	11.01	8.40	11.36	3.65	2.65	4.94	4.43	3.25	3.64	2.56	2.11	2.10	1.14	12.86	13.03	12.71	12.57	12.22
Total	**98.89**	**98.46**	**100.01**	**99.88**	**98.24**	**101.95**	**97.12**	**99.76**	**99.95**	**101.26**	**102.45**	**97.82**	**99.48**	**100.73**	**99.56**	**100.66**	**101.56**	**100.27**	**100.10**	**99.44**	**100.51**	**101.88**
Mg#	**40.92**	**42.12**	**38.85**	**42.75**	**40.17**	**41.10**	**37.62**	**51.78**	**56.93**	**36.96**	**36.52**	**41.02**	**37.84**	**46.56**	**48.48**	**59.25**	**54.43**	**48.69**	**44.68**	**44.22**	**50.11**	**45.76**

Sample	LOD[a]	PCC-1[b] measured	PCC-1 certified	% Diff[c]
FeO	0.001	8.13	7.42	8.67
Al_2O_3	0.500	0.73	0.675	7.08
CaO	0.010	0.55	0.52	5.45
K_2O	0.010	<	0.007	
MgO	0.005	45.56	43.43	4.68
MnO	0.010	0.12	0.12	0.25
Na_2O	0.001	<	0.03	
P_2O_5	0.100	<	0.002	
SiO_2	0.003	46.38	41.7	10.09
TiO_2	0.050	<	0.01	

[a] LOD = limit of detection

[b] PCC-1 = peridotite reference material

[c] % Diff = ((measured - certified)/measured)*100

agreement with previously published data for this sample (LSPET, 1969; Gast et al., 1970; Goles et al., 1970a; Morrison et al., 1970; Rose et al., 1970; Wiesmann and Hubbard, 1975; Duncan et al., 1976; Beaty and Albee, 1978; Rhodes and Blanchard, 1980). In addition, other previously published data indicate a number of samples were collected from the Apollo 11 and 17 sites with high-Al and/or intermediate-Ti compositions (e.g., Turekian and Kharkar, 1970; Kharkar and Turekian, 1971; Wakita et al., 1970; Wänke et al., 1970; Smales et al., 1971; Laul et al., 1975; Warner et al., 1975; Duncan et al., 1976; Neal et al., 1994a). The low-Ti basalts of Apollo 12 and 15 within our sample set show greater scatter in Al_2O_3 content than the high-Ti basalts. Ilmenite basalts 12051 and 12064 contain $\geq$ 11 wt % Al_2O_3, along with Apollo 15 KREEP basalt 15386 and Apollo 14 basalt 14053, which plot in the high-Al region (Figure 4.1a).

Apollo 15 KREEP basalt 15386 displays the highest K_2O (0.61 wt %, Figure 4.1b) within the sample set, followed by the Apollo 11 high-K basalts (0.32 to 0.29 wt %), highlighting the significant K-enrichment in these samples compared to all other basalt groups. Apollo 14 low-Ti, high-Al basalt 14053 contains the next highest K_2O at 0.12 wt %, but this is still less than half of the lowest Apollo 11 high-K value. However, previous data show a number of Apollo 14 mare-basalt samples contain between 0.20 and 0.30 wt % K_2O (e.g., Dickinson et al., 1985; Shervais et al., 1985a; Neal et al., 1988); these samples can therefore be classed as high-K using the classification of Neal and Taylor (1992). The data envelope shown on Figure 4.1b does not include the very high-K (VHK) Apollo 14 basalts, as this group is not represented in our sample set – VHK samples contain between 0.35 and 1.86 wt % K_2O (e.g., Duncan et al., 1975; Shervais et al., 1985b; Neal et al., 1988b; Neal et al., 1989a). All Apollo 12 and 15 low-Ti basalts contain K_2O below 0.2 wt % and are, therefore, classified as low-K according to the classification scheme of Neal and Taylor (1992). The remaining high-Ti basalts do not plot beyond 0.88 wt % K_2O.

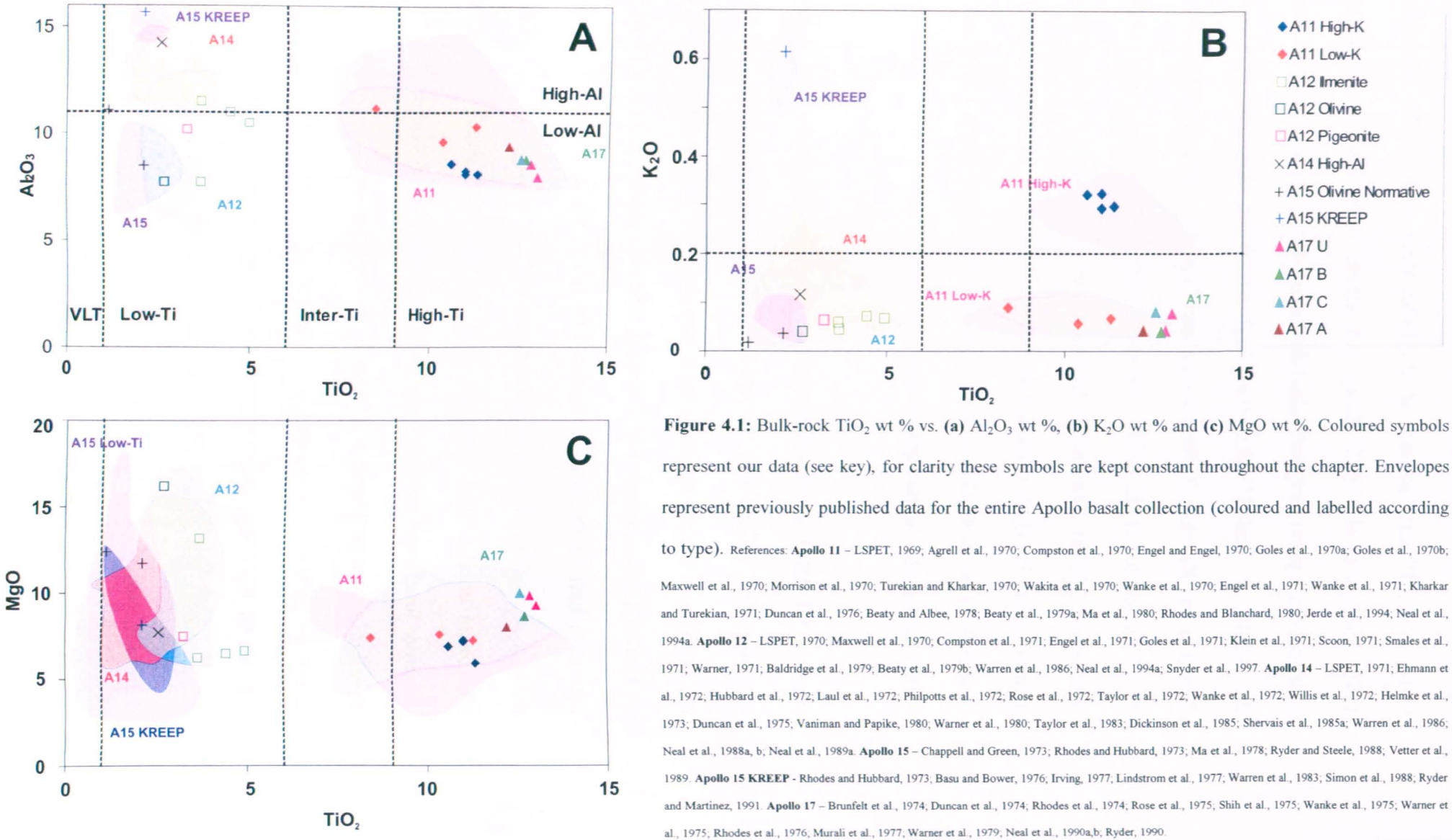

Figure 4.1: Bulk-rock TiO_2 wt % vs. **(a)** Al_2O_3 wt %, **(b)** K_2O wt % and **(c)** MgO wt %. Coloured symbols represent our data (see key), for clarity these symbols are kept constant throughout the chapter. Envelopes represent previously published data for the entire Apollo basalt collection (coloured and labelled according to type). References: **Apollo 11** – LSPET, 1969; Agrell et al., 1970; Compston et al., 1970; Engel and Engel, 1970; Goles et al., 1970a; Goles et al., 1970b; Maxwell et al., 1970; Morrison et al., 1970; Turekian and Kharkar, 1970; Wakita et al., 1970; Wanke et al., 1970; Engel et al., 1971; Wanke et al., 1971; Kharkar and Turekian, 1971; Duncan et al., 1976; Beaty and Albee, 1978; Beaty et al., 1979a; Ma et al., 1980; Rhodes and Blanchard, 1980; Jerde et al., 1994; Neal et al., 1994a. **Apollo 12** – LSPET, 1970; Maxwell et al., 1970; Compston et al., 1971; Engel et al., 1971; Goles et al., 1971; Klein et al., 1971; Scoon, 1971; Smales et al., 1971; Warner, 1971; Baldridge et al., 1979; Beaty et al., 1979b; Warren et al., 1986; Neal et al., 1994a; Snyder et al., 1997. **Apollo 14** – LSPET, 1971; Ehmann et al., 1972; Hubbard et al., 1972; Laul et al., 1972; Philpotts et al., 1972; Rose et al., 1972; Taylor et al., 1972; Wanke et al., 1972; Willis et al., 1972; Helmke et al., 1973; Duncan et al., 1975; Vaniman and Papike, 1980; Warner et al., 1980; Taylor et al., 1983; Dickinson et al., 1985; Shervais et al., 1985a; Warren et al., 1986; Neal et al., 1988a, b; Neal et al., 1989a. **Apollo 15** – Chappell and Green, 1973; Rhodes and Hubbard, 1973; Ma et al., 1978; Ryder and Steele, 1988; Vetter et al., 1989. **Apollo 15 KREEP** - Rhodes and Hubbard, 1973; Basu and Bower, 1976; Irving, 1977; Lindstrom et al., 1977; Warren et al., 1983; Simon et al., 1988; Ryder and Martinez, 1991. **Apollo 17** – Brunfelt et al., 1974; Duncan et al., 1974; Rhodes et al., 1974; Rose et al., 1975; Shih et al., 1975; Wanke et al., 1975; Warner et al., 1975; Rhodes et al., 1976; Murali et al., 1977; Warner et al., 1979; Neal et al., 1990a,b; Ryder, 1990.

The bulk-rock MgO content varies from 5.92 to 16.17 wt % in our sample set (Figure 4.1c), with only the low-Ti Apollo 15 basalts 15016 and 15555, Apollo 12 olivine basalt 12040 and Apollo 12 ilmenite basalt 12016 containing > 10 wt % MgO. The remaining Apollo 12 ilmenite basalts within our sample set show little MgO variation (6.27-6.67 wt %) and the MgO content of Apollo 12 pigeonite basalt 12052 is only slightly higher (7.49 wt %). Apollo 14 high-Al basalt 14053 and Apollo 15 KREEP basalt 15386 show similar MgO contents at 7.71 and 8.21 wt %, respectively. The high-Ti basalts display a more restricted data set, with Apollo 17 basalts showing higher MgO (8.01-9.97 wt %) than the Apollo 11 basalts (5.92-7.59 wt %). Apollo 17 type A basalt 75055 shows the lowest MgO value of the Apollo 17 samples within our sample set (8.01 wt %), and plots closest to Apollo 11 basalt 10020 (7.59 wt %). The limited variation in bulk-rock MgO content within the high-Ti mare basalts compared to the low-Ti basalts is consistent with previous studies (Figure 4.1c).

Figure 4.2 shows Na_2O vs. FeO for our sample set along with all previous mare-basalt data from the Apollo collection. The Apollo 15 KREEP basalt 15386 plots distinctly away from the mare basalts because of its comparatively high Na_2O (0.81 wt %) and low FeO content (9.96 wt %). Apollo 14 high-Al basalt 14053 also shows a slight FeO depletion (15.77 wt %) compared to other mare basalts, but its Na_2O content (0.42 wt %) is still lower than the Apollo 11 high-K basalts (0.45-0.49 wt %). The latter have the second highest Na_2O content, followed by the Apollo 11 low-K basalts (0.34-0.36 wt %) and the Apollo 17 basalts (0.37-0.34 wt %), of which type A basalt 75055 has the highest Na_2O content. The Apollo 12 and 15 low-Ti basalts exhibit low Na_2O values (0.29-0.18 wt %), with olivine basalt 12040 displaying the lowest value. Figure 4.2 highlights the negative correlation between Na_2O and FeO in the Apollo basalts, as Na_2O decreases FeO generally increases. This observation can be related to the mineral modes in these basalts; an increase in the modal proportion of feldspar (the main Na_2O host) is accommodated by concomitant

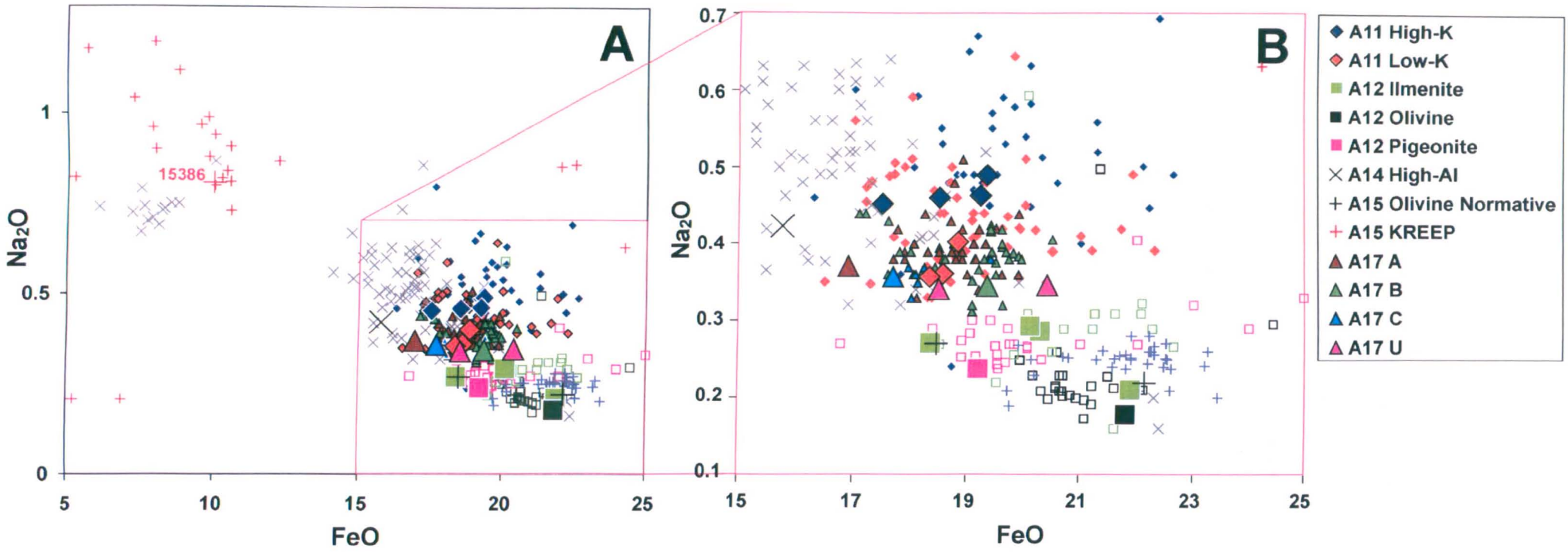

Figure 4.2: Bulk-rock Na_2O vs. FeO. The large scale plot **(a)** shows the high Na_2O and low FeO of the Apollo 15 KREEP basalts, including sample 15386. The smaller scale plot **(b)** highlights the high Na_2O abundance in Apollo 11 and 17 high-Ti basalts compared to the Apollo 12 and 15 low-Ti basalts. Large symbols represent our measured data, whereas smaller symbols represent previously published data (for references see Figure 4.1).

decrease in the amount of olivine and pyroxene present (the main FeO bearing phases). However, ilmenite is not a part of this relationship (as it is not a silicate), hence the high-Ti basalts show a weaker negative correlation than the low-Ti basalts.

Interestingly, despite the fact that low-Ti basalts within the sample set analysed in this study contain the most Cr-rich spinel grains, they do not all contain high Cr_2O_3 contents (Figure 4.3). In fact, Apollo 12 ilmenite basalts 12047, 12051 and 12064 show some of the lowest Cr_2O_3 contents, alongside the Apollo 11 high-K basalts. However, there does appear to be a weak positive relationship between spinel modal abundance and bulk-rock Cr_2O_3 content for a number of samples - for example, the Apollo 15 low-Ti olivine-normative basalts and Apollo 12 ilmenite basalt 12016 contain some of the highest modal spinel and Cr_2O_3 abundances compared to the other samples, whereas Apollo 12 ilmenite basalt 12051 is poor in both (Figure 4.4). However, there are numerous exceptions to this rule, relating to the presence of minor Cr within other phases. This effect is most obvious in Apollo 17 unclassified basalt 70017 and Apollo 15 KREEP basalt 15386; these samples contain little spinel but pyroxene grains contain up to 0.7 wt % Cr, ~ 0.4 wt % above the average for other samples. Sample 15386 also contains slightly elevated Cr_2O_3 wt % within ilmenite grains (section 3.2.4). Neither of these samples shows abnormally high bulk-rock Cr_2O_3 contents. In general, there is a positive correlation between bulk-rock Cr_2O_3 (wt %) and MgO (wt %) contents in most samples, consistent with spinel co-crystallisation with olivine and pyroxene during magma cooling (Table 3.2). For most basalt groups, previous studies have highlighted this relationship, but the Apollo 12 olivine basalts show no change in Cr_2O_3 with increasing MgO.

Bulk-rock SiO_2 content is higher within the low-Ti basalts, with Apollo 15 KREEP basalt 15386 displaying the highest value and the Apollo 17 basalts showing the lowest values (Figure 4.3b). As expected from fractionating magmas, the high- and low-Ti groups exhibit

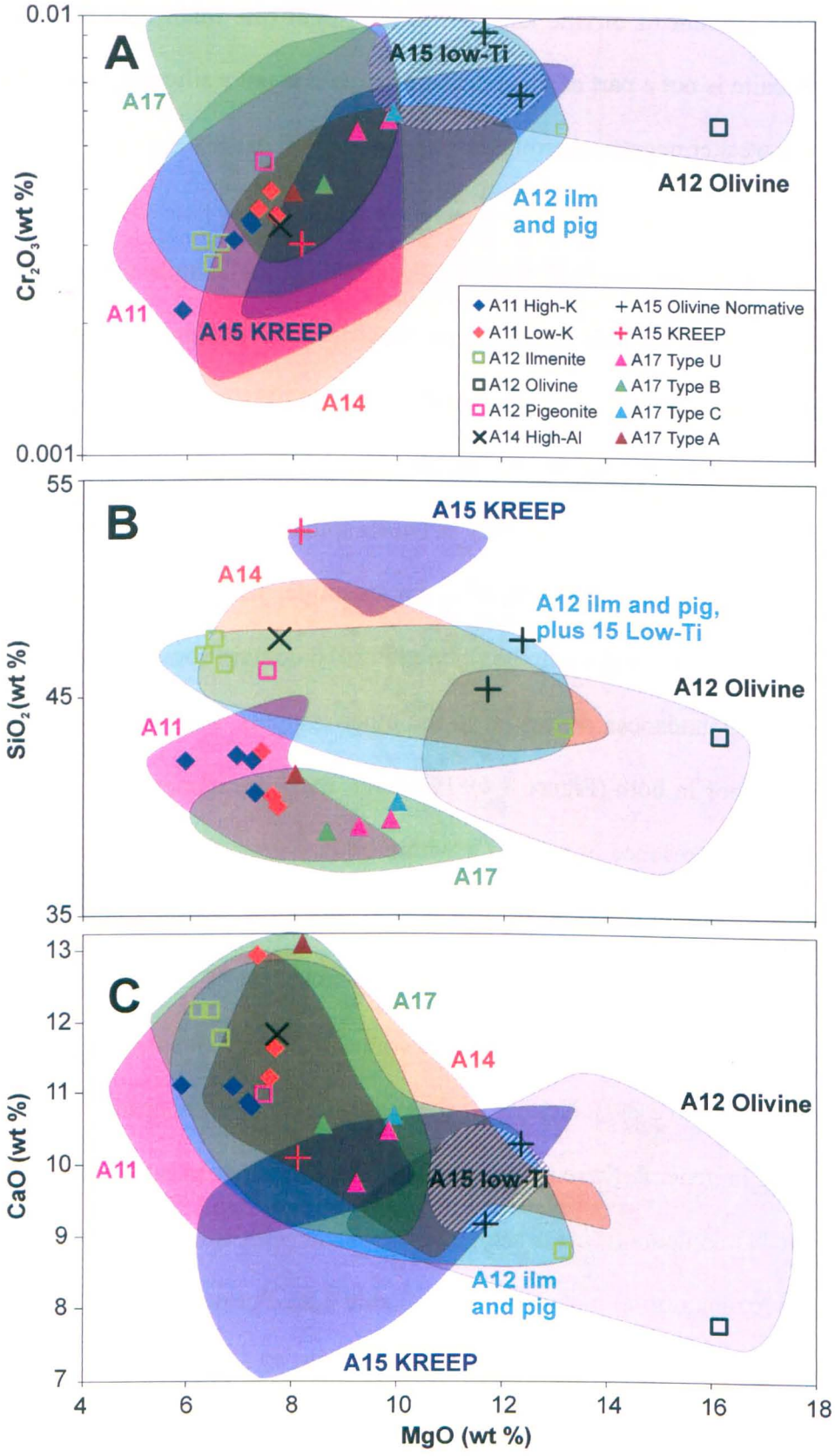

Figure 4.3: Bulk-rock MgO vs. Cr_2O_3 **(a)**, SiO_2 **(b)** and CaO **(c)**. Data from this study are represented by coloured symbols (see key), previously published data for each basalt group is represented by separate coloured envelopes. Apollo 12 pigeonite and ilmenite basalt data and Apollo 15 olivine normative basalt data are represented by the same envelope, whereas a separate envelope represents Apollo 12 olivine basalt data. See Figure 4.1 for previously published data references.

parallel negative correlations between SiO_2 and MgO (The high-Ti basalts contain less SiO_2 as they have higher TiO_2 contents). The CaO contents of most mare-basalt groups are similar, excepting the Apollo 12 olivine basalts, which contain less CaO (and more MgO) than other samples. All mare-basalt groups show a strong decrease in CaO with increasing MgO, whereas the Apollo 15 KREEP basalts display the opposite relationship (Figure 4.3c).

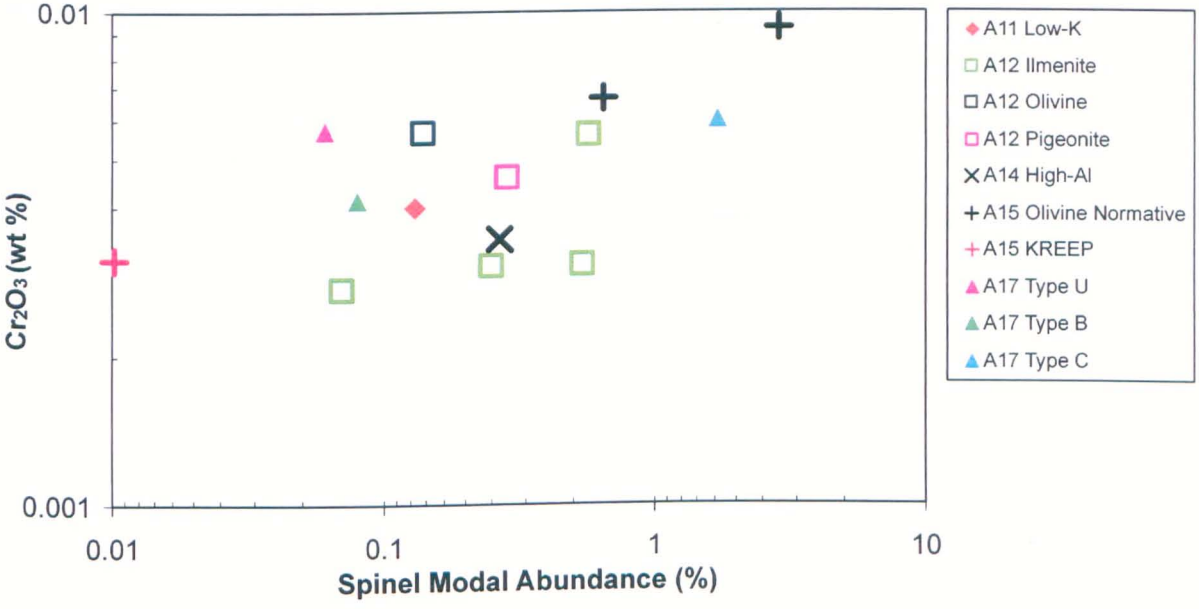

Figure 4.4: Bulk rock Cr_2O_3 vs. spinel modal abundance.

The bulk-rock Ni (ppm) content is variable throughout the sample set – in general, a number of low-Ti basalts contain Ni above the detection limit, whereas a number of high-Ti basalts show Ni below the detection limit, but there are numerous exceptions (Table 4.1). Only the high-K Apollo 11 basalts, Apollo 14 high-Al basalt 14053 and Apollo 15 KREEP basalt 15386 contain bulk P_2O_5 above the detection limit.

4.1.2. MELTS Calculations. By processing the bulk-rock major-element data into MELTS software (Ghiorso and Sack, 1995; Asimow and Ghiorso, 1998) it was possible to calculate the liquidus temperature and the predicted crystallisation sequence for each sample (Table 4.2; Figure 4.5). Data that do not match the petrological observations may indicate that the

Table 4.2: Predicted liquidus temperatures for each sample, based on major-element bulk-rock composition.

Sample	Liquidus (°C)	MELTS Correct?
10017	1157	N - spinel and olv are not present in the sample
10020	1162	Y - although no second Ti-rich spinel phase was found in sample
10049	1148	N - spinel is not present in the sample and merri is very fine grained if present
10050	1159	N - predicted olv have lower Mg# than some cpx in sample, spinel was not observed
10057	1159	N - no olv, spinel or merri present in sample, observations show cpx and ilm crystallise before plag
10058	1144	N - olv and spinel not present in sample, free silica not predicted, observations show cpx, plag and ilm crystallise together
10072	1141	N - olv predicted to crystallise late but aboservations show early olv
12016	1311	N - spinel crystallised early in sample, no uilmentie is predicted
12040	1377	N - no ilmenite or late stage Ti-spinel predicted, Cr-spinel is crystallised early in sample
12047	1146	N - olv crystallises early in sample
12051	1151	N - olv is not present in sample, spinel crystallised earlier in sample
12052	1184	N - olv, spienl and cpx are phenocrysts in sample, everything else is quench textured
12064	1149	Y - although apatite is not predicted and no olv was found in our sample (though 12064 does contain rare olv grains)
14053	1174	Y - although Cr-spinel appears to have crystallised early in the sample
15016	1281	N - ilm and free silica missing from MELTS predictions, spinel crystallised early in sample
15386	1214	Y - although olivine is not present in the sample
15555	1290	N - ilm and free silica missing from MELTS predictions, spinel crystallised early in sample
70017	1218	N - in sample olv crystallises after ilm and cpx, apatite is missing from MELTS prediction
70035	1207	N - olv crystallised after cpx in sample, ilm should be before cpx, and spinel is very rare in sample
70215	1188	Y - correct crystallisation order, although silica is not present in sample (or is very fine grained), In reality sample is mostly quench
74275	1219	N - ilm (and arm) should crsytallise first, Cr-spinel and olv should follow
75055	1153	N - olv is not present in the sample

Pressure is assumed to be 1 bar, but decreasing the pressure to 0 bars has no significant effect on liquidus temperature.

sample contains xenocrysts, or has undergone crystal fractionation or accumulation. Equilibrium crystallisation modelling was performed with an oxygen fugacity equivalent to two log units below the Iron-Wustite buffer (i.e. IW-2) and with a starting liquidus temperature of 1400 °C. Calculated liquidus temperatures vary from 1377 °C to 1141 °C (samples 12040 and 10072, respectively). The higher liquidus temperature for Apollo 12 olivine cumulate basalt 12040 is followed by that of Apollo 12 ilmenite basalt 12016, at 1311 °C. A gap of 22 °C exists before the next highest liquidus temperatures, those of the Apollo 15 low-Ti basalts at 1290 °C and 1281 °C. The liquidus temperature estimates for the remaining Apollo 12 basalts range from 1147 °C to 1151 °C for the ilmenite basalts and 1184 °C for pigeonite basalt 12052. Apollo 14 high-Al basalt 14053 yields a similar estimate of 1174 °C, significantly different from that of Apollo 15 KREEP basalt 15386 (1214 °C). Apollo 11 basalts show liquidus temperatures between 1162 °C and 1141 °C, with no difference between the estimates of high- and low-K samples. Apollo 17 type A basalt 75055 shows a similar liquidus temperature (1153 °C). The remaining Apollo 17 basalts have slightly higher estimates, from 1219 °C to 1188 °C.

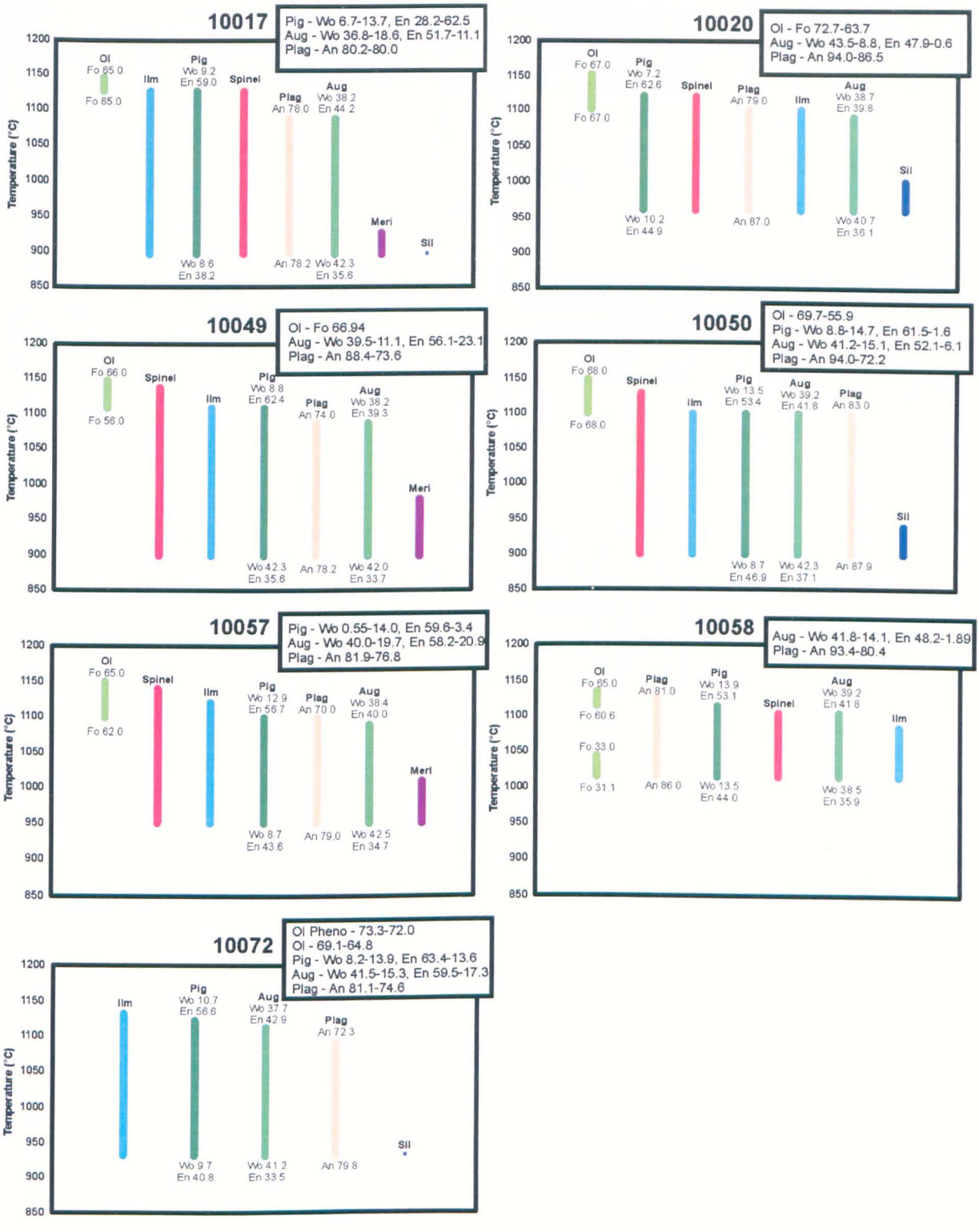

Figure 4.5: Plots showing the equilibrium crystallisation sequence for each sample as temperature decreases, calculated using MELTS. Coloured bars represent individual mineral phases (labelled). For olivine, pigeonite, augite, orthopyroxene and plagioclase, compositional data at the beginning and end of crystallisation are shown next to each bar. As the version of MELTS available did not take into account crystal fractionation a number of calculated crystallisation sequences and mineral compositions vary significantly from those observed in the samples. The box to the top right of each plot shows the observed mineralogical compositions for each sample.

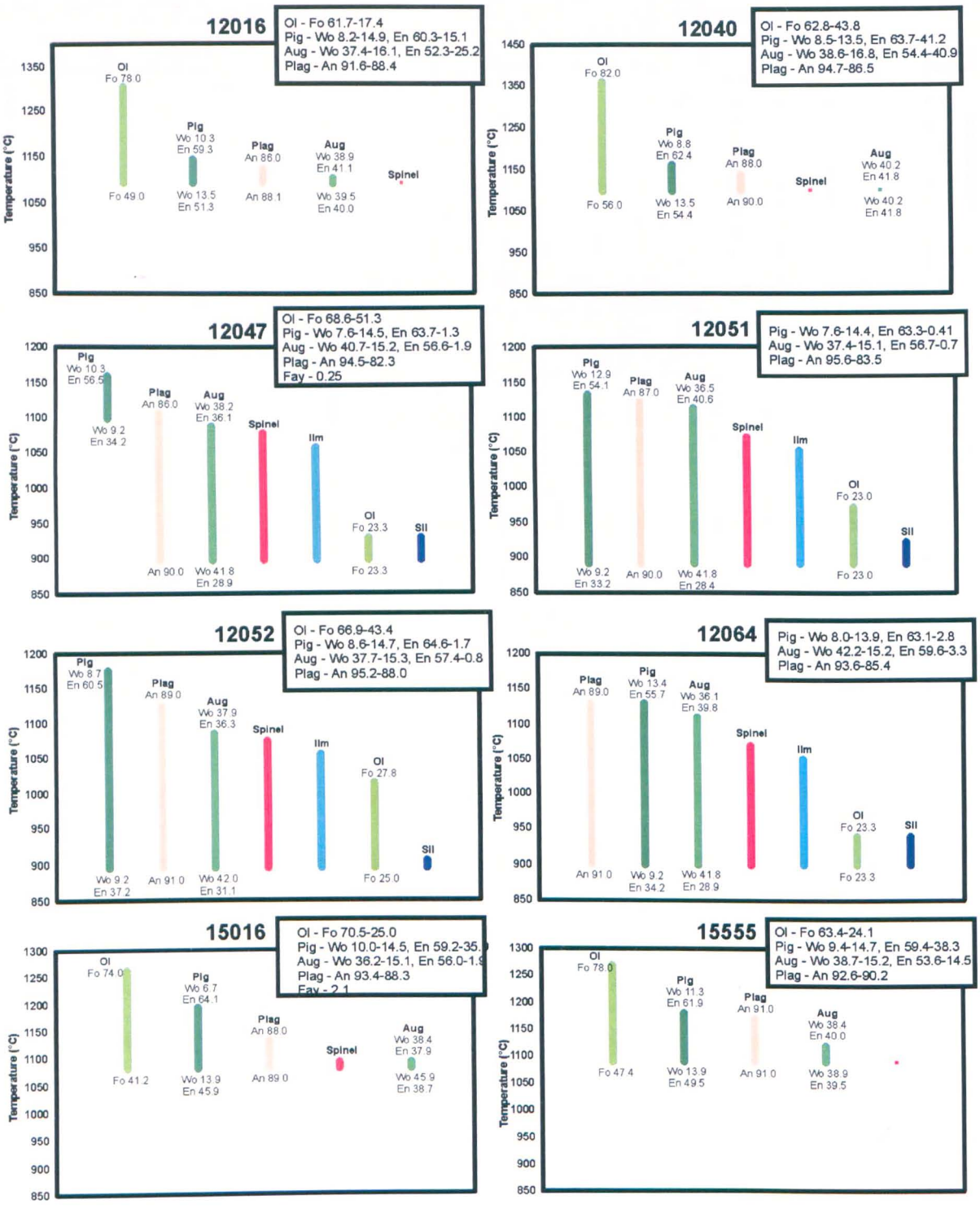

Figure 4.5: cont.

As the available MELTS software did not allow for fractional crystallisation calculations, most crystallisation sequences estimated using the MELTS program were found to be in some disagreement with the textural and mineralogical evidence. For example, MELTS calculations failed to predict the crystallisation of ilmenite in Apollo 12 olivine basalt 12040, ilmenite basalt 12016 and Apollo 15 low-Ti basalts 15016 and 15555, yet ilmenite

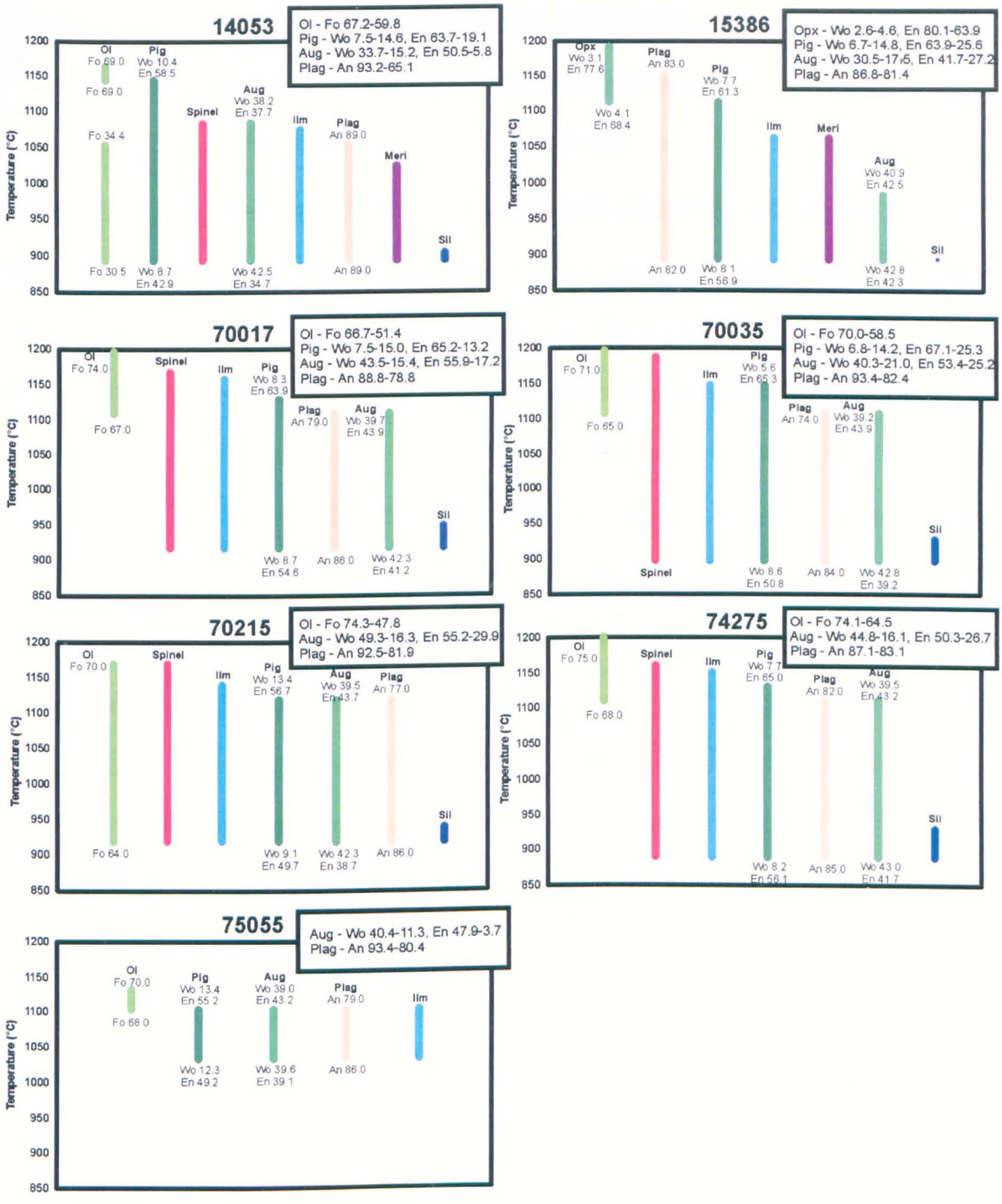

Figure 4.5: cont. 2.

is present in these samples. MELTS also predicted that olivine should be present in a number of samples where none is observed (Figure 4.5). However, in nature, pure fractional or equilibrium crystallisation end-members rarely exist; a continuum between the two end-members is more probable. Therefore, a sample which exhibits major petrological similarities to the MELTS equilibrium-crystallisation calculations must have formed in an environment dominated by this crystallisation mechanism. Equally, a sample

with few petrological similarities to the MELTS equilibrium-crystallisation calculations probably formed in an environment dominated by fractional crystallisation.

Within our sample set equilibrium crystallisation modelling only provides a fair match between the observed and predicted compositional ranges of mineral phases in the Apollo 12 and 15 mare basalts. For Apollo 12 samples 12047, 12051, 12052 and 12064 the calculations predict olivine should crystallise late, with Fo_{28-23}. Such Fe-rich olivine is not encountered in these samples - where present (in samples 12047 and 12052) olivine shows compositions of Fo_{69-43}, and appears to have crystallised as one of the earliest phases. Cr-rich spinel is also observed as an early phase in the Apollo 12 and 15 mare basalts, but MELTS calculations suggests that it should have crystallised late. Pigeonite and augite compositions of these samples do not show as much variation in MELTS crystallisation sequences as is observed, a discrepancy visible for the majority of samples. Plagioclase is predicted with lower and less varied An# than that observed within most samples, excepting samples 15555, 70017 and 74275, where predicted and observed An# are similar. The presence of olivine is predicted but not observed in Apollo 11 sample 10017 and Apollo 17 sample 75055, in contrast Apollo 11 sample 10072 contains olivine but the MELTS calculation for this sample did not. All of the high-Ti basalts contain early crystallising ilmenite, but MELTS calculations indicate that ilmenite should crystallise late in Apollo 11 low-K samples 10020 and 10058, and Apollo 17 sample 75055. In addition, spinel is incorrectly predicated to crystallise late in sample 10020. In contrast, Apollo 11 basalt 10058 does not contain spinel, but the MELTS calculations incorrectly predict its presence in this sample.

Only Apollo 14 high-Al basalt 14053 and Apollo 15 KREEP basalt 15386 yield estimates mostly in line with the observations, though plagioclase still shows more An# variation in the samples than is predicted by MELTS. This is especially true in sample 14053, where

observed values range from An_{93} to An_{65} (at the extreme rim), but the predicted value of MELTS does not change from An_{89}. Overall, with the exceptions of a few samples, the equilibrium MELTS predictions did not fit well with the observed crystallisation sequences of the samples (Table 3.3), indicating crystal fractionation played a roll in the evolution of these basalts parental melts.

4.1.3. Olivine Accumulation and Addition. The Garcia (Garcia et al., 1995) plot is used to determine the equilibrium conditions at the onset of early olivine crystallisation, when other phases do not affect the partitioning of Mg and Fe. Therefore, for the Garcia plot to produce valid interpretations, olivine must be an early crystallising phase with initial Fo# (mol %) higher than ~ 60. Once olivine Fo# falls below 50 the crystallisation of other phases begins to significantly affect the partitioning of Mg and Fe, and Garcia plot interpretations become less straightforward. Incidentally, all the basalts which contain olivine within our sample set show initial olivine (cores) above Fo# 60. Figure 4.6 compares the measured bulk-rock Mg# with forsterite contents in olivines measured by EMPA. If the data points plot below the mare-basalt partition coefficient (Kd) line, olivine accumulation has occurred, whereas if they plot above the line, a xenocrystic origin for the olivine is suggested. Figure 4.6a indicates that a number of mare basalts within our sample set have been subjected to varying amounts of olivine accumulation; Apollo 12 olivine basalt 12040 shows the most accumulation, in agreement with the mineralogical evidence presented in chapter 3, as well as that of Meyer and Wiltshire (1974) and Baldridge et al. (1979). The Garcia plot also indicates that Apollo 15 olivine-normative basalt 15555 and Apollo 12 ilmenite basalt 12016 contain significant amounts of accumulated olivine. Only samples 10020, 12047 and 70215 plot on the equilibrium line, although the single olivine data point for Apollo 11 high-K basalt 10049 plots close enough to suggest that with a more extensive data set this sample would also plot on the line. The only remaining Apollo 11 high-K basalt that contains olivine is sample 10072. Its large olivine phenocryst

(Figures 3.13 and 3.14) plots above the equilibrium line, suggesting it is a xenocryst. Other olivine grains within this basalt plot on the line, indicating they were native to the sample's parental melt. Figure 4.6b shows the Mg# each sample would require for its highest Fo#

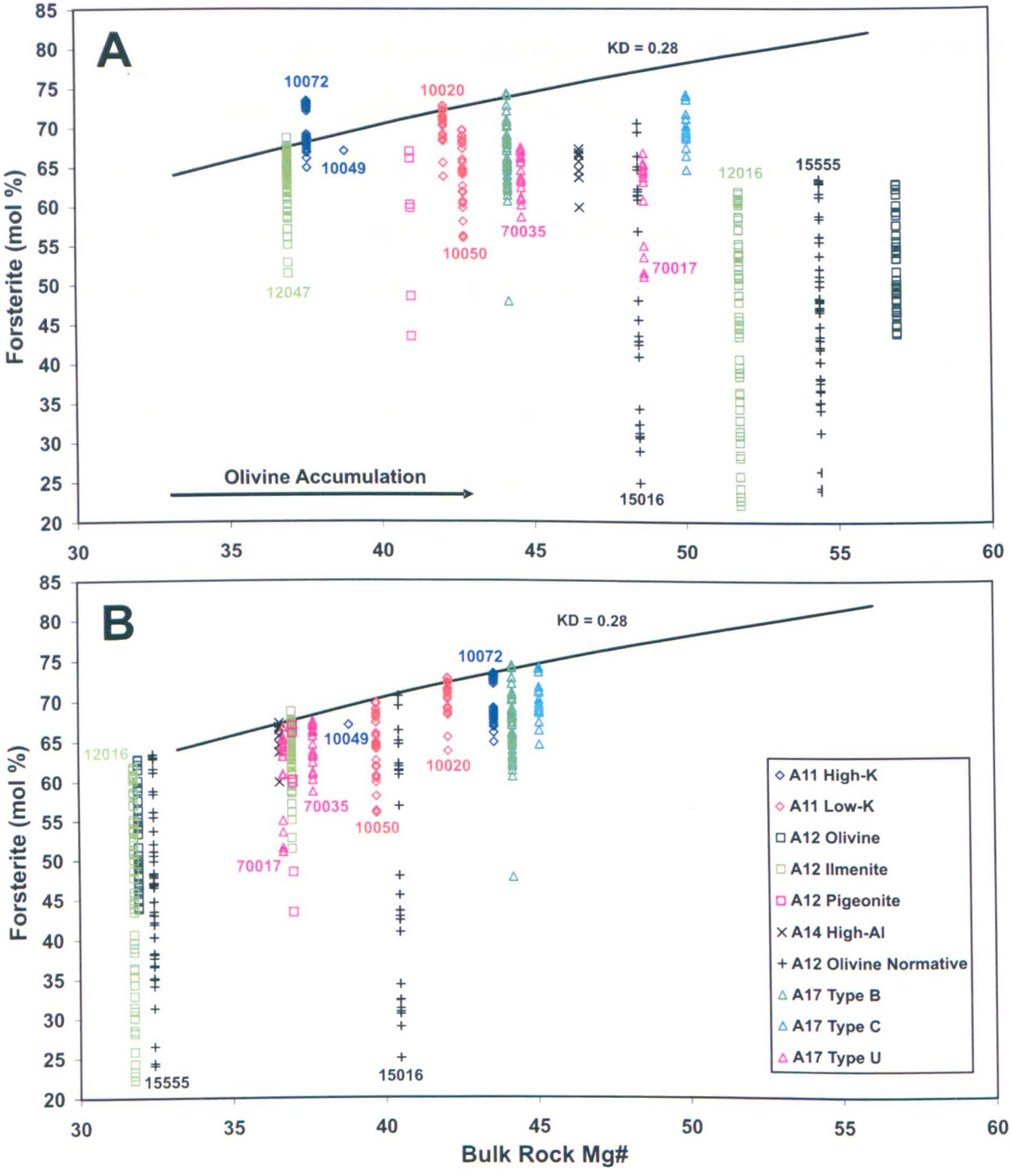

Figure 4.6: Garcia plot showing olivine forsterite number vs. bulk-rock Mg# for individual samples. **(a)** Measured data, if the highest forsterite value within a sample is far below the black equilibrium line olivine accumulation has occurred, if forsterite values plot above the line the sample contains olivine xenocrysts. **(b)** Reducing the Mg# of samples showing olivine accumulation, and increasing that of xenocryst bearing samples, until the highest forsterite data points touch the equilibrium line, gives the original Mg#.

olivine to plot on the equilibrium line. For most samples this value is between 7 and 25 % lower than the measured bulk-rock Mg#, but for samples 12016, 12040 and 15555 the value of Mg# must be 39, 44 and 40 % lower respectively. The Mg# of sample 10072 would have to increase by 16 % in order to fit with the xenocrystic value. This plot indicates that without olivine accumulation, none of these samples would have a bulk-rock Mg# higher than 45 (sample 74275) and the most extensively affected sample would have Mg# 32 (sample 12016). However, there is the possibility that the highest Fo# olivine grains within a bulk-rock sample are not represented in the thin section investigated, especially in those cases in which the thin sections were small (e.g., samples 74275 and 12016). In these cases, the maximum Fo content measured in olivine in this study should be taken as minimum estimates. Another factor which may complicate any straightforward interpretation of the Garcia plot is the possibility of sub-solidus re-equilibration. This would homogenise Fe-Mg distribution in an olivine grain, thereby lowering the Fo content of the core region, and the resulting data point would plot below the equilibrium line at the given bulk-rock Mg#.

4.2. Trace-Elements

4.2.1. Bulk-Rock REE. Bulk-rock REE data for mare basalts within the Apollo sample collection have been published by numerous research groups over the past forty years (see Figures 4.11 for references). As a result there is an extensive existing dataset, but in most cases only a handful of REE's were analysed in a given sample because of the limitations posed by instrumentation and analytical techniques during the early post-Apollo era. This study reports the most extensive mare-basalt REE dataset to date, raw data is presented in Appendix E.

Previously published REE data for Apollo 17 unclassified basalt 70035 plots slightly below our data, 20-78 rather than 33-93 times chondrite-normalised values (Figure 4.7).

Similarly, previous data for Apollo 17 type A basalt 75055 shows slightly higher REE abundances than our data (23-89 vs. 15-50 times chondrite-normalised values). These differences can be attributed to sample heterogeneity, as the previously published data for these two samples shows wide variation. The measured REE abundances in Apollo 15 low-

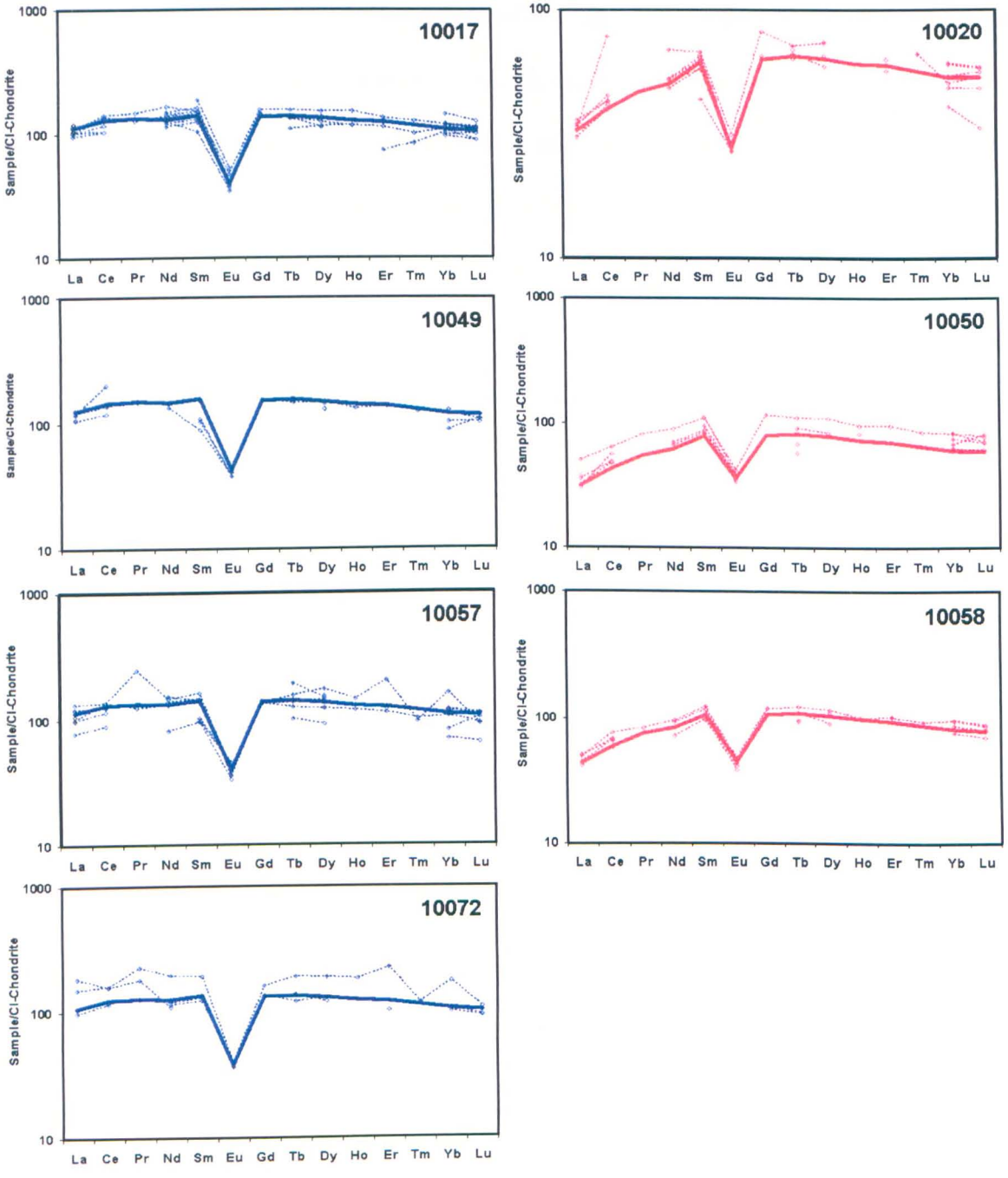

Figure 4.7: Chondrite-normalised REE abundance diagrams comparing previously published bulk-rock data for each sample (see Figure 4.11), to that measured in this study. Previously published data are shown as dotted lines and new data collected in this study are shown as solid lines. Colours and symbols denote sample type (see Figure 4.6 Key).

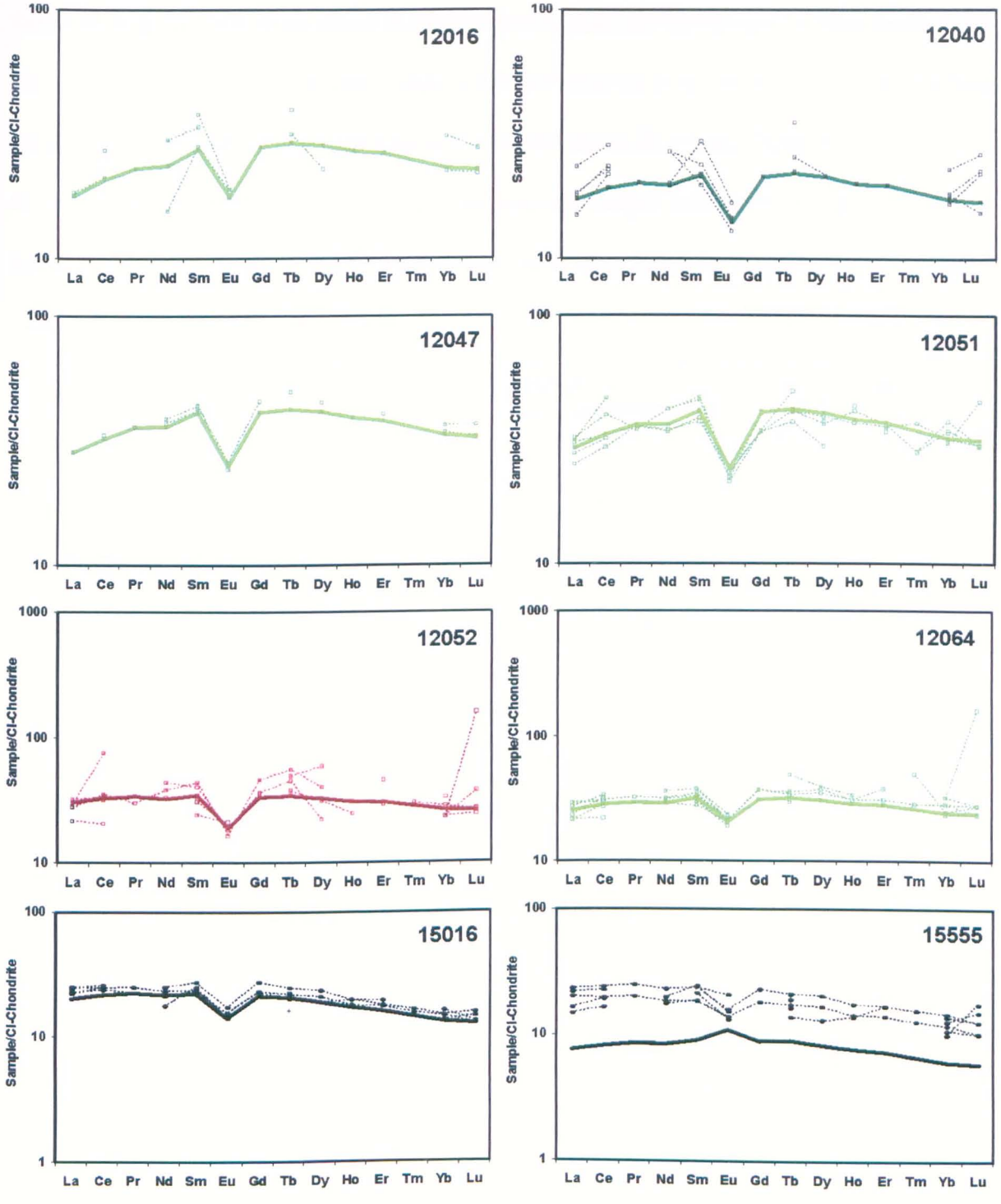

Figure 4.7: cont.

Ti basalt 15555 has a significantly different trend to all previously published data. Not only do our data indicate that this sample contains lower REE abundances than any other, the trend shows a positive europium anomaly (Eu* = 1.21). Previous data for this sample suggest that the europium anomaly should be negative (Eu* = 0.67-0.75), and REE abundances should be slightly higher - around 10-25 rather than 5-11 times chondrite-

normalised values. Significant terrestrial contamination could cause this change in trend and abundance. However, since we received the sample it has been stored and processed in the same manner as all other rock chips within our sample set, none of which show signs of any contamination. Therefore, significant contamination of the sample during this study is unlikely. It is possible that the chip was contaminated before we received it, or that

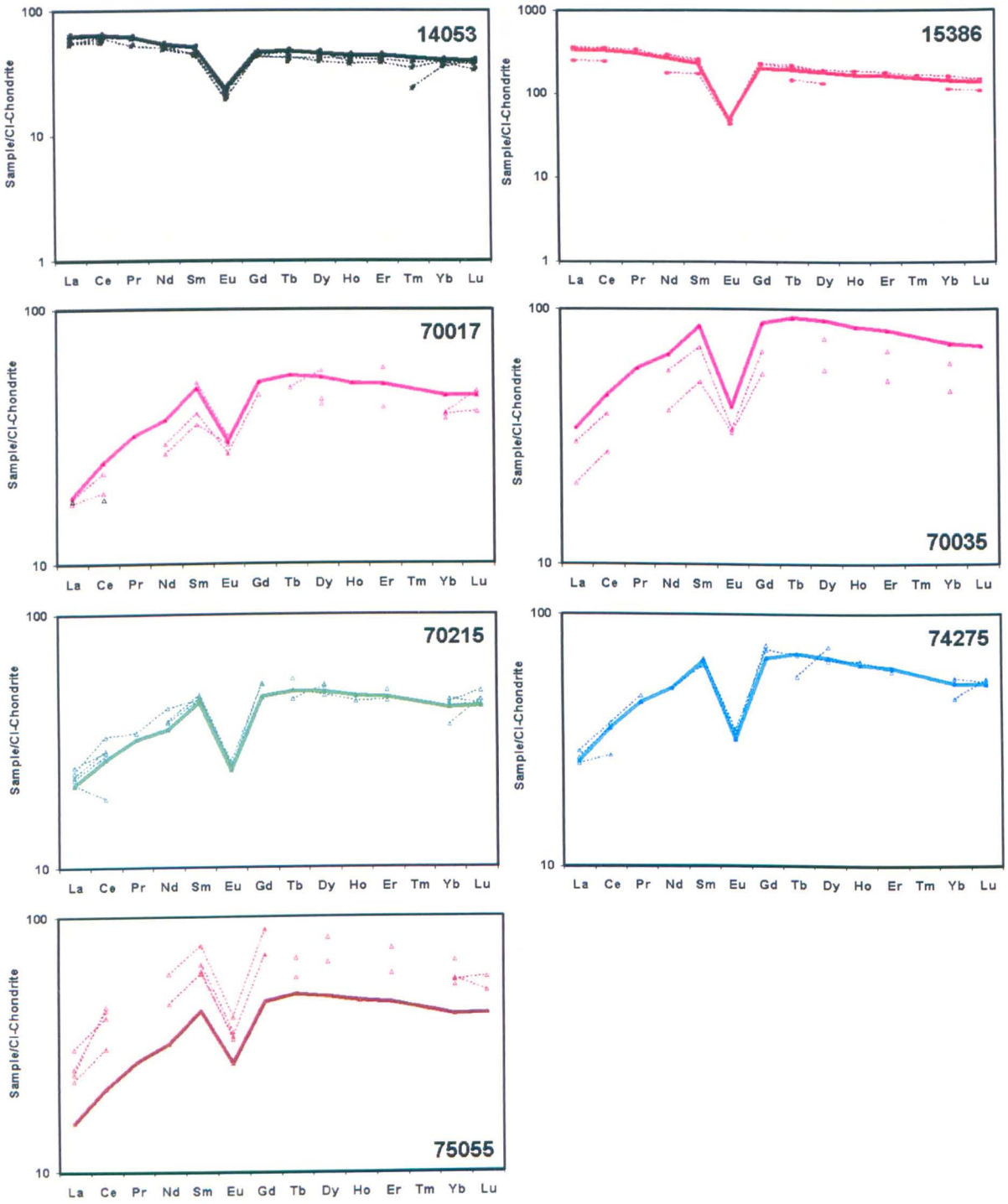

Figure 4.7: cont. 2.

we were mistakenly allocated a chip of a wrong sample. However, taking into account the highly controlled environment the Apollo samples are stored in, the latter possibilities also seem unlikely. The measured REE data of sample 15555,982 must therefore be accounted for by sample heterogeneity and disregarded as unrepresentative of the whole sample. The heterogeneity of this sample was also noted by Ryder and Schuraytz (2001).

Excepting the above sample, Apollo 15 low-Ti basalt 15016 shows the lowest REE abundances, along with Apollo 12 olivine basalt 12040 (12-23 times chondrite-normalised values) (Figure 4.8). The remaining Apollo 12 samples display REE abundances varying from 17 to 43 times chondrite-normalised. All these low-Ti samples show relatively flat trends and weakly negative europium anomalies (Eu* = 0.56-0.65). The high-Ti basalts of Apollo 17 have higher HREE abundances (41-93 times chondrite-normalised values), but LREE depletion means these values overlap with those of the Apollo 12 and 15 samples (15-86 times chondrite-normalised values). Apollo 11 low-K basalts contain lower REE abundances than the high-K basalts, and show a greater spread of data (52-110 vs. 101-154 times chondrite-normalised values for the HREE's). The former contain LREE depletion similar to the Apollo 17 basalts, whereas the latter have much flatter trends and strongly negative europium anomalies (Eu* = 0.28). The REE trends of both Apollo 14 high-Al basalt 14053 and Apollo 15 KREEP basalt 15386 show LREE enrichment. However, in every other sense the trend of sample 14053 fits well with those of the Apollo 12 basalts, whereas KREEP basalt 15386 displays the highest REE abundances and the strongest negative europium anomaly (Eu* = 0.22) among all our samples. Generally, despite a slight overlap, the high-Ti mare basalts contain higher REE abundances than the low-Ti mare basalts. 2σ error bars are smaller than the thickness of the lines on this plot (for values see appendix E), except for sample 15555,982 (because of its low REE abundance).

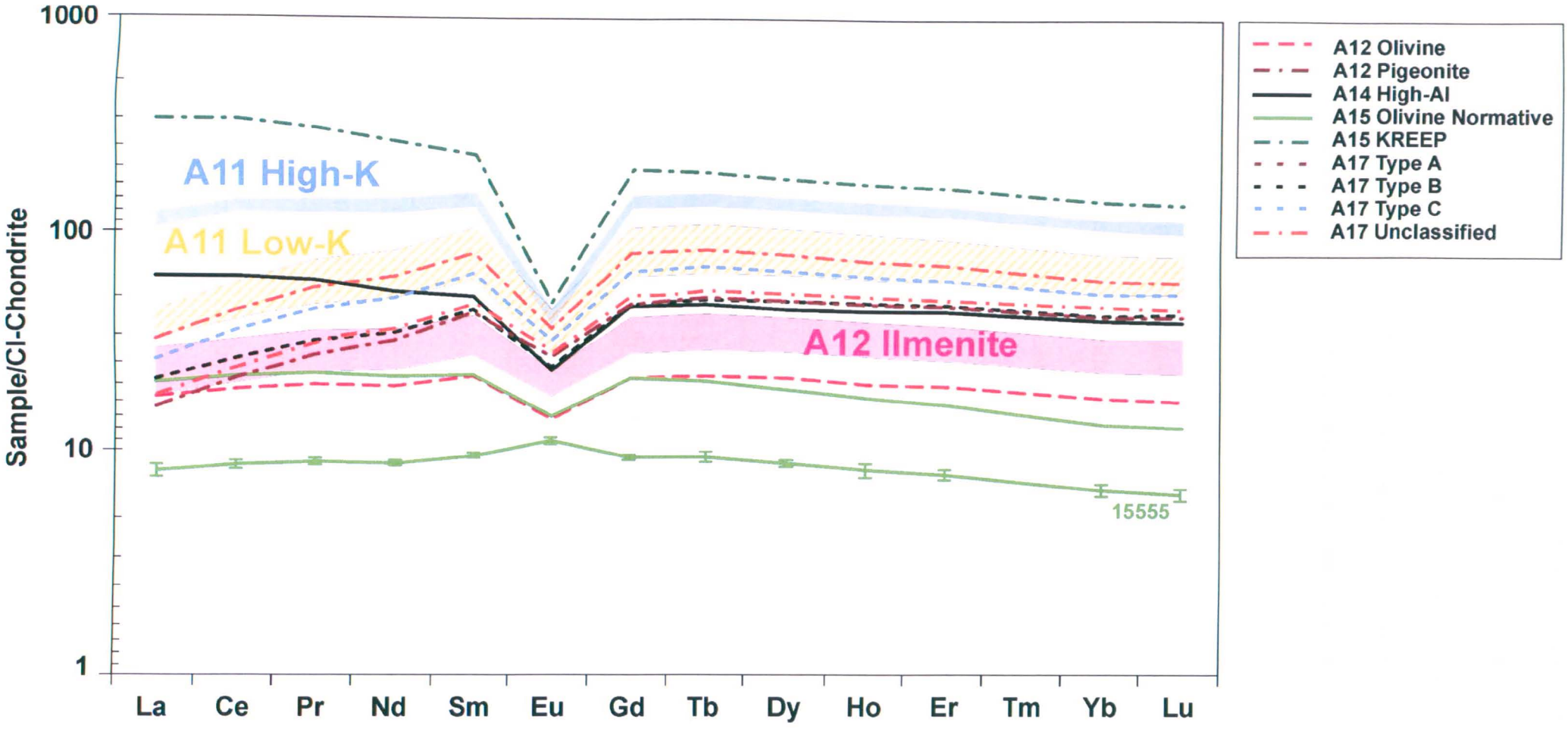

Figure 4.8: Measured bulk-rock REE abundance for all samples. Where the blue envelope represents Apollo 11 high-K basalts, the yellow envelope represents Apollo 11 low-K basalts and the pink envelope represents Apollo 12 ilmenite basalts. Lines represent the remaining samples, coloured according to type. Apollo 15 sample 15555 data (labelled) is disregarded as unreliable. Because this sample has the lowest REE abundance, 2σ error bars are visible – for the other samples the error bars are too small to be observed on this plot.

An additional advantage of having bulk-rock trace-element data is that it can be used to determine the accuracy of the calculated parental melt REE abundances, provided the effects of crystal fractionation and accumulation are taken into account (section 3.3.2). For the Apollo 12 ilmenite basalts, Apollo 15 olivine-normative basalt 15016, Apollo 17 type A basalt 75055, and the Apollo 11 basalts (excepting sample 10058) the two datasets match well (Figure 4.9). The majority of the remaining samples display higher calculated than measured abundances, with the largest difference shown for Apollo 11 low-K basalt 10058, Apollo 12 olivine basalt 12040 and Apollo 17 type B and C basalts 70215 and 74275. The calculated REE melt abundances were based on pyroxene REE content, so the calculated REE values could be higher than the measured values in these samples because pyroxene was not one of the first phases to crystallise, or the pyroxene grains analysed were not among the first to form. Later stage pyroxenes contain higher REE abundances, therefore calculated melt REE abundances would be high compared to the true melt composition of the sample. However, if significant crystal accumulation occurred in the sample the calculated REE values may be more reliable than the bulk-rock values. If a sample contains accumulated grains of a mineral with low REE content (e.g., olivine and/or ilmenite), then the measured bulk-rock REE content will be low compared to that of the original melt (e.g., sample 12040). Apollo 15 KREEP basalt 15386 is the only sample with higher measured REE than the calculated values. Plagioclase (LREE-enriched) and orthopyroxene crystallised in this sample before clinopyroxene, therefore the melt was probably low in LREE's at the time of clinopyroxene crystallisation. This would subsequently result in low calculated REE melt abundances (Figure 4.9).

4.2.2. Incompatible Trace-Elements. Within the mare basalts the large radii alkali elements (K, Rb, Cs), Sr, Ba, Zr, Hf, Nb, Ta, Th and U behave incompatibly, in addition to the REE's. Figure 4.10 shows various incompatible-element bivariate plots to highlight the low abundance of these elements in most lunar basalt groups. Apollo 15 KREEP basalt

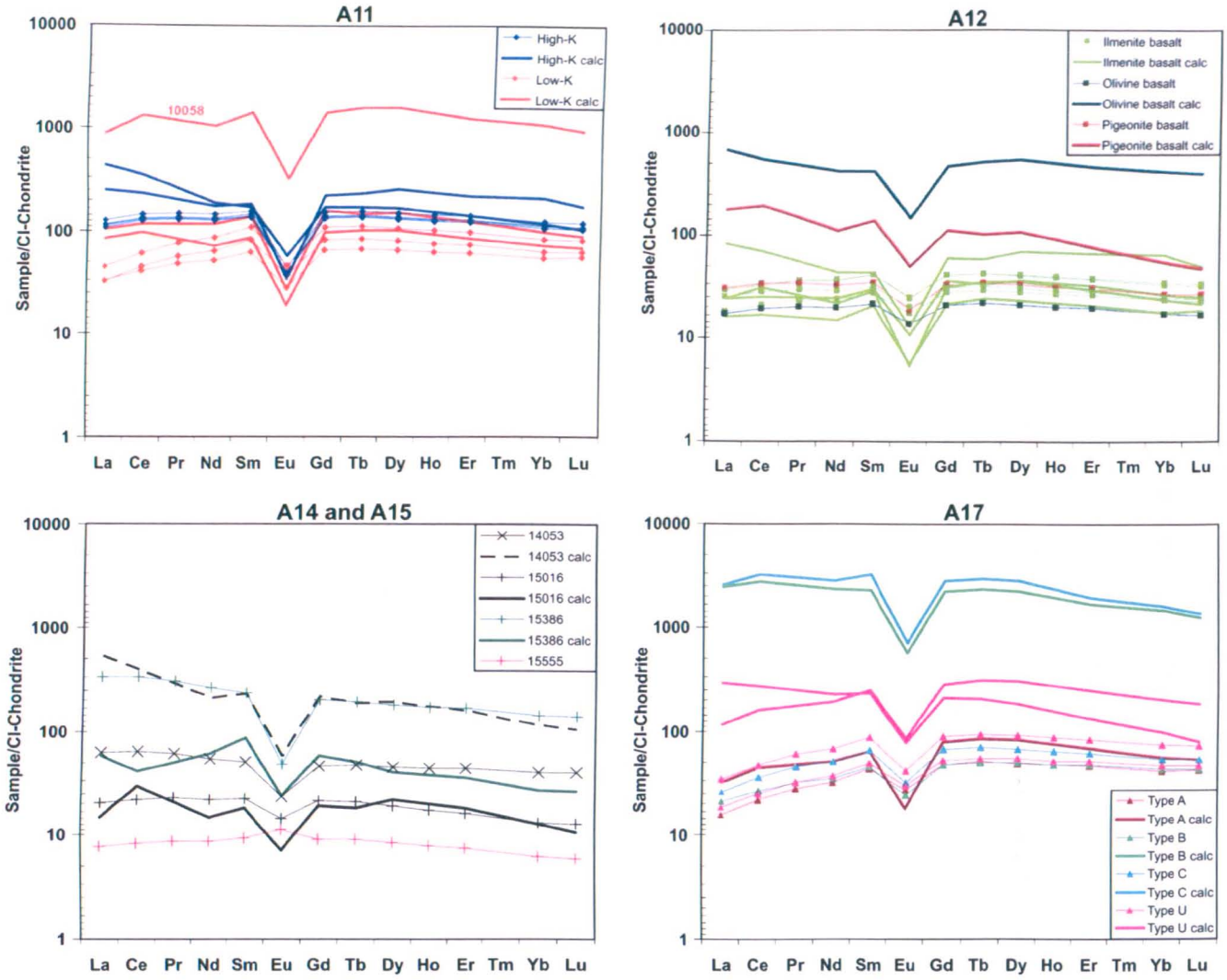

Figure 4.9: Measured bulk-rock REE compared with calculated bulk-rock REE (see Figure 3.49). Only measured data is shown for sample 15555, as pyroxene REE abundance data is unreliable for this thin section. Pyroxene REE abundance was not measured for samples 10049 and 10057, as these were too fine grained for LA-ICP-MS analysis.

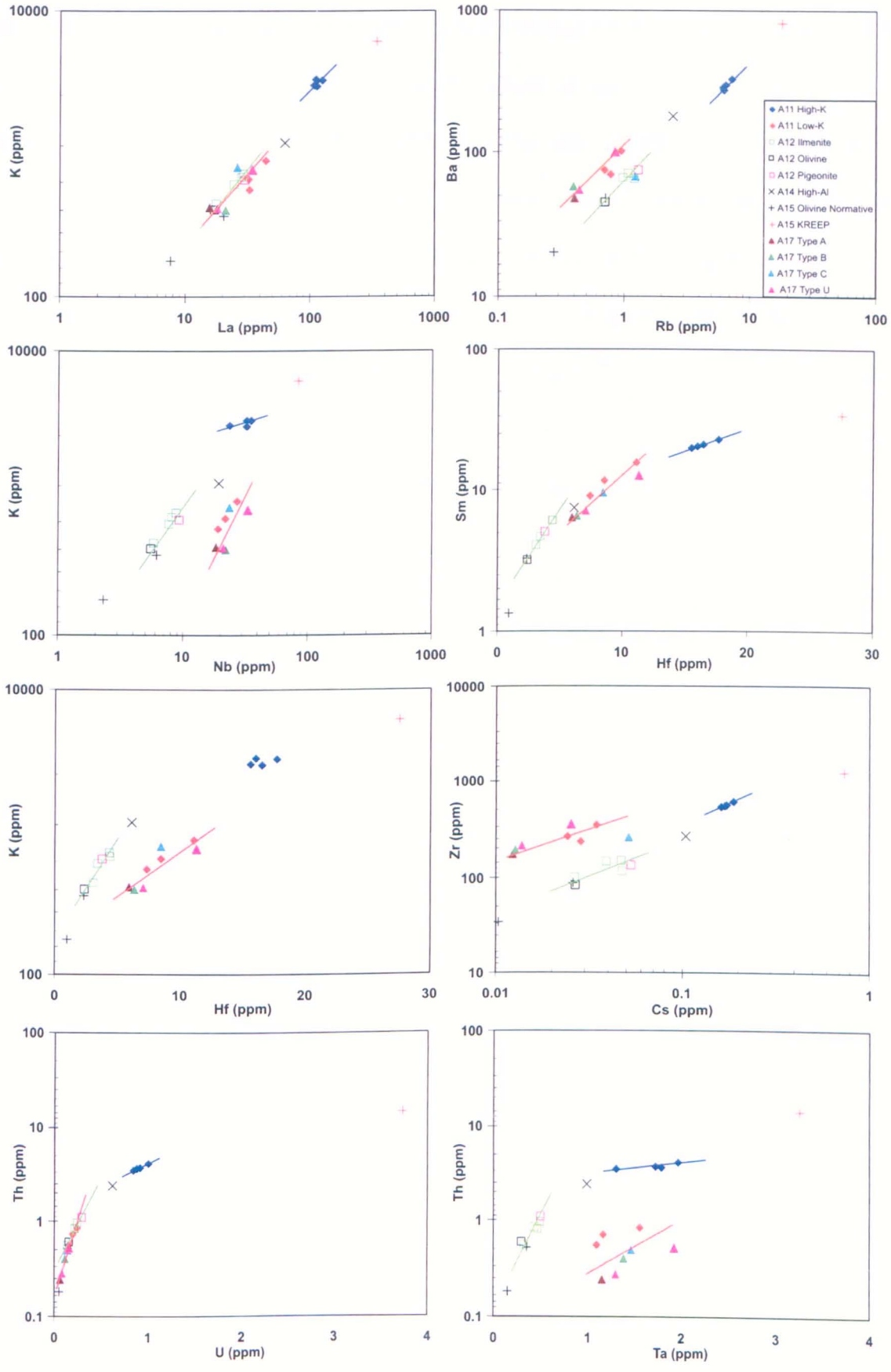

Figure 4.10: Incompatible-element bi-variate plots. Each plot shows the approximate trend line for A11 high-K basalts (blue line), Apollo 11 low-K basalts and Apollo 17 basalts (orange line) and the Apollo 12 and 15 low-K basalts (green line). Sample 15555 shows the lowest abundance for every element, however as these data are almost certainly unreliable it has not been considered when plotting the trend lines.

15386 consistently displays the highest incompatible-element abundance, followed by the tightly clustered Apollo 11 high-K basalts. Apollo 14 high-Al basalt 14053 also contains elevated amounts of K, Rb, Cs, Ba, La, Th and U. Zr, Nb, Sm, Hf, and Ta in this sample plot alongside the remaining mare basalts, often in the gap between the high-and low-Ti groups. Apollo 11 and 17 high-Ti basalts contain higher Zr, Nb, Sm, Hf and Ta than the Apollo 12 and 15 low-Ti basalts. Apollo 17 type A basalt 75055, type B basalt 70215, and unclassified basalt 70017 commonly cluster tightly towards the lower abundances (frequently close to sample 14053), whereas type C basalt 74275 and unclassified basalt 70035 contain slightly higher abundances, similar to the Apollo 11 low-K samples. Apollo 12 olivine basalt 12040 and Apollo 15 olivine-normative basalt 15016 show very similar incompatible-element contents and often (though not always) contain the lowest abundances among all the samples. Apollo 12 ilmenite basalt 12016 commonly plots alongside these two samples, while the remaining ilmenite basalts, along with pigeonite basalt 12052, display slightly higher incompatible-element contents. The Apollo 11 low-K basalts and Apollo 17 basalts commonly plot along a line on these graphs (more defined for some element pairs than for others), indicating these samples have similar ratios of these elements. The Apollo 11 high-K basalts plot along a separate and more defined line, indicating these basalts contain very similar incompatible-element ratios to each other, but significantly different incompatible-element ratios to the other high-Ti basalts within the sample set. Apollo 12 and 15 low-Ti basalts consistently plot along similar incompatible-element trend lines to each other, though the latter appear to contain slightly lower abundances. These basalts commonly plot along entirely separate trend lines to the Apollo 11 low-K and Apollo 17 samples, indicating the low- and high-Ti basalts have significantly different incompatible-element ratios.

Figures 4.11 and 4.12 show previous Rb, Sr, Ba and Pr data alongside the data collected in this study. The Apollo 15 KREEP basalts contain the highest abundances of Ba and Pr,

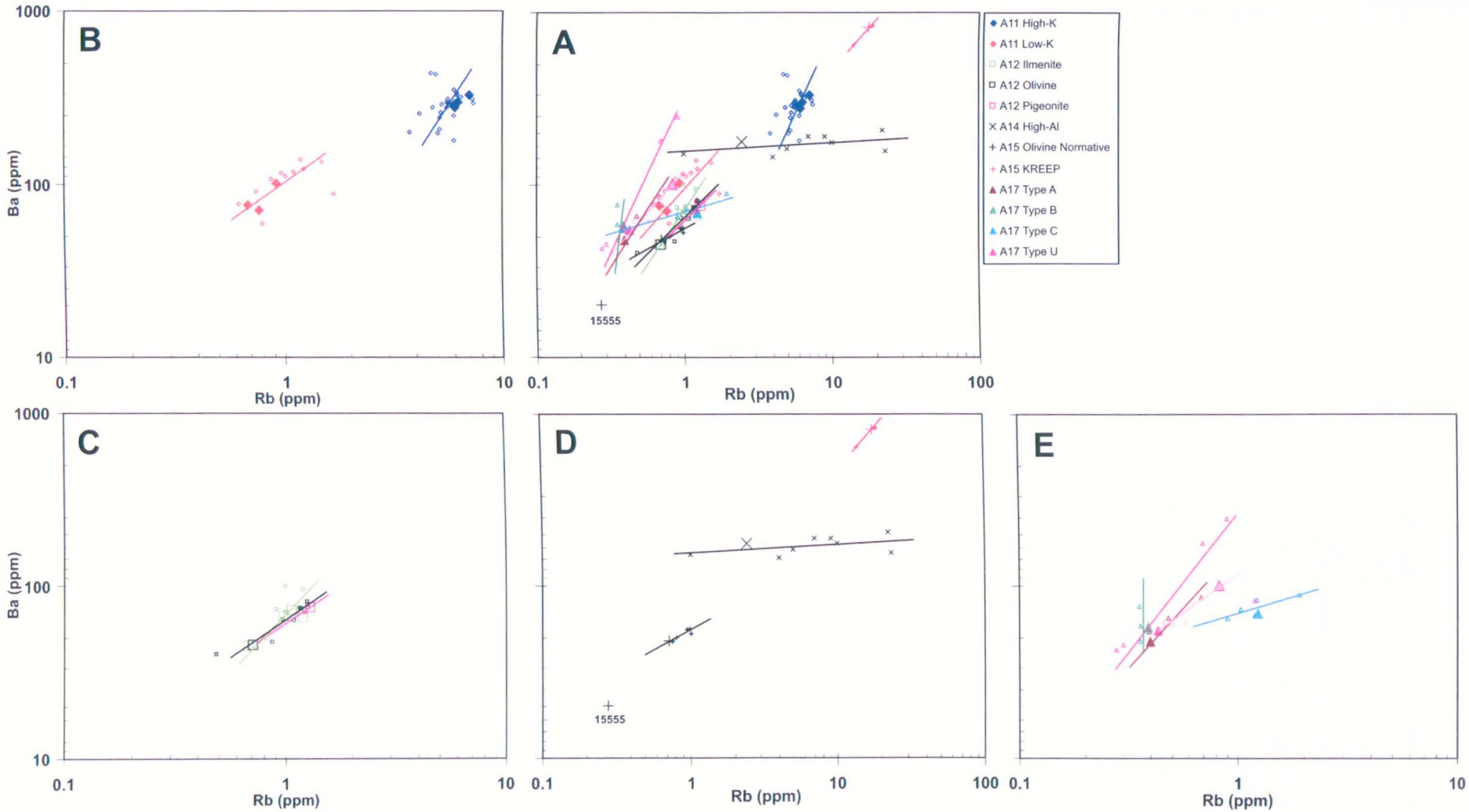

Figure 4.11: Bi-variate plots of Ba vs. Rb, including previously published data. **(a)** Bi-variate plot showing all sample groups represented within our sample set, **(b)** Apollo 11 basalts, **(c)** Apollo 12 basalts, **(d)** Apollo 14 and 15 basalts, and **(e)** Apollo 17 basalts. Trend lines for individual basalt groups correspond to the colour shown for that group in the key. For

Apollo 17 unclassified basalts only previous data for those specific samples are shown. The points and trend line for sample 70017 are shown in bright pink, while sample 70035 data is shown in paler pink to avoid confusion. Large symbols represent our data whereas small symbols represent previously published data.

References: Apollo 11 high-K; LSPET, 1969; Annell and Helz, 1970; Compston et al., 1970; Ganapathy et al., 1970; Gast et al., 1970; Morrison et al., 1970; Murthy et al., 1970; Philpotts and Schnetzler, 1970; Tera et al., 1970; Wakita et al., 1970; Wanke et al., 1970; Wanless et al., 1970; Wassen and Baedecker, 1970; Anders et al., 1971; Smales et al., 1971; Duncan et al., 1976; Nyquist, 1977; Papanastassiou et al., 1977; Beaty and Albee, 1978; Jerde et al., 1994; Snyder et al., 1994; Neal, 2001. **Apollo 11 low-K;** LSPET, 1969; Compston et al., 1970; Tatsumoto, 1970; Tera et al., 1970; Wanless et al., 1970; Duncan et al., 1976; Nyquist, 1977; Rhodes and Blanchard, 1980; Dickinson et al., 1989; Snyder et al., 1994. **Apollo 12 ilmenite;** LSPET, 1970; Gast and Hubbard, 1970; Papanastassiou and Wasserburg, 1970; Anders et al., 1971; Compston et al., 1971; Hubbard and Gast, 1971; Morrison et al., 1971; Papanastassiou and Wasserburg, 1971a; Rhodes et al., 1977; Nyquist, 1977; Nyquist et al., 1977; Unruh et al., 1984; Snyder et al., 1997; Neal, 2001. **Apollo 12 olivine;** LSPET, 1970; Anders et al., 1971; Bottino et al., 1971; Compston et al., 1971; Murthy et al., 1971; Papanastassiou and Wasserburg, 1970; Papanastassiou and Wasserburg, 1971a; Nyquist, 1977; Nyquist et al., 1977; Snyder et al., 1997. **Apollo 12 pigeonite;** LSPET, 1970; Bottino et al., 1971; Compston et al., 1971; Murthy et al., 1971; Schnetzler and Philpotts, 1971; Wanke et al., 1972; Wolf et al., 1979; Warren and Jerde, 1990. **Apollo 14;** LSPET, 1971; Papanastassiou and Wasserburg, 1971b; Ehmann et al., 1972; Hubbard et al., 1972; Morgan et al., 1972; Willis et al., 1972; Neal, 2001; Neal and Kramer, 2006. **Apollo 15 olv. norm.;** Brunfelt et al., 1972; Compston et al., 1972; Christian et al., 1972; Müller, 1972; Murthy et al., 1972; Chappell and Green, 1973; Cuttita et al., 1973; Evensen et al., 1973; Helmke et al., 1973; Mark et al., 1973; Nyquist et al., 1973; Rhodes and Hubbard, 1973; Muller, 1975; Nyquist, 1977; Wolf et al., 1979; Snyder et al., 1998; Neal, 2001; Ryder and Schuraytz, 2001. **Apollo 15 KREEP;** Compston et al., 1972; Hubbard et al., 1974; Nyquist et al., 1974; Nyquist et al., 1975; Vaniman and Papike, 1980; Neal and Kramer, 2003. **Apollo 17 type A;** LSPET, 1973; Shih et al., 1975; Nyquist et al., 1975; Nyquist, 1977. **Apollo 17 type B;** Morgan et al., 1974; Nyquist et al., 1975; Rhodes et al., 1974; Rose et al., 1974; Shih et al., 1975; Wanke et al., 1975; Nyquist, 1977. **Apollo 17 type C;** Duncan et al., 1974; Wanke et al., 1974; Shih et al., 1975; Murthy and Coscio, 1976; Rhodes et al., 1976; Nyquist, 1977; Paces et al., 1991. **Apollo 17 sample 70017;** Brunfelt et al., 1974; Duncan et al., 1974; Philpotts et al., 1974; Rose et al., 1974; Nyquist et al., 1975; Shih et al., 1975; Rhodes et al., 1976. **Apollo 17 sample 70035;** LSPET, 1973; Evensen et al., 1973; Nyquist et al., 1974; Shih et al., 1975.

followed by the Apollo 11 high-K basalts and the Apollo 14 high-Al basalts. The latter group contain a wide spread of Rb and Pr abundance, extending to the highest values of all the samples for Rb, just beyond the Apollo 15 KREEP basalts. Though Sr abundance is high in the KREEP basalts it appears to be more enriched in a number of Apollo 11 and 17 basalts. Apollo 14 high-Al basalts plot amongst the lowest Sr abundances. Element trend lines are drawn for individual groups on these plots. They again highlight the variation between the ratios of Apollo 11 high- and low-K basalts and, in addition, highlight differences between the Apollo 17 basalt groups. The low-Ti basalt groups of Apollo 12

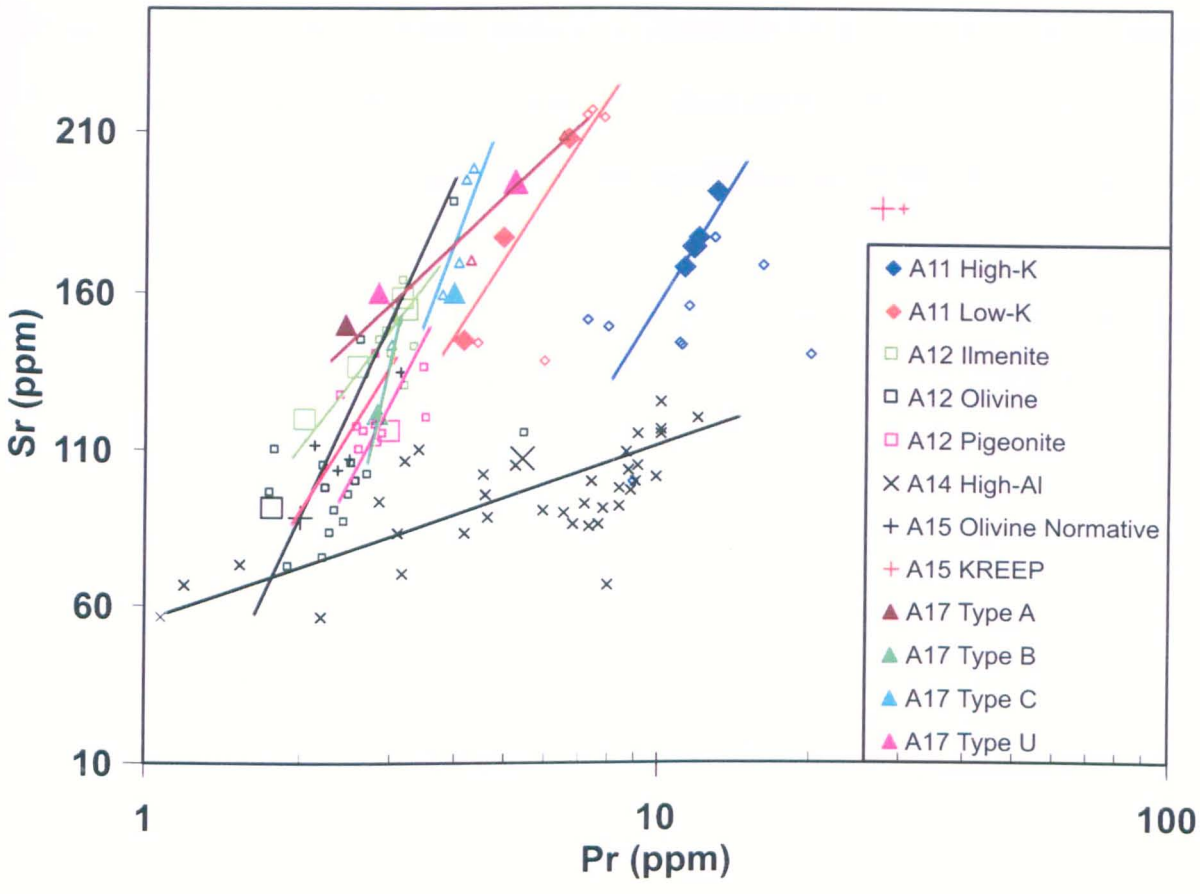

Figure 4.12: Plot showing Sr vs. Pr with previously published data for all groups represented within the sample set. Approximate trend lines are shown for all sample groups in the corresponding colour (see key), except for the trend line of the Apollo 15 olivine normative basalts, which is shown in red for clarity. Sample 15555 does not plot on this graph as its Pr abundance is < 1. Large symbols represent our data, whereas small symbols represent previously published data. References for previously published data as in Figure 4.11.

and 15 show little difference between their incompatible-element ratios, but the low-Ti Apollo 14 high-Al basalts show a completely separate ratio in both Figure 4.11 and 4.12. Neal et al. (1994a) classified the Apollo 12 mare basalts in terms of Rb/Sr ratio and Mg#. According to these authors, the three groups can be separated as follows: olivine basalts have Mg# > 46 and Rb/Sr ratios > 0.008, pigeonite basalts have Mg# < 46 and Rb/Sr ratios > 0.008 and ilmenite basalts have varying Mg# and Rb/Sr ratios < 0.008. Figure 4.13 shows how our data compare with that of this previous study. Apollo 15 KREEP basalt 15386, Apollo 11 high-K basalts and Apollo 14 high-Al basalt 14053 all display Rb/Sr ratios much higher than the Apollo 12 samples analysed by Neal et al. (1994a), as these

basalts have strongly negative strontium anomalies. However, the remaining high-Ti basalts and the Apollo 15 olivine-normative basalts show similar ratios below 0.008. Ignoring sample 15555,982 as unrepresentative of the bulk-rock composition, the high-Ti

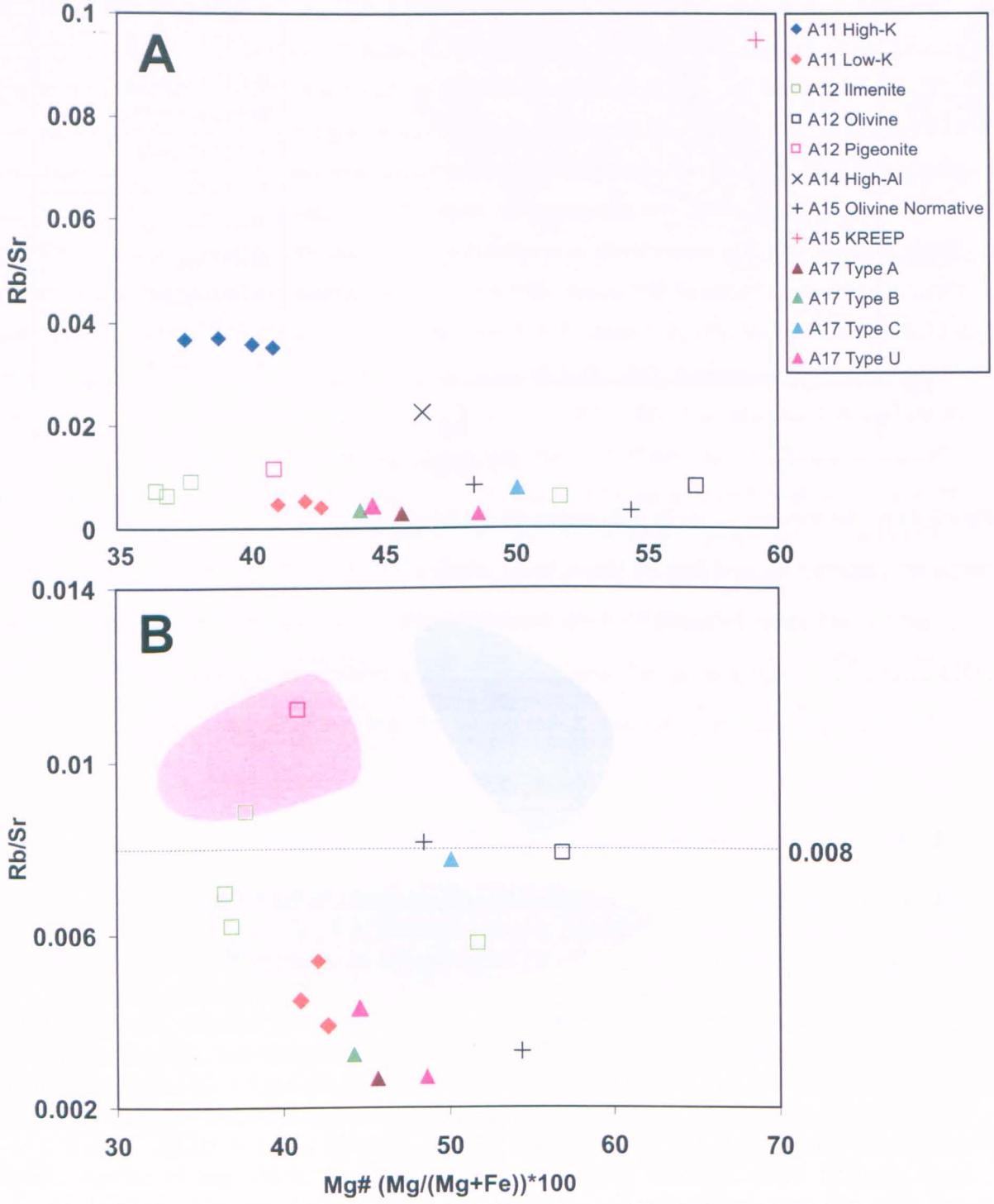

Figure 4.13: Rb/Sr vs. Mg#. The larger scale plot shows all samples **(a),** whereas the smaller scale plot **(b)** focuses on the classification line of Neal et al. (1994a) at Rb/Sr = 0.008. Envelopes on this plot represent the data of this previous study (dark green = A12 olivine basalts, pink = A12 pigeonite basalts and light green = A12 ilmenite basalts).

basalts of Apollo 17 and 11 (low-K) show the lowest Rb/Sr ratios, with the exception of sample 74275 (just below the 0.008 line). Apollo 12 pigeonite basalt 12052 and ilmenite basalts 12016, 12047 and 12051 fit within the relevant regions of the Neal et al. (1994a) classification, but olivine basalt 12040 plots just below the Rb/Sr classification line (0.0079) and ilmenite basalt 12064 plots just above (0.0088) within the pigeonite basalt region.

4.2.3. Compatible Trace-Elements. As the transition metals have small ionic radii and low charge they are generally more compatible in mineral crystal lattices than the REE's and large ion lithophile elements (LILE's) discussed above. The compatibility of these elements causes their abundance to change dramatically as a result of geological processes (e.g., fractional crystallisation). Figure 4.14 shows the variations in bulk-rock Sc, V and Cr contents with bulk-rock Mg# for our measured data, along with previously published data for samples within the same basalt groups. Sc is most abundant within the high-Ti basalts, but its abundance does not change significantly with Mg#. Apollo 15 basalts (both KREEP and olivine-normative) contain the lowest Sc concentrations and also show no change with Mg#. Apollo 12 low-Ti basalts show increasing Sc concentrations with decreasing Mg#, all following roughly the same trend – average olivine and pigeonite basalt Sc abundances are slightly lower than those of the ilmenite basalts, but there is a large degree of overlap between the two groups. V contents are higher in the low-Ti than the high-Ti basalts, but show no significant change with Mg# in the former. Apollo 17 type B, C and unclassified basalts contain slightly higher V abundances than the type A and Apollo 11 basalts, both groups show a decrease in V concentration with decreasing Mg# though the trend is not as coherent as with Apollo 12 Sc content. The same trend is visible for Cr content in the Apollo 17 basalts, this time along with the Apollo 12 basalts. The Apollo 15 and 11 basalts show no trend. Apollo 14 high-Al basalts show increasing Sc, V and Cr contents with decreasing Mg#.

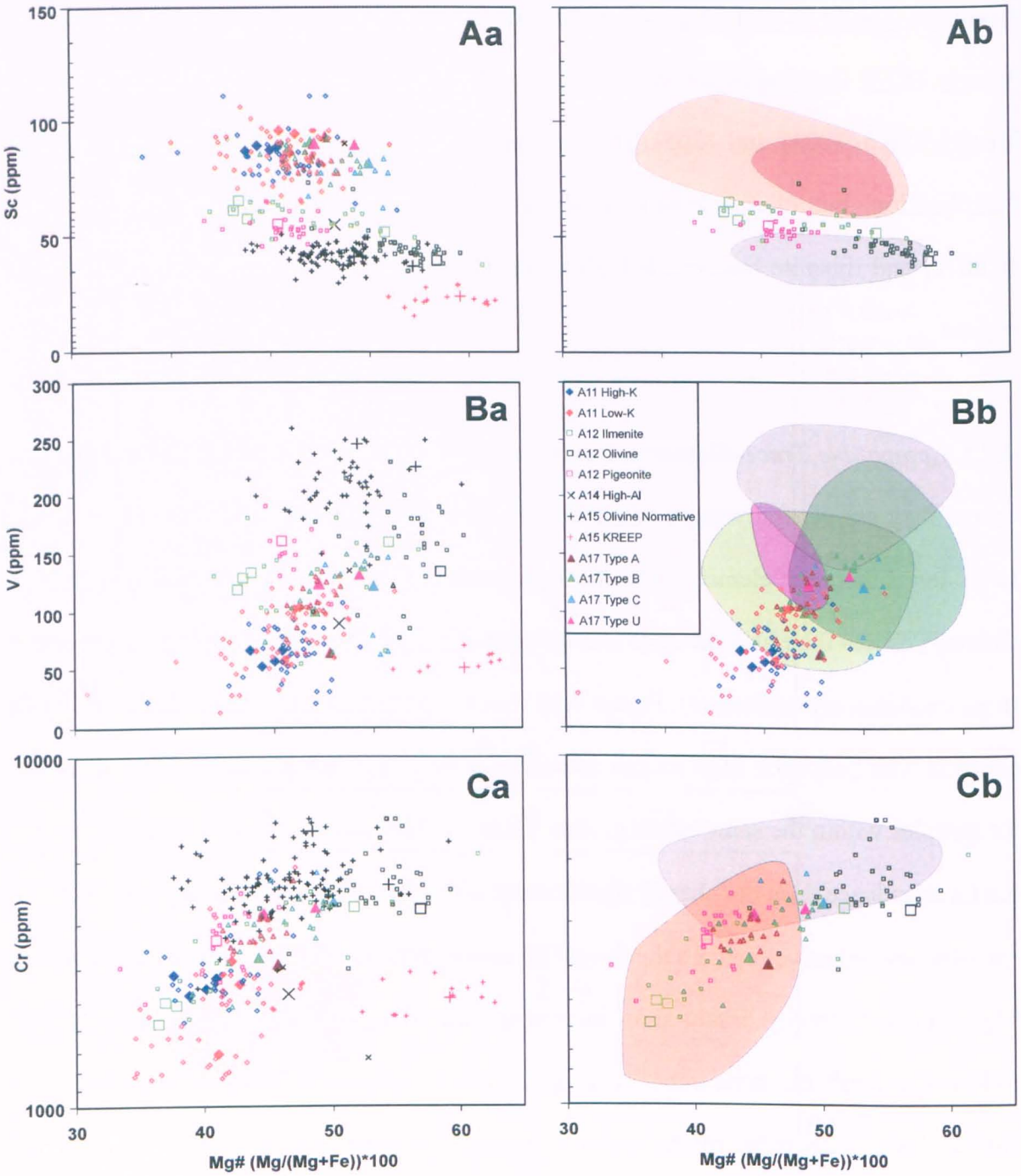

Figure 4.14: Compatible-element plots with previously published data. Mg# vs. Sc **(aa and ab)**, Mg# vs. V **(ba and bb)** and Mg# vs. Cr **(ca and cb)**. Plots **(ab)**, **(bb)** and **(cb)** show basalt groups with the strongest trends as data points, other groups are represented by coloured envelopes (grey envelope = A15 olivine normative, orange envelope = A11 basalts, brown envelope = A17 basalts and light green, dark green and pink envelopes = A12 ilmenite, olivine and pigeonite basalts). Large symbols represent our data, whereas small symbols represent previously published data. References for previously published data as in Figure 4.11.

4.3. Discussion

4.3.1. Apollo 12 and 15 Low-Ti basalts. The wide range in major-element compositions shown from our data set (especially for Al_2O_3, MgO and FeO) and those from previous works (Figure 4.1 and 4.2) indicate that the low-Ti mare basalts are chemically diverse, both between samples collected at different sites and those collected from the same site. For samples within the same group (e.g., the Apollo 12 ilmenite basalts) chemical diversity highlights the role of crystal fractionation (and in some cases accumulation) in the evolution of the mare-basalt melts. These observations are in agreement with our mineralogical data (chapter 3) and previous petrological studies (e.g., Kushiro and Haramura, 1971; Rhodes et al., 1977; Neal and Taylor, 1992; Neal et al., 1994a; Ryder and Schuraytz, 2001; Schnare et al., 2008). Lack of agreement between predicted MELTS equilibrium crystallisation sequences and the observed crystallisation sequences (section 3.4, Table 3.2) also suggests fractional rather than equilibrium crystallisation was the dominant process during the cooling and crystallisation of low-Ti mare-basalt magmas. The spread of bulk-rock REE abundances and compatible-element ratios between samples from the same source (e.g., the Apollo 12 ilmenite basalts) indicates a high degree of fractionation during the crystallisation of these samples. Increasing Sc abundances with decreasing Mg# indicates olivine fractionation occurred in the Apollo 12 mare basalts. In addition, ilmenite basalts 12051 and 12064 contain $\geq$ 11 wt % Al_2O_3, believed to be because of olivine fractionation rather than origin from a high-Al parental melt (Dungan and Brown, 1977; Neal and Taylor, 1992). Both our data and that of previous studies (Figure 4.1 and 4.2) highlight similarities between the major-element data of Apollo 12 and Apollo 15 low-Ti basalts. However, the Apollo 15 olivine-normative basalts do show a slight TiO_2 depletion and Cr_2O_3 enrichment compared to the Apollo 12 samples. Incompatible trace-element bi-variate plots (Figure 4.10-4.12) show comparable incompatible-element ratios for Apollo 12 and 15 low-Ti basalts, but compatible-element data indicate the Apollo 15 low-Ti basalts contain more V and less Sc than Apollo 12 low-

Ti basalts (Figure 4.14), and less variation in Cr with decreasing Mg#. Compatible-elements are more sensitive to post-melting processes such as crystal fractionation (compared to incompatible-elements), therefore major- and trace-element comparisons show that the Apollo 12 and 15 mare-basalts were produced from compositionally similar (though not the same) source regions, but have followed different melt evolution pathways (e.g., the strong decrease in Cr with increasing Mg# in Apollo 12 basalts is probably the result of Cr-rich spinel fractionation).

As would be expected of two basalt groups from separate sources, the Rb/Sr ratios of the Apollo 15 basalts within our sample set do not fit into the Apollo 12 classification of Neal et al. (1994a) (Figure 4.13). Previously recorded Apollo 15 low-Ti Rb/Sr ratios vary from 0.007 to 0.010 (Chappell and Green, 1973; Rhodes and Hubbard, 1973; Ma et al., 1978; Ryder and Steele, 1988; Vetter et al., 1989), straddling the dividing line of Neal et al. (1994a). Our trace-element data place Apollo 15 sample 15016 at the centre of this group, but once again our data for sample 15555,982 are not representative of the whole sample, showing a Rb/Sr ratio of 0.003 compared to previously published values of 0.006-0.009 (Chappell and Green, 1973; Rhodes and Hubbard, 1973; Neal et al., 2001). Both Apollo 15 low-Ti samples within our sample set are classified as olivine-normative; the quartz-normative basalts are not represented. However, previously published data show no distinction between the Rb/Sr ratios of these two Apollo 15 basalt types (e.g., Christian et al., 1972; Compston et al., 1972; Nyquist et al., 1972; Chappell and Green, 1973; Cuttita et al., 1973; Rhodes and Hubbard, 1973; Neal, 2001), indicating they originate from the same source region. Mineralogical and chemical differences between the Apollo 15 quartz- and olivine-normative basalts must therefore be related to post melting fractionation effects, as suggested by Schnare et al. (2008). Though the separation of Apollo 12 low-Ti basalts into olivine, pigeonite and ilmenite basalts had been previously recognised via mineralogical and chemical investigations (James and Wright, 1972; Walker et al., 1976a; Rhodes et al.,

1977; Baldridge et al., 1979), the Rb/Sr classification of Neal et al. (1994a) further validated this separation and re-classified ambiguous samples (e.g., 'feldspathic' basalts 12031 and 12072 were found to be ilmenite basalts). Despite the slightly anomalous Rb/Sr ratios of samples 12040 and 12064 it is clear from our data and the mineralogical modes of these samples (Table 3.1) that all Apollo 12 basalts within our sample set have been correctly classified.

Comparison of olivine forsterite content with bulk-rock Mg# reveals that olivine basalt 12040 contains extensive amounts of accumulated olivine, in agreement with Meyer and Wilshire (1974) and Baldridge et al. (1979). Olivine accumulation explains this sample's high bulk-rock MgO and low Al_2O_3 and CaO abundances, and the lack of correlation between Cr_2O_3 and MgO - accumulated olivine grains are not consistently associated with spinel grains, therefore MgO abundance increases while that of Cr_2O_3 remains relatively constant. The bulk-rock chemistry of sample 12040 also yields an incorrectly high MELTS liquidus temperature, which has been increased by excessive MgO content. Addition of olivine to this sample has significantly lowered the wt % of all elements not present in olivine, hence MELTS calculations incorrectly predict that the parental melt was too Ti-depleted for ilmenite crystallisation. As discussed in section 3.3.2, the calculated parental melt REE data for sample 12040,44 do not match measured bulk-rock REE for sample 12040,206. Olivine accumulation decreases bulk-rock REE content as it is a REE-poor mineral, therefore calculated melt REE data based on abundance within pyroxene may be more reliable than measured bulk-rock REE data for this sample. The calculated data indicate olivine basalt 12040 originated from a melt enriched in these elements compared to the other Apollo 12 and 15 low-Ti basalts. MgO-rich ilmenite grains and high Sc abundances within these measured pyroxenes suggest the parental melt of sample 12040 was Mg- and Sc-rich, therefore probably not highly evolved - indicating the Apollo 12

olivine basalt source may have been inherently enriched in incompatible-elements compared to the other Apollo 12 and 15 low-Ti sources.

MgO enrichment, along with other major- and trace-element depletions, are shown to a lesser extent by ilmenite basalt 12016 (Figures 4.1-4.3, 4.10-4.12 and 4.14). The measured REE content in this sample is slightly lower than the calculated REE content, indicating a small amount of olivine accumulation may have occurred (Figure 4.9), but this process was weak compared to the accumulation within sample 12040. Measured bulk-rock REE abundance matches well with the calculated REE abundance for sample 15016, despite the fact that the Garcia plot indicates a small amount of olivine accumulation may have occurred. This indicates sub-solidus re-equilibration occurred in this sample's olivine grains. Our REE bulk-rock analysis of sample 15555,982 produced unrepresentative data for sample 15555 as a whole, but the Garcia plot suggests significant olivine accumulation occurred within this sample. In agreement, comparisons of previously published data for sample 15555 (Brunfelt et al., 1972; Fruchter et al., 1973; Neal, 2001; Ryder and Schuraytz, 2001) and the Apollo 15 olivine-normative parental melt composition (Vetter et al., 1989; section 4.4.1) indicate varying amounts of crystal accumulation did occur within this heterogeneous basalt. No mineralogical evidence or previous research suggests olivine accumulation occurred in Apollo 12 pigeonite basalt 12052 or Apollo 14 high-Al basalt 14053, comparisons of the measured REE abundance of these samples with their parental melts (Snyder et al., 1997; Neal and Kramer, 2006) indicate crystal fractionation occurred in both.

4.3.2. Apollo 11 and 17 High-Ti basalts. The Apollo 11 low-K basalts show varying trace-element abundances, from type B3 basalt 10020 with the lowest Mg# and REE abundance, to type B1 basalt 10058 with the highest Mg# and REE abundance (Figure 4.8). Despite this apparent evolution, these three samples are members of separate basalt groups which

cannot be related via direct shallow level crystal fractionation (sample 10050 is an unclassified low-K basalt) - La/Sm ratios were found to vary too widely at similar Co abundances (Beaty and Albee, 1978; Beaty et al., 1979a,b; Rhodes and Blanchard, 1980, appendix E). However, Snyder et al. (1992b, 1993) and Jerde et al. (1994) suggest that these two groups may have originated from the same source at different periods in time. To explain differing Sm/Nd (and La/Sm) ratios between the two basalt groups Snyder et al. (1992b, 1993) suggested melting of the source at 3.71 Ga producing the B3 basalts, and later melting (at ~ 3.67 Ga) of a portion of the same source region, with slightly less trapped liquid component, resulting in B3-like basalts which fractionated to the Bl compositions.

Major- and trace-element data collected in this study, along with that of previous studies (e.g., Paces et al., 1991; Neal and Taylor, 1992) suggest that all of the Apollo 11 high-K basalts originate from the same melt. The evolution of this melt can be tracked in our samples - REE abundances are relatively constant for all four Apollo 11 high-K samples, but melt evolution is visible in the increasing abundances of other incompatible-elements (Figure 4.10 - 4.12), where sample 10017 appears to be the most primitive and sample 10049 is the most evolved.

The Apollo 17 basalts within our sample set represent five different basalt groups originating from separate melts (Shih et al., 1975; Rhodes et al., 1976; Warner et al., 1979; Ryder, 1988, 1990). However, the similarities in both major- and trace-element abundances for the Apollo 11 type B3 and Apollo 17 type A basalts (samples 10020 and 75055) indicate that these basalt types originate from similar source compositions, in agreement with Neal et al. (1990a). Snyder et al. (1990) also suggested that the Apollo 11 type B3 and Apollo 17 type C basalts share chemical characteristics, and therefore originate from similar melts. Bulk-rock REE abundances and Sm/Hf ratios within Apollo

11 type B3 basalt 10020 and Apollo 17 type C basalt 74275 are similar, but other trace-element and major-element abundances do not suggest any close relationship between these two samples.

Apollo 17 basalts 70017, 70035 and 74275 display olivine Fo % lower than expected based on their bulk-rock MgO wt %, suggesting olivine accumulated in these samples (Figure 4.6). As with low-Ti Apollo 12 olivine basalt 12040 this accumulation results in artificially low bulk-rock REE's when compared to REE abundances calculated from pyroxene compositions (Figure 4.9). Apollo 17 type C basalt 74275, along with non-cumulate type B basalt 70215, shows calculated REE abundances far higher than unclassified basalts 70017 and 70035. As pyroxene in samples 74275 and 70215 crystallised relatively late, after the crystallisation of the non REE-bearing minerals olivine, spinel, armalcolite and ilmenite (Table 3.2), the REE's were concentrated into pyroxene - leading to an artificially high melt REE calculation for both samples. Interpretation of the REE signature of sample 74275 is further complicated by the observations of Meyer and Wilshire (1974) and Delano and Lindsley (1982), who reported the presence of Mg-rich olivine xenocrysts in this sample. None of these grains was observed within thin section 74275,310, but they may have been present within rock chip sample 74275,323. Heterogeneity of this kind between the two 74275 samples could complicate interpretations of data on the Garcia plot. If sample chip 74275,323 contained olivine xenocrystic material, the measured MgO wt % would be higher than expected for the Fo % of native olivines in thin section 74275,310, thus giving the impression of olivine accumulation as seen on the plot (Figure 4.6). Donohue and Neal (2009) used crystal size distribution calculations to conclude that large olivine xenocrysts accumulated within the source magma chamber of the Apollo 17 type C basalts. These xenocrysts were produced by an Mg-rich melt, but rather than erupting with this melt they sank down and accumulated within the parental melt of Apollo 17 type C basalts. The olivine xenocrysts were carried to the surface upon eruption of this melt.

Donohue and Neal (2009) suggest the native olivines (those analysed in thin section 74275,310) were not accumulated. The measured bulk-rock REE abundances of this sample plot close to those of the proposed parental melt of the Apollo 17 type C basalts (Snyder et al., 1992). As it formed from an evolved melt, the REE abundances in sample 74275 should plot above those of the more primitive parental melt, but the presence of olivine xenocrysts would lower the REE abundances – this comparison may, therefore, suggest olivine xenocrysts were present in rock chip sample 74275,323.

The single embayed olivine phenocryst analysed in Apollo 11 high-K basalt thin-section 10072,40 (section 3.1.7, Figures 3.13 and 3.14) probably has a similar petrogenesis to the olivine xenocrysts of sample 74275. Garcia plot (Figure 4.6) and electron microprobe data (Figure 3.47) show the core of this grain is slightly more Mg-rich than could have been produced from the parental melt of sample 10072. Its trace-element characteristics match those of the other Apollo 11 olivine grains, confirming that it was produced by mare volcanism and is not a country-rock xenocryst. This grain was most probably produced in the same magma body as the parental melt of sample 10072 (and the other Apollo 11 high-K basalts) but at a slightly earlier time, and may have subsequently accumulated within the more evolved parental melt of sample 10072. Alternatively, it may have been trapped within the volcanic vent upon the eruption of its parental melt and released during the eruption of the more evolved Apollo 11 high-K basalt melt. As the Garcia plot does not show any evidence of significant olivine accumulation, and none is discussed in previous studies of this sample (James and Jackson, 1970; Schmitt et al., 1970; McGee et al., 1977; Beaty and Albee, 1978), the latter possibility appears to be more probable.

MELTS equilibrium crystallisation data for the high-Ti basalts show major inconsistencies in the predicted crystallisation sequences (Figure 4.5) compared to those observed in the samples (Table 3.2). This suggests that the high-Ti basalts within our sample set are

significantly affected by crystal fractionation/accumulation (as are the low-Ti basalt samples). This observation is supported by mineralogical evidence (chapter 3) and the studies of previous authors (e.g., Kesson, 1975; Neal et al., 1990a; Paces et al., 1991; Neal and Taylor, 1992). Decrease in the V and Sc content of the high-Ti mare basalts with decreasing Mg# suggests ilmenite and pyroxene fractionation occurred within these melts (V is highly compatible in ilmenite and Sc is compatible in clinopyroxene). The Apollo 17 samples also show a decrease in Cr abundance with decreasing Mg#, indicating Cr-rich spinel also fractionated from these melts.

Apollo 17 basalts extend to higher TiO_2 abundances than the Apollo 11 samples, with several type B, C and unclassified samples containing over 11 wt % TiO_2 (e.g., Brunfelt, 1974; Hodges and Kushiro, 1974; Boynton et al., 1975). The Apollo 17 basalts do not contain as much CaO and Al_2O_3 as the most Ca and Al-rich Apollo 11 basalts - in general these are the low-K Apollo 11 samples, though there is overlap between low and high-K Al_2O_3 contents. A number of unclassified, type B and C Apollo 17 basalts are enriched in MgO, V and Cr compared to the type A samples and Apollo 11 basalts. V and Cr enrichment can be explained by the high ilmenite and spinel modal abundances in Apollo 17 type B, C and unclassified basalt source regions. High MgO abundance suggests these samples are more primitive than the Apollo 17 type A and Apollo 11 basalts, but as the Apollo 11 low-K and Apollo 17 basalts all show similar REE and LILE contents (Apollo 11 high-K REE and LILE content is discussed below) the difference in MgO content cannot be related to the basalt evolution. Therefore, compositional differences between the two basalt groups were probably controlled by fundamental differences in their source regions – the Apollo 17 type B, C and the majority of the unclassified basalts (from now on referred to as the Apollo 17 group) formed from a source enriched in TiO_2, MgO, Cr and V and depleted in Al_2O_3 and CaO compared to the type A and Apollo 11 basalts (from now on referred to as the Apollo 11/17 type A group). Various authors have suggested that the

high-Ti mare-basalt sources formed through mixing of ilmenite and olivine-pyroxene cumulates (section 1.1.5; Ringwood and Kesson, 1976; Ryder, 1991; Snyder et al., 1992; Elkins-Tanton et al., 2002). Snyder et al. (1992) proposed that the modal mineralogy of the cumulate mix required to produce high-Ti mare basalts was 46 % pigeonite, 43 % olivine, 7 % augite, 3 % ilmenite, 1 % plagioclase and a small amount of trapped KREEPy liquid. A cumulate mix with less ilmenite, but more augite, would correspond to the decrease in TiO_2 and increase in CaO observed between the Apollo 17 and Apollo 11/17 type A sample groups. A slight increase in plagioclase content and corresponding decrease in pyroxene/olivine content would further account for the Al_2O_3 enrichment and MgO depletion between the Apollo 17 group and Apollo 11/17 type A group. Therefore, the Apollo 17 group may have been created by a cumulate mix enriched in ilmenite, olivine and pigeonite and depleted in plagioclase and augite compared to the Apollo 11/17 type A group. The amount of trapped KREEPy liquid would have had to be similar in both source types to produce the similar REE and incompatible-element abundances observed in samples from both groups.

Separation of the Apollo 11 low and high-K basalts is not simply based on differing K abundances. Incompatible-elements, P_2O_5 and Na_2O are also more abundant in the high-K basalts, whereas MgO, Al_2O_3 and Cr_2O_3 are depleted in these samples compared to the low-K basalts (Table 4.1, Figures 4.1-4.3). Incompatible-element ratios for our Apollo 11 high-K samples are all similar to each other, but significantly different to those of the low-K samples (Figure 4.10- 4.12). Additionally, the Rb/Sr ratios are much higher in the former (Figure 4.12). Previous studies also highlight these differences (e.g., Haskin et al., 1970; Philpotts and Schnetzler, 1970; Rhodes and Blanchard, 1980; Neal, 2001), indicating these two sample groups did not originate from similar source compositions, and that the high-K samples were probably all from the same melt. Incompatible-elements normally occur in low concentrations in most crystalline mare-basalts and volcanic glasses, either because the

source regions were intrinsically depleted in these elements or because the source region cumulates were composed of minerals that do not readily incorporate them (Wieczorek et al., 2006). Where basalt groups display incompatible-element abundances higher than expected, assimilation/contamination is suspected. Contamination may be the result of either melt assimilation of trace-element enriched crustal material or source region enrichment in incompatible-elements. The elevated abundances of K and P in the high-K basalts, along with strong europium and strontium anomalies, and LREE enrichment compared to the low-K samples (Figure 4.8-4.9), imply that these basalts have undergone KREEP contamination. Granitic contamination can be discounted as La/K ratios within these samples are similar to those of the Apollo 11 low-K basalts rather than the Apollo 14 VHK basalts - the latter are believed to have been contaminated by a granitic component (Shervais et al., 1985b; Neal et al., 1989b; Neal and Kramer, 2006). If the Apollo 11 high-K basalts were the result of KREEP assimilation, the final melt must have contained > 5 % assimilant to produce the observed K concentrations (Neal and Taylor, 1992). Assuming these samples originated from a melt similar to the Apollo 11 low-K basalts this amount of KREEP assimilation would have resulted in basalt samples with strong characteristic KREEP LREE enrichments. As this enrichment is not visible, either the KREEP component was present in the source (as suggested by Paces et al., 1991 and Neal and Taylor, 1992) or the melt composition was significantly different to that of the Apollo 11 low-K basalts (as suggested by Jerde et al., 1994).

4.3.3. Apollo 15 KREEP basalts and Apollo 14 low-Ti, high-Al basalts. In addition to containing high amounts of incompatible trace-elements, K_2O and P_2O_5, the Apollo 15 KREEP basalts are rich in Al_2O_3, SiO_2 and Na_2O compared to the mare basalts, and are relatively poor in FeO, TiO_2 and MnO (Figure 4.1-4.3, Table 4.1). They show a positive correlation between bulk-rock CaO and MgO, in contrast to mare basalts, probably because of the presence of orthopyroxene in association with high-Ca pyroxene. The Apollo 14

high-Al basalts are also Al_2O_3, K_2O and Na_2O rich, though for the latter two elements both the Apollo 11 high-K samples and Apollo 15 KREEP basalts contain higher abundances. Apollo 14 high-Al basalts are FeO depleted, not to the extent of Apollo 15 KREEP basalts but more than the Apollo 11 high-K basalts. This FeO depletion delays the crystallisation of ilmenite and spinel, resulting in V and Cr enrichment in the more evolved Apollo 14 high-Al basalts. Sc abundance also increases with decreasing Mg#, indicating olivine fractionation occurred in these melts. Incompatible-element abundances also highlight the similarities between KREEP basalts and the Apollo 14 high-Al and Apollo 11 high-K mare basalts. Both Apollo 11 high-K basalts and Apollo 14 high-Al basalts show incompatible-element ratios between those of the Apollo 15 KREEP basalts and the other mare basalts, with Apollo 11 high-K basalts always plotting closest to the KREEP compositions (Figure 4.10-4.12). Apollo 15 KREEP basalt 15386 shows a typical KREEPy REE signature, overall high abundance with strong LREE enrichment, relative HREE depletion, deeply negative europium and strontium anomalies, and a slightly convex upwards trend (Figure 4.8). These distinctive characteristics are fingerprints of a parental melt derived from a source region corresponding to the very end of LMO solidification. Apollo 14 high-Al basalt 14053 shows LREE enrichment compared to the HREE's, and does have a slightly convex upwards trend, but its overall REE abundance is in line with the more REE enriched low-Ti mare basalts (excepting the LREE's). The europium and strontium anomalies of sample 14053 are also similar to the low-Ti mare basalts. From the above data, and that of previous studies (see Figure 4.1 and 4.11 Apollo 14 references), it is clear that the Apollo 14 high-Al mare-basalt melts were contaminated with a material rich in incompatible-elements, especially LREE's and Rb. However, as the Apollo 14 high-Al basalts do not appear to be as enriched in incompatible-elements as the Apollo 11 high-K basalts, either the contaminant was of a different composition or contamination was weaker in the former.

Previous studies of the Apollo 14 mare basalts initially grouped the samples into five different types, from LREE enriched to LREE depleted (Dickinson et al., 1985; Shervais et al., 1985a). Subsequent research expanded these groups to form a continuum (Neal et al., 1988a, 1989b), where sample 14053 occupies the centre, the trydimite ferrobasalt group and 14321-type group show relative LREE enrichment, and the 14072-type group and LREE depleted group show relative LREE depletion. Both Dickinson et al. (1985) and Shervais et al. (1985a) noted that the individual groups could not be related via crystal fractionation, and as Dasch et al. (1987) demonstrated that the volcanism represented by these sample groups lasted approximately 300-400 Ma, the same fractional crystallisation process could not have operated for this period of time. Dasch et al. (1987) suggested that the different Apollo 14 mare-basalt groups formed via separate partial melts and varying amounts of KREEP assimilation. Neal and Taylor (1990) used the age data produced by Papanastassiou and Wasserburg (1970) and Dasch et al. (1987) to modify the assimilation with fractional crystallisation (AFC) model to include separate events at 4.3 Ga , 4.1 Ga and 3.9 Ga, suggesting basalts of all five compositions could occur at all proposed ages. Samples within these three age groups were defined as group A, B and C basalts by Neal and Kramer (2006), where sample 14053 fits into group C. Further details of this model have been debated in publications by Shih and Nyquist (1989), Hughes et al. (1990) and Neal and Taylor (1990, 1992), Snyder et al. (2000), Snyder and Taylor (2000, 2001), Kramer and Neal (2003), and Neal and Kramer (2006). While most authors now agree that the Apollo 14 high-Al group B and C basalts have undergone assimilation the exact composition of the assimilant(s) is still debated.

4.3.4. Comparisons of the Low- and High-Ti basalts. Compared to the low-Ti mare basalts, the high-Ti basalts show less variation in MgO and Al_2O_3 content, are relatively enriched in Na_2O and depleted in Cr_2O_3 and SiO_2, when compared to the low-Ti basalts (Figure 4.1 - 4.3). Higher abundances of incompatible-elements and Sc also differentiate

the high-Ti basalts from the low-Ti (Figure 4.10 - 4.14). The bulk-rock REE abundances of the low-Ti samples are generally lower than those of the high-Ti samples within our sample set, and show a weaker negative europium anomaly, reflecting source region compositional variation between the high- and low-Ti mare basalts. Other incompatible-element ratios also highlight differences between the high- and low-Ti source regions, in addition to the separate nature of the Apollo 11 high-K basalts, Apollo 14 high-Al basalt 14053 and Apollo 15 KREEP basalt 15386. In general, the high-Ti basalts of Apollo 11 and 17 contain greater amounts of incompatible-elements than the Apollo 12 and 15 low-Ti basalts, although K, La, U, Th, Cs, Rb and Sr show similar values in both groups. High incompatible-element abundance can be the product of small amounts of partial melting in a source, therefore, if the high-Ti basalts were the product of smaller degrees of partial melting, and the low-Ti basalts were produced form greater percentage partial melts, the high-Ti basalts should contain higher incompatible-element abundances. However, the fact that some incompatible-element abundances are similar in both basalt types suggests the source regions for low and high-Ti basalts contained inherently different amounts of trace-elements, with the high-Ti source being enriched in the majority of incompatible-elements. High Ni abundances (Table 4.1; Taylor, 1982) indicate that it was enriched within the low-Ti source region compared to the high-Ti. Based on this Ni enrichment, Taylor (1982) suggested the low-Ti basalt melts interacted with a primitive lunar source rich in Ni because of primitive olivine accumulation in the LMO. Na_2O appears to have been relatively depleted in the low-Ti source. All of these differences can be explained if the low-Ti basalts were produced from olivine-pyroxene cumulate sources which formed during 0-80 % crystallisation of the LMO, and the high-Ti basalts were formed as a result of mixing of these olivine-pyroxene cumulates with late stage ilmenite cumulates which formed at $\geq$ 95 % LMO crystallisation (e.g., Wood et al., 1970b; Ringwood and Kesson, 1976; Ryder, 1991). As the ilmenite cumulates formed late they would be relatively enriched in incompatible-elements and show a stronger negative europium anomaly,

Table 4.3: Summary of bulk-rock compositional data for each sample.

	Type	Sample	Characteristics
Apollo 11	High-K	10017	K-, incompatible element-, Na- and P-rich. high Rb/Sr ratio. V decrease with Mg# (indicating ilmenite fractionation).
		10049	K-, incompatible element-, Na- and P-rich. high Rb/Sr ratio. V decrease with Mg# (indicating ilmenite fractionation).
		10057	K-, incompatible element-, Na- and P-rich. high Rb/Sr ratio. V decrease with Mg# (indicating ilmenite fractionation).
		10072	K-, incompatible element-, Na- and P-rich. high Rb/Sr ratio. V decrease with Mg# (indicating ilmenite fractionation). Olivine xenocryst.
	Low-K	10020	Low Mg# and REE abundance compared to other 2 A11 low-K samples. REE abundances and Sm/Hf ratios similar to A17 type C basalt 74275.
		10050	Intermediate Mg# and REE abundance compared to other 2 A11 low-K samples. Apears to be generally compositionally interemediate
		10058	High Mg# and REE abundance compared to other 2 A11 low-K samples. Slightly younger than B1 basalts.
Apollo 12	Olivine	12040	High Mg# compared to other A12 samples and all other samples in our suite (because of olivine accumulation). Rb/Sr ratio > 0.008.
	Ilmenite	12016	High Mg# compared to other A12 ilmenite basalts in our sample suite (high olivine vol %). Rb/Sr ratio < 0.008. Increasing Sc abundances with decreasing Mg#
		12047	Rb/Sr ratio < 0.008. Increasing Sc abundances with decreasing Mg# (indicating olivine fractionation). Low REE abundances.
		12051	Rb/Sr ratio < 0.008. Increasing Sc abundances with decreasing Mg# (indicating olivine fractionation). Low REE abundances. > 11 wt % Al
		12064	Rb/Sr ratio < 0.008. Increasing Sc abundances with decreasing Mg# (indicating olivine fractionation). Low REE abundances. > 11 wt % Al
	Pigeonite	12052	Rb/Sr ratio > 0.008, Mg# < 45. Increasing Sc abundances with decreasing Mg# (indicating olivine fractionation). Low REE abundances.
Apollo 14	High-Al	14053	Al-rich. Incompatible element abundances lower than the A11 high-K and A15 KREEP basalt samples, but higher than all other samples withon our suite.
Apollo 15	Olivine Normative	15016	Lower Ti and Sc, and higher Cr and V, abundances than the A12 samples, but otherwise compositionally similar. Low REE abundances.
		15555	Lower Ti and Sc, and higher Cr and V, abundances than the A12 samples, but otherwise compositionally similar. Low REE abundances
	KREEP	15386	Comparable Ti to the A15 mare basalts. LREE enrichment and strongly negative Eu* (characteristic of KREEP). Incompatible element-,
Apollo 17	Type A	75055	Compositionally simialr to A11 low-K samples, specifically A11 B3 sample 10020. Less Ti-rich than other A17 samples. Generally low incompatible element abundacnes compared to other A17 samples.
	Type B	70215	Ti-rich compared to most other lunar basalts. REE enriched compare to other mare-basalts (excluding A11 high-K and A14 high-Al).
	Type C	74275	Ti-rich compared to most other lunar basalts. REE enriched compare to other mare-basalts (excluding A11 high-K and A14 high-Al).
	Unclassified	70017	Low REE abundance compared to other high-Ti mare-basalt samples, but other incompatible elements are in agreement with other samples.
		70035	high REE and incompatible element abundances compared with low-Ti mare-basalts (in agreement with other A17 and A11 samples).

characteristics inherited by the high-Ti basalt source (although weakened by mixture with the olivine-pyroxene cumulates). The olivine-pyroxene cumulates would be enriched in elements compatible in these minerals (such as Ni and Sc), and strongly depleted in any elements incompatible in these minerals (such as Na).

4.4. Chemical Modelling

To determine the petrogenesis of the mare-basalt groups represented in our sample set we have undertaken quantitative geochemical modelling. The main geological processes controlling the chemical composition of igneous rocks include partial melting, fractional crystallisation, crystal accumulation, magma mixing and contamination, all of which affect bulk-rock trace-element abundances. Therefore, by comparing the REE abundance of a sample with theoretically calculated values, its geological history can be ascertained. The aim of our geochemical modelling is to determine if, and how, each sample could have evolved from a low-Ti cumulate source (in the case of low-Ti mare basalts), or different mixtures of low-Ti and high-Ti cumulate end-member sources (in the case of the various types of high-Ti mare basalts), thus testing the heterogeneous source model of mare-basalt formation (e.g., Elkins-Tanton et al., 2002).

4.4.1. Mare-basalt Parental Melt Compositions. Within each Apollo mare-basalt group the most primitive sample is commonly assumed to be comparable to the primary/parental melt of the group. A sample is deemed to be primitive if it contains high Mg# and compatible trace-element abundances, along with low abundances of incompatible-elements, with no petrographic indications of crystal accumulation. Where no single sample of this kind exists in the Apollo collection the compositions of a number of samples may be averaged to produce primary elemental abundances (e.g., Snyder et al., 1992, 1997). Alternatively, experimental petrogenetic modelling can be induced to calculate the probable parental composition (e.g., Neal et al., 1990a). As, by definition, the composition

of a parental melt should have undergone minimal evolution, its REE abundances should be unaffected by crystal fractionation or accumulation, and can therefore be used as an indication of the extent of these processes in other samples within the same basalt group. If a mare-basalt sample contains higher REE abundances than the parental melt, crystal fractionation of low-REE phases (e.g., olivine and ilmenite) and/or assimilation of KREEPy material may have occurred. If a mare-basalt sample contains lower REE abundances than the parental melt then accumulation of low-REE phases has occurred. Table 4.3 shows the REE compositions of these parental melts and the method by which they were calculated. Figure 4.15 compares the REE abundances of the most primitive samples in our sample set with the abundances of their estimated parental melts. Samples 12040, 12016, 15016 and 74275 show lower REE abundances than their parental melts, supporting the evidence obtained from the Garcia plot (Figure 4.6) which indicates olivine accumulation in these samples. Apollo 12 ilmenite basalt 12064 and Apollo 17 type A basalt 75055 also show lower REE abundances than their parental melts. These samples contain little to no olivine, and ilmenite modal abundances are not atypically high (Table 3.1; Brown et al., 1975; Neal et al., 1994). Sample 75055 shows only slightly low HREE abundances but more significantly low LREE abundances, a trend that could have been

Table 4.4: Mare-basalt assumed parental melt compositions.

	Apollo 12			Apollo 14	Apollo 15	Apollo 11	Apollo 17		
	Pigeonite	Olivine	Ilmenite	Group C	Olv Norm	Type B3	Type A	Type B2	Type C
REE	12011	Average[a]	Average[b]	Hybrid[c]	15537	10045	Estimated[d]	Estimated[d]	Average[e]
La	33.11	24.76	26.91	26.21	22.18	28.55	20.45	18.75	26.84
Ce	30.67	27.19	28.11	20.91	24.20	37.30			36.14
Pr	31.31	28.90	32.92						
Nd	31.39	31.83	35.32			46.64			52.61
Sm	32.63	29.50	39.26	10.97	24.58	57.10	47.59	39.43	64.58
Eu	19.82	17.50	21.93	6.46	14.29	26.79	27.68	21.43	32.14
Gd	26.55	26.07	35.97			67.14			75.28
Tb	25.90	27.55	38.55		21.49	57.85			
Dy	24.19	26.12	36.82			59.74			69.63
Ho	23.74	23.74	32.91						
Er	23.47	23.54	32.49			61.04			61.04
Tm	21.07	21.69	29.81						
Yb	23.75	20.43	29.31	9.91	14.00	52.31	43.69	36.31	54.15
Lu	19.34	19.55	26.99	8.89	12.80	49.38			49.38

[a]Average of samples 12009 and 12015 (Snyder et al., 1997). [b]Average of samples 12008, 12022 and 12045 (Snyder et al., 1997). [c]Hybrid taking the lowest elemental abundances for all samples within this group (Neal and Kramer, 2006). [d]Estimation based on element-element plots (Neal et al., 1990b). [e]Average based on samples 74245, 74275 and 74247.

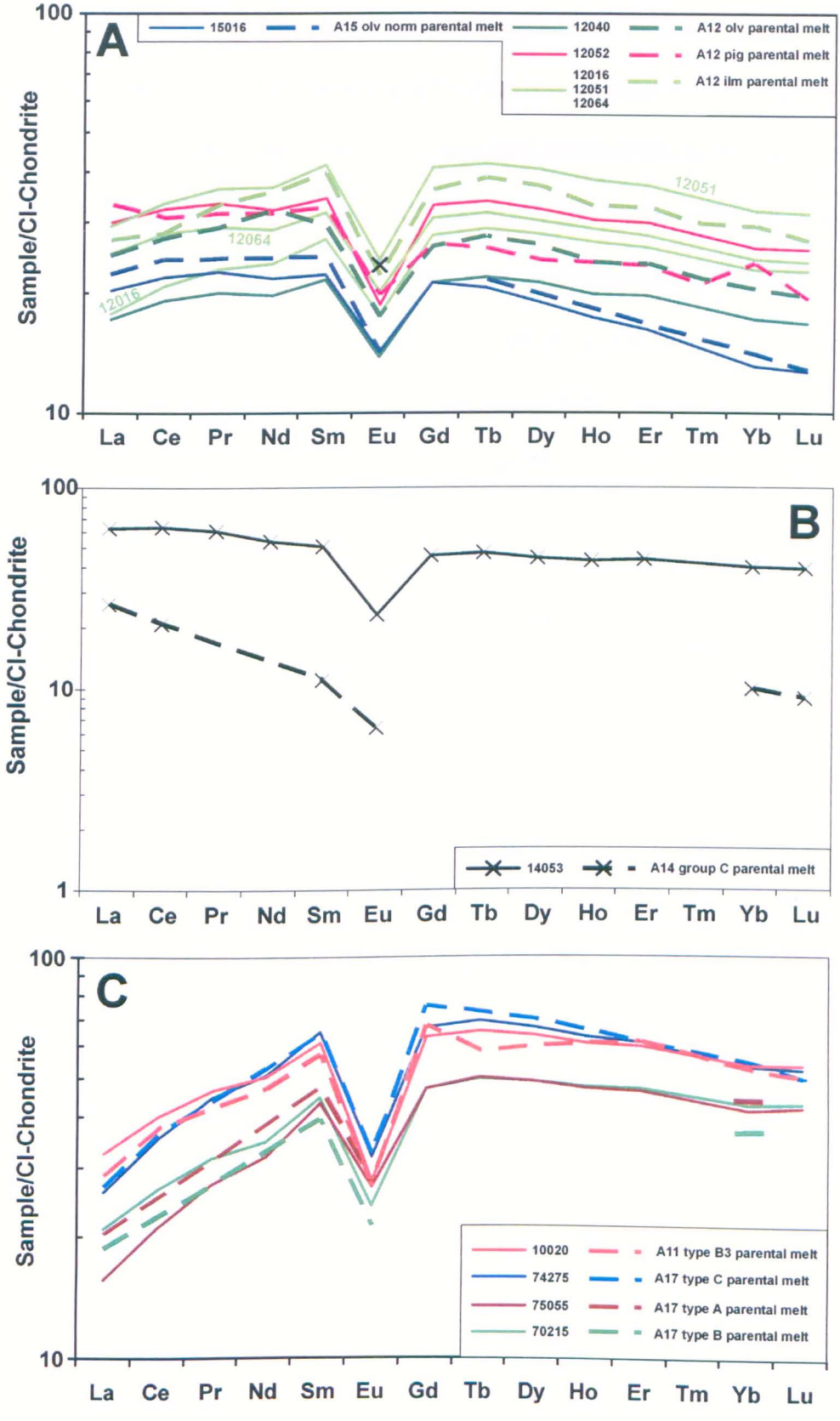

Figure 4.15: REE chondrite-normalised abundance plots showing mare-basalt parental melt compositions. **(a)** Apollo 12 and 15 low-Ti basalts, **(b)** Apollo 14 high-Ti basalts and **(c)** Apollo 11 and 17 high-Ti basalts. These compositions (dashed lines) are compared with the most primitive samples of each mare-basalt group represented within our sample set (solid lines).

produced by small amounts of clinopyroxene accumulation. Sample 12064 shows a more significant difference between its REE abundance and that of the parental melt. The modal abundance of clinopyroxene within this sample is slightly high compared with a number of other Apollo 12 ilmenite basalts (Dungan and Brown, 1977; McGee et al., 1977), indicating some clinopyroxene accumulation may have occurred. However, this slight accumulation can not entirely explain the low REE abundances. An accumulation of trydimite in sample 12064 is perhaps another factor to take into consideration for a lower bulk-rock REE content. The Garcia plot (Figure 4.6) indicates Apollo 14 high-Al basalt 14053 contains accumulated olivine, but the parental melt REE abundances of Neal and Kramer (2006) are significantly lower than those of sample 14053. Neal and Kramer (2006) estimated the parental melt REE composition of Apollo 14 group C basalts by producing a database of all previous measurements for this group of samples, taking the lowest individual measurements of each REE and producing a hybrid composition. This approach assumes no significant crystal accumulation has occurred in these basalts, an assumption that Neal and Kramer (2006) argue is supported by petrography. Therefore, the most probable explanation for the apparent olivine accumulation in sample 14053 is the absence of the most Mg-rich olivine grains within thin section 14053,19. The remaining mare basalts within our sample set (excluding unclassified samples 10050, 70017 and 70035, as their parental melt compositions have not been estimated) have undergone crystal fractionation. For clarity, Apollo 12 ilmenite basalt 12047 has not been included in Figure 4.15, but its REE abundances are similar to sample 12051. Apollo 11 low-K type B1 basalt 10058 is the most primitive sample of the three basalts within the B1 group (e.g., Beaty and Albee, 1978; Rhodes et al., 1980), hence it is not included in Figure 4.15. However, sample 10058 is significantly REE enriched compared to type B3 basalt 10020 and, therefore, may not represent a true B1 parental melt.

Apollo 12 red and Apollo 15 green glasses are rich in MgO with high Mg# (Longhi et al., 1992; Shearer and Papike, 1993), suggesting they may be primitive samples of the low-Ti mare-basalt source. However, the major- and minor-element abundances of these glasses cannot be directly linked to any known mare-basalt composition via crystal fractionation (Longhi, 1992). In addition, high-pressure experimental data indicate that the temperature and pressure of multiple saturation in the Apollo 12 and 15 glass samples generally exceed those of the crystalline mare-basalts, implying the two sample types originated from separate source regions (Longhi, 1992, 1995). The same is true for most of the glasses collected at the Apollo 11 and 17 sites, therefore, these glass samples are generally not suitable as proxies for mare-basalt parental melt compositions (Apollo 11 orange glass is a possible exception, see section 4.4.4). The parental melt compositions of Table 4.3 can be used as an indication of the amount of mare-basalt source partial melting required to produce each basalt group, but first the appropriate source composition(s) must be selected.

4.4.2. Selecting an Appropriate Mare-Basalt Source Composition. McKenzie and O'Nions (1991) made the assumption that the primitive Moon contained the same REE composition as the primitive Earth, and the depleted Moon contained the same REE composition as the depleted Earth with the addition of a negative europium anomaly. This assumption is based on the fact that the Earth and Moon both differentiated to produce ultramafic mantle/cumulate layers beneath feldspar-rich crusts. Ringwood and Essene (1970) and Green et al. (1971) suggested partial melting of a primitive Moon source could result in the production of mare basalts, but this model does not account for the wide variety of mare-basalt compositions, the negative europium and strontium anomalies present in all mare basalts, and the lack of Ni in the high-Ti basalts (indicating they were never in contact with a primitive lunar source) (Taylor 1982; Neal and Taylor, 1992). A depleted Moon parent for the mare basalts would account for these anomalies, but the lack of Ni and the high-Ti content in the Apollo 11 and 17 mare basalts is believed to be caused

Table 4.5: Potential mare-basalt source-region compositions.

	Potential source region compositions			
Element	A15 Green Glass[1]	A11 Green Glass[1]	McKenzie and O'Nions (1991) PMS[2]	McKenzie and O'Nions (1991) DMS[3]
La	1.62	1.4	0.55	0.206
Ce	4	3.37	1.4	0.722
Pr			0.22	0.143
Nd	2.2	2.36	1.08	0.815
Sm	0.75	0.72	0.35	0.299
Eu	0.2	0.25	0.13	0.0805
Gd			0.457	0.419
Tb			0.084	0.077
Dy	1.11	1.39	0.57	0.525
Ho			0.13	0.12
Er	0.75	0.94	0.372	0.347
Tm			0.058	0.054
Yb	0.77	1	0.372	0.347
Lu			0.057	0.054

[1]Shearer and Papike (1993). [2]PMS = Primitive Moon source. [3]DMS = Depleted Moon source.

by source heterogeneity (Ryder, 1991; Elkins-Tanton 2002; section 1.1.5), suggesting that the low and high-Ti mare-basalts were produced from differing source compositions. As it is generally accepted that the ilmenite cumulates only began to crystallise after ~ 95 % solidification of the lunar magma ocean (LMO) (e.g., Wood et al., 1970b; Ringwood and Kesson, 1976; Ryder, 1991), they should be enriched in incompatible-elements compared to the earlier-forming olivine and pyroxene cumulates (which crystallised between 0-80 % LMO solidification). As the high-Ti basalts are thought to originate from sources enriched in ilmenite cumulates compared to the low-Ti basalts, the high-Ti mare-basalt source region should also be enriched in REE. Based on these arguments, and REE abundance comparisons with our sample set (Figure 4.16), the depleted-Moon composition of McKenzie and O'Nions (1991) was deemed the best approximation of the low-Ti mare-basalt source regions. McKenzie and O'Nions' (1991) depleted Moon composition was also chosen as the best initial estimate of the high-Ti mare-basalt source because the majority of cumulate material within these source regions is thought to be the same as that which makes up the low-Ti mare-basalt source. However, this initial source selection was made with the knowledge that a REE enrichment factor would probably be required to model the addition of REE-enriched cumulates to this source.

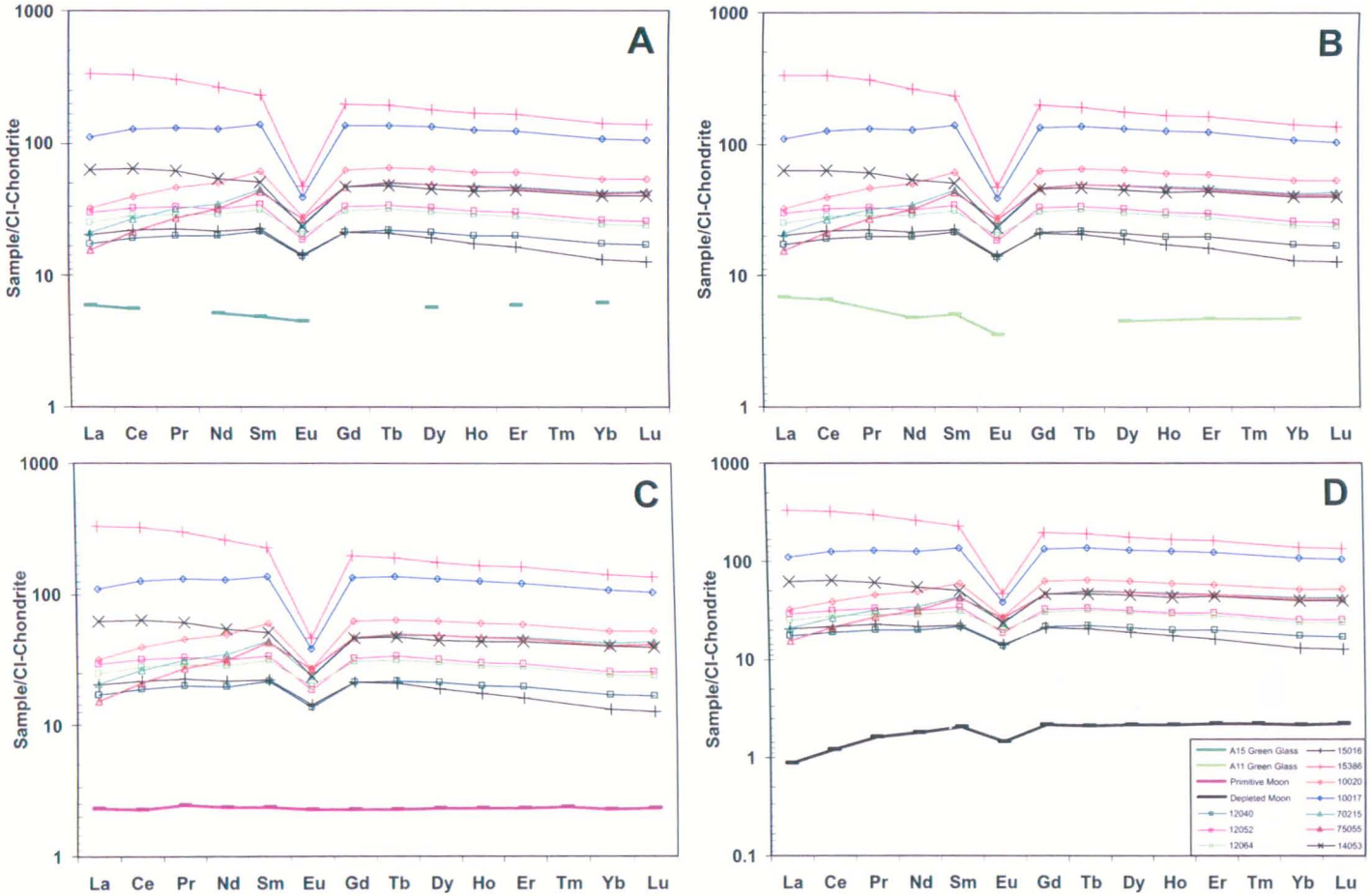

Figure 4.16: REE chondrite-normalised abundance plots of potential mare-basalt source compositions. REE abundance trends within the Apollo 15 green glass **(a)** and Apollo 11 green glass **(b)** are not typical of mare-basalts. The primitive lunar composition **(c)** calculated by McKenzie and O'Nions (1991) is too depleted in REE and does not show the negative europium anomaly visible in mare-basalts. In contrast, the depleted lunar composition **(d)** has the REE abundance and trend expected in a mare-basalt source. The most primitive mare-basalt samples of each group present within our sample set are compared to each potential source composition in these plots.

The difference in Ti-content between the low and high-Ti basalt sources was initially taken into account during partial melting calculations, by using the mare-basalt source modal mineralogies calculated by Snyder et al. (1992a). These authors stated that the low-Ti mare-basalt source region consisted of 46 % pigeonite, 43 % olivine, 10 % augite, 1 % plagioclase and a small amount of residual KREEP material. The high-Ti mare-basalt source was essentially the same, but with less augite (7 %) and the addition of 3 % ilmenite.

4.4.3. Fractional and Batch Partial Melting. It is generally accepted that mare basalts are the product of partially melted sources (e.g., Ringwood and Essene, 1970; Nyquist, 1977; Nyquist et al., 1979; Shervais et al., 1985a; Neal and Taylor, 1992 and references therein; Shearer and Papike, 1993, 1999; Beard et al., 1998). The two end-members of the partial melting process are batch melting and fractional melting. Batch melting describes the formation of a partial melt in which the melt is continually reacting and re-equilibrating with the solid residue at the site of melting, until mechanical conditions allow it to escape as a single batch of magma. During fractional melting a small amount of liquid is produced and instantly isolated from the source, therefore, equilibrium is only achieved between the melt and the surface of the mineral grains in the source region. In reality, partial melting is generally a mixture of these two end-members. The dominant process can be revealed by calculating the progression of trace-element abundance in a melt for 100 % batch and 100 % fractional melting, and comparing these abundances to those observed in a sample, which has not suffered extensive crystal fractionation or accumulation. Where modal melting occurs (each mineral phase melts in proportion to its modal abundance in the source) batch melting can be calculated using equation 4.1. All the following equations were sourced from Rollinson (1993).

$$C_L/C_0 = 1/[D_0 + F(1-D_0)] \quad (4.1)$$

where; C_L = weight concentration of a trace-element in the liquid

C_0 = weight concentration of a trace-element in the original unmelted source

F = weight fraction of melt produced

D_0 = bulk distribution coefficient of the original solid.

The bulk distribution coefficient is calculated by multiplying each mineral partition coefficient by the percentage of that mineral in the source. For example, for a source with 50 % olivine, 40 % pigeonite and 10 % augite, D_0 = (0.5× olivine partition coefficient) + (0.4 × pigeonite partition coefficient) + (0.1 × augite partition coefficient). Fractional melting can be represented by equation 4.2, again assuming each mineral phase melts in proportion to its modal abundance (vol %) in the source:

$$C_L/C_0 = (1/D_0) \times (1 - F)^{((1/D0)-1)} \quad (4.2)$$

Using the depleted Moon as an approximation of the mare-basalt source (C_0) (McKenzie and O'Nions, 1991), the modal mineralogies (vol %) of the high and low-Ti mare-basalt source regions as calculated by Snyder et al. (1992a), and the mineral partition coefficients of Drake and Weill (1975) and those compiled by Snyder et al. (1995) (D_0), the weight concentration of REE in the liquid (C_L) can be calculated for increasing melt fractions (F). Snyder et al. (1997) state that mare-basalt partial melting would have been non-modal, as the trapped KREEPy liquid would have been the first phase to melt. However, as this liquid is not a mineral phase it cannot be included in these calculations, hence the calculated REE abundances may be lower than those actually produced for each partial melt.

Figure 4.17 displays the results of these calculations alongside the various parental melt REE abundances (from Table 4.3). For small amounts of partial melting (0.5 – 5 %) LREE's are enriched in the melt compared to the original depleted Moon source composition, because the values of the LREE partition coefficients are smaller than those of the HREE's (10 to 1000 times smaller depending on the mineral). As the amount of partial melting increases the REE trend of the melt increasingly begins to mirror that of the source, until at ~ 15 % partial melting the trends are only distinguishable by an increased REE abundances in the melt. For small amounts of fractional melting, the overall REE abundances in the melt are higher than for the same percentage of batch melting, especially for LREE's. As the percentage of melting increases this difference decreases, until at ~ 30 % melting the two end-member processes produce very similar REE trends and abundances in the melt.

Figure 4.17a shows that the low-Ti mare-basalt parental melts contain similar europium anomalies and HREE trends to the depleted Moon source, but less LREE depletion. A depleted-Moon partial melt from 5 % batch melting, or 7 % fractional melting, would yield approximately similar REE abundances to those observed in the pigeonite and olivine basalt parental melts, but with a more convex upwards trend. The ilmenite basalts contain slightly higher REE abundances, creating a better match with 3 % batch melting, or 5 % fractional melting. However, the MREE's and HREE's of the calculated partial melts show much similar trends to the flatter Apollo 12 parental melt trends for 10 % partial melting of the depleted-Moon source. Between 5 and 10 % partial melting is in agreement with Snyder et al. (1997), who calculated the olivine and pigeonite basalts could be produced by 9-7 % partial melting of an olivine (48 %), clinopyroxene (30 %), pigeonite (22 %) and trapped residual liquid (0.3-0.5 %) source, while the ilmenite basalts could be produced by 7-5 % partial melting of an olivine (45.5 %), pigeonite (42.5 %) and clinopyroxene (11.5 %) source, with very little trapped residual liquid (< 0.15 %). Nyquist et al. (1977, 1979)

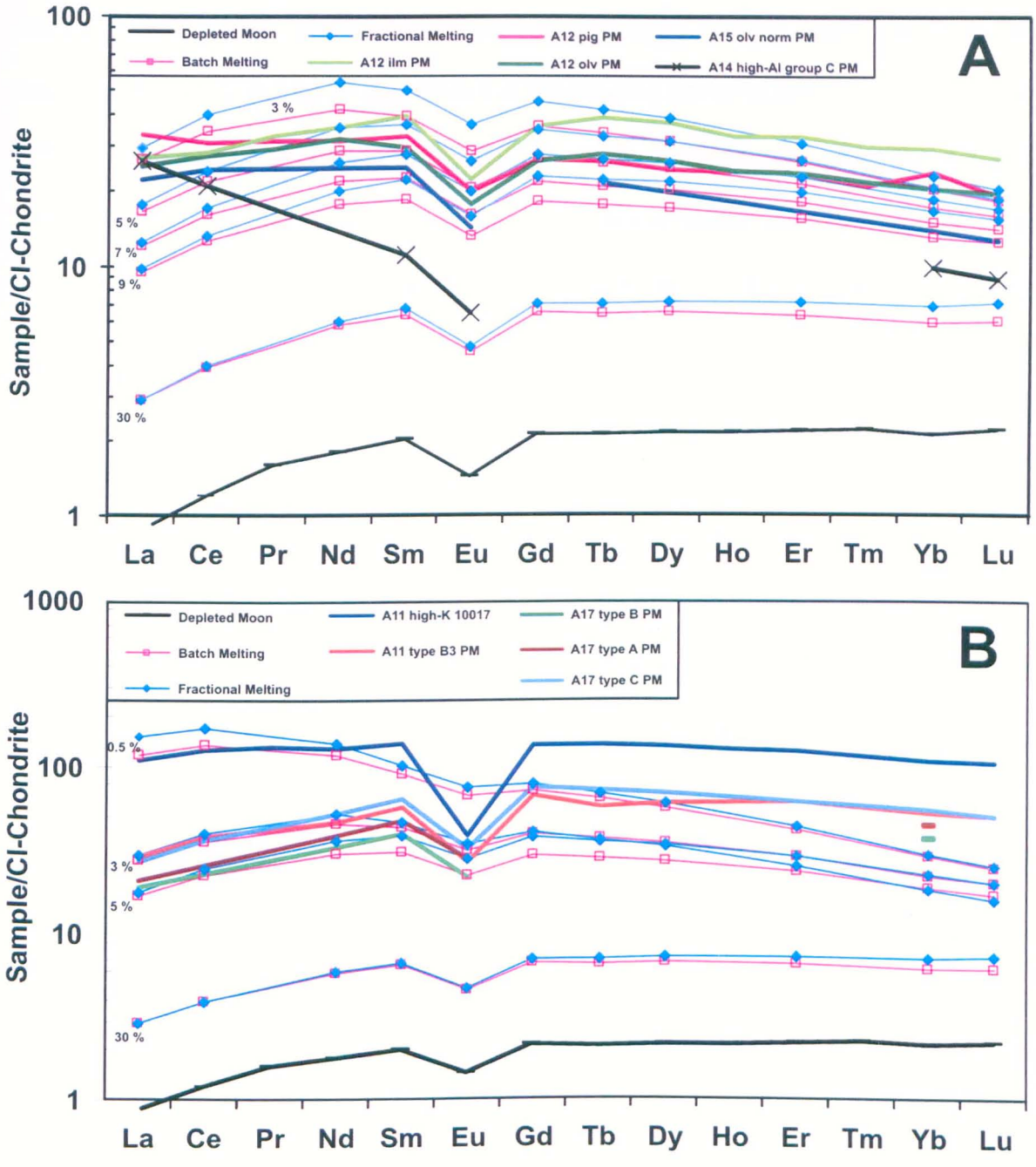

Figure 4.17: Chondrite-normalised REE abundance plots showing partial melts of the depleted Moon source of McKenzie and O'Nions (1991). These plots show increasing melt proportions for both fractional and batch melting, compared with REE abundances in: **(a)** low-Ti Apollo 12 ilmenite and pigeonite basalt, Apollo 15 olivine-normative basalt and Apollo 14 high-Al basalt parental melts, **(b)** high-Ti Apollo 11 low- and high-K and Apollo 17 type B and type A basalt parental melts.

also concluded that the Apollo 12 basalts formed as a result of 2-10 % partial melting of cumulate sources, composed of varying proportions of olivine, orthopyroxene and clinopyroxene. However, as the depleted-Moon source of McKenzie and O'Nions (1991) displays greater La and Ce depletion than the low-Ti Apollo 12 basalts even at 5 % partial

melting, neither fractional nor batch melting REE trends fit the measured REE trends perfectly. These discrepancies can be attributed to variations in source region composition for each basalt group (as taken into account in Neal et al. (1994b) and Snyder et al. (1997)) and the probability of non-modal melting. In fact Nyquist et al. (1977, 1979) state that the cumulate source regions of the Apollo 12 basalts must have had LREE-enriched profiles.

The Apollo 15 olivine-normative parental melt contains lower abundances of REE's than the Apollo 12 parental melts, showing similar abundances to 7 % batch melts, or 9 % fractional melts, of the depleted Moon source of McKenzie and O'Nions (1991). The LREE's are again enriched in the parental melt compared to the calculated partial melts, and the HREE's are slightly depleted compared to both the partial melt REE trends and those of the Apollo 12 parental melts. The experimental models of Hughes et al. (1988) suggest the Apollo 15 olivine-normative basalts could have been produced by as little as 3 % partial melting of an olivine and orthopyroxene (98.5 %), clinopyroxene (0.37 %), plagioclase (0.79 %), ilmenite (0.16 %) and trapped residual liquid (0.13 %) cumulate source. This source was clearly REE depleted compared to the depleted Moon source of McKenzie and O'Nions (1991), as a 3 % partial melt of the latter produces REE abundances too high for even the LREE's of the Apollo 15 olivine-normative parental melt.

The high-Ti Apollo 17 and Apollo 11 low-K parental melts show relatively similar REE trends to the depleted Moon source of McKenzie and O'Nions (1991), with LREE depletion and relatively constant HREE abundance (Figure 4.17b). For calculations using this source the Apollo 17 type A and B parental melts are most comparable to the calculated REE abundances in 2 % and 4 % batch melting, or 3 % and 5 % fractional melting, respectively. REE's are more abundant in Apollo 11 low-K and Apollo 17 type C parental melts, therefore 1-2 % batch melting or 2-3 % fractional melting of the McKenzie

and O'Nions' (1991) depleted-Moon source show the closest match to their REE compositions. For the high-Ti basalts fractional melting matches the parental melt LREE trends slightly better than batch melting.

Because of the small amounts of partial melting required to match the parental melt and calculated REE abundances, especially for the high-Ti basalts, LREE's in the calculated trends are enriched, and HREE's depleted, compared to the measured parental compositions. Therefore, a number of the high-Ti partial-melting estimates are based solely on one or two of the MREE's (Sm and Gd) - where these elements differ considerably, determination of the single most accurate partial melting estimate becomes difficult (hence the variation for high-Ti parental melt estimates). For the calculated and parental melt REE compositions fro high-Ti basalts to show a similar trend, at least 10 % partial melting of the McKenzie and O'Nions (1991) depleted Moon source is required. At this melting proportion, the REE trend of fractional melting matches that of the high-Ti parental melts better than the REE trend of the batch melting calculations, as the HREE's are slightly more enriched in the fractional melting trends. These estimates are supported by previous data indicating the Apollo 17 high-Ti basalts were produced by < 20 % partial melting (Duncan et al., 1976) and the Apollo 11 low-K basalts were produced by ~ 3 % partial melting (Ringwood and Essene, 1970). Trace-element constraints on the modelled high-Ti source of Snyder et al. (1992) also suggest the high-Ti basalts were produced by 1-3 % partial melting.

The europium anomalies of the high-Ti parental melts and the partial melts derived from the depleted-Moon source are not well matched, with the former containing more strongly negative anomalies. As neither partial melting, fractional crystallisation (excepting fractionation of plagioclase, which isn't observed in these samples), nor crystal accumulation can significantly increase the europium anomalies, this discrepancy suggests

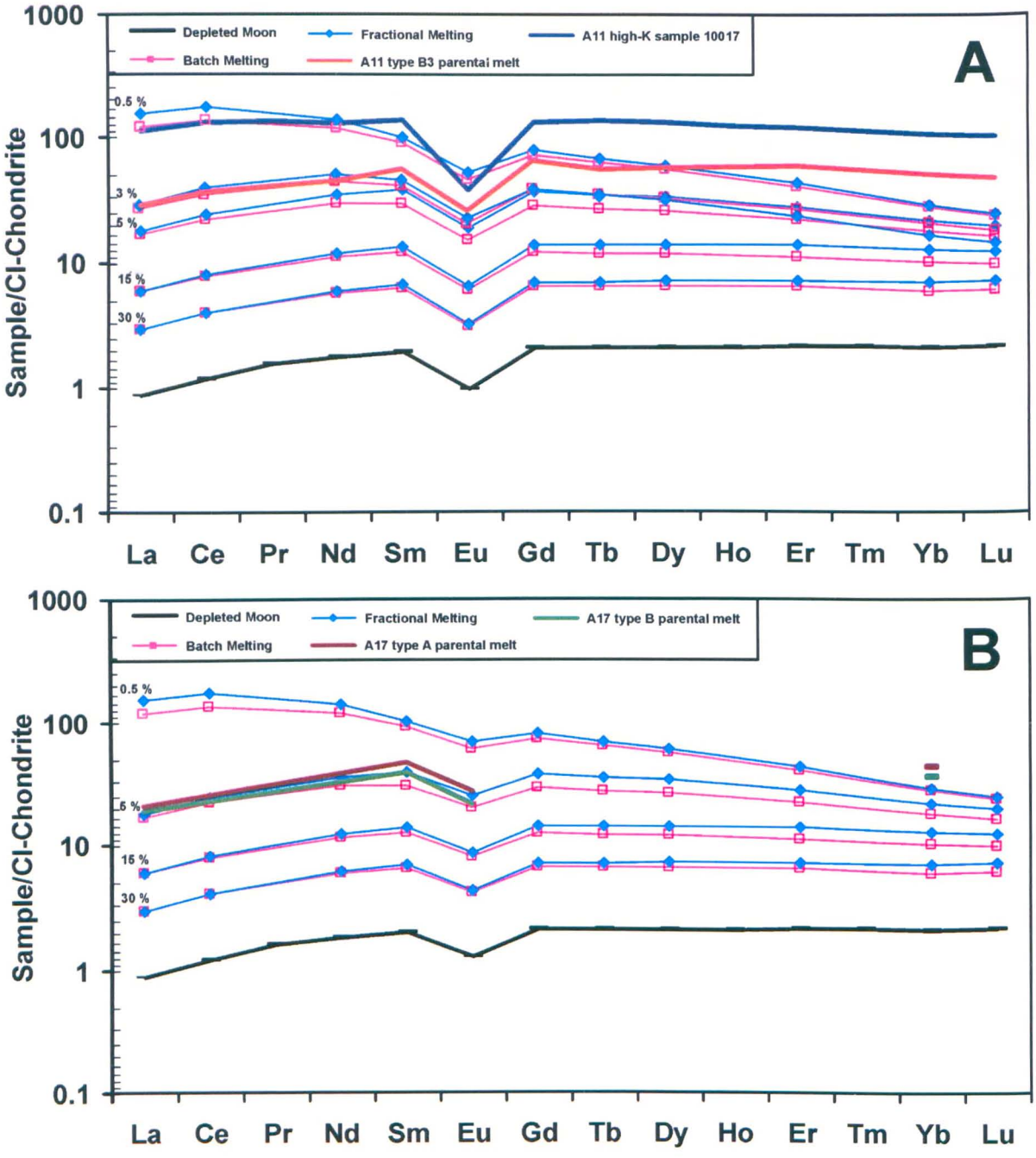

Figure 4.18: Chondrite-normalised REE abundance plots showing partial melts of the depleted Moon source (McKenzie and O'Nions, 1991) with europium anomaly modifications. These plots show increasing melt proportions of both fractional and batch melting, compared with mare-basalt parental melt REE abundances of: **(a)** the high-Ti Apollo 11 low- and high-K basalts (where sample 10017 is assumed to be representative of the latter), and **(b)** the high-Ti Apollo 17 type A and B basalts. The strength of the negative europium anomaly is increased by 29 % **(a)** and 14 % **(b)** based on average observed europium anomalies for each sample group.

that the sources of the high-Ti basalts had stronger europium anomalies than those of the low-Ti basalts (which are well matched with the europium anomaly of the partial melts

derived from the depleted-Moon source). This is in agreement with the ilmenite cumulate mixing model of high-Ti mare-basalt source formation, as late stage ilmenite cumulates would be expected to have strongly negative europium anomalies (similar to KREEPy material). The magnitude of the europium anomaly in the partial melts derived from the depleted-Moon source can only be matched to those of the high-Ti parental melts by subtraction of a certain percentage of Eu. McKenzie and O'Nions (1991) estimated the depleted-Moon Eu abundance based on the fact that the Moon's reduced nature would increase the plagioclase partition coefficient for Eu (as the Eu^{2+}/Eu^{3+} ratio correlates inversely with oxygen fugacity). These authors estimated that this partition coefficient would increase from the Earth's mantle value of 0.73 to a lunar mantle value of 1.1, creating a negative europium anomaly in the depleted-Moon source, similar to those observed in the low-Ti mare basalts. However, the average negative europium anomaly of the low-Ti basalts within our sample set (Apollo 12 and Apollo 15 sample 15016) is 14 % weaker than that of the Apollo 17 samples, and 29 % weaker than that of the Apollo 11 low-K samples. When these percentages were taken into account, the revised Eu composition in the depleted-Moon source matched closely with those of the high-Ti samples (Figure 4.18; see appendix F for calculations).

Figure 4.19 compares the REE trends of the basalts in our sample set and the calculated partial melts, on a plot showing La/Yb vs. Dy/Yb ratios and La/Sm vs. Sm/Yb ratios. Crystal fractionation and accumulation do not affect these ratios, so basalts from the same parental melt should cluster together at a point along the calculated partial melting curves. The Apollo 12 low-Ti basalts plot close to the curve indicating that they were derived from 10-13 % batch melting or 10-12 % fractional melting of the depleted-Moon source. These partial melting estimates are only slightly higher than those of Snyder et al. (1997), Nyquist et al. (1977, 1979) and those in Figure 4.17a, all of which indicate the Apollo 12 mare basalts were produced by $\leq$ 10 % partial melting. Apollo 15 low-Ti olivine-normative

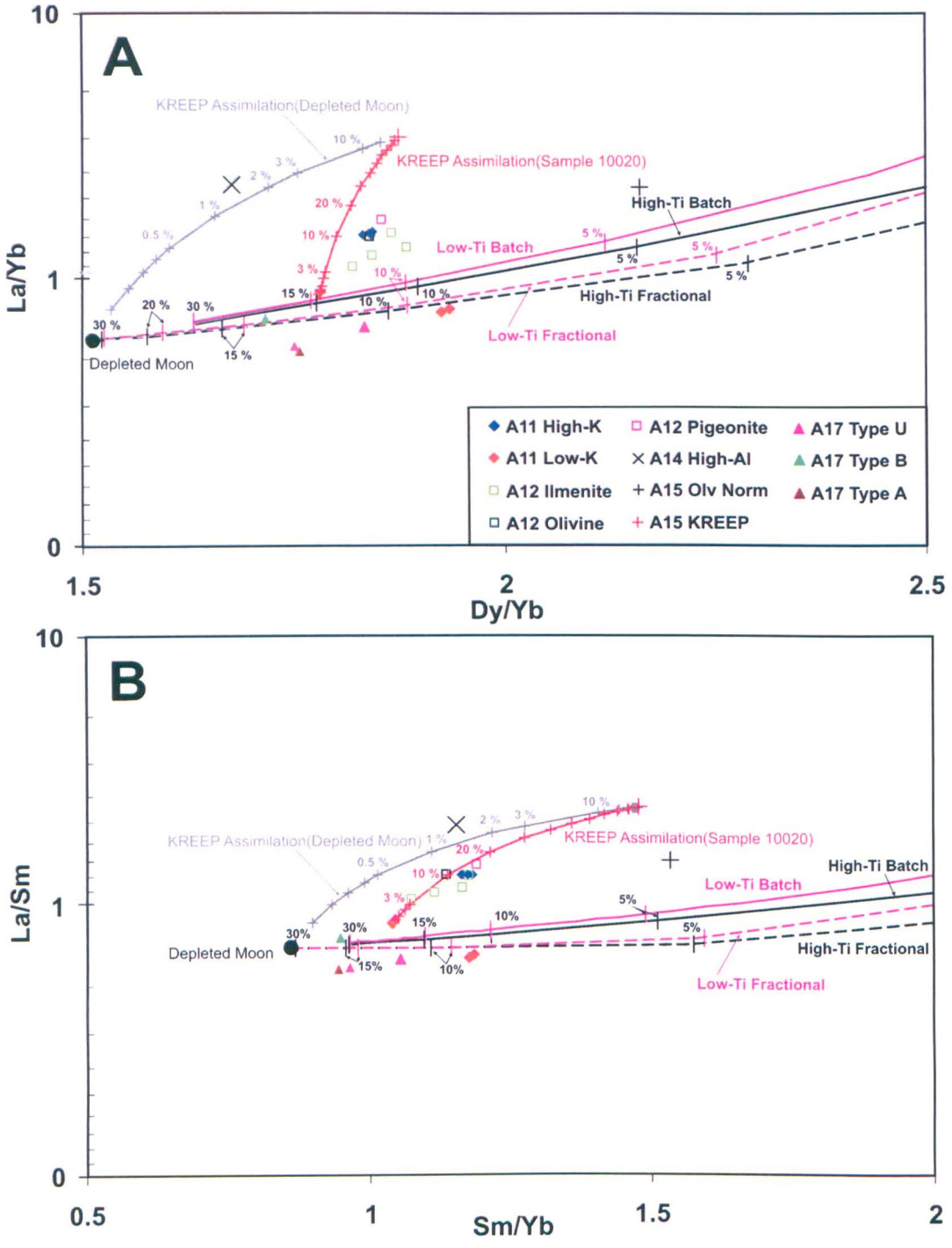

Figure 4.19: Comparative REE ratio plots for Apollo basalt samples and for calculated partial melts based on the depleted Moon source of McKenzie and O'Nions (1991). The modelled variations in low-Ti and high-Ti partial melts for batch and fractional melting are shown as pink and black solid and dashed lines in both plots of **(a)** La/Yb vs. Dy/Yb and **(b)** La/Sm vs. Sm/Yb. Overall the ratios decrease with increasing proportions of partial melting, as the LREE's become more depleted in the melt. The trend of increasing KREEP addition to the depleted Moon source is shown as a solid grey line. The solid red line shows the trend of KREEP addition to a melt with the composition of Apollo 11 low-K basalt 10020. This sample is the most primitive Apollo 11 basalt within our sample set, showing similar REE abundances to the Apollo 11 B3 parental melt.

basalt 15016 seem to be derived from ~ 4 % batch melting or ~ 6 % fractional melting on both plots. These estimates are intermediate between those of Figure 4.17a (7-9 %) and Hughes et al. (1988) (3 %). High-Ti, low-K Apollo 11 B3 basalt 10020 shows similar REE ratios corresponding to 15-19 % batch melting or ~ 12 % fractional melting of a depleted-Moon source. The remaining two Apollo 11 low-K samples compare more favourably with 9-12 % batch melting or 8-9 % fractional melting. The high-Ti Apollo 17 samples show a wide spread, from 13-35 % batch melting, or 11-17 % fractional melting. These high-Ti mare-basalt partial melting estimates are higher than previously published estimates (Ringwood and Essene, 1970; Shih et al., 1975; Duncan et al., 1976) and those modelled using the batch and fractional melting calculations (Figure 4.17b). As previously discussed, the depleted Moon source of McKenzie and O'Nions (1991) is only an approximation of the mare-basalt source region compositions. However, the general agreement of low-Ti mare-basalt melting estimates based on these partial melting curves, Figure 4.17a, and previously published data indicate McKenzie and O'Nions' (1991) depleted-Moon source is a fair estimate of the low-Ti mare-basalt source. In contrast, the large variation between the high-Ti mare-basalt partial melting estimates of Figure 4.19 and Figure 4.17b indicates modification of the depleted-Moon source is required to produce an adequate estimate of the high-Ti mare-basalt source composition. Overall the high-Ti basalts plot closest to the fractional melting line, whereas the low-Ti basalts are closest to the batch melting line. This may be an indication of the dominant melting processes for the two main basalt types.

Sample 10017 is the most primitive Apollo 11 high-K basalt within our sample set. It contains abundant REE's, requiring < 1 % depleted-Moon source partial melting to match the observed abundance (Figure 4.17b). Even with this small proportion of melting, the calculated MREE and HREE abundances are depleted compared to those observed in the sample. As with the other high-Ti mare basalts/parental melts within our sample set, the minimum partial melting required to produce a REE trend similar to that of the sample is

10 %. However, the difference in abundance between the calculated REE's at this melting proportion and the REE abundance in the sample is too great to be accounted for by crystal fractionation. The Apollo 11 high-K samples also display strongly negative europium anomalies, on average 54 % stronger than the average of the low-Ti samples. Figure 4.19 shows how La/Yb, Dy/Yb, La/Sm and Sm/Yb ratios would alter with the addition of increasing percentages of KREEP (REE composition of sample 15386) to a melt with the REE composition of low-K Apollo 11 B3 basalt 10020. The high-K Apollo 11 basalts plot close to this line at ~ 10 % addition of KREEP material to the melt. Apollo 14 high-Al basalt 14053 also shows high REE abundances and a deeper europium anomaly than the other low-Ti samples within our sample set. If KREEP is added in increasing proportions to a melt with the REE composition of the depleted Moon source, Apollo 14 low-Ti, high-Al basalt 14053 plots closest to the line at ~ 1.5 % KREEP addition.

4.4.4. Fractional Crystallisation. Fractional crystallisation is best approximated by Rayleigh fractionation (equation 4.3), the extreme case where crystals are effectively removed from a melt the instant they are formed.

$$C_L/C_0 = F^{(D-1)} \qquad (4.3)$$

where; C_0 = the weight concentration of a trace-element in the parental liquid

C_L = the weight concentration of a trace-element in the evolving liquid

D = the bulk distribution coefficient of the fractionating assemblage

F = the fraction of melt remaining

For our samples, the weight concentration of REE in the parental liquid is governed by the choice of partial melting type, and the melting proportion, of the original depleted-Moon source. As the dominant type of partial melting cannot be determined conclusively, both are calculated. The modified Eu concentrations of Figure 4.18 were utilised for the high-Ti

basalt fractional crystallisation calculations. From Figures 4.6 and 4.15, it is clear that Apollo 12 olivine basalt 12040, Apollo 15 olivine-normative basalt 15016, and Apollo 17 type A and C basalts 75055 and 74275 have undergone crystal accumulation. Therefore, these samples will not be included in the fractional crystallisation calculations. As discussed above, assuming a depleted Moon source composition (McKenzie and O'Nions, 1991) for all samples the Apollo 12 low-Ti parental melt REE abundances appear to be most comparable to 5-7 % (for pigeonite basalts) and 3-5 % (for ilmenite basalts) partial melting. The parental melt of high-Ti Apollo 11 low-K type B3 basalts has REE abundances approximately equivalent to 2-3 % fractional melting, or 1-2 % batch melting, whereas high-Ti Apollo 17 type B basalt parental melt is equivalent to 4 % batch melting, or 5 % fractional melting of the depleted-Moon source. Where necessary, these values were averaged for the crystal fractionation calculations (e.g., high-Ti Apollo 11 type B3 fractional melting was averaged from 2-3 % to 2.5 %).

Figure 4.20 highlights the fractionating assemblages and proportions required to create REE abundances similar to each mare-basalt group, both from the calculated partial melts (Figure 4.20aa, ab, etc.) and from the parental melt compositions (Figure 4.20ba, bb, etc.). Although the calculated REE trends are commonly not accurate representations of those shown within the samples, focusing on the MREE's allows the percentage of crystal fractionation required for the two trends to match to be estimated. Experiments from numerous laboratories have shown that the high-Ti basalts are multi-saturated with silicate and Ti-oxide within 25 °C of their liquidi, and several are multi-saturated within 10 °C (O'Hara et al., 1970; Longhi et al., 1974; Walker et al., 1975; Green et al., 1975). Other experimental investigations have shown that olivine (± minor Cr-spinel) is the major liquidus phase for the more Mg-rich low-Ti mare basalts (A12: Green et al., 1971; Bigger et al., 1971; Kushiro et al., 1971; Grove et al., 1973; Rhodes et al., 1979; A14: Walker et al., 1972; A15: Kesson and Lindsley, 1975; Walker et al., 1977). Therefore, the

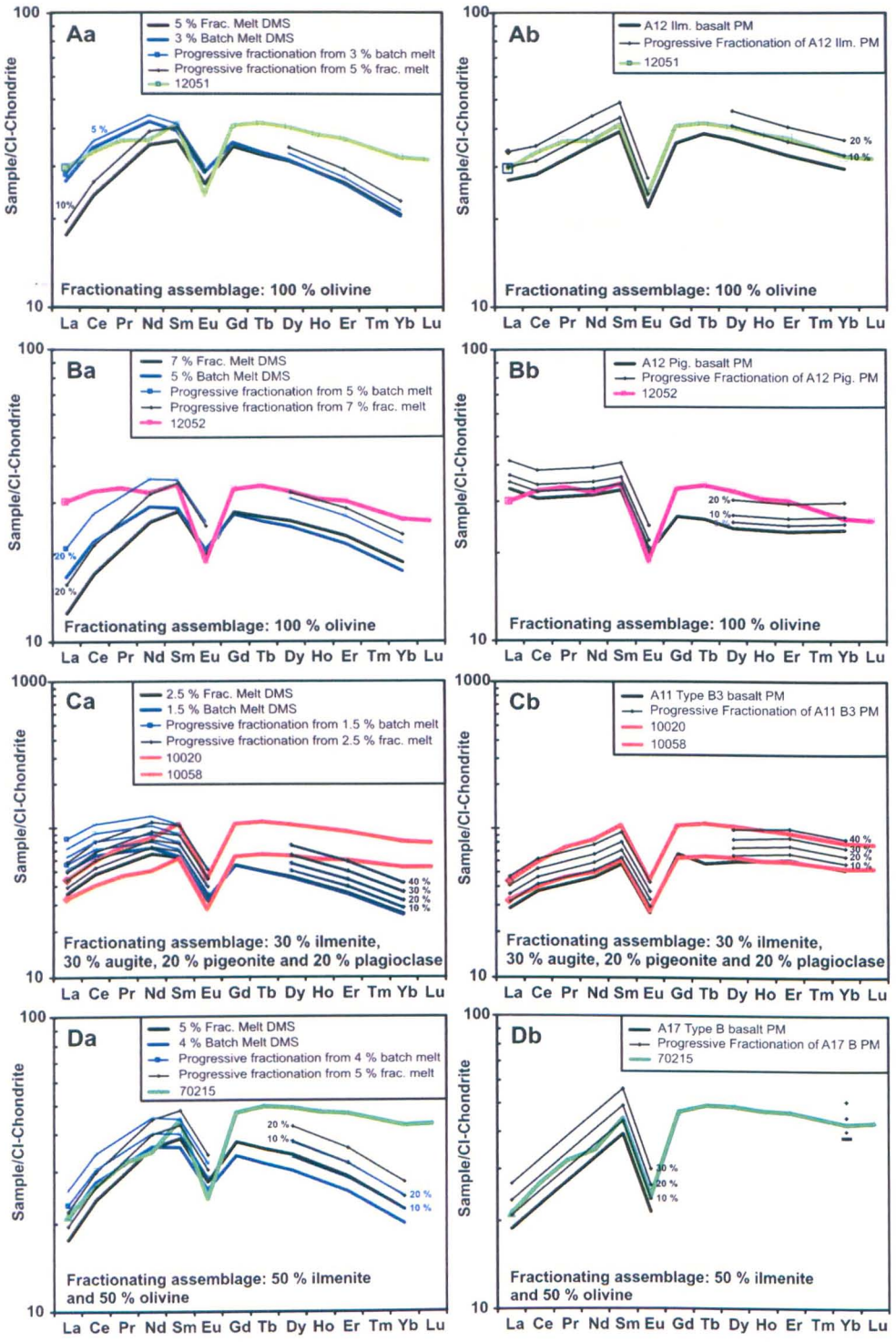

Figure 4.20: Chondrite-normalised REE abundance plots showing increasing amounts of fractional crystallisation, from both the depleted Moon source (McKenzie and O'Nions, 1991) and parental melt compositions, compared with the measured REE trends of mare-basalt samples. Plots **(aa)**, **(ba)**, **(ca)** and **(da)** show crystal fractionation from the calculated depleted Moon source partial melts that show the best match with the parental melt REE abundances for each basalt type. Plots **(ab)**, **(bb)**, **(cb)**, and **(db)** show crystal fractionation from the parental melt of each basalt type. Fractionating assemblages are shown on each plot. The europium anomaly is modified for the high-Ti basalts as in Figure 4.18.

fractionating assemblages of the low-Ti basalts should be dominated by olivine, whereas those of the high-Ti basalts will include multiple phases. These investigations support the petrological interpretations from this study (e.g., sections 4.1.2, 4.1.3, 4.2.3). Fractionating assemblages were therefore chosen for each sample based on our petrological interpretations, previously published data, and the best match for the calculated and measured REE trends.

Reconstruction of the approximate REE abundances of low-Ti Apollo 12 ilmenite basalt 12051 from the calculated partial melts requires 5-10 % olivine fractionation (depending on the dominant partial melting end-member). This amount of fractionation is supported by the data of Neal et al. (1994b), which indicates that all Apollo 12 ilmenite basalts were produced by less than 30 % olivine fractionation. It is also supported by calculations of fractional crystallisation from the Apollo 12 ilmenite basalt parental melt, showing 10 % olivine fractionation increases the REE abundances to match well with those of sample 12051 (Figure 4.20aa and ab). The calculated REE abundances of Apollo 12 pigeonite basalt 12052 require 20 % olivine fractionation. The pigeonite basalt parental melt (based on sample 12011) is LREE enriched compared to sample 12052, therefore, although parental melt HREE's are in line with the calculated data, the LREE's only require 5 % olivine fractionation to match those of sample 12052 (Figure 4.20ba and bb). Neal et al. (1994b) suggested that the Apollo 12 pigeonite basalts did not form in a closed system, but assimilated ~ 3 % of an anorthositic material while fractionating ≤ 10 % olivine (with some Cr-spinel). This assimilation would have caused an increase in LREE abundances in the melt, as anorthite is strongly LREE-enriched. Therefore, the difference in LREE abundances between these two pigeonite basalt samples may be explained if sample 12052 did not assimilate as much anorthositic material, or assimilated a material less LREE enriched, than sample 12011.

Sample 10020 is the most primitive Apollo 11 low-K basalt in our sample set. It shows similar REE abundances to its parental melt composition (type B3 parental melt, Figure 4.20cb), indicating this sample has not undergone large amounts of crystal fractionation (< 10 %). The Sm abundances calculated from 1.5-2.5 % partial melts of the depleted-Moon source also indicate little to no crystal fractionation occurred in this sample (Figure 4.20ca), although the calculated REE trend is so different to the measured trend that the abundances of the other REE's cannot be compared. Snyder et al. (1992b, 1993) and Jerde et al. (1994) suggested that the B1 basalts (including sample 10058) may be linked to the B3 basalts through later melting of the same source region. The isotopic systematics described by Snyder et al. (1992b, 1993) indicate that the Bl basalts are approximately three εNd units higher than the B3 basalts (where one epsilon unit represents a one part per 10,000 deviation from the chondritic uniform reservoir (CHUR) composition). These differences for the B3 and Bl basalt groups were interpreted as resulting from melting of a source region with variable amounts of KREEPy trapped liquid. In this model, melting of the source at 3.71 Ga resulted in the B3 basalts with εNd ~ +4. Later melting (at 3.67 Ga) of a portion of the same source region with slightly less trapped liquid component resulted in B3-like basalts which fractionated to B1 compositions. Snyder et al. (1992b and 1993) suggested the occurrence of 40 % fractionation of an olivine, pyroxene, plagioclase and ilmenite assemblage would produce the most evolved B1 composition, in agreement with our crystal fractionation calculations (Figure 4.20 ca, cb).

Apollo 17 type B2 basalt 70215 appears to have been produced by ~ 10 % fractionation, the REE trends show the best match for a 50 % ilmenite and 50 % olivine fractionating assemblage from the parental melt (Figure 4.20db). However, as with the Apollo 11 low-K basalts (and to a lesser extent the Apollo 12 ilmenite basalts), the HREE's of the calculated REE trends are too low, and the LREE's are too high. As explained in section 4.4.3 the smaller the amount of melting the more the LREE's are enriched in the melt. Every mafic

mineral phase which could plausibly have been present in the high-Ti mare-basalt source has LREE-depleted patterns, therefore, the source must have been LREE-depleted. However, the preservation of LREE depletion at the low degrees of partial melting suggested by the above calculations would require extreme LREE depletion in the source. Because of the formation of the anorthositic primary crust the mare-basalt source regions would be expected to be LREE depleted, therefore, it may be that the McKenzie and O'Nions (1991) depleted Moon source is still LREE enriched compared to the true mare-basalt sources. Alternatively, greater degrees of partial melting of the depleted Moon source would produce REE trends more in line with those measured in the parental melts and the basalt samples. As previously discussed, Snyder et al. (1997) suggested that the mare basalts were produced by non-modal melting, with the KREEPy trapped liquid being the first phase to melt (so if trapped liquid made up 2 % of the source, a 1 % melt would contain 100 % trapped liquid). Non-modal melting of this kind would result in partial melts more enriched in REE's than those calculated above, therefore, greater degrees of partial melting would be required to produce REE abundances similar to the mare-basalt parental melts. This effect would be greatest in the high-Ti basalts, as the trapped KREEPy liquid within these source regions would be more abundant in REE. On the basis of this information, high-Ti basalt REE abundances can be modelled more accurately by greater degrees of partial melting of a source enriched in REE's compared to the depleted Moon source of McKenzie and O'Nions (1991).

A 10 % partial melt (batch or fractional) is the minimum amount of melting of the depleted-Moon source required to produce a REE trend similar to those measured in the high-Ti samples. However, the levels of fractionation required to elevate the REE abundances to match those of the high-Ti samples from a 10 % partial melt are improbable (> 80 %). As no sample is present in the Apollo or meteorite collection which represents the composition of the pure ilmenite cumulates, a straight forward mixture of this

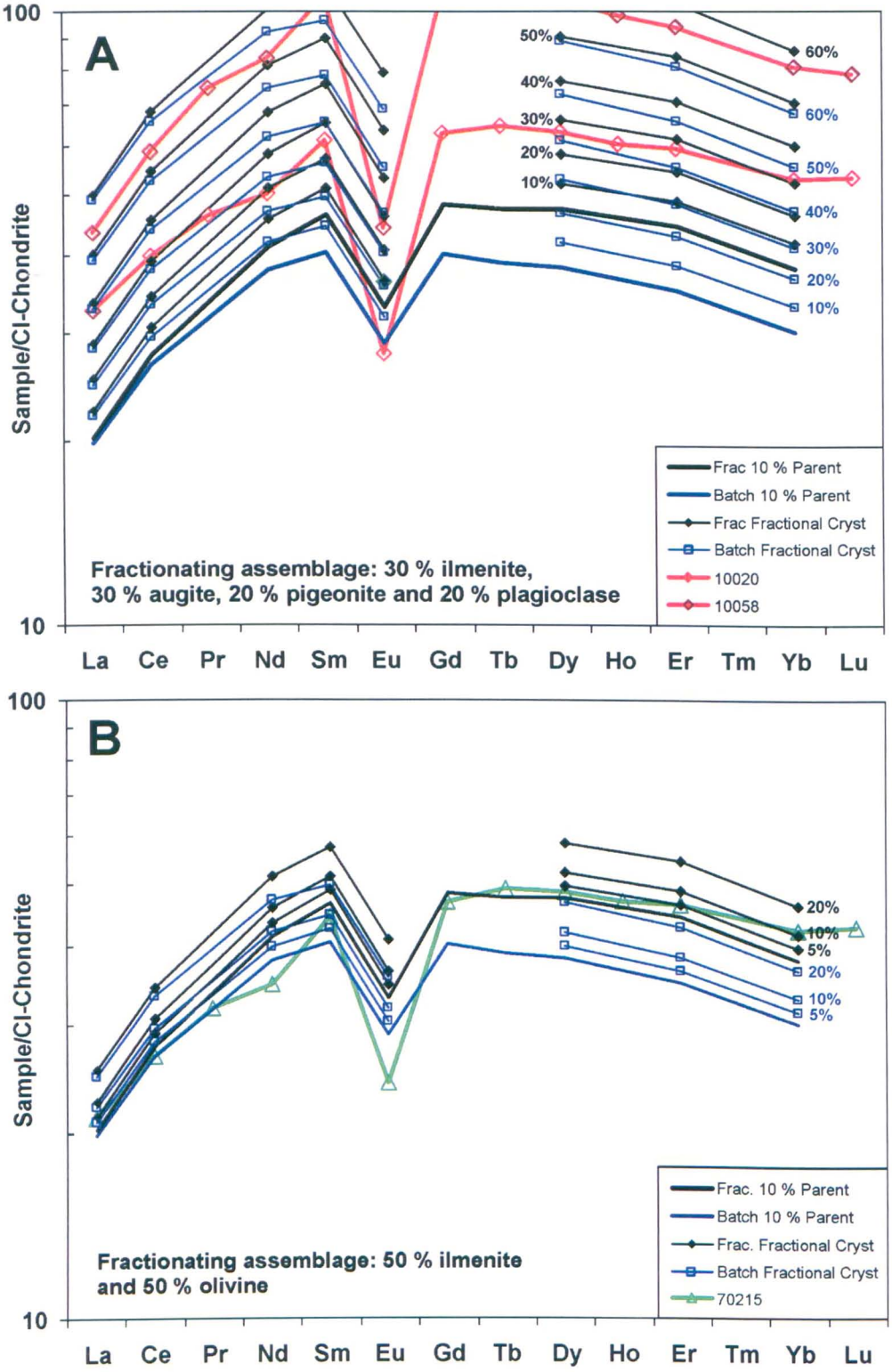

Figure 4.21: Chondrite-normalised REE abundance plots, comparing increasing proportions of fractional crystallisation from 10 % partial melts of a REE enriched depleted Moon source (130 % extra REE), with the REE trends of high-Ti mare-basalt samples. **(a)** Plot showing the Apollo 11 high-Ti, low-K basalts 10020 and 10058. **(b)** Plot showing Apollo 17 high-Ti type B2 basalt 70215. Other than the addition of 130 % REE abundance to the original depleted Moon composition of McKenzie and O-Nions (1991) europium is not modified, therefore the europium anomaly is constant in both plots.

component with the depleted-Moon source to create the high-Ti source cannot be achieved. Therefore, the simplest way to enrich the depleted Moon source in REE's is to proportionally increase the abundances. 130 % extra REE abundance (1 × REE abundance + 1.3 × REE abundance) appears to be the minimum amount of enrichment required to bring a 10 % partial melt within reach of the samples' measured REE abundances. For the Apollo 11 low-K basalt 10020 (type B3), 30 % or 40 % fractionation, respectively, of a 10 % fractional or batch partial melt of this REE-enriched source is required to produce similar measured and calculated REE abundances and trends (Figure 4.21). For Apollo 11 low-K type B1 basalt 10058, the amount of fractionation increases to 60 % (fractional melting) and 70 % (batch melting) – the former end-member appears to fit best with the trends of Apollo 11 low-K basalts. However, Snyder et al. (1992b, 1993) suggest the most evolved Apollo 11 B1 basalts only show 40 % crystal fractionation. The HREE's and LREE's of Apollo 17 type B2 basalt 70215 show the best match with 5 % fractionation of a 10 % fractional melt - a 10 % batch melt of the depleted-Moon source shows a more negative gradient less in line with sample 70215.

Greater degrees of partial melting require larger proportions of clinopyroxene within the source region to produce the Sm abundances and La/Sm_n ratios observed in the samples (Snyder et al., 1992). The presence of this clinopyroxene in the high-Ti basalt source regions is supported by the Sr isotopic modelling of Nyquist et al. (1976) and the Nd-Hf isotopic modelling of Unruh et al. (1984). However, Snyder et al. (1992) suggest that the high-Ti basalts were produced by less than 5 % partial melting, and the clinopyroxene abundance required in the source for larger degrees of partial melting would be too high. Even the amount of clinopyroxene required for a 5 % melt is not suggested by the modelling of Neal et al. (1990a) and Paces et al. (1991), who state that clinopyroxene should be exhausted in the source residue after melting. Beyond 5 % partial melting no more KREEPy trapped liquid would be added to the melt, but more ilmenite would melt

(which is REE-poor), therefore, beginning to lower the REE content. At 5 % partial melting the REE-enriched depleted Moon source and the Apollo 11 B3 parental melt have similar REE abundances (though the trend of the former still contains less abundant HREE's). However, the parental melt of Apollo 17 type B2 basalts contains lower REE abundances than a 5 % partial melt of this source. Assuming the ilmenite cumulates were homogeneous with respect to REE's, at the same amount of partial melting, the parental melt of the Apollo 17 basalts would be expected to contain higher abundances of REE than those of the Apollo 11 basalts, as the former contain more TiO_2 (hence originate from a source more enriched in ilmenite cumulates). As this is not the case, it may be that the Apollo 17 type B2 basalts are the result of higher degrees of partial melting - a 10 % partial melt of the 130 % REE enriched depleted Moon source could produce similar REE abundances to those measured in sample 70215 after ~ 10 % crystal fractionation. Alternatively, the ilmenite cumulate mixture which made up the Apollo 17 type B2 source region may have contained lower abundances of REE than that which produced the Apollo 11 type B3 and B1 basalts. Only 30 % REE enrichment of the McKenzie and O'Nions (1991) depleted Moon source is required for a 5 % partial melt to contain similar REE abundances to the Apollo 17 type B2 parental melt. An additional complication arises when we consider that Paces et al. (1991) suggested that, based on the scatter of Sm-Nd and Rb-Sr isotopic analyses, the Apollo 17 type B2 basalts assimilated several crustal components. As neither the composition of the assimilants, nor that of the source region, has yet been defined, a more in-depth study of this basalt group is required to determine their melt evolution.

4.4.5. Hybrid Source Compositions. As previously stated, the Apollo 11 high-K basalts contain excessively high amounts of REE, and strongly negative europium anomalies, compared to the other high-Ti samples. Apollo 14 high-Al basalt 14053 also shows higher REE abundances and LREE enrichment compared to the other low-Ti basalts within our

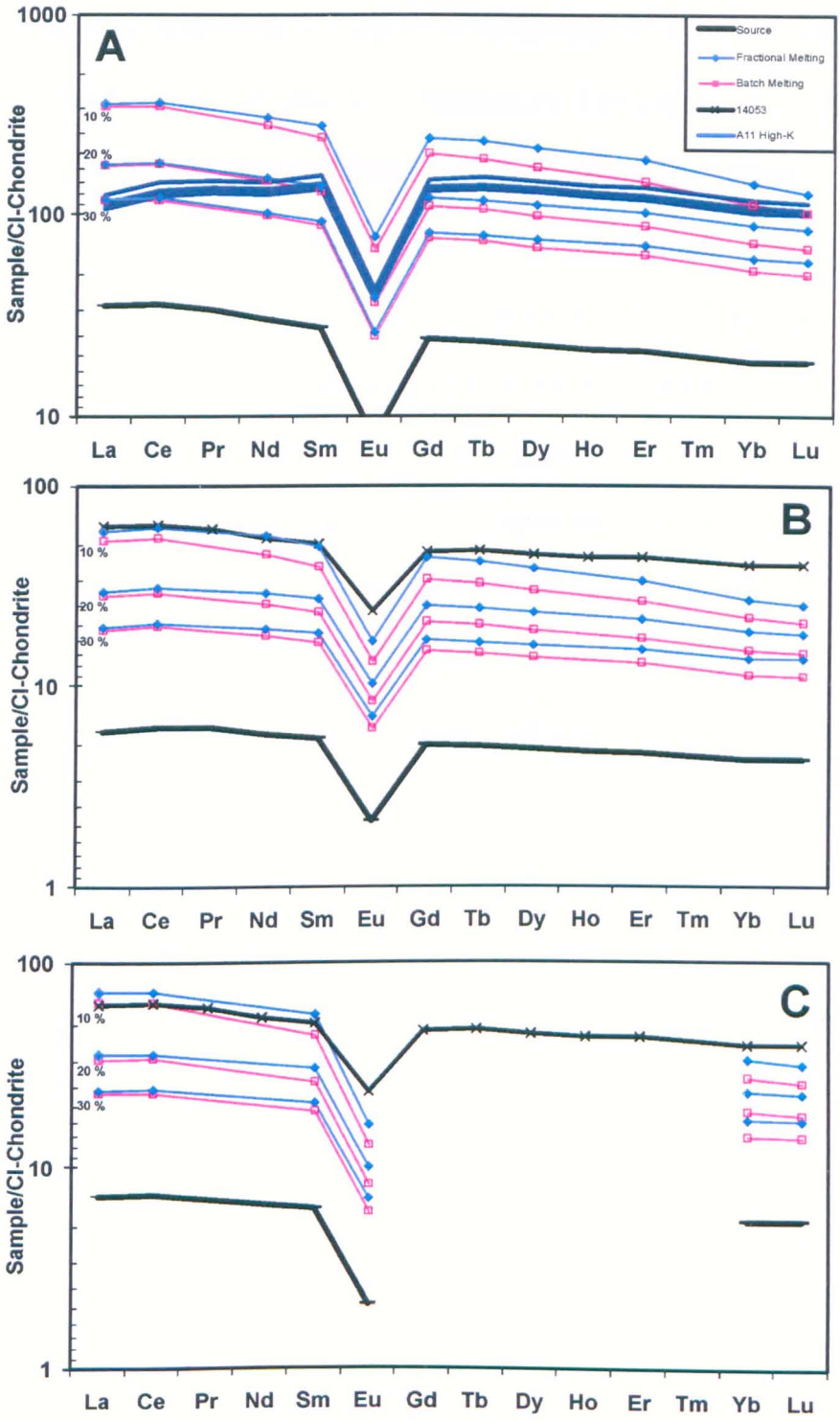

Figure 4.22: The effect of KREEP addition to the depleted Moon source compositions prior to partial melting. The plots show increasing degrees of partial melts from a depleted Moon source (Mckenzie and O'Nions, 1991), **(a)** with 130 % extra REE and 10 % added KREEP, **(b)** 1.5 % added KREEP and **(c)** 0.75 % added KREEP and 0.75 % added granitic component (Neal and Kramer, 2006). The first is compared to the bulk-rock REE abundances of Apollo 11 high-K samples, whereas the latter two plots are compared to the bulk-rock REE abundances of Apollo 14 high-Al basalt 14053. The high-Ti source modal abundances of Snyder et al. (1992) were used in the calculations for the first plot, whereas the low-Ti modal abundances were used in those of the latter two plots.

sample set. As discussed in section 4.3.2 Paces et al. (1991) and Neal and Taylor (1992) stated that lack of LREE enrichment in Apollo 11 high-K basalts suggests the incompatible-element rich contaminant was added to this mare-basalt groups source cumulates during partial melting, rather than assimilated after melt production. To test this theory, we initially added 10 % of a KREEPy material (sample 15386) to the high-Ti, REE enriched (+ 130 %) depleted-Moon source in an attempt to model the production of Apollo 11 high-K basalts via partial melting. Figure 4.22a shows the results of partial melting from this reconstructed source composition. While the europium anomaly of both modelled and observed REE trends match well with a 20 % fractional melt of this source, the LREE's are enriched in both the calculated source and partial melts, in contrast to the strong LREE depletion observed in the Apollo 11 high-K samples. For the LREE's of both the calculated and observed trends to match, the addition of only 1 % KREEPy material to the source is required, but this results in a weaker europium anomaly than that observed in the samples. Jerde et al. (1994) argue that the high-K basalt compositions are consistent with formation from a parental liquid with the composition of Apollo 11 orange glass (in agreement with the fractionation calculations of Longhi, 1987), coupled with 7.5-15 % assimilation of a KREEPy material. These calculations are also in agreement with Hughes et al. (1989) and Figure 4.19, both of which suggest a 10 % KREEP contaminant for the Apollo 11 high-K basalts. Therefore, we attempted to model the REE abundances produced by KREEP assimilation using assimilation and fractional crystallisation (AFC) calculations. DePaolo (1981) and Powell (1984) first derived the equations describing trace-element concentration in a melt, relative to the original magma composition, in terms of AFC processes:

$$C_L/C_0 = f' + (r/(r - 1 + D)) \times ((C_A/C_0) \times (1 - f')) \quad (4.4)$$

where; C_L, C_0, D and F represent the same factors as in equation 4.3,

r is the ratio of the assimilation rate to the fractional crystallisation rate,

C_A is the concentration of the trace-element in the assimilated wallrock,

and f' is represented by the equation;

$$f' = F^{-(r - 1 + D)/(r - 1)} \quad (4.5)$$

The results of these calculations show that for a 15 % fractionally-melted depleted-Moon source (with or without the addition of 130 % REE abundance) the europium anomaly and HREE's show a similar trend to the Apollo 11 high-K basalts when r = 0.7 and the fractionating assemblage is the same as that predicted for the Apollo 11 low-K basalts. However, the use of this source produces modelled data with LREE enrichment compared to the samples (Figure 4.23a). If melt with the composition of Apollo 11 orange glass is used in the AFC calculations, along with the same fractionating assemblage and a ratio (r) of 0.8, the modelled and observed trends are found to match well for the europium anomaly, HREE's and LREE's. Therefore, Apollo 11 orange glass is a good approximation for the parental melt of the Apollo 11 high-K basalts. A similar REE trend to that found within the Apollo 11 orange glass can be produced by 5 % fractional melting of the depleted-Moon source (or ~ 10 % fractional melting of a REE-enriched depleted Moon source with 130 % extra REE). However, the measured and modelled europium anomalies are slightly different (measured = 0.67 (where Sm is substituted for Gd in the Eu* calculation) and modelled = 0.51) This suggests that the Apollo 11 high-K basalt source was less depleted in Eu than the our adapted McKenzie and O'Nions (1991) depleted Moon source (McKenzie and O'Nions' (1991) source - 29 % of its Eu). This may be an indication that the Apollo 11 high-K basalt source was more oxidising than the Apollo low-K basalt sources, because the Eu^{3+}/Eu^{2+} ratio would be higher (and therefore the negative europium anomaly would be weaker) in a more oxidised source.

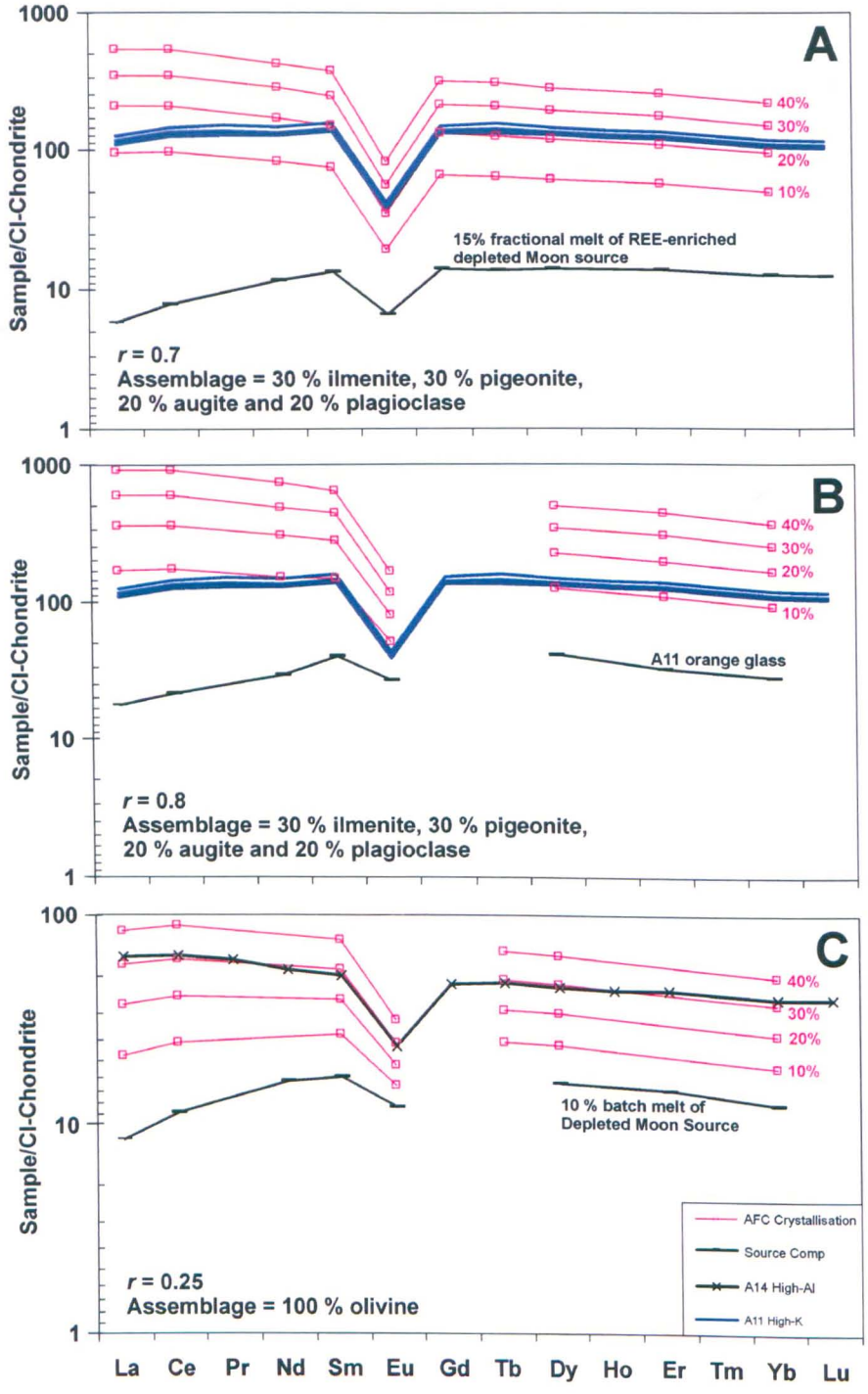

Figure 4.23: Chondrite-normalised REE abundance plots, comparing increasing proportions of AFC crystallisation with the Apollo 11 high-K and Apollo 14 high-Al group C mare-basalts. **(a)** Comparison of the measured REE's of the Apollo 11 high-K basalt samples to a 15 % fractional melt of a depleted Moon source, with the progressive addition of a KREEP assimilant. **(b)** Comparison of the measured REE's of the Apollo 11 high-K basalt samples to a melt with the composition of the Apollo 11 orange glasses, with progressive KREEP assimilation. **(c)** Comparison of Apollo 14 high-Al basalt 14053 to the REE abundance of a 10 % batch melt of a depleted Moon source, with progressive KREEP/granite mix assimilation (75 % KREEP and 25 % granite). Assemblage and ratio of the rate of assimilation to the rate of crystal fractionation (r) are shown on each individual plot.

While most authors agree that the production of the Apollo 14 high-Al basalts included a certain proportion of assimilation, only Neal and Kramer (2006) indicate the inclusion of a granitic component. These authors state that the Apollo 14 high-Al basalts of groups B and C (the latter containing sample 14053) gained elevated LREE abundances through < 5 % assimilation of a mixture of KREEP and granitic material. To exclude the possibility of source region contamination, and confirm an assimilation origin for these basalts, we initially experimented with the addition of various KREEP (sample 15386) and granite (sample 14303,204 – Neal and Kramer, 2006) mixes to the low-Ti depleted-Moon source prior to partial melting (Figure 4.22b and c). 1.5 % assimilant was added to the depleted-Moon source composition, based on the REE ratio plots of Figure 4.19. The best match for Apollo 14 high-Al sample 14053 using this model requires 15 % batch melting, followed by 40 % olivine fractionation. However, even for this situation the modelled europium anomaly is stronger than that observed in the sample (0.14 and 0.49 respectively), and the HREE's are depleted. Discrepancies in REE abundance for both a pure KREEP contaminant and granite/KREEP mix contaminant at the source region support the conclusion of Neal and Kramer (2006) that Apollo 14 group C basalts gained their high LREE content through assimilation. AFC calculations indicate that the production of these basalts involved a 75 % KREEP (sample 15386) and 25 % granite (sample 14303,204) assimilant, where r = 0.25 for 30 % fractionation of a purely olivine assemblage, from a 10 % batch melt of a depleted-Moon source (Figure 4.23b). Under these conditions the modelled data and observed REE abundances match well.

4.5. Conclusions

- Bulk-rock major-element data highlights the dichotomy in TiO_2 content between the low- and high-Ti mare basalts in our sample set (1.14-4.94 and 8.40-13.03 wt % respectively).

Table 4.6: Summary of chemical modelling results.

	Type	Sample	Evolution
Apollo 11	High-K	10017 10049 10057 10072	10 % modal melt of A11 orange glass source, with ~ 10 % KREEP assimilation
	Low-K	10020 10050 10058	low % melting (< 20 %) of a mixed source, composed of depleted Moon and REE-rich ilmenite cumulate sources.
Apollo 12	Olivine	12040	5 % batch, or 7 % fractional melting, of the McKenzie and O'Nions (1991) depleted Moon source, followed by olivine accumulation.
	Ilmenite	12016	3 % batch, or 5 % fractional melting, of the McKenzie and O'Nions (1991) depleted Moon source, followed by a small amount of olivine accumulation.
		12047	4 % batch, or 5 % fractional melting, of the McKenzie and O'Nions (1991) depleted Moon source, followed by 5-10 % olivine fractionation.
		12051	5 % batch, or 5 % fractional melting, of the McKenzie and O'Nions (1991) depleted Moon source, followed by 5-10 % olivine fractionation.
		12064	6 % batch, or 5 % fractional melting, of the McKenzie and O'Nions (1991) depleted Moon source, followed by a small amount of clinopyroxene (and possibly tryimite) accumulation.
	Pigeonite	12052	5 % batch, or 7 % fractional melting, of the McKenzie and O'Nions (1991) depleted Moon source, followed by 20 % olivine fractionation possible anorthosite assimilation (few %).
Apollo 14	High-Al	14053	10 % batch melting of the McKenzie and O'Nions (1991) depleted Moon source, along with ~ 1.5 % assimilation of a KREEP (75 %) and granite (25 %) mix during 30 % olivine fractionation.
Apollo 15	Olivine Normative	15016 15555	7 % batch, or 9 % fractional, melting of the McKenzie and O'Nions (1991) depeleted Moon source, followed by olivine accumulation.
Apollo 17	Type A	75055	low % melting (< 20 %) of a mixed source, composed of depleted Moon and REE-rich ilmenite cumulate sources.
	Type B	70215	
	Type C	74275	

- Bulk-rock major- and trace-element abundances indicate that the Apollo 12 and 15 mare basalts originate from source regions with similar compositions. The Apollo 15 olivine-normative basalts appear to be particularly similar to the Apollo 12 ilmenite basalts.

- The Apollo 11 and 17 basalts share fewer similarities than the Apollo 12 and 15 basalts, probably because of their more varied source compositions. However, the Apollo 11 high-K basalts are all very closely related in terms of chemical composition, suggesting they originated from the same melt, in agreement with previous authors (Paces et al., 1991; Neal and Taylor, 1992). Apollo 17 type A basalt 75055 shows a number of chemical similarities to Apollo 11 type B3 basalt 10020, indicating they originated from similar sources. The close relationship suggested by Snyder et al. (1990) between Apollo 17 type C basalts and Apollo 11 type B3 basalts is not obvious from our dataset.

- The higher MELTS liquidus temperature and low CaO, Al_2O_3, Na_2O, SiO_2 and REE content of Apollo 12 olivine basalt 12040, and the low forsterite content of olivines in this sample in relation to bulk-rock Mg#, indicate that it is a product of open system evolution as a result of olivine accumulation. This is in agreement with previous studies (Meyer and Wilshire, 1974; Baldridge et al., 1979). Parental melt calculations based on early pyroxene REE abundances (see also chapter 3) indicate that the original melt composition of the olivine basalts was REE enriched compared to that of the ilmenite and pigeonite basalts.

- The above factors, along with parental melt REE abundance comparisons indicate that a number of other basalts within our sample set were produced by lesser amounts of crystal accumulation (mostly olivine, though samples 12064 and 75055 show signs of pyroxene accumulation).

- Compatible-element abundance variations with decreasing Mg# indicate olivine fractionation occurred in Apollo 12 and 14 mare basalts, ilmenite fractionation occurred in the high-Ti basalts, and Cr-spinel fractionation occurred in the Apollo 12 and 17 basalts.

- The high-Ti basalts generally contain higher incompatible-element abundances than the low-Ti basalts. This can be explained by the LMO overturn model (e.g., Ringwood and Kesson, 1976; Ryder et al., 1991), whereby late-stage, incompatible-element-enriched ilmenite cumulates mixed with the olivine-pyroxene cumulates of the low-Ti mare-basalt source to produce the source of the high-Ti basalts.

- The relatively high incompatible-element abundances of the Apollo 11 high-K and Apollo 14 high-Al basalts in our sample set, along with other REE characteristics,

indicate that these samples (and by extension the basalt groups to which they belong) have undergone some form of KREEP contamination.

- The REE composition of the depleted-Moon source of McKenzie and O'Nions (1991) was found to be a fair approximation for the low-Ti mare-basalt source regions. Partial melting calculations show that the Apollo 12 pigeonite and olivine basalt REE abundances can be produced from a 5 % batch melt, or 7 % fractional melt, of this source, whereas Apollo 12 ilmenite basalts require 3 % batch or 5 % fractional melting. This is followed by 5-10 % olivine fractionation for ilmenite basalt 12051 and 20 % olivine fractionation (and possible anorthite assimilation) for pigeonite basalt 12052. The Apollo 15 olivine-normative basalts require 7 % batch or 9 % fractional melting of the depleted Moon source, followed by olivine accumulation in sample 15016.

- The depleted-Moon REE source composition of McKenzie and O'Nions (1991) is not suitable for high-Ti basalts. As the high-Ti basalt source regions are believed to be a mixture of the olivine-pyroxene cumulates found in the low-Ti basalt source regions and ilmenite cumulates which formed towards the end of LMO crystallisation, they should contain more REE's (as suggested by the higher REE abundances measured in the samples). REE enrichment of the depleted-Moon source produced some possible models for high-Ti basalt formation (e.g., a 10 % partial melt of the depleted-Moon source, with 130 % extra REE abundance, could produce REE abundances similar to the Apollo 11 B3 basalt parental melt after 30-70 % crystal fractionation), but these models were not in line with previously published isotopic evidence (Neal et al., 1990a; Paces et al., 1991; Snyder et al., 1992b, 1993).

- REE ratios in low-Ti samples are closer to those produced by batch melting than fractional melting (Figure 4.19), indicating the former was dominant in these

samples. As ratio variation along the calculated curves is minimal, this interpretation is open ended, but it does agree with the experimental data of Longhi et al. (2006). The REE ratios in high-Ti basalts plot closer to the fractional melting curves (Figure 4.19), and REE abundance trends share more characteristics with fractional melting calculations (Figure 4.17 and 4.18), indicating that fractional melting may have been a dominant process in the case of high-Ti basalts.

- REE ratios and AFC calculations indicate that the Apollo 11 high-K basalts formed from the assimilation of approximately 10 % KREEPy material into a partial melt with the composition of the Apollo 11 orange glasses, in agreement with Longhi (1987), Hughes et al. (1989) and Jerde et al. (1994). These glasses contain similar REE abundances to a 5 % fractional melt of McKenzie and O'Nions (1991) depleted Moon source (or a 10 % fractional melt of a 130 % REE enriched source).

- REE ratios and AFC calculations for the Apollo 14 high-Al group C basalt 14053,260 suggest this group of basalts originated from a 10 % batch melt of a depleted-Moon source which assimilated ~ 1.5 % of a 75 % KREEP and 25 % granite mix during 30 % fractionation of an olivine assemblage. The presence of a KREEP/granite mixed assimilant within the group B and C Apollo 14 high-Al basalts was also suggested by Neal and Kramer (2006).

While the above calculations give an idea of the conditions each basalt group formed under, they also highlight the variety of different ways the mare basalts evolved. The REE composition of McKenzie and O'Nions (1991) depleted-Moon source appears to be a fair estimate of the low-Ti mare-basalt olivine-pyroxene cumulate source, but simple REE enrichment did not produce accurate REE abundances for the high-Ti basalts. The high-Ti basalt source regions appear to be more complex, with each basalt group evolving from sources with different proportions of late-stage crystallisation products enriched in REE's.

This heterogeneity is an indication of the incomplete mixing of ilmenite, pyroxene and olivine rich cumulates, and KREEPy, granitic and other plutonic components within the source regions. The different degrees and types of partial melting, along with crystal fractionation and possible assimilation, further contribute towards the diversity of mare-basalts in terms of trace- and rare-earth-element compositions.

5. OXYGEN ISOTOPES

A manuscript based on the results presented in this chapter has been submitted to Geochimica et Cosmochimica Acta (Hallis et al., 2010), and is currently under review.

5.1. An Introduction to Oxygen Isotopes

5.1.1. Oxygen Isotopes and the Giant-Impact Theory. As discussed in section 1.1, the formation of the Moon is widely considered to have been the result of a large scale collision in the early solar system, between the proto-Earth and a Mars-sized planetesimal (Hartmann and Davis, 1975; Cameron and Ward, 1976). Similarities between the inferred lunar and silicate Earth compositions (Ringwood, 1979), lack of a large lunar iron core, short-lived radionuclide dating of lunar formation (e.g., Touboul et al., 2007), combined with the abnormally high angular momentum in the Earth-Moon system (Cameron and Ward, 1976) have been cited as evidence in support of this theory. Recent smooth-particle hydrodynamic (SPH) impact simulations suggest that 70-90 % of Moon forming material was derived from the impacting body (Cameron, 2000; Canup and Asphaug, 2001; Canup, 2004a). These results imply that even relatively small isotopic differences between the impacting planetesimal and the proto-Earth should have left an observable difference between the Earth and the Moon. However, previous high-precision oxygen isotope studies have been unable to distinguish between the terrestrial and lunar fractionation lines (Wiechert et al., 2001; Spicuzza et al., 2007). It has been suggested that this isotopic homogeneity may be the result of post-impact isotopic mixing between the Earth's silicate mantle and the lunar forming magma disk (Pahlevan and Stevenson, 2007). However, more recent studies indicate that the high level of mixing needed to achieve homogenisation would equilibrate the angular-momentum of the Earth-Moon system, rendering the current dynamics of this system implausible (Melosh, 2009). Conversely, some authors have

suggested that the impactor and the Earth had virtually identical oxygen isotope compositions (Belbruno and Gott, 2005; Taylor et al., 2006).

5.1.2. Oxygen Isotopes in the Mare-Basalt Source Regions. Previous high-precision oxygen isotope studies have been used successfully to identify important processes that operated during the evolution of the LMO. Wiechert et al. (2001) found a systematic $\delta^{18}O$ difference of 0.4 ‰ between the anorthositic rocks of the primary crust and mare-basalts, an offset explained via equilibrium fractionation between feldspar and the silicate melt during LMO crystallisation. In addition, both Wiechert et al. (2001) and Spicuzza et al. (2007) found an offset of 0.2-0.25 ‰ for bulk-rock $\delta^{18}O$ between the low and the high-Ti mare-basalts, which the latter suggested was a direct consequence of lunar mantle-source heterogeneity.

In order to improve understanding of the evolution of the lunar magma ocean, we have undertaken a high-precision oxygen isotope study of our sample set. Only three other studies report oxygen three-isotope measurements ($^{18}O/^{16}O$ and $^{17}O/^{16}O$) of mare basalts at similarly high precision (Wiechert et al., 2001; Spicuzza et al., 2007; Liu et al., 2009). Of the twenty-two Apollo basalts within our sample set, twelve samples have been analysed for oxygen isotopes in these other studies, thus enabling useful comparisons with our measurements. Liu et al. (2009) analysed a single Apollo 11 mare basalt (sample 10044), but apart from this no other studies have reported the oxygen isotopic composition of Apollo 11 mare basalts - a group which partially bridges the gap between the low-Ti basalts of Apollo 12, 15 and 14 and the high-Ti basalts of Apollo 17.

5.1.3. Oxygen Isotope Notation. The data are reported using the usual δ notation, as per mil (‰) variations from the Vienna standard mean ocean water (VSMOW) reference:

$$\delta^{18}O = \frac{\left(^{18}O/^{16}O\right)_{sample}}{\left(^{18}O/^{16}O\right)_{ref}} - 1 \qquad (1)$$

and similarly for $\delta^{17}O$ using the $^{17}O/^{16}O$ ratio.

We report $\Delta^{17}O$ as the ordinate deviation from a reference (mass-dependent) fractionation line (Figure 5.1) on the logarithmic form of the oxygen three-isotope plot (Miller, 2002):

$$\Delta^{17}O\ (‰) \approx 10^3 \ln(1 + \delta^{17}O) - \lambda 10^3 \ln(1 + \delta^{18}O) \qquad (2)$$

For nearly all $\Delta^{17}O$ values encountered in nature, equation (2) is a very close approximation of the 'exact' linear relationship, given by

$$10^3 \ln(1 + \Delta^{17}O) = 10^3 \ln(1 + \delta^{17}O) - \lambda 10^3 \ln(1 + \delta^{18}O) \qquad (3)$$

which may also be expressed as in equation 4, where λ represents the slope of the line.

$$\Delta^{17}O = \frac{1 + \delta^{17}O}{(1 + \delta^{18}O)^{\lambda}} - 1 \qquad (4)$$

The assignment of a reference value for λ is necessarily somewhat arbitrary. A value of 0.524 was obtained independently in two studies which reported high-precision measurements of many terrestrial silicates from various origins (Miller, 2002; Pack et al., 2007); the same result was also reported by Rumble et al. (2007) to be characteristic of natural silicas (although the associated fractionation line is slightly offset from VSMOW). A λ value of 0.524 (and with no offset) is probably a representative average of numerous

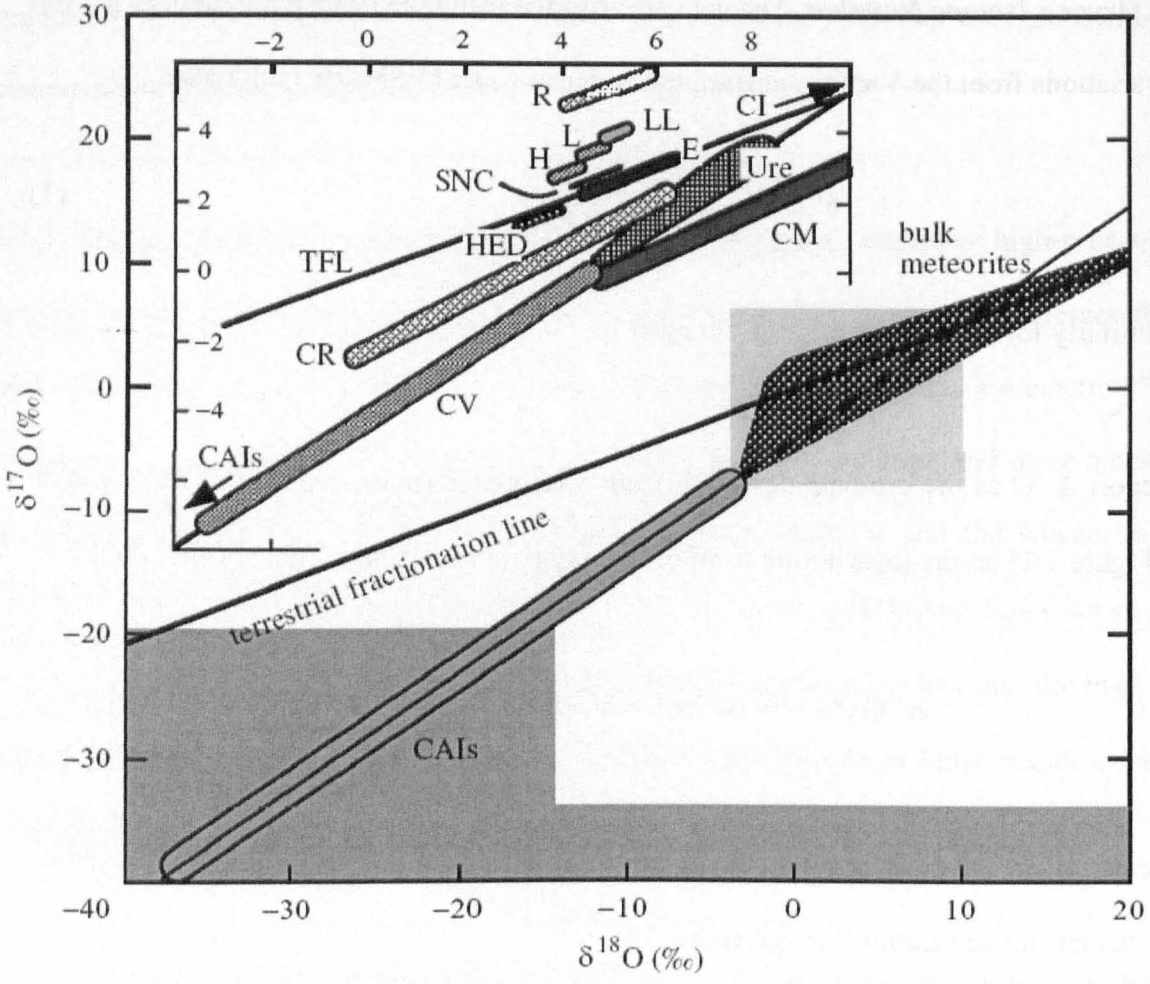

Figure 5.1: Bulk-rock oxygen isotope composition of various meteorite groups relative to the terrestirial fractionation line (TFL). Inset covers area the of the light grey box. The main groups of chondritic and achondritic meteorites, covering the range of values displayed by these types, are shown. TFL = terrestrial fractionation line, which is shown for reference; H, L and LL are all types of ordinary chondrites; R = R chondrites; CR, CV and CM are carbonaceous chondrites; E = enstatite chondrites and aubrites; SNC = shergottites, nakhlites and Chassigny; HED = howardites, eucrites and dioginites; Ure = ureilites; CAIs = calcium-aluminium-rich inclusions. Diagram from Franchi et al. (2001).

terrestrial geological fractionation processes, rather than being applicable specifically to basalts of either terrestrial or lunar origin. Furthermore, we recognise that eclogitic garnets (Rumble et al., 2007) and fractionation lines formed from some specific combinations of silicates (e.g., the four point line reported by Spicuzza et al., 2007) give values of λ that are significantly higher than 0.524. It is also important to recognise that the assigned reference fractionation line may not necessarily pass through VSMOW on the logarithmic form of

the oxygen three-isotope plot. For example, the line formed from eclogitic garnets (Rumble et al., 2007) is offset by -0.026 per mil, as determined using the same experimental facility and 'working standard' O_2 gas used for the present investigation of lunar basalts. The effect of the choice of λ for the present work (and any associated ordinate axis offset of the fractionation line on the logarithmic form of the oxygen three-isotope plot) is discussed further in section 5.2.1.

International standards UWG-2 (Valley et al., 1995) and San Carlos olivine (Kusakabe and Matsuhisa, 2008, and references therein) and an in-house standard, PSSRI obsidian (Miller et al. 1999) were analysed along with the lunar samples in order to monitor system performance. A minimum of two replicates per lunar sample were run and the results averaged to give a single value per sample. Published system precision (2σ), based on replicate analyses of international (NBS-28 quartz, UWG-2 garnet) and internal standards, is approximately ± 0.08 ‰ for $\delta^{17}O$; ± 0.16 ‰ for $\delta^{18}O$; ± 0.05 ‰ for $\Delta^{17}O$ (Miller et al., 1999). The quoted precision (2σ) for the lunar samples is based on 2 or more replicate analyses.

5.2. Oxygen Isotope Data

5.2.1. Comparison of Lunar and Terrestrial $\Delta^{17}O$ values. Table 5.1 shows the $\Delta^{17}O$ results as calculated from $\delta^{17}O$ and $\delta^{18}O$ for lunar samples in conjunction with an assigned λ value of 0.524 and with no ordinate axis offset. On this basis, the average $\Delta^{17}O$ of our lunar sample suite is -0.008 ± 0.021 ‰. The comparable mean $\Delta^{17}O$ value from thirty-seven replicate analyses of the UWG-2 garnet standard (as obtained during a period of one year that fully encompassed the interval in which the lunar samples were run) is -0.017 ± 0.034 ‰, which is clearly indistinguishable from the lunar samples, on the basis of the associated analytical precision. Wiechert et al. (2001) and Spicuzza et al. (2007) were also unable to detect any difference between lunar and terrestrial $\Delta^{17}O$ values.

Table 5.1: Lunar and terrestrial $\delta^{17}O$, $\delta^{18}O$ and $\Delta^{17}O$.

Sample	Basalt Type	n	$\delta^{17}O$‰	2σ	$\delta^{18}O$‰	2σ	$\Delta^{17}O$‰	2σ	TiO_2	Mg#
Apollo 11: 10017	High-Ti, Low-Al, High-K	3	2.99	0.060	5.68	0.079	0.017	0.019	11.01	40.9
Apollo 11: 10020	High-Ti, Low-Al, Low-K (B3)	2	2.95	0.042	5.63	0.061	0.002	0.011	10.34	42.1
Apollo 11: 10049	High-Ti, Low-Al, High-K	2	2.95	0.031	5.65	0.020	-0.010	0.021	10.59	38.9
Apollo 11: 10050	High-Ti, Low-Al, Low-K (Unclassified)	2	2.95	0.088	5.65	0.156	-0.004	0.006	11.30	42.8
Apollo 11: 10057	High-Ti, Low-Al, High-K	2	2.96	0.055	5.66	0.075	-0.006	0.016	11.01	40.2
Apollo 11: 10058	High-Ti, Low-Al, Low-K (B1)	2	2.99	0.083	5.70	0.177	0.003	0.009	8.40	41.1
Apollo 11: 10072	High-Ti, Low-Al, High-K	2	2.92	0.071	5.61	0.110	-0.019	0.013	11.36	37.6
Apollo 12: 12016	Low-Ti, Low-Al, Low-K (ilmenite basalt)	2	2.88	0.096	5.53	0.106	-0.014	0.041	3.65	51.8
Apollo 12: 12040	Low-Ti, Low-Al, Low-K (olivine basalt)	3	2.87	0.122	5.49	0.179	0.000	0.028	2.65	56.9
Apollo 12: 12047	Low-Ti, Low-Al, Low-K (ilmenite basalt)	2	2.97	0.030	5.69	0.042	-0.015	0.008	4.94	37.0
Apollo 12: 12051	Low-Ti, Low-Al, Low-K (ilmenite basalt)	2	3.03	0.023	5.76	0.041	0.009	0.001	4.43	36.5
Apollo 12: 12052	Low-Ti, Low-Al, Low-K (pigeonite basalt)	2	2.95	0.083	5.70	0.017	-0.031	0.074	3.25	41.0
Apollo 12: 12064	Low-Ti, Low-Al, Low-K (ilmenite basalt)	3	2.96	0.212	5.66	0.369	-0.004	0.061	3.64	37.9
Apollo 14: 14053	Low-Ti, High-Al, Low-K (group C)	2	3.03	0.004	5.81	0.095	-0.016	0.045	2.56	46.6
Apollo 15: 15016	Low-Ti, Low-Al, Low-K (olivine normative)	5	2.97	0.131	5.66	0.282	0.003	0.054	2.11	48.5
Apollo 15: 15386	KREEP basalt	2	3.11	0.035	5.95	0.061	-0.007	0.004	2.10	59.3
Apollo 15: 15555	Low-Ti, Low-Al, Low-K (olivine normative)	2	2.96	0.126	5.70	0.100	-0.022	0.073	1.14	54.4
Apollo 17: 70017	High-Ti, Low-Al, Low-K (unclassified)	4	2.85	0.164	5.46	0.285	-0.012	0.037	12.86	48.7
Apollo 17: 70035	High-Ti, Low-Al, Low-K (unclassified)	2	2.84	0.023	5.45	0.057	-0.015	0.052	13.03	44.7
Apollo 17: 70215	High-Ti, Low-Al, Low-K (type B2)	2	2.88	0.037	5.51	0.049	-0.005	0.011	12.71	44.2
Apollo 17: 74275	High-Ti, Low-Al, Low-K (type C)	2	2.89	0.017	5.54	0.031	-0.012	0.001	12.57	50.1
Apollo 17: 75055	High-Ti, Low-Al, Low-K (type A)	2	2.90	0.059	5.56	0.219	-0.013	0.055	12.22	45.8
Average Lunar		**52**	**2.94**	**0.128**	**5.64**	**0.237**	**-0.008**	**0.021**		

Terrestrial Samples	Rock Type	n	$\delta^{17}O$‰	2σ	$\delta^{18}O$‰	2σ	$\Delta^{17}O$‰	2σ
UWG-2 Garnet	Garnet	37	2.96	0.080	5.68	0.146	-0.017	0.034

We eliminated from the UWG-2 garnet dataset any analyses that were run first in a tray, as these often produce elevated blank levels. Furthermore, we consider that UWG-2 is a better standard for this study than are alternative silicates commonly used as oxygen isotope standards, as it has been well characterised (Valley et al., 1995) and has a $\delta^{18}O$ value close to that of the lunar samples (Table 5.1). The average $\delta^{18}O$ value obtained from thirty-seven UWG-2 garnet measurements was 5.68 ‰, which is close to the value of 5.8 ‰ recommended by Valley et al. (1995).

If, instead of assigning λ to be 0.524 and with no ordinate axis offset (Miller, 2002), we use the fractionation line reported by Rumble et al. (2007) for eclogitic garnets, λ becomes 0.5262 ± 0.0010 (95 % confidence level) and the ordinate axis offset becomes -0.026 ± 0.0007. Again, this is on the basis of measurements made using the same analytical facility and using the same O_2 'working standard' gas as for our measurements on the lunar samples. In this case, the mean $\Delta^{17}O$ value for the lunar basalts becomes 0.006 ‰ and the mean of the thirty-seven measurements of UWG-2 becomes -0.003 ‰. Clearly, the reference fractionation line given by the eclogitic garnets appears to be better matched to the lunar basalts and to the UWG-2 garnet, which is not surprising. Alternatively, if we were to use the fractionation line given by natural silicas (Rumble et al., 2007), which has a λ value of 0.524 but an ordinate axis offset of +0.020 ‰ as measured on the same mass spectrometer and with the same 'working standard' O_2 gas as for the lunar basalt analyses reported in this study, the corresponding $\Delta^{17}O$ values are changed accordingly but there is again no detectable difference between the $\Delta^{17}O$ of terrestrial and lunar silicates. The effect of switching between these two reference fractionation lines (silicas versus eclogitic garnets) is illustrated in Figure 5.2. The lack of detectable difference in $\Delta^{17}O$ (within error) between low- and high-Ti basalts is in agreement with previous suggestions that the source regions for these basalts were in oxygen isotopic equilibrium (Spicuzza et al., 2007).

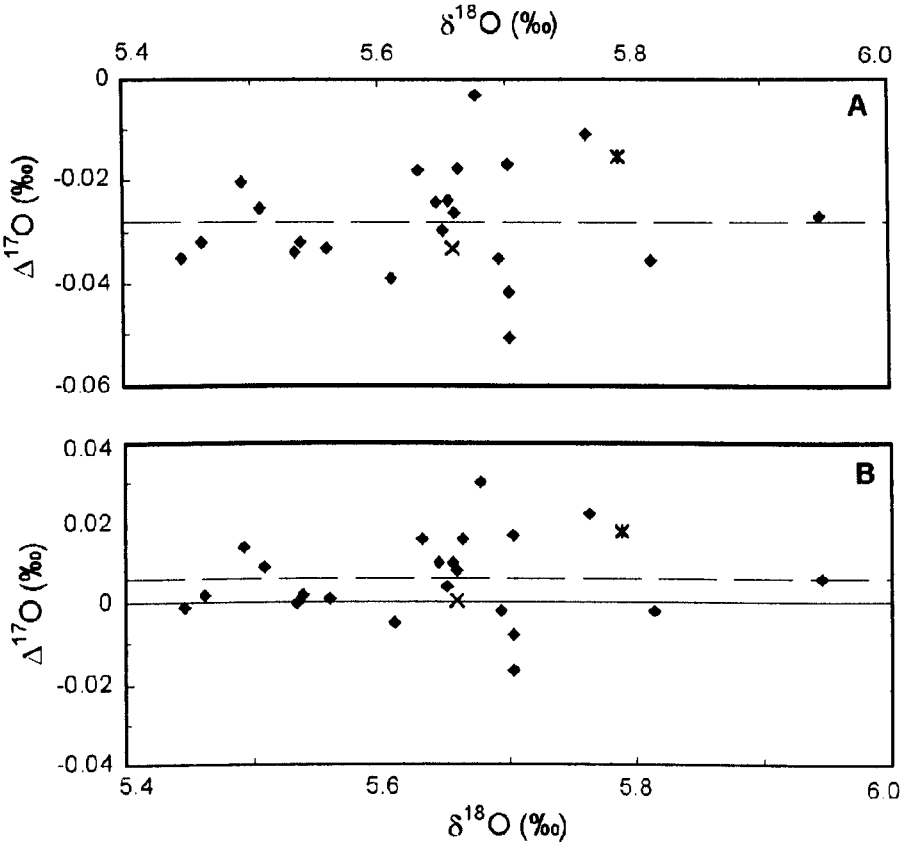

Figure 5.2: The effect of changing reference fractionation line for calculating the $\Delta^{17}O$ data. In **(a)**, λ is assigned as 0.524 and the associated ordinate axis offset on the logarithmic form of the oxygen three-isotope plot is 0.020. These values were as obtained from terrestrial silicas, using the same experimental facility and 'working standard' O_2 gas as for our measurements on the lunar basalts. Changing to $\lambda = 0.5262$ and offset of -0.026 (as given by eclogitic garnets in the same laboratory) produces the plot illustrated in **(b)**. In both cases, terrestrial samples are represented by UWG-2 garnet (a single point, representing the average of thirty-seven replicate analyses) and by a sample of MORB (designated RD32). Lunar basalts data are shown as filled diamonds, UWG-2 as a simple cross and MORB as a star. The mean of the lunar basalt $\Delta^{17}O$ data is shown by the dashed line, in both **(a)** and **(b)**.

5.2.2. Comparison of $\delta^{18}O$ in High and Low-Ti Mare Basalts. Measured $\delta^{18}O$ values for our set of Apollo basalts are presented in Table 5.1. Low-Ti mare basalts generally exhibit higher $\delta^{18}O$ than high-Ti basalts, with the exception of two low-Ti Apollo 12 olivine rich basalts (samples 12016 and 12040, discussed below). The average $\delta^{18}O$ for the high-Ti basalts is 5.59 ± 0.17 and the average of the low-Ti basalts excluding the above mentioned samples and KREEP basalt 15386 is 5.71 ± 0.11. Apollo 15 KREEP basalt 15386 shows

the heaviest $\delta^{18}O$ (5.95 ± 0.06). Apollo 14 high-Al basalt 14053 plots between the KREEP basalt and other mare-basalts (5.81 ± 0.10). Of the high-Ti basalts Apollo 11 samples have heavier bulk-rock $\delta^{18}O$ whereas Apollo 17 samples display lighter values. There is no clear difference between the $\delta^{18}O$ of Apollo 11 high-K and low-K basalts.

Figure 5.3 shows measured bulk-rock $\delta^{18}O$ vs. bulk-rock Mg# for each sample (where Mg# = (Mg/(Fe+Mg))*100, using bulk-rock atomic % values). The fields for high-Ti and low-Ti lunar basalts defined by Spicuzza et al. (2007) are also shown on Figure 5.3 5.2 for reference. At first glance there appears to be no relationship between Mg# and $\delta^{18}O$. Apollo 11 and 17 high-Ti basalts show little $\delta^{18}O$ variation with Mg# while Apollo 14 and 15 low-Ti basalts were not analysed in great enough numbers to display any meaningful relationship. The Apollo 12 basalts do show a slight increase in $\delta^{18}O$ with decreasing Mg# (sample 12040 Mg# = 56.93 and $\delta^{18}O$ = 5.49, whereas sample 12051 Mg# = 36.52 and $\delta^{18}O$ = 5.76), but it is important to note that as sample 12040 is known to be an olivine-cumulate (chapter 4, Baldridge et al., 1979), its bulk-rock Mg# is not representative of the melt from which it crystallised. A trend of decreasing $\delta^{18}O$ with increasing Mg# for low-Ti samples was also reported by Spicuzza et al. (2007) (their low-Ti field in Figure 5.3).

The data of Spicuzza et al. (2007) show a clear difference between the bulk-rock $\delta^{18}O$ of low- and high-Ti samples. However, only Apollo 17 high-Ti mare basalts were analysed in their study. Our Apollo 17 data agree well with those of Spicuzza et al. (2007), but our Apollo 11 high-Ti basalt data stretch well into the low-Ti $\delta^{18}O$ region. Although Apollo 11 basalts generally contain lower abundances of ilmenite than Apollo 17 basalts, they still have much higher ilmenite content than any of the low-Ti basalts (Table 5.2). The bimodal high- and low-Ti $\delta^{18}O$ variation reported by Spicuzza et al. (2007) turns out to be continuous when the Apollo 11 samples measured in the present study are included.

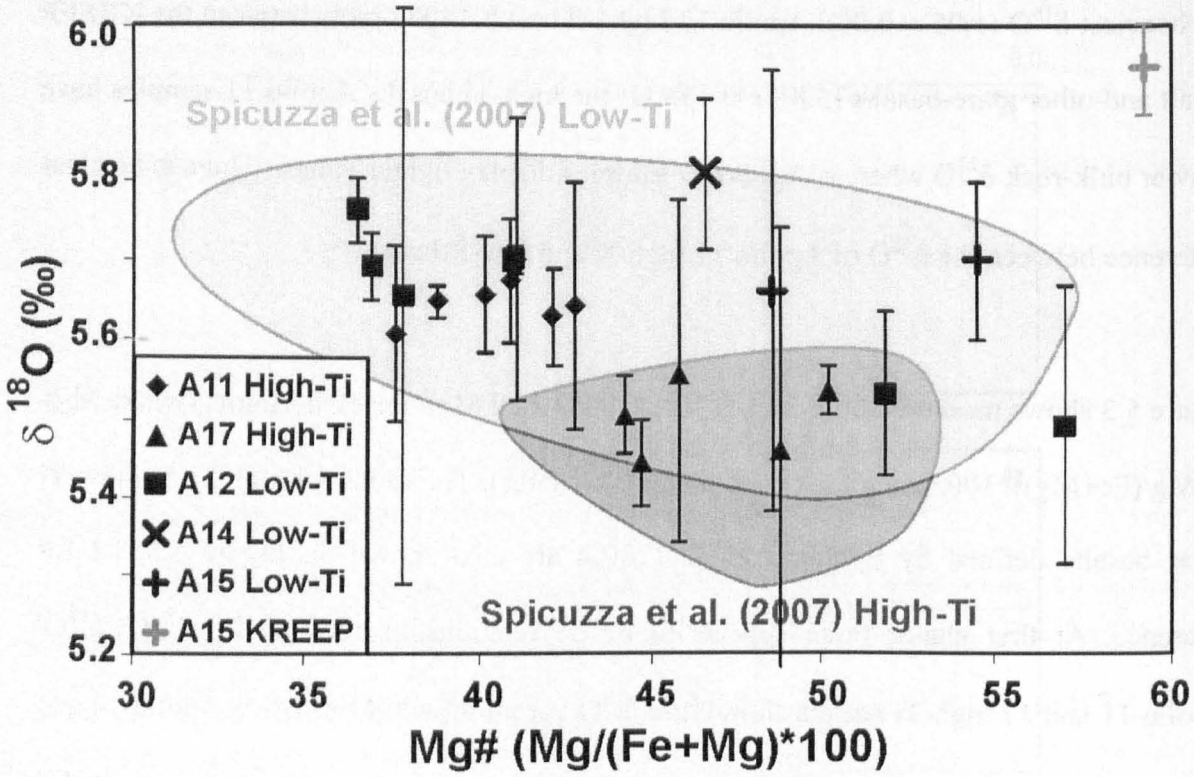

Figure 5.3: Measured $\delta^{18}O$ vs. Mg# for each basalt sample. Shadows represent the data of Spicuzza et al. (2007), light grey for low-Ti and dark grey for high-Ti.

Figure 5.4 shows the $\delta^{18}O$ value of each sample vs. bulk-rock TiO_2 content. TiO_2 was measured from the powdered rock-chips, therefore, it can be used to check sample heterogeneity by comparison with recalculated bulk-rock TiO_2 content based on ilmenite modal abundance (estimated from the thin sections – Figure 5.5a) and microprobe data. High-Ti basalts show an inverse relationship between bulk-rock TiO_2 content and $\delta^{18}O$, but this relationship is not obvious for the low-Ti basalts. The same trend is visible when the ilmenite modal abundance of each sample is plotted against $\delta^{18}O$ (Figure 5.5a), indicating that mineral modes in our thin-sections are broadly representative of the bulk-rock. There is one exception, however, the thin-section of Apollo 17 type A basalt 75055 contains 10 modal % ilmenite, which is anomalously low compared to previous data (12-20 modal % – Kriedelbaugh and Weill, 1973; Brown et al., 1975; Dymek et al., 1975; McGee et al., 1977). Because of this low modal ilmenite value, sample 75055 plots away from the high-Ti basalt trend in Figure 5.4a. In contrast, the measured bulk-rock TiO_2 value (12.22 wt %)

is comparable to previous data (10.4-11.41 wt % - Boynton et al., 1975; Rhodes et al., 1978) and plots alongside data points of other Apollo 17 basalts in Figure 5.4. The ilmenite abundance in rock chip 75055,120 is therefore more representative of the bulk-rock compared to the modal ilmenite data from the thin section. As $\delta^{18}O$ is measured from rock chip 75055,120 and not thin-section 75055,49 the value is considered to be representative of the bulk-rock oxygen isotope composition.

Differing ilmenite content can at least partially explain the difference in $\delta^{18}O$ between low- and high-Ti basalts. Ilmenite has low $\delta^{18}O$ values (4.55 to 3.85 ‰ - Onuma et al., 1970; Taylor and Epstein, 1970). Therefore, high modal abundance of ilmenite decreases bulk-rock $\delta^{18}O$. However, the trend of the high-Ti basalts in Figure 5.5 indicates that as ilmenite abundance in a sample decreases, its effect on bulk-rock $\delta^{18}O$ lessens until (as appears to

Table 5.2: Mineral modal abundances (excluding minor minerals).

Sample*	Clinopyroxene	Plagioclase	Olivine	Ilmenite	Spinel	Armalcolite	Silica	Sum
A11 10017	53.7	35.8		10.2	0.2	0.1		100
A11 10020	47.8	32.9	5.1	14.0	0.1			100
A11 10049	50.4	33.6		14.6			1.4	100
A11 10050	50.9	32.7	0.8	14.1			1.6	100
A11 10057	55.7	36.3		8.0				100
A11 10058	51.5	32.6		11.0			4.9	100
A11 10072	45.5	39.1	0.5	14.9				100
A12 12016	51.0	30.6	14.2	3.6	0.6			100
A12 12040	55.4	19.2	22.1	3.2	0.1	<0.1		100
A12 12047	51.0	38.7	1.0	6.1	0.3		3.0	100
A12 12051	60.2	30.2		6.7	0.1		2.8	100
A12 12052	61.9	32.1	1.6	2.7	0.3		1.4	100
A12 12064	63.1	27.7		4.9	0.5		3.8	100
A14 14053	59.3	34.1	3.2	2.2	0.3		0.9	100
A15 15016	60.6	23.4	12.3	0.9	2.8			100
A15 15386	38.4	56.4		2.6			2.7	100
A15 15555	55.9	30.9	10.7	1.3	0.6		0.5	100
A17 70017	53.1	28.3	1.0	17.1	0.1	0.2	0.3	100
A17 70035	51.8	28.6		17.8	0.2	0.2	1.4	100
A17 70215	63.2	12.5	7.0	17.1	0.1	0.1	<0.1	100
A17 74275	51.0	21.8	9.2	15.1	1.9	0.9	0.3	100
A17 75055	54.9	31.3		10.2			3.6	100

*A11, A12 etc denotes pollo mission. Where vol % of certain minerals are vastly different from those reported in Table 3.1 the sample contains high amounts of mesostasis and minor minerals, which are excluded from these calculations (the remaining minerals are normalised).

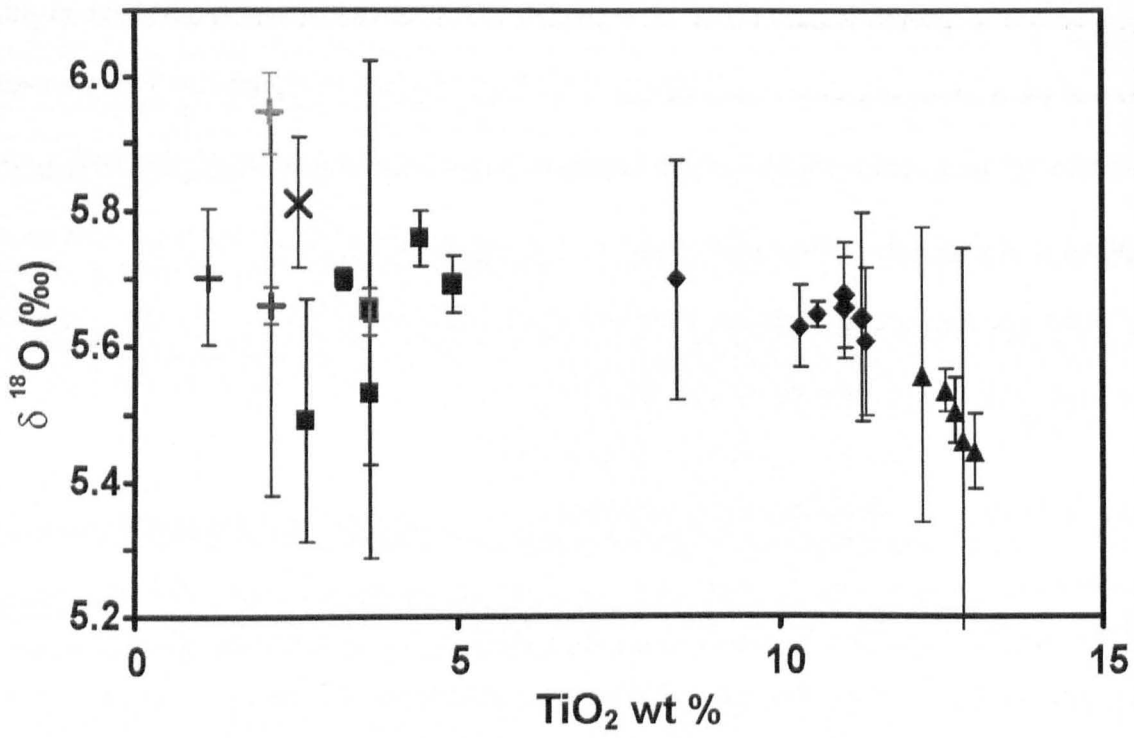

Figure 5.4: Measured $\delta^{18}O$ vs. TiO_2 wt % for each basalt sample. The high-Ti basalts show a clear linear relationship, as TiO_2 decreases, $\delta^{18}O$ increases. No such relationship is visible for the low-Ti basalts. Apollo 12 olivine-cumulate basalt 12040 shows the lowest $\delta^{18}O$ of all the low-Ti basalts. Key as in Figure 5.3. The d18O difference between the Apollo 17 and Apollo 12, 14 and 15 basalts is clearer when anomalous results are excluded from samples 12064 and 15016 (see smaller error bars in red).

be the case for the low-Ti basalts) ilmenite abundance is no longer a significant factor. Apollo 12 olivine-rich basalts 12016 and 12040 display $\delta^{18}O$ similar to Apollo 17 basalts, despite their low ilmenite modal abundance. Olivine also has relatively low $\delta^{18}O$ values (5.24 to 4.99 ‰) (Clayton et al., 1971, 1973), so the high modal abundance of olivine appears to have lowered the bulk-rock $\delta^{18}O$ of these samples in comparison to the other low-Ti basalts. Plagioclase tends to have high $\delta^{18}O$ values (6.31 to 5.67 ‰) (Mayeda et al., 1975; Onuma et al., 1970), therefore, samples with high plagioclase abundance, such as Apollo 14 high-Al basalt 14053 and Apollo 15 KREEP basalt 15386 reflect this in their bulk-rock $\delta^{18}O$ values.

5.2.3. Reconstruction of Bulk-rock $\delta^{18}O$. To check our $\delta^{18}O$ values were accurate for each sample we used modal abundance data based on thin section analyses (Table 5.2), along with previously measured mineral-separate $\delta^{18}O$ from lunar samples (Table 5.3), to reconstruct bulk-rock $\delta^{18}O$ values (Table 5.4). Using this method we aimed to further investigate how individual minerals may have influenced the bulk-rock $\delta^{18}O$ of mare basalts. Table 5.3 shows the extent of variation between published mare-basalt mineral-

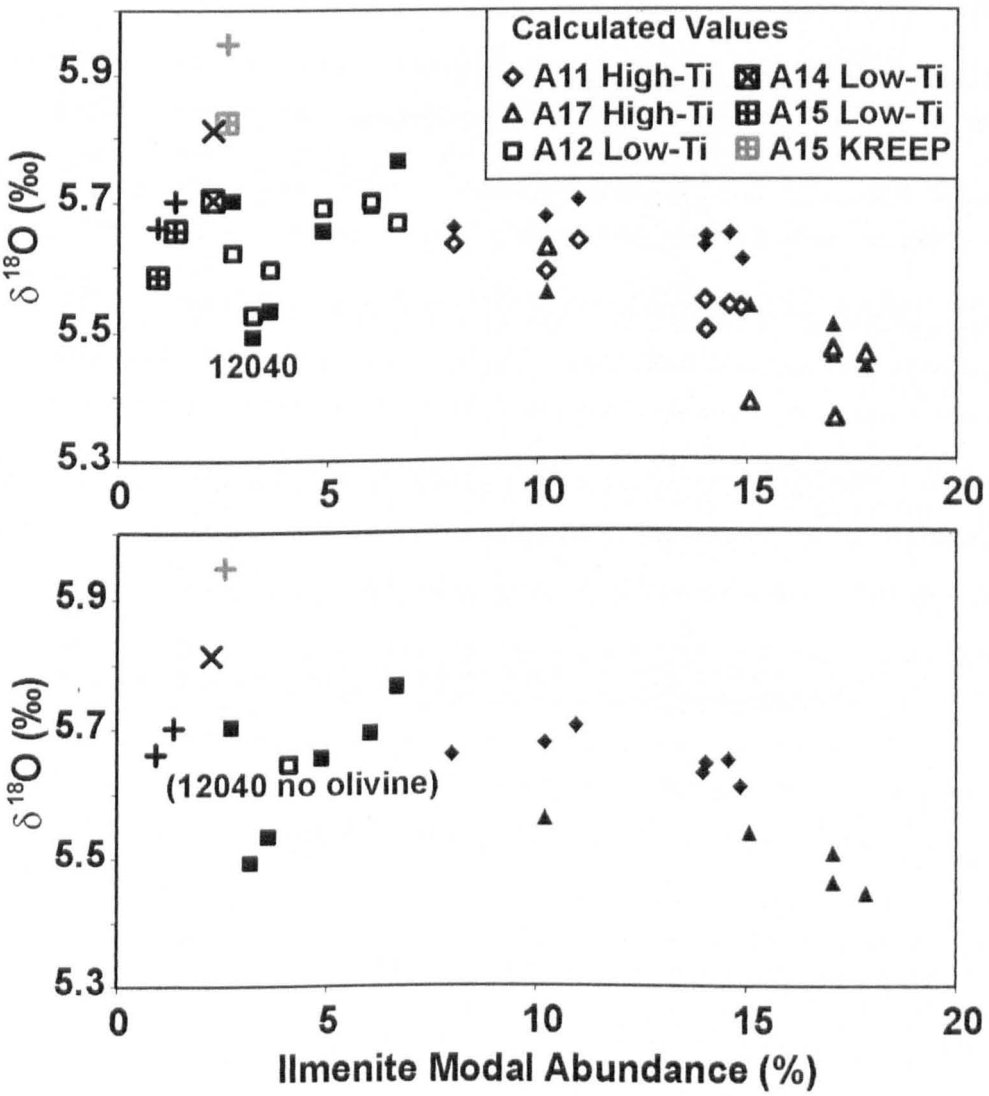

Figure 5.5: Ilmenite modal abundance vs. $\delta^{18}O$. **(a)** Where solid symbols represent measured data (as in Figures 5.3 and 5.4) and open symbols represent calculated data (see key). **(b)** When olivine is removed from the modal abundance of Apollo 12 olivine cumulate basalt 12040, $\delta^{18}O$ becomes similar to other Apollo 12 and 15 low-Ti mare basalts. Key as in Figure 5.3.

separate data. As there appears to be no systematic difference between the values in low- and high-Ti basalts, we decided to calculate the average value for each mineral. Figure 5.5a shows the ilmenite modal abundance in each sample vs. measured bulk-rock $\delta^{18}O$ and calculated values based on mineral-separate data. Measured and calculated bulk-rock $\delta^{18}O$ values agree to within 0.13 ‰ for all samples, demonstrating that the difference in $\delta^{18}O$ between basalts with high- and low-Ti content is real rather than an analysis artefact. The small discrepancies that are present may be ascribed to a number of factors. For example,

Table 5.3: Mare basalt mineral separates ^{18}O data (‰)

	Mineral					
Sample*	**Plagioclase**	**Ca-pyroxene**	**Pigeonite**	**Olivine**	**Ilmenite**	**Silica**
A11 Low-K [a]	6.31	5.71			4.55	
A11 Low-K [a]	6.17	5.72			4.47	
A11 High-K [a]	6.16	5.81			4.51	
A11 High-K [a]	6.18	5.77			4.35	
A11 High-K [a]	6.20	5.76			4.29	
A11 High-K [a]	6.00	5.53			4.24	7.09
Average [a]	**6.17 ± 0.2**	**5.72 ± 0.2**			**4.40 ± 0.25**	**7.09**
A11 10058 (Low-K) [b]	6.07	5.75			3.94	
A11 10044 (Low-K) [b]	6.06	5.67			3.85	7.16
A11 10003 (Low-K) [b]	6.09	5.86			4.10	
A11 10017 (High-K) [b]	6.33	5.95			4.02	
A11 10057 (High-K) [b]	6.30	5.83			4.12	
Average [b]	**6.17 ± 0.27**	**5.81 ± 0.21**			**4.01 ± 0.23**	**7.16**
A11 Average	**6.17 ± 0.22**	**5.76 ± 0.22**			**4.22 ± 0.47**	**7.13**
A17 72155 [c]	5.78	5.22			3.97	7.02
A17 70017 [c]	5.82	5.27			3.99	
A17 71055 [c]	5.82	5.36			4.01	6.75
A17 75075 [c]	5.70	5.39			3.95	
A17 79155 [c]	5.88	5.47			4.03	6.71
A17 75055 [c]	5.67	5.47			3.98	6.86
Average [c]	**5.78 ± 0.16**	**5.36 ± 0.21**			**3.99 ± 0.06**	**6.84 ± 0.28**
High-Ti Average	**6.03 ± 0.43**	**5.62 ± 0.44**			**4.14 ± 0.44**	**6.93 ± 0.37**
A12 12008 [d]				5.05		
A12 12009 [d]				5.20		
A12 12018 [d]	5.92	5.63		5.16	4.15	
A12 12021 [d]	5.96	5.58	5.76		4.06	
A12 12038 [d]	6.19	5.67			4.08	
A12 12040 [d]	5.93	5.61	5.87	5.09	4.10	
A12 12052 [d]	5.89	5.41			4.00	
A12 12063 [d]	5.98	5.64		5.24	4.22	
A12 12064 [d]	5.97	5.56			3.90	7.15
Average [d]	**5.98 ± 0.20**	**5.59 ± 0.17**	**5.82 ± 0.16**	**5.15 ± 0.16**	**4.07 ± 0.21**	**7.15**
A15 15058 [e]	6.13	5.73				
A15 15016 [f]	5.81	5.42	5.56	5.00	4.04	
A15 15065 [f]	5.84	5.47	5.60		4.08	6.72
A15 15495 [f]	5.74		5.34		3.92	
A15 15556 [f]	5.88		5.68	4.99	4.01	
Average [f]	**5.82 ± 0.30**	**5.45 ± 0.33**	**5.55 ± 0.29**	**5.00 ± 0.01**	**4.01 ± 0.14**	**6.72**
Low-Ti Average	**5.94 ± 0.25**	**5.57 ± 0.21**	**5.64 ± 0.37**	**5.10 ± 0.20**	**4.05 ± 0.19**	**6.94 ± 0.61**
Overall Average	**5.99 ± 0.38**	**5.60 ± 0.37**	**5.64 ± 0.37**	**5.10 ± 0.20**	**4.10 ± 0.37**	**6.93 ± 0.39**

*A11, A12 etc denotes Apollo mission. [a]Onuma et al., 1970. [b]Taylor and Epstein, 1970. [c]Mayeda et al., 1975. [d]Clayton et al., 1971. [e]Epstein and Taylor, 1972. [f]Clayton et al., 1973.

Table 5.4: Measured and calculated $\delta^{18}O$ (‰)

	Mineral Separates (Overall Averages)						
	Clinopyroxene	**Plagioclase**	**Olivine**	**Ilmenite**	**Armalcolite****	**Spinel****	**Silica**
$\delta^{18}O$	5.62*	5.99	5.10	4.11	4.11	4.11	6.93

Sample	Calculated $\delta^{18}O$	Measured $\delta^{18}O$	Difference	Relative Difference†
10017	5.59	5.68	0.09	1.52
10020	5.50	5.63	0.13	2.36
10049	5.54	5.65	0.11	1.96
10050	5.55	5.65	0.10	1.81
10057	5.63	5.66	0.03	0.47
10058	5.64	5.70	0.06	1.13
10072	5.54	5.61	0.07	1.30
12016	5.60	5.53	-0.06	-1.13
12040	5.53	5.49	-0.03	-0.60
12047	5.70	5.69	-0.01	-0.13
12051	5.67	5.76	0.10	1.71
12052	5.62	5.70	0.08	1.47
12064	5.69	5.66	-0.03	-0.60
14053	5.70	5.81	0.11	1.91
15016	5.59	5.66	0.08	1.38
15386	5.83	5.95	0.12	2.07
15555	5.66	5.70	0.05	0.82
70017	5.46	5.46	0.00	0.01
70035	5.47	5.45	-0.02	-0.39
70215	5.37	5.51	0.14	2.59
74275	5.39	5.54	0.15	2.82
75055	5.63	5.56	-0.07	-1.22

	With Olivine Removed			
Sample	**Calculated $\delta^{18}O$**	**Measured $\delta^{18}O$**	**Difference**	**Relative Difference†**
12040	5.645	5.492	-0.153	-2.709

*Ca-pyroxene and pigeonite overall mineral separate values (Table 3 averaged). **Assumed to be the same as ilmenite. †Where relative difference = (measured/calculated*100) - 100

slightly unrepresentative modal data, sample heterogeneity and/or impurities within the mineral separates could all contribute to slight variations. As with Figure 5.4, Figure 5.5a highlights the strong relationship between decreasing bulk-rock $\delta^{18}O$ and increasing ilmenite content within the highest high-Ti basalts, and the lack of such a relationship in the low-Ti basalts. The calculated bulk-rock $\delta^{18}O$ value for Apollo 15 KREEP basalt 15386 agrees with the measured $\delta^{18}O$ to within 0.12 ‰ despite the fact that mare-basalt mineral-separate data were used for this calculation.

A simple test to remove the effects of olivine accumulation in Apollo 12 basalt 12040 (e.g., Baldridge et al., 1979) was performed by subtracting olivine from the modal abundance of this sample. Though Champness et al. (1971) suggested the presence of two olivine populations (based on Cr content) only accumulated olivine was observed in thin section 12040,44, therefore 100 % of the olivine mode was subtracted from this sample. This yields a slightly higher bulk-rock $\delta^{18}O$ than the "true" bulk-rock value for sample 12040, indicating the possible presence of a small percentage of phenocrystic olivine. Nevertheless, the calculation is still meaningful and relevant for the purposes of this study. Removal of olivine from sample 12040 increased the bulk-rock $\delta^{18}O$ by 0.11 ‰, bringing this sample more in line with the other low-Ti basalts, specifically Apollo 12 ilmenite basalt 12064 (Table 5.4, Figure 5.5b).

Apollo 12 ilmenite basalt 12016 also contains a high modal abundance of olivine, but unlike olivine basalt 12040 these olivine grains were in equilibrium with the melt (chapter 4, Dungan and Brown, 1977; Neal et al., 1994a). Although Neal et al. (1994a) reported heterogeneous olivine distribution in sample 12016, our measured modal abundance (14.21 modal %) and previously reported modes (Dungan and Brown (1977) and Neal et al. (1994a) both report 12 modal %), demonstrate the olivine-rich nature of 12016 compared to the other Apollo 12 basalts within our sample set (< 2 modal % olivine). High bulk-rock Mg# and phenocrystic olivine, along with low REE abundance (e.g., Rhodes et al., 1977; Neal et al., 1994a) are consistent with sample 12016 being the most primitive of the four Apollo 12 ilmenite basalts analysed in our study.

5.3. Discussion

5.3.1. The Giant Impact. The lack of a distinguishable difference in $\Delta^{17}O$ between terrestrial and lunar samples, as shown by this and previous studies (Spicuzza et al., 2007; Wiechert et al., 2001), is consistent with the post-impact equilibration, volatile mixing

model of Pahlevan and Stevenson (2007). However, Melosh (2009) highlighted some shortcomings in this model, and argued for a more refined modelling which more accurately reproduces the present day angular momentum of the Earth-Moon system. Melosh (2009) theorises that the solution may lie in a partial return to the Darwin fission model (Darwin, 1875), but with a much hotter initial Earth than originally suggested. If the Moon-forming impact was more central then hot silicate gas may have spun out to form the Moon after complete mixing with the proto-Earth.

Alternatively, the oxygen isotope compositions can be understood within the framework of current smooth particle hydrodynamic (SPH) impact models provided the early Earth and the impacting body had $\Delta^{17}O$ values to within about 0.03 ‰ of each other (Wiechert et al., 2001). Chambers (2004) suggested that the size of planetary accretion zones during oligarchic growth of the terrestrial planets is relatively small (0.01 AU). Therefore, assuming radial distribution of oxygen within the solar system at the time of the giant-impact, the two bodies would have to form at very similar heliocentric distances from the Sun to produce the current $\Delta^{17}O$ of the Earth and Moon. Until recently the presence of two bodies of that size occupying such similar orbits around the Sun for a long period of time without colliding was not thought plausible. However, Belbruno and Gott (2005) showed that a Mars-sized body could grow within the L4 or L5 Lagrange points of Earth's orbit and subsequently be thrown into an eccentric orbit via collisions with other planetesimals. If this occurred, they reasoned that the body would very probably collide with the Earth. There are examples of this type of growth within the current solar system, e.g., the Saturnian moons Helene, Telesto and Calypso, although the mass ratio between these bodies and Saturn is much larger than would have been the case for the giant-impact involving the Earth. But can a radial distribution of oxygen in the early solar system be assumed? Recent measurements of the $\Delta^{17}O$ of Mars (+0.30 ‰) and Vesta (-0.24 ‰) suggest oxygen isotope ratios do not have a radial distribution within the current solar

system (Greenwood et al., 2005; Wiechert et al., 2004). However, it does not necessarily follow that such a distribution was absent in the early solar system. It should also be acknowledged that not all other bodies within the solar system have different oxygen compositions to the Earth and Moon. Thus, the enstatite chondrites show $\Delta^{17}O$ mostly within error of the terrestrial fractionation line (Newton et al., 2000). Current models of terrestrial planet formation suggest planetesimals must endure a series of growth stages before they mature into a planet. The first two stages, known as runaway and oligarchic growth, are restricted to the relatively small feeding zone suggested by Chambers et al. (2004), but during the last stage - known as chaotic growth - planetesimals that formed in widely different orbits may collide and merge (Kenyon and Bromley, 2006 - and references therein). The final planets are therefore a mixture of material from a broad region of the inner solar system, although each planet accreted more material from its own locale than elsewhere, giving each a unique mixture. As a result of this chaotic growth primordial chemical and isotopic gradients became less distinct. The giant impact is thought to have occurred during this last period of growth (Canup and Asphaug, 2001; Chambers, 2004). Therefore, the impacting body could have formed anywhere within the inner solar system, but equally an increase in chaotic collisions may have given a Mars-sized body in Earth's L4 or L5 points the push it needed to finally collide with Earth. However, by definition this chaotic growth may have produced oxygen isotopic compositions with greater than 0.03 ‰ difference between the impacting body and the proto-Earth. The delicacy of such a binary system may also pose a problem; it is believed that the Earth accreted from a dozen or more planetary embryos during the chaotic growth period before the giant impact occurred. Any one of those collisions could have disturbed or destroyed a second smaller body so close to Earth. Ultimately further work is needed to aid our understanding of isotopic homogenisation in the early solar system before a definite model for Earth-Moon system formation can be proposed. The evidence from this and previous studies (Spicuzza et al., 2007; Wiechert et al., 2001), indicating that lunar and terrestrial rocks have

indistinguishable $\Delta^{17}O$ values, while not excluding the possibility of a giant impact model for the origin of the Earth-Moon system, strongly suggests that alternative scenarios merit further consideration.

5.3.2. Petrogenesis of Mare Basalts. In contrast to previous studies (Wiechert et al., 2001 and Spicuzza et al., 2007) our bulk-rock $\delta^{18}O$ data show no clear separation between the low-Ti and high-Ti basalt suites. This can most easily be ascribed to the restricted sample set used in previous studies, where no moderate-Ti samples (Apollo 11) were analysed. Close agreement between our measured and calculated bulk-rock $\delta^{18}O$ values indicates that the observed $\delta^{18}O$ variation between samples is real and not an analytical artefact. Variation in mineral modal abundances can account for bulk-rock $\delta^{18}O$ variations both between and within different groups of mare basalts. The causes of this variation are discussed below.

When the bulk-rock $\delta^{18}O$ values of the highest high-Ti samples (Apollo 17) are compared to those of the low-Ti samples the former display lighter bulk-rock $\delta^{18}O$ values than the latter (Table 5.1). As discussed in previous chapters, it is thought the low-Ti partial melts originate from olivine-pyroxene cumulate source regions at depths of ~100-300 km in the lunar interior, whereas the high-Ti basalts originate from mixtures of these cumulates and ilmenite-rich cumulates at similar depths (Ryder 1991; Van Orman and Grove, 2000; Elkins-Tanton et al., 2002; Shearer et al., 2006). Mineralogical differences in the cumulate source regions can also explain the significant Li-Sr-Nd-Hf isotope variations within the mare basalts (Beard et al., 1998; Day et al., 2006; Magna et al., 2006). Snyder et al. (1992a) proposed that the modal mineralogy of the ilmenite cumulate mix required to produce high-Ti mare basalts was 46 % pigeonite, 43 % olivine, 7 % augite, 3 % ilmenite, 1 % plagioclase and a small amount of trapped KREEPy liquid. In contrast, the olivine-

pyroxene cumulate source of the low-Ti basalts contains no ilmenite but more augite (10 %). As ilmenite $\delta^{18}O$ is lighter than that of augite, the low-Ti basalt sources would consequently have inherently heavier bulk-rock $\delta^{18}O$ than the ilmenite enriched high-Ti sources (5.41 ‰ and 5.36 ‰ respectively, based on the average mineral-separate values shown in Table 5.3, and excluding any trapped KREEPy liquid).

Experimental studies have shown the mare magmas are produced via small amounts of non-modal partial melting of the source regions (< 20 % – e.g., Ringwood and Essene, 1970; Duncan et al., 1974, 1976; Shih et al., 1975; Walker et al, 1975; Nyquist, 1977; Nyquist et al., 1979; Hughes et al., 1988, 1989; Shearer and Papike, 1993, 1999; Snyder et al., 1997; Beard et al., 1998). The experimental work of Hess and Finnila (1997) suggests, in agreement with phase-equilibria studies of picritic mare-glasses (Longhi 1992a), that many high-Ti mare basalts are significantly under-saturated with respect to ilmenite. This implies that, during the melting event which produced the high-Ti basalt partial melts, ilmenite is totally removed from the source. Hess and Finnila (1997) show that these high-Ti basalts are generally saturated in both olivine and orthopyroxene, hence olivine and orthopyroxene will be left in the source after melt removal. This suggests that TiO_2 would be concentrated in the mare-basalt partial melts and that the difference in oxygen isotope composition between the low- and high-Ti source types should increase upon cumulate source re-melting (as the low-Ti basalt source would become devoid of TiO_2 after a very small amount of partial melting, well before the high-Ti source).

Unfortunately, there is a lack of high-pressure experimental data that can be used to model the influence of various lunar mantle source compositions on the bulk $\delta^{18}O$ of mare-basalt melts. However, these data do exist for the picritic glasses (Longhi 1992a, 1996). Most authors agree that there is no direct parent-daughter relationship between the melts that produced the picritic glasses and the mare basalts (e.g., Longhi 1992a, Shearer and Papike

1993, Papike et al., 1998) - although Shearer and Papike (1993) do suggest that one possible relationship is that both are derived from a single common picritic parent melt. The picritic glasses do show similar trends to the mare basalts in terms of their TiO_2 contents and there is general agreement that the glasses are better candidates for primary melts than even the most primitive mare basalts (Hess and Finnila, 1997; Papike et al., 1998). Therefore, it seems reasonable to use the experimental data that exist for the glasses to try and understand how partial melting of potential lunar-mantle source compositions influences the oxygen isotope composition of lunar basalts. Longhi (1992a) provides two possible low-Ti mantle sources, the first is a modification of Taylor's (1982) lunar-mantle composition and the second the author's own calculated green-glass magma source. These sources have relatively low TiO_2 contents (hence low modal ilmenite at ~ 0.4 %) and slightly differing calculated $\delta^{18}O$ values (5.36 ‰ and 5.29 ‰ respectively, Table 5.5). Partial melting of these sources at 25 kbar (500 km depth according to the steep depth/pressure gradient of 20 km/kbar in the outer portion of the Moon (Longhi, 1992b) yield liquids with higher TiO_2 (1.89 and 3.34 wt %) values and slightly heavier $\delta^{18}O$ values (5.59 ‰ and 5.50 ‰ respectively) than their potential sources. It should be noted that all the picritic glasses give slightly lower calculated $\delta^{18}O$ values than the mare basalts because they have less normative plagioclase and more normative olivine. Longhi (1996) provides experimental results relevant to the high TiO_2 picritic glasses. This author's model suggests a source composition containing 2.7 wt % TiO_2 (3.7 % ilmenite) with a calculated $\delta^{18}O$ value of 5.25 ‰ (Table 5.5) – only slightly lower than the low-TiO_2 sources of the green picritic glass. Longhi (1996) gives compositions for a number of high-Ti liquids produced during high-pressure melting of this source. Using these compositions we calculated that the $\delta^{18}O$ value for a very high-Ti melt (19.7 wt % TiO_2), produced at 25 kbar and 1435 °C, is 5.19 ‰. Therefore, these high-Ti melts can have lower $\delta^{18}O$ values than their sources, and significantly lower values than melts produced by partial melting of a low-Ti source

Table 5.5: Possible mare-basalt source region and partial melt compositions.

	Pricritic GG[a] Source		Pricritic GG Partial Melts[d]		VHT Source[e]	VHT Partial Melt[f]	A14 RPG[g]
	TS[b]	GGMS[c]	2.4 % TS	2.4 % GGMS		1435 °C	
SiO_2	44.30	43.50	43.90	42.00	41.70	31.15	34.14
TiO_2	0.28	0.27	1.89	3.34	2.70	19.70	17.01
Al_2O_3	4.10	1.43	12.80	8.96	1.48	5.00	3.80
Cr_2O_3	0.67	0.72	0.45	0.59	0.66	0.30	0.74
FeO	11.40	16.00	13.60	17.80	17.90	28.60	23.48
MgO	35.60	36.00	15.30	14.20	33.00	7.01	13.60
MnO	0.15	0.18	0.23	0.27	0.19	0.28	0.35
CaO	3.36	1.84	10.90	12.00	2.41	6.81	6.39
K_2O	<0.00	<0.00	0.11	0.11	<0.00	0.60	0.20
Na_2O	0.05	0.03	0.80	0.59	0.32	1.00	0.45
Total	**99.91**	**99.97**	**99.98**	**99.86**	**100.36**	**100.45**	**100.16**
Mineralogical Mode							
Plag	13.70	5.00	44.90	32.70	6.80	26.60	17.10
Cpx	4.60	4.50	18.00	31.10	7.90	23.70	21.30
Opx	21.50	23.40	5.10	0.00	16.50	5.40	23.00
Ol	59.80	66.80	29.60	31.80	65.10	15.50	13.90
Ilm	0.40	0.40	2.40	4.40	3.70	28.70	24.70
Total	**99.97**	**99.99**	**100.00**	**100.00**	**100.02**	**99.99**	**100.00**
$\delta^{18}O$	**5.36**	**5.29**	**5.59**	**5.50**	**5.25**	**5.19**	**5.24**

[a]GG = green glass. [b]TS = green glass source of Taylor (1982). [c]GGMS = green glass magma source of Longhi et al. (1992b). [d]GG 2.4 % partial melts at 25 kbar. [e]VHT source = very high-Ti source of Longhi et al. (1996). [f]VHT partial melt at 25 kbar and 1435 °C. [g]A14 RPG = Apollo 14 red picritic glass.

(i.e. those that produced the green picritic glasses). This behaviour is very similar to that seen in our mare-basalt $\delta^{18}O$ dataset. Longhi (1996) points out that these very high TiO_2-rich liquids would be relatively dense and in fact slightly denser than the source composition. However, picritic glasses close to this composition have reached the lunar surface (e.g., the red Apollo 14 picritic glass, Table 5.5). If the possibility of ilmenite assimilation can be excluded on the basis of Lu/Hf and Sm/Nd ratios (Beard et al., 1998) then our oxygen isotope data support the proposition that the high and low-Ti basalts were produced by melting of sources with differing ilmenite contents (in agreement with Spicuzza et al., 2007).

The fact that experimental and measured data indicate there is a continuum in TiO_2 contents in both the picritic glasses and mare basalts has important implications for the distribution of ilmenite in the source rocks. Rather than two discrete sources, one high- and one low-Ti, these data indicates that ilmenite is heterogeneously distributed in the source regions. The experimental data of Longhi (1992b) indicate that primitive mare basalts show

multiple saturation in the range 5 to 12.5 kbars (100 to 250 km), whereas picritic glasses are in the range 18 to 25 kbars (360 to 500 km). There is also experimental evidence to support the possibility that melting may initiate at depths >1000 km (Longhi, 1992b). In view of these data, ilmenite heterogeneity must be present over an extremely wide depth range within the lunar mantle. Thus, our oxygen isotope data agree with the results of a recent study of the stability of ilmenite/armalcolite in the lunar mantle (Thacker et al. 2009), which suggests that the postulated late overturn of the mantle during crystallisation of the lunar magma ocean extended to great depths, but that mixing was inefficient, with TiO_2-bearing phases being heterogeneously distributed. Because of the heterogeneity of the mantle at mare-basalt source region depths, subsequent re-melting and mixing of the lunar-mantle cumulates led to the formation of mare-magmas with a range of TiO_2 abundances rather than purely low- and high-Ti basalts (e.g., Elkins-Tanton et al., 2002; Shearer et al., 2006). The moderate ilmenite abundance and $\delta^{18}O$ values within the Apollo 11 mare-basalt suite can therefore be explained if the source region of these mare-magmas contained less ilmenite-rich cumulate than the source of the highest-Ti mare-basalts of Apollo 17, but more ilmenite than the sources of the low-Ti mare-basalts. This inference is supported by remote sensing observations of mare basalts with a range of TiO_2 abundances on the lunar surface (Giguere et al., 2000).

Bulk-rock $\delta^{18}O$ variations within mare-basalt groups suggest further $\delta^{18}O$ modification via fractional crystallisation processes. The effect of ilmenite fractional crystallisation is most pronounced in the highest-Ti Apollo 17 basalts within our sample set, where a strong correlation exists between the bulk-rock $\delta^{18}O$ value and TiO_2 content (Figure 5.4 5.3). Fractional crystallisation of ilmenite has a less pronounced effect on the Apollo 11 basalts and no apparent influence on the $\delta^{18}O$ values of the low-Ti basalts within our sample set. Shallow level, dominantly olivine, crystal fractionation is known to have occurred during the formation of the low-Ti basalts (chapter 4; Rhodes et al., 1977; Ryder, 1991; Neal et al.,

1994b; Neal and Taylor, 1992; Schnare et al., 2008), and the presence of a weak inverse relationship between $\delta^{18}O$ and Mg# in these samples appears to indicate that this process may also have had some influence on bulk-rock $\delta^{18}O$ values (Figure 5.3). This relationship is most apparent for the four Apollo 12 ilmenite-basalts within our sample set. The Apollo 12 ilmenite-basalts are all thought to originate from the same parental melt (chapter 4; James and Wright, 1972; Rhodes et al., 1977; Walker et al., 1976; Baldridge et al., 1979; Neal et al., 1994a). Bulk-rock Mg# and bulk-rock REE abundance indicate sample 12016 is the most primitive basalt within this group, and sample 12051 is the most evolved. The value of $\delta^{18}O$ increases with increasing basalt evolution (and decreasing bulk-rock Mg#) - from 5.53 ‰ in sample 12016 to 5.76 ‰ in sample 12051. Therefore, olivine fractional crystallisation clearly had an effect on bulk-rock $\delta^{18}O$ within the low-Ti basalt group.

Apollo 12 olivine mare basalt 12040 can not be included in the fractional crystallisation evolutionary trend as it crystallised in an open system (chapter 4; Baldridge et al., 1979). Olivine accumulation within this sample produced an inaccurately high bulk-rock Mg# and a low $\delta^{18}O$ value unrelated to that of original parental melt. Once the effect of accumulated olivine is removed in sample 12040, it shows a bulk-rock $\delta^{18}O$ value similar to the low olivine Apollo 12 samples, specifically ilmenite basalt 12064 (Table 5.4, Figure 5.5b). This illustrates the effect of olivine modal abundance on the value of $\delta^{18}O$ in low-Ti mare basalts. It also indicates that the major-element chemistry of the original Apollo 12 olivine basalt melt was similar to that of the Apollo 12 ilmenite-basalts, although the possible presence of a small native olivine population within the olivine basalts does add uncertainty to the $\delta^{18}O$ value of sample 12040 (Champness et al., 1971).

Our modal calculations show that the comparatively heavy $\delta^{18}O$ value of Apollo 15 KREEP basalt 15386 is because of its high plagioclase content. Spudis and Hawke (1986)

stated that KREEP basalts typically contain 40-50 % plagioclase, 30-40 % low-Ca pyroxene, and minor cristobalite, ilmenite, apatite, REE-merillite and Si- and K-rich glass. This high-plagioclase content relative to the mare-basalts within our sample set (13-39 modal % plagioclase) indicates that the KREEP source region was comparatively plagioclase-rich. As plagioclase has a heavy $\delta^{18}O$ value (5.99 ± 0.38 ‰ – Onuma et al., 1970; Taylor and Epstein, 1970; Clayton et al., 1971; Epstein and Taylor, 1972; Clayton et al., 1973; Mayeda et al., 1975) the KREEP source region is also likely to have had a heavy $\delta^{18}O$ value compared to the mare-cumulate sources.

Apollo 14 low-Ti, high-Al group C mare-basalt 14053 contains the next heaviest $\delta^{18}O$ value after Apollo 15 KREEP basalt 15386. This heavy $\delta^{18}O$ value is produced by high-plagioclase modal abundance (plagioclase $\delta^{18}O$ = 5.99 ± 0.38 ‰ – Onuma et al., 1970; Taylor and Epstein, 1970; Clayton et al., 1971; Epstein and Taylor, 1972; Clayton et al., 1973; Mayeda et al., 1975). As only one Apollo 14 high-Al sample was analysed the effects of crystal fractionation within this basalt group cannot be detected. However, AFC calculations (section 4.4.5; Neal and Kramer, 2006) indicate Apollo 14 high-Al group C mare-basalts were produced by 40 % crystal fractionation along with < 5 % assimilation of a granite/KREEP mixture. The fractionating assembledge is dominated by olivine until the late stages of crystallisation, therefore future analysis of other Apollo 14 group C samples should reveal bulk-rock $\delta^{18}O$ variation controlled by olivine content. The effect of this amount of KREEP assimilation on bulk-rock $\delta^{18}O$ appears to be minimal, as no consistant $\delta^{18}O$ difference is visible between the Apollo 11 low-K and high-K basalts. The latter are thought to have assimilated 10 % KREEPy material (section 4.4.5; Longhi et al.; 1987; Hughes et al.,1989; Jerde et al., 1994) while the low-K basalts are not believed to contain a KREEP component (chapter 4; Beaty and Albee, 1978; Beaty et al., 1979a,b; Rhodes and Blanchard, 1980). As granite is by definition more abundant in silica and feldspar than

basalt, and these phases are enriched in ^{18}O, granite assimilation may be expected to increase the $\delta^{18}O$ value of the Apollo 14 group C mare-basalt melt, but whether this small amount of assimilation would produce a measureable difference in the $\delta^{18}O$ value of Apollo 14 high-Al basalts has not yet been studied.

5.4. Conclusions

- We have employed a high-precision laser fluorination technique to analyse the oxygen isotope composition of a suite of lunar Apollo basalts. Using mineral separates and modal mineralogy data for each sample we were able to calculate bulk-rock $\delta^{18}O$ to within 0.13 ‰ of measured values.

- The excellent agreement between calculated and analysed $\delta^{18}O$ values demonstrates that the observed differences in $\delta^{18}O$ values between basalts with high- and low-Ti content are real.

- Our results, combined with evidence from experimental investigations, indicate that the main control on bulk-rock $\delta^{18}O$ variation between different mare-basalt groups (low, high and higher-Ti) primarily reflects source region heterogeneity. However, we suggest that rather than a bi-modal variation in bulk-rock $\delta^{18}O$ between high and low-Ti basalts a continuum of values exists, reflecting highly heterogeneous ilmenite contents in the source region. This is in agreement with the mineralogical and chemical evidence of chapters 3 and 4.

- In conjunction with the results of previous studies, our data suggest that this ilmenite heterogeneity probably developed during the later stages of the crystallisation of the lunar magma ocean and may be present to depths of at least 1000 km within the lunar mantle.

- Bulk-rock $\delta^{18}O$ variation within mare-basalt groups is also controlled by fractional crystallisation, for example, our Apollo 17 samples show a strong correlation between decreasing ilmenite modal abundance/TiO_2 wt % and increasing bulk-rock $\delta^{18}O$. In contrast, the low-Ti basalts show no systematic variation with ilmenite content. However, these samples do show increasing bulk-rock $\delta^{18}O$ with decreasing Mg#, indicating olivine fractional crystallisation was a major control on low-Ti mare-basalt bulk-rock $\delta^{18}O$ variation. Fractional crystallisation of olivine and ilmenite within the low- and high-Ti mare basalts is in agreement with our petrogenetic and chemical evidence (chapters 3 and 4).

- Within Apollo 12 sample 12040, when the effect of this accumulation is removed, the sample displays a similar bulk-rock $\delta^{18}O$ value to the majority of the other low-Ti, Apollo 12 samples.

- The heavy bulk-rock $\delta^{18}O$ value of Apollo 15 KREEP basalt 15386 is caused by this sample's high plagioclase abundance, as all KREEP basalts appear to share this characteristic (Spudis and Hawke, 1986), it probably reflects high plagioclase abundance in the KREEP source region.

- In agreement with previous studies, our data reveal no difference between the $\Delta^{17}O$ of the Earth and Moon. SPH models predict the Giant Impact would produce a Moon made up of 70-90 % impactor. Assuming these models are correct there is now a wealth of oxygen isotopic evidence indicating the Giant Impact Model for the formation of the Earth-Moon system is not viable in its present form.

- Recent doubts raised by Melosh (2009) concerning the mechanism of Pahlevan and Stevenson's (2007) post-impact volatile mixing model suggest that this model also requires further refinements to account for the current dynamics of the Earth-Moon system.

- Possible alternative models which may explain the observed homogeneous oxygen isotopic composition of the Earth and Moon include an altered Darwin fission model (Melsoh, 2009) and the double planet growth model of Belbruno and Gott (2005). The possibility of these models has yet to be fully explored but it is clear that the Giant Impact theory is in need of re-assessment.

6. AGES OF MARE-BASALTS

As discussed in chapter one, the crater counting evidence from remote sensing images of mare-basalt flows does not support the positively correlated relationship between age and TiO_2 content measured in the Apollo sample collection. In fact, a number of remote sensing studies have found that the low-Ti basalts are, in general, older than the high-Ti basalts. For example, Bugiolacchi and Guest (2008) suggested that the Imbrium basin was filled with increasingly Ti-rich mare basalts over a period of 800 million years, from 3.3-2.5 Ga. Combining previously published age data on mare-basalts with the new age data obtained in this study, we aim to provide additional constraints on the relationship between mare-basalt type and crystallisation age.

6.1. Previous Age Data

Previously published age data for our sample set is shown in Table 6.1. The Ar/Ar and Rb^{87}-Sr^{87} geochronometers appear to have been most exclusively applied to date mare-basalts, with only a handful of studies reporting Pb-Pb data (e.g., Andersen and Hinthorne, 1973). All of these data were collected between 1970 and 1979, excepting the Sm^{147}-Nd^{143} data by Nyquist et al. (1991). During the 1970's the SHRIMP technique was in its infancy, therefore, at this time, *in-situ* age dating was not an established methodology. Contemporary Pb-Pb and U-Pb dating involved the separation of minor incompatible-element-rich phases (e.g., phosphates or zircons) from a sample, followed by destructive analysis via mass spectrometry (e.g., Tera and Wasserburg, 1974). In contrast, Ar^{40}-Ar^{39} and Rb^{87}-Sr^{87} techniques relied on the separation of more abundant mineral phases in lunar basalts (feldspar and pyroxene), and therefore produced more extensive datasets.

Table 6.1: Previously published age data.

	Ages (Ga)											
Sample	Ar^{40}-Ar^{39}	Error	Rb^{87}-Sr^{87}	Error	K^{40}-Ar^{40}	Error	Sm^{147}-Nd^{143}	Error	Pb-Pb	Error	Average	2σ
14053	3.94[a]	0.04	3.96[d]	0.04							3.94	0.03
	3.94[b]	0.05										
	3.92[c]	0.08										
15386			3.94[e]	0.01			3.85[f]	0.08			3.90	0.20
74275	3.81[g]	0.32									3.83	0.06
	3.85[h]	0.08										
75055	3.82[i]	0.05	3.83[l]	0.10							3.80	0.06
	3.78[j]	0.02	3.77[m]	0.06								
	3.76[j]	0.05										
	3.82[k]	0.05										
70215	3.84[n]	0.04									3.79	0.14
	3.74[o]	0.11										
70035	3.75[s]	0.07	3.82[p]	0.06							3.77	0.09
			3.73[q]	0.11								
10050	3.75[r]	0.03									3.75	
	3.75[t]	0.03										
70017	3.67[u]	0.12	3.67[v]	0.18							3.71	0.15
	3.80[i]	0.03										
10058	3.71[w]	0.04	3.63[x]	0.20							3.67	0.11
10072	3.52[y]	0.05	3.64[w]	0.05			3.57[w]	0.03			3.63	0.18
	3.62[z]	0.05	3.78[x]	0.10								
	3.57[r]	0.04	3.71[y]	0.11								
10057			3.63[y]	0.01							3.63	
10020	3.77[r]	0.04			3.36[t]	0.02					3.57	0.58
10017	3.23[w]	0.06	3.59[w]	0.05			3.58[z]	0.20			3.53	0.41
			3.71[y]	0.11								
15016	3.38[x]	0.08	3.29[y]	0.05					3.75[w]	0.27	3.47	0.49
10049	3.45[r]	0.04									3.45	
15555	3.33[aa]	0.05	3.54[ab]	0.13			3.32[ac]	0.04	3.36[w]	0.06	3.33	0.16
	3.22[w]	0.03	3.32[ad]	0.06			3.23[ae]	0.02	3.46[w]	0.09		
	3.28[af]	0.06	3.30[ag]	0.08								
	3.31[w]	0.05	3.34[w]									
	3.31[w]	0.03	3.32[ah]	0.04								
			3.34[ai]	0.09								
12051	3.16[s]	0.05	3.19[aj]	0.06							3.31	0.32
	3.32[ak]	0.06	3.26[w]	0.10								
	3.15[s]	0.07	3.52[w]	0.30								
	3.27[s]	0.05	3.58[al]	0.30								
12040			3.30[d]	0.04							3.22	0.15
			3.21[al]	0.10								
			3.15[w]	0.10								
12064	3.18[w]	0.01	3.18[d]	0.09							3.19	0.02
	3.20[w]	0.04										
12052			2.92[am]	0.18							3.14	0.39
			3.28[al]	0.19								
			3.22[w]	0.19								

[a]Stettler et al. (1973), [b]Turner, (1971), [c]Husain et al. (1972), [d]Papanastassiou and Wasserburg (1971b), [e]Nyquist et al.(1975), [f]Carlson and Lugmair (1979), [g]Nyquist et al. (1976), [h]Murthy and Coscio (1977), [i]Huncke et al. (1973), [j]Turner et al. (1973), [k]Kirsten et al. (1973), [l]Tatsumoto et al. (1973), [m]Tera et al. (1974), [n]Kirsten and Horn (1974), [o]Schaeffer et al. (1977), [p]Evensen et al. (1973), [q]Nyquist et al. (1974), [r]Geiss et al. (1977), [s]Guggisberg et al. (1979), [t]Phinney et al. (1975), [u]Papanastassiou et al. (1970), [v]Turner (1970), [w]Papanastassiou et al. (1977), [x]Compston et al. (1970), [y]DeLaeter et al. (1973), [z]Gopalan et al. (1970), [aa]Anderson and Hinthorne (1973), [ab]Alexander et al. (1971), [ac]Podosek et al. (1971), [ad]Husain et al. (1971), [ae]York et al. (1972), [af]Chappell et al. (1972), [ag]Wasserburg and Papanastassiou (1971). [ah]Murthy et al. (1971), [ai]Cliff et al. (1972), [aj]Papanastassiou and Wasserburg (1973), [ak]Birck et al. (1975), [al]Nyquist et al. (1991), [am]Alexander et al. (1972), [an]Nyquist et al. (1979). [ao]Papanastassiou and Wasserburg (1970), [ap]Nyquist (1977) (recalculated), [aq]Compston et al. (1971), [ar]Horn et al. (1975).

Calculating the average age of each sample clarifies the chronology of our sample set (Table 6.1). Apollo 14 low-Ti, high-Al basalt 14053 appears to be the oldest basalt among our samples at 3.94 ± 0.03 Ga. Apollo 15 KREEP basalt 15386 shows a slightly younger average age at 3.90 ± 0.20 Ga, but a relatively large uncertainty produces an overlap with sample 14053. The high-Ti Apollo 11 and 17 basalts are the next oldest samples, with average ages ranging from 3.80 to 3.71 Ga for the Apollo 17 samples, and 3.75 to 3.45 Ga for the Apollo 11 samples. The Apollo 11 low-K basalts are thought to be older than the high-K basalts from the same site (Papike et al., 1998). Because of the anomalously low

average age of sample 10020 (suggested by the K^{40}-Ar^{40} data of Guggisberg et al. (1979)), no significant difference between the ages of these two groups is observed in our sample set. However, if the K^{40}-Ar^{40} age is ignored, the ages of the high-Ti basalts can be constrained to 3.77 to 3.63 Ga, a time period which only slightly overlaps (including 2σ error) with the age of the high-K basalts at 3.63 to 3.45 Ga. Apollo 17 basalts show very similar ages, with only 0.04 Ga between type C basalt 74275 and type B basalt 70215, the age of type A basalt 75055 lies between the two. Apollo 17 unclassified basalts 70035 and 70017 exhibit slightly younger average ages, but these samples are still within 2σ error of the other Apollo 17 samples. The low-Ti basalts of Apollo 15 and 12 display the lowest average ages, at 3.47 to 3.33 Ga and 3.31 to 3.14 Ga, respectively. The anomalously low Rb-Sr age data of Murthy et al. (1971) for pigeonite basalt 12052, and the anomalously high Rb^{87}-Sr^{87} age data of Compston et al. (1971) for ilmenite basalt 12051, were excluded from the average age calculations of the Apollo 12 basalts. It should also be noted that the data of Compston et al. (1971) were recalculated by Nyquist (1977), giving a slightly lower age estimation of 3.52 Ga, which was also excluded on the basis of its high value. The refined dataset gives ages ranging from 3.25 ± 0.09 Ga for pigeonite basalt 12052 to 3.19 ± 0.02 Ga for ilmenite basalt 12064, illustrating that the Apollo 12 low-Ti basalt ages are indistinguishable. Apollo 12 ilmenite basalts 12016 and 12047 have never previously been dated.

Previously published age data for the wider Apollo sample collection can be used to indicate whether the basalts within our sample set have typical ages for their basalt type. Radiometric ages of the Apollo 11 high-K basalts not represented within our sample set are similar to the ages of our Apollo 11 high-K samples (3.48-3.68 Ga - Papanastassiou et al., 1970; Turner et al., 1970; Papanastassiou and Wasserburg, 1971a; Stettler et al., 1973; Geiss et al., 1977; Guggisburg et al., 1979). The only sample that does not fit chronologically with this group is sample 10062 (not within our sample set) which appears

to be older (4.01-3.82, Turner et al., 1970; Papanastassiou et al., 1977). Previous data for the low-K type B1 and B3 basalts are consistent with data for these basalt types within our sample set (3.71-3.75 Ga – Papanastassiou et al., 1970; Turner et al., 1970; Stettler et al., 1974; Geiss et al., 1977; Papanastassiou et al., 1977; Guggisburg et al., 1979; Hinthorne et al., 1979; Rassmussen et al., 2008). Apollo 11 low-K B2 basalts (not represented in our sample set) are older than the B1 and B3 basalts (3.92-3.84 Ga - Turner et al., 1970; Stettler et al., 1974; Papanastassiou and Wasserburg, 1975). The full Apollo 17 basalt collection has a wider range of ages than the samples we studied (3.84-3.64 Ga - Tera et al., 1974; Turner and Cadogen, 1974; Murthy and Coscio, 1976; Nyquist et al., 1976; Schaeffer and Schaeffer, 1977), whereas the full Apollo 12 and 15 basalt collections have the same range as our sample set (3.40-3.34 Ga and 3.16-3.36 Ga, respectively – Papanastassiou and Wasserburg, 1970; Alexander et al., 1971; Papanastassiou and Wasserburg, 1971a; Turner, 1971; Alexander et al., 1972; Horn et al., 1975; Nyquist et al., 1977; Nyquist et al., 1979). Therefore, all our samples have ages representative of their basalt groups within the Apollo collection.

6.2. Pb-Pb data

6.2.1. Pb-Pb Isochron Calculations. Using the Isoplot/Ex v. 2.49 program (Ludwig, 2000) to plot $^{207}Pb/^{206}Pb$ vs. $^{204}Pb/^{206}Pb$, a Pb-Pb isochron was created for each sample. The line of best fit was determined using the weighted least squares regression method (York et al., 1969). This calculation is the most precise way to determine the isochron as it allows for the individual weighting of different data points, a useful technique for a dataset such as this where data points have different uncertainties (σ errors). Measured ^{206}Pb and ^{207}Pb both consist of radiogenic and initial components. In contrast, because ^{204}Pb is not a radiogenic isotope, its measured value only reflects the initial amount present in the mineral structure at the time of crystallisation. In order to calculate Pb-Pb age the radiogenic ratio of $^{207}Pb^*/^{206}Pb^*$ must be known, therefore, the initial Pb components must

be subtracted. On the plot of $^{207}Pb/^{206}Pb$ vs. $^{204}Pb/^{206}Pb$, at the point where $^{204}Pb/^{206}Pb$ equals zero ^{204}Pb must be zero. Therefore, at this point the initial Pb is zero and the intercept on the y-axis shows the value of the radiogenic $^{207}Pb/^{206}Pb$ ratio ($^{207}Pb^*/^{206}Pb^*$). As the two separate decay constants of ^{207}Pb and ^{206}Pb are known (equations 1 and 2) $^{207}Pb^*/^{206}Pb^*$ can be used to determine Pb-Pb age (equation 3).

$$^{238}U \rightarrow {}^{206}Pb = 0.155125 \times 10^{-9}\ yr^{-1}\ (\lambda_{238}) \quad (1)$$

$$^{235}U \rightarrow {}^{207}Pb = 0.98485 \times 10^{-9}\ yr^{-1}\ (\lambda_{235}) \quad (2)$$

$$Pb(t) = U(t)\ [(e^{\lambda_{235}t} - 1)/(e^{\lambda_{238}t} - 1)]$$

$$= 1/137.88^*\ [(e^{\lambda_{235}t} - 1)/(e^{\lambda_{238}t} - 1)] \quad (3)$$

where; $U(t)$ = the present day ratio of $^{238}U/^{235}U$ (1/137.88)

$Pb(t)$ = value of the Pb-Pb isochron intercept on the y-axis ($^{207}Pb^*/^{206}Pb^*$)

λ_{235} and λ_{238} = the separate decay constants of U^{235} and U^{238} (equations 1 and 2)

t = the age of the sample

This method of Pb-Pb age calculation does not require the assumption of a value for the initial Pb content within the sample, as is the case with conventional $^{207}Pb/^{204}Pb$ vs. $^{206}Pb/^{204}Pb$ plots.

6.2.2. MSWD Calculations. It is important that the isochron regression calculations provide a realistic measure of uncertainty in the age and initial ratios. The mean square weighted deviation (MSWD) is a measure of the fit of the line to the data within the limits of analytical error. Ideally, an isochron should have a MSWD value of ≤ 1 - anything greater than this is not strictly an isochron, as the data scatter cannot be explained solely by

experimental error. However, an MSWD value of ≤ 1 is only applicable to isochrons involving infinitely large numbers of samples, therefore, 2.5 is generally taken as the cut off point for the definition of an isochron (Brooks et al., 1972). The origin of scatter on an isochron with an MSWD value ≤ 2.5 can be assumed to be analytical. The weighted MSWD is calculated as follows:

$$\text{MSWD}^{w} = \frac{\sum_{i=1}^{N} w_i}{(\sum_{i=1}^{N} w_i)^2 - \sum_{i=1}^{N} w_i^2} \cdot \sum_{i=1}^{N} \frac{w_i.(x_i - \overline{x}^*)^2}{(\sigma_{x_i})^2} \qquad (4)$$

where; xi = the measured value

wi = the weighting of that value

σ_{xi} = the associated error for that value

N = number of data points

The weighted mean is calculated as follows:

$$\overline{x}^* = \frac{\sum_{i=1}^{N} w_i x_i}{\sum_{i=1}^{N} w_i} \qquad (5)$$

The MSWD value can be reduced by excluding unrepresentative data points from the isochron calculations. This is done in two stages. Firstly any obviously anomalous points are excluded - anomalous results frequently occur during the first few analyses of an analytical run, as machine conditions are less stable at this time. Occasionally, they can also be produced by electrostatic field and/or magnetic field drift during the analyses, which required careful monitoring and appropriate corrections. Secondly, once the obvious anomalous points have been excluded from the dataset, a statistical f-test is applied to the remaining data. In very basic terms, the f-test can be defined for our dataset as the

observed variance of a data point from the isochron divided by the expected variance from the isochron based on the data point weighting.

6.2.3. Sample Ages. Table 6.2 shows the $^{204}Pb/^{206}Pb$ and $^{207}Pb/^{206}Pb$ ratios for the three mare-basalt samples dated during this study. Low-Ti Apollo 12 ilmenite basalts 12047 and 12064, and high-Ti Apollo 17 unclassified basalt 70035, were selected on the basis of their phosphate abundance and grain size, basalt type, and the quality of previous datasets. Both phosphates and plagioclase feldspar were analysed in samples 12064 and 70035 (Table 6.3) to obtain a spread of data along the isochron (plagioclase contains lower radiogenic Pb values than phosphate). Both apatite and whitlockite were analysed in sample 70035, but there is no large variation between the Pb-Pb ratios of these phases. The remaining samples only contain apatite. As mentioned above sample 12047 had never been dated previously.

$^{204}Pb/^{206}Pb$ ratios are relatively similar within all three samples, ranging from 0.0859-0.0003 (errors in Table 6.2). As expected, plagioclase grains show higher $^{204}Pb/^{206}Pb$ ratios than phosphates, at 0.049-0.086 and 0.314-9.945 $\times 10^{-3}$, respectively. $^{207}Pb/^{206}Pb$ ratios show more variation, though there is still substantial overlap between samples. Sample 12047 contains the lowest $^{207}Pb/^{206}Pb$ (0.2556-0.8505), followed by sample 12064 (0.2633-0.9215), and finally sample 70035 (0.3615-0.9775). Of the 16 spot analyses performed on sample 12047, five were excluded on the basis of the statistical f-test. These exclusions reduced the MSWD value from 2.1 to 1.1 (Figure 6.1). In addition, one point was excluded from the isochron calculations of both samples 12064 and 70035, producing MSWD values of 0.082 and 0.47 respectively (Figure 6.2). From these calculations, sample 12064 was determined to be the youngest at 3.24 ± 0.11 Ga, well within error of all preceding data. Sample 12047 is shown to be slightly older (3.32 ± 0.07 Ga), while sample 70035 is by far the oldest (3.79 ± 0.27 Ga) in agreement with previous data. These ages all show 2σ error.

Table 6.2: Pb-Pb data for samples 12047, 12064 and 70035.

	$^{204}Pb/^{206}Pb$	Error (2σ)	$^{207}Pb/^{206}Pb$	Error (2σ)
12047-phos 1	0.001295	0.000333	0.306290	0.033560
12047-phos 2	0.006054	0.000816	0.332060	0.006481
12047-phos 3	0.000642	0.000099	0.266590	0.010509
12047-phos 5*	0.003401	0.000218	0.298980	0.017310
12047-phos 6	0.005335	0.000295	0.310500	0.017293
12047-phos 7	0.001874	0.000353	0.255630	0.025568
12047-phos 8	0.001014	0.001045	0.310290	0.032978
12047-plag 1	0.058602	0.006478	0.850450	0.043403
12047-plag 2	0.070254	0.011980	0.779000	0.042832
12047-plag 6**	0.072658	0.005983	0.778730	0.032095
12047-plag 7	0.055735	0.012237	0.753440	0.159990
12064-plag 1	0.069646	0.007161	0.877320	0.035697
12064-plag 2	0.066916	0.006970	0.921500	0.046950
12064-plag 4*	0.053104	0.007712	0.751700	0.068439
12064-plag 5	0.049091	0.009883	0.710780	0.113360
12064-plag 6	0.069801	0.009467	0.909050	0.040214
12064-phos 1	0.001135	0.000169	0.269190	0.011713
12064-phos 2	0.000314	0.000035	0.263330	0.014222
70035-phos 2*	0.002519	0.000370	0.361490	0.063473
70035-phos 3	0.008194	0.001489	0.393480	0.070225
70035-phos 4	0.009945	0.000964	0.462220	0.075631
70035-phos 5	0.006866	0.001241	0.478590	0.094975
70035-phos 6	0.006138	0.002162	0.438940	0.050604
70035-plag 1	0.066829	0.006060	0.879300	0.055360
70035-plag 2	0.085901	0.019116	0.977530	0.071694
70035-plag 3	0.060093	0.006413	0.956980	0.055616
70035-plag 4	0.069871	0.007061	0.938040	0.052983
70035-plag 5	0.078012	0.011714	0.863910	0.133250
70035-plag 6	0.059194	0.004671	0.874710	0.038157
70035-plag 7	0.065439	0.003022	0.873620	0.024000

*Previous point has been masked. **Previous three points have been masked.

Adding these ages to the data in Table 6.1 increases the average age of sample 12064 by 0.01 Ga to 3.20 Ga, but does not change the average age of sample 70035 (3.77 Ga). Sample 12047 is younger than low-Ti Apollo 15 olivine-normative basalt 15555 (3.33 Ga), but older than low-Ti Apollo 12 olivine basalt 12040 (3.22 Ga). Including this new data, the average age of the low-Ti basalts is 3.28 ± 0.28 Ga and the average age of the high-Ti basalts is 3.67 ± 0.42 Ga.

6.2.4. Analytical Limitations and Challenges. The biggest limitation for successful SHRIMP analysis was the size and quality of the target grains. Phosphates form towards

Table 6.3: Typical phosphate and plagioclase major element data for samples 12047, 12064 and 70035.

Sample	Mineral	F	Na_2O	MgO	SiO_2	P_2O_5	CaO	SO_3	Cl	FeO	SrO	La_2O_3	Ce_2O_3	Pr_2O_3	Nd_2O_3	Sm_2O_3	Y_2O_3	Total	Final Total*
12047	apatite	3.16	-0.06	0.02	1.09	39.23	53.50	0.06	0.09	1.04	0.21	0.12	0.36					98.87	96.46
12064	apatite	2.67	-0.04	0.00	0.83	40.47	53.39	0.06	0.26	1.14	0.13	0.12	0.37					99.45	97.36
70035	apatite	3.06	0.05	-0.01	1.55	39.83	51.62		0.14	0.45	0.31	0.30	0.86	0.12	0.62	0.15	1.08	100.16	97.91
70035	whitlockite	-0.14	0.02	1.63	0.74	42.01	38.17		0.00	3.34	0.17	0.65	2.20	0.37	2.15	0.68	4.82	97.00	96.99

Sample	Mineral	Na_2O	MgO	Al_2O_3	SiO_2	K_2O	CaO	TiO_2	Cr_2O_3	MnO	FeO	CoO	NiO	Total
12064	plagioclase	0.73	0.20	33.61	45.62	0.02	19.34	0.07	0.00	0.03	0.44	0.01	0.00	100.08
70035	plagioclase	1.64	0.17	31.88	48.09	0.11	16.15	0.32	-0.02	0.01	0.84	0.00	0.01	99.23

*Where the final total includes subtraction of the extra oxygen incorrectly added to F and Cl by the electron microprobe software during the calculation of the original total.

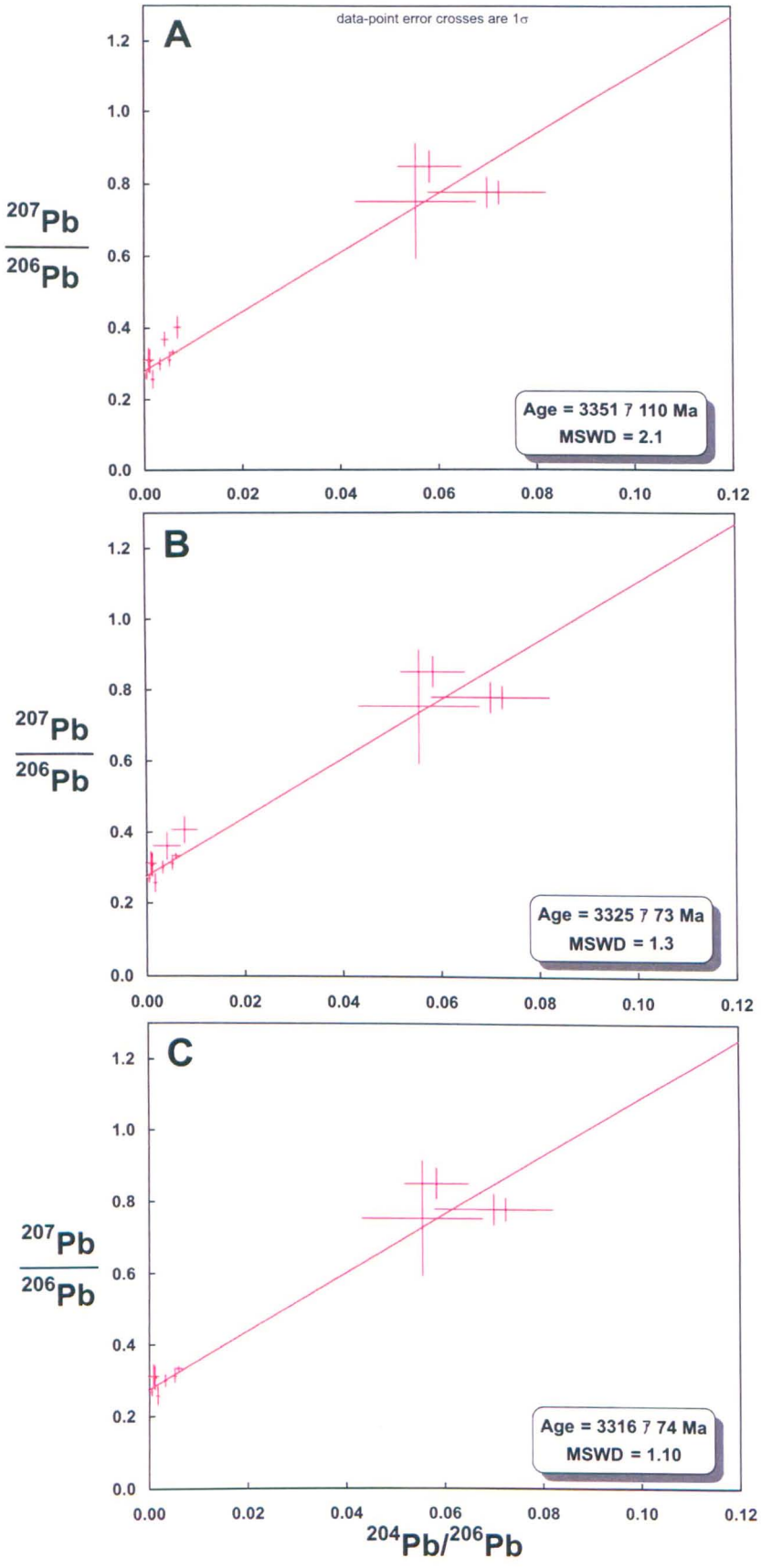

Figure 6.1: $^{207}Pb/^{206}Pb$ vs. $^{204}Pb/^{206}Pb$ isochrons, illustrating the change in MSWD with the exclusion of certain anomalous values. **(a)** Isochron calculated using all data points. **(b)** Isochron calculated with the exclusion of three plagioclase data points. **(c)** Isochron calculated with the exclusion of three plagioclase and two apatite data points, showing the lowest MSWD.

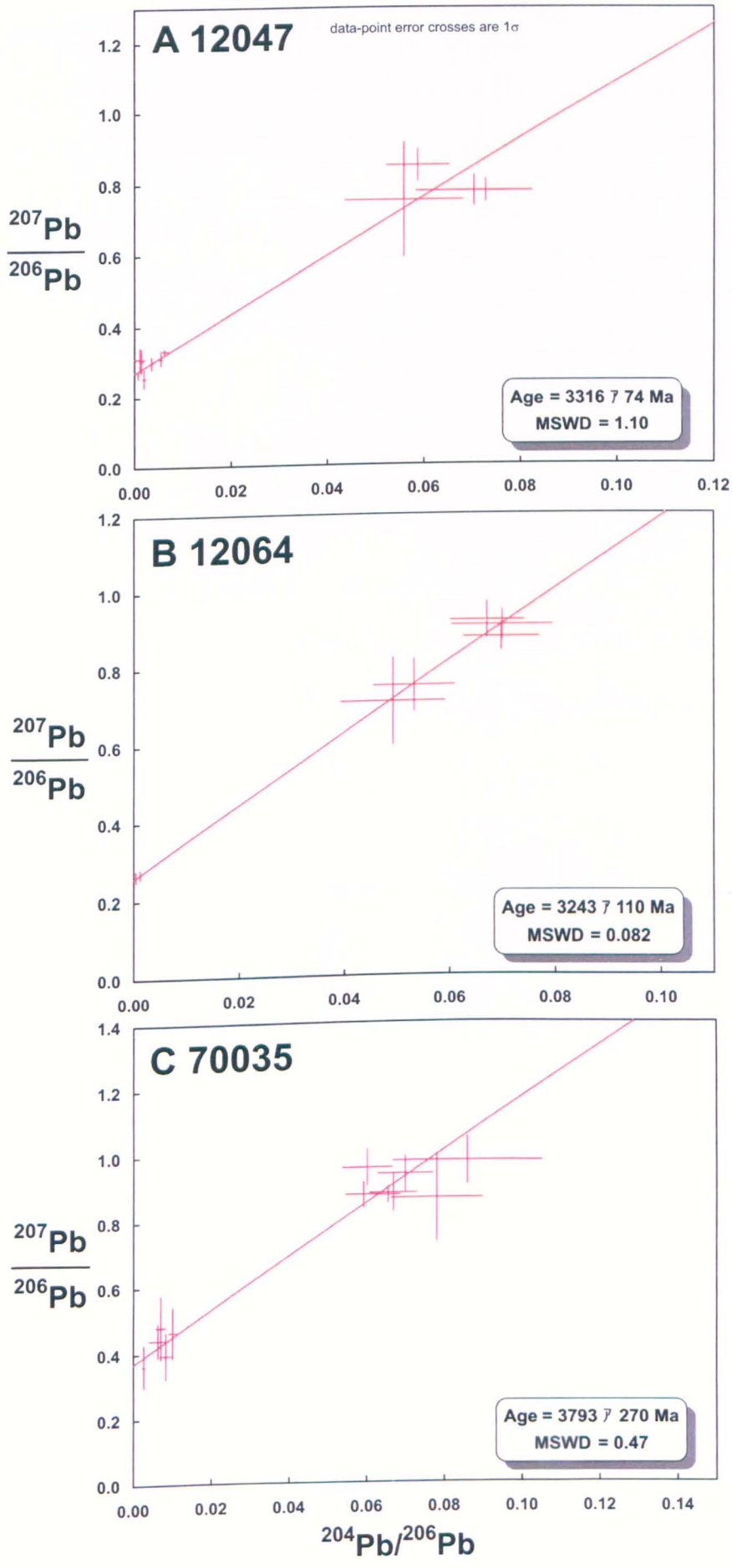

Figure 6.2: Our final Pb-Pb sample ages. The final $^{207}Pb/^{206}Pb$ vs. $^{204}Pb/^{206}Pb$ isochrons for **(a)** sample 12047 (the same as Figure 6.1c), **(b)** sample 12064 and **(c)** sample 70035.

the very end of mare-basalt crystallisation, so they contain relatively higher amounts of incompatible-elements, such as U and Th. For this reason phosphates are ideal targets for U-Pb dating. However, most phosphates in mare-basalts occur as small grains (mostly 5-50 μm), associated with mesostasis areas. These grains often have cracks, and in some cases contain inclusions of other minerals (e.g., ilmenite, plagioclase and sulphides - Figure 6.3). Analysis of these small grains in our samples could only be performed with a 4 μm beam size, rather than the usual 10 μm beam.

The 10 μm beam creates a spot on the sample surface of 10 by 14 μm - slightly elliptical because of the 45 ° angle at which the beam hits the surface. A smaller beam reduces the spot size, but also weakens the signal strength reaching the detector by approximately four times, thus increasing the error on individual data points and the isochron as a whole. The size of the error on isochron age is also dependent on phosphate composition. If a sample contains both whitlockite and apatite, it is likely that Pb-Pb ratios will vary within these two phases, thereby creating sufficient spread to allow a meaningful isochron to be defined. If only one of these phases is analysed the Pb-Pb ratios of all grains will be very similar and the data points usually cluster together, increasing the uncertainty on isochron age determination. In this case, another end-member mineral must be analysed to define the isochron, preferably a phase with a very different Pb-Pb content (e.g., plagioclase).

The SHRIMP facility at Hiroshima University encountered some major technical issues leading to significant machine downtime during the last two years. Because of the logistical requirements, laboratory visits had to be planned several months in advance, and, therefore, a successful outcome for a trip could not be guaranteed. Since it takes approximately 72 hours of machine time to age date one sample, the restricted availability allowed dating of far fewer samples than originally planned.

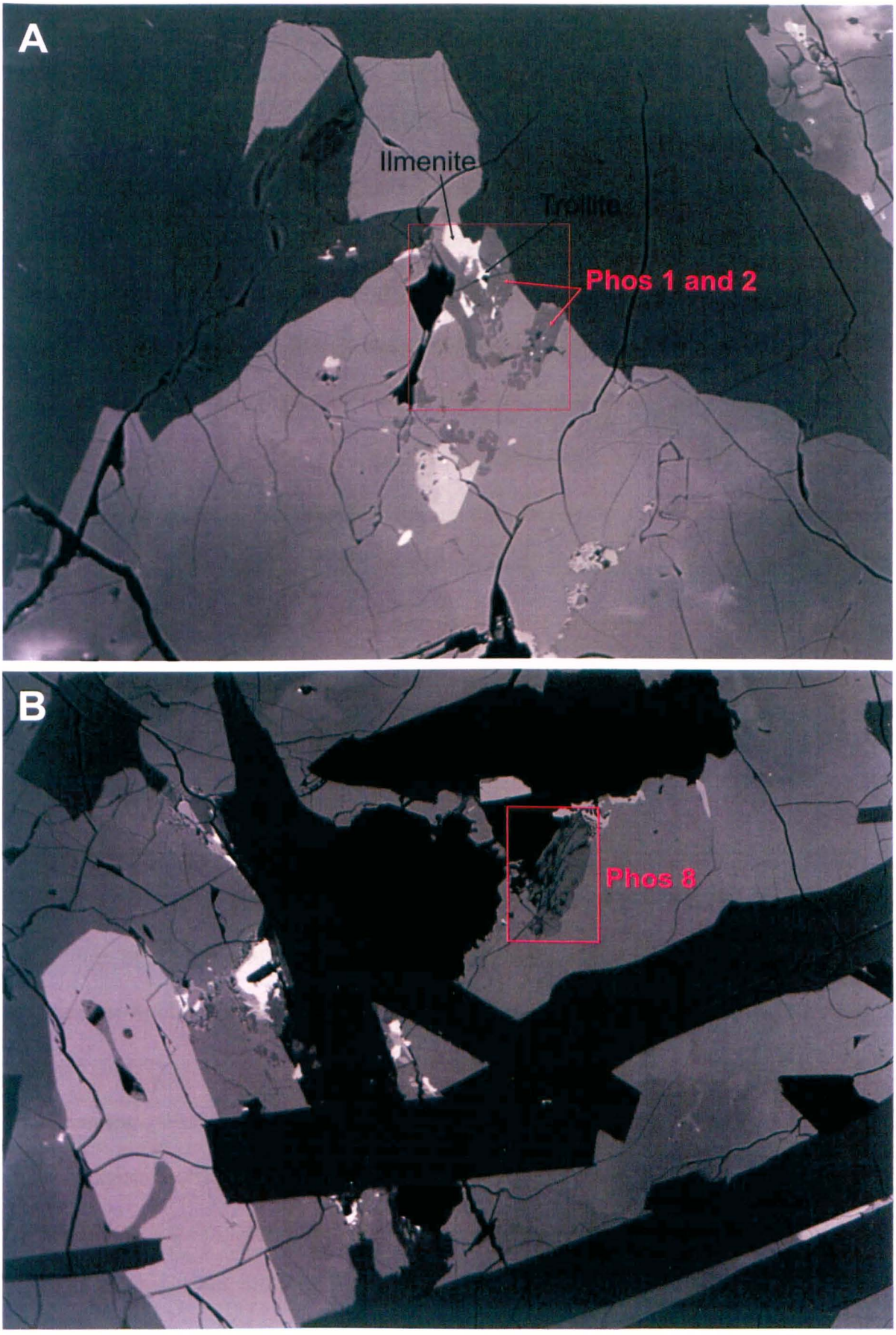

Figure 6.3: Backscatter electron images of apatite grains within sample 12047. These images illustrate the cracked **(a)** and included **(b)** nature of phosphate grains within all our samples.

6.3. Discussion

6.3.1. Geochronological Data. Our Pb-Pb results confirm that the high-Ti basalts of Apollo 11 and 17 are older than the low-Ti basalts of Apollo 12 and 15, in agreement with previous geochronological studies of these two main mare-basalt groups. These age relationships are consistent with the suggestion of Head and Wilson (1992) and Head et al. (1997) that although a variety of magma types erupted in nearside mare basins during the period 3.8 to 3.2 Ga, the early and intermediate phases of eruption within individual basins were dominated by high-Ti basalts. Later periods of eruption within a basin were predominantly low-Ti. These studies suggested that this may be the result of increasing depth of mantle sources for various magma types, but this conclusion is not consistent with high pressure experimental results for mare-basalts (Stopler, 1974; Green et al., 1975; Delano, 1980, 1986; Chen et al., 1982; Chen and Lindsley, 1983; Longhi, 1987, 1992). Although the sample record implies the high Ti-basalts of the Apollo 11 site are at least 3.37 Ga (see Table 6.1), high-Ti volcanic activity as young as 1 Ga has been suggested by Schultz and Spudis (1983) based on photogeologic evidence. In addition, VLT basalt fragments in Apollo 17 soils were located within a breccia with a melt-rich matrix older than 4 Ga (Taylor et al., 1991). The oldest mare basalt discovered to date is also a VLT basalt, fragmental meteorite Kalahari 009, which is believed to be a sample of cryptomare (a mare basalt flow covered by subsequent flows/regolith an therefore hidden from direct view) that crystallised around 4.35 Ga (Terada et al., 2007). This evidence, along with the fact that the oldest sample within our sample set is low-Ti basalt 14053, further raises doubts on the hypothesis that the mare-basalts became globally Ti-depleted over time.

Although the low-Ti Apollo 12 olivine, pigeonite and ilmenite basalts cannot be discriminated in terms of their age, the geology of the Apollo 12 site indicates that the ilmenite basalts overlie the pigeonite basalts, which in turn overlie the olivine basalts (Rhodes et al., 1977). As the ilmenite basalts contain more TiO_2 than the pigeonite basalts,

and these contain more than the olivine basalts, this stratagraphic sequence suggests the mare flows in this area became Ti-enriched over time. This enrichment is in direct contrast to the observed Ti-depletion of the Apollo collection as a whole, indicating the Ti-composition of mare basalts may be more dependant on local conditions than was initially recognised. The mantle overturn model of Ringwood and Kesson (1976) suggested that shallow formed ilmenite-rich cumulates sank deeper into the Moon's mantle over time, because of density instability. However, it is believed that this overturn was not complete, and as a result a heterogeneous mare-basalt source region was produced (Van Orman and Grove, Elkins-Tanton et al., 2002). This heterogeneous source would explain why basalts of different Ti-contents appear to have erupted from similar depths on to the lunar surface (Stopler, 1974; Green et al., 1975; Delano, 1980, 1986; Chen et al., 1982; Chen and Lindsley, 1983; Longhi, 1987, 1992).

6.3.2. Remote Sensing Data. As the samples returned by the Apollo missions present an incomplete picture of the relationship between magma composition and time (Papike et al., 1976), many authors have relied on remote sensing methods to gain a more global picture of mare-basalt evolution. Using crater size frequency ages on well defined volcanic units Hiesinger et al. (2000) concluded that the main phase of mare volcanism on the lunar near side spanned from approximately 4 to 2 Ga. However, the patches of youngest mare-basalt areas are low-Ti extrusions found within the Procellarum and Imbrium basins, which appear to be as young as 1.1 Ga (Hiesinger et al., 2002, 2003). As the eruptive flux was not constant, separate basins show different phases of mare eruption. For example, older regions such as the Tranquillitatis basin (containing the Apollo 11 site) show a single phase of mare volcanism, from 3.3 to 3.9 Ga, whereas the younger multi-ring basins exhibit a second weaker phase of eruption, from 3.3 to 3.5 Ga (Shearer et al., 2006). Following this phase, volcanic eruptions became low volume and episodic, accounting for < 5 % of the total volume of mare basalts (Schaber, 1973; Schultz and Spudis, 1983; Head and Wilson,

1992; Head et al., 1997). Mare-basalt eruption on the far side, though comparatively sparse, was also a long lived process (Pieters et al., 2001; Harkyama et al., 2009).

The most extensive remote-sensing studies of nearside mare basaltic units to date were performed by Hiesinger et al., (2000, 2002, 2003). These authors used crater size frequency age calculations, along with Clementine and Lunar Prospector compositional data (e.g., Lucey et al., 2000; Lawrence et al., 2000; Elphic et al., 2000; Feldman et al., 2002), to recreate the volcanic history of Oceanus Procellarum, Mare Nubium, Cognitum, Insularum, Humorum, Imbrium, Serenitatis, Tranquillitatis, Humboldtianum, Australe, Frigoris, Nectaris, Vaporum, Smythii, and Marginis. These investigations revealed no link between the Ti-content and age of mare basalts, and in many cases a single basin was found to contain high- and low-Ti mare units of the same age (Hiesinger et al., 2002). These observations support the heterogeneous source model of Elkins-Tanton et al. (2002) mentioned above.

However, in some cases, major basins analysed in detail using the remote sensing algorithms of Lucey et al. (1998, 2000) show mare-basalt evolution from low-Ti to high-Ti compositions. For example, the investigations of Bugiolacchi and Guest (2008) and Otake and Mizutani (2006) both indicate the basaltic units of Mare Imbrium evolve to high-Ti compositions, as does the study of Mare Nubium and Mare Cognitum by Bugiolacchi et al. (2006). Otake and Mizutani (2006) produced a model in which the low-Ti mare-basalts are the product of primitive magma generated in the undifferentiated interior of the Moon, and the high-Ti basalts are the product of this primitive magma being assimilated by a late stage Ti-rich magma. These authors used the impact associated thermal model of Arkani-Hamed, 1974 and Strangway and Sharpe (1975) to argue that the high-Ti hybrid sources re-melted more extensively hundreds of million years after Imbrium basin formation to produce relatively young high-Ti mare-basalts. The impact associated thermal model

proposes that radiogenic heat from the deep undifferentiated interior is accumulated under the rims of giant impact craters, where it has the maximum insulation effect of thick, low-thermal conductivity ejecta blankets. Arkani-Hamed (1974), and Strangway and Sharpe (1975), estimated that this heat is adequate to allow delayed re-heating and re-melting of materials in these region hundreds of million years after the basin forming impact event. Otake and Mizutani (2006) claimed that this model explains the variation in chemical composition, the change of eruption volume with time, and the long period of volcanic activity within the Imbrium basin. However, the model does not specify that the high-Ti basalts must erupt later than the low-Ti basalts, it simply gives a possible explanation as to why they did.

6.4. Conclusions

- Our radiogenic Pb-Pb dating of Apollo 12 low-Ti mare-basalts 12047 and 12064, and Apollo 17 high-Ti basalt 70035, indicate the latter is older than the former (12047 = 3.32 ± 0.07 Ga, 12064 = 3.24 ± 0.11 Ga, and 70035 = 3.79 ± 0.27 Ga.

- These ages support previously recorded ages for these individual samples, and the mare-basalt groups to which they belong.

- Both geochronological and remote sensing data show that there is no unifying model linking the global composition and age of mare basalts, but rather indicate that composition is dependant on the heterogeneity of the cumulate source regions at a more localised level.

7. DISCUSSION

7.1. Mare Basalt Petrogenesis

7.1.1. Origins. Analysis of the data collected in this study has shown that the high and low-Ti mare basalts form two distinct groups, both mineralogically and chemically. SEM images, mineral compositions, major- and trace-element data, combined with oxygen isotopes, indicate that the Apollo 12 and 15 low-Ti basalts were produced from similar source regions, whereas the Apollo 11 and 17 basalts show greater source-region compositional variation. Chemical modelling suggests that the low-Ti mare basalts formed from < 10 % partial melting of sources with similar REE abundances to McKenzie and O'Nions' (1991) depleted-Moon source, followed by olivine fractionation or accumulation. REE abundance estimations of the high-Ti mare-basalt source-regions were not as straightforward, as the McKenzie and O'Nions' (1991) depleted-Moon source was not an accurate representation of the REE content within these source regions. However, the high-Ti basalts were probably formed as a result of < 15 % partial melting of comparatively incompatible-element enriched source regions, followed by multi-phase crystal fractionation and/or accumulation (including ilmenite, olivine, augite, pigeonite and plagioclase) (sections 4.43- 4.45). Trace-element data also indicate that the low-Ti basaltic melts were dominantly produced by batch melting, whereas high-Ti basalt melt production was dominated by fractional melting (section 4.43, Figures 4.19 and 7.1). The REE content of Apollo 14 low-Ti, high-Al basalt 14053 can be reproduced by ~ 10 % partial melting of the depleted-Moon source, followed by olivine fractionation and 1.5 % simultaneous assimilation of a crustal component, probably a mixture of KREEPy and granitic material. The Apollo 11 high-Ti, high-K basalt samples' REE contents match well with 10 % pure KREEP assimilation, along with ilmenite, augite, pigeonite and plagioclase fractionation from a parental melt with the same composition as Apollo 11 orange glass (section 4.4.5;

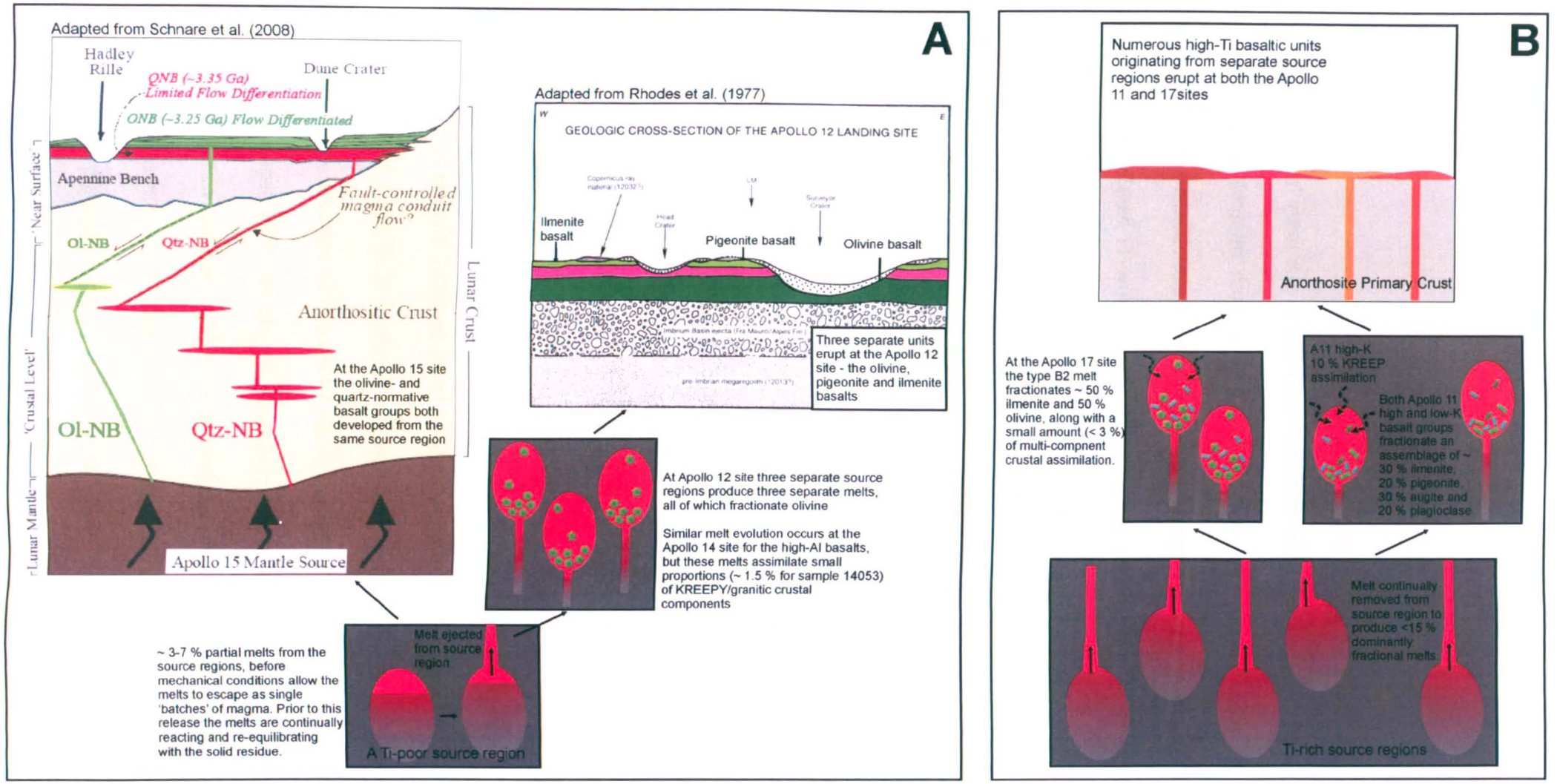

Figure 7.1: Batch vs. fractional partial melting in the mare-basalt source regions. **(a)** The possible evolution of Apollo 12, 14 and 15 low-Ti basalts from dominantly batch melted source regions. **(b)** The possible evolution of the Apollo 11 and 17 high-Ti basalts from source regions dominated by fractional partial melting.

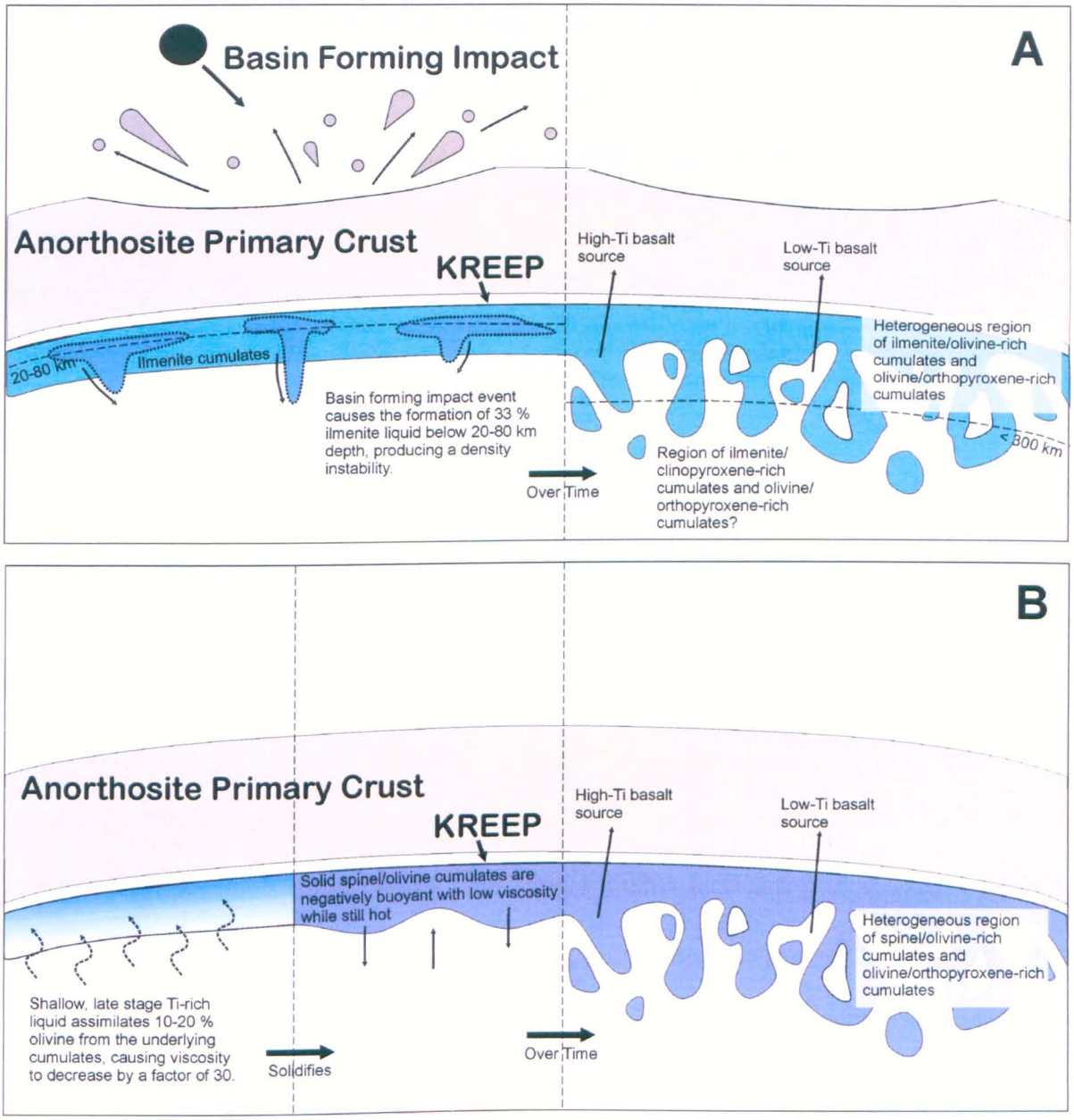

Figure 7.2: The mare-basalt heterogeneous source region model of Elkins-Tanton (2002). **(a)** The possible formation of the heterogeneous source regions via shallow level ilmenite-cumulate melting and subsequent diapir formation. **(b)** An alternative model, involving the assimilation of 10-20 % olivine by shallow level Ti-rich liquids.

The second plausible model of Elkins-Tanton et al. (2002) requires the late stage Ti-rich liquid to assimilate 10-20 % of the underlying olivine-rich cumulates. The change in bulk-composition would subsequently alter liquidus relations, causing spinel rather than ilmenite cumulates to crystallise at these shallow levels. The solidus temperature of this material would be higher, allowing a negatively buoyant cumulate layer to form while the

layer remained hot, and had lower viscosity. The MELTS calculations of Ghiorso and Sack (1995) predict that the solidus of this spinel-rich cumulate would be ~ 115°C higher than the original ilmenite-clinopyroxene cumulate, leading to a reduction in viscosity by a factor of ~ 30. This spinel cumulate could, therefore, travel deeper into the lunar interior as a solid due to density instabilities (Figure 7.2b). In possible support of this model, Wagner and Grove (1997) found orthopyroxene, olivine and spinel, not ilmenite, on the liquidus of the Ti-rich Apollo 14 black glass.

In conclusion, Elkins-Tanton et al. (2002) state that both mechanisms may have occurred, but that only early solid spinel cumulates could have sunk into the lunar interior as the model requires that they were hot (therefore less viscous). Which ever way mare-basalt source heterogeneity was caused, its presence indicates that the separation of the Apollo basalts into high and low-Ti groups may not be justified – source heterogeneity suggests the eruption of basalts with a wide spectrum of TiO_2 contents, as implied by remote sensing data (e.g., Giguere et al., 2000; Elphic et al., 2002; Gillis et al., 2003). Our $\delta^{18}O$ data also suggest an oxygen isotope compositional continuum rather than the previously reported bi-modal system (Wiechert et al., 2001; Spicuzza et al., 2007) - from the light $\delta^{18}O$ values of the highest-Ti Apollo 17 basalts through the moderate values of Apollo 11 to the heaviest values of the Apollo 12 and 15 low-Ti basalts. This TiO_2 spectrum can be best explained by the mixing of two end-member source compositions, where one contains a significant amount of TiO_2. Based on geochemical modelling Snyder et al. (1992a) suggested the source region of the low-Ti basalts contained 46 % pigeonite, 43 % olivine, 10 % clinopyroxene, 1 % plagioclase and 1-2 % trapped KREEPy liquid. These authors calculated the probable source of the high-Ti basalts was a 80:20 % mix of the low-Ti mafic cumulates and late-stage ilmenite cumulates, yielding a high-Ti basalt source with 3 % ilmenite and less clinopyroxene than the low-Ti source (7 %). The Lu-Hf-Sm-Nd data of Beard et al. (1998) indicate similar high- and low-Ti mare-basalt source mineralogies.

The presence of these small scale reversals in TiO_2 content evolution within the Imbrium region reflect the Apollo sample collection's localised TiO_2 variability. Both Otake and Mizutani (2006) and Bugiolacchi and Guest (2008) focused on the Imbrium region - studies of other regions do not share the same conclusions. The most extensive studies of nearside mare basaltic units to date revealed no link between the Ti-content and age of mare basalts (Hiesinger et al., 2000, 2002, 2003). These authors used crater-size-frequency age calculations along side Clementine and Lunar Prospector compositional data (Lucey et al., 2000; Lawrence et al., 2000; Elphic et al., 2000; Feldman et al., 2000) to recreate the volcanic history of Oceanus Procellarum, Mare Nubium, Cognitum, Insularum, Humorum, Imbrium, Serenitatis, Tranquillitatis, Humboldtianum, Australe, Frigoris, Nectaris, Vaporum, Smythii, and Marginis (Figure 7.3). In many cases, a single basin was found to contain high- and low-Ti mare-basalt units of the same age (Hiesinger et al., 2002). Neither do these authors report any link between unit Ti content and size, although the youngest eruptions are less numerous. These observations support the heterogeneous source model of Elkins-Tanton et al. (2002) mentioned above, as this model would not require global scale Ti content evolution over time, and would allow localised variability. On the smaller scale of a single magma chamber/source region the units may be expected to become Ti-richer over time, as dense ilmenite crystals accumulate at the bottom of the magma body, and, therefore, produce late stage ilmenite-rich units. This may account for the small scale reversals in TiO_2 enrichment visible in the Imbrium region.

7.1.3. Origin of the Moon. In agreement with previous studies (Wiechert et al., 2001; Spicuzza et al., 2007), our data reveal no detectable difference between the $\Delta^{17}O$ of the Earth and Moon. The recent doubts raised by Melosh (2009), concerning the mechanism of Pahlevan and Stevenson's (2007) post-Giant-Impact volatile mixing model, suggest that this model requires further refinements to account for the current dynamics of the

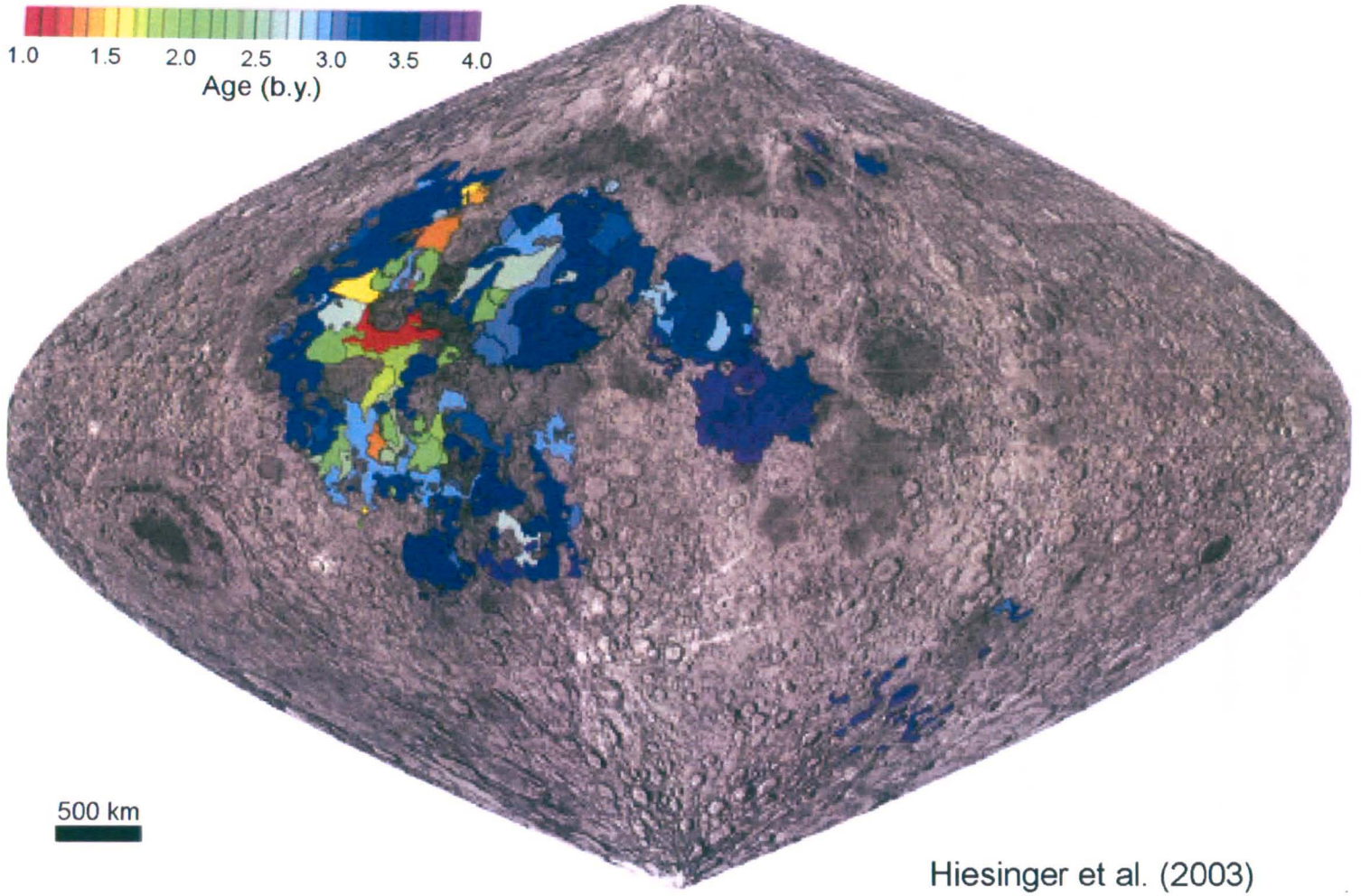

Figure 7.3: Global map of mare basalts, coloured according to age (after Hiesinger et al., 2003).

Figure 4.23). Setting aside the different parental melt evolutions, bulk-rock elemental evidence clearly indicates that the high- and low-Ti mare-basalts were produced by compositionally separate source regions. This is supported by different oxygen isotope compositions of the high- and low-Ti basalts. However, this data implies that rather than a bi-modal system a mare-basalt compositional continuum exists, where the Apollo 11 basalts show compositions between those of the other high-Ti basalts and the low-Ti basalts (both in terms of oxygen isotopes and TiO_2 abundance).

The differing oxygen isotope compositions and TiO_2 contents between the high- and low-Ti mare-basalts can best be explained by the lunar cumulate overturn model (Ringwood and Kesson, 1976). A number of authors have investigated the possibility of ilmenite assimilation at the base of the lunar crust as an alternative to the lunar mantle overturn hypothesis (e.g., Hubbard and Minear, 1975; Wagner and Grove, 1997; Elkins et al., 2000; Thacker et al., 2009), but mare basalt Hf-Nd ratios (e.g., Beard et al. 1998) argue against ilmenite assimilation as the cause of Ti variation in mare basalts. As ilmenite is not thought to have crystallised a depths below 100-150 km within the lunar interior (Ryder, 1991; Hess and Parmentier, 1995; Van Orman and Grove, 2000), its crystallisation is believed to have formed a shallow region of relatively dense material compared to the underlying olivine-pyroxene cumulates (e.g., Snyder et al., 1992; Hess and Parmentier, 1995). Ringwood and Kesson (1976) argued that this density instability was dissipated by cumulate overturn, whereby the ilmenite cumulates form diapirs into the olivine-pyroxene cumulates and vice-versa. However, this mixing is unlikely to have completely homogenised the cumulate region, leaving some areas more enriched in ilmenite than others at mare-basalt source depths (200-300 km – Elkins-Tanton et al., 2002). Based on viscosity constraints, Elkins-Tanton et al. (2002) suggested that the traditional view of ilmenite-rich cumulate solids sinking deeper into the lunar interior during mantle overturn (e.g., Ringwood and Kesson, 1976; Hess and Parmentier, 1995; Zhong et al., 2000) is

improbable. Various alternative scenarios were examined by Elkins-Tanton et al (2002) via numerical modelling, only two were found to be plausible. The first involves re-melting of shallow level (60-100 km) ilmenite and clinopyroxene cumulates to form a liquid denser than the underlying cumulates. This liquid would have had a maximum of 33 % ilmenite content (as ilmenite and clinopyroxene melt with a 1:2 ratio), making it negatively buoyant below depths of 20-80 km, depending on the assumed mantle composition. Shallow level re-melting could have been caused by basin forming impact events or radiogenic heating from nearby KREEP-rich materials. The steep liquidus of this ilmenite-clinopyroxene liquid indicates the downward percolating liquid would begin to crystallise ilmenite at < 200 km depth and ~ 1200 °C (Hess et al., 1978; Van Orman and Grove, 2000). This model also indicates that at shallow depths, the liquid will probably crystallise olivine and dissolve pyroxene, whereas at greater depths it will be in its pyroxene primary phase volume, and will dissolve olivine and crystallise pyroxene. This makes the formation of a heterogeneous, hybrid mantle possible, where clinopyroxene cumulates are more abundant than olivine cumulates at deeper levels (Figure 7.2a). However, the clinopyroxene within these cumulates would be mostly low-Ca pigeonite (Elkins-Tanton, personal communication), so the depth of mare-basalt origin cannot be constrained by Ca-content - no difference is visible between the bulk rock CaO content of high and low-Ti Apollo mare-basalts (Figure 4.3c; section 4.1.1), therefore, both appear to have originated from source regions with similar CaO contents. The Lu-Hf and Sm-Nd data of Beard et al. (1998) suggest that low-Ti basalts were probably produced from cumulate sources rich in orthopyroxene and olivine with small amounts of clinopyroxene (2 %) and trapped liquid (< 10 %). These authors argued that the production of high-Ti basalts would only require the addition of a small amount of ilmenite (< 2 %) to this mixture. These mineral proportions are in close agreement with those produced by the chemical modelling of Snyder et al. (1992).

Ilmenite does not contain significant amounts of REE, therefore if this was the only difference in source region mineralogy, and if modal partial melting proportions were similar for the high and low-Ti basalt sources, the high-Ti source would be expected to produce melts with lower REE contents than the low-Ti melts (as the latter contain 3 % more clinopyroxene – a REE-rich phase). However, our bulk rock REE data indicate the opposite relationship is found in the Apollo mare-basalts (in agreement with previous studies – chapter 4). Snyder et al. (1997) stated that partial melting was non-modal in the mare-basalt source regions, and that the first phase to melt would be REE-rich trapped KREEPy liquid. Therefore, the high REE contents of the high-Ti basalts could be explained if these basalts are products of smaller proportions of partial melting than the low-Ti mare basalts (as a 1 % melt would contain 100 % trapped KREEPy liquid, whereas a 10 % melt would only contain 10 % of his phase). However, neither our data, nor that of previously published work (e.g., Nyquist et al., 1977, 1979; Hughes et al., 1988; Snyder et al., 1992, 1997) suggests there is a significant difference in the proportion of partial melting which produced the high- and low-Ti mare basalts. Alternatively, the melting proportions in source regions for both types could have been similar if the high-Ti sources trapped KREEPy liquid contained higher REE abundances than that within the low-Ti sources (as may be expected from source regions containing late-stage cumulates). Our measured $\delta^{18}O$ values, alongside those calculated from mineral separates data and modal mineralogies, show how oxygen isotopic composition evolves from the cumulate source region to the parental partial-melt and finally (after melt evolution, including crystal fractionation/accumulation) to the mare-basalt samples. In some cases, assimilation of KREEPy and/or granitic material further expand the possible mare basalt major-, minor- and trace-element compositions, of which the Apollo collection probably only represent a small fraction. However, the samples which were collected have allowed the complex nature of the lunar interior to be investigated and used as a possible analogy for other small planetary bodies.

7.1.2. Type, Age and Distribution. Our mineral and bulk-rock major- and trace-element data, and that of other authors (e.g., Rhodes et al., 1976; Beaty and Albee, 1978; Beaty et al., 1979a,b; Warner et al., 1979; Ma et al., 1980; Rhodes and Blanchard, 1980), show that at least five separate high-Ti parental melt compositions were sampled at the Apollo 11 site (type A, B1, B2, B3 and unclassified basalt 10050), and five separate Apollo 17 high-Ti melts are represented in our sample set alone (types A, B and C, and unclassified basalts 70017 and 70035). In contrast, only three melts are represented from the Apollo 12 site (the low-Ti olivine, ilmenite and pigeonite basalts – e.g., Rhodes et al., 1977; Neal et al., 1994a), and the Apollo 15 low-Ti olivine-normative and quartz-normative basalts appear to all have originated from the same source (Schnare et al., 2008). Therefore, the Apollo sample collection suggests that basaltic eruptions at sites dominated by high-Ti mare-basalts are more numerous than those at the low-Ti sites. This apparent difference may have been produced by sampling bias, as remote sensing observations do not support the sampling evidence (e.g., Hiesinger et al., 2000, 2002, 2003; Otake and Mizutani, 2006; Bugiolacchi and Guest, 2008). However, the nature of remote sensing studies only allows large scale investigation, therefore, the analysis of individual basalt flows is not currently possible. Radiogenic age dating of these samples (including those measured during this study) also indicates a difference in age between the two main basalt types, where the high-Ti basalts are older than the low-Ti basalts (3.92-3.48 Ga for the high-Ti basalts of Apollo 11 and 17 and 3.40-2.92 Ga for the low-Ti basalts of Apollo 12 and 15 – chapter 6).

Otake and Mizutani (2006), and Bugiolacchi and Guest (2008) employed Clementine remotely-sensed data to derive the TiO_2 abundance of mare-basalt units within the Imbrium region of the lunar nearside. Both studies show the opposite relationship to the Apollo basalt sample suite. Low-Ti mare-units tend to be older than the high-Ti basalts within this region. However, Bugiolacchi and Guest (2008) reported localised variations in TiO_2 evolution, with some small areas showing older Ti-rich and younger Ti-poor units.

Earth-Moon system. This may be taken as an indication that the Giant-Impact model cannot plausibly explain the isotopic and dynamic components within the Earth-Moon system. Possible alternative models, which may explain the observed homogeneous oxygen isotopic composition of the Earth and Moon, include a modified version of the Darwin fission model (Melsoh, 2009) and the double planet growth model of Belbruno and Gott (2005). This latter model suggests that a body the size of Mars could have grown within the L4 or L5 Lagrange points of Earth's orbit, and subsequently been thrown into an eccentric orbit via collisions with other planetesimals. If this occurred, Belbruno and Gott (2005) reasoned that the body would very probably have collided with the Earth, causing a giant impact and the subsequent formation of the Moon. However, this model assumes the impacting body would have had the same oxygen isotope composition as the Earth, simply because it formed in the same region of space. Although it does not necessarily follow that the oxygen isotopic distribution of the current solar system is the same as that of the early solar system, recent measurements of the $\Delta^{17}O$ of Mars (+0.30 ‰) and Vesta (-0.24 ‰) suggest oxygen isotope ratios do not have a radial distribution within the current solar system (Greenwood et al., 2005; Wiechert et al., 2004). This, along with the chaotic planetary growth model (Kenyon and Bromley, 2006 - and references therein), argue against Belbruno and Gott's (2005) double planet model of lunar formation. The possibility of alternative models has yet to be fully explored, but it is clear that the Giant-Impact theory is in need of re-assessment.

7.2. 40 Years after Apollo – What's left to Achieve?

7.2.1. The Importance of Apollo Scientific Results to Subsequent Lunar Exploration.

Not only did the Apollo and Luna missions return the only lunar samples from known locations, but they also made photographic, geophysical and spectral observations and measurements of the Moon (Metzger et al., 1977; Haines et al., 1978; Andre et al., 1979; Andre and El-Baz, 1981; Hawke and Bell, 1981; Taylor, 1982). One of the most significant

discoveries made through these observations and measurements was the detection of the thicker lunar farside crust based on iron concentrations which are directly related to density (e.g., Bills and Ferrari, 1977; Haines and Metzger, 1980; Wieczorek et al., 2006). Another significant discovery from the Apollo orbital data was that the Moon's centre of mass was offset from the centre by ~ 2.5 km (Kaula et al., 1972; 1974; Haines and Metzger, 1980). Wieczorek et al. (2006) refined this estimate based on global datasets from post-Apollo missions to ~1.9 km. Integrating sample analysis with orbital data to provide ground truth made the remote sensing datasets of the Clementine and Lunar Prospector missions much more important. These missions extended the Apollo datasets and allowed global maps of FeO, TiO_2, Th and H abundances to be produced (Lucey et al., 1995, 1998, 2000; Elphic et al., 1998, 2002; Feldmann et al., 1998a, 2000; Lawerence et al., 1998, 2000). These global maps highlighted a number of features:

1. The Apollo and Luna mare-basalt samples were not fully representative of the compositional diversity on the lunar surface, which appears to show a mare-basalt Ti-content continuum rather than the bi-modal separation visible in the sample suite (e.g., Giguere et al., 2000).

2. There is a Th 'hotspot' centred on mare Imbrium on the lunar nearside (Lawrence et al., 1998, 2000), interpreted as a concentration of KREEP-rich material exposed by the Imbrium basin forming impact.

3. There is only a minor positive Th anomaly at the South Pole-Aitken basin, indicating KREEP is heterogeneously distributed at global scale (Lawrence et al., 1998, 2000).

4. The polar regions are enriched in H (Feldman et al., 1998b, 2000, 2004) and the enriched areas are at least partly correlated with permanently shadowed areas.

Preliminary data from the Lunar Crater Observation and Sensing Satellite (LCROSS) indicates that the mission successfully detected water in the permanently shadowed region of Cabeus crater near the Moon's south pole, during the 9th October 2009 impact.

5. Recognition of evolved lithologies in the sample collection and high Th areas on the lunar surface (Metzger et al., 1977; Lawrence et al., 1998) has allowed Lawrence et al. (2005, 2007) to define the locations of potential outcrops of these rocks on the surface by reinterpreting the Th abundances derived from Lunar Prospector gamma-ray spectrometer data. Establishing the abundance of these lithologies on the Moon will aid in understanding the growth and evolution of the lunar crust.

*7.2.2. **Why go back to the Moon?*** Since the last Apollo mission there have been a number of publications and reports stating the reasons why the moon is still important both scientifically and for exploration purposes (e.g., Mendell, 1986; Spudis et al., 1986; Taylor and Spudis, 1990; Spudis, 2003). President Bush summarised these reasons in his speech 'A Renewed Spirit of Discovery' (Bush, 2004);

"Returning to the Moon is an important step for our space program. Establishing an extended human presence on the Moon could vastly reduce the cost of further space exploration, making possible ever more ambitious missions. Also the Moon is home to abundant resources. Its soil contains raw materials that might be harvested and processed into rocket fuel or breathable air. We can use our time on the Moon to develop and test new approaches and technologies and systems that will allow us to function in other, more challenging, environments. The Moon is a logical step towards further progress and achievement. With the experience and knowledge gained on the Moon, we will then be ready to take the next steps of space exploration: human missions to Mars and to worlds beyond."

In terms of the geological evolution of the Moon we have still to discover:

1. If a substantial record is available for events prior to ~ 4 Ga or if this history has been masked by later impact events. The presence of such early lithologies could help elucidate the events of the early solar system.

2. What is the full extent of lithological variation within the mare basalt/anorthositic highlands and KREEP terrains; the Apollo and lunar sample collections do not appear to fully represent any of these regions (e.g., Giguere et al., 2000; Korotev, 2005).

3. What is the structure of the lunar interior – Apollo and subsequent orbital missions have told us very little about the deep interior of the Moon or the heterogeneity within the lunar crust and mantle.

4. How abundant are volatile elements on the Moon, and how are they distributed? This knowledge is important for future manned missions to the Moon (e.g., are there large enough quantities of accessible H_2O?) and also for the confirmation or rejection of the giant impact hypothesis (which requires that the Moon be depleted in volatile elements).

These questions demonstrate the limited lunar sampling and exploration that has been undertaken. This is reflected in the small number of impact craters that have been sampled (and accurately dated), leaving questions regarding the possible late-heavy-bombardment (~3.9 Ga). It is evident, therefore, that there is plenty of science which still needs to be conducted on the Moon, requiring robotic and human exploration. Robotic exploration includes both orbital and surface systems, as well as networked monitoring stations for geophysics (seismic stations, heat flow, magnetism), solar wind, and lunar exosphere studies. This research should be conducted prior to or during the next human exploration of

the Moon (so the natural lunar exosphere can be studied and seismic and radiation hazards evaluated etc (Joosten and Guerra, 1993). Once humans have returned to the lunar surface exploration could continue robotically or by human-robotic partnerships (e.g., telepresence operations – Cooper et al., 2005). Not only could future human return to the Moon enhance our understanding of the Moon itself, a lunar base would provide the perfect low gravity, uncontaminated environment for clean laboratory and high precision science. A base at the South Pole-Aitken basin would also allow for telescopic observations of deep space without atmospheric and radio wave 'noise' from the Earth. In addition, *in situ* resource utilization (ISRU) can reduce the risk and cost of maintaining a lunar outpost. Products of ISRU could be used for life support (O_2, H_2O), or as propellants (H_2, O_2), construction materials, metals and energy (ilmenite ore, Helium-3, solar power) (e.g., Cameron, 1987, 1991; Allen et al., 1992, 1994a,b, 1996; McCullogh and Hall, 2001; Schmitt, 2006).

However, at the end of January 2010 NASA's plans to build a permanent base on the Moon via the proposed Constellation missions were put on hold by the American government, who propose to significantly reduce funding for these missions. Instead they propose NASA would invest in space technology research and spend $6 billion to pay private space groups to develop and build new rockets to take astronauts into orbit (Sutter, 2010). Under the proposed plan, NASA eventually will return to the Moon but it leaves many open questions about the future of U.S. space travel, including if and when NASA will ever build rockets of its own again, when astronauts will return to the Moon and in what kind of spacecraft. Despite this set back the next two decades should see numerous spacecraft heading to the Moon in order to answer at least some of the questions the Apollo missions left unanswered. The major difference between this new age of lunar exploration and the space race of the 1960's and 70's is that it is broader in scope and is a multinational effort. It will therefore require international co-operation at a level not before seen in space exploration.

REFERENCES

Agrell S. O., Scoon J. H., Muir I. D., Long J. V. P., McConnell J. D. C. and Peckett A. (1970) Observations on the chemistry, mineralogy and petrology of some Apollo 11 lunar samples. *Proc. 1st Lunar Sci. Conf.* pp. 93-128.

Albee A. L. and Chodos A. A. (1970) Microscope investigations on Apollo 11 samples. *Proc. 1st Lunar Sci. Conf.* pp. 135-157.

Albee A. L., Chodos A. A., Gancarz A. J., Haines E. L., Papanastassiou D. A., Ray L., Tera F., Wasserburg G. J. and Wen T. (1972) Mineralogy, petrology, and chemistry of a Luna 16 basaltic fragment, sample B-1. *Earth Planet. Sci. Lett.* **13**, 353-367.

Alexander E. C. (1971) Spallogenic Ne, Kr, and Xe from a depth study of 12002. *Proc. 2nd Lunar Sci. Conf.* pp. 1643-1650.

Alexander E. C., Davis P. K. and Reynolds J. H. (1972) Rare-gas analysis on neutron irradiated Apollo 12 samples. *Proc. 3rd Lunar Sci. Conf.* pp. 1787-1795.

Allen C. C., Hines J. A., McKay D. S. and Morris R. V. (1992) Sintering of glass and basalts. In *Engineering, Construction and Operations in Space, vol. III* (eds. W. Z. Sadeh, S. Sture and R. J. Miller). Am. Soc. Civil Eng. pp. 1209-1218.

Allen C. C., Morris R. V. and McKay D. S. (1994a) experimental reduction of lunar mare soil and volcanic glass. *J. Geophys. Res.* **99**, 23173-23185.

Allen C. C., Graf J. C. and McKay D. S. (1994b) Sintering bricks on the Moon. In *Engineering, Construction and Operations in Space, vol. IV* (eds. R. G. Galloway and S. Lokaj). Am. Soc. Civil Eng. pp. 1220-1229.

Allen C. C., Morris R. V. and McKay D. S. (1996) Oxygen extraction from lunar soils and pyroclastic glass. *J. Geophys. Res.* **101**, 26085-26095.

Anand M., Taylor L. A., Misra K. C., Demidova S. I. and Nazarov M. A. (2003) KREEPy lunar meteorite Dhofar 287A: A new lunar mare basalt. *Met. Planet. Sci.* **38**, 483-664.

Anand M., James S., Johnson D., Greenwood R. C., Franchi I. A. and Grady M. M. (2008) Mineralogy and geochemistry of shergottite RBT 04262. *Lunar Planet. Sci. XXXIX.* **2173**.

Anders E. and Grevesse N. (1989) Abundances of the elements: Meteoritic and solar. *Geochem. Cosmochim. Acta* **53**, 197-214.

Anders E., Ganapathy R., Keays R. R., Laul J. C., and Morgan J. W. (1971) Volatile and siderophile elements in lunar rocks: Comparsion with terrestrial and meteoritic basalts. *Proc. 2nd Lunar Sci. Conf.* pp. 1021-1036.

Andersen C. A. and Hinthorne J. R (1973) $^{207}Pb/^{206}Pb$ ages of individual mineral phases in Luna 20 material by ion microprobe mass analysis. *Geochim. Cosmochim. Acta* **37**, 745-754.

Andre C. G. and El-Baz F. (1981) Regional chemical setting of the Apollo 16 landing site and the importance of the Kant Plateau. *Proc. 12th Lunar Planet. Conf.* pp. 767-779.

Andre C. G., Wolf R. W. and Adler I. (1979) Are early magnesium-rich basalts widespread on the Moon? *Proc. 10th Lunar Planet. Sci. Conf.* pp. 1739-1751.

Annell C. S. and Helz A. W. (1970) Emission spectrographic determination of trace elements in lunar samples from Apollo 11. *Proc. 1st Lunar Sci. Conf.* pp. 991-994.

Araki H., Tazawa S., Noda H., Ishihara Y., Goossens S., Sasaki S., Kawano N., Kamiya I., Otake H., Oberst J. and Shum C. (2009) Lunar global shape and polar topography derived from Kaguya-LALT laser altimetry. *Science* **323**, 897-900.

Arkani-Hamed J. (1974) Effect of a giant impact on the thermal evolution of the Moon. *The Moon* **9**, 183-209.

Asimow P. D. and Ghiorso M. S. (1998) Algorithmic modifications extending MELTS to calculate sub-solidus phase relations. *Am. Min.* **83**, 1127-1131.

Baldridge W. S., Beaty D. W., Hill S. M. R. and Albee A. L. (1979) The petrology of the Apollo 12 pigeonite basalt suite. *Proc. 10th Lunar Planet. Sci. Conf.* pp. 141-179.

Barsukov V. L., Tarasov L. S., Dimitriev L. V., Kolesov G. M., Shevaleevsky I. D. and Garanin A. V. (1977) The geochemical and petrochemical features of regolith and rocks from Mare Crisium (preliminary data). *Proc. 8th Lunar Sci. Conf.* pp. 3319-3332.

Basu A. and Bower J. F. (1976) Petrography of KREEP basalt fragments from Apollo 15 soils. *Proc. 7th Lunar Sci. Conf.* pp. 659-678.

Beard B. L., Taylor L. A., Scherer E. E., Johnson C. M. and Snyder G. A. (1998) The source region and melting mineralogy of high-titanium and low-titanium lunar basalts deduced from Lu-Hf isotope data. *Geochim. Cosmochim. Acta* **62**, 525-544.

Beaty D. W. and Albee A. L. (1978) Comparative petrology and possible genetic relations among the Apollo 11 basalts. *Proc. 9th Planet Sci. Conf.* pp. 359-463.

Beaty D. W. and Albee A. L. (1980) The geology and petrology of the Apollo 11 landing site. *Proc. 11th Lunar Planet. Sci. Conf.* pp. 23-35.

Beaty D. W., Hill S. M. R., Albee A. L., Ma M-S. and Schmitt R. A. (1979a) The petrology and chemistry of basaltic fragments from the Apollo 11 soil, part 1. *Proc.10th Lunar Sci Conf.* pp. 41-75.

Beaty D. W., Hill S. M. R., Albee A. L. and Baldridge W. S. (1979b) Apollo 12 feldspathic basalts 12031, 12038, and 12072: Petrology, comparison and interpretations. *Proc.10th Lunar Sci Conf.* pp. 115-139.

Belbruno E. and Gott J. R. (2005) Where did the Moon come from? *Astro. J.* **129**, 1724-1745.

Belton M. J. S., Greeley R., Greenberg R., McEwen A., Klaasen K. P., Head J. W., Pieters C., Neukum G., Chapman C. R., Geissler P., Heffernan C., Breneman H., Anger C.,

Carr M. H., Davies M. E., Fanale F. P., Gierasch P. J., Ingersoll A. P., Johnson T. V., Pilcher C. B., Thompson W. R., Veverka J. and Sagan C. (1994) Galileo multispecral imaging of the north polar and eastern limb regions of the Moon. *Science* **264**, 1112-1115.

Bence A. E. and Papike J. J. (1972) Pyroxenes as recorders of lunar basalt petrogenesis: Chemical trends due to crystal-liquid interaction. *Proc. 3rd Lunar Sci. Conf.* pp. 431-469.

Bence A. E., Papike J. J. and Prewitt C. T. (1970) Apollo 12 clinopyroxene chemical trends. *Earth Planet. Sci. Lett.* **8**, 393-399.

Biggar G. M., O'Hara M. J., Peckett A. and Humphries D. J. (1971) Lunar lavas and the achondrites: petrogenesis of proto-hypersthene basalts in the maria lava lakes. *Proc. 2nd Lunar Planet. Sci. Conf.* pp. 617-643.

Bills B. G. and Ferrari A. J. (1977) A lunar density model consistent with topographic, gravitational, librational and sesmic data. *J. Geophys. Res.* **82**, 1306-1314.

Bindeman I. N., Sigmarsson O. and Eiler J. (2006) Time constraints on the origin of large volume basalts derived from O-isotope and trace element mineral zoning and U-series disequilibria in the Laki and Grimsvötn volcanic system. *Earth Planet. Sci. Lett.* **245**, 245–259.

Binder A. B. (1998) Lunar Prospector: Overview. *Science* **281**, 1475-1476.

Birck J. L., Fourcade S. and Allegre C. J. (1975) $^{87}Rb/^{86}Sr$ age of rocks from the Apollo 15 landing site and significance of internal isochron. *Earth Planet. Sci. Lett.* **26**, 29-35.

Blewett D. T., Lucey P. G., Hawke B. R. and Jolliff B. L. (1997) Clementine images of the lunar sample-return stations: Refinement of FeO and TiO_2 mapping techniques. *J. Geophys. Res.* **102**, 16319-16325.

Bottino M. L., Fullagar P. D., Schnetzler C. C. and Phillpotts J. A. (1971) Sr isotopic measurements in Apollo 12 samples. *Proc. 2nd Lunar Sci. Conf.* pp. 1487-1491.

Boynton W. V., Baedecker P. A., Chou C-L., Robinson K. L. and Wasson J. T. (1975) Mixing and transport of lunar surface materials: Evidence obtained by the determination of lithophile, siderophile, and volatile elements. *Proc. 6th Lunar Sci. Conf.* pp. 2241-2259.

Brett R., Butler P. J., Meyer C. J., Reid A. M., Takeda H. and Williams R. (1971) Apollo 12 igneous rocks 12004, 12008, 12009 and 12022: A mineralogical and petrological study. *Proc. 2nd Lunar Sci. Conf.* pp. 301-317.

Brooks C., Hart S. R. and Wendt T. (1972) Realistic use of two error regression treatments as applied to Rb-Sr data. *Rev. Geophys. Space Phys.* **10**, 551-577.

Brown G. M., Emeleus C. H., Holland J. G., Peckett A. and Phillips R. (1971) Picrite basalts, ferrobasalts, feldspathic norites, and rhyolites in a strongly fractionated lunar crust. *Proc. 2nd Lunar Sci. Conf.* pp. 583-600.

Brown G. M., Emeleus C. H., Holland G. J., Peckett A. and Phillips R. (1972) Mineral-chemical variations in Apollo 14 and Apollo 15 basalts and granitic fractions. *Proc. 3rd Lunar Sci. Conf.* pp. 141-157.

Brown G. M., Peckett A., Emeleus C. H., Phillips R. and Pinsent R. H. (1975) Petrology and mineralogy of Apollo 17 mare basalts. *Proc 6th Lunar Sci. Conf.* pp. 1-13.

Brunfelt A. O., Heier K. S., Nilssen B., Steiennes E. and Sundvoll B. (1972) Elemental composition of Apollo 15 samples. In *The Apollo 15 Lunar Samples* (eds. J.W. Chamberlain and C. Watkins). Lunar and Planetary Institute, Houston. pp. 195-197.

Brunfelt A. O., Heier K. S., Nilssen B., Steinnes E. and Sundvoll B. (1974) Elemental composition of Apollo 17 fines and rocks. *Proc. 5th Lunar Sci. Conf.* pp. 981-990.

Bugiolacchi R. and Guest J. E. (2008) Compositional and temporal investigation of exposed lunar basalts in the Mare Imbrium region. *Icarus* **197**, 1-18.

Bugiolacchi R., Spudis P. D. and Guest J. E. (2006) Stratigraphy and composition of lava flows in mare Nubium and mare Cognitum. *Met. Planet. Sci.* **41**, 285-304.

Burgess R. and Turner G. (1998) Laser ^{40}Ar-^{39}Ar age determinations of Luna 24 mare basalts. *Meteorit. Planet. Sci.* **33**, 921-935.

Busche F. D., Conrad G. H., Keil K., Prinz M., Bunch T. E., Erlichman J. and Quaide W. L. (1971) Electron microprobe analysis of minerals from Apollo 12 lunar samples. *Special Pub. 3, UNM Institute of Meteoritics.*

Bush G. (2004) A Renewed Spirit of Discovery. The White House. URL: www.whitehouse.gov/space/renewed_spirit.html

BVSP (Basaltic Volcanism Study Project) (1981) *Basaltic Volcanism on the Terrestrial Planets.* Pergamon Press, New York. pp. 1286.

Cameron A. G. W. (2000) Higher Resolution Simulations of the Giant Impact. In *Origin of the Earth and Moon* (eds. K. Righter and R. Canup) Univ. Arizona Press, Tucson. pp. 133-144.

Cameron A. G. W. and Ward W.R. (1976) The origin of the Moon. *Lunar Science VII* pp. 120-122.

Cameron E. N. (1987) Titanium in lunar regoliths and its use in selecting He-3 mining sites. *Wisconsin Center for Space Automation and Robotics* **Report No. WCSAR-TR-AR3-9107-1** pp. 48.

Cameron E. N. (1991) A review of helium-3 resources and acquisition for use as a fusion fuel. *Wisconsin Center for Space Automation and Robotics* **Report No. WCSAR-TR-AR3-8708** pp. 68.

Canup R. M. (2004) Simulations of a late lunar forming impact. *Icarus* **168,** 433-456.

Canup R. M. and Asphaug E. (2001) Origin of the Moon in a giant impact near the end of the Earth's formation. *Nature* **412**, 708–712.

Carlson R. W. and Lugmair G. W. (1979) Sm-Nd constraints on early lunar differentiation and the evolution of KREEP. *Earth Planet. Sci. Lett.* **45**, 123-132.

Carter J. L. and MacGregor I. D. (1970) Mineralogy, petrology, and surface features of lunar samples 10062,35, 10067,9, 10069,30, and 10085,16. *Science* **167**, 661-663.

Cashore J. and Woronow A. (1985) A new Monte Carlo model of lunar megaregolith development. *J. Geophys. Res.* **90**, 811-816.

Chambers J. E. (2004) Planetary accretion in the inner Solar System. *Earth Planet. Sci. Lett.* **223**, 241–252.

Champness P. E., Dunham A. C., Gibb F. G. F., Giles H. N., MacKenzie W. S., Stumpel E. F. and Zussman J. (1971) Mineralogy and petrology of some Apollo 12 lunar samples. *Proc. 2nd Lunar Sci. Conf.* pp. 359-376.

Chao E. C. T., Minkin J. A., Frondel C., Klein C. J., Drake J. C., Fuchs L., Tani B., Smith J. V., Anderson A.T., Moore P. B., Zechman G. R., Trail R. J., Plant A. G., Douglas J. A. V. and Dence M. R. (1970a) Pyroxferroite: A new calcium-bearing iron silicate from Tranquility Base. *Proc. 1st Lunar Sci. Conf.* pp. 65-79.

Chao E. C. T., James O. B., Minkin J. A., Boreman J. A., Jackson E. D. and Raleigh C. B. (1970b) Petrology of unshocked crystalline rocks and evidence of impact metamorphism in Apollo 11 returned lunar samples. *Proc. 1st Lunar Sci. Conf.* pp. 287-314.

Chappell B. W., Compston W., Green D. H. and Ware N. G. (1972) Chemistry, geochronology and petrogenesis of lunar sample 15555. *Science* **175**, 415-416.

Chappell B. W. and Green D. H. (1973) Chemical compositions and petrogenetic relationships in Apollo 15 mare basalts. *Earth Planet. Sci. Lett.* **18**, 237-246.

Chen H-K. and Lindsley D. H. (1983) Apollo 14 very low titanium glasses: Melting experiments in iron-platinum alloy capsules. *J. Geophys. Res.* **88**, B335-342.

Chen H-K., Delano J. W. and Lindsley D. H. (1982) Chemistry and phase relations of VLT volcanic glasses from Apollo 14 and Apollo 17. *Proc. 13th Lunar Planet. Sci. Conf., J. Geophys. Res.* **87**, A171-A181.

Christian R. P., Annell C. S., Carron M. K., Cuttitta F., Dwornik E. J., Ligon D. T. and Rose H. J. (1972) Chemical composition of some Apollo 15 igneous rocks. In *The*

Apollo 15 Lunar Samples (eds. J. W. Chamberlain and C. Watkins). The Lunar Science Institute, Houston. pp. 1206-1209.

Claoué-Long J., Compston W., Roberts J. and Fanning C. M. (1995) Two carboniferous ages: A comparison of SHRIMP zircon dating with conventional zircon ages and $^{40}Ar/^{39}Ar$ analysis. In *Geochronology, Time Scales and Global Stratigraphic Correlation.* pp. 3-21.

Clayton R. N., Onuma N. and Meyeda, T.K. (1971) Oxygen isotope fractionation in Apollo 12 rocks and soils. *Lunar Sci. II.* pp. 1417-1420.

Clayton R. N., Hurd J. M. and Mayeda T. K. (1973) Oxygen isotopic compositions of Apollo 15, 16 and 17 samples, and their bearing on lunar origin and peterogenesis. *Geochim. Cosmochim. Acta* **2**, 1535-1542.

Cliff R. A., Lee-Hu C. and Wetherill G. W. (1972) K, Rb and Sr measurements in Apollo 14 and 15 material. *Lunar Sci. III* pp. 146-147.

Cohen B. A., Snyder G. A. and Taylor L. A. (2000) Argon-40-Argon-39 geochronology of basalt and highland rock fragments from Luna 16, 20, and 24 soils. *Met. Planet. Sci.* **35**, A43.

Compston W., Chappell B. W., Arriens P. A. and Vernon M. J. (1970) The chemistry and age of Apollo 11 lunar material. *Proc. 1st Lunar Sci. Conf.* pp. 1007-1027.

Compston W., Berry H. and Rudowski R. (1971) Rb-Sr chronology and chemistry of lunar material from the ocean of storms. *Proc. 2nd Lunar Sci. Conf.* pp. 1471-1485.

Compston W., Laeter J. R. and Vernon M. J. (1972) Strontium isotope geochemistry of Apollo 15 basalts. In *The Apollo 15 Lunar Samples* (eds. J. W. Chamberlain and C. Watkins). Lunar Science Institute, Houston. pp. 347-351.

Compston W., Williams I. S. and Meyer C. E. (1984) U-Pb geochronology of zircons from lunar breccia 73217 using a sensitive high mass-resolution ion microprobe. *J. Gephys. Res.* **89,** B525-B534.

Coombs, C. R. and B. R. Hawke (1992) Pyroclastic deposits on the western limb of the Moon. *Proc 22nd Lunar Planet. Sci. Conf.* pp. 303-312.

Cooper B. L., Sharpe B., Schrunk D., Thangavelu M. (2005) Telerobotic exploration and development of the Moon. *J. Earth Syst. Sci.* **114**, 815-822.

Cuttita R., Rose H. J., Annell C. S., Carron M. K., Christian R. P., Ligon D. T., Dwornik E. J., Wright T. L. and Greenland L. P. (1973) Chemistry of twenty-one igneous rocks and soils returned by the Apollo 15 mission. *Proc. 4th lunar Sci. Conf.* pp. 1081-1096.

Dalrymple G. B. and Ryder G. (1993) $^{40}Ar/^{39}Ar$ age spectra of Apollo 15 impact melt rocks by laser step-heating and their bearing on the history of lunar basin formation. *J. Geophys. Res.* **98**, 13085-13095.

Dalton J. and Hollister L. S. (1974) Spinel-silicate co-crystallization relations in sample 15555. *Proc. 5th Lunar Sci. Conf.* pp. 421-429.

Darwin G. H. (1875) History of the Earth and Moon. In *Tides (Part 50); Encyclopaedia Britannica, Ninth Edition.*

Dasch E. J., Shih C-Y., Bansal B. M.,Wiesmann H. and Nyquist L. E. (1987) Isotopic analysis of basaltic fragments from lunar breccia 14321: Chronology and petrogenesis of pre-Imbrium mare volcanism. *Geochim. Cosmochim. Acta* **51**, 3241-3254.

Day J. M. D., Taylor L. A., Floss C., Patchen A. D., Schnare D.W. and Pearson D. G. (2006) Comparative petrology, geochemistry and petrogenesis of evolved, low-Ti lunar mare basalt meteorites from the LaPaz Icefield, Antarctica. *Geochim. Cosmochim. Acta* **70**, 1581–1600.

Deer W. A., Howie R. A. and Zussman J. (1966) *An Introduction to the Rock Forming Minerals.* Longman Group Ltd, London.

De Laeter J. R., Vernon M. J. and Compston W. (1973) Revision of lunar Rb-Sr ages. *Geochem. Cosmochim. Acta* **37**, 700-702.

Delano J. W. (1979) Apollo 15 green glass: Chemistry and possible origin. *Proc. 10th Lunar Planet. Sci. Conf.* pp. 275-300.

Delano J. W. (1980) Chemistry and liquidus relations of Apollo 15 red glass: Implications for the deep lunar interior. *Proc. 11th Lunar Planet. Sci. Conf.* pp. 251-288.

Delano J. W. (1986) Pristine lunar glasses: Criteria, data and implications. *Proc. 16th Lunar Planet. Sci. Conf., J. Geophys. Res.* **91**, D201-D213.

Delano J. W. (1990) Buoyancy-driven melt segregation in the Earth's moon, I, numerical results. *Proc. 20th Lunar Sci. Conf.* pp. 3-12.

Delano J. W. and Lindsley D. H. (1982) Chromium, nickel, and titanium abundances in 74275 olivines: More evidence for a high-pressure origin of high-titanium mare basalts. *Lunar Planet. Sci. XIII* pp. 160-161.

DePaolo D. J. (1981) Neodymium isotopes in the Colorado Frant range and crust-mantle evolution in the Proterozoic. *Nature* **291**, 193-196.

Dence M. R., Douglas J. A. V., Plant A. G. and Trail R. J. (1970) Petrology, mineralogy and deformation of Apollo 11 samples. *Proc. 1st Lunar Science Conf.* **3**, 15-340.

Dickinson T., Taylor G. J., Keil K., Schmitt R. A., Hughes S. S. and Smith M. R. (1985) Apollo 14 aluminous mare basalts and their possible relationship to KREEP. *J. Geophys. Res.* **90**, C365-C374.

Dickinson T., Taylor G. J., Keil K., and Bild R. W. (1989) Germanium abundances in lunar basalts: Evidence of mantle metasmatism. *Proc. 19th Lunar Planet. Sci. Conf.* pp. 189-198.

Donaldson C. H., Usselman T. M., Williams R. J. and Lofgren G. E. (1975) Experimental modeling of the cooling history of Apollo 12 olivine basalts. *Proc. 6th Lunar Sci. Conf.* pp. 843-869.

Donohue P. and Neal C. R. (2009) Apollo 17 high-titanium basalt petrogenesis revealed by crystal size distributions and mineral geochemistry. *Lunar Planet. Sci. XL* **1805**.

Dowty E., Prinz M. and Keil K. (1973) Composition, mineralogy, and petrology of 28 mare basalts from Apollo 15 rake samples. *Proc. 4th Lunar Sci. Conf.* pp. 423-444.

Dowty E., Keil K., Prinz M., Gros J. and Takahashi H. (1976) Meteorite-free Apollo 15 crystalline KREEP. *Proc. 7th Lunar Sci. Conf.* pp. 1833-1844.

Drake M. J. (1986) Is lunar bulk material similar to Earths mantle? In *Origin of the Moon* (eds. W. K. Hartmann, R. J. Phillips, G. J. Taylor). Lunar and Planetary Institute. pp. 105-124.

Drake M. J. and Weill D. F. (1975) Partition of Sr, Ba, Ca, Y, Eu^{2+}, Eu^{3+}, and other REE between plagioclase feldspar and magmatic liquid: An experimental study. *Geochim. Cosmochim. Acta.* **89**, 689-712.

Duncan A. R., Erlank A. J., Willis J. P., Sher M. K. and Ahrens L. H. (1974) Trace element evidence for a two-stage origin of some titaniferous mare basalts. *Proc. 5th Lunar Sci. Conf.* pp. 1147-1157.

Duncan A. R., McKay S. M., Stoeser J. W., Lindstrom M. M., Lindstrom D. J., Fruchter J. S. and Goles G. C. (1975) Lunar polymict breccia 14321: A compositional study of its principal components. *Geochim. Cosmochim. Acta* **39**, 247-260.

Duncan A. R., Sher M. K., Abraham Y. C., Erlank A. J., Willis J. P. and Marens L. H. (1976) Source region constraints for lunar basalt types inferred from trace element chemistry. *Proc. 6th Lunar Sci. Conf.* pp. 218-220.

Dungan M. A. and Brown R. W. (1977) The petrology of the Apollo 12 basalt suite. *Proc. 8th Lunar Sci. Conf.* pp. 1339-1381.

Dymek R. F., Albee A. L. and Chodos A. A. (1975) Comparative mineralogy and petrology of Apollo 17 mare basalts: Samples 70215, 71055, 74255, and 75055. *Proc. 6th Lunar Sci. Conf.* pp. 49-77.

Eggins S. M., Woodhead J. D., Kinsley L. P. J., Mortimer G. E., Sylvester P., McCulloch M. T., Hergt J. M. and Handler M. R. (1997) A simple method for the precise

determination of ≥40 trace elements in geological samples by ICPMS using enriched isotope internal standardisation. *Chem. Geol.* **134**, 311-326.

Ehmann W. D., Gillum D. E. and Morgan J. W. (1972) Oxygen and bulk element composition studies of Apollo 14 and other lunar rocks and soil. *Proc. 3rd Lunar Sci. Conf.* pp. 1149-1160.

El Gorsey A., Ramdohr P. and Taylor L. A. (1971a) The geochemistry of opaque minerals in Apollo 14 crystaline rocks. *Earth Planet. Sci. Lett.* **13**, 121-129.

El Gorsey A., Ramdohr P. and Taylor L. A. (1971b) Opaque minerals in the lunar crust from Oceanus Procellarum. *Proc. 2nd Lunar Sci. Conf.* pp. 219-235.

El Gorsey A., Taylor L. A. and Ramdohr P. (1972) Fra mauro crystalline rocks: Mineralogy, geochemistry and sub-solidus reducton of opaque minerals. *Proc. 3rd Lunar Sci. Conf.* pp. 333-349.

Elkins L. T., Fernandes V. A., Delano J. W. and Grove T. L. (2000) Origin of lunar ultramafic green class: Constraints from phase equilibrium studies. *Geochim. Cosmochim. Acta* **64**, 2339-2350.

Elkins-Tanton L. T., Van Orman J. A., Bradford H. H. and Grove T. L. (2002) Re-examination of the Lunar Magma Ocean cumulate overturn hypothesis: Melting or mixing is required. *Earth Planet. Sci. Lett.* **196**, 239-249.

Elkins-Tanton L. T., Hager B. H. and Grove T. L. (2004) Magmatic effects of the lunar late heavy bombardment. *Earth Planet. Sci. Lett.* **222**, 17-27.

Elphic R.C., Lawrence D. J., Feldman W. C., Barraclough B. L., Maurice S., Binder A. B. and Lucey P. G. (1998) Lunar Fe and Ti abundacnes: Comparison of the Lunar Prospector and Clementine data. *Science* **281**, 1493-1496.

Elphic R.C., Lawrence D. J., Feldman W. C., Barraclough B. L., Maurice S., Binder A. B. and Lucey P. G. (2000) Lunar rare earth element distribution and ramifications for FeO and TiO_2: Lunar Prospector neutron spectrometer observations. *J. Geophys. Res.* **105**, 20333-20345.

Elphic R. C., Lawrence D. J., Feldman W. C., Barraclough B. L., Gasnault O. M., Maurice S., Lucey P. G., Blewett D. T. and Binder A. B. (2002) Lunar Prospector neutron spectrometer constraints on TiO_2. *J. Geophys. Res.* **107** (E4), 5024.

Engel A. E. J. and Engel C. G. (1970) Lunar rock compositions and some interpretations. *Proc. 1st Lunar Sci. Conf.* pp. 1081-1084.

Engel A. E. J., Engel C. G., Sutton A. L. and Myers A. T. (1971) Composition of five Apollo 11 and Apollo 12 rocks and one Apollo 11 soil and some petrogenetic considerations. *Proc. 2nd Lunar Sci. Conf.* pp. 439-448.

Epstein S. and Taylor H. P. (1972) O^{18}/O^{16}, Si^{30}/Si^{28}, C^{13}/C^{12}, and D/H studies of Apollo 14 and 15 samples. *Proc. 3rd Lunar Sci. Conf.* **2**, 1429-1454.

Evensen N. M., Murthy V. R., and Coscio M. R. (1973) Rb-Sr ages of some mare basalts and the isotopic and trace element systematics in lunar fines. *Proc. 4th Lunar Sci. Conf.* pp. 1707-1724.

Feldman W. C., Barraclough B. L., Maurice S., Elphic R.C., Lawrence D. J., Thomsen D. R. and Binder A. B. (1998a) Major compositional units of the Moon: Lunar Prospector thermal and fast neutrons. *Science* **281**, 1489-1493.

Feldman W. C., Maurice S., Binder A. B., Barraclough B. L., Elphic R.C. and Lawrence D. J. (1998b) Fluxes of fast and epithermal neutrons from lunar prospector: Evidence for water ice at the lunar poles. *Science* **281**, 1496-1500.

Feldman W. C., Lawrence D. J, Elphic R. C., Vaniman D. T., Thomsen D. R., Barraclough B. L. and Binder A. B. (2000) Chemical information content of lunar thermal and epithermal neutrons. *J. Geophys. Res.* **105**, 20347-20363.

Feldman W. C., Gasnault O., Maurice S., Lawrence D. J., Elphic R. C. Lucey P. G. and Binder A. B. (2002) Global distribution of lunar composition: New results from Lunar Prospector. *J. Geophys. Res.* **107**(E3), 5016.

Feldman W. C., Ahola K., Barraclough B. L., Belian R. D., Black R. K., Elphic R. C., Everett D. T., Fuller K. R., Kroesche J., Lawrence D. J., Lawson S. L., Longmire J.

L., Maurice S., Miller M. C., Prettyman T. H., Storms S. A. and Thornton G. W. (2004) Gamma-ray, neutron and alpha-particle spectrometers for the Lunar Prospector mission. *J. Geophys. Res.* **109**, E07S06. doi 10. 1029/2003JE002207.

Fernandes A. V. (2000) Petrologic and chemical studies of samples from Luna 16 and Luna 20 regolith cores. In *Proc. 4th International Conference on Exploration and Utilisation of the Moon* (eds. B. H. Foing and M. Perry). European Space Agency, Noordwijk, The Netherlands. pp. 381.

Fogel R. A. and Rutherford M. J. (1995) Magmatic volatiles in primitive lunar glasses: FTIR and EMPA analyses of Apollo 15 green and yellow glasses and revision of the volatile assisted fire-fountaining theory. *Geochim. Cosmochim. Acta* **59**, 201-215.

Freeman V. F. (1981) regolith of the Apollo 16 site. In *Geology of the Apollo 16 area, central highlands* (eds. G. E. Ulrich, C. A. Hodges and W. R. Muehlberger). USGS Prof. Paper **1048**, 147-159.

French B. M., Walter L. S. and Heinrich K. F. J. (1970) Quantitative mineralogy of an Apollo 11 lunar sample. *Proc. 1st Lunar Science Conf.* pp. 433-444.

Friel J. J. and Goldstein J. I. (1977) Metallic phases in the Luna 24 soil samples. *Geophys. Res. Lett.* **10**, 481-483.

Fruchter J. S., Stoeser J. W., Lindstrom M. M. and Goles G. G. (1973) Apollo 15 clastic materials and their relationship to local geologic features. *Proc. 4th Lunar Sci. Conf.* pp. 1227-1237.

Gaddis L. R., Pieters C. M. and Hawke B. R. (1985) Remote sensing of lunar pyroclastic mantling deposits. *Icarus* **61**, 461-489.

Gaddis L. R., Hawke B. R., Robinson M. S. and Coombs C. (1999) Compositional analyses of small lunar pyroclastic deposits using Clementine multispectral data. *J. Geophys. Res.* **105** (E2), 4245–4262.

Garcia M. O., Hulsebosch T. P. and Rhodes J. M. (1995) Olivine-rich submarine basalts from the southwest rift zone of Mauna Loa volcano: Implications for magmatic processes and geochemical evolution. *Geophysical Monograph* **92**, 219-239.

Garrick-Bethell I., Weiss B. P., Shuster D. L. and Buz J. (2009) Early Lunar Magnetism. *Science* **323**, 356-359.

Ganapathy R., Keays R. R., Laul J. C., and Anders E. (1970) Trace elements in Apollo 11 lunar rocks: Implications for meteorite influx and origin of moon. *Proc. 1st Lunar Sci. Conf.* pp. 1117-1142.

Gancarz A. J., Albee A. L. and Chodos A. A. (1971) Petrologic and mineralogic investigation of some crystalline rocks returned by Apollo 14 mission. *Earth Planet. Sci. Lett.* **12**, 1-18.

Gast P. W. and Hubbard N. J. (1970) Rare earth abundances in soil and rocks from the Ocean of Storms. *Earth Planet. Sci. Lett.* **10**, 94-101.

Gast P. W., Hubbard N. J. and Wiesmann H. (1970) Chemical composition and peterogenesis of basalts from Tranquillity Base. *Proc. 1st Lunar Sci. Conf.* pp. 1143-1163.

Geiss J., Eberhardt P., Grogler N., Guggisbert S., Maurer P. and Stettler A. (1977) Absolute time scale of lunar mare formation and filling. *Phil. Trans. Royal Soc. Lond.* **A285**, 151-158.

Gerstenkorn H. (1955) Uber Gezeitenreibung beim Zweikorper-problem. *Zeit Astrophys* **36**, 245-274.

Ghiorso M. S. and Sack R. O. (1995) Chemical mass transfer in magmatic processes. IV. A revised and internally consistant thermodynamic model for the interpolation and extrapolation of liquid-solid equillibria in magmatic systems at elevated temperatures and pressures. *Cont. Mineralog. Petrolog.* **119**, 197-212.

Giguere T. A., Taylor G. J., Hawke B. R. and Lucey P. G. (2000) The titanium contents of lunar mare basalts. *Meteor. Planet. Sci.* **35**, 193-200.

Gillis J. J., Jolliff B. L. and Elphic R. C. (2003) A revised algorithm for calculating TiO2 from Clementine UVVIS data: A synthesis of rock, soil and remotley sensed TiO_2 concentrations. *J. Geophys Res.* **108**(E2), doi: 10.1029/2001JE001515.

Goldstein J. I., Hewins R. H. and Axon H. J. (1974) Metal silicate relationships in Apollo 17 soils. *Proc. 5th Lunar Sci. Conf.* pp. 653-671.

Goldstein J. I., Newbury D. E., Echlin P., Joy D. C., Fiori C. and Lifshin E. (1981) *Scanning electron microscopy and x-ray microanalysis*. Plenum Press, New York.

Goldstein J., Newbury D. E., Joy D. C., Echlin P., Lyman C. E. and Lifshin E. (2003) *Scanning electron microscopy and x-ray microanalysis.* Springer.

Goles G., Randle K., Osawa M., Schmitt R. A., Wakita H., Ehmann W. D. and Morgan J. W. (1970a) Elemental abundances by instrumental activiation analyses in chips from 27 lunar rocks. *Proc. 1st Lunar Sci. Conf.* pp. 1165-1176.

Goles G. G., Randle K., Osawa M., Lindstrom D. J., Jerome D. Y., Steinborn T. L., Beyer R. L., Martin M. R. and McKay S. M. (1970b) Interpretations and speculations on elemental abundances in lunar samples. *Proc. 1st Lunar Sci. Conf.* pp. 1177-1194.

Goles G. G., Duncan A. R., Lindstrom D. J.,Martin M. R., Beyer R. L., Osawa M., Randle K., Meek L. T., Steinborn T. L. and McKay S. M. (1971) Analyses of Apollo 12 specimens: Compositional variations, differentiation processes, and lunar soil mixing models. *Proc. 2nd Lunar Sci. Conf.* pp. 1063-1081.

Goodrich C. A., Taylor L. A., Keil K., Kallemeyn G. W. and Warren P. H. (1986) Alkali norite, troctolites and VHK mare baslats from breccia 14304. *Proc. 16th Lunar Sci. Conf., J. Geophys. Res.* **91**, D305-D318.

Gopalan K., Kaushal S., Lee-Hu C. and Wetherill G. W. (1970) Rb-Sr and U, Th-Pb ages of lunar materials. *Proc. 1st Lunar Sci. Conf.* pp. 1195-1206.

Greeley R., Kadel S. D., Williams D. A., Gaddis L. R., Head J. W., McEwen A. S., Murchie S. L., Nagel E., Neukum G., Pieters C. M., Sunshine J. M., Wagner R. and

Belton M. J. S. (1993) Galileo imaging observations of lunar maria and related deposits. *J. Geophys. Res.* **98**, 17183-17206.

Green D. H., Ringwood A. E., Ware N. G., Hibberson W. O., Major A. and Kiss E. (1971) Experimental petrology and petrogenesis of Apollo 12 basalts. *Proc. 2nd Lunar Sci. Conf.* pp. 601-615.

Green D. H., Ringwood A. E., Ware N.G. and Hibberson W. O. (1975) Experimantal petrology and petrogenesis of Apollo 17 mare basalts. *Proc. 6th Lunar Sci. Conf.* pp. 871-893.

Greenwood J. P., Itoh S., Sakamoto N., Taylor L.A., Warren P.H. and Yurimoto H. (2010) Water in Apollo rock samples and the D/H of lunar apatite. *41st Lunar Planet. Sci. Conf.* **2439**.

Greenwood R. C., Franchi I. A., Jambon A. and Buchanan P. C. (2005) Widespread magma oceans on asteroidal bodies in the early Solar System. *Nature* **435**, 916-918.

Grove T. L, and Beaty D. W. (1980) Classifcation, experimental petrology and possible volcanic histories of the Apollo 11 high-K basalts. *Proc. 11th Lunar Sci. Conf.* pp. 149-177.

Grove T. L, Walker D., Longhi J., Stolper E. and Hays J. F. (1973) Petrology of 12002 and the origin of picritic basalts. *Proc. 4th Lunar Sci. Conf.* pp. 995-1011.

Guggisberg S., Eberhardt P., Geiss J., Grogler N., Stettler A., Brown G. M. and Pecket A. (1979) Classification of the Apollo 11 basalts according to Ar^{39}/Ar^{40} ages and petrological properties. *Proc. 10th Lunar Planet. Sci. Conf.* pp. 1-39.

Günther D. and Heinrich C. A. (1999) Enhanced sensitivity in laser-abaltion ICP mass spectrometry using helium-argon mixtures as aerosol carriers. *J. Analytic. Atom. Spectrom.* **14**, 1363-1368.

Hafner S. S. and Virgo D. (1970) Temperature dependent cation distributions in lunar and terrestrial distribution. *Geochim. Cosmochim. Acta.* **Supplement I**.

Hagerty J. J., Shearer C. K. and Papike J. J. (2003) Trace element characterisitics of minerals in the Apollo 14 high-Al basalts: Implications for an igneous versus an impact origin. *Lunar Planet. Sci. Conf. XXXIV* **1773.**

Hagerty J. J., Shearer C. K., Papike J. J. (2005) Petrogenesis of the Apollo 14 high-alumina basalts: Implications from ion microprobe analyses. *Geochim. Cosmochim. Acta* **69**, 5831-5845.

Haggerty S. E., Boyd F. R., Bell P. M. Finger L. W. and Bryan W. B. (1970) Opaque minerals and olivine in lavas and breccias from mare tranquillitatis. *Proc. 1st Lunar Sci. Conf.* **3**, 513-538.

Haggerty S. E. (1972) Apollo 14 subsolidus reduction and compositional variations of spinels. *Proc. 3rd Lunar Sci. Conf.* pp. 305-333.

Haggerty S. E. (1973) Armacolite and genetically associated opaque minerals in the lunar samples. *Proc. 4th Lunar Sci. Conf. 4th.* pp. 777-797.

Haggerty S. E. (1978) Luna 24: Systematics in spinel mineral chemistry in the context of an intrusive petrogenetic grid. In *Mare Crisium: The Veiw from Luna 24.* (eds. R. B. Merrill and J. J. Papike). Pergamon, New York. pp. 523-536.

Haines E. L. and Metzger A. E. (1980) Lunar highland crustal models based on iron concentrations: Isostasy and center-of-mass displacement. *Proc. 11th Lunar Planet. Sci. Conf.* 689-718.

Haines E. L., Etchegaray-Ramirez M. I. and Metzger A. E. (1978) Thorium concentrations in the lunar surface II. Deconvolution, modelling and its application to the regions of Aristarchus and Mare Smythii. *Proc. 9th Lunar Planet. Sci. Conf.* pp. 2985-3013.

Halliday A. N. (1995) Processes involved in the formation of the magnisian-suite plutonic rocks from the highlands of the Earth's moon. *J. Geophys. Res.* **100**, 9365-9388.

Halliday A. N. (2003) The origin and earliest history of the Earth. In *Treatise on Geochemistry vol. 1 Meteoritics, Comets and Planets* (eds. A. M. Davis, H. D. Holland, K. K. Turekian). Elsevier-Pergamon. pp. 509-557.

Halliday A. N. (2004) Mixing, volatile loss and compositional change during impact driven accretion of the Earth. *Nature* **427**, 505-509.

Hallis L. J., Anand M., Greenwood R. C., Miller M. F., Franchi I. A. and Russell S. S. (2010) Oxygen isotope evidence for large-scale compositional variation within the lunar magma ocean. *Geochim. Cosmochim. Acta.* (submitted).

Hammond S. (2006) Lithium and Li isotopes as tracers of subduction zone processes. PhD thesis, The Open University.

Hanan B. B. and Tilton G. R. (1987) 60025: relict of primitive lunar crust? *Earth Planet. Sci. Lett.* **84**, 15-21.

Hartmann W. K. and Davis D.R. (1975) Satalite sized planetesimals and lunar origin. *Icarus* **24**, 504-515.

Haruyama J., Ohtake M., Matsunaga T., Morota T., Honda C., Yokota Y., Abe M., Ogawa Y., Miyamoto H., Iwasaki A., Pieters C. M., Asada N., Demura H., Hirata N., Terazono J., Sasaki S., Saiki K., Yamaji A., Torii M. and Josset J. L. (2009) Long-lived volcanism on the lunar farside revealed by SELENE terrain camera. *Science* **323**, 905-908.

Haskin L. A., Allen R. O., Helmke P. A., Paster T. P., Anderson M. R., Korotev R. L. and Zweifel K. A. (1970) Rare earths and other trace elements in Apollo 11 lunar samples. *Proc. 1st Lunar Sci. Conf.* pp. 1213-1231.

Haskin L. A., Gillis J. J., Korotev R. L. and Jolliff B. L. (2000) The materials of the lunar Procellarum KREEP terrain: A synthesis of data from geomorphological mapping, remote sensing and sample analysis. *J. Geophys. Res.* **105**, 20403-20415.

Haskin L. A., Korotev R. L., Gillis J. J. and Jolliff B. L. (2002) Stratigraphies of Apollo and Luna landing sites and provenances of materials from the prespective of basin impact ejecta modelling. *Lunar Planet. Sci. Conf. XXXIII* **1364**.

Hathorne E. C., Alard O., James R. H. and Rogers N. W. (2003) Determination of intratest variability of trace elements in foraminifera by laser ablation inductively coupled plasma-mass spectrometry. *Geochem. Geophys. Geosyst.* **4**, 1-14.

Hawke B. R. and Bell J. F. (1981) Remote sensing studies of luanr dark-halo craters: Preliminary results and implications for early volcanism. *Proc. 12th Lunar Planet Sci. Conf.* pp. 665-678.

Head J. W. (1975) Some geologic observations concerning lunar geophysical models. *Proc. Soviet-American Conf. on the Cosmochem. of the Moon and Planets, Moscow.* pp. 407-416.

Head J. W. and Wilson L. (1992) Lunar mare volcanism: Stratigraphy, eruption conditions, and the evolution of secondary crusts. *Geochim. Cosmochim. Acta* **55**, 2155-2175.

Head J. W., Adams J. B., McCord T. B., Pieters C. and Zisk S. (1978) Regional stratigraphy and geologic history of Mare Crisium. In *Mare Crisium: The View from Luna 24* (eds. R. B. Merrill and J. J. Papike). Pergamon, New York. pp. 43-74.

Head J. W., Murchie S., Mustard J. F., Pieters C. M., Neukum G., McEwen A., Greeley R., Nagel E. and Belton M. J. S. (1993) Lunar impact basins: New data for the western limb and far side (Orientale and South Pole-Aitken basins) from the first Galileo flyby. *J. Geophys. Res.* **98**, 17149-17182.

Head J. W., Wilson L. and Wilhelms D. (1997) Lunar mare basalt volcanism: Early stages of secondary crustal formation and implications for petrogenetic evolution and magma emplacement processes. *Lunar Planet. Sci. XXVIII* pp. 545-546.

Heiken G. and McEwen M. C. (1972) The geologic setting of the Luna 20 site. *Earth Planet. Sci. Lett.* **17**, 3-6.

Heiken G. and McKay D. S. (1977) A model for eruption behaviour of a volcanic vent in eastern Mare Serenitatis. *Proc. 8th Lunar Sci. Conf.* pp. 3243-3255.

Heiken G. and McKay D. S. (1978) Petrology of a sequence of pyroclastic rocks from the valley of Taurus-Littrow (Apollo 17 landing site). *Proc. 9th Lunar Planet. Sci. Conf.* pp. 1933-1943.

Heiken G. H., Vaniman D. T. and French B. M. (1991) *The Lunar Sourcebook.* Cambridge Univeristy Press, Cambridge.

Helmke P. A., Blanchard D. P., Haskin L. A., Telander K., Weiss C. and Jacobs J. W. (1973) Major and trace elements in igneous rocks from Apollo 15. *The Moon* **8**, 129-148.

Hess P.C. and Finnila A. (1997) Depths of segregation of Hi-TiO_2 picritic mare glasses. *Lunar Planet. Sci. 28.* abstract#**1665**.

Hess P. C. and Parmentier E. M. (1995) A model for the thermal and chemical evolution of the Moon's interior: Implications for the onset of mare magmatism. *Earth Planet. Sci. Lett.* **134**, 501-514.

Hess P.C., Rutherford M.J. and Campbell H.W. (1978) Ilmenite crystallization in non-mare basalt: Genesis of KREEP and high-Ti mare basalt. *Proc. 9th Lunar Planet. Sci. Conf.* pp. 705-724.

Hiesinger H. and Head J. W. (2006) New views of lunar geoscience; An introduction and overview. *Reviews in Minerology and Geochemistry* **60**, 1-81.

Hiesinger H., Jaumann R., Neukum G. and Head J. W. (2000) Ages of mare basalts on the lunar nearside. *J. Geophys. Rev.* **105**, 29239-29275.

Hiesinger H., Head J. W., Wolf U., Jaumann R. and Neukum G. (2002) Lunar mare basalt flow units: Thicknesses determined from crater size frequency distributions. *Geophys. Res. Lett.* **29**(8), 1248.

Hiesinger H., Head J. W., Wolf U., Jaumann R. and Neukum G. (2003) Ages and stratigraphy of mare basalts in Oceanus Procellarum, Mare Nubium, Mare Cognitum, and Mare Insularum. *J. Geophys. Res.* **108** (E7), 5065.

Hiesinger H., Head J. W., Wolf U., Jaumann R. and Neukum G. (2010): Ages and stratigraphy of lunar mare basalts in Mare Frigoris and other nearside maria based on crater size-frequency distribution measurements. *J. Geophys. Res.* **115** E03003 (doi:10.1029/2009JE003380).

Hinthorne J. R., Andersen C. A., Conrad R. L and Lovering J. F. (1979) Single-grain $^{207}Pb/^{206}Pb$ and U/Th age determinations with a 10-micron spatial resolution using the ion microporbe mass analyzer (IMMA). *Chem. Geology* **25**, 271-303.

Hodges F. N. and Kushiro I. (1974) Apollo 17 petrology and experimental determination of differentiation sequences in model Moon compositions. *Proc. 5th Lunar Sci. Conf.* pp. 505-520.

Hollister L. S. and Hargraves R. B. (1970) Compositional zoning and its significance in pyroxenes from two coarse grained Apollo 11 samples. *Proc. 1st Lunar Sci. Conf., Geochim. Cosmochim. Acta.* **1**, 541-550.

Hood L. L. and Zuber M. T. (2000) Recent refinments on geophysical constraints on lunar origin and evolution. In *Origin of the Earth and Moon.* (eds. R. M. Canup and K. Righter). Univ. Arizona Press, Tucson. pp. 397-412.

Hood L. L., Coleman P. J. and Wilhelms D. E. (1979) Lunar nearside magnetic anomalies. *Proc 10th Lunar Planet. Sci. Conf.* pp. 99-113.

Hood L. L., Zakharian A., Halekas J., Mitchell D. L., Lin R. P., Acuna M. H. and Binder A. B. (2001) Initial mapping and interpretation of lunar crustal magnetic anomalies using Lunar Prospector magnetometer data. *J. Geophys. Res.* **106**, 27825-27840.

Horn P., Kirsten T. and Jessberger E. K. (1975) Are there Apollo 12 basalts younger than 3.1 b.y.? Unsuccessful search for A12 mare basalts with crystallization ages below 3.1 b.y. *Meteoritics* **10**, 417-418.

Hörz F. (1978) How thick are lunar mare basalts? *Proc. 9th Lunar Planet. Sci. Conf.* pp. 3311-3331.

Hörz F., Morrison D. A., Gault D. E., Oberbeck V. R., Quaide W. L., Vedder J. F., Brownlee D. E. and Hartung J. B. (1977) The micrometeoroid complex and evolution of the lunar regolith. In *The Soviet-American Conference on Cosmochemistry of the Moon and Planets*. pp. 605-635.

Hörz F., Grieve R., Heiken G., Spudis P. and Binder A. (1991) Lunar surface processes. In *Lunar Sourcebook* (eds. G. H. Heiken, D. T. Vaniman and B. M. French). Cambridge Univeristy Press, Cambridge. pp. 61-120.

Howard K. A. and Head J. W. (1972) Regional geology of the Hadley Rille. *Preliminary Science Report, Apollo 15*. pp 25-53.

Hubbard N. J. and Gast P. W. (1971) Chemical composition and origin of non-mare lunar basalts. *Proc. 2nd Lunar Sci. Conf.* 999-1020.

Hubbard N. J., Gast P. W., Meyer C., Nyquist L. E. and Shih C.-Y. (1971) Chemical composition of lunar anorthosites and their parent liquids. *Earth Planet. Sci. Lett.* **13**, 71-75.

Hubbard N. J., Gast P. W., Rhodes J. M., Bansal B. M., Wiesmann H. and Church S. E. (1972) Non-mare basalts: Part II. *Proc. 3rd Lunar Sci. Conf.* 1161-1179.

Hubbard N. J., Rhodes J. M., Wiesmann H., Shih C-Y. and Bansal B. M. (1974) The chemical definition and interpretation of rock types returned from the non-mare regions of the Moon. *Proc. 5th Lunar Sci. Conf.* pp. 1227-1246.

Hubbard N. J. and Minear J. W. (1975) A chemical and physical model for the genesis of lunar rocks: Part II. Mare basalts. *Lunar Sci. IV* pp. 405-407.

Hughes S. S., Delano J. W. and Schmitt R. A. (1988) Apollo 15 yellow-brown volcanic glass: Chemistry and petrogenetic relations to green volcanic glass and olivine-normative basalts. *Geochim. Cosmochim. Acta* **52**, 2379-2391.

Hughes S. S., Delano J. W. and Schmitt R. A. (1989) Petrogenetic modelling of 74220 high-Ti orange volcanic glasses and the Apollo 11 and 17 high-Ti mare basalts. *Proc. 19th Lunar Planet. Sci. Conf.* pp. 175-188.

Hughes S. S., Neal C. R. and Taylor L. A. (1990) Petrogenesis of Apollo 14 high-alumina (HA) parental basaltic magma. *Lunar Planet. Sci. Conf. XXI* pp. 540-541.

Huneke J. C., Jessberger E. K., Podosek F. A. and Wasserburg G. J. (1973) Ar^{40}/Ar^{39} measurements in Apollo 16 and 17 samples and the chronology of metamorphic and volcanic activity in the Taurus-Littrow region. *Proc. 4th Lunar Sci. Conf.* pp. 1725-1756.

Husain L., Sutter J. F. and Schaeffer O. A. (1971) Ages of crystalline rocks from Fra Mauro. *Science* **173**, 1235-1236.

Husain L., Schaeffer O. A., Funkhouser J. and Sutter J. (1972) The ages of lunar material from Fra Mauro, Hadley Rille and Spur Crater. *Proc. 3rd Lunar Sci. Conf.* pp. 1557-1567.

Irving A. J. (1977) Chemical variation and fractionation of KREEP basalt magmas. *Proc. 8th Lunar Sci. Conf.* pp. 2433-2448.

James O. B. and Jackson E. D. (1970) Petrology of the Apollo 11 ilmenite basalts. *J. Geophys. Res.* **75**, 5793-5824.

James O. B. and McGee J. J. (1980) Petrology of mare-type basalt clasts from consortium breccia 73255. *Proc. 11th Lunar Planet. Sci. Conf.* pp. 67-86.

James O. B. and Wright T. L. (1972) Apollo 11 and 12 mare basalts and gabbros: Classification, compositional variations and possible petrogenetic relations. *Geologic. Soc. Am. Bull.* **83**, 2357-2382.

James O. B., Floss C. and McGee J. J. (1998) Rare earth distributions in pyroxenes from a lunar mafic-magnesian ferroan anorthosite. *29th Lunar Planet. Sci. Conf.* **1292**.

Jerde E. A., Snyder G. A., Taylor L. A., Liu Y-G. and Schmitt R. A. (1994) The origin and evolution of lunar high-Ti basalts: Periodic melting of a single source at Mare Tranquillitatis. *Geochim. Cosmochim. Acta* **58**, 515-527.

Jolliff B. L. (1999) Clementine UVVIS multispectral data and the Apollo 17 landing site: What can we tell and how well? *J. Geophys. Res.* **104**, 14123-14148.

Jolliff B. L., Haskin L. A., Colson R. O. and Wadhwa M. (1993) Partioning in REE-saturating minerals: Theory, experiment, and modelling of whitlockite, apatite, and evolution of lunar residual magmas. *Geochim. Cosmochim. Acta* **57**, 4069-4094.

Jolliff B. L., Gillis J. J., Haskin L. A., Korotev R. L. and Wieczorek M. A. (2000) Major lunar crustal terrances: Surface expressions and crust-mantle origins. *J. Geophys. Res.* **105**, 4197-4216.

Jolliff B. L., Hughes J. M., Freeman J. J. and Zeigler R. A. (2006) Crystal chemistry of lunar merrillite and comparison to other meteoritic and planetary suites of whitlockite and merrilite. *Am. Min.* **91**, 1583-1595.

Joosten B. K. and Guerra L. A. (1993) Early lunar resource utilization: A key to human exploration. *AIAA Space Programs and Technologies Conf., Huntsville.* **AIAA 93-4784.**

Kaula W. M., Schubert G., Lingenfelter R.E., Sjogren W. L., Wollenhaupt W. R. (1972) Analysis and interpretation of lunar laser altimetry. *Proc. 2nd Lunar Sci Conf.* pp. 3049-3058.

Keil K., Bunch T. E. and Prinz M. (1970) Mineralogy and composition of Apollo 11 lunar samples. *Proc. 1st Lunar Sci. Conf.* pp. 561-598.

Keil K., Prinz M. and Bunch T. E. (1971) Mineralogy, petrology and chemistry of some Apollo 12 samples. *Proc. 2nd Lunar Sci. Conf.* pp. 319-341.

Kenyon S. J. and Bromley B. C. (2006) Terrestrial planet formation I. The transition from oligarchic to chaotic growth. *Astro. J.* **131**, 1837–1850.

Kesson S. E. (1975) Mare basalts: Melting experiemnts and petrogenetic interpretations. *Proc. 6th Lunar Sci. Conf.* pp. 921-944.

Kesson E. and Lindsley H. (1975) The effects of Al^{3+}, Cr^{3+}, and Ti^{3+} on the stability of armalcolite. *Proc. 6th Lunar Sci. Conf.* pp. 911-920.

Kharkar D. P. and Turekian K. K. (1971) Analyses of Apollo 11 and Apollo 12 rocks and soils by neutron activation. *Proc. 2nd Lunar Sci. Conf.* pp. 1301-1305.

Kirsten T. and Horn P. (1974) Chronology of the Taurus-Littrow region III: Ages of mare basalts and highland breccias and some remarks about the interpretation of lunar highland rock ages. *Proc. 5th Lunar Sci. Conf.* pp. 1451-1475.

Kirsten T., Horn P. and Heymann D. (1973) Chronology of the Taurus-Littrow region. Ages of two major rock types from the Apollo 17 site. *Earth Planet. Sci. Lett.* **20**, 125-130.

Klein C., Drake J. C. and Frondel C. (1971) Mineralogical, petrological, and chemical features of four Apollo 12 lunar microgabbros. *Proc. 2nd Lunar Sci. Conf.* 265-284.

Kliene T., Münker C., Mezger K., Palme H. (2002) Rapid accretion and early core formation on asteroids and the terrestrial planets from Hf-W chronometry. *Nature* **418**, 952-955.

Konopliv A. S., Binder A. B., Hood L. L., Kucinskas A. B., Sjogren W. L. and Williams J. G. (1998) Improved gravity field of the Moon from lunar prospector. *Science* **281**, 1476-1480.

Konopliv A. S., Asmar S. W. and Yuan D. N. (2001) Recent gravity models as a result of the Lunar Prospector mission. *Icarus* **150**, 1-18.

Korotev R. L. 2005. Invited review: Lunar geochemistry as told by lunar meteorites. *Chem. Der Erde Geochem.* **65**, 297-346.

Korotev R. L. and Gillis J. J. (2001) A new look at the Apollo 11 regolith and KREEP. *J. Geophys. Res.* **106**, 12339-123353.

Kramer G. Y. and Neal C. R. (2003) Petrogenesis of the Apollo 14 high-al basalts revisited: Distinct magmatic events, source metasomatism, and AFC. *Lunar Planet. Sci. XXXIV* **2035**.

Kramer G. Y., Jolliff B. L. and Neal C. R. (2008) Distinguishing high-alumina mare basalts using Clementine UVVIS and Lunar Prospector GRS data: Mare Moscoviense and Mare Nectaris. *J. Geophys. Res.* **113**, E01002, doi:10.1029/2006JE002860.

Kridelbaugh S. J. and Weill D. F. (1973) The mineralogy and petrology of ilmenite basalt 75055. *EOS Trans. AGU* **54**, 597-598.

Kusakabe M. and Matsuhisa Y. (2008) Oxygen three-isotope ratios of silicate reference materials determined by direct comparison with VSMOW-oxygen. *Geochemical Journal* **42**, 309-317.

Kushiro I. (1972) Petrology of some Apollo 15 basalts. In *The Apollo 15 Lunar Samples* (eds. Chamberlain and Watkins). Lunar Science Institute, Houston. pp. 128-130.

Kushiro I. and Haramura H. (1971) Major element variation and possible source materials of Apollo 12 crystalline rocks. *Science* **171**, 1235-1237.

Kushiro I., Nakamura Y., Kitayama K. and Akimoto S-I. (1971) Petrology of some Apollo 12 crystalline rocks. *Proc. 2nd Lunar Sci. Conf.* pp. 481-495.

Kushiro I., Ikeda Y. and Nakamura Y. (1972) Petrology of Apollo 14 high-alumina basalt. *Proc. 3rd Lunar Sci. Conf.* pp. 115-129.

Laul J. C., Wakita H., Showalter D. L., Boynton W. V. and Schmitt R. A. (1972) Bulk, rare earth, and other trace elements in Apollo 14 and 15 and Luna 16 samples. *Proc. 3rd Lunar Sci. Conf.* pp. 1181-1200.

Laul J. C., Schmitt R. A., Robyn M. and Goles G. G. (1975) Chemical composition of 18 Apollo 17 rake basalts and one basalt-breccia. *Proc. 6th Lunar Sci. Conf.* pp. 492-494.

Laul J. C., Vaniman D. T. and Papike J. J. (1978) Chemistry, mineralogy and petrology of seven > 1 mm fragments from Mare Crisium. In *Mare Crisium: The View from Luna 24* (eds. R. B. Merrill and J. J. Papike). Pergamon, New York. pp. 537-568.

Lawrence D. J., Feldman W. C., Barraclough B. L., Binder A. B., Elphic R. C., Maurice S. and Thomsen D. R. (1998) Global elemental maps of the Moon: The lunar prospector gamma ray spectrometer. *Science* **281**, 1484-1489.

Lawrence D. J., Feldman W. C., Barraclough B. L., Binder A. B., Elphic R. C., Maurice S., Miller M. C. and Prettyman T. H. (2000) Thorium abundances on the lunar surface. *J. Geophys. Res.* **105**, 20307-20331.

Lawrence D. J., Elphic R. C., Feldman W. C., Prettyman T., Gasnault O. and Maurice S. (2003) Small area thorium features on the lunar surface. *J. geophys. Res.* **108**, doi:10.1029/2003/JE002050.

Lawrence D. J., Hawke B. R., Hagerty J. J., Elphic R. C., Feldman W. C., Prettyman T. H. and Vaniman D. T. (2005) Evidence for a high-Th, evolved lithology on the Moon at Hanstenn Alpha. *Geophys. Res. Lett.* **32**, L07201.

Lawrence D. J., Puetter R. C., Elphic R. C., Feldman W. C., Hagerty J. J., Prettyman T. H. and Spudis P.D. (2007) Global spatial deconvolution of Lunar Prospector Th abundances. *Geophys. Res. Lett.* **34**, L03201.

Lawson S. L., Jakosky B. M., Park H-S. and Mellon M. T. (2000) Brightness temperature of the lunar surface: Calibration and global analysis of the Clementine long-wave infared camera data. *J. Geophys. Res.* **105**, 4273-4290.

Lindsley D. H. Papike J. J. Bence A. E. (1972) Pyroxferroite: Breakdown at low pressure and high temperature. In *Lunar Sci. III.* Lunar Science institute, Houston. pp. 483-485.

Lindstrom M. M., Nielsen R. L. and Drake M. J. (1977) Petrology and geochemistry of lithic fragments separated from the Apollo 15 deep-drill core. *Proc. 8th Lunar Sci. Conf.* pp. 2869-2888.

Liu Y., Spicuzza M. J. and Valley J. W. (2009) Oxygen isotopes of lunar rocks: Different sources for different high-Ti basalts? *Lunar Planet. Sci. XXXX.* **2291**.

Liu Y., Boyce J. W., Rossman J. R., Guan Y., Eiler J. and Taylor L. A. (2010) Water in lunar mare basalt: Confirmation from apatite in lunar basalt 14053. *41st Lunar Planet. Sci. Conf.* **2647**.

Long J. V. P. (1967) Electron microprobe analysis. In: *Physical methods in determinative mineralogy* (ed. J. Zussman). Academic Press, New York. pp. 215-260.

Longhi J. (1987) On the conection between mare basalts and picritic volcanic glasses. *Proc. 17th Lunar Planet. Sci. Conf., J. Geophys. Res.* **92**, E349-E360.

Longhi J. (1992a) Origin of Picritic Green Glass Magmas by Polybaric Fractional Fusion. *Proc. Lunar Planet. Sci.* **22**, 343-353.

Longhi J. (1992b) Experimental petrology and petrogenesis of mare volcanics. *Geochim. Cosmochim. Acta* **56**, 2235-2251.

Longhi J. (1995) Liquidus equilibria of some primary lunar and terrestrial melts in the garnet stability field. *Geochim. Cosmochim. Acta* **56**, 2375-2386.

Longhi J. (1996) Investigation of the origin of Hi-Ti basalts by polybaric fractional fusion. *Lunar Planet. Sci.* **27**, 767-768.

Longhi J. (2006) Petrogenesis of picritic mare magmas: Constraints on the extent of early lunar differentiation. *Geochim. Cosmochim. Acta.* **70**, 5919-5934.

Longhi J., Walker D. and Hays J. F. (1972) Petrology and crystallization history of basalts 14310 and 14072. *Proc. 3rd Lunar Sci. Conf.* pp. 131-139.

Longhi J., Walker D., Grove T. L., Stopler E. M. and Hays J. F. (1974) The petrology of the Apollo 17 mare basalts. *Proc. 5th Lunar Sci. Conf., Geochim. Cosmochim. Acta.* **1**, Supplement 5, pp. 447-469.

Longhi J., Walker D. and Hays J. F. (1976) Fe and Mg in plagioclase. *Proc. 7th Lunar Sci. Conf.* pp. 1281-1300.

Lovering J. F. and Ware N. G. (1970) Electron probe microanalyses of minerals and glasses in Apollo 11 lunar samples. *Proc. 1st Lunar Sci. Conf.* pp. 633-654.

The Lunar Sample Preliminary Examination Team (LSPET) (1969) Preliminary examination of lunar samples from Apollo 11. *Science* **165**, 1211-1227.

The Lunar Sample Preliminary Examination Team (LSPET) (1970) Preliminary examination of lunar samples from Apollo 12. *Science* **167**, 1325-1339.

The Lunar Sample Preliminary Examination Team (LSPET) (1971) Preliminary examination of lunar samples from Apollo 14. *Science* **173**, 681-693.

The Lunar Sample Preliminary Examination Team (LSPET) (1973) Preliminary examination of Lunar samples from Apollo 17. *Science* **182**, 659-672.

Lucchitta B.K. (1977) Crater clusters and light mantle at the Apollo 17 site: A result of secondary impact from Tycho. *Icarus* **30**, 80-96.

Lucey P. G., Spudis P. D., Zuber M., Smith D. and Malaret E. (1994) Topographic-compositional units on the Moon and the early evolution of the lunar crust. *Science* **266**, 1855-1858.

Lucey P. G, Taylor G. J. and Malaret E. (1995) Abundance and distribution of iron on the Moon. *Science* **268**, 1150-1153.

Lucey P. G., Blewett D. T. and Hawke B. R. (1998) Mapping the FeO and TiO2 content of he lunar surface multispectral imagery. *J. Geophys. Res.* **103**, 3679-3699.

Lucey P. G., Blewett D. T. and Jolliff B. L. (2000) Lunar iron and titanium abundance algorithms based on initial processing of Clementine ultraviolet-visible images. *J. Geophys. Res.* **105**, 20,297-20,305.

Lucey P. G., Korotev R. L., Gillis J. J., Taylor L. A., Lawrence D., Campbell B. A., Elphic R., Feldman B., Hood L. L., Hunten D. (2006) Understanding the Lunar Surface and Space-Moon Interactions. *Reviews in Mineralogy and Geochemistry* **60**, 83-219.

Ludwig K. R. (2000) Users manual for isoplot/ex, version 2.2. *Berkeley Geochronology Center Special Publication* **No. 1a**.

Ma M-S., Schmitt R. A., Nielson R. L., Taylor G. J., Warner R. D. and Keil K. (1979) Petrogenesis of Luna 16 aluminous mare basalt. *Geophys. Res. Lett.* **6**, 909-912.

Ma M-S., Schmitt R. A., Taylor G. J., Warner R. D., Lange D. E. and Keil K. (1977) Luna 24 soils: A chemical study. In *Papers Presented to the Conference on Luna 24.* Lunar Science Institute, Houston. pp. 102-105.

Ma M-S., Schmitt R. A., Taylor G. J., Warner R. D., Lange D. E. and Keil K. (1978a) Chemistry and petrology of Luna 24 lithic fragments and < 250 μm soils: Constraints on the origin of VLT basalts. In *Mare Crisium: The View from Luna 24* (eds. R. B. Merrill and J. J. Papike). Pergamon, New York. pp. 569-592.

Ma M-S., Schmitt R. A., Warner R. D., Taylor G. J. and Keil K. (1978b) Genesis of Apollo 15 olivine normative mare basalts: Trace element correlations. *Proc. 9th Lunar Sci. Conf.* pp. 523-533.

Ma M-S., Schmitt R. A., Beaty D. W. and Albee A. L. (1980) The petrology and chemistry of basaltic fragments from the Apollo 11 soil: Drive tubes 10004 and 10005. *Proc. 11th Lunar Planet. Sci. Conf.* pp. 37-47.

McCallum I. S. and Charette M. P. (1978) Zr and Nb partition coefficients: Implications for the genesis of mare basalts, KREEP, and sea floor basalts. *Geochim. Cosmochim. Acta* **42**, 859-869.

Magna T., Wiechert U. and Halliday A. N. (2006) New constraints on the lithium isotope compositions of the Moon and terrestrial planets. *Earth Planet. Sci. Lett.* **243**, 336-353.

Mark R. K., Cliff R. A., Lee-Hu C. and Wetherill G.W. (1973) Rb-Sr studies of lunar breccias and soils. *Proc. 4th Lunar Sci. Conf.* pp. 1785-1795.

Marvin U. B. (1971) Lunar niobian rutile. *Earth Planet. Sci. Lett.* **11**, 7-9.

Maxwell J. A., Peck L. C., and Wiik H. B. (1970) Chemical composition of Apollo 11 lunar samples 10017, 10020, 10072, and 10084. *Proc. 1st Lunar Sci. Conf.* pp. 1369-1374.

Maxwell J. A., Bouvier J.-L. and Wiik H. B. (1972) Chemical composition of some Apollo 15 lunar samples. In *The Apollo 15 Lunar Samples* (eds. J. W. Chamberlain and C. Watkins). The Lunar Science Institute, Houston. pp. 233-238.

Mayeda T. K., Shearer J. and Clayton R. N. (1975) Oxygen isotope fractionation in Apollo 17 rocks. *Proc. 6th Lunar Sci. Conf.* pp. 1799-1802.

McCauley J. F. and Scott D. H. (1972) Geologic setting of the Luna 16 landing site. *Earth Planet. Sci. Lett.* **13**, 225-232.

McCubbin F. M., Steele A., Nekvasil H., Schnieders A., Rose T., Fries M., Carpenter P. K. and Jolliff B. L. (2010) Detection of structurally bound hydroxyl in apatite from Apollo mare basalt 15058,128 using TOF-SIMS. *41st Lunar Planet. Sci. Conf.* **2468**.

McCullogh E. D. and Hall A. (2001) ISRU lunar processing research at Boeing. *Am. Inst. Aeronaut. Astronaut.* **01-0938**, 1-11.

McEwen A. S., Gaddis L. R., Neukum G., Hoffmann H., Pieters C. M. and Head J. W. (1993) Galileo observations of post-Imbrium lunar craters during the first Earth-Moon flyby. *J. Geophys. Res.* **98**, 17207-17234.

McGee P. E., Warner J. L. and Simonds C. H. (1977) *Introduction to the Apollo Collections. Part I: Lunar Igneous Rocks.* Curators Office, Johnson Space Centre.

McKay G. A. and Weill D. F. (1976) Peterogenesis of KREEP. *Proc. 7th Lunar Sci Conf.* pp. 2427-2447.

McKay D. S. and Wentworth S. J. (1992) Morphology and composition of condensates on Apollo 17 orange and black glass. *Workshop on the Geology of the Apollo 17 Landing Site.* pp. 31.

McKay G., Wagstaff J. and Yang S-R. (1986) Clinopyroxene REE distribution coefficients for shergottites: The REE content of the Shergotty melt. *Geochim. Cosmochim. Acta* **50**, 927-937.

McKay G. A., Wagstaff J., and Le L. (1991) REE distribution coefficients for pigeonite: Constraints on the origin of the mare basalt europium anomaly, III. In *Mare Volcanism and Basalt Petrogenesis Workshop: LPI Tech. Rpt.* **91-03**, 27-28.

McKenzie D. and O'Nions R. K. (1991) Partial melt distributions from inversion of rare earth element concentrations. *J. Petrol.* **32**, 1021-1091.

Melosh H. J. (2009) An isotopic crisis for the giant impact origin of the Moon? *Met. Planet. Sci. XXXXIV.* **A139.**

Mendell W. W. (1986) *Lunar Bases and Space Activities of the 21st Century.* Lunar and Planetary Institute, Houston.

Mermet J. M. (2005) Is it Still Possible, Necessary and Beneficial to Perform Research in ICP-Atomic Emission Spectrometry? *J. Anal. At. Spectrom* **20,** 11-16.

Metzger A. E., Haines E. L., Parker R. E. and Radoncinski R. G. (1977) Thorium concentrations on the lunar surface. I: Regional values and crustal content. *Proc. 8th Lunar Sci. Conf.* pp. 940-999.

Meyer H. O. A. and Boctor N. Z. (1974) Opaque mineralogy: Apollo 17, rock 75035. *Proc. 5th Lunar Sci. Conf.* pp. 707-716.

Meyer C. E. and Wilshire H. G. (1974.) 'Dunite' inclusion in lunar basalt 74275. In *Lunar Sci. V.* Lunar Planetary Institute, Houston. pp. 503-505.

Miller M. F. (2002) Isotopic fractionation and the quantification of ^{17}O anomalies in the oxygen three-isotope system: An appraisal and geochemical significance. *Geochim. Cosmochim. Acta* **66,** 1881-1889.

Miller M. F., Franchi I. A., Sexton A. S. and Pillinger C. T. (1999) High precision $\Delta^{17}O$ isotope measurements of oxygen from silicates and other oxides: Method and applications. *Rapid Commun. Mass Spectrom.* **13,** 1211–1217.

Morgan J. W., Laul J. C., Krahenbuhl U., Ganapathy R. and Anders E. (1972) Major impacts on the Moon: Characterization from trace elements in Apollo 12 and 14 samples. *Proc. 3rd Lunar Sci. Conf.* pp. 1377-1395.

Morgan J. W., Ganapathy R., Higuchi H., Krahenbuhl U. and Anders E. (1974) Lunar basins: Tentative characterization of projectiles from meteoritic elements in Apollo 17 boulders. *Proc. 5th Lunar Sci. Conf.* pp. 1703-1736.

Morishima R. and Watanabe S-I. (2001) Two types of co-accretion scenarios for the origin of the Moon. *Earth, Planets, Space* **53,** 213-231.

Morrison R. H. and Oberbeck V. R. (1975) Geomorphology of crater and basin deposits – emplacement of the Fra Mauro formation. *Proc. 6th Lunar Sci. Conf.* pp. 2503-2530.

Morrison G. H., Gerard J. T., Kashuba A. T., Gangadharam E. V., Rothenberg A. M., Potter N. M. and Miller G. B. (1970) Elemental abundances of lunar soil and rocks. *Proc. 1st Lunar Sci. Conf.* pp. 1383-1392.

Morrisson G. H., Gerard J. T., Potter N. M., Gangadharam E. V., Rothenberg A. M. and Burdo R. A. (1971) Elemental abundances of lunar soil and rocks from Apollo 12. *Proc. 2nd Lunar Sci. Conf.* pp. 1169-1185.

Müller O. (1972) Alkali and alkaline earth elements, La, and U in Apollo 14 and Apollo 15 samples. In *The Apollo 15 Lunar Samples* (J. W. Chamberlain and C. Watkins). The Lunar Science Institute, Houston. pp. 240-243.

Müller O. (1975) Lithophile trace and major elements in Apollo 16 and 17 lunar samples. *Proc. 6th Lunar Sci. Conf.* pp. 1303-1311.

Murali A. V., Ma M-S., Laul J. C. and Schmitt R. A. (1977) Chemical composition of breccias, feldspathic basalt and anorthosites from Apollo 15 (15308, 15359,15382, and 15362), Apollo 16 (60618 and 65785), Apollo 17 (72434, 72536, 72559, 72735, 72738, 78526, and 78527) and Luna 20 (22012 and 22013). *Lunar Sci. Conf. VIII* pp. 700-702.

Murthy V. R. and Coscio M. R. (1976) Rb-Sr ages and isotopic systematics of some Serenitatis mare basalts. *Proc. 7th Lunar Sci. Conf.* pp. 1529-1544.

Murthy V. R. and Coscio C. (1977) Rb-Sr isotopic systematics and initial Sr considerations for some lunar samples. *Lunar Sci. VIII* pp. 706-708.

Murthy V. R., Evensen N. M., and Coscio M. R. Jr. (1970) Distribution of K, Rb, Sr, and Ba and Rb-Sr isotopic relations in Apollo 11 lunar samples. *Proc. 1st Lunar Sci. Conf.* pp. 1393-1406.

Murthy V. R., Evensen N. M., Jahn B-M. and Coscio M. R. (1971) Rb-Sr ages and elemental abundances of K, Rb, Sr, and Ba samples from the Ocean of Storms. *Geochim. Cosmochim. Acta* **35**, 1139-1153.

Murthy V. R., Evensen N. M., Jahn B-M. and Coscio M. R., Jr. (1972) Apollo 14 and 15 samples: Rb-Sr ages, trace elements, and lunar evolution. *Proc. 3rd Lunar Sci. Conf.* pp. 1503-1514.

Nava D. F. (1974) Chemical compositions of some soils and rock types from the Apollo 15, 16, and 17 lunar sites. *Proc. 5th Lunar Sci. Conf.* pp. 1087-1096.

Neal C. R. (2001) Interior of the moon: The presence of garnet in the primitive deep lunar mantle. *J. Geophys. Res.* **106**, 27865-27885.

Neal C. R. and Kramer G. Y (2003) The composition of KREEP: A detailed study of KREEP basalt 15386. *Lunar Planet. Sci. XXXIV* **1665**.

Neal C. R. and Kramer G. Y. (2006) The petrogenesis of the Apollo 14 high-Al mare basalts. *Am. Min.* **91**, 1521-1535.

Neal C. R. and Taylor L. A. (1990) Modelling of lunar basalt petrogenesis: Sr isotopic evidence from Apollo 14 high-alumina basalts. *Proc. 20th Lunar Planet. Sci. Conf.* pp. 101-108.

Neal C. R. and Taylor L. A. (1992) Petrogenesis of mare basalts - A record of lunar volcanism. *Geochim. Cosmochim. Acta* **56**, 2177-2211.

Neal C. R. and Taylor L. A. (1993) *Catalog of Apollo 17 Rocks, Central Valley.* Lunar and Planetary Science Institute, Houston. pp. 2-3.

Neal C. R., Taylor L. A. and Lindstrom M. M. (1988a) Apollo 14 mare basalt petrogenesis: Assimilation of KREEP-like components by a fractionating magma. *Proc. 18th Lunar Planet. Sci. Conf.* pp. 139-153.

Neal C. R., Taylor L. A. and Lindstrom M. M. (1988b) Importance of lunar granite and KREEP in very high potassium (VHK) basalt petrogenesis. *Proc.18th Lunar Planet. Sci. Conf.* pp. 121-137.

Neal C. R., Taylor L. A., Schmitt R. A., Hughes S. S. and Lindstrom M. M. (1989a) High alumina (HA) and very high potassium (VHK) basalt clasts from Apollo 14 breccia, Part 1: Mineralogy and petrology: Evidence of crystallization from evolving magmas. *Proc. 19th Lunar Planet. Sci. Conf.* pp. 137-145.

Neal C. R., Taylor L. A., Patchen A. D., Schmitt R. A., Hughes S. S. and Lindstrom M. M. (1989b) High alumina (HA) and very high potassium (VHK) basalt clasts from Apollo 14 breccias, part 2 - whole-rock geochemistry; Further evidence for combined assimilation and fractional crystallization within the Lunar crust. *Proc. 19th Lunar Planet. Sci. Conf.* pp. 147-162.

Neal C. R., Taylor L. A., Hughes S. S. and Schmitt R. A. (1990a) The significance of fractional crystallisation in the peterogenesis of Apollo 17 type A and B high-Ti basalts. *Geochim. Cosmochim. Acta* **54**, 1817-1833.

Neal C. R., Paces J. B., Taylor L. A. and Hughes S. S. (1990b) Two new Type C basalts: Petrogenetic implications for source evolution and magma genesis at the Apollo 17 site. *Lunar Planet. Sci. XXI*, pp. 855-856.

Neal C. R., Hacker M. D., Taylor L. A., Schmitt R. A. and Liu Y-G. (1992) The Petrogenesis of Apollo 12 mare basalts, part 1: The 'lumpers' versus the 'splitters'. *Lunar Planet. Sci. XXIII.* Lunar and Planetary Institute, Houston. pp. 975-976.

Neal C. R., Hacker M. D., Snyder G. A., Taylor L. A., Liu Y-G. and Schmitt R. A. (1994a) Basalt generation at the Apollo 12 site, Part 1: New data, classification and re-evaluation. *Meteoritics* **29**, 334-348.

Neal C. R., Hacker M. D., Snyder G. A., Taylor L. A., Liu Y.-G. and Schmitt R. A. (1994b) Basalt generation at the Apollo 12 site, Part 2: Source heterogeneity, multiple melts and crustal contamination. *Meteoritics* **29,** 349-361.

Nemchin A. A., Whitehouse M. J., Pidgeon R. T. and Meyer C. (2006) Oxygen isotopic signature of 4.4–3.9 Ga zircons as a monitor of differentiation processes on the Moon. *Geochim. Cosmochim. Acta* **70**, 1864–1872.

Nemchin A. A., Pidgeon R. T., Whitehouse M. J., Vaughan J.P. and Meyer C. (2008) SIMS U-Pb study of zircon from Apollo 14 and 17 breccias: Implications for the evolution of lunar KREEP. *Geochim. Cosmochim. Acta.* **72**, 668-689.

Newton J., Franchi I. A. and Pillinger C. T. (2000) The oxygen isotopic record in enstatite meteorites. *Met. Planet. Sci.* **35**, 698-698.

Nicholis M. G. and Rutherford M. J. (2005) Pressure dependence of graphite C-O phase equilibria and its role in lunar volcanism. *Lunar Planet. Sci. Conf. XXXVI.* **1726**.

Nicholis M. G. and Rutherford M. J. (2009) Graphite oxidation in the Apollo 17 orange glass magma: Implications for the generation of a lunar volcanic gas phase. *Geochim. Cosmochim. Acta* **73**, 5905-5917.

Nozette S., Rustan P., Pleasance L. P., Horan D. M., Regeon P., Shoemaker E. M., Spudis P. D., Acton C. H., Baker D. N., Blamont J. E., Buratti B. J., Corson M. P., Davies M. E., Duxbury T. C., Eliason E. M., Jakosky B. M., Kordas J. F., Lewis I. T., Lichtenberg C. L., Lucey P. G., Malaret E., Massie M. A., Resnick J. H., Rollins C. J., Park H. S., McEwen A. S., Priest R. E., Pieters C. M., Reisse R. A., Robinson M. S., Simpson R. A., Smith D. E., Sorenson T. C., Breugge R. W. V. and Zuber M. T. (1994) The Clementine Mission to the Moon – Scientific Overview. *Science* **266**, 1835-1839.

Nozette S., Lichtenberg C. L., Spudis P. D., Bonner R., Ortr W., Malaret E., Robinson M. and Shoemaker E. M. (1996) The Clementine bistatic radar experiment. *Science* **274**, 1495-1498.

Nyquist L. E. (1977) Lunar Rb-Sr chronology. *Phys. Chem. Earth* **10**, 103-142.

Nyquist L. E. and Shih C.-Y. (1992) The isotopic record of lunar volcanism. *Geochim. Cosmochim. Acta* **56**, 2213-2234.

Nyquist L. E., Gast P. W., Church S. E., Wiesmann H. and Bansal B. M. (1972) Rb-Sr systematics for chemically defined Apollo 15 materials. In *The Apollo 15 Lunar*

Samples (eds. J. W. Chamberlain and C. Watkins). The Lunar Science Institute, Houston. pp. 380-384.

Nyquist L. E., Hubbard N. J., Gast P. W., Bansal B. M., Wiesmann H. and Jahn B. (1973) Rb-Sr systematics for chemically defined Apollo 15 and 16 materials. *Proc. 4th Lunar Sci. Conf.* pp. 1823-1846.

Nyquist L. E., Bansal B. M., Wiesmann H. and Jahn B-M. (1974) Taurus-Littrow chronology: Some constraints on early lunar crustal development. *Proc. 5th Lunar Sci. Conf.* pp. 1515-1539.

Nyquist L. E., Bansal B. M. and Wiesmann H. (1975) Rb-Sr ages and initial $^{87}Sr/^{86}Sr$ for Apollo 17 basalts and KREEP basalt 15386. *Proc. 6th Lunar Sci. Conf.* pp. 1445-1465.

Nyquist L. E., Bansal B. M. and Wiesmann H. (1976) Sr isotopic constraints on the petrogenesis of Apollo 17 mare basalts. *Proc. 7th Lunar Sci. Conf.* pp. 1507-1528.

Nyquist L. E., Bansal B. M., Wooden J. L., and Wiesmann H. (1977) Sr-isotopic constraints on the petrogensis of Apollo 12 mare basalts. *Proc. 8th Lunar Sci. Conf.* pp. 1383-1415.

Nyquist L. E., Shih C-Y., Wooden J. L., Bansal B. M. and Wiesmann H. (1979) The Sr and Nd isotopic record of Apollo 12 basalts: Implications for lunar geochemical evolution. *Proc. 10th Lunar Planet. Sci. Conf.* pp. 77-114.

Nyquist L. E., Bogard D. D., Garrison D. H., Bansal B. M., Wiesmann H. and Shih C-Y. (1991) Thermal resetting of radiometric ages. I: Experimental Investigations. *Lunar Planet. Sci. XXII* pp. 985-986.

O'Hara M. J., Biggar G. M., Richardson S. W., Ford C. E. and Jamieson B. G. (1970) The nature of seas, mascons, and the lunar interior in light of experimental studies. *Proc. 1st Lunar Sci. Conf.* pp. 695-710.

Onuma N., Higuchi H., Wakita H. and Nagasawa H. (1968) Trace element partitioning between two pyroxenes and the host lava. *Earth Planet Sci. Lett.* **5**, 47-51.

Onuma N., Clayton R. N., and Mayeda T. K. (1970) Oxygen isotope fractionation between minerals and an estimate of the temperature of formation. *Science* **167**, 536-538.

Otake H. and Mizutani H. (2006) Subsurface chemistry of the Imbrium basin inferred from Clementine UVVIS spectroscopy. *Earth Planets Space* **58**, 1499-1510.

Oxford-instruments. www.xraymicroanalysis.com.

Paces J. B., Nakai S., Neal C. R., Taylor L. A., Halliday A. N. and Lee D-C. (1991) A strontium and neodymium isotopic study of Apollo 17 high-Ti mare basalts: Resolution of ages, evolution of magmas, and origins of source heterogenities. *Geochim. Cosmochim. Acta* **55**, 2025-2043.

Pack A., Toulouse C. and Przybilla R. (2007) Determination of oxygen triple isotope ratios of silicates without cryogenic separation of NF_3 – technique with application to analyses of technical O_2 gas and meteorite classification. *Rapid Commun. Mass Spectrom.* **21**, 3721-3728.

Pahlevan K. and Stevenson D. J. (2007). Equilibration in the aftermath of the lunar-forming giant impact. *Earth Planet. Sci. Lett.* **262**, 438-449.

Papanastassiou D. A. and Wasserburg G. J. (1970) Rb-Sr ages from the Ocean of Storms. *Earth Planet. Sci. Lett.* **8**, 269-278.

Papanastassiou D. A. and Wasserburg G. J. (1971a) Lunar chronology and evolution from Rb-Sr studies of Apollo 11 and 12 samples. *Earth Planet. Sci. Lett.* **11**, 37-62.

Papanastassiou D. A. and Wasserburg G. J. (1971b) Rb-Sr ages of igneous rocks from the Apollo 14 mission and the age of the Fra Mauro formation. *Earth Planet. Sci. Lett.* **12**, 36-48.

Papanastassiou D. A. and Wasserburg G. J. (1973) Rb-Sr ages and initial strontium in basalts from Apollo 15. *Earth Planet. Sci. Lett.* **17**, 324-337.

Papanastassiou D. A. and Wasserburg G. J. (1975) Rb-Sr study of a lunar dunite and evidence for early lunar differentiates. *Proc. 6th Lunar Sci. Conf.* pp. 1467-1489.

Papanastassiou D. A., DePaolo D. J. and Wasserburg G. J. (1977) Rb-Sr and Sm-Nd chronology and genealogy of mare basalts from the Sea of Tranquility. *Proc. Lunar Sci. Conf. 8th* pp. 1639-1672.

Papike J. J. (1987) Chemistry of the rock-forming silicates: Ortho, ring and single-chain structures. *Rev. Geophys.* **25**, 1483-1526.

Papike J. J. (1988) Chemistry of the rock forming silicates: Multiple-chain, sheet and framework silicates. *Rev. Geophys.* **26**, 407-444.

Papike J. J. and Bence A. E. (1978) Lunar mare verses terrestrial midocean ridge basalts: Planetary constraints on basaltic volcanism. *Geophys. Res. Lett.* **5**, 803-806.

Papike J. J. and Vaniman D. T. (1978) The lunar mare basalt suite. *Geophys. Res. Lett.* **5**, 433-436.

Papike J. J., Bence A. E., Brown G. E., Prewitt C. T. and Wu C. H. (1971) Apollo 12 clinopyroxenes: Exsolution and epitaxy. *Earth Planet. Sci. Lett.* **10**, 307-315.

Papike J. J., Bence A. E. and Lindsley D. H. (1974) Mare basalts from the Taurus-Littrow region of the moon. *Proc. 5th Lunar Sci. Conf.* 471-504.

Papike J. J., Hodges F. N., Bence A. E., Cameron M. and Rhodes J. M. (1976) Mare basalts: Crystal chemistry, mineralogy and petrology. In *Mare Crisium: The View From Lunar 24.* (eds. R. B. Merrill and J. J. Papike). Pergamon, New York. pp. 371-401.

Papike J. J., Ryder G., and Shearer C. K., (1998) Lunar Samples. *Reviews in Mineralogy and Geochemistry* **36**, 5-1 to 5-234.

Papike J. J., Fowler G. W., Adcock C. T. and Schearer C. K. (1999) Systematics of Ni and Co in olivine from planetary melt systems: Lunar mare basalts. *Am. Min.* **84**, 392-399.

Parmentier E. M., Zhong S. and Zuber M. T. (2002) Gravitational differentiation due to initial chemical stratification: Origin od lunar asymmetry by the creep of dense KREEP? *Earth Planet. Sci. Lett.* **201**, 473-480.

Patchen A. P. and Taylor L. A. (2004) The most reduced rock from the Moon - Apollo 14 basalt 14053: Extreme reduction entirely from a re-heating event. *Lunar Planet Sci. Conf. XXXV* **1762**.

Pearce N. J. G., Perkins W. T., Westgate J. A., Gorton M. P., Jackson S. E., Neal C. R. and Chenery S. P. (1997) A compilation of new and published major and trace element data for NIST SRM 610 and NIST SRM 612 glass reference materials. *J. Geostandards and Geoanal.* **21**, 115-144.

Philpotts J. A. (1978) The law of constant rejection. *Geochim. Cosmochim. Acta* **42**, 909-920.

Philpotts J. A. and Schnetzler C. C. (1970) Potassium, rubidium, strontium, barium and rare-earth concentrations in lunar rocks and separated phases. *Science* **167**, 493-495.

Philpotts J. A., Schnetzler C. C., Nava D. F., Bottino M. L., Fullagar P. D., Thomas H. H., Schumann S. and Kouns C. W. (1972) Apollo 14: Some geochemical aspects. *Proc. 3rd Lunar Sci. Conf.* 1293-1305.

Philpotts J. A., Schuhmann S., Kouns C. W., Lum R. K. L. and Winzer S. (1974) Origin of Apollo 17 rocks and soils. *Proc. 5th Lunar Sci. Conf.* pp. 1255-1267.

Phinney D., Kahl S. B. and Reynolds J. H. (1975) ^{40}Ar-^{39}Ar dating of Apollo 16 and 17 rocks. *Proc. 6th Lunar Sci. Conf.* pp. 1593-1608.

Pieters C. M. (1978) Mare basalt types of the front side of the Moon: A summary of spectral reflectance data. *Proc. 9th Lunar Planet. Sci. Conf.* pp. 2825-2849.

Pieters C. M. and McCord T. B. (1975) Classification and distribution of lunar mare basalts. In *Papers Presented to the Conference on Origins of Mare Basalts and Their Implications for Lunar Evolution.* Lunar Science Institute, Houston. pp. 125-129.

Pieters C. M., Sunshine J. M., Fischer E. M., Murchie S. L., Belton M., McEwen A., Gaddis L., Greeley R., Neukum G., Jaumann R. and Hoffmann H. (1993) Crustal

diversity of the Moon: Compositional analysis of Galileo solid state imaging data. *J. Geophys. Res.* **98**, 17127-17148.

Pieters C. M., Staid M. I., Fischer E. M., Tompkins S. and He G. (1994) A sharper view of imapct craters from Clementine data. *Science* **266**, 1844.

Pieters C. M., Head J. W., Gaddis L., Jollif B. and Duke M. (2001) Rock types of South Pole-Aitken basin and extent of basaltic volcanism. *J. Geophys. Res.* **106**, 28001-28022.

Podosek F. A., Huneke J. C., Burnett D. S. and Wasserburg G. J. (1971) Isotopic composition of xenon and krypton in the lunar soil and in the solar wind. *Earth Planet. Sci. Lett.* **10**, 199-216.

Poldervaart A. and Hess H. H. (1951) Pyroxenes in the crystallisation of basaltic magma. *J. Geol.* **59**, 472.

Powell R. (1984) Inversion of the assimilation and fractional crystallisation (AFC) equations; Charateristation of contaminants from isotope and trace element relationships in volcanic suites. *J. Geol. Soc. Lond.* **141**, 447-452.

Premo W. R. and Tatsumoto M. (1992) Isotopic ages and characteristics of ancient (pre-Serenitatis) lunar crustal rocks at Apollo 17. *Workshop on the Geology of the Apollo 17 Landing Site.* LPI Tech. Rpt. 92-09. Lunar Planetary Institute, Houston. pp. 45-48.

Pritchard M. E. and Stevenson D. J. (1999) How has the Moon released its internal heat? In *Lunar and Planetary Science XXX* pp. 1981.

Pritchard M. E. and Stevenson D. J. (2000) Thermal aspects of a lunar origin by giant impact. In *Origin of the Earth and Moon* (eds. R. M. Canup and K. Righter). Univ. Arizona Press, Tucson. pp. 179-196.

Rankenburg K., Brandon A.D. and Norman M. D. (2007) A Rb–Sr and Sm–Nd isotope geochronology and trace element study of lunar meteorite LaPaz Icefield 02205. *Geochim. Cosmochim. Acta.* **71**, 2120-2135.

Rasmussen B., Fletcher I. R. and Muhling J. R. (2008) Pb/Pb geochronology, petrography and chemistry of Zr-rich accessory minerals (zirconolite, tranquillityite and baddeleyite) in mare basalt 10047. *Geochim. Cosmochim. Acta* **72**, 5799-5818.

Reid A. M., Meyer C., Harmon R. S. and Brett R. (1970) Metal grains in Apollo 12 igneous rocks. *Earth Planet. Sci. Lett.* **9**, 1-5.

Rhodes J. M. (1972) Major element chemistry of Apollo 15 mare basalts. In *The Apollo 15 Lunar Samples.* Lunar Science Institute, Houston. pp. 250-252.

Rhodes J. M. and Blanchard D. P. (1980) Chemistry of Apollo 11 low-K basalts. *Proc. 11th Lunar Planet. Sci. Conf.* pp. 49-66.

Rhodes J. M. and Hubbard N. J. (1973) Chemistry, classification, and petrogenesis of Apollo 15 mare basalts. *Proc. 4th Lunar Sci. Conf.* pp. 1127-1148.

Rhodes J. M., Rodgers K. V., Shih C., Bansal B. M., Nyquist L. E., Wiesmann H. and Hubbard N. J. (1974) The relationships between geology and soil chemistry at the Apollo 17 landing site. *Proc. 5th Lunar Sci. Conf.* pp. 1097-1117.

Rhodes J. M., Hubbard N. J., Wiesmann H., Rodgers K. V., Brannon J. C. and Bansal B. M. (1976) Chemistry, classification, and petrogenesis of Apollo 17 mare basalts. *Proc. 7th Lunar Sci. Conf.* pp. 1467-1489.

Rhodes J. M., Blanchard D. P., Dungan M. A., Brannon J. C. and Rodgers K. V. (1977) Chemistry of the Apollo 12 mare basalts: Magma types and fractionation processes. *Proc. 8th Lunar Sci. Conf.* pp. 1305-1338.

Rhodes J. M., Lofgren G. E. and Smith D. P. (1979) One atmosphere melting experiments on ilmenite basalt 12008. *Proc. 10th Lunar Planet. Sci. Conf.* pp. 407-422.

Ridley W. I. and Brett R. (1973) Petrogenesis of basalt 70035: A multistage cooling history. *EOS Trans. AGU* **54**, 611-612.

Ringwood A. E. (1979) *Origin of the Earth and Moon.* Springer-Verlag, New York.

Ringwood A. E and Essene E. (1970) Petrogenesis of Apollo 11 basalts, internal constitution and origin of the moon. *Proc. 1st Lunar Sci. Conf.* pp. 769-799.

Ringwood A. E and Kesson S. E. (1976) A dynamic model for mare basalt petrogenesis. *Proc. 7th Lunar Sci. Conf.* pp. 1697-1722.

Robinson M. S. and Jolliff B. L. (2002) Apollo 17 landing site: Topography, photometric corrections and heterogenaity of the surrounding highland massifs. *J. Geophys. Res.* **107**, doi 10.1029/2001JE001614.

Robinson M., Shoemaker E. M. and Hawke B. R. (1996) Spectral heterogeneity of lunar local dark mantle deposits. *Lunar Planet. Sci. Conf. XXVII.* **1087**.

Robinson M. S., Hapke B. W., Garvin J. B., Skillman D., Bell J. F., Ulmer M. P. and Pieters C. M. (2007) High resolution mapping of TiO_2 abundances on the Moon using the Hubble Space Telescope. *Geophys. Res. Lett.* **34**, L13203, doi:10.1029/2007GL029754.

Rollinson H. (1993) *Using geochemical data: Evaluation, presentation, interpretation.* Longman, UK.

Rose H. J., Cuttitta F., Dwornik E. J., Carron M. K., Christian R. P., Lindsay J. R., Ligon D. T. and Larson R. R. (1970) Semimicro chemical and X-ray fluorescence analysis of lunar samples. *Science* **167**, 520-521.

Rose H. J., Cuttitta F., Annell C. S., Carron M. K., Christian R. P., Dwornik E. J., Greenland L. P. and Ligon D. T. (1972) Compositional data for twenty-one Fra Mauro lunar materials. *Proc. 3rd Lunar Sci. Conf.* 1215-1229.

Rose H. J., Cuttitta F., Berman S., Brown F. W., Carron M. K., Christian R. P., Dwornik E. J. and Greenland L. P. (1974) Chemical composition of rocks and soils at Taurus-Littrow. *Proc. 5th Lunar Sci. Conf.* pp. 1119-1133.

Rose H. J., Baedecker P. A., Berman S., Christian R. P., Dwornik E. J., Finkelman R. B. and Schnepfe M. M. (1975) Chemical composition of rocks and soils returned by the Apollo 15, 16, and 17 missions. *Proc. 6th Lunar Sci. Conf.* pp. 1363-1373.

Ross M., Bence A. E., Dwornik E. J., Clark J. R., Papike J. J. (1970) Mineralogy of lunar clinopyroxenes, augite and pigeonite. *Proc. 1st Lunar Sci. Conf.* pp. 839-848.

Rubin A. E. (1997) Mineralogy of meteorite groups. Meteorit. Planet Sci. **32**, 231-247.

Rumble D., Miller M. F., Franchi I. A. and Greenwood R. C. (2007) Oxygen three-isotope fractionation lines in terrestrial silicate minerals: An inter-laboratory comparison of hydrothermal quartz and eclogitic garnet. *Geochim. Cosmochim. Acta* **71**, 3592-3600.

Ryder G. (1988) A new Apollo 17 high-Ti mare basalt variant and the intricacy of melting of the lunar mantle. *Trans. Amer. Geophys. Union* **69**, 292.

Ryder G. (1990) A distant variant of high-titanium mare basalt from the Van Serg Core, Apollo 17 landing site. *Meteoritics* **25**, 249-258.

Ryder G. (1991) Lunar ferroan anorthosites and mare basalt sources: The mixed connection. *Geophys. Res. Lett.* **18**, 2065-2068.

Ryder G. (1994) Coincidence in time of the Imbrium basin impact and Apollo 15 KREEP volcanic flows: The case for impact-induced melting in large meteorite impacts. *Geochim. Cosmochim. Acta* Special Paper **293**, 11-18.

Ryder G. and Martinez R. R. (1991) Evolved hyperbyssal rocks from Station 7, Apennine Front, Apollo 15. *Proc. 21st Lunar Planet Sci. Conf.* pp. 137-150.

Ryder G. and Marvin U. B. (1978) On the origin of Luna 24 basalts and soils. In *Mare Crisium: The View from Luna 24.* (eds. R. B. Merrill and J. J. Papike) Pergamon, New York. pp. 339-355.

Ryder G. and Schuraytz B. C. (2001) Chemical variations of the large Apollo 15 olivine-normative mare basalt rock samples. *J. Geophys. Res.* **106**, 1435-1451.

Ryder G. and Steele A. (1988) Chemical dispersion among Apollo 15 olivine-normative mare basalts. *Proc. 18th Lunar Planet. Sci. Conf.* 273-282.

Ryder G., Norman M. D. and Score R. A. (1980) The distinction of pristine from meteorite-contaminated highlands rocks using metal compositions. *Proc. 11th Lunar Planet. Sci. Conf.* pp. 471-479.

Saal A. E., Hauri E. H., Lo Cascio M., Van Orman J. A., Rutherford M. C., Cooper R. F. (2008) Volatile content of lunar volcanic glasses and the presence of water in the Moon's interior. *Nature* **454**, 192-195.

Sano Y., Oyama T., Terada K., Hidaka H. (1999) Ion microprobe U–Pb dating of apatite. *Chem. Geol.* **153**, 249-258.

Sasada T., Hiyagon H., Bell K. and Ebihara M. (1997) Mantle-derived noble gases in carbonatites. *Geochim. Cosmochim. Acta* **19**, 4219–4228.

Sato M. and Helz R. T. (1971) Oxygen fugacity values of Apollo 12 basaltic rocks. In *Lunar Sci. II.* Lunar and Planetary Science Institute, Houston. pp. 144-145.

Sato M., Hicklin N. L. and McLane J. E. (1973) Oxygen fugacity values of lunar samples. *Proc. 4th Lunar Sci. Conf.* pp. 1061-1079.

Schaber G. G. (1973) Lava flows in mare Imbrium: Geologic evaluation from Apollo orbital photography. In *Lunar Sci. IV.* Lunar and Planetary Science Institute, Houston. pp. 653-654.

Schaeffer G. A. and Schaeffer O. A. (1977) $^{39}Ar/^{40}Ar$ ages of lunar rocks. *Proc. 8th Lunar Sci. Conf.* pp. 2253-2300.

Schaeffer O. A., Muller H. W. and Grove T. L. (1977) Laser ^{39}Ar-^{40}Ar study of Apollo 17 basalts. *Proc. 8th Lunar Sci. Conf.* pp. 1489-1499.

Schmidt O. Y. (1959) *A theory of the origin of the Earth.* Lawrence and Wishart, London. pp. 139.

Schmitt H. H. (1989) Apollo 17 orange soils: Interpretation of geologic setting. In *Lunar Volcanic Glasses: Scientific and research Potential.* (eds. J. W. Delano and G. H. Heiken). Lunar and Planetary Institute, Houston. pp. 56-57.

Schmitt H. H. (2006) *Return to the Moon.* Praxis Publishing Ltd., Copernicus Books, Springer, New York. pp. 335.

Schmitt H. H., Lofgren G., Swann G. A. and Simmons G. (1970) The Apollo 11 samples: Introduction. *Proc. 1st Lunar Sci. Conf.* pp. 1-54.

Schnare D. W., Day J. M. D., Norman M. C., Liu Y. and Taylor L. A. (2008) A laser-ablation ICP-MS study of Apollo 15 low-titanium olivine-normative and quartz-normative mare basalts. *Geochim. Cosmochim. Acta* **72**, 2556-2572.

Schnetzler C. C. and Philpotts J. A. (1971) Alkali, alkaline earth, and rare earth element concentrations in some Apollo 12 soils, rocks, and separated phases. *Proc. 2nd Lunar Sci. Conf.* pp. 1101-1122.

Schultz P. H. and Spudis P. D. (1983) Beginning and end of lunar mare volcanism. *Nature* **302**, 233-236.

Schulz T., Sokol A., Palme H., Weckwerth G., Münker C. and Bischoff A. (2007) Chemical composition and Lu/Hf-age of the lunar mare basalt meteorite Kalahari 009. *Meteor. Planet. Sci. Supplement.* **5151**.

Scoon J. H. (1971) Chemical analyses of lunar samples 12040 and 12064. *Proc. 2nd Lunar Sci. Conf.* pp. 1259-1260.

Shearer C. K. and Borg L. (2004) KREEP-rich basaltic magmatism: Diversity of composition and consistency of age. *Lunar Planet. Sci. Conf. XXXV.* **1390**.

Shearer C. K. and Papike J. J. (1993) Basaltic magmatism on the Moon: A perspective from volcanic picritic glass beads. *Geochim. Cosmochim. Acta* **57**, 4785-4812.

Shearer C. K. and Papike J. J. (1999) Magmatic evolution of the Moon. *Am. Miner.* **84**, 1469-1494.

Shearer C. K., Hess P. C., Wieczorek M. A., Pritchard M. E., Parmentier E. M., Borg L. E., Longhi J., Elkins-Tanton L. T., Neal C. R., Antonenko I., Canup R. M., Halliday A. N., Grove T. L., Hager B. H., Lee D-C. and Wiechert U. (2006) Thermal and magmatic evolution of the Moon. *Reviews in Mineralogy and Geochemistry* **60**, 365-518.

Shearer C.K., Sharp Z. D., Brearley A., King P.L. and Fischer T. (2010) A "dry" versus a "wet" Moon: The effect of potential indigenous water on the composition of lunar volcanic gases and sublimates. *41st Luanr Planet. Sci. Conf.* **1941**.

Shervais J. W. (1989) Highland crust at the Apollo 14 site: A review. In *Workshop on Moon in Transition: Apollo 14, KREEP, and Evolved Lunar Rocks.* (eds. G. J. Taylor and P. H. Warren). pp. 118–127.

Shervais J.W. and McGee J.J. (1998) Ion and electron microprobe study of trotolites, norites and anorthosites from Apollo 14: Evidence for urKREEP assimilation during petrogenesis of Apollo 14 Mg-suite rocks. *Geochim. Cosmochim. Acta* **62**, 3009-3023.

Shervais J. W. and Vetter S. K. (1990) Lunar mare volcanism: Mixing of distinct mantle source regionswith KREEP-like component. *Lunar Planet. Sci. Conf. XXI* pp. 1142-1143.

Shervais J. W., Taylor L. A., Laul J. C. and Smith M. R. (1984a) Pristine highlands clasts in consortium breccia 14305: Pterology and geochemeistry. *Proc. 15th Lunar Sci. Conf., J. Geophys. Res.* **89**, C25-C40.

Shervais J. W., Taylor L. A. and Laul J. C. (1984b) Very high potasium (VHK) basalt: A new type of alluminous mare basalt from Apollo 14. *Lunar Planet. Sci. XV.* Lunar and Planetary Institute, Houston. pp. 768-769.

Shervais J. W., Taylor L. A. and Lindstrom M. M. (1985a) Apollo 14 mare basalts: petrology and geochemistry of clasts from consortium breccia 14321. *Proc. 15th Lunar Planet. Sci. Conf., J. Geophys. Res.* **89**, C375-395.

Shervais J. W., Taylor L. A., Laul J. C., Shih C-Y. and Nyquist L. E. (1985b) Very high potassium (VHK) basalt: Complications in mare basalt petrogenesis. *J. Geophys. Res.* **90**, D3-D18.

Shih C-Y. and Nyquist L. E. (1989) Isotopic and chemical constraints on models of Aluminous mare basalt genesis. *Lunar Planet. Sci. Conf. XX* pp. 1002-1003.

Shih C.-Y., Haskin L. A., Wiesmann H., Bansal B. M. and Brannon J. C. (1975) On the origin of high-Ti mare basalts. *Proc. 6th Lunar Sci. Conf.* 1255-1285.

Shih C-Y., Nyquist L. E., Bogard D. D., Bansal B. M., Wiesmann H., Johnson P., Shervais J. W. and Taylor L. A. (1986) Geochronology and petrogenesis of Apollo 14 very high potassium mare basalts. *Proc. 16th Lunar Planet. Sci. Conf., J. Geophys. Res.* **91**, D214-D228.

Shoemaker E. M., Bailey N. G., Batson R. M., Dahlem D. H., Foss T. H., Grolier M. J., Goddard E. M., Hait M. H., Holt H. E. and Larson K. B. (1970). Geologic setting of the lunar samples returned by the Apollo 11 mission. In *Apollo 11 Preliminary Science Report.* NASA Spec. Publ. **214**, 41-84.

Shoemaker E. M., Robinson M. S. and Eliason E. M. (1994) The south pole region of the Moon as seen by Clementine. *Science* **266**, 1851-1854.

Short N. M. and Forman M. L. (1972) Impact crater ejecta on the lunar surface. *Modern Geol.* **3**, 69-91.

Simon S. B., Papike J. J. and Laul J. C. (1988) Chemistry and petrology of the Apennine Front, Apollo 15, Part I: KREEP basalts and plutonic rocks. *Proc. 18th Lunar Planet. Sci. Conf.* pp. 187-201. Lunar Planetary Institute, Houston.

Smales A. A., Mapper D., Webb M. S. W., Webster R. K., Wilson J. D. and Hislop J. S. (1971) Elemental composition of lunar surface material (part 2). *Proc. 2nd Lunar Sci. Conf.* pp. 1253-1258.

Smith J. V. (1974) Lunar mineralogy: A heavenly detective story. Pres. Address. *Am. Mineral.* **59**, 231-243.

Smith J. V., Anderson A. T., Newton R. C., Oslen E. J., Wyllie P. J., Crewe A. V., Isaacson M. S. and Johnson D. (1970) Petrologic history of the Moon inferred from petrography, mineralogy and petrogenesis of Apollo 11 rocks. *Proc. 1st Lunar Sci. Conf.* pp. 897-925.

Snyder G. A. and Taylor L. A. (2000) Impact processes and isotopic closure on planetary bodies and the Moon. *Lunar Planet. Sci. XXXI* **1220**.

Snyder G. A. and Taylor L. A. (2001) Oldest mare basalts or Impact melts? The role of differential melting of plagioclase in Apollo 14 high-Al basalts. *Met. Planet. Sci.* **36**, A194.

Snyder G. A., Taylor L. A. and Neal C. R. (1990) The sources of mare basalts: A model involving lunar magma ocean crystallisation, plagioclase flotation, and trapped instanatious residual liquid. *Workshop on mare basalt petrogenesis.* Lunar and Palnetary Institute, Houston. pp. 43-44 (abs.).

Snyder G. A., Taylor L. A. and Neal C. R. (1992a) A chemical model for generating the sources of mare basalts: Combined equillibrium and fractional crystallisation of the lunar magmasphere. *Geochim. Cosmochim. Acta* **56**, 3809-3823.

Snyder G. A., Lee D-C., Taylor L. A., Jerde E. A. and Halliday A. N. (1992b) Nd and Sr isotopic constraints on high-Ti basalt volcanism at Mare Tranquillitatis. *Lunar Planet Sci. XXIII* pp. 132 l-1322 (abs.).

Snyder G. A., Lee D-C., Taylor L. A., Halliday A. N. and Jerde E. A. (1993) Enrichment and depletion in the lunar mantle: Nd and Sr isotopic constraints from high-Ti mare basalts. *Geochim. Cosmochim. Acta* **58,** 4795-4808.

Snyder G. A., Lee D., Taylor L. A., Halliday A. N. and Jerde E. A. (1994) Evolution of the upper mantle of the Earths moon: Neodymium and strontium isotopic constraints from high-Ti mare basalts. *Geochim. Cosmochim. Acta* **58**, 4795-4808.

Snyder G. A., Neal C. R., Taylor L. A. and Halliday A. N. (1995) Processes involved in the formation of magnesian-suite plutonic rocks from the highlands of the Earth's moon. *J. Geophys. Res.* **100**, 9365–9388.

Snyder G.A., Neal C.R., Taylor L.A. and Halliday A.N. (1997) Anataxis of lunar cumulate mantle in time and space: Clues from trace-element, strontium and neodymium isotopic chemistry of parental Apollo 12 basalts. *Geochim. Cosmochim. Acta* **61**, 2731-2747.

Snyder G. A., Borg L. E., Taylor L. A., Nyquist L. E. and Halliday A. N. (1998) Volcanism in the Hadley-Apennine region of the Moon: Geochronology, Nd-Sr isotopic systematics and depths of melting. *Lunar Planet Sci. Conf. XXIX* **1141**.

Snyder G. A., Borg L. E., Nyquist L. E. and Taylor L. A. (2000) Chronology and isotopic constraints on lunar evolution. In *Origin of the Earth and Moon.* (eds. R. M. Canup and K. Righter). Uni. Arizona Press, Tucson. pp. 361-396.

Sokol A. K and 12 authors (2008) Kalahari 008 and 009: New constraints on early lunar evolution. *Geochim. Cosmochim. Acta* **72**, 4845-4873.

Soloman S. C. and Longhi J. (1977) Magma oceanography: Thermal evolution. *Proc. 8th Lunar Sci. Conf.* pp. 583-599.

Spangler R. R., Warasila R. and Delano J. W. (1984) ^{39}Ar-^{40}Ar ages for the Apollo 15 green and yellow volcanic glasses. *Proc. 14th Lunar Planet. Sci. Conf., J. Geophys. Res.* **89**, B487-497.

Spicuzza M. J., Day J. M. D., Taylor L. A. and Valley J. W. (2007) Oxygen isotope constraints on the origin and differentiation of the Moon. *Earth Planet. Sci. Lett.* **253**, 254–265.

Spudis P. D. (1978) Composition and origin of the apennine bench formation. *Proc. 9th Lunar Planet. Sci.* pp. 3379-3394.

Spudis P. D. (2003) Harvest the Moon. *Astronomy* **06**, 42-47.

Spudis P. D. and Hawke B. R. (1986) The Apennine Bench formation. In *Workshop on the Geology and Petrology of the Apollo 15 Landing Site. LPI Tech. Rep.* **86-03**, 105–107.

Spudis P. D., Hawke B. R., Hood L. L., Schultz P. H., Taylor G. J. and Wilhelms D. E. (1986) Status and future of lunar geoscience. *Lunar Geoscience Working Group* **NASA SP-484**, pp. 58.

Spudis P. D., Reisse R. A. and Gillis J. J. (1994) Ancient multiring basins on the Moon revealed by Clementine laser altimetry. *Science* **266**, 1848-1851.

Steele I. M., Smith J. V. and Grossman L. (1972) Mineralogy and petrology of Apollo 15 rake samples: I. Basalts. In *The Apollo 15 Lunar Samples*. Lunar Planetary Institute, Houston. pp. 158-160.

Stettler A., Eberhardt P., Geiss J., Grogler N. and Maurer P. (1973) Ar^{39}-Ar^{40} ages and Ar^{37}-Ar^{38} exposure ages of lunar rocks. *Proc. 4th Lunar Sci. Conf.* pp. 1865-1888.

Stettler A., Eberhardt P., Geiss J., Grogler N. and Maurer P. (1974) On the duration of the lava flow activity in Mare Tranquillitatis. *Proc. 5th Lunar Sci. Conf.* pp. 1865-1888.

Stevenson D. J. (1980) Lunar asymmetry and paleomagnetism. *Nature* **287**, 520-521.

Stewart D. B., Appleman D. E., Huebner J. S. and Clark J. R. (1970) Crystallography of Some Lunar Plagioclases. *Science* **167**, 634-635.

Strangway D. W. and Sharpe H. N. (1975) A model of lunar evolution. *The Moon* **12**, 369-397.

Stöffler D. and Ryder G. (2001) Stratigraphy and isotopic ages of lunar geologic units: Chronological standard for the inner solar system. *Space Science Rev.* **96**, 9-54.

Stöffler D., Bischoff A., Borchardt R., Burghele A., Deutsch A., Jessberger E. K., Ostertag R., Palme H., Spettel B., Reimold W. U., Wacker K. and Wänke H. (1985) Composition and evolution of the lunar crust in the Decartes highlands. *Proc. 15th Lunar Planet. Sci. Conf., J. Geophys. Res.* **90**, C449-C506.

Stolper E. M. (1974) Lunar ultramafic glasses. *A. B. thesis. Harvard Univ.*

Sutter J. D. (2010) Will NASA ever return to the Moon. *CNN (Tech)*. URL: http://www.cnn.com/2010/TECH/space/02/02/nasa.constellation.reaction/index.html

Takeda H., Miyamoto M., Ishii T. and Lofgren G. E. (1975) Relative cooling rates of mare basalts at the Apollo 12 and 15 sites as estimated from pyroxenes exsolution data. *Proc. 6th Lunar. Sci. Conf.* pp. 987-996.

Takeda H., Miyamoto M., Duke M. B. and Ishii T. (1978) Crystallisation of pyroxene in lunar KREEP basalt 15386 and meteoritic basalts. *Proc. 9th Lunar Sci. Conf.* pp. 1157-1171.

Tatsumoto M. (1970) Age of the Moon: An isotopic study of U-Th-Pb systematics of Apollo 11 lunar samples - II. *Proc. 1st Lunar Sci. Conf.* pp. 1595-1612.

Tatsumoto M., Nunes P. D., Knight R. J., Hedge C. E. and Unruh D. M. (1973) U-Th-Pb, Rb-Sr, and K measurements of two Apollo 17 samples. *EOS Trans. AGU* **54**, 614-615.

Taylor G. J. (1989) Phenocyst content of mare volcanics: Inferrences for magma migration mechanisms on the Moon. In: *Lunar Volcanic Glasses: Scientific and research Potential.* (eds. J. W. Delano and G. H. Heiken). Lunar and Planetary Institute, Houston. pp. 68-70.

Taylor G. J. and Spudis P. D. (1990) Geoscience and a lunar base: A comprehensive plan for lunar exploration. *NASA Conf. Pub.* **3070**, 75.

Taylor G. J., Keil K. and Warner R. D. (1977) Very Low-Ti Mare Basalts. *Geophys. Res. Lett.* **4**, 207-210.

Taylor G. J., Warren P., Ryder G., Delano J., Pieters C. (1991) Lunar Rocks. In *The Lunar Sourcebook, A Users Guide to the Moon* (eds. G. H. Heiken, D. T. Vaniman and B. M. French). Cambridge University Press, Cambridge. pp. 183-284.

Taylor H. P. and Epstein S. (1970) O^{18}/O^{16} ratios of Apollo 11 lunar rocks and minerals. *Proc 1st Lunar Sci. Conf.* **2**, 1613-1626.

Taylor L. A. and McCallister R. H. (1972) An experimental investigation of the significance of zirconium partitioning in lunar ilmenite and ulvospinel. *Earth Planet. Sci. Lett.* **17**, 105-109.

Taylor L. A. and Williams K. L. (1973) Cu-Fe-S phases in lunar rocks. *Am. Mineral.* **58**, 952-954.

Taylor L. A., McCallister R. H. and Sardi O. (1973) Cooling histories of lunar rocks based on opaque mineral geothermometers. *Proc. 4th Lunar Sci. Conf.* pp. 819-828.

Taylor L. A., Uhlmann D. R., Hopper R. W. and Misra K. C. (1975) Absolute cooling rates of lunar rocks: Theory and application. *Proc. 6th Lunar Sci. Conf. 6th.* pp. 181-191.

Taylor L. A., Onorato P. I. K., Uhlman D. R. and Coish R. A. (1978) Subophitic basalts from Mare Crisium: Cooling rates. In *Mare Crisium: The view from Luna 24* (eds. R. B. Merrill and J. J. Papike). Pergamon, New York. *Geochim. Cosmochim. Acta* Supplement 9. pp. 473-482.

Taylor L. A., Shervais J. W., Hunter R. H., Shih C.-Y., Nyquist L. E., Bansal B. M., Wooden J. and Laul J. C. (1983) Pre-4.2 AE mare-basalt volcanism in the lunar highlands. *Earth Planet. Sci. Lett.* **66**, 33-47.

Taylor S. R. (1982) *Planetary Science: A Lunar Perspective.* Lunar and Planetary Science Institute, Houston. pp. 481.

Taylor S. R., Kaye M., Muir P., Nance W., Rudowski R. and Ware N. (1972) Composition of the lunar uplands: Chemistry of Apollo 14 samples from Fra Mauro. *Proc. 3rd Lunar Sci. Conf.* pp. 1231-1249.

Taylor S. R. and Jakes P. (1974) The geochemical evolution of the moon. *Proc. 5th Lunar Sci. Conf.* pp. 1287-1305.

Taylor S. R. Norman M. D. and Esat T. M. (1993) The Mg-suite and the highland crust: An unsolved enigma. *Lunar Planet. Sci. XXIV.* pp. 1413-1414.

Taylor S. R., Pieters C. M., and MacPherson G. J. (2006) Earth-Moon System, Planetary Science, and Lessons Learned. *Reviews in Mineralogy and Geochemistry* **60**, 657-704.

Tera F. and Wasserburg G.J. (1974) U-Th-Pb systematics on lunar rock: and inferences about lunar evolution and the age of the Moon. *Proc. 5th Lunar Sci. Conf.* pp. 1571-1599.

Tera F., Eugster O., Burnett D. S. and Wasserburg G. J. (1970) Comparative study of Li, Na, K, Rb, Cs, Ca, Sr, and Ba abundances in achondrites and in Apollo 11 lunar samples. *Proc. 1st Lunar Sci. Conf.* pp. 1637-1657.

Tera F., Papanastassiou D. A. and Wasserburg G. J. (1974) Isotopic evidence for a terminal lunar cataclysm. *Earth Planet. Sci. Lett.* **22**, 1-21.

Terada K, Anand M, Sokol A. K., Bischoff A. and Sano Y. (2007) Cryptomare Magmatism 4.35 Gyr ago recorded in lunar meterorite Kalahari 009. *Nature* **450**, 849-853.

Thacker C., Liang Y., Peng Q. and Hess P. (2009) The stability and major element partitioning of ilmenite and armalcolite during lunar cumulate manlte overturn. *Geochim. Cosmochim. Acta.* **73**, 820-836.

Thompson C. and Stevenson D. J. (1988) Gravitatinoal instability of two-phase disks and the origin of the Moon. *Astrophys. J.* **333**, 452-481.

Toksöz M. N., Dainty A. M., Soloman S. C. and Anderson K. R. (1973) Velocity structure and evolution of the Moon. *Proc. 4th Lunar Sci. Conf.* pp. 25-29.

Touboul M., Kleine T., Bourdon B. and Plame H. (2007) The duration of magma ocean crystallisation on the Moon: Evidence from new W isotope data for metals from high and low-Ti mare basalts. *Lunar Planet. Sci. Conf. XXXVIII.* **2385.**

Turekian K. K. and Kharkar D. P. (1970) Neutron activation analysis of milligram quantities of Apollo 11 lunar rocks and soil. *Proc. 1st Lunar Sci. Conf.* pp. 1659-1664.

Turkevich A. (1971) Comparison of the analytical results from the Surveyor, Apollo and Luna missions. *Proc. 2nd Lunar. Sci. Conf.* pp. 1209-1215.

Turner G. (1970) $^{40}Ar/^{39}Ar$ dating of lunar rock samples. *Proc. 1st Lunar Sci. Conf.* pp. 1665-1684.

Turner G. (1971) ^{40}Ar-^{39}Ar ages from the lunar maria. *Earth Planet. Sci. Lett.* **11**, 169-191.

Turner G. and Cadogan P. H. (1974) Possible effects of ^{39}Ar recoil in ^{40}Ar-^{39}Ar dating. *Proc. 5th Lunar Sci. Conf.* pp. 1601-1615.

Turner G., Cadogan P. H. and Yonge C. J. (1973) Apollo 17 age determinations. *Nature* **242**, 513-515.

Unruh D. M., Stille P., Patchett P. J., and Tatsumoto M. (1984) Lu-Hf and Sm-Nd evolution in lunar mare basalts. *Proc. 14th Lunar Planet. Sci. Conf., J. Geophys. Res.* **89**, B459-B477.

Urey H. C. (1966) The capture hypothesis of the origin of the Moon. In *The Earth-Moon system.* (eds. B. G. Marsden and A. G. W. Cameron). Plenum, New York. pp. 210-212.

Urey H. C., Marti K., Hawkins J. W. and Liu M. K. (1971) Model history of the lunar surface. *Proc. 2nd Lunar Sci. Conf.* pp. 987-998.

Valley J. W, Kitchen N., Kohn M. J., Niendorf C. R. and Spicuzza M. J. (1995) UWG-2, a garnet standard for oxygen isotope ratios: Strategies for high precision and accuracy with laser heating. *Geochim. Cosmochim. Acta* **59**, 5223-5231.

Van Achterbergh E., Ryan C. G., Jackson S. E. and Griffin W. L. (2001) Data reduction software for LA-ICP-MS. In: *Laser-ablation-ICPMS in the Earth Sciences: Principles and Applications* (ed. P. Sylvester). Mineralogical Association of Canada. pp. 239-243.

Vaniman D. T. and Papike J. J. (1977a) The Apollo 17 drill core: Characterisation, of the mineral and lithic component (sections 70007, 70008, 70009). *Proc. 8th Lunar Sci. Conf.* pp. 3123-3159.

Vaniman D. T. and Papike J. J. (1977b) The Apollo 17 drill core: Modal petrology and glass chemistry (sections 70007, 70008, 70009). *Proc. 8th Lunar Sci. Conf.* pp. 3161-3193.

Vaniman D. T. and Papike J. J. (1977c) Very low-Ti (VLT) basalts: A new mare rock type from the Apollo 17 drill core. *Proc. 8th Lunar Sci. Conf.* pp. 1443-1471.

Vaniman D. T. and Papike J. J. (1980) Lunar highland melt rocks: Chemistry, petrology and silicate mineralogy. In *Proc. Conf. Lunar Highlands Crust* (eds. J. J. Papike and R. B. Merrill). Lunar Planetary Institute, Houston. Pergamon, New York. pp. 271-337.

Vaniman D. T., Reedy R., Heiken G., Olhoeft G. and Mendell W. (1991) The Lunar Environment. In *The Lunar Sourcebook: A Users Guide to the Moon* (eds. G. H. Heiken, D. T. Vaniman and B. M. French). Cambridge University Press, Cambridge. pp. 27-60.

Van Orman J. A. and Grove T. L. (2000) Origin of lunar high-titanium ultramafic glasses: constraints from phase relations and dissolution kinetics of clinopyroxene-ilmenite cumulates. *Meteorit. Planet. Sci. Lett.* **35**, 783-794.

Vetter S. K., Shervais J. W. and Lindstrom M. M. (1989) Petrology and geochemistry of olivine-normative and quartz-normative basalts from regolith breccia 15498: New diversity in Apollo 15 mare basalts. *Proc. 18th Lunar Planet. Sci. Conf.* pp. 255-271.

Vinogradov A. P. (1971) Preliminary data on lunar ground brought to Earth by Automatic Probe "Luna 16". *Proc. 2nd Lunar Sci. Conf.* pp. 1-16.

Wagner T.P. and Grove T.L. (1997) Experimental constraints on the origin of lunar high-Ti ultramafic glasses. *Geochim. Cosmochim. Acta* **61**, 1315-1327.

Wakita H., Schmitt R. A. and Rey P. (1970) Elemental abundances of major, minor, and trace elements in Apollo 11 lunar rocks, soil, and core samples. *Proc. 1st Lunar Sci. Conf.* pp. 1685-1717.

Walker D., Longhi J. and Hays J. F. (1972) Experimental petrology and origin of Fra Mauro rocks and soil. *Proc. 3rd Lunar Sci. Conf.* pp. 797-817.

Walker D., Longhi J., Stolper E. M., Grove T. L. and Hays J. F. (1975) Origin of titaniferous lunar basalts. *Geochim. Cosmochim. Acta* **39**, 1219-1235.

Walker D., Kirkpatrick R. J., Longhi J. and Hays J. F. (1976a) Crystallization history of lunar picritic basalt sample 12002: Phase-equilibria and cooling-rate studies. *Geologic. Soc. Am. Bull.* **87**, 646-656.

Walker D., Longhi J. and Hays J. F. (1976b) Heterogeneity in titaniferous lunar basalts. *Earth Planet. Sci. Lett.* **30**, 27-36.

Walker D., Longhi J., Lasaga A. C., Stolper E. M., Grove T. L. and Hays J. F. (1977) Slowly cooled microgabbros 15555 and 15056. *Proc. 8th Lunar Sci. Conf.* pp. 1521-1547.

Wänke H., Rieder R., Baddenhausen H., Spettler B., Teschke F., Quijano-Rico M. and Balacescu A. (1970) Major and trace elements in lunar material. *Proc. 1st Lunar Sci. Conf.* pp. 1719-1727.

Wänke H., Wlotzka F. M. and Rieder R. (1971) Apollo 12 samples: Chemical composition and its relation to sample locations and exposure ages, the two component origin of the various soil samples and studies on lunar metallic particles. *Proc. 2nd Lunar Sci. Conf.* pp. 1187-1208.

Wänke H., Baddenhausen H., Balacescu A., Teschke F., Spettel B., Dreibus G., Palme H., Quijano-Rico M., Kruse H., Wlotzka F. and Begemann F. (1972) Multi-element analysis of lunar samples and some implications of the results. *Proc. 3rd Lunar Sci. Conf.* pp. 1251-1268.

Wänke H., Palme H., Baddenhausen H., Dreibus G., Jagoutz E., Kruse H., Spettel B., Teshke F. and Thacker R. (1974) Chemistry of Apollo 16 and 17 samples: Bulk composition, late stage accumulation and early differentiation of the Moon. *Proc. 5th Lunar Sci. Conf.* pp. 1307-1335.

Wänke H., Palme H., Baddenhausen H., Dreibus G., Jagoutz E., Kruse H., Palme C., Spettel B., Teschke F. and Thacker R. (1975) New data on the chemistry of lunar samples: Primary matter in the lunar highlands and the bulk composition of the moon. *Proc. 6th Lunar Sci. Conf.* pp. 1313-1340.

Wanless R. K., Loveridge W. D., and Stevens R. D. (1970) Age determinations and isotopic abundance measurements on lunar samples (Apollo 11). *Proc. Lunar Sci. Conf. 1st* pp. 1729-1739.

Ware N. G. and Lovering J. F. (1970) Electron microscope analysis of phases in lunar samples. *Science* **167**, 517-520.

Warner J. L. (1971) Lunar crystalline rocks: Petrology and geology. *Proc. 2nd Lunar Sci. Conf.* pp. 469-480.

Warner R. D., Keil K., Prinz M., Laul J. C., Murali A. V. and Schmitt R. A. (1975) Mineralogy, petrology, and chemistry of mare basalts from Apollo 17 rake samples. *Proc. 6th Lunar Sci. Conf.* pp. 193-220.

Warner R. D., Taylor G. J., Keil K., Planner H. N., Nehru C. E., Ma M-S. and Schmitt R. A. (1978) Green glass vitrophyre 78526: An impact melt of very low-Ti mare basalt composition. *Proc. 9th Lunar Planet. Sci. Conf.* pp. 547-563.

Warner R. D., Taylor G. J., Conrad G. H., Northrop H. R., Barker S., Keil K., Ma M.-S. and Schmitt R. (1979) Apollo 17 high-Ti mare basalts: New bulk compositional data, magma types, and petrogenesis. *Proc. 10th Lunar Planet. Sci. Conf.* pp. 225-247.

Warner R. D., Taylor G. J., Keil K., Ma M.-S. and Schmitt R. (1980) Aluminous mare basalts: New data from Apollo 14 coarse-fines. *Proc. 11th Lunar Planet. Sci. Conf.* pp. 87-104.

Warren P. H. (1985) The magma ocean concept and lunar evolution. *Ann. Rev. Earth Planet. Sci.* **13**, 201-240.

Warren P. H. (1993) A concise compilation of petrologic information on possibly pristine non-mare Moon rocks. *Am. Mineral.* **78**, 360-376.

Warren P.H. (2001) Early lunar crustal genesis: The ferroan anorthosite epsilon-neodymium paradox as a possible result of crustal overturn. *Meteorit. Planet. Sci.* **36**, (supplement) A219.

Warren P. H. and Jerde E. A. (1990) Olivine-porphyritic vitrophyre 12024,15: A sample of the margin of a lunar lava flow. *Lunar Planet. Sci. Conf. XXI* pp. 1293-1294.

Warren P. H. and Wasson J. T. (1977) Pristine non-mare rocks and the nature of the lunar crust. *Proc. 8th Lunar Sci. Conf.* pp. 2215-2235.

Warren P. H. and Wasson J. T. (1979a) The origin of KREEP. *Rev. Geophys. Space Phys.* **17**, 73-88.

Warren P. H. and Wasson J. T. (1979b) The compositional-petrographic search for pristine non-mare rocks: Third foray. *Proc. 10th Lunar Planet. Sci. Conf.* 583-610.

Warren P. H. and Wasson J. T. (1980) Further foraging of pristine non-mare rocks: Correlations between geochemistry and longitude. *Proc. 11th Lunar Planet. Sci. Conf.* 431-470.

Warren P. H., Taylor G. J., Keil K., Kallemeyn G. W., Shirley D. and Wasson J. T. (1983) Seventh foray: Whitlockite-rich lithologies, a diopside-bearing troctolitic anorthosite, ferroan anorthosite and KREEP. *Proc. 14th Lunar Planet. Sci. Conf., J. Geophys. Res.* **88**, B151-B164.

Warren P. H., Shirley D. N. and Kallemeyn G. W. (1986) A potpourri of pristine moon rocks, including a VHK mare basalt and a unique, augite-rich Apollo 17 anorthosite. *Proc. 16th Lunar Planet. Sci. Conf., J. Geophys. Res.* **89**, D319-D330.

Warren P. H., Jerde E. A. and Kallemeyn G. W. (1987) Pristine moon rocks: A large felsite and a metal rich ferroan anorthosite. *Proc. 17th Lunar Planet. Sci. Conf., J. Geophys. Res.* **92**, E303–E313.

Warren P. H., Jerde E. A. and Kallemeyn G. W. (1990) Pristine moon rocks: An alkali anorthosite with coarse augite exsolution from plagioclase, a magnesian harzburgite, and other oddities. *Proc. 20th Lunar Planet. Sci. Conf.* pp. 31–59.

Wasserburg G. J. and Papanastassiou D. A. (1971) Age of an Apollo 15 mare basalt: lunar crust and mantle evolution. *Earth Planet. Sci. Lett.* **13**, 97-104.

Wasson J. T. (1971) Volatile elements on the Earth and Moon. *Earth Planet. Sci. Lett.* **11**, 219-225.

Wasson J. T. and Baedecker P. A. (1970) Ga, Ge, In, Ir, and Au in lunar terrestrial and meteoritic basalts. *Proc. 1st Lunar Sci. Conf.* pp. 1741-1750.

Wechsler B. A., Prewitt C. T. and Papkie J. J. (1976) Chemistry and structure of lunar synthetic armacolite. *Earth Planet. Sci. Lett.* **9**, 91-103.

Weigand P. W. (1973) Petrology of a coarse-grained Apollo 17 ilmenite basalt. *EOS Trans. AGU* **54**, 621-622.

Weill D. F. and McKay G. (1975) The partitioning of Mg, Fe. Sr, Ce, Sm, Eu, and Yb in lunar igneous systems and a possible origin of KREEP by equilibrium partial melting. *Proc. 6th Lunar Sci. Conf.* pp. 1143-1158.

Weitz C. M., Rutherford M. J. and Head J. W. (1997) Oxidation states during ascent and eruption of the volcanic glasses as inferred from metal-melt equilibria in the 74001/2 core. *Geochim. Cosmochim. Acta* **61**, 2765-2775.

Weitz C. M., Head J. W. and Pieters C. M. (1998) Lunar regional dark mantle deposits: Geologic, multispectral and modelling studies. *J. Geophys. Res.* **103**, 22725-22760.

Wellman T. R. (1970) Gaseous species in equillibrium with Apollo 11 holocrystalline rocks during their crystallisation. *Nature* **225**, 716-717.

Wentworth S. J. (1994) Apollo 12 ropy glasses revisited. *Meteoritics* **29**, 323-333.

Wiechert U., Halliday A. N., Lee D-C., Snyder G. A., Taylor L. A. and Rumble D. (2001) Oxygen isotopes and the Moon-forming giant impact. *Science* **294**, 345-348.

Wiechert U., Halliday A. N., Palme H. and Rumble D. (2004) Oxygen isotope evidence for rapid mixing of the HED meteorite parent body. *Earth Planet. Sci. Lett.* **221**, 373-382.

Wieczorek M.A. and Phillips R.J. (1999) Lunar multiring basins and the cratering process. *Icarus* **139**, 246-259.

Wieczorek M.A. and Phillips R.J. (2000) The Procellarum KREEP Terrane: Implications for mare volcanism and lunar evolution. *J. Geophys. Res. - Planets* **105**, 20417-20430.

Wieczorek M. A. and Zuber M. T. (2001) The composition and origin of the lunar crust: Constraints from central peaks and crustal thickness modelling. *Geophys. Res. Lett.* **28**, 4023-4026.

Wieczorek M. A., Jolliff B. L., Khan A, Pritchard M. E., Weiss B. P., Williams J. G., Hood L. L., Righter K, Neal C. R. and Shearer C. K. (2006) The constitution and structure of the lunar interior. *Reviews in Mineralogy and Geochemistry* **60**, 221-364.

Wiesmann H. and Hubbard N. J. (1975) A compilation of the lunar sample data generated by the Gast, Nyquist and Hubbard Lunar Sample PI-Ships. *Unpublished, Johnson Space Centre.*

Wilhelms D. E. (1987) *Geologic History of the Moon.* US Geol. Survey Prof. Paper **1348**.

Williams K. L. and Taylor L. A. (1974) Optical properties and chemical compositions of Apollo 17 armacolites. *Geology* **2**, 5-8.

Williams J. G., Boggs D. H., Yoder C. F., Ratcliff J. T. and Dickey J. O. (2001) Lunar rotational dissipation in solid body and molten core. *J. Geophys. Res.* **106**, 27933-27968.

Willis J. P., Erlank A. J., Gurney J. J., Theil R. H., and Ahrens L. H. (1972) Major, minor, and trace element data for some Apollo 11, 12, 14, and 15 samples. *Proc.3rd Lunar Sci. Conf.* pp. 1269-1273.

Wolf R., Woodrow A. and Anders E. (1979) Lunar basalts and pristine highland rocks: Comparison of siderophile and volatile elements. *Proc. 10th Lunar Planet. Sci. Conf.* pp. 2107-2130.

Wood J. A., Dickey J. S., Marvin U. B. and Powell B. N. (1970a) Lunar anorthosites. *Science* **167**, 602-604.

Wood J. A., Dickey J. S., Marvin U. B. and Powell B. N. (1970b) Lunar anorthosites and a geophysical model of the Moon. *Proc. 1st Lunar Sci. Conf.* pp. 965-988.

York D., Macintyre R. M. and Gittins G. (1969) Excess radiogenic ^{40}Ar in cancrinite and sodalite. *Earth Planet. Sci. Lett.* **7**, 25-28.

York D., Kenyon W. J. and Doyle R. J. (1972) ^{40}Ar-^{39}Ar ages of Apollo 14 and 15 samples. *Proc. 3rd Lunar Sci. Conf.* pp. 1613-1622.

Zhong S., Parmentier E. M. and Zuber M. T. (2000) A dynamic origin for the global asymmetry of lunar mare basalts. *Earth Planet. Sci. Lett.* **177**, 131-140.

Zuber M. T., Smith D. E., Lemoine F. G., Neumann G. A. (1994) The shape and internal structure of the Moon from the Clementine mission. *Science* **266**, 1839-1843.